Constraining the chemical and mineralogical composition of Earth's lower mantle through high-pressure crystallography and mineral elasticity

DISSERTATION

zur Erlangung des akademischen Grades eines Doktors der Naturwissenschaften (Dr. rer. nat.)
in der Bayreuther Graduiertenschule für Mathematik und Naturwissenschaften (BayNAT)
der Universität Bayreuth

vorgelegt von

Giacomo Criniti
aus *Venedig (Italien)*

Bayreuth, 2023

Die vorliegende Arbeit wurde in der Zeit von Oktober 2019 bis März 2023 in Bayreuth am Bayerischen Geoinstitut unter Betreuung von Herrn Professor Dr. Daniel J. Frost angefertigt.

Vollständiger Abdruck der von der Bayreuther Graduiertenschule für Mathematik und Naturwissenschaften (BayNAT) der Universität Bayreuth genehmigten Dissertation zur Erlangung des akademischen Grades eines Doktors der Naturwissenschaften (Dr. rer. nat.).

Dissertation eingereicht am: 29.03.2023

Zulassung durch das Leitungsgremium: 05.04.2023

Wissenschaftliches Kolloquium: 03.07.2023

Amtierender Direktor: Prof. Dr. Hans Keppler

Prüfungsausschuss:

Prof. Dr. Daniel J. Frost (Gutachter)
Prof. Dr. Leonid Dubrovinsky (Gutachter)
PD. Dr. Catherine McCammon (Vorsitz)
PD. Dr. Gerd Steinle-Neumann

(Weiterer Gutachter: Prof. Dr. Hauke Marquardt)

Abstract

The lower mantle, spanning from 660 to 2890 km depth, comprises more than half of the total volume of the Earth. Nevertheless, its chemical composition is still poorly constrained. Compositional models have been often derived from the comparison of seismic observation with laboratory experiments aimed at constraining the density and elastic properties of lower mantle minerals. Bridgmanite, (Mg,Fe,Al)(Si,Al)O_3 with a distorted perovskite structure, is the most abundant mineral in both chondritic and pyrolitic lower mantle assemblages. Current experimental estimates of the elastic properties of bridgmanite mainly come from Brillouin scattering measurements of polycrystalline samples compressed in the diamond anvil cell (DAC). These measurements typically allow to only constrain the shear wave velocity (v_S) of the sample at lower mantle pressures, as the compressional velocity (v_P) overlaps with the much more intense signal from the diamond anvils. To overcome this issue, I performed single-crystal X-ray diffraction and Brillouin scattering measurements in the DAC to determine the anisotropic elastic properties of $MgSiO_3$ bridgmanite from room pressure up to 79 GPa. By carefully selecting the appropriate mutual orientation of bridgmanite samples and diamond anvils, I obtained the first direct experimental constraints on the v_P of bridgmanite at mid-lower mantle pressures. Combining these new data with the thermoelastic properties of other minerals and bridgmanite components, a mineral physical model was built that predicts the mineral compositions and sound wave velocities of a simplified pyrolitic rock in the CaO-FeO-MgO-SiO_2 system, showing good agreement with one-dimensional seismic models of Earth's lower mantle.

Al is incorporated in the crystal structure of bridgmanite through the $Fe^{3+}AlO_3$ and $AlAlO_3$ charge coupled (CC) mechanisms and the $MgAlO_{2.5}$ oxygen vacancy (OV) mechanism. Oxygen vacancies can affect significantly the transport properties of bridgmanite (e.g., viscosity) and have been argued to substantially increase its compressibility as well. However, to date, there is no conclusive experimental evidence supporting this hypothesis. Therefore, I synthesised Al-bearing bridgmanite single-crystals having different CC, OV, and bulk Al contents in a multi-anvil press. Three crystals were subsequently loaded in resistively heated DACs to determine their isothermal and thermal equations of state by synchrotron X-ray diffraction. Combining high-pressure structural refinement and bulk compressibility data, I found that the main factor controlling the bulk modulus systematics is the Si-Al substitution in the octahedral site. On the other hand, the effect of oxygen vacancies on the bulk modulus and its derivatives does not seem to be significant.

Although the lower mantle is often regarded as being chemically homogeneous, three-dimensional seismic models have highlighted the presence of seismic heterogeneities at various scales. Among these, the scattering of seismic waves from bodies of a few-km size in the top- to mid-lower mantle has been primarily attributed to remnants of metabasaltic rocks transported by subduction. Stishovite, rutile-structured SiO_2, constitutes up to 25 vol.% of subducted metabasalt and is known to undergo a second-order ferroelastic transformation to $CaCl_2$-type post-stishovite in the mid-mantle. This transformation

induces a softening of the v_S of stishovite and could explain the mentioned anomalies in mid-mantle scatterers. As Al and H stabilise post-stishovite at lower pressure, I conducted high-pressure X-ray diffraction and Raman spectroscopy measurements on single crystals of $Al_{0.05}Si_{0.95}O_{1.98}H_{0.02}$ (Al5) stishovite and $Al_{0.11}Si_{0.89}O_{1.98}H_{0.07}$ (Al11) post-stishovite in the DAC up to 50 GPa. From X-ray diffraction, I found that the Al5 sample transformed to post-stishovite at about 16 GPa, while the Al11 sample displayed the post-stishovite structure from room pressure to 50 GPa. Combining structural refinements and Raman data on the characteristic mode associated with the post-stishovite transition, I found that neither sample displays second-order ferroelastic behaviour and that the evolution of the unit-cell lattice parameters is somehow decoupled from that of the characteristic Raman mode and octahedral tilting. The presence of hydrous Al-bearing silica with the Al5 composition in a hydrous basaltic assemblage may therefore explain the negative velocity anomalies in seismic scatterers located at 700-900 km depth.

Out of the hydrous phases that have been synthesised at mantle transition zone and topmost lower mantle pressures, Al-phase D, nominally $(Al,Fe^{3+})_2SiO_6H_2$, is one of the most stable at high temperatures, possibly due to the presence of strong H-bonds. I have investigated the crystal structure and compressibility of Fe-bearing Al-phase D with a composition of $Al_{1.53(2)}Fe_{0.22(1)}Si_{0.86(1)}O_6H_{3.33(9)}$ by means of single-crystal X-ray diffraction. The incorporation of Fe^{3+} was found to induce partial ordering of the cations over the octahedral sites of Al-phase D, resulting in a change of the space group symmetry from $P6_3/mcm$ to $P6_322$. X-ray diffraction measurements in the DAC revealed that the unit-cell volume decreases smoothly from room pressure to 30 GPa, suggesting that the symmetrisation of H-bonds has no effect on the compressibility of Al-phase D. Furthermore, a change in the electronic configuration of Fe^{3+} from high- to low-spin is likely to explain the enhanced compressibility of Al-phase D observed above 30 GPa and up to at least 65 GPa.

Zusammenfassung

Der untere Erdmantel, der sich in einer Erdtiefe von 660 bis 2890 km erstreckt, macht mehr als die Hälfte des Gesamtvolumens der Erde aus. Dennoch ist seine chemische Zusammensetzung noch immer nicht ausreichend geklärt. Aktuelle Schätzungen wurden hauptsächlich aus dem Vergleich seismischer Beobachtungen mit Laborexperimenten abgeleitet, die darauf abzielen, die Dichte und die elastischen Eigenschaften der Minerale des unteren Erdmantels zu bestimmen. Bridgmanit, (Mg,Fe,Al)(Si,Al)O_3 mit einer verzerrten Perowskitstruktur ist das am häufigsten vorkommende Mineral sowohl in chondritischen als auch in pyrolitischen Mineralparagenesen des unteren Erdmantels. Aktuelle experimentelle Abschätzungen der elastischen Eigenschaften von Bridgmanit stammen hauptsächlich aus Brillouin-Streuungsmessungen an polykristallinen Proben, die in der Diamantstempel-Zelle (DSZ) komprimiert wurden. Diese Messungen erlauben in der Regel nur eine Bestimmung der Scherwellengeschwindigkeit (v_S) der Probe bei niedrigeren Manteldrücken, da sich die Kompressionswellengeschwindigkeit (v_P) mit dem viel intensiveren

Signal der Diamantstempel überschneidet. Um dieses Problem zu überwinden, führte ich in der DSZ Einkristall-Röntgenbeugungs- und Brillouin-Streuungsmessungen durch, um die anisotropen elastischen Eigenschaften von $MgSiO_3$-Bridgmanit von Raumdruck bis zu 79 GPa zu bestimmen. Durch die sorgfältige Auswahl der geeigneten gegenseitigen Ausrichtung von Bridgmanit-Proben und Diamantstempeln zueinander erhielt ich die ersten direkten experimentellen Bestimmungen für die v_P von Bridgmanit bei Drücken des mittleren bis tiefen Erdmantels. Durch die Kombination dieser neuen Daten mit den thermoelastischen Eigenschaften anderer Minerale und Bridgmanit-Komponenten wurde ein mineralphysikalisches Modell erstellt, das die Mineralzusammensetzungen und Schallwellengeschwindigkeiten eines vereinfachten pyrolitischen Gesteins im CaO-FeO-MgO-SiO_2-System vorhersagt und eine gute Übereinstimmung mit eindimensionalen seismischen Modellen des unteren Erdmantels zeigt.

Al wird in die Kristallstruktur von Bridgmanit durch den Ladungs-gekoppelten $Fe^{3+}AlO_3$ und $AlAlO_3$-Mechanismus (CC) und den $MgAlO_{2.5}$-Sauerstoffleerstellenmechanismus (OV) eingebaut. Sauerstoffleerstellen können die Transporteigenschaften von Bridgmanit (z. B. die Viskosität) erheblich beeinflussen, und es wird behauptet, dass sie auch seine Kompressibilität wesentlich erhöhen. Bislang gibt es jedoch keine schlüssigen experimentellen Beweise für diese Hypothese. Daher habe ich Al-haltige Bridgmanit-Einkristalle mit unterschiedlichem CC-, OV- und Al-Gehalt in einer Multi-Anvil-Presse synthetisiert. Drei Kristalle wurden anschließend in widerstandsbeheizte DSZ geladen, um ihre isothermen und thermischen Zustandsgleichungen mittels Synchrotron-Röntgenbeugung zu bestimmen. Durch die Kombination von Hochdruck-Strukturverfeinerung und Daten zur Volumenkompressibilität konnte ich feststellen, dass der Hauptfaktor, der die Systematik des Kompressionsmoduls steuert, die Si-Al-Substitution im oktaedrisch koordinierten Gitterplatz ist. Andererseits scheinen die Auswirkungen von Sauerstoffleerstellen auf den Kompressionsmodul und seine Ableitungen nicht signifikant zu sein.

Obwohl der untere Erdmantel häufig als chemisch homogen angesehen wird, haben dreidimensionale seismische Modelle das Vorhandensein seismischer Heterogenitäten auf verschiedenen Ebenen aufgezeigt. Die Streuung seismischer Wellen von Körpern mit einer Größe von einigen Kilometern im oberen bis mittleren unteren Erdmantel wird in erster Linie auf Reste von metabasaltischen Gesteinen zurückgeführt, die durch Subduktion transportiert wurden. Stishovit, SiO_2 mit Rutilstruktur, macht bis zu 25 Vol.-% des subduzierten Metabasalts aus und unterliegt bekanntermaßen im mittleren Erdmantel einer ferroelastischen Umwandlung zweiter Ordnung in Poststishovit vom $CaCl_2$-Strukturyp. Diese Umwandlung führt zu einer Verringerung der v_S von Stishovit und könnte die erwähnten Anomalien in den Reflektoren des mittleren Mantels erklären. Da Al und H Poststishovit bei niedrigerem Druck stabilisieren, führte ich Hochdruck-Röntgenbeugungs- und Raman-Spektroskopie-Messungen an Einkristallen von $Al_{0.05}Si_{0.95}O_{1.98}H_{0.02}$ (Al5) Stishovit und $Al_{0.11}Si_{0.89}O_{1.98}H_{0.07}$ (Al11) Poststishovit in der DSZ bis zu 50 GPa durch. Aus

der Röntgenbeugung ging hervor, dass sich die Al5-Probe bei etwa 16 GPa in Poststishovit umwandelte, während die Al11-Probe die Poststishovit-Struktur von Raumdruck bis 50 GPa aufwies. Durch die Kombination von Strukturverfeinerungen und Raman-Daten über die charakteristischen Moden, die mit dem Poststishovit-Übergang verbunden sind, fand ich heraus, dass keine der beiden Proben ein ferroelastisches Verhalten zweiter Ordnung zeigt und dass die Entwicklung der Gitterparameter der Einheitszelle in gewisser Weise von den charakteristischen Raman-Moden und der oktaedrischen Kippung entkoppelt ist. Das Vorhandensein von H- und Al-haltigem Siliziumdioxid mit der Al5-Zusammensetzung in einer wasserhaltigen basaltischen Mineralparagenese könnte daher die negativen Geschwindigkeitsanomalien in seismischen Heterogenitäten in 700-900 km Tiefe erklären.

Von den wasserhaltigen Phasen, die sich in der Mantelübergangszone und bei den höchsten Drücken im unteren Mantel als stabil erwiesen haben, ist die Al-Phase D, nominell $(Al,Fe^{3+})_2SiO_6H_2$, eine der stabilsten bei hohen Temperaturen, was möglicherweise auf das Vorhandensein von starken H-Bindungen zurückzuführen ist. Ich habe die Kristallstruktur und das Hochdruckverhalten der Fe-haltigen Al-Phase D mit einer Zusammensetzung von $Al_{1.53(2)}Fe_{0.22(1)}Si_{0.86(1)}O_6H_{3.33(9)}$ mit Hilfe der Einkristall-Röntgenbeugung untersucht. Es wurde festgestellt, dass der Einbau von Fe^{3+} zu einer teilweisen Ordnung der Kationen auf den oktaedrischen Stellen der Al-Phase D führt, was eine Änderung der Raumgruppensymmetrie von $P6_3/mcm$ zu $P6_322$ zur Folge hat. Röntgenbeugungsmessungen in der DSZ ergaben, dass das Volumen der Einheitszelle von Raumdruck bis 30 GPa gleichmäßig abnimmt, was darauf hindeutet, dass die Symmetrisierung der H-Bindungen keine Auswirkung auf die Kompressibilität der Al-Phase D hat. Darüber hinaus ist eine Änderung der elektronischen Konfiguration von Fe^{3+} von High-Spin zu Low-Spin wahrscheinlich die Erklärung für die verstärkte Kompressibilität der Al-Phase D, die oberhalb von 30 GPa und bis zu mindestens 65 GPa beobachtet wurde.

Acknowledgments

First and foremost, I would like to thank my supervisors, Tiziana Boffa Ballaran and Dan Frost, for guiding me and supporting me throughout my PhD, exchanging sceintific ideas, putting up with my stubbornness, and always granting me the freedom to work independently, collaborate extensively with other scientists and satisfy my scientific curiosity. I also thank Alex Kurnosov for his invaluable support in the preparation of diamond anvil cells and resistive heaters, and in conducting the Brillouin scattering measurements. I am grateful to Takayuki Ishii, Niccolò Satta, Nicki Siersch, Serena Dominijanni, Luca Faccincani, Narangoo Purevjav, Johannes Buchen, Hauke Marquardt, and Biao Wang for collaborating with me and getting me involved in their projects, from which I learned a lot. I acknowledge Konstantin Glazyrin for his extensive support and assistance during all synchrotron beamtimes at the P02.2 beamline of PETRA-III in Hamburg. I am grateful to Leonid Dubrovinsky for assistance with some of the single-crystal XRD measurements at BGI, as well as for fruitful discussions on DAC and resistive heating techniques. I also acknowledge Hans Keppler and Cathrine McCammon for allowing me to use the FTIR and Mössbauer laboratories at BGI, Detlef Krausse and Anke Potzel for their support with the EPMA measurements, Nobuyoshi Miyajima and Dorothea Wiesner for their help with the FIB milling, and Raphael Njul for preparing the samples for DAC experiments. I am also grateful to Florian Heidelbach for translating the abstract of my thesis to German. For the fun time outside the institute, I would like to thank my friends Adriano, Andrea, Arne, Egor, Elena, Enrico, Giulia, Greta, Iuliia, Laura, Luca, Matej, Niccolò, Sara, Serena, Sumith and Tim.

Contents

Chapter 1

Introduction

In this thesis, I have studied the relations between the crystal structure, cation substitutions, and physical properties of bridgmanite, stishovite, and hydrous Al-phase D to constrain the density and elastic properties of lower mantle assemblages as a function of depth. Seismic methods allow for a direct comparison of the elastic properties of mineral assemblages with those of the deep and inaccessible regions of Earth's mantle. Therefore, the interpretation of seismic reference models and local velocity anomalies offers unique opportunities to infer the average bulk composition of the mantle and trace the abundance and path of chemical heterogeneities, such as subducted oceanic plates sinking deep into the lower mantle. In this chapter, I will first describe the structure of Earth's mantle based on the interpretation of seismic data, followed by a comparison of current mineralogical and petrological models of the lower mantle, with a particular focus on the high-pressure phases of interest for this thesis.

1.1 The internal structure of the Earth from seismic observations

Whenever an earthquake occurs, seismic waves are produced, propagate inside the Earth, and are eventually recorded by seismometers on the Earth's surface. Depending on the relation between propagation and oscillation directions, body waves are divided into compressional or primary (P) waves and shear or secondary (S) waves, whose propagation velocities (v_{P} and v_{S}) depend on the density (ρ) and elastic properties of the material they travel through (e.g., Poirier, 2000):

$$v_P = \sqrt{\frac{K + \frac{4}{3}G}{\rho}}, \quad v_S = \sqrt{\frac{G}{\rho}} \tag{1.1}$$

where K and G, called bulk and shear moduli, represent the response of an elastically isotropic material to compression and shearing, respectively. The path of a body wave travelling inside the Earth is perturbed whenever it encounters a region where physical properties, such as ρ, K, or G, change discontinuously (Stein and Wysession, 2003). Depending on the orientation, sharpness, and physical property contrast of the discontinuity, reflection, scattering, and S-to-P or P-to-S conversion of the incident wave can take place. By interpreting the arrival times and waveforms of seismic waves at several seismic

stations, the phases (i.e., paths) of seismic waves can be inferred and used to calculate depth-dependent (i.e., radial) average models of the Earth's interior or identify lateral anomalies linked to the presence of chemical and/or thermal heterogeneities in mantle rocks.

1.1.1 Seismic reference models

As a first approximation, the composition of the Earth's interior can be deciphered by comparing laboratory data on the elastic properties of rock-forming minerals with the depth-dependent radial average of density and seismic velocities of the Earth's interior. As minerals are compressed to extreme conditions of pressure and temperature, they transform to denser and generally stiffer structures than their lower-pressure polymorphs (Irifune and Ringwood, 1987a; Irifune and Ringwood, 1987b). Global discontinuities in Earth's density and velocity structure are therefore interpreted as evidence for pressure-induced isochemical phase transformations or changes in the bulk chemical composition of mantle rocks. Major seismic discontinuities define, for instance, the boundaries between the crust, the upper mantle and the low velocity zone within it, the mantle transition zone, the lower mantle, the liquid outer core, and the solid inner core. To constrain the depth, topography, and contrast in seismic velocities and density of the mentioned discontinuities, the reflection of seismic waves is typically used. For instance, the top of the lower mantle is marked by the post-spinel transformation of $(Mg,Fe)_2SiO_4$ ringwoodite into $(Mg,Fe)SiO_3$ bridgmanite and (Mg,Fe)O ferropericlase. The depth of this discontinuity has been deduced using precursors of P waves (PP) and S waves (SS). The paths of SS or PP phases and their precursors (SdS or PdP, with d being the depth of the discontinuity, Figure 1.1a) are similar, except that the precursors reflect at the discontinuity of interest rather than at the Earth's surface (Deuss, 2009). Fixed the depth and the contrast of physical properties for a given set of discontinuities, low-order polynomial functions are then employed to create density and seismic velocities models (Figure 1.1b) through the inversion of large datasets of body waves travel times, surface waves, and/or free oscillations. In addition to the elastic model, other features such as anelastic dispersion, attenuation, and anisotropy are taken into account to obtain a satisfactory fit to the input data (Dziewonski and Anderson, 1981). The currently most used reference models are the Preliminary Reference Earth Model (Dziewonski and Anderson, 1981), iasp91 (Kennett and Engdahl, 1991), and ak135 (Kennett et al., 1995). Although most of the mineral reactions responsible for the mentioned discontinuities are rather sharp (Frost et al., 2004; Ishii et al., 2019a), they still take place over a finite pressure range in which mineral properties change continuously. Therefore, an alternative approach to that described above is to integrate seismic velocity datasets with experimental estimates for the depth intervals in which mineral transformations take place. Rather than imposing discontinuous jumps in density and seismic velocities, steep gradients are introduced to make a seismic model more meaningful from a mineral physical perspective (Cammarano et al., 2005; Cammarano and Romanowicz, 2007). It should be noted that one-dimensional (1D) radial approximations are far from accurate in the crust

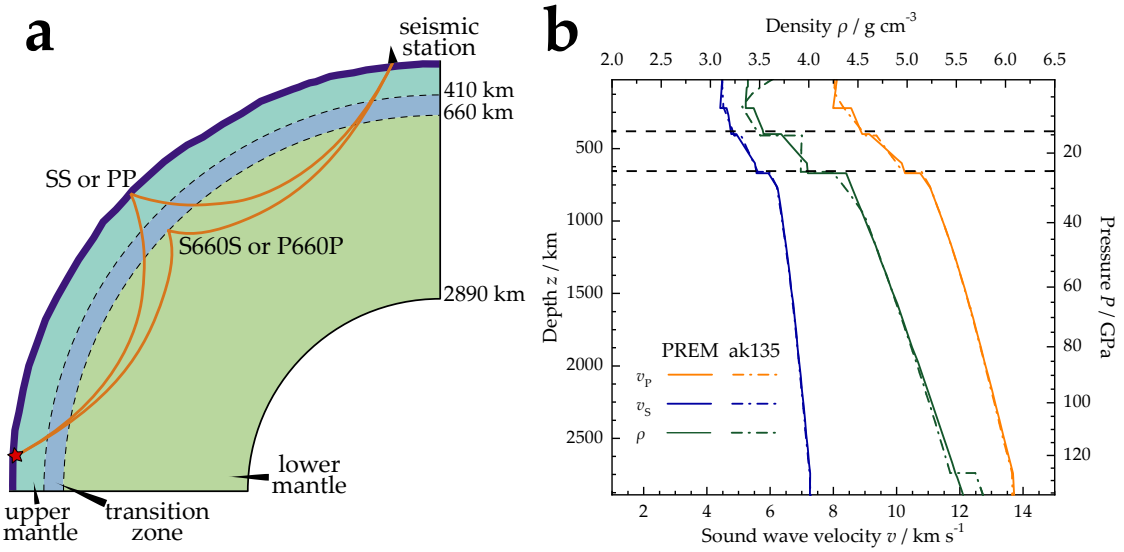

Figure 1.1. (a) Schematic representation of the propagation of SS or PP waves and their precursors reflected at the 660 km discontinuity (S660S and P660P) in a spherically symmetric Earth. (b) One-dimensional (1D) average models of density and seismic velocities in the Earth as a function of depth according to the reference models PREM and ak135 (Dziewonski and Anderson, 1981; Kennett et al., 1995).

and lithospheric mantle due to the heterogeneous nature and topography of these layers. However, they are still relevant for deeper regions of the Earth, such as the lower mantle, where lateral heterogeneities are less frequent and pronounced.

1.1.2 Seismic tomography and large-scale mantle heterogeneities

The increasing availability of seismic data over the last decades has allowed the creation of both local and global three-dimensional reconstructions of the Earth's interior, highlighting the presence of several large-scale lateral variations in density and seismic velocities within the mantle transition zone and lower mantle (Houser et al., 2008; Simmons et al., 2010; Ritsema et al., 2011; Fukao and Obayashi, 2013; Lu et al., 2019). Of particular interest to this thesis is the presence of positive velocity anomalies associated with cold subducted oceanic plates in the transition zone and shallow lower mantle (Figure 1.2). First mapped in the early 1990s (van der Hist et al., 1991; van der Hilst and Seno, 1993) and systematically classified by Fukao and Obayashi (2013), subducted oceanic plates are known to either stagnate at (i.e., flatten on) the 660 km discontinuity, penetrate the 660 km discontinuity, be trapped between 660 and 1000 km depth, or sink deeply into the lower mantle. The stagnation of slabs at the 660 km discontinuity can be explained by the slightly negative Clapeyron slope of the post-spinel transformation (Ishii et al., 2011; Kojitani et al., 2016; Chanyshev et al., 2022). In fact, slabs are generally colder than the ambient mantle (Kirby et al., 1996; Eberle et al., 2002; Syracuse et al., 2010), causing the post-spinel transformation and its related density increase to be delayed to greater depths. This mechanism likely

prevents some slabs from penetrating further in the lower mantle. Other factors, such as the dip angle of the slab and a viscosity contrast between transition zone and lower mantle assemblages have also been suggested (Torii and Yoshioka, 2007). On the other hand, no seismic discontinuities hinting the presence of a phase transformation are observed at about 1000 km depth in 1D velocity models (Dziewonski and Anderson, 1981; Kennett et al., 1995). Marquardt and Miyagi (2015) suggested that the increase in yield strength (and thus viscosity) of ferropericlase between 20 and 65 GPa could be responsible for this phenomenon. A second factor that would enhance the viscosity of the ambient mantle could be the pressure-dependent concentration of oxygen vacancies defects in bridgmanite (Liu et al., 2017a), which are believed to reduce the viscosity of bridgmanite. At the depths of the bottom lower mantle, a second class of heterogeneities characterised by negative velocity and positive density anomalies has been detected beneath the African and Pacific plates in the bottom 1000 km of the lower mantle (van der Hilst and Kárason, 1999). These structures, called large low shear velocity provinces (LLSVPs), have the shape of domes extending for hundreds and thousands of kilometres in vertical and lateral directions, respectively. To date, the origin, dynamic stability, and exact composition of these regions remain largely debated (McNamara, 2019). However, an interplay of temperature and enrichment in relatively heavy atoms (e.g., Fe, Ca) has been often invoked by experimental studies to reconcile geophysical observation with mineral physical data of lower mantle minerals (e.g., Wolf et al., 2015; Thomson et al., 2019).

1.1.3 Seismic scattering and small-scale mantle heterogeneities

In addition to the thermal and chemical variations giving rise to the large-scale heterogeneities discussed in Section 1.1.2, additional smaller-scale chemical anomalies have been detected by seismic methods in the topmost- to mid-lower mantle (e.g., Kaneshima, 2019). As mentioned above, seismic waves can be converted and scattered when they encounter an interface with a sufficiently large contrast in density and elastic properties. In order for the wave to interact with the heterogeneity, the wavelength of the former should be comparable with the thickness of the latter (Stein and Wysession, 2003). Therefore, short period ($\sim$ 1 s) waves proved to be the most effective in detecting small-scale heterogeneities in the lower mantle, (Kaneshima and Helffrich, 1999; Kaneshima and Helffrich, 2003; Rost et al., 2008; Niu, 2014). Seismic arrays (Rost and Thomas, 2009), initially assembled to detect underground nuclear explosions, are typically employed to map small-scale heterogeneities as they benefit from a high spatial resolution. Depending on the source-receiver geometry and type of scattering, the shape, orientation, and contrast in seismic properties of the scatterer can also be computed from the difference in travel time, slowness, and azimuth relative to the non-scattered wave (Kaneshima and Helffrich, 1999; Niu et al., 2003; Niu, 2014). Among several types of scattering (Kaneshima, 2016), P waves originating from incident S waves (S-to-P scattering, Figure 1.2) in the coda region of direct P arrivals have been the most utilised to identify and characterise small-scale lower mantle heterogeneities due to their high signal to noise ratio (Niu, 2014; Kaneshima, 2016; Kaneshima, 2019). Seismic

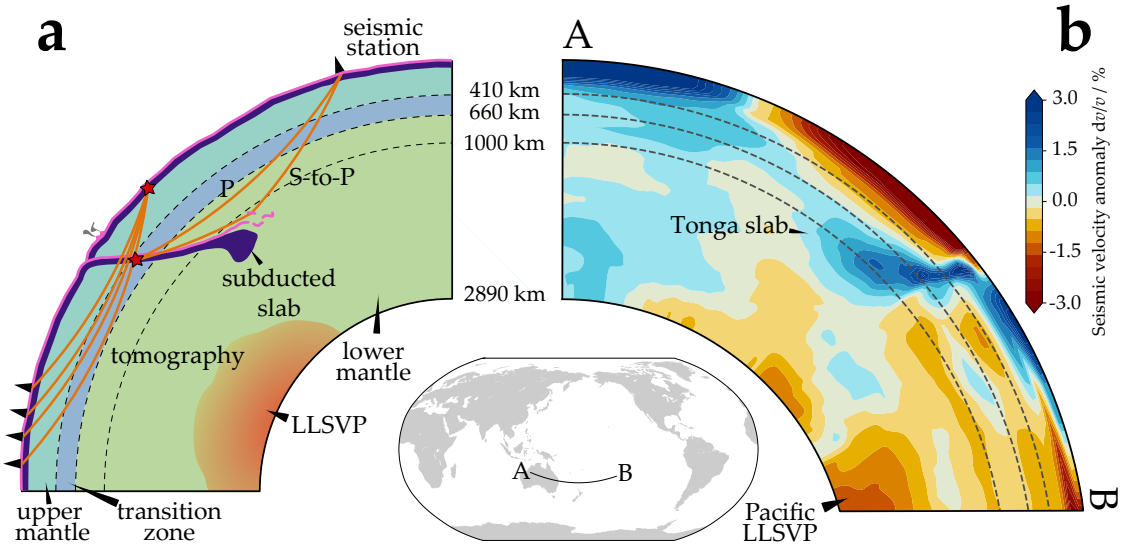

Figure 1.2. (a) Schematic representation of the principles of seismic tomography and seismic scattering to map large- and small-scale heterogeneities in the mantle transition zone and lower mantle. (b) An example of a tomographic section displaying the shear velocity anomalies (Lu et al., 2019) relative to a combined TNA/SNA 1D model (Grand and Helmberger, 1984) beneath the Tonga subduction zone. The presence of a subducted slab penetrating down to at least 1000 km depth is highlighted by the positive velocity anomaly (blue colour) dipping at an approximately constant angle from the surface straight into the lower mantle. The western edge of the Pacific LLSVP is also visible as a negative velocity anomaly just above the core-mantle boundary. The tomographic section was generated using the web-based tool SubMachine (Hosseini et al., 2018).

scatterers identified with this method have typical thicknesses of 5-12 km, positive density and negative shear velocity anomalies compared to the surrounding mantle (Kaneshima and Helffrich, 1999; Niu, 2014). The plate-like shape of the scatterers and the contrast in density and elastic properties with a pyrolitic lower mantle are compatible with those of subducted oceanic crust at depths of 1400-1800 km, where the second-order transformation of SiO_2 stishovite is expected to cause shear elastic softening (Carpenter et al., 2000). Scatterers with similar characteristics but located at much shallower depths of 660-1000 km have been detected in the proximity of subducted slabs, for instance beneath the Tonga and South American subduction zones (Kaneshima, 2019). As discussed more in detail in Section 1.3.2, the incorporation of small amounts of Al and H and the lower temperature in the slab can decrease the transition pressure of the post-stishovite transformation to some extent. However, the individual effect of each of the mentioned factors is still unclear and requires further investigation.

1.2 Mineralogy of the lower mantle

Insights on the composition of Earth's upper mantle can be obtained from the study of natural peridotitic samples (i.e., xenoliths) representing fragments of upper mantle rocks that are transported to the Earth's surface by ascending magmas. Combining information from mantle xenoliths and basaltic lavas erupted at mid ocean ridges, Ringwood (1962) proposed a hypothetical pyrolite rock to represent the composition of a primitive upper mantle. This kind of xenoliths, however, rarely originate from regions below 200 km depth (e.g., Pearson et al., 2003). Although some petrological and geochemical information about deeper regions of the Earth can still be obtained by studying mineral inclusions in diamonds (Pearson et al., 2014; Nestola et al., 2018; Tschauner et al., 2021; Gu et al., 2022; Lorenzon et al., 2022), open questions remain concerning the bulk chemical composition of the mantle transition zone and lower mantle. Therefore, it is the role of high-pressure experiments to investigate the phase relations and mineral transformations of pyrolite and other candidate rock compositions to identify what phases are stable at such depths (Irifune and Ringwood, 1987b; Irifune, 1994; Hirose, 2002; Irifune et al., 2010; Ishii et al., 2011; Ishii et al., 2018) and compare their physical properties with geophysical observations (Murakami et al., 2007; Murakami et al., 2012; Irifune et al., 2008; Kurnosov et al., 2017; Gréaux et al., 2019). Of particular relevance for this thesis is the study of the lower mantle, which is the deepest layer of Earth's interior to be composed of silicate rocks. As mentioned above, the top of the lower mantle, located at about 660 km, is defined by the transition of ringwoodite to an assemblage of bridgmanite and ferropericlase. Bridgmanite remains the dominant mineral phase down to about 2700 km, where a polymorphic reaction to the so-called post-perovskite phase takes place (Murakami et al., 2004; Oganov and Ono, 2004; Catalli et al., 2009). Current estimates for the volume fraction of bridgmanite in a lower mantle assemblage oscillate between approximately 75% and 100%, based on the comparison of experimental and computational mineral physical data with seismic models (Xu et al., 2008; Murakami et al., 2012; Zhang et al., 2013; Kurnosov et al., 2017). Additionally, as shown in the previous section, seismically heterogeneous regions in the lower mantle ranging from 10^1 to 10^3 km have been identified from 3D seismic models. The nature of these heterogeneities is diverse and cannot be attributed to variations in temperature alone. Resolving the interplay between temperature and mineralogy of these anomalies is possible by modelling the contrast in physical properties between the average mantle composition and other lithologies, which can be done combining mineral physics and thermodynamic data (e.g., Satta et al., 2021). Particularly relevant to this thesis is the mineral chemistry of dry pyrolite, dry basalt, and hydrous basalt at lower mantle conditions, which will be discussed in more detail in the following sections.

1.2.1 Bulk chemical composition of the lower mantle

As mentioned above, geophysical observations and high-pressure-temperature laboratory experiments indicate that bridgmanite comprises at least 75 vol.% of lower mantle rocks

down to approximately 2700 km depth. However, the exact proportion of this mineral relative to other phases, which defines to a first approximation the bulk chemical composition of the lower mantle, remains uncertain. Previously proposed models ranged between two end members, reflecting different scenarios of mantle differentiation and convection regimes. The former assumes that the lower mantle is relatively enriched in silica, with a molar ratio of Mg/Si of about 1.0, such as in the carbonaceous chondritic materials from which the Earth is believed to have accreted (McDonough and Sun, 1995; Mcdonough and Rudnick, 1998; Palme and O'Neill, 2014). The latter postulates that the bulk composition of the lower mantle is the same as in the primitive upper mantle (i.e., pyrolite), which in turn is obtained from a weighted average of mid-ocean ridge basalt (MORB) and the residual harzburgite from which the basaltic magma was extracted (McDonough and Sun, 1995; Mcdonough and Rudnick, 1998; Palme and O'Neill, 2014; Ringwood, 1962). The pyrolite model has a higher molar ratio of Mg/Si of about 1.3, corresponding to a volume fraction of ferropericlase of about 15-18% at lower mantle conditions (Irifune et al., 2010; Ishii et al., 2018), while in the chondrite model this can be as low as few vol.% (Figure 1.3). To reconcile the composition of a pyrolitic mantle with the initial composition of carbonaceous chondrites during Earth's accretion, it was argued that the missing silicon had partitioned in the core during core-mantle differentiation (e.g., Allègre et al., 1995). This model seems to be supported by the observation of a lower core density relative to that of pure Fe-Ni alloy (Wänke, 1981; Poirier, 1994). On the other hand, the existence of a Si-rich lower mantle, as in the chondrite model, would require bridgmanite to have fractionally crystallised from a magma ocean during core-mantle differentiation (Solomatov, 2007; Elkins-Tanton, 2012), in agreement with recent estimates of melt viscosity (Xie et al., 2020; Xie et al., 2021), and that such chemical layering has been preserved until today. As a consequence, a layered mantle convection regime is required to explain the chondrite model, while a pyrolitic lower mantle is more compatible with a whole mantle convection regime where upper and lower mantle have been effectively mixed throughout Earth's geological history.

1.2.2 Phase relations of pyrolite in the lower mantle

At the top of the lower mantle, between 660 and 730 km depth, corresponding to pressures of 23-26 GPa, at least two mineral reactions take place that involve the formation of (Mg,Fe,Al)(Si,Al)O_3 bridgmanite, i.e., the post-spinel transformation (Liu, 1976; Ito and Takahashi, 1989; Ishii et al., 2011) and the post-garnet transformation (Liu, 1974; Irifune et al., 1996; Kubo and Akaogi, 2000). Immediately after the post-spinel transformation, bridgmanite is enriched in Mg and Si, and relatively depleted in Al, which partitions into majoritic garnet (Irifune, 1994; Ishii et al., 2011). With increasing pressure, majoritic garnet disappears and the Al concentration in bridgmanite therefore increases (Irifune, 1994; Irifune et al., 2010; Ishii et al., 2011). At approximately 26-27 GPa, bridgmanite contains approximately 5 mol.% Al_2O_3 and 5 mol.% FeO-Fe_2O_3, depending on redox conditions. Additionally, chemical analyses of bridgmanite samples synthesised at these conditions often found that the total number of cations normalised by 3 oxygens is larger than 2. If the stoichiometry is

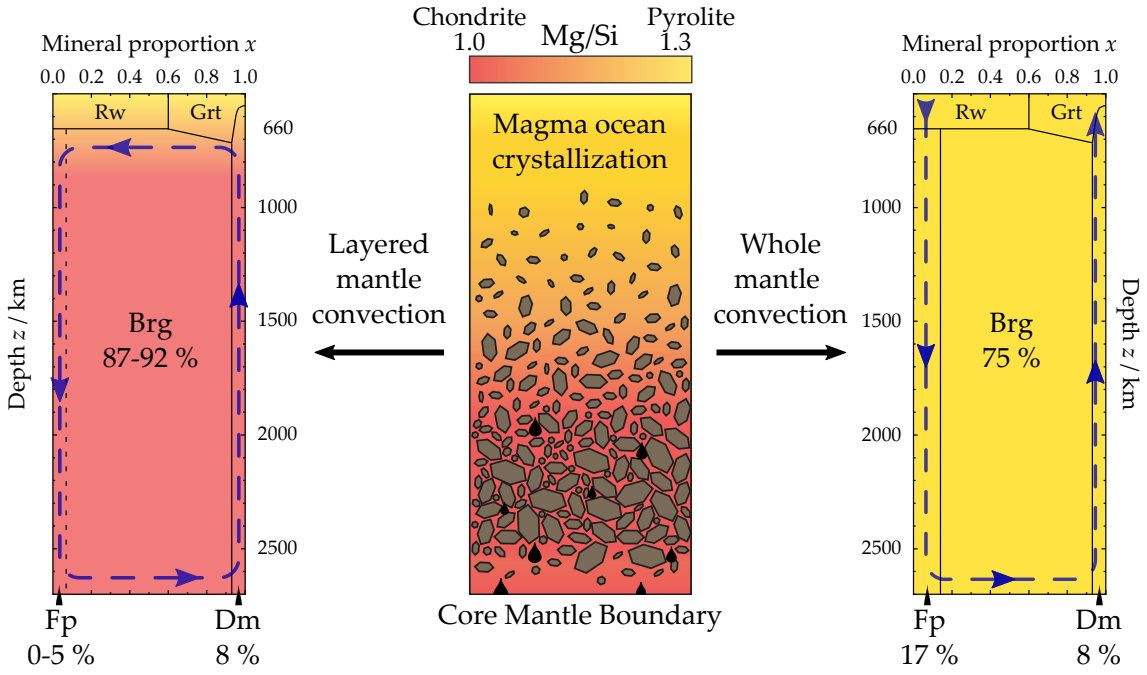

Figure 1.3. Schematic representation of a possible magma ocean scenario (middle) with fractional crystallisation of bridgmanite (brown) and metal droplets (black) percolating towards the core mantle boundary. The colour in the background indicates the changes in Mg/Si ratio resulting from the crystallisation of the magma ocean and enrichment in Mg in the upper layers of the mantle. On the left and right are shown the volume fraction of the three most abundant phases in chondrite and pyrolite, respectively. Brg, Fp, and Dm indicate bridgmanite, ferropericlase, and $CaSiO_3$ perovskite (recently named davemaoite), respectively. Blue arrows indicate the lower mantle convection regime compatible with each model.

instead normalised by two cations, it is found that part of the oxygen sites must be vacant to keep the charge balance. This is consistent with experiments performed in simpler chemical systems, such as MgO-$AlO_{1.5}$-SiO_2, which reported the presence of an $MgAlO_{2.5}$ component in bridgmanite at topmost lower mantle conditions and under MgO saturation (Navrotsky et al., 2003; Kojitani et al., 2007; Liu et al., 2019c). As the volume fraction of $CaSiO_3$ perovskite, recently named davemaoite (Tschauner et al., 2021), is limited to about 8% and the concentration of Al in ferropericlase is very limited, bridgmanite is the main Al sink in a pyrolitic lower mantle (Irifune, 1994). Therefore, rather than constraining the partitioning of Al between lower mantle phases, previous studies have attempted to charecterise its distribution among the two crystallographic sites of bridgmanite (Lauterbach et al., 2000; Navrotsky et al., 2003; Kojitani et al., 2007; Liu et al., 2017a; Grüninger et al., 2019; Liu et al., 2019c; Liu et al., 2019b) and its effect on the partitioning of Fe with ferropericlase (Frost and Langenhorst, 2002; Huang et al., 2021a). The distribution of Fe and Al is tightly related to the redox conditions of the system and in particular to oxygen fugacity (f_{O_2}). Low f_{O_2} conditions can trigger the disproportionation of Fe^{2+} in ferropericlase and lead to the incorporation of Fe^{3+} in bridgmanite, as well as the formation of an Fe-rich metal alloy (Frost et al., 2004; Frost and McCammon, 2008; Huang et al., 2021a). Under reducing conditions and absence of Al, on

the other hand, Fe in bridgmanite is mostly ferrous (Frost and Langenhorst, 2002; Nakajima et al., 2012). The distribution coefficient (K_D) of ferrous iron between bridgmanite (*brg*) and ferropericlase (*fp*) is derived from the following equilibrium reaction:

$$MgSiO_3(brg) + Fe^{2+}O(fp) = Fe^{2+}SiO_3(brg) + MgO(fp) \tag{1.2}$$

$$K_D = \frac{X^{brg}_{Fe^{2+}SiO_3} X^{fp}_{MgO}}{X^{brg}_{MgSiO_3} X^{fp}_{Fe^{2+}O}} \tag{1.3}$$

where X_i^α represents the molar fraction of component i in the phase α. However, information on the oxidation state of Fe is not always available, which makes it impossible to distinguish between ferrous and ferric iron in chemical analyses. Therefore, the apparent distribution coefficient $K_{D,app}$ is often used, which instead makes use of the total molar concentrations of Mg and Fe atoms per formula unit:

$$K_{D,app} = \frac{X^{brg}_{Fe} X^{fp}_{Mg}}{X^{brg}_{Mg} X^{fp}_{Fe}} \tag{1.4}$$

As Fe significantly affects the density and elasticity of bridgmanite and ferropericlase, several previous studies have attempted to experimentally determine possible K_D values as a function of pressure and temperature both in the absence (e.g., Auzende et al., 2008; Sakai et al., 2009; Tange et al., 2009a; Nakajima et al., 2012; Arimoto et al., 2019) and in the presence of Al (e.g., Prescher et al., 2014; Shim et al., 2017). Note that the obtained K_D values change depending on the bulk chemical composition of the system, such as the (Mg+Fe)/Si ratio. For instance, in a $Mg_{1.8}Fe_{0.2}SiO_4$ starting composition, K_D values were found to decrease from about 0.3 in the topmost lower mantle to 0.1-0.2 before the post-perovskite transition. On the other hand, in more Si-rich systems such as $MgSiO_3$-$FeSiO_3$, the proportion of bridgmanite to ferropericlase is higher and the observed K_D values span from 0.15 at the top of the lower mantle to virtually zero in the proximity of the core-mantle boundary (Figure 1.4). The presence of Al further complicates the crystal chemistry of bridgmanite, as it favours the incorporation of other trivalent cations, such as Fe^{3+}, and the formation of oxygen vacancies (see Section 1.3.1). Several previous studies attempted to investigate the effect of pressure on the Mg-Fe partitioning in Al-bearing system by both multi-anvil and diamond anvil cell techniques (Prescher et al., 2014; Shim et al., 2017; Irifune et al., 2010), reporting contrasting results. Sudden jumps in either K_D or the $Fe^{3+}/\Sigma Fe$ of bridgmanite were often observed (Irifune et al., 2010; Shim et al., 2017) and explained by occurrence of a pressure induced spin-crossover of octahedrally coordinated Fe^{3+} in bridgmanite (Kupenko et al., 2015; Sinmyo et al., 2017) and/or Fe^{2+} in ferropericlase (Badro et al., 2003; Lin et al., 2005). However, similar changes in the electronic properties of these two minerals would be expected to take place in Al-free systems as well, where K_D was found to smoothly decrease with pressure (Figuer 1.4). Recently, Huang et al. (2021a) conducted multi-anvil experiments showing that the redox conditions and initial $Fe^{3+}/\Sigma Fe$ of the system can have an even more prominent effect on the phase relations of bridgmanite and

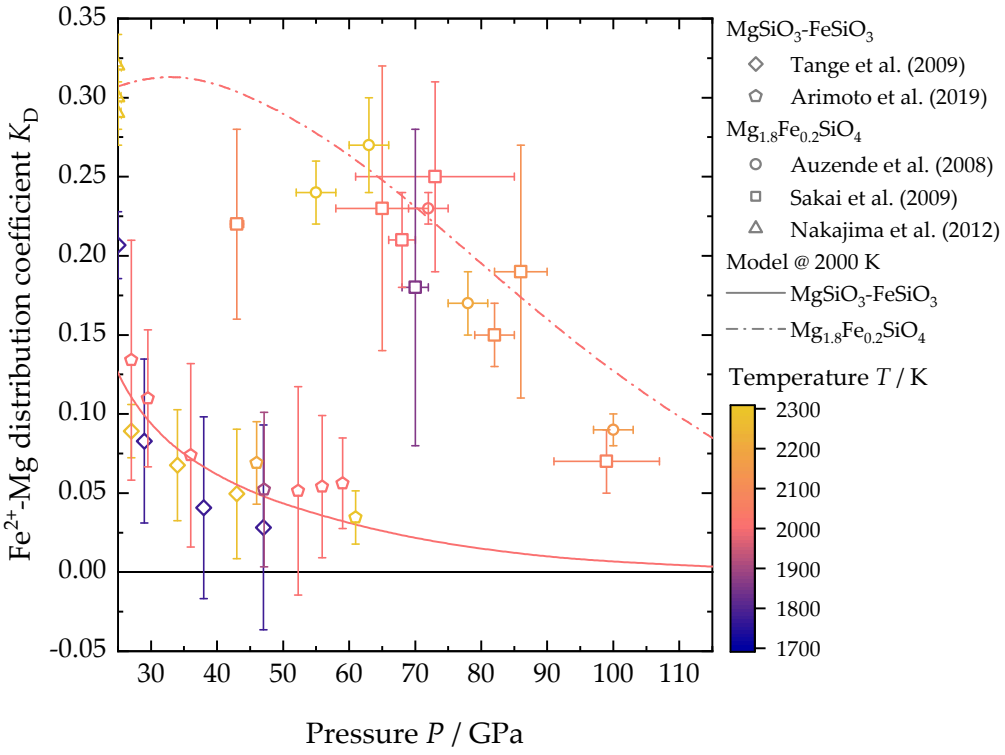

Figure 1.4. Experimentally determined K_D values (equation 1.3) for the Fe^{2+}-Mg partitioning between bridgmanite and ferropericlase in pyroxene ($MgSiO_3$-$Fe^{2+}SiO_3$) and Fo90 olivine ($Mg_{1.8}Fe_{0.2}SiO_4$) starting material at lower mantle pressures. Temperature is expressed by the colour scale. Modelled curves at 2000 K are calculated using the thermoelastic and interaction parameters of bridgmanite and ferropericlase suggested by Nakajima et al. (2012).

ferropericlase at 25 GPa. Thermodynamic calculations were then performed to extrapolate these results to 50 GPa, where both Fe^{3+} in bridgmanite and Fe^{2+} in ferropericlase are still in the high-spin state, and showed that this could indeed reconcile the apparently contrasting results reported in previous studies. Future experiments at deeper lower mantle conditions will hopefully help improving our understanding of the combined effect of oxygen fugacity and Fe spin state, thus providing us with a formalism to model element partitioning in complex systems, such as pyrolite, throughout the entire lower mantle pressure range.

1.2.3 Inferring the average composition of the lower mantle from mineral elasticity data

Seismic data are the primary source of information on the density, elastic and anelastic properties of lower mantle rocks, as seen in Section 1.1. Therefore, several previous studies have attempted to infer the bulk composition of the lower mantle by comparing experimentally and computationally determined sound velocities of candidate lower mantle minerals with seismic velocities reported in 1D reference models (Murakami et al., 2007;

Murakami et al., 2012; Xu et al., 2008; Chantel et al., 2012; Zhang et al., 2013; Kurnosov et al., 2017; Mashino et al., 2020). Numerical simulations have suggested that the composition of the lower mantle should become increasingly more enriched in bridgmanite with depth (Ballmer et al., 2017). However, the absence of steep velocity and density gradients in 1D and averaged 3D models have motivated previous studies to compute pressure-dependent sound velocities and densities assuming a constant bulk chemical composition. One of the limitations of most previous models is that mineral compositions and volume fractions were either arbitrarily fixed or refined to match the velocities reported in seismic models (Murakami et al., 2007; Murakami et al., 2012; Mashino et al., 2020), which is not thermodynamically consistent. Kurnosov et al. (2017), instead, proposed a more complex mineral physical model based on the formalism of Stixrude and Lithgow-Bertelloni (2005) and Stixrude and Lithgow-Bertelloni (2011) where the distribution of Fe and Mg between bridgmanite and ferropericlase was calculated from experimental and thermodynamic data on phase equilibria (Irifune et al., 2010; Nakajima et al., 2012) and the mineral proportion in the lower mantle assemblage were obtained at each pressure-temperature condition from a mass balance calculation. In Chapter 4, the same approach of Kurnosov et al. (2017) has been employed to compute seismic velocities in the CaO-MgO-FeO-SiO_2 (CMFS) system with simplified pyrolitic composition using novel elasticity data of $MgSiO_3$ bridgmanite determined in this thesis. Although simplified, the model uses the same framework of equations to calculate both mineral compositions and sound velocities in an internally consistent way between 800 and 2600 km depth, i.e., between the post-garnet and post-perovskite transformations in the lower mantle. At the time of publication, the influence of oxygen fugacity on the partitioning of Fe between bridgmanite and ferropericlase and of Fe and Al between the crystallographic sites of bridgmanite had not been constrained experimentally and was therefore neglected by the model. However, a recent publication by Huang et al. (2021a) provided both experimental results and a robust thermodynamic description of these features at topmost lower mantle conditions, which will allow future studies to compute velocities and density for more relevant and complete chemical systems at lower mantle conditions.

1.2.4 Mineralogy of dry MORB in the lower mantle

Subducted oceanic plates are typically composed of an apical basaltic layer (6-10 km), an intermediate residual peridotitic layer (harzburgite and lherzolite, 30-40 km), and a basal depleted pyrolitic layer (Ringwood and Irifune, 1988). Basalt is the more chemically distinct rock composition, with higher Na_2O, CaO, Al_2O_3, and SiO_2 concentrations at expenses of that of MgO. As a consequence, when basaltic crust is subducted in the lower mantle, its mineralogy will differ from that of pyrolite and peridotite (Figure 1.5). Due to its enrichment in SiO_2 relative to MgO, about 20-25 vol.% of basaltic assemblages is constituted by stishovite, the high-pressure polymorph of SiO_2 with rutile-type structure. Upon compression to about 50 GPa and room temperature, a displacive phase transition to a $CaCl_2$-type post-stishovite phase takes place (Kingma et al., 1995; Andrault et al.,

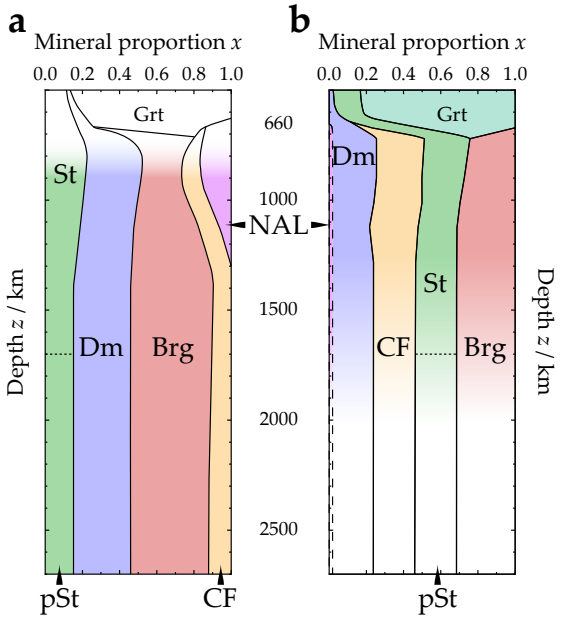

Figure 1.5. Phase proportions in a normal MORB composition determined from (a) diamond anvil cell (Ricolleau et al., 2010) and (b) multi-anvil experiments (Ishii et al., 2019b; Ishii et al., 2022b) at lower mantle pressures. Bright colours indicate the depth (i.e., pressure) interval where the experiments were conducted. Grt: majoritic garnet. St: stishovite. pSt: post-stishovite. Dm: davemaoite (i.e., $CaSiO_3$ perovskite). NAL: new hexagonal aluminous phase. CF: $CaFe_2O_4$-type aluminous phase. Brg: bridgmanite.

1998), with the transition pressure increasing at high temperature (Nomura et al., 2010). At pressures and temperatures of the core mantle boundary, post-stishovite further transforms into a α-PbO_2-type phase called seifertite (Murakami et al., 2003). A second major phase, also constituting about 25 vol.% of the entire assemblage, has $CaFe_2O_4$-type structure (CF) and is the main host of Na and Al. Similarly to bridgmanite, the CF phase is a solid solution of many end member components, with $NaAlSiO_4$ being the most abundant, followed by $MgAl_2O_4$, $Fe^{2+}Al_2O_4$, Mg_2SiO_4, $CaAl_2O_4$, and $Fe^{2+}Fe^{3+}{}_2O_4$ (Guignot and Andrault, 2004; Ricolleau et al., 2010; Ishii et al., 2022b). Laser-heated diamond anvil cell experiments suggested that the CF phase is stable throughout the entire lower mantle pressure range. However, the boundary of CF-type to $CaTi_2O_4$-type (CT) $MgAl_2O_4$ shifts to significantly lower pressures with increasing temperatures (Ishii et al., 2021). Therefore, the transition of $NaAlSiO_4$-rich CF phase to a CT phase could take place in hotter regions of the lower mantle, such as upwelling plumes. Another Al-rich phase, known as new hexagonal aluminous (NAL) phase, has been recovered in basaltic phase assemblages at topmost lower mantle conditions together with or instead of the CF phase (Ricolleau et al., 2010; Ishii et al., 2022b). Results from multi-anvil studies have shown that the NAL phase seems to be stabilised by the presence of potassium in the starting bulk composition, while its volume fraction is limited to a few vol.% and does not change with pressure (Ishii et al., 2019b; Ishii et al., 2022b). A diamond anvil cell study, on the other hand, suggested that NAL is the main aluminous phase in the topmost lower mantle and gradually transforms to CF phase upon further compression (Ricolleau et al., 2010). In the absence of potassium and for intermediate $NaAlSiO_4$-$MgAl_2O_4$ compositions, NAL is stable under shallow lower mantle conditions and transforms to the CF phase with increasing pressure (Imada et al., 2011; Ono et al., 2009). The remaining portion of the basaltic phase assemblage is constituted by silicate perovskite phases, i.e., bridgmanite (25-30 vol.%) and davemaoite (25 vol.%). The composition of davemaoite is close to $CaSiO_3$, as it is in pyrolite,

while basaltic bridgmanite is significantly more enriched in Fe and Al with respect to pyrolitic and peridotitic bridgmanite (Ricolleau et al., 2010; Ishii et al., 2019b; Ishii et al., 2022b).

1.2.5 Hydrous phases in MORB at lower mantle conditions

Basalt is also considered to be a possible candidate to host structurally bound hydrogen (i.e., water) within its constituent minerals. For decades it was believed that basaltic crust subducted into the Earth's interiors would dehydrate under upper mantle conditions after the destabilisation of lawsonite (Poli and Schmidt, 1995; Okamoto and Maruyama, 1999) and remain essentially dry down to the topmost lower mantle. At these depths, hydrous fluids were argued to migrate from the underlying peridotitic layers and react with the dry basaltic lithology to form Al-rich dense hydrous phases, such as $Al_2SiO_6H_2$ Al-phase D and δ-AlOOH (phase δ). These hydrous phases proved to be stable along subduction geotherms or even at ambient mantle temperature in the pressure range corresponding to the bottom mantle transition zone and lower mantle (Ohira et al., 2014; Pamato et al., 2015; Li et al., 2022). A recent experimental study, however, showed that a continuous chain of hydrous phases can be actually found in metabasaltic rocks along the entire pressure-temperature path of a subducting oceanic plate down to the topmost lower mantle (Liu et al., 2019a). Results showed that Al-phase D transforms into a solid solution of δ-AlOOH and isostructural compound $MgSiO_4H_2$ phase H in the shallow lower mantle. In this scenario, rehydration of basaltic crust after dehydration of the harzburgitic layer would not be necessary to transport water into the lower mantle.

Among nominally anhydrous minerals, bridgmanite is known to host only limited amounts of water, with current estimates ranging from few tens of ppm wt. to approximately 1000 ppm wt. H_2O under water saturated conditions (e.g., Fu et al., 2019; Liu et al., 2021, and reference threin). As far as the CF phase is concerned, our recent high-pressure-temperature synthesis experiments under water saturated conditions always produced a mixture of phase δ, bridgmanite, and Na-rich melt, implying that CF has a very low water solubility (Ishii et al., 2023). $CaSiO_3$ davemaoite was found to host some amounts of water based on recent in situ infrared spectroscopy measurements (Chen et al., 2020), although quantitative estimates of the water content are extremely challenging as davemaoite tends to become amorphous upon decompression to ambient conditions. In recent years, a number of studies have argued that SiO_2 stishovite and post-stishovite can incorporate wt.%-levels of water at pressures and temperature of the top- to mid-lower mantle based on its volume expansion upon reaction with water in laser heated diamond anvil cells (Lin et al., 2020; Lin et al., 2022; Nisr et al., 2020). Note, however, that infrared spectroscopy measurements on the quenched samples were not always possible to conduct and concerns remain about the validity of the volume expansion calibration against the estimated water content. Nonetheless, silica phases remain the most likely candidate to transport and host water in subducted basaltic rocks in the lower mantle in the

absence of a nominally hydrous phase, especially in the presence of Al (Litasov et al., 2007a).

1.3 Bridgmanite and stishovite: crystal structure, chemistry, and elasticity

The substitution of cations with different radii and/or charge at the same crystallographic site affects the stability and physicochemical properties of minerals. Understanding the link between the two is critical to the construction of suitable mineral physical models of Earth's lower mantle that accurately describe the elastic behaviour of rocks as a function of pressure and temperature. In this section, I will describe the crystal structures and crystal chemistries of bridgmanite and stishovite, with particular emphasis on how they affect the high-pressure behaviour of these two minerals, which is of central importance for Chapters 4, 5, and 6 of this thesis. The relationship between crystal structure and cation substitutions in phase D, on the other hand, is directly reported in Chapter 7.

1.3.1 Bridgmanite

Bridgmanite belongs to the structural group of perovskites, whose chemical formula is expressed as ABX_3. Perovskites are comprised of a framework of corner-sharing BX_6 octahedra creating large AX_{12} cavities, which can be more or less distorted depending on the charge and relative size of the A and B cations and of the X anion. In bridgmanite, the X anion is an oxygen, the octahedral B-site is occupied by Si, Al, and possibly Fe^{3+}, while the pseudo-dodecahedral A-site hosts Mg, Fe^{2+}, Fe^{3+} and Al (Figure 1.6). The distortion of perovskites is mainly controlled and classified by the solid rotation of the octahedral units around the crystallographic axes of an ideal and undistorted cubic structure, called aristotype (Glazer, 1972). Octahedral tilting can be either in-phase, when neighbouring octahedra along the tilt axis rotate in the same direction, or out-of-phase, if they rotate in opposite directions. Bridgmanite has a $GdFeO_3$-type structure, which is characterised by an in-phase rotation of the octahedra about the [001] crystallographic direction of the aristotype structure, and out-of-phase rotation about the [110] direction (Yagi et al., 1978; Horiuchi et al., 1987). As a consequence of octahedral tilting, the unit-cell edge parallel to the in-phase tilting axis doubles, and the symmetry decreases from cubic to orthorhombic. Although the standard space group of bridgmanite would be *Pnma*, the bridgmanite structure is usually described in the non-standard configuration *Pbnm*, having unit-cell dimensions $a < b < c$, so that the doubled unit cell dimension is c, while the a and b directions are aligned along $[\bar{1}10]$ and [110] directions of the pseudo-cubic cell, respectively (Figure 1.6). A useful way to charecterise the overall distortion of perovskites using the unit-cell lattice parameters is by calculating the symmetry-adapted lattice strains (e_i) that express the fractional stretching or shortening of the pseudo-cubic axes relative to the theoretical axis of the aristotype structure (a^0). Since the unit cell volume (V) of bridgmanite is four times that of its aristotype, a^0 can be obtained

as the cubic root of $V/4$. The symmetry adapted strains e_{tx} and e_4 in the non-standard setting ($a < b < c$) are then calculated to quantify the degree of tetragonal and orthorhombic distortion, respectively (Carpenter et al., 2001):

$$e_1 = \frac{\frac{c}{2} - a^0}{a^0}, \quad e_2 + e_3 = \frac{\frac{b}{\sqrt{2}} - a^0}{a^0} + \frac{\frac{a}{\sqrt{2}} - a^0}{a^0} \tag{1.5}$$

$$e_{\mathrm{tx}} = \frac{1}{\sqrt{3}} (2e_1 - e_2 - e_3) \tag{1.6}$$

$$|e_4| = \left| \frac{\frac{b}{\sqrt{2}} - a^0}{a^0} - \frac{\frac{a}{\sqrt{2}} - a^0}{a^0} \right| \tag{1.7}$$

Lattice strains can be used at both ambient and non-ambient conditions as proxies to infer the overall degree of distortion of the perovskite structure of bridgmanite (Boffa Ballaran et al., 2012), showing that strains correlate positive with the Al content in the B-site. However, an accurate assessment of the structural distortion is only possible by applying group theoretical methods to the analysis of structural refinements (Stokes et al., 1991; Howard and Stokes, 1998), which is typically carried out by computer programs (Campbell et al., 2006; Orobengoa et al., 2009). This method is particularly used in materials science, where the onset of octahedral tilting (i.e., X-anion displacement) or B-cation displacement is correlated with ferroic or multiferroic behaviour of perovskite-related materials. Recently, the same type of analysis has been applied to earth sciences to charecterise the local effect of cation substitutions on structural distortion of bridgmanite (Huang et al., 2021b), which is ultimately related to the stability of the perovskite structure at high pressure and temperature (Martin and Parise, 2008). In Section 3.3, a more in-depth description of what these distortions are and how they change as a function of pressure, temperature, and composition is presented.

From a crystal chemical point of view, the replacement of Mg and/or Si by Fe and/or Al at the A and B crystallographic sites gives rise to several possible substitution mechanisms, such as $Fe^{2+}SiO_3$, $Fe^{3+}AlO_3$, $AlAlO_3$, $Fe^{3+}Fe^{3+}O_3$, and $MgAlO_{2.5}$. The physical properties and thermodynamic behaviour of bridgmanite solid solutions is, however, not always well constrained. In fact, all end member components other than $MgSiO_3$ are not thermodynamically stable. The solubility of $Fe^{2+}SiO_3$ and $AlAlO_3$, for instance, is limited to approximately 40 and 30 mol.%, respectively, based on most recent high-pressure-temperature multi-anvil experiments up to 60 GPa (Liu et al., 2017b; Liu et al., 2020a; Arimoto et al., 2019). Diamond anvil cell studies conducted at higher pressure have suggested that the miscibility gap in the $MgSiO_3$-$Fe^{2+}SiO_3$ system narrows significantly at higher pressure (Dorfman et al., 2013), although the introduction of $Fe^{3+}_{2/3}SiO_3$ component might be required to stabilise a pure iron silicate perovskite phase (Ismailova et al., 2016). The solubility of the $Fe^{3+}AlO_3$ component can be up to about 70 mol.% (Liu et al., 2020b), although compositions that are more enriched that 50 mol.% revert to $LiNbO_3$-type phase upon decompression (Liu et al., 2019d) and cannot be used to determine material properties at ambient conditions. In the

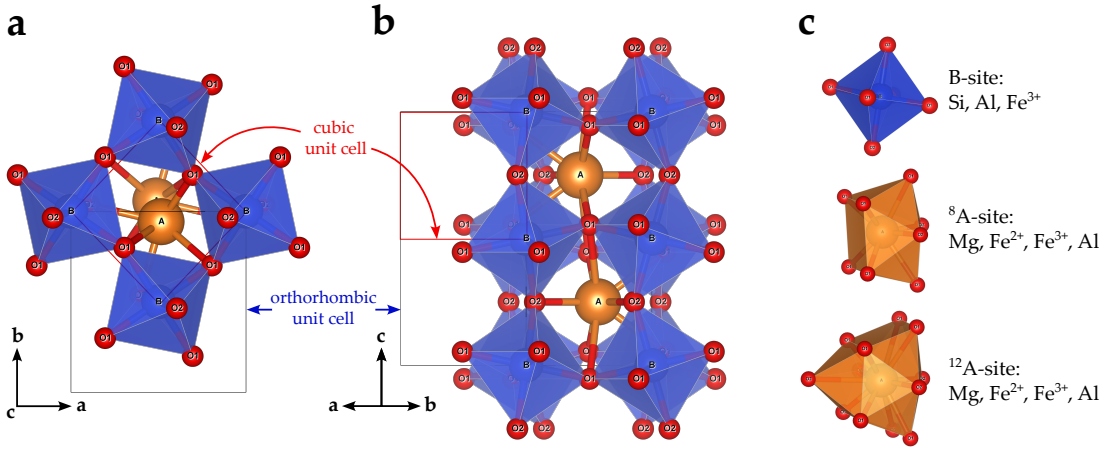

Figure 1.6. Crystal structure of bridgmanite (a) along and (b) perpendicular to the *c*-axis. The unit-cell of the cubic aristotype is shown in red. (c) Geometries, coordination polyhedra, and cation contents of the octahedral B-site, 8-fold-coordinated A site (^{8}A, bicapped prism), and 12-fold-coordinated A site (^{12}A, pseudo-dodecahedron).

case of the oxygen vacancy component $MgAlO_{2.5}$, its solubility is of the order of 5 mol.% (Liu et al., 2019c; Liu et al., 2019b). Therefore, in order to obtain the relevant information on the thermodynamic properties of these end member components, such as the molar volume and the elastic moduli, it is necessary to define trends in the compositional range where experimental data are available and then extrapolate them to the end member composition. For instance, on a first approximation, it is accepted that the Fe^{2+} substitution at the A site and the Al or Fe^{3+} substitutions at the B site both increase the molar volume of $MgSiO_3$ bridgmanite (Huang et al., 2021b). However, making accurate estimates for the molar volumes of end member components can be problematic for multiple reasons, such as the limited solubility of some components (e.g., $MgAlO_{2.5}$), the experimental challenge in synthesising suitable samples, and the reproducibility of the experimental data acquired using different techniques. These issues are even more relevant when defining compositional trends in the elastic properties, where available experimental data are much scarcer. Part of my Ph.D. has therefore been devoted to determining the sound velocities and thermoelastic properties of well-characterised bridgmanite samples with $MgSiO_3$ and $MgSiO_3$-$AlAlO_3$-$MgAlO_{2.5}$ compositions. Combining the experimental results with a reanalysis of literature data, the thermoelastic properties of the relevant end member components have then been obtained and used to model the composition of bridgmanite and/or its elastic properties as a function of pressure and temperature.

1.3.2 Stishovite and post-stishovite

The stability field of stishovite spans from about 8-10 GPa at 900-1800 K in the upper mantle (Hemley et al., 1994; Zhang et al., 1996) to 50-55 GPa at 300 K and 70-80 GPa at 2300 K in the mid-lower mantle, where a structural phase transition to post-stishovite takes place (Kingma et al., 1995; Andrault et al., 1998; Nomura et al., 2010; Fischer et al.,

2018). Post-stishovite remains stable down to the bottom lower mantle, where it transforms to seifertite (α-PbO_2-type structure) at pressures and temperatures in excess of 110 GPa and 2000 K (Murakami et al., 2003; Hirose et al., 2005; Andrault et al., 2014). The crystal structure of stishovite is tetragonal with space group $P4_2/mnm$ (i.e., rutile-type structure), with chains of corner-sharing SiO_6 octahedra stacked parallel to the crystallographic *c*-axis and connected to each other through vertices (Figure 1.7a). Silicon atoms sit at the corner of the unit cell at positions equivalent to (0,0,0), while oxygen atoms lie along the face diagonal at positions equivalent to (*x*,-*x*,0). When viewed along the *c*-axis, this configuration results in empty cages also running parallel to the *c*-axis with a characteristic square section (Figure 1.7a). Upon transformation to post-stishovite, oxygen atoms start to move away from the face diagonal as the *y*-coordinate acquires one more degree of freedom (i.e., *x*,*y*,0). As a result, octahedral chains start to rotate relatively to each other, and the space group symmetry decreases from $P4_2/mnm$ to $Pnnm$ (i.e., $CaCl_2$-type structure). Visually, this structural change can be appreciated by the change from square to rhombic section of the channels in the octahedral framework (Figure 1.7b). As the transformation from stishovite to post-stishovite is of the displacive type, the space groups of the two phases are tightly related to each other, the only difference being the presence of a 4-fold screw axis in the stishovite space group which is lost at the phase transition. Since all the symmetry elements of the post-stishovite space group are contained in that of stishovite, according to group theory $Pnnm$ is called a sub-group of $P4_2/mnm$. Therefore, irreducible representations of the high-symmetry space group can be used to classify structural distortion mechanisms, decompose them into simple displacive modes, and compute their individual amplitudes (Stokes et al., 1991). As I will discuss in Chapter 6, in the case of stishovite there is only one displacive mode, Γ_2^+, which displaces the oxygen atom from the face diagonal of the unit cell in the *a*-*b* plane. The symmetry of the Γ_2^+ mode is the same as the Raman-active B_{1g} optic mode. High-pressure experiments showed that the frequency of B_{1g} initially decreases upon compression and starts to increase only once the transition pressure to post-stishovite is reached (Kingma et al., 1995; Zhang et al., 2021). The softening behaviour of the B_{1g} mode is also coupled with the transverse acoustic velocity along the [110] crystallographic direction of stishovite, which in turn depends on the difference between the elastic coefficients $c_{11} - c_{12}$ (see Section 2.4.1). As the transition pressure is approached, this difference vanishes, leading to a violation of the Born stability criterion $c_{11} - c_{12} > 0$ (Jiang et al., 2009; Zhang et al., 2021). Combining group theory considerations with experimental measurements of the unit-cell lattice parameters and optic mode frequencies of stishovite and post-stishovite at high pressure, the elastic behaviour of both phases can be modelled by means of Landau theory (Carpenter et al., 2000). Landau theory further allows to compute the excess thermodynamic properties, such as heat capacity and entropy, of the two phases (e.g., Salje, 1991), which are required to model phase equilibria of lower mantle basaltic rocks.

In more complex chemical systems, the only relevant substitution mechanism in stishovite under dry conditions is the replacement of Si by Al with the formation of half

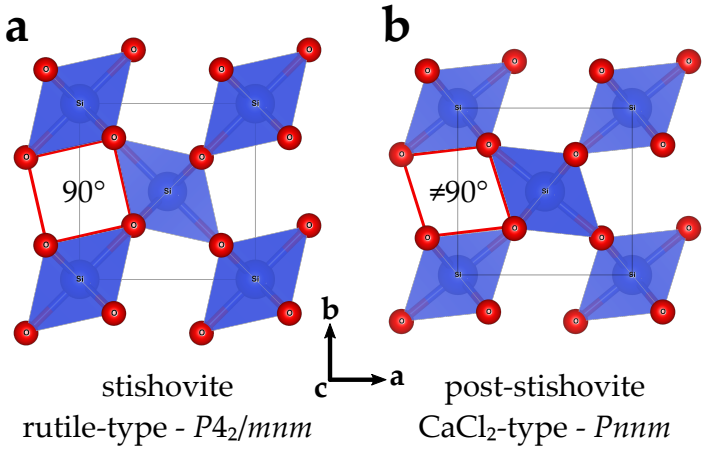

Figure 1.7. Crystal structures of (a) stishovite and (b) post-stishovite viewed along the *c*-axis. Red polygons highlight the (a) square or (b) rhombic section of the characteristic channels that extend parallel to *c*.

an oxygen vacancy for charge balance (Kröger and Vink, 1956): $Si_{Si}^{x} = Al'_{Si} + 1/2V_{O}^{\bullet}$. This substitution mechanism is limited to few wt.% $AlO_{1.5}$ at transition zone and lower mantle conditions, as reported by high-pressure-temperature phase relations experiments in the SiO_2-$AlO_{1.5}$ system (Liu et al., 2006) and in MORB (Ono et al., 2001; Hirose et al., 2005; Ishii et al., 2019b; Ishii et al., 2022b). In the presence of water, the $AlO_{1.5}$ solubility is enhanced, possibly by the charge couple substitution of SiO_2 with an AlOOH component (Litasov et al., 2007a; Ishii et al., 2022a). The incorporation mechanism of H and its position in the stishovite unit cell are, however, still unclear. Fourier-transform infrared (FTIR) spectroscopy data collected on single crystals of hydrous Al-bearing stishovite display a strong polarisation of the absorption bands in the *a*-*b* plane, i.e., perpendicular to the *c*-axis (Pawley et al., 1993; Litasov et al., 2007a; Thomas et al., 2009). Based on neutron diffraction data on isostructural TiO_2 rutile, Smyth et al. (1995) argued that the position of H in stishovite should be close to the shared edge of SiO_6 octahedra. However, H in the isostructural compound δ-AlOOH sits in the *a*-*b* plane, close to the central position of the channels (Sano-Furukawa et al., 2018). The addition of H and Al were found to expand the stability field of post-stishovite to lower pressure (Lakshtanov et al., 2007b; Bolfan-Casanova et al., 2009; Nisr et al., 2017). Note also that δ-AlOOH has the same space group (i.e., *Pnnm*) as post-stishovite at transition zone and shallow lower mantle conditions, where Al- and H-bearing stishovite samples are typically synthesised (Litasov et al., 2007a). Therefore, when Al > H, it is reasonable to expect that H is located in the channels extending parallel to the *c*-axis and is coupled with Al, as in phase δ. This fits well with our recent findings that silica samples with $AlO_{1.5}$ and H_2O contents of at least 6 and 0.8 wt.%, respectively, display the post-stishovite structure even after being recovered to room pressure and temperature (Ishii et al., 2022a). Note that silica with about 6 wt.% Al and 0.2 wt.% H_2O from another study was recovered to ambient conditions as stishovite and found to transform to post-stishovite upon compression to 25 GPa (Lakshtanov et al., 2007b). This further suggests that hydrogen has an important role in determining the stability of silica

phases and that further experimental work is needed to accurately constrain the individual and combined effects of Al and H substitution in silica under lower mantle conditions.

References

Allègre, C. J., J. P. Poirier, E. Humler, and A. W. Hofmann (1995). "The chemical composition of the Earth". In: *Earth and Planetary Science Letters* 134 (3-4), pp. 515–526. DOI: 10.1016/0012-821X(95)00123-T.

Andrault, D., G. Fiquet, F. Guyot, and M. Hanfland (1998). "Pressure-induced Landau-type transition in stishovite". In: *Science* 282 (5389), pp. 720–724. DOI: 10.1126/science.282.5389.720.

Andrault, D., R. G. Trønnes, Z. Konôpková, W. Morgenroth, H. P. Liermann, G. Morard, and M. Mezouar (2014). "Phase diagram and *P-V-T* equation of state of Al-bearing seifertite at lowermost mantle conditions". In: *American Mineralogist* 99 (10), pp. 2035–2042. DOI: 10.2138/AM-2014-4697.

Arimoto, T., T. Irifune, M. Nishi, Y. Tange, T. Kunimoto, and Z. Liu (2019). "Phase relations of $MgSiO_3$-$FeSiO_3$ system up to 64FIX ME!!!!GPa and 2300FIX ME!!!!K using multianvil apparatus with sintered diamond anvils". In: *Physics of the Earth and Planetary Interiors* 295. DOI: 10.1016/j.pepi.2019.106297.

Auzende, A. L., J. Badro, F. J. Ryerson, P. K. Weber, S. J. Fallon, A. Addad, J. Siebert, and G. Fiquet (2008). "Element partitioning between magnesium silicate perovskite and ferropericlase: New insights into bulk lower-mantle geochemistry". In: *Earth and Planetary Science Letters* 269 (1-2), pp. 164–174. DOI: 10.1016/j.epsl.2008.02.001.

Badro, J., G. Fiquet, F. Guyot, J. P. Rueff, V. V. Struzhkin, G. Vankó, and G. Monaco (2003). "Iron partitioning in earth's mantle: Toward a deep lower mantle discontinuity". In: *Science* 300 (5620), pp. 789–791. DOI: 10.1126/SCIENCE.1081311/SUPPL_FILE/BADRO.SOM.PDF.

Ballmer, M. D., C. Houser, J. W. Hernlund, R. M. Wentzcovitch, and K. Hirose (2017). "Persistence of strong silica-enriched domains in the Earth's lower mantle". In: *Nature Geoscience* 10 (3), pp. 236–240. DOI: 10.1038/ngeo2898.

Boffa Ballaran, T., A. Kurnosov, K. Glazyrin, D. J. Frost, M. Merlini, M. Hanfland, and R. Caracas (2012). "Effect of chemistry on the compressibility of silicate perovskite in the lower mantle". In: *Earth and Planetary Science Letters* 333-334, pp. 181–190. DOI: 10.1016/j.epsl.2012.03.029.

Bolfan-Casanova, N., D. Andrault, E. Amiguet, and N. Guignot (2009). "Equation of state and post-stishovite transformation of Al-bearing silica up to 100 GPa and 3000 K". In: *Physics of the Earth and Planetary Interiors* 174 (1-4), pp. 70–77. DOI: 10.1016/j.pepi.2008.06.024.

Cammarano, F., A. Deuss, S. Goes, and D. Giardini (2005). "One-dimensional physical reference models for the upper mantle and transition zone: Combining seismic and mineral

physics constraints". In: *Journal of Geophysical Research: Solid Earth* 110 (1), pp. 1–17. DOI: 10.1029/2004JB003272.

Cammarano, F. and B. Romanowicz (2007). "Insights into the nature of the transition zone from physically constrained inversion of long-period seismic data". In: *Proceedings of the National Academy of Sciences of the United States of America* 104 (22), pp. 9139–9144. DOI: 10.1073/pnas.0608075104.

Campbell, B. J., H. T. Stokes, D. E. Tanner, and D. M. Hatch (2006). "*ISODISPLACE*: A web-based tool for exploring structural distortions". In: *Journal of Applied Crystallography* 39 (4), pp. 607–614. DOI: 10.1107/S0021889806014075.

Carpenter, M. A., A. I. Bacerro, and F. Seifert (2001). "Strain analysis of phase transitions in (Ca,Sr)TiO_3 perovskites". In: *American Mineralogist* 86 (3), pp. 348–363. DOI: 10.2138/am-2001-2-319.

Carpenter, M. A., R. J. Hemley, and H. kwang Mao (2000). "High-pressure elasticity of stishovite and the $P4_2/mnm$ - $Pnnm$ phase transition". In: *Journal of Geophysical Research* 105, pp. 807–816.

Catalli, K., S. H. Shim, and V. Prakapenka (2009). "Thickness and Clapeyron slope of the post-perovskite boundary". In: *Nature* 462 (7274), pp. 782–785. DOI: 10.1038/nature08598.

Chantel, J., D. J. Frost, C. A. McCammon, Z. Jing, and Y. Wang (2012). "Acoustic velocities of pure and iron-bearing magnesium silicate perovskite measured to 25 GPa and 1200 K". In: *Geophysical Research Letters* 39 (19). DOI: 10.1029/2012GL053075.

Chanyshev, A., T. Ishii, D. Bondar, S. Bhat, E. J. Kim, R. Farla, K. Nishida, Z. Liu, L. Wang, A. Nakajima, B. Yan, H. Tang, Z. Chen, Y. Higo, Y. Tange, and T. Katsura (2022). "Depressed 660-km discontinuity caused by akimotoite–bridgmanite transition". In: *Nature* 601 (7891), pp. 69–73. DOI: 10.1038/s41586-021-04157-z.

Chen, H., K. Leinenweber, V. Prakapenka, C. Prescher, Y. Meng, H. Bechtel, M. Kunz, and S.-H. Shim (2020). "Possible H_2O storage in the crystal structure of $CaSiO_3$ perovskite". In: *Physics of the Earth and Planetary Interiors* 299, p. 106412. DOI: 10.1016/j.pepi.2019.106412.

Deuss, A. (2009). "Global observations of mantle discontinuities using SS and PP precursors". In: *Surveys in Geophysics* 30 (4-5), pp. 301–326. DOI: 10.1007/s10712-009-9078-y.

Dorfman, S. M., Y. Meng, V. B. Prakapenka, and T. S. Duffy (2013). "Effects of Fe-enrichment on the equation of state and stability of (Mg,Fe)SiO_3 perovskite". In: *Earth and Planetary Science Letters* 361, pp. 249–257. DOI: 10.1016/j.epsl.2012.10.033.

Dziewonski, A. M. and D. L. Anderson (1981). "Preliminary reference Earth model". In: *Physics of the Earth and Planetary Interiors* 25 (4), pp. 297–356. DOI: 10.1016/0031-9201(81)90046-7.

Eberle, M. A., O. Grasset, and C. Sotin (2002). "A numerical study of the interaction between the mantle wedge, subducting slab, and overriding plate". In: *Physics of the Earth and Planetary Interiors* 134 (3-4), pp. 191–202. DOI: 10.1016/S0031-9201(02)00157-7.

Elkins-Tanton, L. T. (2012). "Magma oceans in the inner solar system". In: *Annual Review of Earth and Planetary Sciences* 40, pp. 113–139. DOI: 10.1146/annurev-earth-042711-105503.

Fischer, R. A., A. J. Campbell, B. A. Chidester, D. M. Reaman, E. C. Thompson, J. S. Pigott, V. B. Prakapenka, and J. S. Smith (2018). "Equations of state and phase boundary for stishovite and $CaCl_2$-type SiO_2". In: *American Mineralogist* 103 (5), pp. 792–802. DOI: 10.2138/am-2018-6267.

Frost, D. J. and F. Langenhorst (2002). "The effect of Al_2O_3 on Fe-Mg partitioning between magnesiowustite and magnesium silicate perovskite". In: *Earth and Planetary Science Letters* 199, pp. 227–241.

Frost, D. J., C. Liebske, F. Langenhorst, C. A. McCammon, R. G. Trønnes, and D. C. Rubie (2004). "Experimental evidence for the existence of iron-rich metal in the Earth's lower mantle". In: *Nature* 428, pp. 409–412. DOI: 10.1029/200/JC000964.

Frost, D. J. and C. A. McCammon (2008). "The Redox State of earth's mantle". In: *Annual Review of Earth and Planetary Sciences* 36, pp. 389–420. DOI: 10.1146/annurev.earth.36.031207.124322.

Fu, S., J. Yang, N. Tsujino, T. Okuchi, N. Purevjav, and J.-F. F. Lin (2019). "Single-crystal elasticity of (Al,Fe)-bearing bridgmanite and seismic shear wave radial anisotropy at the topmost lower mantle". In: *Earth and Planetary Science Letters* 518, pp. 116–126. DOI: 10.1016/j.epsl.2019.04.023.

Fukao, Y. and M. Obayashi (2013). "Subducted slabs stagnant above, penetrating through, and trapped below the 660 km discontinuity". In: *Journal of Geophysical Research: Solid Earth* 118 (11), pp. 5920–5938. DOI: 10.1002/2013JB010466.

Glazer, A. M. (1972). "The classification of tilted octahedra in perovskites". In: *Acta Crystallographica Section B Structural Crystallography and Crystal Chemistry* 28 (11), pp. 3384–3392. DOI: 10.1107/s0567740872007976.

Grand, S. P. and D. V. Helmberger (1984). "Upper mantle shear structure of North America". In: *Geophysical Journal of the Royal Astronomical Society* 76 (2), pp. 399–438. DOI: 10.1111/j.1365-246X.1984.tb05053.x.

Gréaux, S., T. Irifune, Y. Higo, Y. Tange, T. Arimoto, Z. Liu, and A. Yamada (2019). "Sound velocity of $CaSiO_3$ perovskite suggests the presence of basaltic crust in the Earth's lower mantle". In: *Nature* 565 (7738), pp. 218–221. DOI: 10.1038/s41586-018-0816-5.

Grüninger, H., Z. Liu, R. Siegel, T. B. Ballaran, T. Katsura, J. Senker, and D. J. Frost (2019). "Oxygen Vacancy Ordering in Aluminous Bridgmanite in the Earth's Lower Mantle". In: *Geophysical Research Letters* 46 (15), pp. 8731–8740. DOI: 10.1029/2019GL083613.

Gu, T., M. G. Pamato, D. Novella, M. Alvaro, J. Fournelle, F. E. Brenker, W. Wang, and F. Nestola (2022). "Hydrous peridotitic fragments of Earth's mantle 660 km discontinuity sampled by a diamond". In: *Nature Geoscience*, pp. 1–5. DOI: 10.1038/s41561-022-01024-y.

Guignot, N. and D. Andrault (2004). "Equations of state of Na-K-Al host phases and implications for MORB density in the lower mantle". In: *Physics of the Earth and Planetary Interiors* 143 (1-2), pp. 107–128. DOI: 10.1016/j.pepi.2003.09.014.

Hemley, R. J., C. T. Prewitt, and K. J. Kingma (1994). "High-Pressure Behavior of Silica". In: *Reviews in Mineralogy* 29, pp. 41–81.

Hirose, K. (2002). "Phase transitions in pyrolitic mantle around 670-km depth: Implications for upwelling of plumes from the lower mantle". In: *Journal of Geophysical Research: Solid Earth* 107 (B4). DOI: 10.1029/2001JB000597.

Hirose, K., N. Takafuji, N. Sata, and Y. Ohishi (2005). "Phase transition and density of subducted MORB crust in the lower mantle". In: *Earth and Planetary Science Letters* 237 (1-2), pp. 239–251. DOI: 10.1016/j.epsl.2005.06.035.

Horiuchi, H., E. Ito, and D. J. Weidner (1987). "Perovskite-type $MgSiO_3$: Single-crystal X-ray diffraction study". In: *American Mineralogist* 72 (5), pp. 357–360.

Hosseini, K., K. J. Matthews, K. Sigloch, G. E. Shephard, M. Domeier, and M. Tsekhmistrenko (2018). "SubMachine: Web-Based Tools for Exploring Seismic Tomography and Other Models of Earth's Deep Interior". In: *Geochemistry, Geophysics, Geosystems* 19 (5), pp. 1464–1483. DOI: 10.1029/2018GC007431.

Houser, C., G. Masters, P. Shearer, and G. Laske (2008). "Shear and compressional velocity models of the mantle from cluster analysis of long-period waveforms". In: *Geophysical Journal International* 174 (1), pp. 195–212. DOI: 10.1111/j.1365-246X.2008.03763.x.

Howard, C. J. and H. T. Stokes (1998). "Group-theoretical analysis of octahedral tilting in perovskites". In: *Acta Crystallographica Section B: Structural Science* 54, pp. 782–789. DOI: 10.1107/S0108768198004200.

Huang, R., T. B. Ballaran, C. A. McCammon, N. Miyajima, D. Dolejš, and D. J. Frost (2021a). "The composition and redox state of bridgmanite in the lower mantle as a function of oxygen fugacity". In: *Geochimica et Cosmochimica Acta* 303, pp. 110–136. DOI: 10.1016/J.GCA.2021.02.036.

Huang, R., T. B. Ballaran, C. A. McCammon, N. Miyajima, and D. J. Frost (2021b). "The effect of Fe–Al substitution on the crystal structure of $MgSiO_3$ bridgmanite". In: *Journal of Geophysical Research: Solid Earth*, e2021JB021936. DOI: 10.1029/2021jb021936.

Imada, S., K. Hirose, and Y. Ohishi (2011). "Stabilities of NAL and Ca-ferrite-type phases on the join $NaAlSiO_4$-$MgAl_2O_4$ at high pressure". In: *Physics and Chemistry of Minerals* 38 (7), pp. 557–560. DOI: 10.1007/s00269-011-0427-2.

Irifune, T. (1994). "Absence of an aluminous phase in the upper part of the Earth's lower mantle". In: *Nature* 370 (6485), pp. 131–133. DOI: 10.1038/370131a0.

Irifune, T., Y. Higo, T. Inoue, Y. Kono, H. Ohfuji, and K. Funakoshi (2008). "Sound velocities of majorite garnet and the composition of the mantle transition region". In: *Nature* 451 (7180), pp. 814–817. DOI: 10.1038/nature06551.

Irifune, T., T. Koizumi, and J. I. Ando (1996). "An experimental study of the garnet-perovskite transformation in the system $MgSiO_3$-$Mg_3Al_2Si_3O_{12}$". In: *Physics of the Earth and Planetary Interiors* 96 (2-3), pp. 147–157. DOI: 10.1016/0031-9201(96)03147-0.

Irifune, T. and A. E. Ringwood (1987a). "Phase transformations in a harzburgite composition to 26 GPa: implications for dynamical behaviour of the subducting slab". In: *Earth and Planetary Science Letters* 86 (2-4), pp. 365–376. DOI: 10.1016/0012-821X(87)90233-0.

— (1987b). "Phase Transformations in Primitive MORB and Pyrolite Compositions to 25 GPa and Some Geophysical Implications". In: *High-Pressure Research in Mineral Physics*, pp. 231–242.

Irifune, T., T. Shinmei, C. A. McCammon, N. Miyajima, D. C. Rubie, and D. J. Frost (2010). "Iron Partitioning and Density Changes of Pyrolite in Earth's Lower Mantle". In: *Science* 327 (5962), pp. 193–195. DOI: 10.1126/science.1181443.

Ishii, T., G. Criniti, E. Bykova, L. Dubrovinsky, T. Katsura, H. Arii, H. Kojitani, and M. Akaogi (2021). "High-pressure syntheses and crystal structure analyses of a new low-density $CaFe_2O_4$-related and $CaTi_2O_4$-type $MgAl_2O_4$phases". In: *American Mineralogist* 106 (7). DOI: 10.2138/am-2021-7619.

Ishii, T., G. Criniti, E. Ohtani, N. Purevjav, H. Fei, T. Katsura, and H. K. Mao (2022a). "Superhydrous aluminous silica phases as major water hosts in high-temperature lower mantle". In: *Proceedings of the National Academy of Sciences of the United States of America* 119 (44), pp. 1–6. DOI: 10.1073/pnas.2211243119.

Ishii, T., G. Criniti, X. Wang, K. Glazyrin, and T. B. Ballaran (2023). "Synthesis and structural analysis of $CaFe_2O_4$-type single crystals in the $NaAlSiO_4$-$MgAl_2O_4$-Fe_3O_4 system". In: *American Mineralogist* 108 (1), pp. 217–221. DOI: 10.2138/am-2022-8748.

Ishii, T., R. Huang, R. Myhill, H. Fei, I. Koemets, Z. Liu, F. Maeda, L. Yuan, L. Wang, D. Druzhbin, T. Yamamoto, S. Bhat, R. Farla, T. Kawazoe, N. Tsujino, E. Kulik, Y. Higo, Y. Tange, and T. Katsura (2019a). "Sharp 660-km discontinuity controlled by extremely narrow binary post-spinel transition". In: *Nature Geoscience* 12 (10), pp. 869–872. DOI: 10.1038/s41561-019-0452-1.

Ishii, T., H. Kojitani, and M. Akaogi (2011). "Post-spinel transitions in pyrolite and Mg_2SiO_4 and akimotoite-perovskite transition in $MgSiO_3$: Precise comparison by high-pressure high-temperature experiments with multi-sample cell technique". In: *Earth and Planetary Science Letters* 309 (3-4), pp. 185–197. DOI: 10.1016/j.epsl.2011.06.023.

— (2018). "Phase relations and mineral chemistry in pyrolitic mantle at 1600–2200FIX ME!!!!°C under pressures up to the uppermost lower mantle: Phase transitions around the 660-km discontinuity and dynamics of upwelling hot plumes". In: *Physics of the Earth and Planetary Interiors* 274, pp. 127–137. DOI: 10.1016/j.pepi.2017.10.005.

— (2019b). "Phase Relations of Harzburgite and MORB up to the Uppermost Lower Mantle Conditions: Precise Comparison With Pyrolite by Multisample Cell High-Pressure Experiments With Implication to Dynamics of Subducted Slabs". In: *Journal of Geophysical Research: Solid Earth* 124 (4), pp. 3491–3507. DOI: 10.1029/2018JB016749.

Ishii, T., N. Miyajima, G. Criniti, Q. Hu, K. Glazyrin, and T. Katsura (2022b). "High pressure-temperature phase relations of basaltic crust up to mid-mantle conditions". In: *Earth and Planetary Science Letters* 584, p. 117472. DOI: 10.1016/j.epsl.2022.117472.

Ismailova, L., E. Bykova, M. Bykov, V. Cerantola, C. McCammon, T. B. Ballaran, A. Bobrov, R. Sinmyo, N. Dubrovinskaia, K. Glazyrin, H. P. Liermann, I. Kupenko, M. Hanfland, C. Prescher, V. Prakapenka, V. Svitlyk, and L. Dubrovinsky (2016). "Stability of Fe,Al-bearing bridgmanite in the lower mantle and synthesis of pure Fe-bridgmanite". In: *Science Advances* 2 (7). DOI: 10.1126/sciadv.1600427.

Ito, E. and E. Takahashi (1989). "Postspinel transformations in the system Mg_2SiO_4-Fe_2SiO_4 and some geophysical implications". In: *Journal of Geophysical Research: Solid Earth* 94 (B8), pp. 10637–10646. DOI: 10.1029/JB094IB08P10637.

Jiang, F., G. D. Gwanmesia, T. I. Dyuzheva, and T. S. Duffy (2009). "Elasticity of stishovite and acoustic mode softening under high pressure by Brillouin scattering". In: *Physics of the Earth and Planetary Interiors* 172 (3-4), pp. 235–240. DOI: 10.1016/j.pepi.2008.09.017.

Kaneshima, S. (2016). "Seismic scatterers in the mid-lower mantle". In: *Physics of the Earth and Planetary Interiors* 257, pp. 105–114. DOI: 10.1016/j.pepi.2016.05.004.

— (2019). "Seismic scatterers in the lower mantle near subduction zones". In: *Geophysical Journal International* 218 (3), pp. 1873–1891. DOI: 10.1093/gji/ggz241.

Kaneshima, S. and G. Helffrich (1999). "Dipping low-velocity layer in the mid-lower mantle: Evidence for geochemical heterogeneity". In: *Science* 283 (5409), pp. 1888–1891. DOI: 10.1126/science.283.5409.1888.

— (2003). "Subparallel dipping heterogeneities in the mid-lower mantle". In: *Journal of Geophysical Research: Solid Earth* 108 (B5). DOI: 10.1029/2001jb001596.

Kennett, B. L. N., E. R. Engdahl, and R. Buland (1995). "Constraints on seismic velocities in the Earth from traveltimes". In: *Geophysical Journal International* 122 (1), pp. 108–124. DOI: 10.1111/j.1365-246X.1995.tb03540.x.

Kennett, B. L. and E. R. Engdahl (1991). "Traveltimes for global earthquake location and phase identification". In: *Geophysical Journal International* 105 (2), pp. 429–465. DOI: 10.1111/j.1365-246X.1991.tb06724.x.

Kingma, K. J., R. E. Cohen, R. J. Hemley, and H. K. Mao (1995). "Transformation of stishovite to a denser phase at lower-mantle pressures". In: *Nature* 374 (6519), pp. 243–245. DOI: 10.1038/374243a0.

Kirby, S. H., S. Stein, E. A. Okal, and D. C. Rubie (1996). "Metastable mantle phase transformations and deep earthquakes in subducted oceanic lithosphere". In: *Reviews of Geophysics* 34 (2), pp. 261–306. DOI: 10.1029/96RG01050.

Kojitani, H., T. Inoue, and M. Akaogi (2016). "Precise measurements of enthalpy of post-spinel transition in Mg_2SiO_4 and application to the phase boundary calculation". In: *Journal of Geophysical Research: Solid Earth* 121 (2), pp. 729–742. DOI: 10.1002/2015JB012211.

Kojitani, H., T. Katsura, and M. Akaogi (2007). "Aluminum substitution mechanisms in perovskite-type $MgSiO_3$: An investigation by Rietveld analysis". In: *Physics and Chemistry of Minerals* 34 (4), pp. 257–267. DOI: 10.1007/s00269-007-0144-z.

Kröger, F. A. and H. J. Vink (1956). "Relations between the Concentrations of Imperfections in Crystalline Solids". In: *Solid State Physics - Advances in Research and Applications* 3 (C), pp. 307–435. DOI: 10.1016/S0081-1947(08)60135-6.

Kubo, A. and M. Akaogi (2000). "Post-garnet transitions in the system $Mg_4Si_4O_{12}$-$Mg_3Al_2Si_3O_{12}$ up to 28 GPa: Phase relations of garnet, ilmenite and perovskite". In: *Physics of the Earth and Planetary Interiors* 121 (1-2), pp. 85–102. DOI: 10.1016/S0031-9201(00)00162-X.

Kupenko, I., C. McCammon, R. Sinmyo, V. Cerantola, V. Potapkin, A. I. Chumakov, A. Kantor, R. Rüffer, and L. Dubrovinsky (2015). "Oxidation state of the lower mantle: In situ observations of the iron electronic configuration in bridgmanite at extreme conditions". In: *Earth and Planetary Science Letters* 423, pp. 78–86. DOI: 10.1016/j.epsl.2015.04.027.

Kurnosov, A., H. Marquardt, D. J. Frost, T. B. Ballaran, and L. Ziberna (2017). "Evidence for a Fe^{3+}-rich pyrolitic lower mantle from (Al,Fe)-bearing bridgmanite elasticity data". In: *Nature* 543, pp. 543–546. DOI: 10.1038/nature21390.

Lakshtanov, D. L., S. V. Sinogeikin, K. D. Litasov, V. B. Prakapenka, H. Hellwig, J. Wang, C. Sanches-Valle, J. P. Perrillat, B. Chen, M. Somayazulu, J. Li, E. Ohtani, and J. D. Bass (2007b). "The post-stishovite phase transition in hydrous alumina-bearing SiO_2 in the lower mantle of the earth". In: *Proceedings of the National Academy of Sciences of the United States of America* 104 (34), pp. 13588–13590. DOI: 10.1073/pnas.0706113104.

Lauterbach, S., C. A. McCammon, P. V. Aken, F. Langenhorst, and F. Seifert (2000). "Mössbauer and ELNES spectroscopy of (Mg,Fe)(Si,Al)O_3 perovskite: A highly oxidised component of the lower mantle". In: *Contributions to Mineralogy and Petrology* 138 (1), pp. 17–26. DOI: 10.1007/PL00007658.

Li, X., S. Speziale, M. Koch-Müller, R. J. Husband, and H. P. Liermann (2022). "Phase Stability of Al-Bearing Dense Hydrous Magnesium Silicates at Topmost Lower Mantle Conditions: Implication for Water Transport in the Mantle". In: *Geophysical Research Letters* 49 (16). DOI: 10.1029/2022GL098353.

Lin, J. F., V. V. Struzhkin, S. D. Jacobsen, G. Shen, V. B. Prakapenka, H. K. Mao, and R. J. Hemley (2005). "X-ray emission spectroscopy with a laser-heated diamond anvil cell: A new experimental probe of the spin state of iron in the Earth's interior". In: vol. 12. International Union of Crystallography, pp. 637–641. DOI: 10.1107/S0909049505020741.

Lin, Y., Q. Hu, Y. Meng, M. Walter, and H. K. Mao (2020). "Evidence for the stability of ultrahydrous stishovite in Earth's lower mantle". In: *Proceedings of the National Academy of Sciences of the United States of America* 117 (1), pp. 184–189. DOI: 10.1073/pnas.1914295117.

Lin, Y., Q. Hu, M. J. Walter, J. Yang, Y. Meng, X. Feng, Y. Zhuang, R. E. Cohen, and H. K. Mao (2022). "Hydrous SiO_2 in subducted oceanic crust and H_2O transport to the core-mantle boundary". In: *Earth and Planetary Science Letters* 594, p. 117708. DOI: 10.1016/j.epsl.2022.117708.

Litasov, K. D., H. Kagi, A. Shatskiy, E. Ohtani, D. L. Lakshtanov, J. D. Bass, and E. Ito (2007a). "High hydrogen solubility in Al-rich stishovite and water transport in the lower mantle". In: *Earth and Planetary Science Letters* 262 (3-4), pp. 620–634. DOI: 10.1016/j.epsl.2007.08.015.

Liu, L. G. (1976). "Orthorhombic perovskite phases observed in olivine, pyroxene and garnet at high pressures and temperatures". In: *Physics of the Earth and Planetary Interiors* 11 (4), pp. 289–298. DOI: 10.1016/0031-9201(76)90016-9.

Liu, L. (1974). "Silicate perovskite from phase transformations of pyrope-garnet at high pressure and temperature". In: *Geophysical Research Letters* 1 (6), pp. 277–280. DOI: 10.1029/GL001i006p00277.

Liu, X., N. Nishiyama, T. Sanehira, T. Inoue, Y. Higo, and S. Sakamoto (2006). "Decomposition of kyanite and solubility of Al_2O_3 in stishovite at high pressure and high temperature conditions". In: *Physics and Chemistry of Minerals* 33 (10), pp. 711–721. DOI: 10.1007/s00269-006-0122-x.

Liu, X., K. N. Matsukage, Y. Nishihara, T. Suzuki, and E. Takahashi (2019a). "Stability of the hydrous phases of Al-rich phase D and Al-rich phase H in deep subducted oceanic crust". In: *American Mineralogist* 104 (1), pp. 64–72. DOI: 10.2138/am-2019-6559.

Liu, Z., M. Akaogi, and T. Katsura (2019b). "Increase of the oxygen vacancy component in bridgmanite with temperature". In: *Earth and Planetary Science Letters* 505, pp. 141–151. DOI: 10.1016/j.epsl.2018.10.014.

Liu, Z., T. B. Ballaran, R. Huang, D. J. Frost, and T. Katsura (2019c). "Strong correlation of oxygen vacancies in bridgmanite with Mg/Si ratio". In: *Earth and Planetary Science Letters* 523, p. 115697. DOI: 10.1016/j.epsl.2019.06.037.

Liu, Z., L. Dubrovinsky, C. McCammon, S. Ovsyannikov, I. Koemets, L. Chen, Q. Cui, N. Su, J. Cheng, T. Cui, B. Liu, and T. Katsura (2019d). "A new $(Mg_{0.5}Fe^{3+}{}_{0.5})(Si_{0.5}Al^{3+}{}_{0.5})O_3$ $LiNbO_3$ -type phase synthesized at lower mantle conditions". In: *American Mineralogist* 104, pp. 1213–1216.

Liu, Z., H. Fei, L. Chen, C. McCammon, L. Wang, R. Liu, F. Wang, B. Liu, and T. Katsura (2021). "Bridgmanite is nearly dry at the top of the lower mantle". In: *Earth and Planetary Science Letters* 570, p. 117088. DOI: 10.1016/j.epsl.2021.117088.

Liu, Z., T. Ishii, and T. Katsura (2017a). "Rapid decrease of $MgAlO_{2.5}$ component in bridgmanite with pressure". In: *Geochemical Perspectives Letters* 5, pp. 12–18. DOI: 10.7185/geochemlet.1739.

Liu, Z., R. Liu, Y. Shang, F. Shen, L. Chen, X. Hou, M. Yao, T. Cui, B. Liu, and T. Katsura (2020a). "Aluminum solubility in bridgmanite up to 3000 K at the top lower mantle". In: *Geoscience Frontiers*. DOI: 10.1016/j.gsf.2020.04.009.

Liu, Z., C. McCammon, B. Wang, L. Dubrovinsky, T. Ishii, D. Bondar, A. Nakajima, Y. Tange, Y. Higo, T. Cui, B. Liu, and T. Katsura (2020b). "Stability and Solubility of the $FeAlO_3$ Component in Bridgmanite at Uppermost Lower Mantle Conditions". In: *Journal of Geophysical Research: Solid Earth* 125 (2), e2019JB018447. DOI: 10.1029/2019JB018447.

Liu, Z., M. Nishi, T. Ishii, H. Fei, N. Miyajima, T. B. Ballaran, H. Ohfuji, T. Sakai, L. Wang, S. Shcheka, T. Arimoto, Y. Tange, Y. Higo, T. Irifune, and T. Katsura (2017b). "Phase Relations in the System $MgSiO_3$-Al_2O_3 up to 2300 K at Lower Mantle Pressures". In: *Journal of Geophysical Research: Solid Earth* 122 (10), pp. 7775–7788. DOI: 10.1002/2017JB014579.

Lorenzon, S., D. Novella, P. Nimis, S. D. Jacobsen, E. Thomassot, M. G. Pamato, L. Prosperi, A. Lorenzetti, M. Alvaro, F. Brenker, F. Salvadego, and F. Nestola (2022). "Ringwoodite and zirconia inclusions indicate downward travel of super-deep diamonds". In: *Geology* 50 (9), pp. 996–1000. DOI: 10.1130/G50111.1.

Lu, C., S. P. Grand, H. Lai, and E. J. Garnero (2019). "TX2019slab: A New P and S Tomography Model Incorporating Subducting Slabs". In: *Journal of Geophysical Research: Solid Earth* 124 (11), pp. 11549–11567. DOI: 10.1029/2019JB017448.

Marquardt, H. and L. Miyagi (2015). "Slab stagnation in the shallow lower mantle linked to an increase in mantle viscosity". In: *Nature Geoscience* 8 (4), pp. 311–314. DOI: 10.1038/ngeo2393.

Martin, C. D. and J. B. Parise (2008). "Structure constraints and instability leading to the post-perovskite phase transition of $MgSiO_3$". In: *Earth and Planetary Science Letters* 265 (3-4), pp. 630–640. DOI: 10.1016/j.epsl.2007.11.001.

Mashino, I., M. Murakami, N. Miyajima, and S. Petitgirard (2020). "Experimental evidence for silica-enriched Earth's lower mantle with ferrous iron dominant bridgmanite". In: *Proceedings of the National Academy of Sciences of the United States of America* 117 (45), pp. 27899–27905. DOI: 10.1073/pnas.1917096117.

McDonough, W. F. and S. s. Sun (1995). "The composition of the Earth". In: *Chemical Geology* 120 (3-4), pp. 223–253. DOI: 10.1016/0009-2541(94)00140-4.

Mcdonough, W. F. and R. L. Rudnick (1998). "Mineralogy and composition of the upper mantle". In: *Reviews in Mineralogy and Geochemistry* (37), pp. 139–164. DOI: 10.1515/9781501509179-006.

McNamara, A. K. (2019). "A review of large low shear velocity provinces and ultra low velocity zones". In: *Tectonophysics* 760, pp. 199–220. DOI: 10.1016/j.tecto.2018.04.015.

Murakami, M., K. Hirose, K. Kawamura, N. Sata, and Y. Ohishi (2004). "Post-Perovskite Phase Transition in $MgSiO_3$". In: *Science* 304, pp. 855–858. DOI: 10.1126/science.1095932.

Murakami, M., K. Hirose, S. Ono, and Y. Ohishi (2003). "Stability of $CaCl_2$ -type and α-PbO_2 -type SiO_2 at high pressure and temperature determined by in-situ X-ray measurements". In: *Geophysical Research Letters* 30 (5). DOI: 10.1029/2002GL016722.

Murakami, M., Y. Ohishi, N. Hirao, and K. Hirose (2012). "A perovskitic lower mantle inferred from high-pressure, high-temperature sound velocity data". In: *Nature* 485 (7396), pp. 90–94. DOI: 10.1038/nature11004.

Murakami, M., S. V. Sinogeikin, H. Hellwig, J. D. Bass, and J. Li (2007). "Sound velocity of $MgSiO_3$ perovskite to Mbar pressure". In: *Earth and Planetary Science Letters* 256 (1-2), pp. 47–54. DOI: 10.1016/j.epsl.2007.01.011.

Nakajima, Y., D. J. Frost, and D. C. Rubie (2012). "Ferrous iron partitioning between magnesium silicate perovskite and ferropericlase and the composition of perovskite in the Earth's lower mantle". In: *Journal of Geophysical Research: Solid Earth* 117 (8), pp. 1–12. DOI: 10.1029/2012JB009151.

Navrotsky, A., M. Schoenitz, H. Kojitani, H. Xu, J. Zhang, D. J. Weidner, and R. Jeanloz (2003). "Aluminum in magnesium silicate perovskite: Formation, structure, and energetics of magnesium-rich defect solid solutions". In: *Journal of Geophysical Research: Solid Earth* 108 (B7). DOI: 10.1029/2002jb002055.

Nestola, F., N. Korolev, M. Kopylova, N. Rotiroti, D. G. Pearson, M. G. Pamato, M. Alvaro, L. Peruzzo, J. J. Gurney, A. E. Moore, and J. Davidson (2018). "$CaSiO_3$ perovskite in diamond indicates the recycling of oceanic crust into the lower mantle". In: *Nature* 555 (7695), pp. 237–241. DOI: 10.1038/nature25972.

Nisr, C., K. Leinenweber, V. Prakapenka, C. Prescher, S. Tkachev, and S. H. Shim (2017). "Phase transition and equation of state of dense hydrous silica up to 63 GPa". In: *Journal of Geophysical Research: Solid Earth* 122 (9), pp. 6972–6983. DOI: 10.1002/2017JB014055.

Nisr, C., H. Chen, K. Leinenweber, A. Chizmeshya, V. B. Prakapenka, C. Prescher, S. N. Tkachev, Y. Meng, Z. Liu, and S. H. Shim (2020). "Large H_2O solubility in dense silica

and its implications for the interiors of water-rich planets". In: *Proceedings of the National Academy of Sciences of the United States of America* 117 (18), pp. 9747–9754. DOI: 10.1073/pnas.1917448117.

Niu, F. (2014). "Distinct compositional thin layers at mid-mantle depths beneath northeast China revealed by the USArray". In: *Earth and Planetary Science Letters* 402 (C), pp. 305–312. DOI: 10.1016/j.epsl.2013.02.015.

Niu, F., H. Kawakatsu, and Y. Fukao (2003). "Seismic evidence for a chemical heterogeneity in the midmantle: A strong and slightly dipping seismic reflector beneath the Mariana subduction zone". In: *Journal of Geophysical Research: Solid Earth* 108 (B9), pp. 1–12. DOI: 10.1029/2002jb002384.

Nomura, R., K. Hirose, N. Sata, Y. Ohishi, D. Suetsugu, C. Bina, T. Inoue, D. Wiens, and M. Jellinek (2010). "Precise determination of post-stishovite phase transition boundary and implications for seismic heterogeneities in the mid-lower mantle". In: *Physics of the Earth and Planetary Interiors* 183 (1-2), pp. 104–109. DOI: 10.1016/j.pepi.2010.08.004.

Oganov, A. R. and S. Ono (2004). "Theoretical and experimental evidence for a post-perovskite phase of $MgSiO_3$ in Earth's D" layer". In: *Nature* 430 (6998), pp. 445–448. DOI: 10.1038/nature02701.

Ohira, I., E. Ohtani, T. Sakai, M. Miyahara, N. Hirao, Y. Ohishi, and M. Nishijima (2014). "Stability of a hydrous δ-phase, AlOOH-$MgSiO_2(OH)_2$, and a mechanism for water transport into the base of lower mantle". In: *Earth and Planetary Science Letters* 401, pp. 12–17. DOI: 10.1016/j.epsl.2014.05.059.

Okamoto, K. and S. Maruyama (1999). "The high-pressure synthesis of lawsonite in the MORB+H2O system". In: *American Mineralogist* 84 (3), pp. 362–373. DOI: 10.2138/am-1999-0320.

Ono, A., M. Akaogi, H. Kojitani, K. Yamashita, and M. Kobayashi (2009). "High-pressure phase relations and thermodynamic properties of hexagonal aluminous phase and calcium-ferrite phase in the systems $NaAlSiO_4$–$MgAl_2O_4$ and $CaAl_2O_4$–$MgAl_2O_4$". In: *Physics of the Earth and Planetary Interiors* 174 (1-4), pp. 39–49. DOI: 10.1016/J.PEPI.2008.07.028.

Ono, S., E. Ito, and T. Katsura (2001). "Mineralogy of subducted basaltic crust (MORB) from 25 to 37 GPa, and chemical heterogeneity of the lower mantle". In: *Earth and Planetary Science Letters* 190 (1-2), pp. 57–63. DOI: 10.1016/S0012-821X(01)00375-2.

Orobengoa, D., C. Capillas, M. I. Aroyo, and J. M. Perez-Mato (2009). "*AMPLIMODES*: Symmetry-mode analysis on the Bilbao Crystallographic Server". In: *Journal of Applied Crystallography* 42 (5), pp. 820–833. DOI: 10.1107/S0021889809028064.

Palme, H and H. O'Neill (2014). "Cosmochemical Estimates of Mantle Composition". In: *Treatise on Geochemistry: Second Edition* 3, pp. 1–39. DOI: 10.1016/B978-0-08-095975-7.00201-1.

Pamato, M. G., R. Myhill, T. B. Ballaran, D. J. Frost, F. Heidelbach, and N. Miyajima (2015). "Lower-mantle water reservoir implied by the extreme stability of a hydrous aluminosilicate". In: *Nature Geoscience* 8 (1), pp. 75–79. DOI: 10.1038/ngeo2306.

Pawley, A. R., P. F. McMillan, and J. R. Holloway (1993). "Hydrogen in stishovite, with implications for mantle water content". In: *Science* 261 (5124), pp. 1024–1026. DOI: 10.1126/science.261.5124.1024.

Pearson, D. G., F. E. Brenker, F Nestola, J McNeill, L Nasdala, M. T. Hutchison, S Matveev, K Mather, G Silversmit, S Schmitz, B Vekemans, and L Vincze (2014). "Hydrous mantle transition zone indicated by ringwoodite included within diamond." In: *Nature* 507 (7491), pp. 221–4. DOI: 10.1038/nature13080.

Pearson, D. G., D. Canil, and S. B. Shirey (2003). "Mantle Samples Included in Volcanic Rocks: Xenoliths and Diamonds". In: *Treatise on Geochemistry* 2-9, pp. 171–275. DOI: 10.1016/B0-08-043751-6/02005-3.

Poirier, J. P. (1994). "Light elements in the Earth's outer core: A critical review". In: *Physics of the Earth and Planetary Interiors* 85 (3-4), pp. 319–337. DOI: 10.1016/0031-9201(94)90120-1.

— (2000). *Introduction to the Physics of the Earth's Interior*. Cambridge University Press. DOI: 10.1017/CBO9781139164467.

Poli, S. and M. W. Schmidt (1995). "H_2O transport and release in subduction zones: experimental constraints on basaltic and andesitic systems". In: *Journal of Geophysical Research* 100 (B11). DOI: 10.1029/95jb01570.

Prescher, C., F. Langenhorst, L. S. Dubrovinsky, V. B. Prakapenka, and N. Miyajima (2014). "The effect of Fe spin crossovers on its partitioning behavior and oxidation state in a pyrolitic Earth's lower mantle system". In: *Earth and Planetary Science Letters* 399, pp. 86–91. DOI: 10.1016/j.epsl.2014.05.011.

Ricolleau, A., J. P. Perrillat, G. Fiquet, I. Daniel, J. Matas, A. Addad, N. Menguy, H. Cardon, M. Mezouar, and N. Guignot (2010). "Phase relations and equation of state of a natural MORB: Implications for the density profile of subducted oceanic crust in the Earth's lower mantle". In: *Journal of Geophysical Research: Solid Earth* 115 (8). DOI: 10.1029/2009JB006709.

Ringwood, A. E. (1962). "A model for the upper mantle: 2." In: *Journal of Geophysical Research* 67 (11), pp. 4473–4478. DOI: 10.1029/jz067i011p04473.

Ringwood, A. E. and T. Irifune (1988). "Nature of the 650–km seismic discontinuity: implications for mantle dynamics and differentiation". In: *Nature* 331 (6152), pp. 131–136. DOI: 10.1038/331131a0.

Ritsema, J., A. Deuss, H. J. V. Heijst, and J. H. Woodhouse (2011). "S40RTS: A degree-40 shear-velocity model for the mantle from new Rayleigh wave dispersion, teleseismic traveltime and normal-mode splitting function measurements". In: *Geophysical Journal International* 184 (3), pp. 1223–1236. DOI: 10.1111/j.1365-246X.2010.04884.x.

Rost, S., E. J. Garnero, and Q. Williams (2008). "Seismic array detection of subducted oceanic crust in the lower mantle". In: *Journal of Geophysical Research: Solid Earth* 113 (6), pp. 1–11. DOI: 10.1029/2007JB005263.

Rost, S. and C. Thomas (2009). "Improving seismic resolution through array processing techniques". In: *Surveys in Geophysics* 30 (4-5), pp. 271–299. DOI: 10.1007/s10712-009-9070-6.

Sakai, T., E. Ohtani, H. Terasaki, N. Sawada, Y. Kobayashi, M. Miyahara, M. Nishijima, N. Hirao, Y. Ohishi, and T. Kikegawa (2009). "Fe-Mg partitioning between perovskite and

ferropericlase in the lower mantle". In: *American Mineralogist* 94 (7), pp. 921–925. DOI: 10.2138/am.2009.3123.

Salje, E. K. (1991). *Phase Transitions in Ferroelastic and Co-elastic Crystals*. Cambridge University Press. DOI: 10.1017/cbo9780511586460.

Sano-Furukawa, A., T. Hattori, K. Komatsu, H. Kagi, T. Nagai, J. J. Molaison, A. M. dos Santos, and C. A. Tulk (2018). "Direct observation of symmetrization of hydrogen bond in δ-AlOOH under mantle conditions using neutron diffraction". In: *Scientific Reports* 8 (1), pp. 1–9. DOI: 10.1038/s41598-018-33598-2.

Satta, N., G. Criniti, A. Kurnosov, T. B. Ballaran, T. Ishii, and H. Marquardt (2021). "High-Pressure Elasticity of δ-(Al,Fe)OOH Single Crystals and Seismic Detectability of Hydrous MORB in the Shallow Lower Mantle". In: *Geophysical Research Letters* 48 (23). DOI: 10.1029/2021GL094185.

Shim, S. H., B. Grocholski, Y. Ye, E. E. Alp, S. Xu, D. Morgan, Y. Meng, and V. B. Prakapenka (2017). "Stability of ferrous-iron-rich bridgmanite under reducing midmantle conditions". In: *Proceedings of the National Academy of Sciences of the United States of America* 114 (25), pp. 6468–6473. DOI: 10.1073/pnas.1614036114.

Simmons, N. A., A. M. Forte, L. Boschi, and S. P. Grand (2010). "GyPSuM: A joint tomographic model of mantle density and seismic wave speeds". In: *Journal of Geophysical Research: Solid Earth* 115 (12), pp. 1–24. DOI: 10.1029/2010JB007631.

Sinmyo, R., C. McCammon, and L. Dubrovinsky (2017). "The spin state of Fe^{3+} in lower mantle bridgmanite". In: *American Mineralogist* 102 (6), pp. 1263–1269. DOI: 10.2138/am-2017-5917.

Smyth, J. R., R. J. Swope, and A. R. Pawley (1995). "H in rutile-type compounds: II. Crystal chemistry of Al substitution in H-bearing stishovite". In: *American Mineralogist* 80 (5-6), pp. 454–456. DOI: 10.2138/am-1995-5-605.

Solomatov, V. (2007). "Magma Oceans and Primordial Mantle Differentiation". In: *Treatise on Geophysics* 9, pp. 81–104. DOI: 10.1016/B978-0-444-53802-4.00155-X.

Stein, S. and M. Wysession (2003). *An Introduction to Seismology, Earthquakes, and Earth Structure*. Blackwell Publishing Ltd. ISBN: 9781118687451.

Stixrude, L. and C. Lithgow-Bertelloni (2005). "Thermodynamics of mantle minerals - I. Physical properties". In: *Geophysical Journal International* 162 (2), pp. 610–632. DOI: 10.1111/j.1365-246X.2005.02642.x.

— (2011). "Thermodynamics of mantle minerals - II. Phase equilibria". In: *Geophysical Journal International* 184 (3), pp. 1180–1213. DOI: 10.1111/j.1365-246X.2010.04890.x.

Stokes, H. T., D. M. Hatch, and J. D. Wells (1991). "Group-theoretical methods for obtaining distortions in crystals: Applications to vibrational modes and phase transitions". In: *Physical Review B* 43 (13), pp. 11010–11018. DOI: 10.1103/PhysRevB.43.11010.

Syracuse, E. M., P. E. van Keken, G. A. Abers, D. Suetsugu, C. Bina, T. Inoue, D. Wiens, and M. Jellinek (2010). "The global range of subduction zone thermal models". In: *Physics of the Earth and Planetary Interiors* 183 (1-2), pp. 73–90. DOI: 10.1016/j.pepi.2010.02.004.

Tange, Y., Y. Nishihara, and T. Tsuchiya (2009a). "Unified analyses for *P-V-T* equation of state of MgO: A solution for pressure-scale problems in high *P-T* experiments". In: *Journal of Geophysical Research* 114 (B3), B03208. DOI: 10.1029/2008JB005813.

Thomas, S. M., M. Koch-Müller, P. Reichart, D. Rhede, R. Thomas, R. Wirth, and S. Matsyuk (2009). "IR calibrations for water determination in olivine, r-GeO2, and SiO_2 polymorphs". In: *Physics and Chemistry of Minerals* 36 (9), pp. 489–509. DOI: 10.1007/s00269-009-0295-1.

Thomson, A. R., W. A. Crichton, J. P. Brodholt, I. G. Wood, N. C. Siersch, J. M. Muir, D. P. Dobson, and S. A. Hunt (2019). "Seismic velocities of $CaSiO_3$ perovskite can explain LLSVPs in Earth's lower mantle". In: *Nature* 572 (7771), pp. 643–647. DOI: 10.1038/s41586-019-1483-x.

Torii, Y. and S. Yoshioka (2007). "Physical conditions producing slab stagnation: Constraints of the Clapeyron slope, mantle viscosity, trench retreat, and dip angles". In: *Tectonophysics* 445 (3-4), pp. 200–209. DOI: 10.1016/j.tecto.2007.08.003.

Tschauner, O., S. Huang, S. Yang, M. Humayun, W. Liu, S. N. G. Corder, H. A. Bechtel, J. Tischler, and G. R. Rossman (2021). "Discovery of davemaoite, $CaSiO_3$-perovskite, as a mineral from the lower mantle". In: *Science* 374 (6569), pp. 891–894. DOI: 10.1126/science.abl8568.

van der Hilst, R. and H. Kárason (1999). "Compositional heterogeneity in the bottom 1000 kilometers of earth's mantle: Toward a hybrid convection model". In: *Science* 283 (5409), pp. 1885–1888. DOI: 10.1126/science.283.5409.1885.

van der Hilst, R. and T. Seno (1993). "Effects of relative plate motion on the deep structure and penetration depth of slabs below the Izu-Bonin and Mariana island arcs". In: *Earth and Planetary Science Letters* 120 (3-4), pp. 395–407. DOI: 10.1016/0012-821X(93)90253-6.

van der Hist, R., R. Engdahl, W. Spakman, and G. Nolet (1991). "Tomographic imaging of subducted lithosphere below northwest Pacific island arcs". In: *Nature* 353 (6339), pp. 37–43. DOI: 10.1038/353037a0.

Wolf, A. S., J. M. Jackson, P. Dera, and V. B. Prakapenka (2015). "The thermal equation of state of (Mg,Fe)SiO_3 bridgmanite (perovskite) and implications for lower mantle structures". In: *Journal of Geophysical Research: Solid Earth* 120 (11), pp. 7460–7489. DOI: 10.1002/2015JB012108.

Wänke, H. (1981). "Constitution of terrestrial planets". In: *Philosophical Transactions of the Royal Society of London. Series A, Mathematical and Physical Sciences* 303 (1477), pp. 287–302. DOI: 10.1098/rsta.1981.0203.

Xie, L., A. Yoneda, T. Katsura, D. Andrault, Y. Tange, and Y. Higo (2021). "Direct Viscosity Measurement of Peridotite Melt to Lower-Mantle Conditions: A Further Support for a Fractional Magma-Ocean Solidification at the Top of the Lower Mantle". In: *Geophysical Research Letters* 48 (19), e2021GL094507. DOI: 10.1029/2021GL094507.

Xie, L., A. Yoneda, D. Yamazaki, G. Manthilake, Y. Higo, Y. Tange, N. Guignot, A. King, M. Scheel, and D. Andrault (2020). "Formation of bridgmanite-enriched layer at the top lower-mantle during magma ocean solidification". In: *Nature Communications* 11 (1), pp. 1–10. DOI: 10.1038/s41467-019-14071-8.

Xu, W., C. Lithgow-Bertelloni, L. Stixrude, and J. Ritsema (2008). "The effect of bulk composition and temperature on mantle seismic structure". In: *Earth and Planetary Science Letters* 275 (1-2), pp. 70–79. DOI: 10.1016/j.epsl.2008.08.012.

Yagi, T., H. kwang Mao, and P. M. Bell (1978). "Structure and Crystal Chemistry of Perovskite-Type $MgSiO_3$". In: *Physics and Chemistry of Minerals* 3, pp. 97–110.

Zhang, J, B Li, W Utsumi, R. C. Liebermann, J. Z. Baosheng, L. W. Utsumi, and R. C. Liebermann (1996). "In situ X-ray observations of the coesite-stishovite transition: reversed phase boundary and kinetics". In: *Phys Chem Minerals* 23, pp. 1–10.

Zhang, Y., S. Fu, B. Wang, and J. F. Lin (2021). "Elasticity of a Pseudoproper Ferroelastic Transition from Stishovite to Post-Stishovite at High Pressure". In: *Physical Review Letters* 126 (2), p. 25701. DOI: 10.1103/PhysRevLett.126.025701.

Zhang, Z., L. Stixrude, and J. Brodholt (2013). "Elastic properties of $MgSiO_3$-perovskite under lower mantle conditions and the composition of the deep Earth". In: *Earth and Planetary Science Letters* 379, pp. 1–12. DOI: 10.1016/j.epsl.2013.07.034.

Chapter 2

Methods

In this thesis, I aimed to characterise the structural and elastic properties of lower-mantle minerals both at ambient conditions and at high pressure and temperature. The aim of this chapter is to describe the experimental procedures, theoretical background, and principles of data analysis involved in the study of the samples presented in this thesis. In the first section, I will focus on the experimental strategies and techniques adopted to synthesise high-quality bridgmanite samples. In the second section, the characterisation of the chemical and structural properties of crystalline materials using both in-house and large-scale facility instrumentation is described. In the third section, the preparation of diamond anvil cells for measurements of the structural and elastic properties of materials at high pressure and high temperature is presented. In the fourth section, I will then introduce the principles of linear and non-linear elasticity and equations of state used to fit experimental data and model elastic properties at high pressure and temperature, followed by a description of the theory and instrumental setup necessary for the measurement of sound wave velocities using Brillouin scattering. Lastly, in the fifth section, the thermodynamic framework used to model the chemical and elastic properties of end member mineral components and their solid solutions at high pressure and temperature is presented.

2.1 High-pressure and high-temperature synthesis experiments

All the samples employed in this study were synthesised at high-pressure and high-temperature conditions using multi-anvil techniques. In this section, I will focus on the synthesis of samples of Al-bearing bridgmanite. $MgSiO_3$ bridgmanite single crystals used for the study of sound wave velocities at high pressure and room temperature (Chapter 4) were provided by Daniel J. Frost and their synthesis and characterisation has been described elsewhere (Boffa Ballaran et al., 2012). One of the Al-bearing bridgmanite samples employed in high-pressure-temperature X-ray diffraction measurements (run I701 and sample name CC4OV2, see Table 5.1) was provided by Zhaodong Liu and synthesised following the method described by Liu et al. (2021). Hydrous Al-bearing silica polymorphs were provided by Takayuki Ishii and details about their synthesis procedure are provided in Chapter 6 and in our recent publication (Ishii et al., 2022a). The high-pressure experiment aimed at synthesising hydrous Al-phase D was also performed by Takayuki Ishii and is

described in detail in Chapter 7.

2.1.1 Synthesis of large Al-bearing bridgmanite single crystals

Bridgmanite is known to be stable at pressures in excess of 23 GPa, meaning that high-pressure devices, such as the diamond anvil cell (DAC) or the multi-anvil press, need to be employed to achieve the pressure-temperature conditions of its stability field. In addition, bridgmanite samples need to be chemically homogeneous and to have sizes of up to 100 micrometres in order for their structural and elastic properties to be accurately constrained by single-crystal methods. The multi-anvil press allows to achieve such conditions, because of the relatively large volume of synthesised samples and homogeneous temperature distribution during experiments. Bridgmanite crystals with $MgSiO_3$ composition up to 1 mm in size were synthesised at lower mantle conditions by annealing mixtures of oxides, hydroxides and/or liquid water at pressures of the lower mantle (Shatskiy et al., 2007; Okuchi et al., 2015). Large single crystals of Fe-bearing, Al-bearing, and Fe,Al-bearing bridgmanite up to several hundred micrometres were also synthesised using similar methods (Okuchi et al., 2015; Liu et al., 2021). The role of water as flux material seems therefore to be critical in the synthesis of large and homogeneous bridgmanite single crystals. However, the presence of water also leads to highly oxidising conditions, which can turn most iron into its ferric state. Moreover, the high water activity promotes the crystallisation of hydrous phases that could potentially deplete bridgmanite of Fe and/or Al (Okuchi et al., 2015; Ishii et al., 2022c). Carbonate and chloride fluxes have also been used for the high-pressure synthesis of mantle minerals (Shatskiy et al., 2009), but were never applied to Fe-bearing and Al-bearing bridgmanite. These substances have the advantage of enhancing crystal growth while keeping both the water activity and the oxygen figacity low, thus leaving the oxidation state of iron basically unaffected and avoiding the crystallisation of accessory phases.

To synthesise large Al-bearing bridgmanite single crystals, synthetic $MgSiO_3$ enstatite and reagent grade Al_2O_3 corundum were mixed together in different molar ratios (Table 2.1) under ethanol in an agate mortar. To synthesise $MgSiO_3$ enstatite, reagent grade SiO_2 and MgO in a 1:1 molar ratio were ground in an agate mortar for 30 min, placed in a Pt crucible and melted in a furnace at 1873 K for 6 h. The sample was subsequently quenched by dropping the Pt crucible in cold water to obtain a glass. The $MgSiO_3$ glass was ground

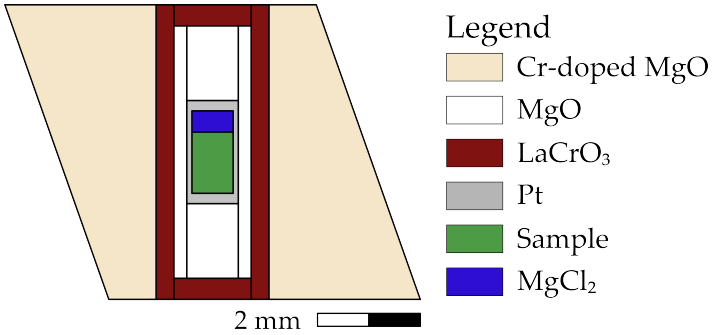

Figure 2.1. Cross sections of the cell assembly 7/3 used in high-pressure and high-temperature multi-anvil experiments aimed at synthesising large crystals of Al-bearing bridgmanite.

Table 2.1. Synthesis conditions of Al-bearing bridgmanite samples employed in this study. Brg, bridgmanite; Hym, hydrous melt; Clm, Cl-rich melt; Grt, garnet (traces).

Run	Starting material	Flux material	P (GPa)	T (K)	Duration (h)	Run products	Max grain size (μm)
I701	En95-Cor5	$Mg(OH)_2$	28	1973	6	Brg+Hym	100
S7412	En90-Cor10	$MgCl_2$	24	1873	4	Brg+Clm±Grt	100
S7464	En95-Cor5	$MgCl_2$	24	1973	3	Brg+Clm	70
S7585	En85-Cor15	$MgCl_2$	24	1773	8	Brg+Clm±Grt	70

in an agate mortar under ethanol for 1 h, then placed again in a Pt crucible and annealed in a furnace at 1473 K for 5 h to convert it to enstatite, which was later confirmed by powder X-ray diffraction. A Pt-tube capsule was then filled using approximately 80 vol.% of $MgSiO_3$-Al_2O_3 mixture and 20 vol.% of reagent grade $MgCl_2$, chosen as flux material. Before preparing the capsule, both the starting silicate mixture and the $MgCl_2$ solvent were stored at 413 K to prevent the adsorption of moisture from the air and were loaded in the Pt-tube while still warm. Each capsule was closed with Pt lids and sealed using an arc welder (Lampert PUK U3) in "micro" mode (i.e., power: 5-7%, impulse length: 5-9 ms). The capsule was then inserted in a MgO sleeve and sandwiched between MgO rods to electrically insulate it from the furnace, consisting of $LaCrO_3$ tube and lids. The furnace was placed in the centre of a Cr-doped MgO octahedral pressure medium having sides of 7 mm. A cross section of the cell assembly is shown in Figure 2.1. Experiments were carried out in the 12 MN Kawai-type multi anvil press (Sumitomo) installed at the Bayerisches Geoinstitut, University of Bayreuth. Tungsten carbide cubes (7% Co content, hawedia) with 3 mm truncated edges (7/3 assembly) were used to compress the sample under a load of 8.2 MN, corresponding to a pressure of approximately 24 GPa (Keppler and Frost, 2005), and subsequently heated to the desired temperature at a rate of $\sim$ 100 K/min. The temperature was estimated based on the power generated by the $LaCrO_3$ heater, which was calibrated in previous runs using a D-type (W3%Re-W25%Re) thermocouple. The high-temperature conditions were kept for 3-8 h (Table 2.1), after which the sample was quenched by switching off the electrical power supply and decompressed to room pressure over 15 h.

After recovering the cell assembly, each capsule was manually opened using a razorblade and the run products were observed using a polarising microscope. In all experimental runs, bridgmanite crystals measuring up to 300 μm were found in the upper and lower portion of the capsule, while grey-coloured Cl-rich quenched melt was localised in the middle of the capsule. The largest crystals often presented cracks and resulted not suitable for structural analyses and elasticity measurements. Nevertheless, single crystals of up to 100 μm and presenting no visible cracks or inclusions were also found and resulted suitable for structural characterisation. An attempt was made to double-side polish a few high-quality single crystals of Al-bearing bridgmanite for elasticity measurements. However, the samples always fractured during polishing, making the crystal platelets

unusable. Smaller samples with dimensions of 10-20 μm were also found to be of very high quality and were later employed in high-pressure and high-temperature single-crystal X-ray diffraction measurements aimed at determining the thermal equation of state of Al-bearing bridgmanite.

2.2 Chemical and structural characterisation of minerals

In this section, I will describe the analytical techniques that were employed in the characterisation of the chemical composition and structural properties of mineral phases at ambient and/or high-pressure conditions. As mineral properties change as a function of chemical composition and concentration of defects, an adequate characterisation of samples at ambient conditions is critical to correctly interpret results and trends obtained at high pressures and temperatures. While the bulk chemical composition and homogeneity of a sample can be inferred by electron probe microanalyses, the concentration of hydrogen and the oxidation state of iron, which are of particular interest for mantle minerals, need to be constrained using additional analytical methods, such as infrared spectroscopy and Mössbauer spectroscopy. The detailed characterisation of the crystal and defect chemistry of minerals is also complementary to volume and structural information obtained by X-ray diffraction methods, and can be used to infer their stability, density and physical properties as a function of pressure and temperature.

2.2.1 Chemical analyses by electron microprobe

The bulk chemical composition and homogeneity of samples synthesised at high pressure and temperature can be determined using the electron probe microanalyser (EPMA). When an electron beam is focused on the surface of the sample, it is scattered both elastically and inelastically, depending on the topology and mean atomic composition of the sample, and stimulates the emission of characteristic X-ray, carrying information on the elemental composition of the sample. The EPMA is equipped with wavelength dispersive spectrometers (WDS) that identify the emitted characteristic lines and quantify their intensity. To do so, each WDS employs a crystal analyser that is cut and oriented along a given crystallographic plane which Bragg-diffracts (see equation 2.1) the incoming X-ray signal. The crystal analyser is then rotated over a certain angular range over which the X-ray intensity is integrated. Quantitative determinations of the sample composition is finally made by comparing the measured intensities of each characteristic X-ray lines with those measured in a reference standard material with known composition. For a more detailed description of the working principles and potential applications of this technique, see Reed (2005). Here, I will simply list the analytical conditions employed for the analysis of the high-pressure phases of interest for this thesis.

Table 2.2. Parameters used for electron probe microanalyses.

			Counting time (s)		
Element	Spectrometer	Fluor. line	Sample	Background	Standard material
Mg	TAP	Kα	10	5	$MgSiO_3$ enstatite
Si	TAP	Kα	10	5	$MgSiO_3$ enstatite
Al	TAP	Kα	10	5	Al_2O_3 corundum
Fe	LiFH	Kα	10	5	Fe metal
Cl	LiFH	Kα	10	5	$Pb_5(VO_4)_3Cl$ vanadinite

Prior to the EPMA measurements, the samples were embedded in epoxy resin, polished on one side until fully exposed and coated with a 12 nm-thick layer of carbon. Quantitative chemical analyses were subsequently carried out on a JEOL JXA-8200 EPMA operated at an acceleration voltage of 10 kV and beam current of 5 nA, due to the sensitivity of high-pressure phases to electron beam damage. A full list of measured elements, as well as utilised standards and spectrometers for Al-bearing bridgmanite and Fe-bearing Al-phase D is provided in Table 2.2.

2.2.2 Mössbauer spectroscopy

As mantle minerals often contain Fe, it is critical to assess the proportion of ferrous (Fe^{2+}) and ferric (Fe^{3+}) iron in samples recovered from high-pressure and high-temperature experiments in order to accurately model mineral properties as a function of chemical composition and cation substitutions. For solid samples, this can be carried out by Mössbauer spectroscopy, which makes use of the recoilless nuclear resonance absorption of gamma rays by ^{57}Fe nuclei, a phenomenon also known as Mössbauer effect (Mössbauer, 1958). In a conventional Mössbauer spectrometer, gamma rays are obtained from the decay of ^{57}Co to ^{57}Fe by electron capture (half-life $\sim$ 272 days). During this process, the ^{57}Fe daughter nucleus decays to an excited energy level of 136.3 keV, followed by deexcitation to either a 14.4 keV energy level (91% probability) or directly to the ground state (9% probability), as shown in Figure 2.2. The 14.4 keV excited state has a half-life of 97.7×10^{-9} s and its decay to the ground state results either in the excitation of an electron orbiting around the nucleus (89% probability) or in the emission of a gamma photon (11% probability). The emitted 14.4 keV gamma rays are then used to probe the sample, where ^{57}Fe nuclei can be excited via Mössbauer effect and the energies and intensities of the absorption peaks carry information on the oxidation state, atomic environment, and relative abundance of Fe species in the sample. The exact nuclear resonance energy of ^{57}Fe is affected by the interaction between the nucleus and the surrounding electrons, meaning that in general it will be different in the source and in the absorber (i.e., the sample). This difference, called isomer shift (IS) or central shift (CS), arises from electrostatic interactions between the nuclear and electronic charge distributions and depends mainly on the density of *s*-electrons around the nucleus. If the point symmetry at the nucleus is not cubic, the interaction of the nuclear quadrupole

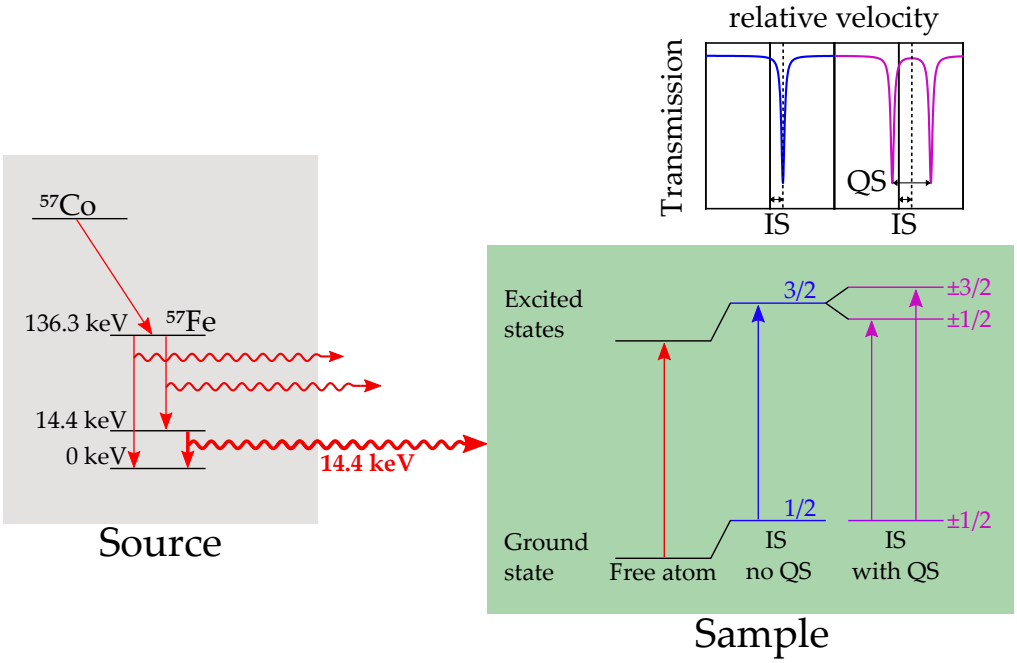

Figure 2.2. Schematic representation of the Mössbauer effect for ^{57}Fe (modified from Dyar et al., 2006). On the left, illustration of the decay process of ^{57}Co to ^{57}Fe leading to the emission of 14.4 keV gamma rays. On the right, effect of the hyperfine parameters isomer shift (IS) and quadrupole splitting (QS) on the energy levels of ^{57}Fe in the absorber (i.e., the sample), and their expression in the Mössbauer spectrum. Numbers in blue and purple indicate the possible nuclear spin states of ^{57}Fe for each energy level.

moment with the electric field gradient existing between Fe and its nearest neighbours will cause the excited nuclear energy levels to split into two sublevels. This phenomenon, referred to as quadrupole splitting (QS), is defined as the energy difference between the two nuclear energy sublevels (Figure 2.2). Therefore, in order to obtain information on the IS, the QS, and the relative abundance of the Fe species present in the sample, a sufficiently wide energy range needs to be probed. This is practically achieved by moving the ^{57}Co source relatively to the absorber, which causes the 14.4 keV line to be shifted to higher and lower energies by Doppler effect. As the energy shift depends on the velocity of the source, the horizontal axis of Mössbauer spectra is typically reported in mm/s, with IS and QS values given with respect to a reference standard material (e.g., α-Fe foil). As the absorption of 14.4 keV gamma rays is directly proportional to the concentration of ^{57}Fe in the absorber, the area of the absorption peaks in a Mössbauer spectrum yields the exact proportion of absorbing species in the sample, e.g., the ratio of Fe^{2+} and Fe^{3+} in a single-phase mineral sample. For a more comprehensive treatment of the principles of Mössbauer spectroscopy see McCammon (2004) and Dyar et al. (2006).

In this thesis, Mössbauer spectroscopy was used to characterise the oxidation state of iron in Fe-bearing Al-phase D (Chapter 7). As the amount of material recovered from

high-pressure multi-anvil experiments is often limited, a Mössbauer milliprobe operated in transmission mode and equipped with a high specific activity source was used (McCammon, 1994). Inclusion-free phase D single crystals were arranged to form a mosaic with 0.5 mm diameter and sandwiched between two pieces of transparent plastic sheet using silicone grease. A Ta mask with a 0.5 mm hole was applied in front of the plastic holder to ensure that only the signal transmitted through the sample was collected by the detector. Since the concentration of Fe in the sample was relatively low, the spectrum was acquired for several days until the desired signal to noise ratio was obtained. Data analysis was carried out using *MossA* (Prescher et al., 2012), where the experimental data were fitted using an asymmetric Lorentzian doublet and the full transmission integral (see Figure 7.1). The refined hyperfine parameters are compatible with those of Fe^{3+} in octahedral coordination, while the asymmetricity is likely due to the sample being constituted by few large grains rather than a fine powder with randomly oriented crystallites.

2.2.3 Single-crystal X-ray diffraction

According to the International Union of Crystallography[1], a crystal is, by definition, a material that exhibits essentially a sharp diffraction pattern or, alternatively, a solid constituted of atoms and/or molecules with a long-range ordered arrangement. The two definitions are equivalent for most crystals and reveal the critical importance of diffraction methods in the characterisation of crystalline materials. Interpreting the diffraction pattern of a crystal or aggregate of crystals, typically obtained using radiations with wavelengths on the order of 1 Å (e.g., photons, electrons, neutrons), constitutes the most utilised approach to the identification and structural characterisation of crystalline materials. The degree of crystallinity of a crystal, its unit-cell lattice parameters, and the exact arrangement of atoms in the crystal structure can be derived by looking at different aspects of the diffraction pattern. When this kind of information is collected over a range of different pressure and/or temperature conditions, insights on the stability and on the thermodynamic and physical properties of the crystal can also be obtained. Known the wavelength λ of the utilised X-ray radiation, the measured 2θ angle between the transmitted and diffracted beams carries information on the distance between a given family of crystallographic planes spaced by a constant value d. This relation, formulated by W.H. Bragg and W.L. Bragg between 1912 and 1913 (Bragg and Bragg, 1913), is known as Bragg's law and constitutes the fundamental equation of X-ray crystallography:

$$n\lambda = 2d\sin\theta \tag{2.1}$$

with n neing an integer number. To categorise the different families of crystallographic planes within a given crystal, indices are assigned to each distance d observed in the diffraction pattern. Indices depend on the intercepts of these planes on the three edges **a**, **b**, and **c** of the unit cell, i.e., the smallest portion of crystal containing all its characteristic symmetry elements, including translational symmetry. For orthorhombic crystals, such as bridgmanite

[1] https://dictionary.iucr.org/Crystal

and post-stishovite, peaks are indexed so that they satisfy the following relation:

$$\frac{1}{d_{hkl}^2} = \frac{h^2}{a^2} + \frac{k^2}{b^2} + \frac{l^2}{c^2} \tag{2.2}$$

with *h*, *k*, and *l* being integer numbers known as Miller indices and *a*, *b*, and *c* corresponding to the length of the three edges of the unit cell. It follows that by assigning the Miller indices to each peak or spot appearing in an experimentally measured powder or single-crystal diffraction pattern, respectively, it is possible to identify the phases constituting the investigated sample and obtain their unit-cell lattice parameters and volume. This procedure is used both to characterise samples recovered from high-pressure and high-temperature synthesis experiments and to define pressure-temperature-volume relations of samples loaded in high-pressure cells (see Section 2.4). For a description of modern powder diffraction mwthods applied to mineralogy, see Altomare et al. (2017). In the present thesis, diffraction patterns of crystalline materials were mainly acquired using single-crystal diffractometers or experimental setups optimised for measurements of single crystals. Therefore, only aspects related to single-crystal diffraction will be discussed.

Single-crystal diffractometers

A single-crystal diffractometer comprises three main elements: a source, a goniometer, and a detector. The source, which can be a conventional X-ray tube, a rotating anode, or a synchrotron facility, produces the X-ray beam. One or multiple sets of X-ray optics are typically used to collimate and focus the X-ray beam on the sample, which in turn is mounted on the goniometer. The goniometer consists of one to several motorised circles that allow to rotate the sample while illuminated by the X-ray beam. In this way, diffraction conditions for several *hkl* planes can be achieved and the intensities of the diffracted beams recorded on the detector. In this thesis, single-crystal diffractometers with 4 motorised circles were used for in-house measurements (see Chapters 4, 5, and 7), while the experimental setup at the beamline P02.2 of the PETRA-III synchrotron in Hamburg, Germany (see Chapters 5, 6, and 7) consisted of a 1-circle device only capable of rotating the sample or high-pressure cell about their vertical axis (Liermann et al., 2015). In a 4-circle diffractometer, in general, one circle moves the detector and the remaining three drive the crystal to diffraction conditions. The angular relations for 4-circle diffractometers with Eulerian geometry, whose angles are referred to as 2-theta (2θ), omega (ω), chi (χ), and phi (ϕ), can be found in Busing and Levy (1967) and are schematically represented in Figure 2.3. The 2θ and ω circles are coaxial and rotate the detector and the χ circle, respectively, about the z-axis of the Cartesian reference system of the instrument. The χ circle is mounted on the ω motor and, therefore, its axis is always perpendicular to that of ω. Lastly, the ϕ motor is mounted on the χ circle and rotates the goniometer head where the sample is mounted about its vertical axis. A variation of this setup is constituted by the kappa (κ) geometry, where the χ circle is replaced by a κ circle which is inclined by a fixed angle α with respect to the z-direction of the diffractometer

reference system (e.g., Paciorek et al., 1999).

Single-crystal diffractometers with Eulerian geometry equipped with point detectors were used in this thesis to characterise the unit-cell lattice parameters of crystals with high precision and accuracy at both ambient and high-pressure conditions. The high accuracy of single-crystal diffraction measurements with a point detector is achieved by accounting for experimental aberrations (e.g., crystal offset from the centre of the goniometer, incorrect zero positions of 2θ, ω, and χ) that can be refined if the same reflection is measured in several equivalent orientations, allowing for the true diffraction angles to be calculated. Known the orientation of the crystal in the Cartesian reference system of the diffractometer (i.e., its UB matrix), there is an infinite number of combinations of ω, χ, and ϕ that can be calculated to bring a given set of *hkl* planes into diffraction conditions (Busing and Levy, 1967). If the value of one of these three circles is fixed, a set of 8 equivalent angular combinations (i.e., 2θ and the two remaining circles) is calculated, for which Bragg's law is satisfied (King and Finger, 1979). In diffractometers operated in "bisecting" mode, ω is coupled with 2θ and its position is zero when the diffraction vector is bisecting the directions of incident and diffracted beam (Busing and Levy, 1967). This means that the absolute value of ω at diffraction conditions is half of 2θ, or simply θ. Alternatively,

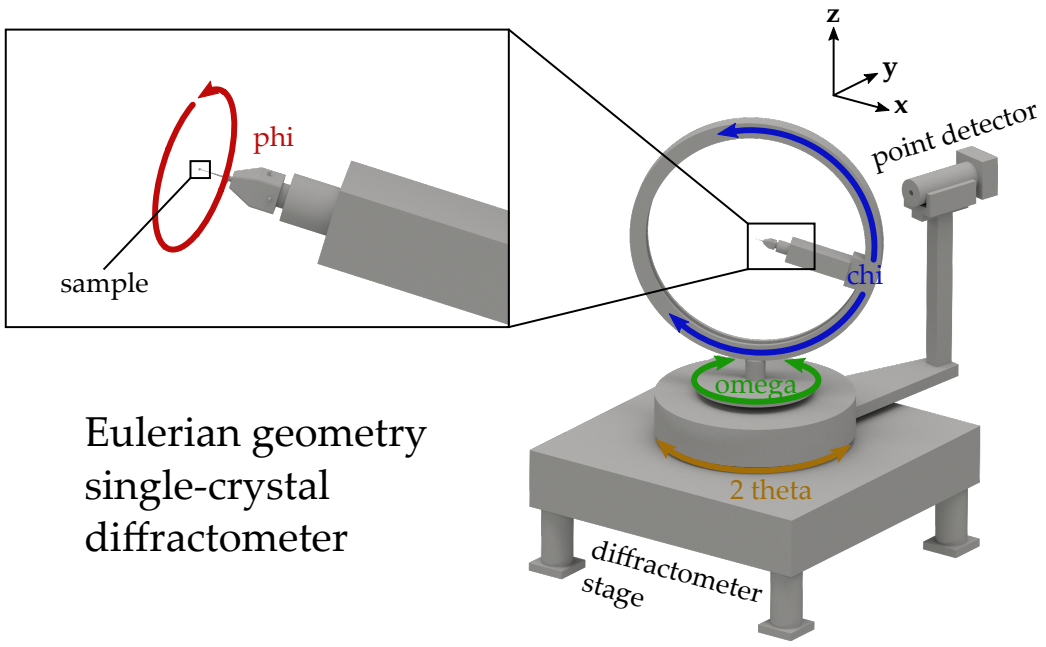

Figure 2.3. Simplified representation of the Eulerian goniometer and detector components of a single-crystal diffractometer. The spatial relations between the diffractometer angles and the Cartesian reference system is shown, according to the conventions reported by Busing and Levy (1967).

in the "fixed-ϕ" mode, ϕ is constrained to be either 0° or 180°, with 2θ, ω, and χ being free to vary. The 8-position centring procedure in fixed-ϕ mode is particularly useful for measurements in the DAC, where the sample alignment procedure using a camera or telescope is not as accurate as for crystals in air mounted on glass fibres. In this thesis, two Huber diffractometers with Eulerian geometry were used, both installed at the Bayerisches Geoinstitut, University of Bayreuth, and driven by the software SINGLE (Angel and Finger, 2011). The first diffractometer is equipped with a conventional Mo-Kα X-ray glass tube and was only used to characterise samples at ambient conditions in bisecting mode. The second diffractometer is coupled with a FR-E+ SuperBright ultra-high intensity rotating anode from Rigaku (Mo-Kα radiation) and is equipped with multilayer VaryMax^{TM} X-ray optics arranged in Kirkpatrick-Baez geometry (Trots et al., 2011). The Eulerian goniometer of this diffractometer is part of the Brillouin scattering setup, described in Section 2.4.5, and was used mainly for measurements in the DAC at high-pressure.

Diffractometers with κ geometry are better suited for measurements with position-sensitive (e.g., charge-coupled device, CCD) detectors as they grant a higher freedom of movement than Eulerian goniometers and are much more compact, thus allowing for shorter sample-detector distances. This has the effect of enhancing the intensity of the diffracted X-rays when they hit the detector and increasing the coverage of reciprocal space recorded with each scan, which turns to be particularly useful to collect intensity data up to high 2θ angles to be used for structural refinements (see Section 2.2.3). In this thesis, a κ geometry Xcalibur diffractometer (Rigaku, Oxford Diffraction) equipped with Mo-Kα and a graphite crystal monochromator to select only the Kα_1 line of Mo was employed. A Sapphire2 CCD detector was used to record the diffracted beams, with the sample-detector distance set to either 41 or 70 mm and calibrated using a ruby (i.e., Cr-doped α-Al_2O_3) single-crystal standard.

Assessment of crystal quality and orientation procedure

In order to assess whether a single crystal is suitable for physical properties measurements at ambient conditions, as well as for compression experiments in the DAC, preliminary X-ray diffraction measurements need to be performed to determine its degree of crystallinity. This is typically achieved by measuring the rocking curve (or diffraction profile) of the sample and looking at its peak shape. To do so, a candidate crystal is first observed under both parallel and cross polarised light with an optical microscope to ensure that no visible cracks, inclusions, or twinning are present. Depending on the chemical composition, crystals of the order of 70-150 micrometres typically provided a good compromise between high peak intensities and low absorption using the in-house diffractometers described above. Once a crystal is selected, it is then fixed to the tip of a silica glass fibre with a diameter of 10-50 μm using super glue and is then mounted on a goniometer head for diffraction measurements. A preliminary data collection is carried out on the κ geometry Xcalibur diffractometer to confirm the absence of twinning and determine a preliminary

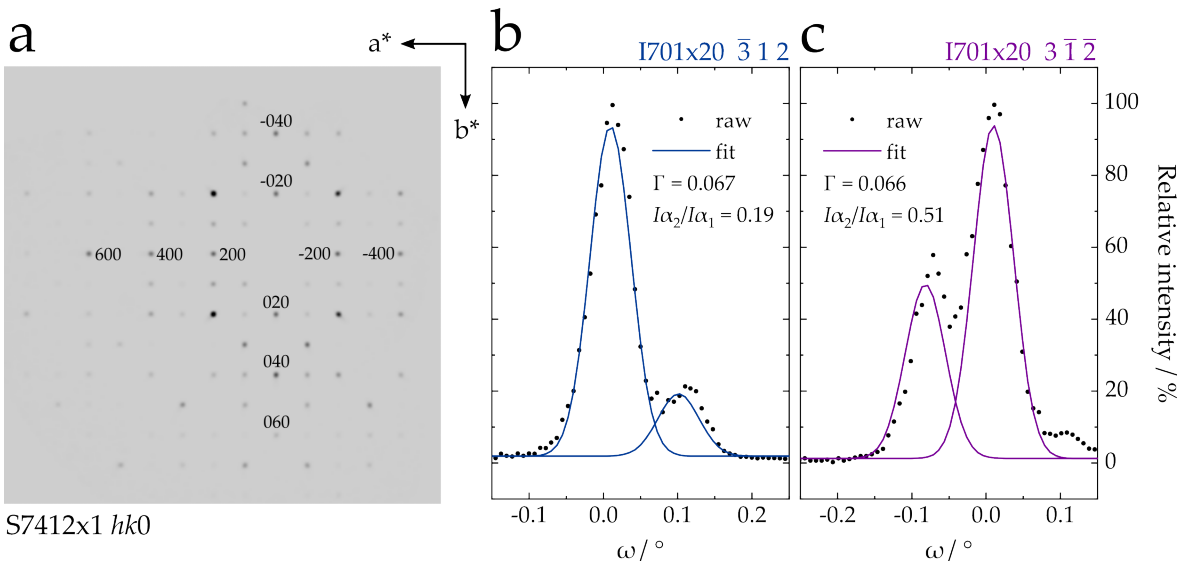

Figure 2.4. (a) Unwarp reconstruction of the reciprocal *hk*0 plane of a high-quality single crystal of Al-bearing bridgmanite of approximately 80 μm obtained using the κ geometry Xcalibur single-crystal diffractometer equipped with an area detector. (b-c) Peak profiles a 60 μm single crystal of Al-bearing bridgmanite measured on a Eulerian geometry Huber single-crystal diffractometer upon ω rotations at positive and negative 2θ values. The different intensity ratios ($I\alpha_2/I\alpha_1$) and relative positions of Kα_2 with respect to Kα_1 stem from the geometry of the VaryMax^{TM} focusing optics.

UB matrix. The crystal is then transferred to one of the Eulerian geometry Huber diffractometers, where the UB matrix is used to calculate the approximate position of a set of *hkl* reflections. Several diffraction profiles are recorded by rotating the sample about the ω circle and Gaussian line shapes are used to fit the contribution of the α_1 and α_2 lines (Angel, 2003). The larger is the width of the peak profile, the higher is the crystal mosaicity, which is the degree of misorientation between crystalline domains inside a single crystal. Crystals with Gaussian peak shapes having a full width half maximum (FWHM or Γ) below 0.1° in ω were usually considered to be ideal for the purposes of this thesis. Examples of a high-quality X-ray diffraction two-dimensional pattern and one-dimensional ω profiles of Al-bearing bridgmanite samples are shown in Figure 2.4.

Measurements of the physical properties of single crystals using spectroscopic techniques sometimes require that the sample is a platelet having a plane normal with specific *hkl* indices. This is the case, for example, of samples employed for Brillouin scattering (Chapter 4) and polarised infrared spectroscopy measurements (Section 2.2.4). After assessing the quality of the single-crystal sample on a Eulerian geometry single-crystal diffractometer, the circles are driven to diffraction conditions for the desired *hkl* plane. The Huber diffractometer used for this purpose has its reference *z*-axis not in the vertical direction, but parallel to the ground. Consequently, negative χ values result in the glass needle – and thus the sample – pointing downwards. Since the diffractometer operates in "bisecting" mode, the selected *hkl* plane is set parallel to the ground by driving the ω motor from 0 to -θ. At this point, a glass slide lying parallel to the ground and to the selected

hkl plane is placed below the crystal, which can then be embedded in UV glue previously placed on top of the glass slide. Single-crystal X-ray diffraction measurement of the samples after double-side polishing typically show that the crystal orientation is retained within ± 2°.

Structural refinements

While the positions of Bragg reflections in reciprocal space (or diffraction angles in direct space) carry information on the unit-cell lattice parameters of a crystal, it is the intensity of the diffracted X-rays that allow us to gain insights on the exact arrangement of atoms within crystalline samples. The intensity of a given *hkl* reflection (I_{hkl}) in a single-crystal diffraction experiment is given by (Giacovazzo et al., 2011):

$$I_{hkl} = I_0 k_1 k_2 LPTE \left|F_{hkl}\right|^2 \tag{2.3}$$

where I_0 is the intensity of the incident beam, k_1 is a combination of universal constants (i.e., mass, charge, and speed of the electron), k_2 depends on the wavelength, the volume of the crystal and of its unit cell, L and P are the Lorentz and polarisation factors and depend on the diffraction angle, T is the transmission factor and depends on the X-ray absorption coefficient of the material, E is the extinction factor and F_{hkl} is the structure factor, which carries all the information on the distribution of atoms in the unit cell of the crystal.

The intensities of *hkl* reflections obtained from a given single-crystal data collection were integrated from two dimensional scans using *CrysAlisPro* (Rigaku, Oxford Diffraction). First, a peak search algorithm was employed to find all the reflections recorded during the data collection. In the case of high-pressure measurements in the DAC, undesired signals arising from the interaction of the X-ray beam with the diamond anvils, the gasket, and/or the pressure medium are also present and need to be excluded from the reflection list in order to properly index the reflections of the sample. This was practically done using the Ewald Explorer tool available in *CrysAlisPro*, where a three-dimensional representation of the reciprocal space allows to identify and manually select different domains of reflections, thus isolating reflections belonging to the sample from those generated by the diamond anvil, pressure transmitting medium, and gasket material (Figure 2.5). After the sample peaks were correctly indexed, their intensities were integrated and corrected for Lorentz and polarisation factors. Intensities also need to be corrected to account for absorption from the crystal in air or from the DAC in high-pressure datasets, which depends on the path of the X-ray beam before and after being diffracted by the sample. To do so, an empirical absorption correction based on spherical harmonics was applied using the Scale3 Abspack algorithm implemented in *CrysAlisPro*. Finally, the corrected structure factors were calculated. To assess the quality of the integrated intensities, the discrepancy between symmetry-equivalent reflections was evaluated through the R_{int} factor, defined as:

$$R_{\text{int}} = \frac{\sum \left|F^2_{\text{obs}} - \left\langle F^2_{\text{obs}} \right\rangle\right|}{\sum F^2_{\text{obs}}} \tag{2.4}$$

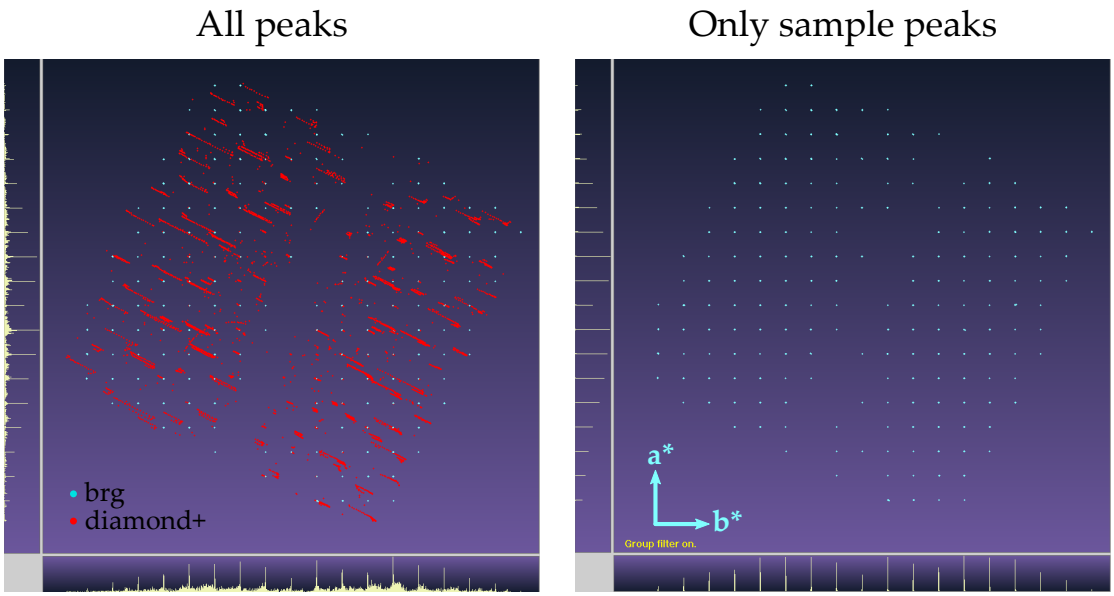

Figure 2.5. Representation of the reciprocal space of Al-bearing bridgmanite using the Ewald Explorer tool of *CrysAlisPro*. The dataset was collected at 50 GPa and 300 K in a DAC loaded with He as pressure transmitting medium. Peaks belonging to the bridgmanite (brg) sample are shown in cyan, while signals from the diamond anvils, pressure transmitting medium and Re gasket, as well as background noise (diamond+) are shown in red.

where the angled brackets indicate the averaged structure factor over a given set of symmetry-equivalent reflections. High-quality R_{int} values are typically below 0.05 (or 5%), while higher values suggest either a poorly diffracting sample, an under-exposed sample, or wobbling of the sample in and out of the X-ray beam. For a detailed description of how to recognise such issues and fix the collection strategy, see Bykova (2015).

The structure factor of a unit cell consisting of n atoms for a given hkl reflection can be written as the sum of scattered radiation from each atom j contained in the unit cell:

$$F_{hkl} = \sum_{j=1}^{n} f_{0,j} \exp\left[-B_j \left(\frac{\sin\theta}{\lambda}\right)^2\right] \exp\left[2\pi i \left(hx_j + ky_j + lz_j\right)\right] \tag{2.5}$$

where $f_{0,j}$ is the scattering factor of the j^{th} atom at $\theta = 0$, λ is the wavelength of the diffracted X-rays, and B_j takes into account the spreading of charge (i.e., the distribution of electrons) around the equilibrium position of the j^{th} atom (x_j,y_j,z_j) in direct space due to thermal motion or structural disorder. In general, B takes the form of a 3×3 matrix (β_{st}) whose entries are called anisotropic displacement parameters (ADPs) and describe the three-dimensional distribution of charge around the crystallographic site. In some cases, such as high-pressure experiments, the low ratio of observed reflections to refined parameters (e.g., less than 7) does not allow to accurately constrain all the entries of the β_{st} matrix. In such cases, a spherical charge distribution is preferred, whose radius is defined as the isotropic displacement

parameter (β_{iso} = B). The distribution of electron density (ρ) in direct space around a given (x,y,z) position is related to structure factors through a Fourier transform:

$$\rho_{xyz} = \frac{1}{V} \sum_{h,k,l} F_{hkl} \exp\left[-2\pi i \left(hx + ky + lz\right)\right] \tag{2.6}$$

with V being the unit-cell volume of the crystal.

In this thesis, structural analyses were carried out using the software package *SHELX* (Sheldrick, 2015b; Sheldrick, 2015a) in the *Shelxle* graphic user interface (Hübschle et al., 2011). In a structural refinement, atomic positions and displacement parameters (isotropic or anisotropic) are refined so that the difference between observed (F_{obs}) and calculated (F_{calc}) structure factors is minimised. Additional parameters, known as site occupancy factors, can account for the presence of vacancies or the coexistence of different atomic species at a given crystallographic site. Additionally, primary and secondary extinction of X-ray (E factor in equation 2.3), arising from the size and degree of misorientation of crystalline domains within a single-crystal sample, respectively, can be corrected by refining an extinction parameter (EXTI), which is especially useful in the analysis of high-pressure data collected in the DAC. Discrepancy factors (or crystallographic R factors) are used to express the mismatch between F_{obs} and F_{calc} and, therefore, between the observed intensities and the refined structural model:

$$R_1 = \frac{\sum ||F_{obs}| - |F_{calc}||}{\sum |F_{obs}|}, \quad wR_2 = \sqrt{\frac{\sum w \left(F_{obs}^2 - F_{calc}^2\right)^2}{\sum w \left(F_{obs}^2\right)^2}} \tag{2.7}$$

where w is a weighting factor calculated as a function of the scaling parameters a and b:

$$w = \frac{1}{\sigma^2 \left(F_{obs}^2\right) + \left(aP\right)^2 + bP}, \quad P = \frac{\max\left(F_{obs}^2, 0\right)}{3} \tag{2.8}$$

The goodness of fit (*GooF* or S), equal to the square root of the chi-square value (χ^2), can also be obtained as:

$$S = \sqrt{\chi^2} = \sqrt{\frac{\sum w \left(F_{obs}^2 - F_{calc}^2\right)^2}{n - p}} \tag{2.9}$$

where n and p are the number of reflection and number of refined parameters, respectively. Threshold values indicating a well-converged refinement and reliable structural model are typically 0.05 (or 5%) and 0.8-1.2 for R_1 and S, respectively.

2.2.4 Fourier transform infrared spectroscopy

Hydrogen can be incorporated in nominally anhydrous minerals as structural defects (i.e., hydroxyl groups), affecting the thermodynamic and physical properties of mantle rocks. O-H bonds in minerals have vibrational frequencies of the order of 2600-3700

cm^{-1} (Libowitzky, 1999) and can be excited by absorbing infrared light. Therefore, the concentration of hydroxyl species in minerals is often quantified by measuring the intensity of the absorption bands related to O-H stretching modes in infrared spectra by applying the Beer-Lambert law (e.g., Libowitzky and Rossman, 1996). As the orientation of O-H bonds in the crystal structure is anisotropic, oriented crystal sections of minerals can be probed with polarised infrared radiation to infer the orientation of the O-H bond vectors in the crystal structure (Libowitzky and Rossman, 1996). Determining the concentration of the absorbing O-H species in the sample requires knowledge of the molar absorption coefficient (ε) of the mineral of interest. As the O-H distance and O-H$\cdots$O angle typically affect the frequency at which the absorption bands are observed (Libowitzky, 1999), mineral-specific calibrations are often required to convert the intensity of absorption bands into water contents. For most upper mantle minerals, ε values are well known and calibrated using complementary techniques, such as second ion mass spectrometry (SIMS) and elastic recoil detection analysis (ERDA) (e.g., Thomas et al., 2009; Withers et al., 2012). For mineral phases stable at mantle transition zone and lower mantle conditions, on the other hand, such calibrations are not always available. In this case, non-mineral-specific calibrations have been often used (e.g., Bolfan-Casanova et al., 2000; Litasov et al., 2007a)S, which rely on empirical relations between the frequency of O-H stretching modes and the known molar absorption coefficients of selected nominally anhydrous and hydrous phases (Paterson, 1982; Libowitzky and Rossman, 1996).

Fourier-transform infrared spectroscopy (FTIR) was used in this thesis to determine the water concentration in Al-bearing silica single-crystals. According to the dimension of the synthesised crystals, FTIR measurements were carried out on randomly oriented crystal platelets or platelets oriented parallel to the (100) and (010) crystallographic planes. Each platelet was polished on both sides to obtain slices approximately 10 μm thick. Further details on the sample preparation procedure are provided in Chapter 6 and in our recent publication (Ishii et al., 2022b). The setup used to acquire FTIR spectra consisted of a Bruker IFS 120 HR spectrometer coupled to an infrared microscope with all-reflective optics. A tungsten lamp was used as light source, while absorption spectra were recorded on a high-sensitivity, narrow-band MCT detector. Spectra were collected between 1000 and 5000 cm^{-1} with a resolution of 4 cm^{-1} by averaging 100 to 200 scans. A manual baseline subtraction was operated using a script in the *OriginPro2021* software (OriginLab corporation, Northampton, MA, USA). Few mineral-specific calibrations for Al-bearing stishovite have been proposed so far (Pawley et al., 1993; Thomas et al., 2009), which predict higher molar absorption coefficient of water relative to the empirical relations of Paterson (1982) and Libowitzky and Rossman (1996), resulting in up to 50% lower water concentration estimates. Note, however, that SIMS measurements were performed only on deuterated samples due to the low concentration of H in hydrogenated stishovite (Pawley et al., 1993) and the derived ε value carries significant uncertainties. Similarly, confocal micro-Raman spectroscopy measurements by Thomas et al. (2009) were conducted on samples bearing less than 200 ppm wt. H_2O and carried similarly large uncertainties. Therefore, the empirical relation proposed

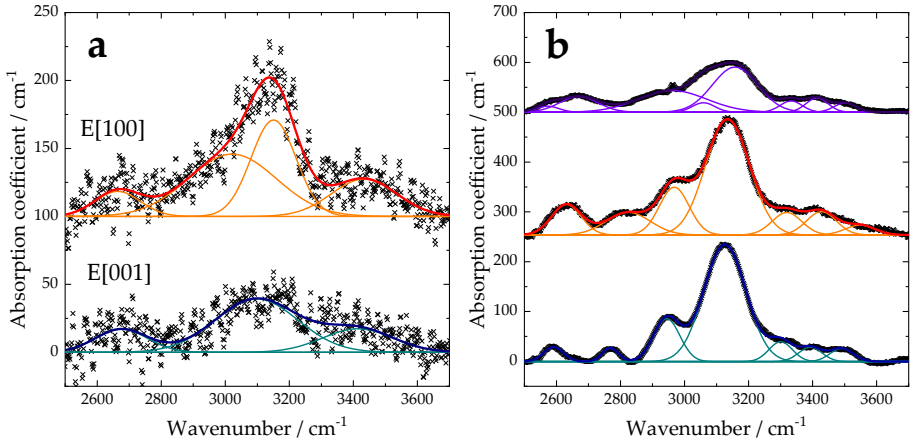

Figure 2.6. Example of polarised (a, sample I1072) and unpolarised (b, sample I1063) FTIR spectra of hydrous Al-bearing silica samples studied at high pressure in Chapter 6.

by Paterson (1982) was used instead, similarly to some of the relevant previous studies on stishovite samples (Bolfan-Casanova et al., 2000; Litasov et al., 2007a):

$$C_{\mathrm{H_2O}} = \frac{X_i}{150\zeta} \int \frac{K(\nu)}{3780 - \nu} d\nu \tag{2.10}$$

where $C_{\mathrm{H_2O}}$ is the water concentration in ppm wt., ζ is an orientation factor equal to 1 for polarised spectra and 1/3 for unpolarised spectra, X_i depends on the density of the sample, ν is the wavenumber and $K(\nu)$ is the absorption coefficient (i.e., measured absorbance divided by sample thickness) expressed in cm^{-1}. An example of polarised and unpolarised FTIR spectra collected on hydrous Al-bearing stishovite and post-stishovite at ambient conditions is shown in Figure 2.6.

2.2.5 Raman spectroscopy

Raman scattering is the process of inelastic scattering of light by internal vibrations in molecules or lattice vibrations (phonons) in ordered crystalline materials (Raman and Krishnan, 1928). At room temperature, only vibrations in the lowest-energy level (ground state) are present. However, upon irradiation by visible light, photons are absorbed to excite virtual higher-energy states that are only defined by the frequency of the incident light (ω_i). If a photon is immediately re-emitted and the molecule reverts to its ground state, the frequency of the incident and scattered photon (ω_s) is the same and the process is called Rayleigh scattering. Raman scattering, on the other hand, occurs when the excitation or de-excitation of the virtual state involves the transition to or from a higher-energy vibrational level. Thus, ω_s will differ from ω_i by an amount equal to the frequency (ω) of the vibrational state involved. In the case of excitation, ω_s = ω_i - ω and the process is referred to as a Stokes event. Conversely, an anti-Stokes event occurs upon de-excitation and is defined by ω_s = ω_i + ω. Vibrational levels in molecules and crystals are quantised,

i.e., only certain energy levels (and thus frequencies) are allowed. The motion of atoms in such states can be described assuming that their displacement from the equilibrium position is well represented by a harmonic oscillator. In this sense, the integer multiples of the characteristic frequency of the oscillator correspond to the allowed energy levels in the molecule or crystal. From an atomistic point of view, Raman scattering is related to how oscillations of atoms around their equilibrium positions affect the polarisability of the molecule or structural unit when irradiated with an oscillating electric field. This process is analogous to that discussed later for Brillouin scattering (see Section 2.4.5). In particular, if the derivative of the polarisability with respect to the displacement for a given vibrational mode is non-zero, then the mode is Raman-active. For a more detailed description of the physical principles of this technique, see for example Rull (2012).

Vibrational modes in crystals depend on the crystal symmetry and, in particular, they are invariant with respect to a given subset of symmetry elements of the crystal point group. This means that each vibrational mode will comply only with a given subset of symmetry elements. This is particularly useful when studying structural phase transitions driven by changes in pressure and/or temperature. In fact, structural phase transitions follow the same symmetry rules as vibrational modes and thus are associated to the same irreducible representations[2] (Stokes et al., 1991; Carpenter and Salje, 1998; Rull, 2012). It follows that when the point group symmetry of a crystal changes, this will have direct consequences for the type and number of Raman-active modes. Thus, phase transitions can be identified by looking at the appearance, disappearance or splitting of Raman-active modes in the Raman spectrum as a function of pressure and/or temperature. A special case is then represented by so-called soft modes. In general, ω of a given Raman mode scales as the square root of the force constant of chemical bonds. Therefore, at high pressure, ω generally increases as a result of atoms being pushed closer and closer to each other (see also Section 2.4.2). If, however, the symmetry of a given mode is the same as the irreducible representation associated with the phase transition, the frequency of that mode will progressively decrease as the crystal approaches the transition pressure or temperature. When the crystal undergoes the phase transition, either the pressure/temperature derivatives of the frequency of the soft mode change abruptly or the vibrational mode vanishes. Thus, the transition pressure (P_C^*) or temperature (T_C^*) can be found by calculating the interception between the trends of the two equivalent vibrational modes in the high- and low-symmetry phases (e.g., Kingma et al., 1995).

In this thesis, Raman spectroscopy was used to characterise samples of hydrous Al-bearing silica at both room and high pressure to understand the effect of chemical impurities (i.e., H and Al) on the ferroelastic transition of tetragonal stishovite to orthorhombic post-stishovite (see Chapter 6). Measurements were performed on Dilor XY Spectrometer equipped with a 50× microscope objective and a 1800 groove/mm diffraction grating

[2] A complete list of the irreducible representations of point groups can be found at: https://global.oup.com/uk/orc/chemistry/qchem2e/student/tables/

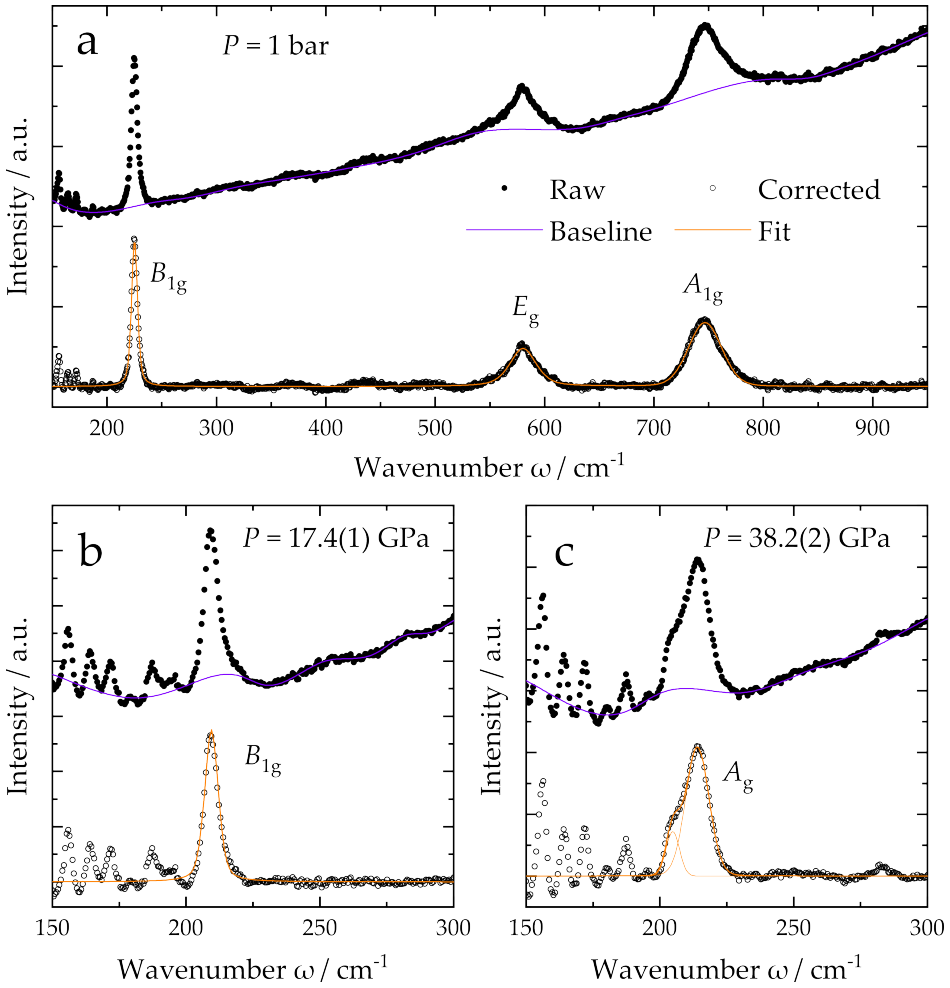

Figure 2.7. Raman spectra of hydrous Al-bearing silica (Al5: $Al_{0.05}Si_{0.95}O_{1.98}H_{0.02}$) collected (a) between 150 and 950 cm^{-1} at room pressure and (b-c) between 150 and 300 cm-1 at high pressure. Labels next to the peaks correspond to the irreducible representations of optic modes. Fringes in the spectral region below 200 cm^{-1} are artifacts that appear when measuring the sample inside the DAC.

operating in backscattering geometry. The system employs a solid state 532 nm ventus532 green laser from Laser Quantum and a TE cooled SynapseTM CCD detector (1024×256 resolution) from HORIBA Jobin Yvon, and was driven by LABRAM 5 software. Raman spectra were acquired using a laser power of 200-800 mW between 150 and 500 cm^{-1} with an estimated resolution on the peak position of ±2 cm^{-1}. For each spectrum, the background was subtracted using a spline function and peak positions and widths were determined by fitting pseudo-Voigt functions to the background-corrected data. This procedure was carried out using the software package *Origin2019* (OriginLab corporation, Northampton, MA, USA) and an example is shown in Figure 2.7.

2.3 High-pressure and high-temperature experiments using diamond anvil cells

The extremely high hardness and fracture toughness of single-crystal diamond, its optical transparency, and low absorption of electromagnetic radiation in the X-ray energy region make it the ideal anvil material for high-pressure experiments (Jayaraman, 1983; Shen and Mao, 2017). The diamond anvil cell (DAC) is a device that uses two oriented single-crystal diamond anvils with small, truncated tips (culets) to subject materials to high-pressure conditions. The working principle of the DAC is that by applying a relatively large force (F) to a very small area (S), extreme pressures (P) in excess of one million atmospheres can be generated according to the equation:

$$P = \frac{F}{S} \tag{2.11}$$

It follows that extremely small samples of the order of tens of micrometres and less than 10 micrometres thick are required to carry out diffraction and spectroscopic measurements in the DAC at such extreme conditions. In the following sections, a procedure for the selection of single crystals for high-pressure experiments and a description of the preparation of diamond anvil cells are presented.

2.3.1 Selection and preparation of single crystals for high-pressure measurements

Single crystals recovered from high-pressure and high-temperature synthesis experiments not always have the ideal dimensions to be loaded directly in the sample chamber of a DAC and thus require additional preparation prior to the high-pressure measurements. In particular, samples employed in Brillouin scattering measurements at high pressures (see section 2.4.4) need to be oriented and double-side polished. High-quality single crystals of at least 100 μm were tested and oriented parallel to a given *hkl* plane using the procedure described in Section 2.2.3. A focus ion beam (FIB) device can then be used to cut the double-side polished crystals to the desired shape (e.g., disk or half-disk). This procedure proved to be useful to arrange multiple samples inside the same DAC (Schulze et al., 2017), so that platelets from the same crystal batch but with different orientations can be analysed at the same pressure conditions and their anisotropic elastic properties can be determined with higher accuracy (Kurnosov et al., 2017; Buchen et al., 2018b; Schulze et al., 2018). Before performing the FIB milling, crystal platelets of $MgSiO_3$ bridgmanite were placed inside an open DAC and analysed with single-crystal X-ray diffraction at ambient conditions, so that their UB matrices could be determined. After the mutual orientations of the platelets were calculated, the crystals were moved to a polished Al holder and fixed on the sides with a thin layer of super glue. Note that this step is required only when trying to minimise the range of orientations where the Brillouin signals of the two samples and of diamond anvil overlap (see Chapter 4). Alternatively, the crystal platelets can be placed on the Al holder directly after polishing. A FEI Scios dual beam device was used to cut the

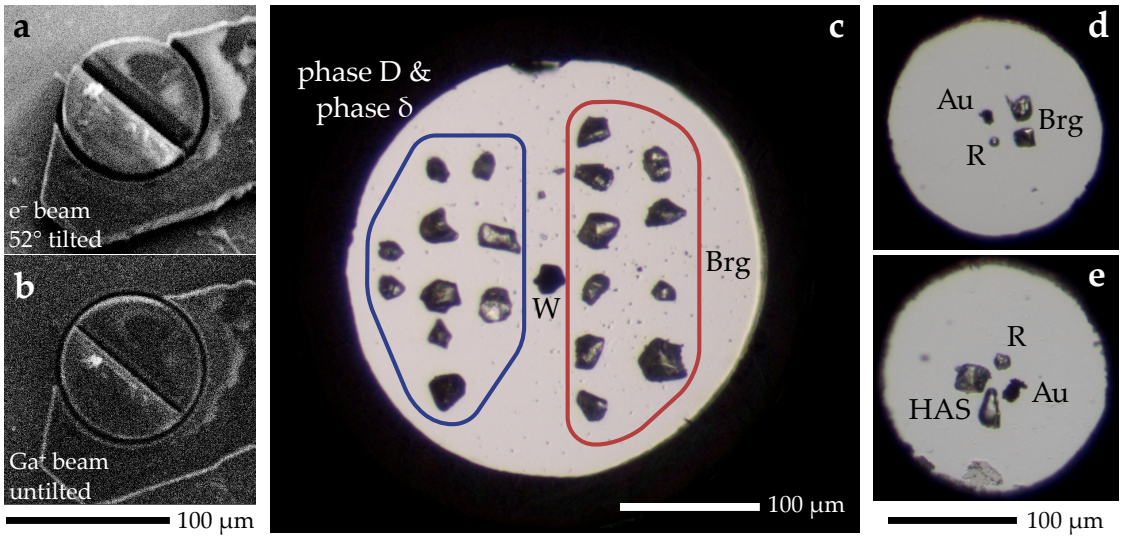

Figure 2.8. (a-b) Secondary electron images of a crystal platelet of $MgSiO_3$ bridgmanite oriented parallel to the (011) plane after FIB milling. (c) Single crystals of Al-bearing bridgmanite (Brg), Fe-bearing Al-phase D and Fe,Si-bearing phase δ inside a "test-DAC" for preliminary synchrotron X-ray diffraction measurements; the W grain in the centre of the culet is used for alignment purposes. (d-e) Single crystals of Al-bearing bridgmanite (Brg) and hydrous Al-bearing silica (HAS) in their respective sample chambers together with Au powder and a ruby sphere (R). Both cells were loaded with He gas to 0.13 GPa.

samples into the desired shapes. A focused Ga^+ ion beam was accelerated at a voltage of 30 kV, while the beam current was varied depending on the thickness of the sample and its sensitivity of the Ga^+ beam. In the case of $MgSiO_3$ bridgmanite, 3 nA were used to avoid amorphisation of the sample. The shape and size of patterns for FIB milling depends on the target pressure of the measurement (i.e., on the size of the culet of the diamond anvils) and on the abundance of material. For instance, half disks with a diameter of approximately 90 μm (Figure 2.8a-b) are ideal for loading two platelets in the same DAC if the diamond anvils have culets of 350-400 μm (see Chapter 4).

The selection of single crystals for synchrotron X-ray diffraction measurements is much simpler than for Brillouin scattering, since a grain size of 10-20 μm usually provides a high enough signal/noise ratio and still allows to reach pressures up to 50 GPa (see Chapters 5 and 6). Smaller crystals are typically required when the pressure range approaches the megabar as smaller culets and thinner gaskets need to be employed. Single crystals displaying sharp optical extinction are selected and arranged on a relatively large culet to form a grid (Figure 2.8c), so that diffraction measurements can be efficiently carried out is series. The X-ray absorption profiles of a piece of Au or W located at the centre of the culet are used to align the DAC on the stage of the synchrotron beamline and accurately determine the position of each single crystal grain using a camera. Note that the DAC is not loaded with a pressure transmitting medium and crystals are analysed at ambient

conditions. Single crystals that exhibit sharp and intense diffraction peaks, low mosaicity, and no twinning are finally selected for high-pressure measurements and moved to their respective DAC (Figure 2.8d-e).

2.3.2 Preparation of diamond anvil cells

The acquisition of high-quality Brillouin scattering and X-ray diffraction data from single crystal samples often requires the use of DACs, anvils, and seats with large opening angles. The BX90-type DAC (Kantor et al., 2012), with a nominal opening of 90°, was designed exactly for this type of measurements and was thus employed in the present studies. WC conical seats with 90° openings and (100)-oriented diamond anvils with Almax-Boehler geometry and an X-ray opening angle of 80° (Boehler and Hantsetters, 2004) were also used to maintain the large opening angles of the BX90 DACs (Figure 2.9). In order to prevent failure of the anvils upon compression, it is critical that the two diamonds are well aligned, meaning that their culets need to overlap perfectly and be parallel to each other. To do so, the first anvil was glued to its seat while pressed against a flat diamond plate. Then the second anvil was placed in its seat inside the DAC, which was gently closed until the tips of the two diamonds touched each other. The position of the second anvil was subsequently adjusted until no interference optical fringes (or Newton's rings) were observed and the edges of the two culets perfectly overlapped. In the case of Brillouin scattering measurements, an additional requirement is that the in-plane orientation of the two crystals should also match. In this case, the shear wave velocity (v_S) of the two diamond anvils was measured by Brillouin scattering as a function of the χ rotation angle of the diffractometer in "fixed-ϕ" mode (see Section 2.4.4). If the v_S peak of diamond was split in two, the unglued anvil was rotated inside its seat and realigned to the other diamond. This procedure was repeated until only one v_S peak of diamond was observed in a χ angle range of 90°. Finally, the second anvil was also fixed to its seat using superglue. To check that the cell remains properly aligned upon compression, stainless steel and rhenium foil gaskets were indented to relatively low pressures by tightening the screws of the DAC. If the alignment of the anvils did not change after releasing pressure, a new rhenium gasket was indented to pressures of 15-20 GPa, depending on the culet size of the anvil and on the target pressure to be achieved in the experiment. A cylindrical hole, whose diameter depended on the culet size, target pressure and type of pressure transmitting medium of choice, was then drilled at the centre of the indented area using an infrared laser to create the sample chamber. For instance, to achieve pressures up to 80 GPa, a pair of diamonds with 250 μm culets was used, the Re gasket was indented to approximately 45 μm and a sample chamber of 160-170 μm diameter was drilled. At this point, samples and pressure sensors (e.g., ruby, Au powder) were placed on the diamond culet and pre-compressed Ne or He gases at 0.13 GPa were loaded in the sample chamber using the gas loading system installed at the Bayerisches Geoinstitut, University of Bayreuth (Kurnosov et al., 2008) or at the PETRA-III synchrotron in Hamburg, Germany. Ne and He are known to retain high hydrostaticity up to pressures of at least 15 or 20 GPa and quasi-hydrostatic conditions at

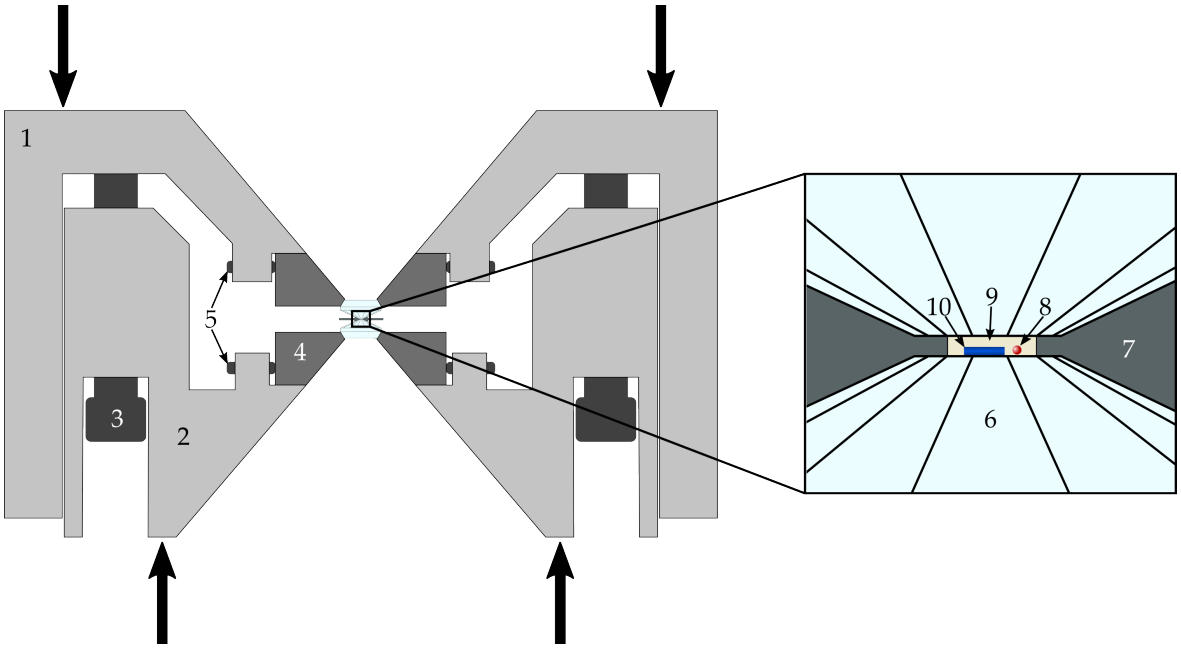

Figure 2.9. Schematic representation of the diamond anvil cell (DAC) design used in this study. Black arrows show the directions of the applied force when tightening the screws. 1: BX90 DAC cylinder. 2: BX90 DAC piston. 3: load screws for pressure generation. 4: WC conical seats with large opening angles. 5: set screws for seats alignment. 6: Almax-Boehler-type diamond anvils. 7: Re gasket. 8: ruby sphere for pressure determination. 9: Ne or He pressure transmitting medium. 10: crystal platelet for Brillouin scattering and/or X-ray diffraction measurements.

higher pressure (Klotz et al. 2009), proving to be the best choice for the study of single crystals at lower mantle pressures. During in-house measurements of the sound velocities of $MgSiO_3$ bridgmanite, pressure was increased by tightening the screws of DAC, while in the case of synchrotron X-ray diffraction measurements, a gas-driven membrane was employed to remotely control the pressure while the cell was positioned on the beamline.

2.3.3 High-temperature generation using resistive heaters

Simultaneous high-pressure and high-temperature conditions for single-crystal X-ray diffraction in the DAC are typically achieved using either a resistive heater (e.g., graphite disk or Pt-wire) or an infrared laser-heating system (e.g. Yb:YAG, CO_2). Although their temperature range rarely exceeds 1200 K (e.g., Carl et al., 2018), resistive heaters provide a more homogeneous temperature distribution in the sample chamber and more stable heating conditions compared to laser heating. Moreover, any sample can be heated in a resistively heated DAC, while transparent crystals are extremely difficult to laser-heat because of their limited interaction with the near-infrared laser radiation. In this thesis, high temperatures were generated using a 0.5 mm-thick and 0.5 m-long Pt-wire heater wrapped around a MACOR®[3] glass ceramic ring that was inserted in the upper part of a

[3]Corning Inc., Corning, New York, USA, https://www.corning.com

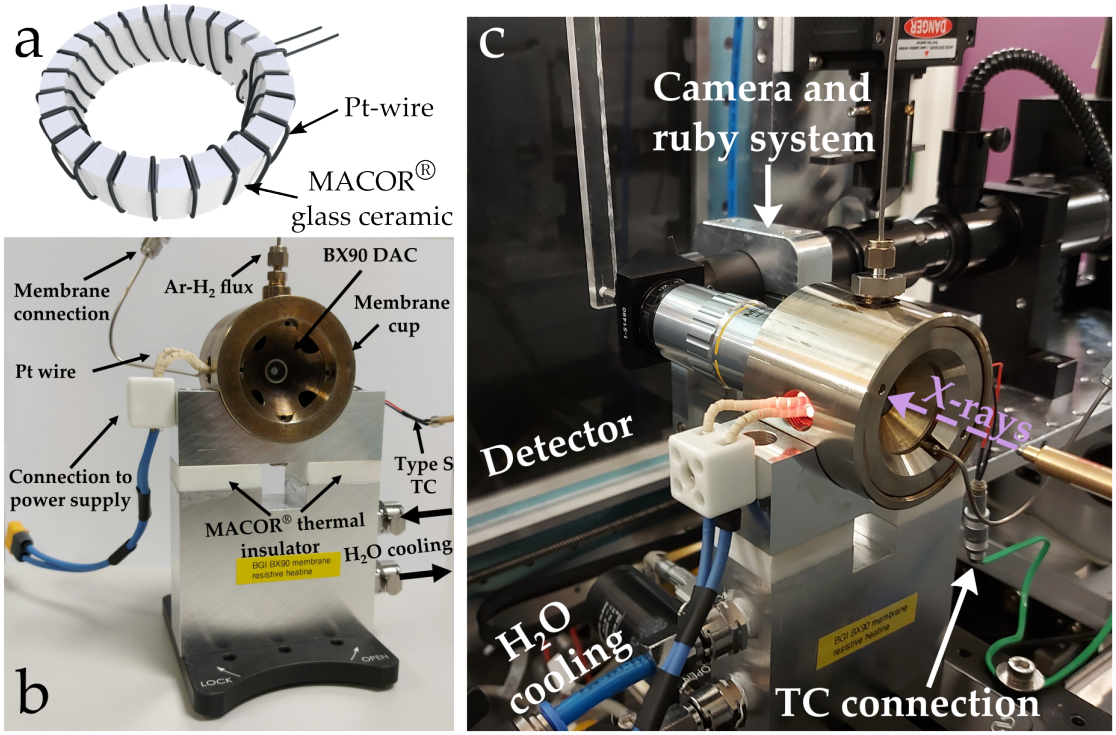

Figure 2.10. (a) A three-dimensional model of Pt-wire heater and ceramic ring used for high-temperature generation in the DAC. (b) Sample holder and resistivey-heated DAC prior to high-pressure and high-temperature experiments. (c) Sample holder and resistivey-heated DAC at approximately 900 K mounted on the P02.2 beamline at PETRA-III (Hamburg, Germany).

BX90 DAC (Figure 2.10a). The ceramic ring was 6 mm thick, with inner and outer diameters of 18 and 22 mm, respectively. A Pt/Pt-Rh thermocouple (type S) was passed through a hole previously drilled on the side of the ceramic ring and placed at approximately 0.5 mm distance from the culet of the diamond anvil. The heater and thermocouple wires were electrically insulated from the WC body of the DAC using ceramic cement. The electrical resistance of the Pt-wire at ambient condition was 0.4 Ω and the heater was able to generate temperatures up to 1000 K at a power of approximately 230 W. To perform the high-pressure and high-temperature measurements, a customised setup for BX90 DACs (Figure 2.10b-c) was built at the beamline P02.2 of PETRA-III (Hamburg, Germany). The DAC was inserted in a membrane cup and fixed to the upper part of the DAC holder using an Allen screw. The bottom part of the holder was connected to a chiller and water cooled in order to prevent damage to the beamline stage and instrumentation. Two slabs of MACOR® were used as thermal insulators between the bottom and top part of the holder to reduce heat dissipation due to water cooling and increase the efficiency of the heater. Furthermore, to prevent the oxidation of Re gasket, WC seats and diamond anvils, a mixture of argon and hydrogen gases in a ratio of Ar:H_2 = 99:1 was continuously flushed inside the membrane cup.

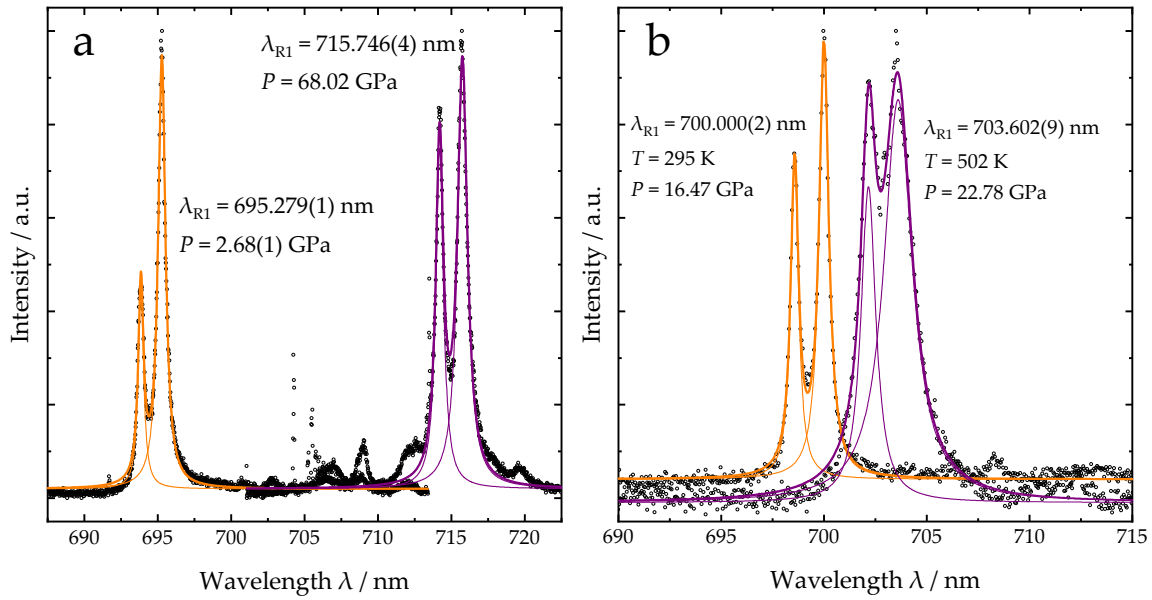

Figure 2.11. Examples of ruby fluorescence spectra collected at different pressures and temperature using the online ruby system at beamline P02.2 of PETRA-III (Hamburg, Germany). (a) shows a comparison of fluorescence spectra measured at room temperature and different pressures in the same compression run. (b) shows fluorescence spectra measured at different pressures and temperature in the same compression run, highlighting the significant broadening of the ruby lines already at 500 K.

2.3.4 Pressure and temperature determination

To determine the pressure conditions in the sample chamber at room temperature, the shift in wavelength of the R1 ruby fluorescence line (Figure 2.11a) was used (Jacobsen et al., 2008; Shen et al., 2020). During in-house measurements of the sound velocities of $MgSiO_3$ bridgmanite and Raman spectroscopy measurements of hydrous Al-bearing silica, a HORIBA Jobin Yvon spectrometer was used, while an online ruby system was employed at the beamline P02.2 of PETRA-III (Hamburg, Germany) (Liermann et al., 2015, and Figure 2.10c). Reference spectra of ruby at room pressure and temperature were recorded for every pressure determination during in-house measurements and at the beginning of every beamtime at the beamline P02.2 of PETRA-III. The position of the R1 line in both reference and high-pressure fluorescence spectra was determined by fitting Lorentzian functions, whereas the error on pressure determination was taken as the half difference between pressures determined before and after the X-ray diffraction and/or sound velocity measurements.

At high temperature, the peak width of the R1 and R2 ruby lines increases significantly (Datchi et al., 2007), to the point that they can be barely distinguished at 500 K (Figure 2.11b), and merge completely at higher temperature. Thus, for measurements at higher temperature, we avoided using the ruby fluorescence scale due to the high uncertainties on the peak position of the R1 line. In principle, less temperature-sensitive

fluorescence scales, such as that of samarium-doped yttrium aluminium garnet (Sm:YAG, Trots et al., 2013), can be used in this temperature interval, but the instrumental setup at the beamline P02.2 of PETRA-III did not allow for such measurements. Therefore, the thermal equations of state of metals were used instead (see Section 2.4.3). For this purpose, a tungsten (W) crystal and/or gold (Au) powder were loaded in the pressure chambers of all DACs used for synchrotron X-ray diffraction measurements. At each pressure-temperature point, a still frame or wide-scan image of W and/or Au was collected immediately before measuring the sample. The one-dimensional diffraction patterns of the materials were integrated from two-dimensional diffraction images using the software *DIOPTAS* (Prescher and Prakapenka, 2015), where the instrument parameters were previously calibrated by analysing the diffraction pattern of a reference CeO_2 sample (Liermann et al., 2015). The unit-cell volume of W and/or Au was then obtained from a full profile Le Bail fit of the diffraction pattern using *JANA2006* (Petrícek et al., 2014) and pressure was calculated using the thermal equation of state of the material (Dorogokupets and Dewaele, 2007; Litasov et al., 2013) in combination with the temperature redout of the thermocouple. To test the accuracy of the thermocouple, a cross correlation function between the ruby fluorescence scale and Au and W equations of state was also used at temperatures up to 500 K, yielding consistent pressure-temperature estimates (see Chapter 5).

2.4 Elastic properties from sound velocity measurements and X-ray diffraction

2.4.1 Linear elasticity

According to Hooke's law, if the deformation (or strain) of a stressed material is sufficiently small, the relation between stress and strain is linear. Following Nye (1985), a generalised version of Hooke's law for anisotropic materials can be obtained by considering the tensorial forms of stress (σ), strain (ε), and elastic properties:

$$\sigma_{ij} = c_{ijkl}\varepsilon_{kl}, \quad \varepsilon_{ij} = s_{ijkl}\sigma_{kl} \tag{2.12}$$

where c_{ijlk} and s_{ijkl} are 4$^{\text{th}}$-rank tensors representing the elastic stiffness and elastic compliance of the material. From equation 2.12 follows that $c_{ijlk} = {s_{ijkl}}^{-1}$. Under the assumption of no body translation and rotation of the sample, the stress and strain tensor are symmetric (i.e., $\sigma_{ij} = \sigma_{ji}$ and $\varepsilon_{kl} = \varepsilon_{lk}$). Additionally, the elastic energy of a crystal, calculated as $1/2 c_{ijkl}\varepsilon_{ij}\varepsilon_{kl}$, must not depend on the order of factorisation, which implies $c_{ijkl}\varepsilon_{ij}\varepsilon_{kl} = c_{ijkl}\varepsilon_{kl}\varepsilon_{ij}$ and thus proves that also the elastic tensors are symmetric (i.e., $c_{ijkl} = c_{klij}$ and $s_{ijkl} = s_{klij}$). Using Voigt notation, the order of symmetric tensor can be halved and indices are changed according to the rule: 11 $\rightarrow$ 1, 22 $\rightarrow$ 2, 33 $\rightarrow$ 3, 23 $\rightarrow$ 4, 13 $\rightarrow$ 5, 12 $\rightarrow$ 6 (e.g., Nye, 1985). The average elastic response of a material subjected to compression or shear deformation is quantified by its bulk (K) and shear (G) moduli. These two elastic moduli can be derived from the spatial averages of the elastic stiffness and elastic

compliance tensors, in which case they represent different bounds of isotropic strain (Voigt) and isotropic stress (Reuss) conditions, respectively. For an orthorhombic crystal, such as bridgmanite, the Voigt bounds of the elastic moduli K_V and G_V assume the following form:

$$K_V = \frac{c_{11} + c_{22} + c_{33} + 2(c_{12} + c_{13} + c_{23})}{9} \tag{2.13}$$

$$G_V = \frac{(c_{11} + c_{22} + c_{33}) - (c_{12} + c_{13} + c_{23}) + 3(c_{44} + c_{55} + c_{66})}{9} \tag{2.14}$$

while for the Reuss bound K_R and G_R are calculated as:

$$K_R = \frac{1}{s_{11} + s_{22} + s_{33} + 2(s_{12} + s_{13} + s_{23})} \tag{2.15}$$

$$G_R = \frac{15}{4(s_{11} + s_{22} + s_{33}) - 4(s_{12} + s_{13} + s_{23}) + 3(s_{44} + s_{55} + s_{66})} \tag{2.16}$$

Because the Reuss and Voigt bounds are not equivalent in elastically anisotropic materials, Hill (1963) proposed to use the arithmetical mean of these two bounds to describe the elastic behaviour of crystalline aggregates with randomly orientated crystallites, which is now known as Voigt-Reuss-Hill (VRH) averaging scheme:

$$K_{VRH} = \frac{K_V + K_R}{2} \tag{2.17}$$

$$G_{VRH} = \frac{G_V + G_R}{2} \tag{2.18}$$

In this thesis, the aggregate sound wave velocities of monomineralic and polymineralic assemblages were calculated using the VRH average of the elastic moduli and equation 1.1 in order to be compared with seismic observations.

2.4.2 Non-linear elasticity and isothermal equations of state

When a material experiences large strains, atoms are pushed closer to each other and the repulsive forces between them increase. As a consequence, the material becomes stiffer and the relation between stress and strain is non-linear. It follows that Hooke's low cannot be employed to describe the volume evolution of a crystal subjected to pressures of the Earth's interior and equations of state must be used instead. First, the infinitesimal strain is replaced by more appropriate finite strain formalisms (Murnaghan, 1937). Depending on whether the strained or unstrained state of the material is chosen as a reference, the Eulerian (f_E) or Lagrangian (f_L) finite strain is chosen:

$$f_E = \frac{1}{2}\left[\left(\frac{V_0}{V}\right)^{\frac{2}{3}} - 1\right], \quad f_L = \frac{1}{2}\left[\left(\frac{V}{V_0}\right)^{\frac{2}{3}} - 1\right] \tag{2.19}$$

Second, an adequate choice of equation of state is necessary to relate finite strains to pressure. Although equations of state are only empirical relations and not thermodynamically

defined, the Birch-Murnaghan formalism based on Eulerian finite strains (Birch, 1947) provides an excellent fit to experimental data. This formalism is based on the assumption that the variation of Helmholtz free energy in a material under compression ($\mathcal{F}_c$) is approximated by a Taylor series expansion in f_E. A series truncated at the fourth order is written as (e.g., Stixrude and Lithgow-Bertelloni, 2005):

$$\frac{\mathcal{F}_c}{V_0} = \frac{\mathcal{F}_0}{V_0} + \frac{1}{2}b^{(1)}_{iikk}f_E^2 + \frac{1}{6}b^{(2)}_{iikkmm}f_E^3 + \frac{1}{24}b^{(3)}_{iikkmmoo}f_E^4 + \cdots \tag{2.20}$$

where the subscript 0 indicates values at the reference state and the coefficients are functions of the isothermal bulk modulus (K_T) and its pressure derivatives at the reference state:

$$b^{(1)}_{iikk} = 9K_{T0} \tag{2.21}$$

$$b^{(2)}_{iikkmm} = 27K_{T0}\left(K'_{T0} - 4\right) \tag{2.22}$$

$$b^{(3)}_{iikkmmoo} = 81K_{T0}\left[K_{T0}K'_{T0} + K''_{T0}\left(K'_{T0} - 7\right) + \frac{143}{9}\right] \tag{2.23}$$

Then, pressure (P) and the bulk modulus are obtained by differentiation of the Helmholtz free energy:

$$P = -\left(\frac{\partial \mathcal{F}}{\partial V}\right)_T \tag{2.24}$$

$$K_{T0} = -V\left(\frac{\partial P}{\partial V}\right)_{T,P=0} \tag{2.25}$$

$$K'_{T0} = \left(\frac{\partial K}{\partial P}\right)_{T,P=0} \tag{2.26}$$

$$K''_{T0} = \left(\frac{\partial^2 K}{\partial P^2}\right)_{T,P=0} \tag{2.27}$$

By truncating 2.20 to the third order in f_E, the 3rd-order Birch-Murnaghan equation of state is obtained (e.g., Birch, 1947; Angel et al., 2014):

$$P = \frac{1}{3}\left(1 + 2f_E\right)^{5/2}\left(b^{(1)}_{iikk} + \frac{1}{2}b^{(2)}_{iikkmm}f_E\right) = 3K_{T0}f_E\left(1 + 2f_E\right)^{5/2}\left[1 + \frac{3}{2}\left(K'_{T0} - 4\right)f_E\right] \tag{2.28}$$

$$K_T = K_{T0}\left(1 + 2f_E\right)^{5/2}\left[1 + \left(3K'_{T0} - 5\right)f_E + \frac{27}{2}\left(K'_{T0} - 4\right)f_E^2\right] \tag{2.29}$$

$$K'_T = \frac{K_{T0}}{K_T}\left(1 + 2f_E\right)^{5/2}\left[K'_{T0} + \left(16K'_{T0} - \frac{143}{3}\right)f_E + \frac{81}{2}\left(K'_{T0} - 4\right)f_E^2\right] \tag{2.30}$$

whereas the second derivative K''_{T0} has an implied value of:

$$K''_{T0} = -\frac{1}{K_{T0}}\left[\left(3 - K'_{T0}\right)\left(4 - K'_{T0}\right) + \frac{35}{9}\right] \tag{2.31}$$

An anisotropic generalisation of equation 2.20 as a function of the Eulerian finite strain (f_{ij}) was proposed by Stixrude and Lithgow-Bertelloni (2005):

$$\frac{\mathcal{F}_c}{V_0} = \frac{\mathcal{F}_0}{V_0} + \frac{1}{2}b^{(1)}_{ijkj}f_{ij}f_{kl} + \frac{1}{6}b^{(2)}_{ijklmn}f_{ij}f_{kl}f_{mn} + \frac{1}{24}b^{(3)}_{ijklmnop}f_{ij}f_{kl}f_{mn}f_{op} + \cdots \tag{2.32}$$

from which an expression for c_{ij} can be derived by assuming $f_E = -f_{ij}\delta_{ij}$ under conditions of both isotropic strain and isotropic stress:

$$c_{ijkl} = (1+2f_E)^{7/2}\left[b^{(1)}_{ijkl} + b^{(2)}_{ijklmn}f_E + b^{(3)}_{ijklmnop}f_E^2\right] - P\delta^{ij}_{kl} \tag{2.33}$$

with:

$$\delta^{ij}_{kl} = -\delta_{ij}\delta_{kl} - \delta_{ik}\delta_{jl} - \delta_{il}\delta_{jk} \tag{2.34}$$

While, strictly speaking, this approach is only valid for elastically isotropic and cubic materials and is not fully internally consistent when applied to lower symmetry minerals (Myhill, 2022), it still provides a flexible enough framework of equations to fit experimental elasticity data of lower-symmetry minerals at high pressure, from which isotropic properties can be calculated (Kurnosov et al., 2017; Buchen et al., 2018b; Siersch et al., 2021, and Chapter 4). By evaluating 2.33 and its pressure derivatives (i.e., $c_{ijkl,0}$, $c'_{ijkl,0}$, and $c''_{ijkl,0}$) at ambient conditions, the coefficients in 2.33 can be obtained:

$$b^{(1)}_{ijkl} = c_{ijkl,0} \tag{2.35}$$

$$b^{(2)}_{ijklmn} = 3K_{T0}\left(c'_{ijkl,0} + \delta^{ij}_{kl}\right) - 7c_{ijkl,0} \tag{2.36}$$

$$b^{(3)}_{ijklmnop} = 9K^2_{T0}c''_{ijkl,0} + 3K_{T0}\left(c'_{ijkl,0} + \delta^{ij}_{kl}\right)\left(3K'_{T0} - 16\right) + 63c_{ijkl,0} \tag{2.37}$$

which yield equations 2.21-2.23 for the isotropic case when Einstein summation is applied. By substituting equations 2.28, 2.35, and 2.36 into equation 2.33 and truncating to the third order in f_E, a formulation of c_{ijkl} as a function of strain is obtained:

$$c_{ijkl} = (1+2f_E)^{5/2}\left\{c_{ijkl,0} + \left(3K_0c'_{ijkl,0} - 5c_{ijkl,0}\right)f_E + \left[6K_0c'_{ijkl,0} - 14c_{ijkl,0} - 3/2K_0\delta^{ij}_{kl}\left(3K'_0 - 16\right)\right]f_E^2\right\} \tag{2.38}$$

This will be used in Chapter 4 to experimentally determine elastic coefficients obtained from Brillouin scattering and X-ray diffraction measurements. Substituting equation 2.38 into 2.14, a formulation for the shear modulus in the Voigt bound can be obtained:

$$G = (1+2f_E)^{5/2}\left[G_0 + \left(3K_0G'_0 - 5G_0\right)f_E + \left(6K_0G'_0 - 24K_0 - 14G_0 + \frac{9}{2}K_0K'_0\right)f_E^2\right] \tag{2.39}$$

where G_0 is the shear modulus in the reference state and its pressure derivative G'_0 is defined as:

$$G'_0 = \left(\frac{\partial G}{\partial P}\right)_{P=0} \tag{2.40}$$

2.4.3 Thermal equations of state

Equations of state aimed at reproducing the volume and elasticity of materials at high-pressure and high-temperature conditions can be categorised in two groups: high-temperature isothermal equations of state and thermal pressure equations of state. In the former case, first the volume expansion at room pressure is calculated through the thermal expansion coefficient (α) and then a pressure correction is applied through an isothermal equation of state at high temperature. To do so, one or more pressure-temperature cross derivatives of the elastic parameters [e.g.,$(\partial K/\partial T)_P$, $(\partial \alpha/\partial P)_T$] are defined to account for elastic softening at high temperature (Anderson, 1995; Angel et al., 2017). This approach is convenient for minerals that are stable at upper mantle conditions. However, when extrapolated to very high pressures it may lead to negative thermal expansion coefficients due to K'_0 being typically assumed to be temperature-independent (Helffrich and Connolly, 2009). In thermal pressure equations of state, on the other hand, pressure is first calculated at room temperature and then the temperature effect is evaluated along an isochoric path. Heating at constant volume causes an increase in pressure due to changes in the frequency of lattice vibrations within the quasi-harmonic approximation (e.g., Poirier, 2000). Pressure can thus be expressed as:

$$P(V,T) = P(V,T_0) + \Delta P_{\text{th}}(V,T) \tag{2.41}$$

where P_{th} is the so-called thermal pressure that develops along the isochoric path. Several thermal pressure models have been proposed that differ from each other on how vibrational frequencies in crystals are described (e.g., Stixrude and Lithgow-Bertelloni, 2005; Holland and Powell, 2011). The most frequent choice is that of a Debye model (Debye, 1912), where the quasi-harmonic part of the internal energy (E_{th}) is a function of the characteristic temperature θ_{D}, the Debye temperature:

$$E_{\text{th}} = 9nRT\left(\frac{T}{\theta_{\text{D}}}\right)^3 \int_0^{\frac{\theta_{\text{D}}}{T}} \frac{t^3}{e^t - 1} dt \tag{2.42}$$

where n is the number of atoms per formula unit and R is the gas constant. By differentiating 2.42 with respect to T, the isochoric heat capacity is found:

$$C_V = 9nR\left(\frac{T}{\theta_{\text{D}}}\right)^3 \int_0^{\frac{\theta_{\text{D}}}{T}} \frac{e^t t^4}{\left(e^t - 1\right)^2} dt = 9nR\left[4\left(\frac{T}{\theta_{\text{D}}}\right)^3 \int_0^{\frac{\theta_{\text{D}}}{T}} \frac{t^3}{e^t - 1} dt - \frac{\theta_{\text{D}}/T}{e^{\theta_{\text{D}}/T} - 1}\right] \tag{2.43}$$

The Debye temperature also changes as a function of pressure and temperature and, more specifically, it increases with compression. Thus, a parametrisation for volume dependency

of θ_D is needed to fit thermal equations of state to experimental datasets. If the Debye temperature and its volume derivatives are assumed to be functions of volume only, the Mie-Grüneisen formalism can be used (e.g., Anderson, 1995):

$$\theta_D(V) = \theta_D(V_0)\exp\left[\frac{\gamma(V_0)-\gamma(V)}{q}\right] = \theta_{D0}\exp\left[\frac{\gamma_0-\gamma}{q}\right] \tag{2.44}$$

$$\gamma(V) = -\frac{d\ln\theta_D(V)}{d\ln V} = \gamma(V_0)\left(\frac{V}{V_0}\right)^q = \gamma_0\left(\frac{V}{V_0}\right)^q \tag{2.45}$$

$$q = \frac{d\ln\gamma(V)}{d\ln V} \tag{2.46}$$

where γ is the Grüneisen parameter and q is a constant. In the Mie-Grüneisen-Debye equation of state, γ as defined in 2.45 is assumed to be numerically equivalent to the thermal Grüneisen parameter $\gamma_{th} = V(\partial P/\partial E)_V$, from which an expression for the thermal pressure can be obtained (Poirier, 2000):

$$\Delta P_{th}(V,T) = \frac{\gamma}{V}\left[E_{th}(V,T) - E_{th}(V,T_0)\right] \tag{2.47}$$

Alternative formulations for θ_D, γ and q have also been proposed, which assume that vibrational frequencies are functions of the Eulerian finite strain (Davies, 1974). In this thesis (see Chapters 4 and 5), the formulation of Stixrude and Lithgow-Bertelloni (2005) was mainly adopted:

$$\theta_D^2 = \theta_{D0}^2\left[1 + a_{ii}^{(1)}f_E + \frac{1}{2}a_{iikk}^{(2)}f_E^2\right] \tag{2.48}$$

$$\gamma = \frac{1}{6}\frac{\theta_{D0}^2}{\theta_D^2}(1+2f_E)\left[a_{ii}^{(1)} + a_{iikk}^{(2)}f_E\right] \tag{2.49}$$

$$q = \frac{\eta_V}{\gamma} = \frac{\left[18\gamma^2 - 6\gamma - \frac{1}{2}\frac{\theta_{D0}^2}{\theta_D^2}(1+2f_E)^2 a_{iikk}^{(2)}\right]}{9\gamma} \tag{2.50}$$

$$\eta_S = -\gamma - \frac{1}{2}\frac{\theta_{D0}^2}{\theta_D^2}(1+2f_E)^2 a_S^{(2)} \tag{2.51}$$

where η_V and η_S are the volume strain and shear strain derivatives of γ. By evaluating equations 2.48-2.51 at ambient conditions, $a_{ii}^{(1)}$, $a_{iikk}^{(2)}$, and $a_S^{(2)}$ are found:

$$a_{ii}^{(1)} = 6\gamma_0 \tag{2.52}$$

$$a_{iikk}^{(2)} = -12\gamma_0 + 36\gamma_0^2 - 18\gamma_0 q_0 \tag{2.53}$$

$$a_S^{(2)} = -2\gamma_0 - 2\eta_{S0} \tag{2.54}$$

Including the thermal pressure correction into equations 2.29 and 2.39, the high-temperature formulation of K and G is obtained:

$$K_{\mathrm{T}} = K_{\mathrm{T0}}\left(1+2f_{\mathrm{E}}\right)^{5/2}\left[1+\left(3K'_{\mathrm{T0}}-5\right)f_{\mathrm{E}}+\frac{27}{2}\left(K'_{\mathrm{T0}}-4\right)f_{\mathrm{E}}^2\right] + \left(1+\gamma-q\right)\frac{\gamma}{V}\Delta E_{\mathrm{th}}-\frac{\gamma^2}{V}\Delta(C_V T) \quad (2.55)$$

$$G = \left(1+2f_{\mathrm{E}}\right)^{5/2}\left[G_0+\left(3K_0G'_0-5G_0\right)f_{\mathrm{E}} + \left(6K_0G'_0-24K_0-14G_0+\frac{9}{2}K_0K'_0\right)f_{\mathrm{E}}^2\right]-\frac{\eta_S}{V}\Delta E_{\mathrm{th}} \quad (2.56)$$

from which the adiabatic bulk modulus K_{S} can also be obtained:

$$K_{\mathrm{S}} = K_{\mathrm{T}}\left(1+\alpha\gamma T\right) = K_{\mathrm{T}}+\frac{\gamma^2 C_V T}{V} \quad (2.57)$$

This set of equations was used in this thesis (see Chapter 4) and in previous works (e.g., Kono et al., 2010) to fit experimental sound velocity datasets and compute seismic velocities at high pressure and temperature in mineral physical models (Stixrude and Lithgow-Bertelloni, 2011; Kurnosov et al., 2017).

2.4.4 Sound velocity determination by Brillouin scattering

When an oscillating electromagnetic field excites the thermal motion of atoms in a dense medium (i.e., liquid or solid), it induces periodic perturbations of its electrical polarisability (Dil, 1982; Speziale et al., 2014). This process results in density fluctuations within the medium that can scatter inelastically the incident electromagnetic radiation depending on the wavenumber (q) and frequency (Ω) of the fluctuations, in a way that resembles Bragg's diffraction of X-rays (equation 2.1). This process takes the name of Brillouin scattering (Brillouin, 1922). The resulting wavenumber (k_{s}) and frequency (ω_{s}) of the scattered radiation are:

$$k_{\mathrm{s}} = k_{\mathrm{i}} \pm q \quad (2.58)$$

$$\omega_{\mathrm{s}} = \omega_{\mathrm{i}} \pm \Omega \quad (2.59)$$

where the subscript i refers to properties of the incident electromagnetic radiation and the negative/positive sign can be seen as an event of phonon creation/annihilation, taking the name of Stokes/anti-Stokes event, as described for Raman scattering (Section 2.2.5). As the wavenumbers of incident and scattered radiation is approximately the same (i.e., $k_{\mathrm{i}} \sim k_{\mathrm{s}}$), the wavenumber of the scattered radiation only depends on its scattering angle:

$$q = 2k_{\mathrm{i}}\sin\left(\frac{\theta}{2}\right) \quad (2.60)$$

The phase velocity of the periodic fluctuation in the medium, defined by the ratio of its frequency and wavenumber ($v = \Omega/q$), can therefore be obtained from equation 2.60:

$$\Omega = 2vk_{\mathrm{i}}\sin\left(\frac{\theta}{2}\right) = \frac{2v}{\lambda_0}\sin\left(\frac{\theta}{2}\right) \tag{2.61}$$

Where λ_0 is the wavelength of the incident radiation. For a scattering angle of 90° and an incident wavelength of 532 nm, q is approximately 37600 cm^{-1}, which is smaller by approximately two orders of magnitude than the edge of the first Brillouin zone of a crystal with unit-cell edges 10 Å. Therefore, acoustic phonons are located close to the centre of the Brillouin zone, where the phase velocity of the periodic fluctuations is equal to the speed of sound, or acoustic velocity, in the medium, yielding (Speziale et al., 2014):

$$v = \frac{\Omega\lambda_0}{2\sin\left(\frac{\theta}{2}\right)} \tag{2.62}$$

In an anisotropic solid medium, one quasi-longitudinal and two quasi-transverse (horizontally and vertically polarised) acoustic modes are present. The velocity, and thus the frequency, of these modes depend on the elastic stiffness coefficients of the material according to Christoffel's equation (Every, 1980):

$$\left|c_{\mathrm{ijkl}}q_{\mathrm{j}}q_{\mathrm{l}} - \rho v_{\mathrm{i}}^2\delta_{\mathrm{ik}}\right| = 0 \tag{2.63}$$

where q_{j} and q_{l} are components of the propagation wavevector, ρ is the density of the material, and δ_{ik} is the Kronecker delta. Note that equation 2.63 cannot be directly employed to obtain the elastic coefficient of crystals that are not centrosymmetric, where an additional coupling term between strain and electrical polarisability exists to account for the piezoelectric effect (Every, 1980). In such a case, equation 2.63 will yield the piezoelastic coefficients, which are not material constants at given pressure and temperature conditions as they also depend on the propagation direction of the wavevector. The determinant of equation 2.63 can be developed to find an analytical solution for this equation, as shown in Chapter 5 of Buchen (2018). By setting $-v^2\rho = x$ and defining the Christoffel's determinants Γ_{ik} as:

$$\Gamma_{\mathrm{ik}} = c_{\mathrm{ijkl}}q_{\mathrm{j}}q_{\mathrm{l}} = \sum_{\mathrm{j}=1}^{3}\sum_{\mathrm{k}=1}^{3} c_{\mathrm{ijkl}}q_{\mathrm{j}}q_{\mathrm{l}} \tag{2.64}$$

it is possible to rewrite equation 2.63 as:

$$\left|c_{\mathrm{ijkl}}q_{\mathrm{j}}q_{\mathrm{l}} - \rho v_{\mathrm{i}}^2\delta_{\mathrm{ik}}\right| = \begin{vmatrix} \Gamma_{11}+x & \Gamma_{12} & \Gamma_{13} \\ \Gamma_{21} & \Gamma_{22}+x & \Gamma_{23} \\ \Gamma_{31} & \Gamma_{32} & \Gamma_{33}+x \end{vmatrix} = A_3x^3 + A_2x^2 + A_1x + A_0 = 0 \tag{2.65}$$

where

$$A_3 = 1 \tag{2.66}$$

$$A_2 = \Gamma_{11} + \Gamma_{22} + \Gamma_{33} \tag{2.67}$$

$$A_1 = \Gamma_{11}\Gamma_{22} + \Gamma_{11}\Gamma_{33} + \Gamma_{22}\Gamma_{33} - \Gamma_{12}\Gamma_{21} - \Gamma_{13}\Gamma_{31} - \Gamma_{23}\Gamma_{32} \tag{2.68}$$

$$A_0 = \Gamma_{11}\Gamma_{22}\Gamma_{33} + \Gamma_{12}\Gamma_{23}\Gamma_{31} + \Gamma_{13}\Gamma_{32}\Gamma_{21} - \Gamma_{23}\Gamma_{32}\Gamma_{11} - \Gamma_{13}\Gamma_{31}\Gamma_{22} - \Gamma_{12}\Gamma_{21}\Gamma_{33} \tag{2.69}$$

It is possible to transform the right-hand side of equation 2.65 into a depressed cubic of the type $t^3 + pt + s = 0$ by applying a change of variable:

$$t = x + \frac{A_2}{3A_1} \tag{2.70}$$

$$p = \frac{3A_3A_1 - A_2^2}{3A_3^2} \tag{2.71}$$

$$s = \frac{2A_2^3 - 9A_1A_2A_3 + 27A_3^2A_0}{27A_3^3} \tag{2.72}$$

so that the three real roots of 2.65 can be found by applying the trigonometric solution formula:

$$v_{\mathrm{P}} = \sqrt{\frac{1}{\rho}\left\{\sqrt{-\frac{4}{3}p}\cos\left[\frac{1}{3}\cos^{-1}\left(-\frac{s}{2}\sqrt{-\frac{27}{p^3}}\right) - \frac{\pi}{3}\right] + \frac{A_2}{3A_3}\right\}} \tag{2.73}$$

$$v_{\mathrm{S2}} = \sqrt{\frac{1}{\rho}\left\{\sqrt{-\frac{4}{3}p}\cos\left[\frac{1}{3}\cos^{-1}\left(-\frac{s}{2}\sqrt{-\frac{27}{p^3}}\right) + \frac{\pi}{3}\right] + \frac{A_2}{3A_3}\right\}} \tag{2.74}$$

$$v_{\mathrm{S1}} = \sqrt{\frac{1}{\rho}\left\{-\sqrt{-\frac{4}{3}p}\cos\left[\frac{1}{3}\cos^{-1}\left(-\frac{s}{2}\sqrt{-\frac{27}{p^3}}\right)\right] + \frac{A_2}{3A_3}\right\}} \tag{2.75}$$

with $v_{\mathrm{P}} > v_{\mathrm{S2}} > v_{\mathrm{S1}}$. Knowing the orientation of the crystal platelets in the DAC, the equations listed above (equations 2.63-2.75) allow the c_{ijkl} to be determined from a least square refinement. Therefore, it is necessary to define a reference system that relates propagation directions of sound wave velocities and crystallographic directions. A Cartesian system with basis vectors $\mathbf{e}_{\mathrm{i}}$ is thus defined according to the following relations with the crystallographic reference system (Haussühl, 2008):

$$\mathbf{e}_1 = \mathbf{e}_2 \times \mathbf{e}_3 \tag{2.76}$$

$$\mathbf{e}_2 = \frac{\mathbf{b}^*}{b^*} \tag{2.77}$$

$$\mathbf{e}_3 = \frac{\mathbf{c}}{c} \tag{2.78}$$

where the star refers to the reciprocal space vectors. The plane normal of a crystal platelet employed in high-pressure experiments is then defined by the vector **n**:

$$\mathbf{n} = \begin{pmatrix} n_1 = \cos\phi \sin\theta \\ n_2 = \sin\phi \sin\theta \\ n_3 = \cos\theta \end{pmatrix} \tag{2.79}$$

where θ is the angle between $\mathbf{e}_3$ and n and ϕ is the angle between $\mathbf{e}_1$ and the projection of n on the plane perpendicular to $\mathbf{e}_3$. In the so-called "forward scattering" or "platelet" geometry (Whitfield et al., 1976; Speziale et al., 2014), the crystal platelet bisects the directions of incident and scattered light, thus the propagation vector **q** is always perpendicular to the plane normal **n**. It is useful to consider changes in the propagation direction within the crystal platelet as a function of the rotation angle χ of the diffractometer, whose axis is ideally parallel to the plane normal **n**. First a reference unit vector $\mathbf{q}_0$ is defined as the cross product of $\mathbf{e}_3$ and **n**:

$$\mathbf{q}_0 = \frac{\mathbf{e}_3 \times \mathbf{n}}{|\mathbf{e}_3 \times \mathbf{n}|} = \begin{pmatrix} q_{01} = -n_2/\sin\theta \\ q_{02} = n_1/\sin\theta \\ q_{03} = 0 \end{pmatrix} \tag{2.80}$$

A new reference system $\mathbf{e'}_i$ having $\mathbf{e'}_1 = \mathbf{q}_0$, $\mathbf{e'}_2 = \mathbf{n} \times \mathbf{q}_0$, and $\mathbf{e'}_3 = \mathbf{n}$ is then defined, so that for any rotation of the crystal about the rotation angle χ, the propagation vector $\mathbf{q'}$ can be expressed as:

$$\mathbf{q'} = \begin{pmatrix} q'_1 = \cos(\chi - \chi_0) \\ q'_2 = \sin(\chi - \chi_0) \\ q'_3 = 0 \end{pmatrix} \tag{2.81}$$

where χ_0 is the angle between $\mathbf{q}_0$ and **q**. A change in coordinates from $\mathbf{e'}$ to **e** is finally obtained by multiplying $\mathbf{q'}$ by the transformation matrix **A**:

$$\mathbf{q} = \mathbf{A}\mathbf{q'} = \begin{pmatrix} q_{01} & n_2 q_{03} - n_3 q_{02} & n_1 \\ q_{02} & n_3 q_{01} - n_1 q_{03} & n_2 \\ q_{03} & n_1 q_{02} - n_2 q_{01} & n_3 \end{pmatrix} \mathbf{q'} \tag{2.82}$$

For a more detailed description of the formalism, see Chaper 5 of Buchen (2018).

2.4.5 Brillouin scattering measurements at high pressure

Measurements of the sound velocities of $MgSiO_3$ bridgmanite presented in this thesis were conducted on the combined X-ray diffraction and Brillouin scattering setup installed at the Bayerisches Geoinstitut, University of Bayreuth (Figure 2.12) and described in detail by Trots et al. (2011) and Trots et al. (2013). The X-ray diffraction component is constituted by a four-circle Eulerian goniometer, a micro-focused rotating anode, and a single-count scintillation detector, as described in Section 2.2.3. The Brillouin scattering setup employs a solid state Nd:YVO_4 green laser (V2 Verdi, Coherent Inc.) with wavelength λ_0 = 532 nm

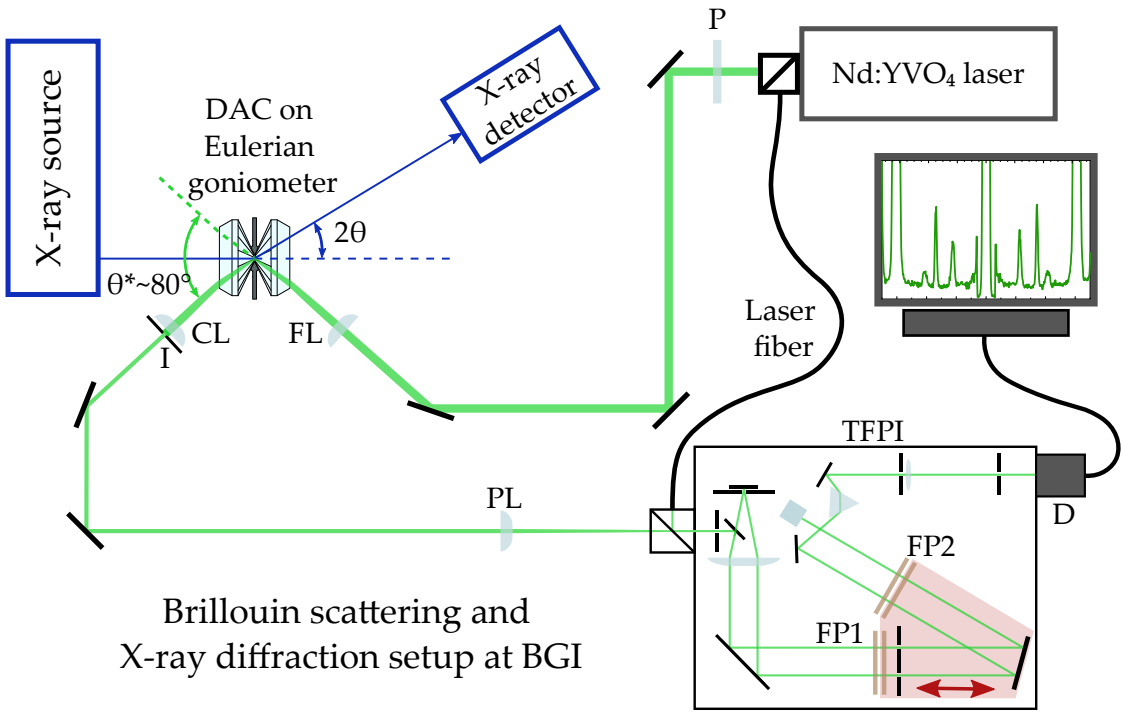

Figure 2.12. Schematic representation of the Brillouin scattering and X-ray diffraction setup installed at the Bayerisches Geoinstitut (BGI), University of Bayreuth. P: laser polariser. FL: Focusing lens. CL: collecting lens. I: iris. PL: lens focusing the scattered laser in the pinhole. TFPI: tandem six-pass Fabry-Perot interferometer. FP1 and FP2: interferometer mirrors. D: detector. 2θ: diffraction angle. θ^*: external scattering angle between transmitted and scattered laser radiation.

and is optimised for measurements in forward scattering (or platelet) geometry (Whitfield et al., 1976; Speziale et al., 2014), where the incident and scattered beam enter and exit the DAC with the same angle (Figure 2.12). The external scattering angle (θ^*) is then defined as the angle between scattered and transmitted beam outside of the DAC on the side of the collecting optics (Figure 2.12). Lenses with 25.4 mm diameter and focal lengths of 100 mm are placed before and after the DAC to focus the incident beam on the sample and collect the scattered light, respectively. An iris of 25(H) $\times$ 6(V) mm^2 is also present behind the collecting lens to further select only the central part of the light cone coming out of the DAC and reduce the intensity of the signal coming from the diamond anvils. The selected portion of the scattered light is then focused on the entrance of a pinhole with 200 or 150 μm aperture that is placed in front of a TFP-1 multi-pass tandem Fabry-Perot interferometer (Lindsay et al., 1981). The signal is then recorded by a Hamamatsu H11202-050 single photon counting module and sent to a multi-channel analyser synchronised with the motion of the translation stage of the interferometer.

In this thesis, a laser power of 100-200 mW, corresponding to 40-80 mW before entering

the DAC, was used to excite and probe the acoustic modes of the sample. The scattering angle was calibrated and checked periodically using a fused silica glass standard inter-calibrated with GHz-ultrasonic interferometry measurements. Deviations from the 80° geometry were within ±0.2°, corresponding to a difference of at most 0.2% in the obtained velocities. The Fabry-Perot interferometer was operated with a plate spacing (FP1 in Figure 2.12) of 4 or 3 mm and a nominal scanning amplitude of 500 or 400 nm for measurements below and above 60 GPa, respectively. By reducing the FP1 plate spacing and the scanning amplitude at the highest pressures, the free spectral range of the instrument was enhanced, while the frequency range investigated remained virtually the same. In this way, it was possible to avoid overlapping between the ghost peaks of the elastically scattered light and the longitudinal acoustic modes of the sample. To convert Brillouin shifts from channels to frequency, the distance between the ghost peaks was calibrated using the "align mode" of the interferometer before every set of measurements. Peak positions were then obtained using the software *Brillouin Win1024* written by S. Sinogeikin for the Brillouin system installed the 13-BM-D station (GSECARS) of the Advanced Photon Source (Argonne National Laboratory, USA) (Sinogeikin et al., 2006). Uncertainties on peak positions were evaluated from their signal-to-noise ratio, following Kurnosov et al. (2017). Further details on the calibration procedure and assessment of errors are provided in Appendix A.

2.5 Thermodynamic and physical properties of multiphase lower mantle assemblages

In Section 2.4.3, it was shown that a total of 9 thermoelastic parameters are required to fully describe the high-pressure and high-temperature elasticity of minerals: V_0, K_{T0}, K'_{T0}, θ_{D0}, γ_0, q_0, G_0, G'_0, η_{S0}. An additional parameter, the Helmholtz free energy at the reference state ($\mathcal{F}_0$), is required to model phase equilibria and mineral composition as a function of pressure and temperature. In this section, I will describe how to calculate the thermodynamic properties of pure mineral (i.e., end members) and solid solutions to be employed in the calculation of phase equilibria and sound velocities at high pressure and high temperature for candidate lower mantle rocks.

2.5.1 End member properties

Under equilibrium conditions, the stability of mineral phases in rocks and their chemical composition in terms of end member components is determined by their Gibbs free energy. The natural variables defining the Gibbs free energy are pressure (P) and temperature (T), while in the previous section it has been shown that physical properties are more easily described starting from the Helmholtz free energy, which is a function of volume (V) and T.

Following Stixrude and Lithgow-Bertelloni (2011), we make use of Legendre transformations to swap from one thermodynamic potential to the other:

$$\mathcal{G}(P,T) = \mathcal{F}(V,T) + P(V,T)V \tag{2.83}$$

where pressure is calculated from the equation of state of the material using the relations discussed in Section 2.4.3. To derive an expression for the Helmholtz free energy at a given P and T, the same Debye model employed in the derivation of a thermal equation of state is used to calculate the quasi-harmonic (or thermal) contribution to $\mathcal{F}$:

$$\mathcal{F}_{\text{th}}(V,T) = 9nRT\left(\frac{T}{\theta_{\text{D}}(V)}\right)^3 \int_0^{\theta_{\text{D}}(V)/T} \ln(1-e^{-t})dt \tag{2.84}$$

This yields:

$$\mathcal{F}(V,T) = \mathcal{F}(V_0,T_0) + \Delta\mathcal{F}_{\text{c}}(V,T_0) + \Delta\mathcal{F}_{\text{th}}(V,T) \tag{2.85}$$

where $\mathcal{F}(V_0,T_0) = \mathcal{F}_0$ is usually a tabulated value and $\Delta\mathcal{F}_{\text{c}}(V,T_0)$ is obtained from equation 2.20. From this expression of the Helmholtz free energy, other thermodynamic quantities, such as entropy (S), are derived by taking the appropriate derivatives (e.g., Anderson, 1995):

$$\begin{aligned} S(V,T) = -\left(\frac{\partial\mathcal{F}(V,T)}{\partial T}\right)_V = \\ = 3nR\left[4\left(\frac{T}{\theta_{\text{D}}(V)}\right)^3 \int_0^{\theta_{\text{D}}(V)/T} \frac{t^3}{e^t-1}dt - \ln(1-e^{-\theta_D(V)/T})\right] \end{aligned} \tag{2.86}$$

Although neglected in the present study, additional contributions to $\mathcal{F}$ may be added to account for the Landau free energy in the proximity of structural phase transition (Salje, 1991; Carpenter et al., 1998) or the change in electronic configuration of transition metal cations (e.g., Fe^{2+} and Fe^{3+}) across spin transitions (Sturhahn et al., 2005; Stixrude and Lithgow-Bertelloni, 2011; Buchen, 2021).

2.5.2 Ideal mixing behaviour

The composition of mineral phases in multiphase assemblages (i.e., rocks) is typically not fixed but changes as a function of pressure, temperature, and bulk composition of the system. It is convenient to describe minerals and their thermodynamic properties in terms of a solid solution of distinct end members. As a first approximation, the Gibbs free energy of a given phase can be expressed as an ideal solution of its end member components. The contributions of an end member is given by its chemical potential μ_i, which is calculated as the partial derivative of $\mathcal{G}$ with respect to the molar fraction n_i while keeping constant the

fractions of all the other *m* components:

$$\mu_i = \left(\frac{\partial \mathcal{G}}{\partial n_i} \right)_{n_{m \neq i}} \tag{2.87}$$

The chemical potential is composed of two parts: the first is the Gibbs free energy of the pure end member component, while the second accounts for the configurational entropy due to mixing at a given crystallographic site (Stixrude and Lithgow-Bertelloni, 2011):

$$\mathcal{G}(P,T) = \sum_{i}^{\text{comps}} n_i \mu_i(P,T) = \sum_{i}^{\text{comps}} n_i \left[\mathcal{G}_i + RT \sum_{k}^{\text{sites}} \left(\sum_{j}^{\text{atoms}} s_{ijk} \ln x_{jk} - S_{ik} \ln X_k \right) \right] \tag{2.88}$$

where the first sum in *i* is over the end member components (comps), the second sum in *k* is over each crystallographic site (sites), the third sum in *j* is over the atomic species in the same site or phase (atoms). The remaining coefficients in 2.88 are thus defined:

$$x_{jk} = \sum_{i}^{\text{comps}} s_{ijk} n_i \tag{2.89}$$

$$X_k = \sum_{j}^{\text{atoms}} x_{jk} \tag{2.90}$$

$$S_{ik} = \sum_{j}^{\text{atoms}} s_{jkl} \tag{2.91}$$

where s_{ijk} is the stoichiometric coefficient of the atomic species *j* (e.g., 1 for Mg and Si in $MgSiO_3$) in site *k* (e.g., A and B sites of bridgmanite) of the end member component *i*, x_{jk} is the fraction of atomic species *j* in site *k*, X_k is the total occupancy of site *k*, and S_{ik} is the total occupancy of site *k* in the end member component *i*. In this study, mixing of different cations was modelled only in sites with a stoichiometric coefficient of 1, while vacancies were taken explicitly into account and treated as an atomic species *j*. Therefore, $S_{ik} = s_{ijk} = X_k = 1$, which allows to simplify equation 2.88 to:

$$\mathcal{G}(P,T) = \sum_{i}^{\text{comps}} n_i \mu_i(P,T) = \sum_{i}^{\text{comps}} n_i \left[\mathcal{G}_i + RT \sum_{k}^{\text{sites}} \left(\sum_{j}^{\text{atoms}} \ln x_{jk} \right) \right] \tag{2.92}$$

A similar expression can be found for other thermodynamic parameters needed to model the sound velocities of lower mantle phase assemblages (Stixrude and Lithgow-Bertelloni, 2011). Of particular interest here is the expression for the molar volume *V* and the elastic

moduli *M*:

$$V = \sum_i n_i V_i \tag{2.93}$$

$$\frac{V}{M} = \sum_i n_i \frac{V_i}{M_i} \tag{2.94}$$

$$\frac{V\,(1+M')}{M^2} = \sum_i n_i \frac{V_i\,(1+M_i')}{M_i^2} \tag{2.95}$$

Where *M* can be either *K* or *G*. Equations 2.93-2.94 are also used to compute the molar volume (and thus the density) and Reuss elastic moduli of an aggregate of mineral phases at high pressure and temperature (Cottaar et al., 2014). To calculate the Voigt-Reuss-Hill average of the elastic moduli and thus the aggregate sound velocities of the material through equations 2.17-2.18, similar expressions to 2.13-2.14 are used to model mixing under the conditions of isotropic strain (i.e., Voigt bound):

$$M = \sum_i \frac{n_i V_i}{V}\, M_i \tag{2.96}$$

2.5.3 Non-ideal mixing behaviour and excess molar properties

The assumption of ideal mixing behaviour in minerals is in general not valid, meaning that molar properties, such as volume and enthalpy, change non-linearly between two end member components of a given solid solution. Therefore, excess contributions to said properties need to be defined to fit the experimental data and model phase equilibria (e.g., Philpotts and Ague, 2009). In this thesis, non-ideal contributions to the chemical potential are relevant to model the phase relations of bridgmanite and ferropericlase in the lower mantle (Nakajima et al., 2012; Huang et al., 2021a). Following these studies, I used a symmetric solid solution model (i.e., excess molar properties are approximated by a function that is symmetric about its midpoint) to define the excess contribution term to the Gibbs free energy $\mathcal{G}_{\text{ex}}$:

$$\mathcal{G}_{\text{ex}} = \sum_{l>j} x_{jk} x_{lk} W_{jlk} \tag{2.97}$$

where W_{jlk} are Margules interaction parameters describing non-ideal mixing of atoms *j* and *l* at site *k*. By taking the appropriate derivatives of 2.97, the excess contribution to the chemical potential is derived and added to 2.92:

$$\mu_i(P,T) = \mathcal{G}_i + RT \sum_k^{\text{sites}} \left(\sum_j^{\text{atoms}} \ln x_{jk} \right) + \sum_k^{\text{sites}} \left[\sum_{l \neq j}^{\text{atoms}} (1 - x_{jk})^2\, W_{jlk} \right] \tag{2.98}$$

In the case of a single site mixing with multiplicity one (e.g., Mg-Fe^{2+} in ferropericlase and bridgmanite), equation 2.97 is rewritten as:

$$\mu_i(P,T) = \mathcal{G}_i + RT \ln a_i = \mathcal{G}_i + RT \ln n_i \gamma_i = \mathcal{G}_i + RT \ln n_i + (1 - n_i)^2\, W_{im} \tag{2.99}$$

Where a_i is the activity of component i in the solid solution and γ_i the activity coefficient. More details on the derivation of the working equations for the case of Al-bearing bridgmanite is presented in Chapter 5 and Appendix B.

References

Altomare, A., C. Cuocci, G. D. Gatta, A. Moliterni, and R. Rizzi (2017). *Methods of crystallography: Powder x-ray diffraction*. Vol. 19, pp. 79–138. DOI: 10.1180/EMU-notes.19.3.

Anderson, O. L. (1995). *Equations of state of solids for geophysics and ceramic science*. Oxford University Press, p. 405. ISBN: 9780195056068.

Angel, R. J. (2003). "Automated profile analysis for single-crystal diffraction data". In: *Journal of Applied Crystallography* 36 (2), pp. 295–300. DOI: 10.1107/S0021889803001134.

Angel, R. J., M. Alvaro, and F. Nestola (2017). "40 Years of Mineral Elasticity: a Critical Review and a New Parameterisation of Equations of State for Mantle Olivines and Diamond Inclusions". In: *Physics and Chemistry of Minerals*, pp. 1–19. DOI: 10.1007/s00269-017-0900-7.

Angel, R. J. and L. W. Finger (2011). "SINGLE: A program to control single-crystal diffractometers". In: *Journal of Applied Crystallography* 44 (1), pp. 247–251. DOI: 10.1107/S0021889810042305.

Angel, R. J., J. Gonzalez-Platas, and M. Alvaro (2014). "EosFit7c and a Fortran module (library) for equation of state calculations". In: *Zeitschrift fur Kristallographie* 229 (5), pp. 405–419. DOI: 10.1515/zkri-2013-1711.

Birch, F. (1947). "Finite elastic strain of cubic crystals". In: *Physical Review* 71 (11), pp. 809–824. DOI: 10.1103/PhysRev.71.809.

Boehler, R. and K. D. Hantsetters (Sept. 2004). "New anvil designs in diamond-cells". In: *High Pressure Research* 24 (3), pp. 391–396. DOI: 10.1080/08957950412331323924.

Boffa Ballaran, T., A. Kurnosov, K. Glazyrin, D. J. Frost, M. Merlini, M. Hanfland, and R. Caracas (2012). "Effect of chemistry on the compressibility of silicate perovskite in the lower mantle". In: *Earth and Planetary Science Letters* 333-334, pp. 181–190. DOI: 10.1016/j.epsl.2012.03.029.

Bolfan-Casanova, N., H. Keppler, and D. C. Rubie (2000). "Water partitioning between nominally anhydrous minerals in the MgO-SiO_2-H2O system up to 24 GPa: Implications for the distribution of water in the Earth's mantle". In: *Earth and Planetary Science Letters* 182 (3-4), pp. 209–221. DOI: 10.1016/S0012-821X(00)00244-2.

Bragg, W. H. and W. L. Bragg (1913). "The Reflection of X-rays by Crystals." In: *Proceedings of the Royal Society of London. Series A, Containing Papers of a Mathematical and Physical Characte* 88 (605), pp. 428–438. URL: https://www.jstor.org/stable/93501.

Brillouin, L. (1922). "Diffusion de la lumière et des rayons X par un corps transparent homogène". In: *Annales de Physique* 9 (17), pp. 88–122. DOI: 10.1051/anphys/192209170088.

Buchen, J. (2018). "The Elastic Properties of Wadsleyite and Stishovite at High Pressures". URL: https://epub.uni-bayreuth.de/4410/.

— (2021). *Seismic Wave Velocities in Earth's Mantle from Mineral Elasticity*, pp. 51–95. DOI: 10.1002/9781119528609.ch3.

Buchen, J., H. Marquardt, S. Speziale, T. Kawazoe, T. B. Ballaran, and A. Kurnosov (2018b). "High-pressure single-crystal elasticity of wadsleyite and the seismic signature of water in the shallow transition zone". In: *Earth and Planetary Science Letters* 498, pp. 77–87. DOI: 10.1016/j.epsl.2018.06.027.

Busing, W. R. and H. A. Levy (1967). "Angle calculations for 3- and 4-circle X-ray and neutron diffractometers". In: *Acta Crystallographica* 22 (4), pp. 457–464. DOI: 10.1107/s0365110x67000970.

Bykova, E. (2015). "Single-crystal X-ray diffraction at extreme conditions in mineral physics and material sciences". University of Bayreuth, p. 1. URL: https://epub.uni-bayreuth.de/2124/.

Carl, E. R., H. P. Liermann, L. Ehm, A. Danilewsky, and T. Kenkmann (2018). "Phase transitions of α-quartz at elevated temperatures under dynamic compression using a membrane-driven diamond anvil cell: Clues to impact cratering?" In: *Meteoritics and Planetary Science* 53 (8), pp. 1687–1695. DOI: 10.1111/maps.13077.

Carpenter, M. A. and E. K. Salje (1998). "Elastic anomalies in minerals due to structural phase transitions". In: *European Journal of Mineralogy* 10 (4), pp. 693–812. DOI: 10.1127/ejm/10/4/0693.

Carpenter, M. A., E. K. Salje, and A. Graeme-Barber (1998). "Spontaneous strain as a determinant of thermodynamic properties for phase transitions in minerals". In: *European Journal of Mineralogy* 10 (4), pp. 621–691. DOI: 10.1127/ejm/10/4/0621.

Cottaar, S., T. Heister, I. Rose, and C. Unterborn (2014). "BurnMan: A lower mantle mineral physics toolkit". In: *Geochemistry, Geophysics, Geosystems* 15, 1164–1179. DOI: doi:10.1002/2013GC005122.

Datchi, F., A. Dewaele, P. Loubeyre, R. Letoullec, Y. L. Godec, and B. Canny (2007). "Optical pressure sensors for high-pressure–high-temperature studies in a diamond anvil cell". In: *High Pressure Research* 27 (4), pp. 447–463. DOI: 10.1080/08957950701659593.

Davies, G. (1974). "Effective Elastic Moduli Under Hydrostatic Stress - Quasi-Harmonic Theory". In: *Journal of Physics and Chemistry of Solids* 35, pp. 1513–1520. DOI: 10.1016/S0022-3697(74)80279-9.

Debye, P. (1912). "Zur Theorie der spezifischen Wärmen". In: *Annalen der Physik* 344 (14), pp. 789–839. DOI: 10.1002/ANDP.19123441404.

Dil, J. G. (1982). "Brillouin scattering in condensed matter". In: *Reports on Progress in Physics* 45 (3), pp. 285–334. DOI: 10.1088/0034-4885/45/3/002.

Dorogokupets, P. I. and A. Dewaele (2007). "Equations of state of MgO, Au, Pt, NaCl-B1, and NaCl-B2: Internally consistent high-temperature pressure scales". In: *High Pressure Research* 27 (4), pp. 431–446. DOI: 10.1080/08957950701659700.

Dyar, M. D., D. G. Agresti, M. W. Schaefer, C. A. Grant, and E. C. Sklute (2006). "Mössbauer spectroscopy of Earth and planetary materials". In: *Annual Review of Earth and Planetary Sciences* 34, pp. 83–125. DOI: 10.1146/annurev.earth.34.031405.125049.

Every, A. G. (1980). "General closed-form expressions for acoustic waves in elastically anisotropic solids". In: *Physical Review B* 22 (4), pp. 1746–1760. DOI: 10.1103/PhysRevB.22.1746.

Giacovazzo, C., H. L. Monaco, G. Artioli, D. Viterbo, M. Milanesio, G. Gilli, P. Gilli, G. Zanotti, G. Ferraris, and M. Catti (2011). "Fundamentals of Crystallography". In: *Fundamentals of Crystallography*. DOI: 10.1093/ACPROF:OSO/9780199573653.001.0001.

Haussühl, S. (2008). *Physical Properties of Crystals: An Introduction*. Wiley-VCH, pp. 1–433. ISBN: 9783527405435. DOI: 10.1002/9783527621156.

Helffrich, G. and J. A. Connolly (2009). "Physical contradictions and remedies using simple polythermal equations of state". In: *American Mineralogist* 94 (11-12), pp. 1616–1619. DOI: 10.2138/am.2009.3262.

Hill, R. (1963). "Elastic properties of reinforced solids: Some theoretical principles". In: *Journal of the Mechanics and Physics of Solids* 11 (5), pp. 357–372. DOI: 10.1016/0022-5096(63)90036-X.

Holland, T. J. B. and R. Powell (2011). "An improved and extended internally consistent thermodynamic dataset for phases of petrological interest, involving a new equation of state for solids". In: *Journal of Metamorphic Geology* 29 (3), pp. 333–383. DOI: 10.1111/j.1525-1314.2010.00923.x.

Huang, R., T. B. Ballaran, C. A. McCammon, N. Miyajima, D. Dolejš, and D. J. Frost (2021a). "The composition and redox state of bridgmanite in the lower mantle as a function of oxygen fugacity". In: *Geochimica et Cosmochimica Acta* 303, pp. 110–136. DOI: 10.1016/J.GCA.2021.02.036.

Hübschle, C. B., G. M. Sheldrick, and B. Dittrich (2011). "ShelXle: A Qt graphical user interface for SHELXL". In: *Journal of Applied Crystallography* 44 (6), pp. 1281–1284. DOI: 10.1107/S0021889811043202.

Ishii, T., G. Criniti, E. Ohtani, N. Purevjav, H. Fei, T. Katsura, and H. K. Mao (2022a). "Superhydrous aluminous silica phases as major water hosts in high-temperature lower mantle". In: *Proceedings of the National Academy of Sciences of the United States of America* 119 (44), pp. 1–6. DOI: 10.1073/pnas.2211243119.

Ishii, T., N. Miyajima, G. Criniti, Q. Hu, K. Glazyrin, and T. Katsura (2022b). "High pressure-temperature phase relations of basaltic crust up to mid-mantle conditions". In: *Earth and Planetary Science Letters* 584, p. 117472. DOI: 10.1016/j.epsl.2022.117472.

Ishii, T., E. Ohtani, and A. Shatskiy (2022c). "Aluminum and hydrogen partitioning between bridgmanite and high-pressure hydrous phases: Implications for water storage in the lower mantle". In: *Earth and Planetary Science Letters* 583, p. 117441. DOI: 10.1016/j.epsl.2022.117441.

Jacobsen, S. D., C. M. Holl, K. A. Adams, R. A. Fischer, E. S. Martin, C. R. Bina, J. F. Lin, V. B. Prakapenka, A. Kubo, and P. Dera (2008). "Compression of single-crystal magnesium oxide to 118 GPa and a ruby pressure gauge for helium pressure media". In: *American Mineralogist* 93 (11-12), pp. 1823–1828. DOI: 10.2138/am.2008.2988.

Jayaraman, A. (1983). "Diamond anvil cell and high-pressure physical investigations". In: *Reviews of Modern Physics* 55 (1), pp. 65–108. DOI: 10.1103/RevModPhys.55.65.

Kantor, I., V. Prakapenka, A. Kantor, P. Dera, A. Kurnosov, S. Sinogeikin, N. Dubrovinskaia, and L. Dubrovinsky (2012). "BX90: A new diamond anvil cell design for X-ray diffraction and optical measurements". In: *Review of Scientific Instruments* 83 (12), p. 125102. DOI: 10.1063/1.4768541.

Keppler, H. and D. J. Frost (2005). "Introduction to minerals under extreme conditions". In: *EMU notes in Mineralogy*, pp. 1–30. DOI: 10.1180/emu-notes.7.1.

King, H. E. and L. W. Finger (1979). "Diffracted beam crystal centering and its application to high-pressure crystallography". In: *Journal of Applied Crystallography* 12 (4), pp. 374–378. DOI: 10.1107/S0021889879012723.

Kingma, K. J., R. E. Cohen, R. J. Hemley, and H. K. Mao (1995). "Transformation of stishovite to a denser phase at lower-mantle pressures". In: *Nature* 374 (6519), pp. 243–245. DOI: 10.1038/374243a0.

Kono, Y., T. Irifune, Y. Higo, T. Inoue, A. Barnhoorn, D. Suetsugu, C. Bina, T. Inoue, D. Wiens, and M. Jellinek (2010). "*P-V-T* relation of MgO derived by simultaneous elastic wave velocity and in situ X-ray measurements: A new pressure scale for the mantle transition region". In: *Physics of the Earth and Planetary Interiors* 183 (1-2), pp. 196–211. DOI: 10.1016/j.pepi.2010.03.010.

Kurnosov, A., I. Kantor, T. Boffa-Ballaran, S. Lindhardt, L. Dubrovinsky, A. Kuznetsov, and B. H. Zehnder (2008). "A novel gas-loading system for mechanically closing of various types of diamond anvil cells". In: *Review of Scientific Instruments* 79 (4). DOI: 10.1063/1.2902506.

Kurnosov, A., H. Marquardt, D. J. Frost, T. B. Ballaran, and L. Ziberna (2017). "Evidence for a Fe^{3+}-rich pyrolitic lower mantle from (Al,Fe)-bearing bridgmanite elasticity data". In: *Nature* 543, pp. 543–546. DOI: 10.1038/nature21390.

Libowitzky, E. and G. R. Rossman (1996). "Principles of quantitative absorbance measurements in anisotropic crystals". In: *Physics and Chemistry of Minerals* 23 (6), pp. 319–327. DOI: 10.1007/BF00199497.

Libowitzky, E. (1999). "Correlation of O-H Stretching Frequencies and O-H O Hydrogen Bond Lengths in Minerals". In: *Hydrogen Bond Research* 1059, pp. 103–115. DOI: 10.1007/978-3-7091-6419-8_7.

Liermann, H. P., Z. Konôpková, W. Morgenroth, K. Glazyrin, J. Bednarčik, E. E. McBride, S. Petitgirard, J. T. Delitz, M. Wendt, Y. Bican, A. Ehnes, I. Schwark, A. Rothkirch, M. Tischer, J. Heuer, H. Schulte-Schrepping, T. Kracht, and H. Franz (2015). "The Extreme Conditions Beamline P02.2 and the Extreme Conditions Science Infrastructure at PETRA III". In: *Journal of Synchrotron Radiation* 22, pp. 908–924. DOI: 10.1107/S1600577515005937.

Lindsay, S. M., M. W. Anderson, and J. R. Sandercock (1981). "Construction and alignment of a high performance multipass vernier tandem Fabry-Perot interferometer". In: *Review of Scientific Instruments* 52, p. 1478. DOI: 10.1063/1.1136479.

Litasov, K. D., P. N. Gavryushkin, P. I. Dorogokupets, I. S. Sharygin, A. Shatskiy, Y. Fei, S. V. Rashchenko, Y. V. Seryotkin, Y. Higo, K. Funakoshi, and E. Ohtani (2013). "Thermal equation of state to 33.5 GPa and 1673 K and thermodynamic properties of tungsten". In: *Journal of Applied Physics* 113 (13). DOI: 10.1063/1.4799018.

Litasov, K. D., H. Kagi, A. Shatskiy, E. Ohtani, D. L. Lakshtanov, J. D. Bass, and E. Ito (2007a). "High hydrogen solubility in Al-rich stishovite and water transport in the lower mantle". In: *Earth and Planetary Science Letters* 262 (3-4), pp. 620–634. DOI: 10.1016/j.epsl.2007.08.015.

Liu, Z., H. Fei, L. Chen, C. McCammon, L. Wang, R. Liu, F. Wang, B. Liu, and T. Katsura (2021). "Bridgmanite is nearly dry at the top of the lower mantle". In: *Earth and Planetary Science Letters* 570, p. 117088. DOI: 10.1016/j.epsl.2021.117088.

McCammon, C. A. (1994). "A Mössbauer milliprobe: Practical considerations". In: *Hyperfine Interactions* 92 (1), pp. 1235–1239. DOI: 10.1007/BF02065761.

McCammon, C. A. (2004). "Mössbauer spectroscopy: applications". In: *EMU notes in Mineralogy* 6, pp. 369–398.

Murnaghan, F. D. (1937). "Finite Deformations of an Elastic Solid". In: *American Journal of Mathematics* 59 (2), pp. 235–260. URL: 10.2307/2371405.

Myhill, R. (2022). "An anisotropic equation of state for high-pressure, high-temperature applications". In: *Geophysical Journal International* 231 (1), pp. 230–242. DOI: 10.1093/gji/ggac180.

Mössbauer, R. L. (1958). "Kernresonanzfluoreszenz von Gammastrahlung in Ir191". In: *Zeitschrift für Physik 1958 151:2* 151 (2), pp. 124–143. DOI: 10.1007/BF01344210.

Nakajima, Y., D. J. Frost, and D. C. Rubie (2012). "Ferrous iron partitioning between magnesium silicate perovskite and ferropericlase and the composition of perovskite in the Earth's lower mantle". In: *Journal of Geophysical Research: Solid Earth* 117 (8), pp. 1–12. DOI: 10.1029/2012JB009151.

Nye, J. F. (1985). *Physical properties of crystals: their representation by tensors and matrices*. Oxford University Press. ISBN: 9780198511656.

Okuchi, T., N. Purevjav, N. Tomioka, J. F. Lin, T. Kuribayashi, L. Schoneveld, H. Hwang, N. Sakamoto, N. Kawasaki, and H. Yurimoto (2015). "Synthesis of large and homogeneous single crystals of water-bearing minerals by slow cooling at deep-mantle pressures". In: *American Mineralogist* 100 (7), pp. 1483–1492. DOI: 10.2138/am-2015-5237.

Paciorek, W. A., M. Meyer, and G. Chapuis (1999). "On the geometry of a modern imaging diffractometer". In: *Acta Crystallographica Section A: Foundations of Crystallography* 55 (3), pp. 543–557. DOI: 10.1107/S0108767398015037.

Paterson, M. S. (1982). "The determination of hydroxyl by infrared adsorption in quartz, silicate glasses and similar materials." In: *Bulletin de Mineralogie* 105 (1), pp. 20–29. DOI: 10.3406/bulmi.1982.7582.

Pawley, A. R., P. F. McMillan, and J. R. Holloway (1993). "Hydrogen in stishovite, with implications for mantle water content". In: *Science* 261 (5124), pp. 1024–1026. DOI: 10.1126/science.261.5124.1024.

Petrícek, V., M. Dušek, and L. Palatinus (2014). "Crystallographic computing system JANA2006: General features". In: *Zeitschrift fur Kristallographie* 229 (5), pp. 345–352. DOI: 10.1515/zkri-2014-1737.

Philpotts, A. and J. Ague (2009). *Principles of Igneous and Metamorphic Petrology*. Cambridge University Press. ISBN: 9780521880060. DOI: 10.1017/cbo9780511813429.

Poirier, J.-P. (2000). *Introduction to the Physics of the Earth's Interior*. Cambridge University Press. DOI: 10.1017/CBO9781139164467.

Prescher, C., C. McCammon, and L. Dubrovinsky (2012). "MossA : a program for analyzing energy-domain Mössbauer spectra from conventional and synchrotron sources". In: *Journal of Applied Crystallography* 45 (2), pp. 329–331. DOI: 10.1107/S0021889812004979.

Prescher, C. and V. B. Prakapenka (2015). "DIOPTAS: A program for reduction of two-dimensional X-ray diffraction data and data exploration". In: *High Pressure Research* 35 (3), pp. 223–230. DOI: 10.1080/08957959.2015.1059835.

Raman, C. V. and K. S. Krishnan (1928). "A New Type of Secondary Radiation". In: *Nature* 121 (3048), pp. 501–502. DOI: 10.1038/121501c0.

Reed, S. J. (2005). *Electron Microprobe Analysis and Scanning Electron Microscopy in Geology*. Cambridge University Press, pp. 1–197. DOI: 10.1017/CBO9780511610561.

Rull, F. (2012). "The Raman effect and the vibrational dynamics of molecules and crystalline solids". In: *European Mineralogical Union Notes in Mineralogy* 12 (1), pp. 1–60. DOI: 10.1180/EMU-notes.12.1.

Salje, E. K. (1991). *Phase Transitions in Ferroelastic and Co-elastic Crystals*. Cambridge University Press. DOI: 10.1017/cbo9780511586460.

Schulze, K., J. Buchen, K. Marquardt, and H. Marquardt (2017). "Multi-sample loading technique for comparative physical property measurements in the diamond-anvil cell". In: *High Pressure Research* 37 (2), pp. 159–169. DOI: 10.1080/08957959.2017.1299719.

Schulze, K., H. Marquardt, T. Kawazoe, T. B. Ballaran, C. McCammon, M. Koch-Müller, A. Kurnosov, and K. Marquardt (2018). "Seismically invisible water in Earth's transition zone?" In: *Earth and Planetary Science Letters* 498, pp. 9–16. DOI: 10.1016/j.epsl.2018.06.021.

Shatskiy, A., H. Fukui, T. Matsuzaki, K. Shinoda, A. Yoneda, D. Yamazaki, E. Ito, and T. Katsura (2007). "Growth of large (1 mm) $MgSiO_3$ perovskite single crystals: A thermal gradient method at ultrahigh pressure". In: *American Mineralogist* 92 (10), pp. 1744–1749. DOI: 10.2138/am.2007.2415.

Shatskiy, A., K. D. Litasasov, T. Matsuzaki, K. Shinodada, D. Yamaamaamazaki, A. Yonedada, E. Ito, and T. Katsura (2009). "Single crystal growth of wadsleyite". In: *American Mineralogist* 94 (8-9), pp. 1130–1136. DOI: 10.2138/am.2009.3150.

Sheldrick, G. M. (2015a). "Crystal structure refinement with *SHELXL*". In: *Acta Crystallographica Section C: Structural Chemistry* 71, pp. 3–8. DOI: 10.1107/S2053229614024218.

— (2015b). "Foundations and Advances *SHELXT*-Integrated space-group and crystal-structure determination". In: *Acta Cryst* 71, pp. 3–8. DOI: 10.1107/S2053273314026370.

Shen, G. and H. K. Mao (2017). "High-pressure studies with x-rays using diamond anvil cells". In: *Reports on Progress in Physics* 80 (1). DOI: 10.1088/1361-6633/80/1/016101.

Shen, G., Y. Wang, A. Dewaele, C. Wu, D. E. Fratanduono, J. Eggert, S. Klotz, K. F. Dziubek, P. Loubeyre, O. V. Fat'yanov, P. D. Asimow, T. Mashimo, and R. M. Wentzcovitch (2020). "Toward an international practical pressure scale: A proposal for an IPPS ruby gauge (IPPS-Ruby2020)". In: *High Pressure Research*, pp. 1–16. DOI: 10.1080/08957959.2020.1791107.

Siersch, N. C., A. Kurnosov, G. Criniti, T. Ishii, T. B. Ballaran, and D. J. Frost (2021). "The elastic properties and anisotropic behavior of $MgSiO_3$ akimotoite at transition zone pressures". In: *Physics of the Earth and Planetary Interiors* 320, p. 106786. DOI: 10.1016/j.pepi.2021.106786.

Sinogeikin, S., J. Bass, V. Prakapenka, D. Lakshtanov, G. Shen, C. Sanchez-Valle, and M. Rivers (2006). "Brillouin spectrometer interfaced with synchrotron radiation for simultaneous x-ray density and acoustic velocity measurements". In: vol. 77. American Institute of Physics, p. 103905. DOI: 10.1063/1.2360884.

Speziale, S., H. Marquardt, and T. S. Duffy (2014). "Brillouin scattering and its application in geosciences". In: *Reviews in Mineralogy and Geochemistry* 78 (1), pp. 543–603. DOI: 10.2138/rmg.2014.78.14.

Stixrude, L. and C. Lithgow-Bertelloni (2005). "Thermodynamics of mantle minerals - I. Physical properties". In: *Geophysical Journal International* 162 (2), pp. 610–632. DOI: 10.1111/j.1365-246X.2005.02642.x.

— (2011). "Thermodynamics of mantle minerals - II. Phase equilibria". In: *Geophysical Journal International* 184 (3), pp. 1180–1213. DOI: 10.1111/j.1365-246X.2010.04890.x.

Stokes, H. T., D. M. Hatch, and J. D. Wells (1991). "Group-theoretical methods for obtaining distortions in crystals: Applications to vibrational modes and phase transitions". In: *Physical Review B* 43 (13), pp. 11010–11018. DOI: 10.1103/PhysRevB.43.11010.

Sturhahn, W., J. M. Jackson, and J. F. Lin (2005). "The spin state of iron in minerals of Earth's lower mantle". In: *Geophysical Research Letters* 32 (12), pp. 1–5. DOI: 10.1029/2005GL022802.

Thomas, S. M., M. Koch-Müller, P. Reichart, D. Rhede, R. Thomas, R. Wirth, and S. Matsyuk (2009). "IR calibrations for water determination in olivine, r-GeO2, and SiO_2 polymorphs". In: *Physics and Chemistry of Minerals* 36 (9), pp. 489–509. DOI: 10.1007/s00269-009-0295-1.

Trots, D. M., A. Kurnosov, T. B. Ballaran, S. Tkachev, K. Zhuravlev, V. Prakapenka, M. Berkowski, and D. J. Frost (2013). "The Sm:YAG primary fluorescence pressure scale". In: *Journal of Geophysical Research: Solid Earth* 118 (11), pp. 5805–5813. DOI: 10.1002/2013JB010519.

Trots, D. M., A. Kurnosov, L. Vasylechko, M. Berkowski, T. B. Ballaran, and D. J. Frost (2011). "Elasticity and equation of state of $Li_2B_4O_7$". In: *Physics and Chemistry of Minerals* 38 (7), pp. 561–567. DOI: 10.1007/s00269-011-0428-1.

Whitfield, C. H., E. M. Brody, and W. A. Bassett (1976). "Elastic moduli of NaCl by Brillouin scattering at high pressure in a diamond anvil cell". In: *Review of Scientific Instruments* 47 (8), pp. 942–947. DOI: 10.1063/1.1134778.

Withers, A. C., H. Bureau, C. Raepsaet, and M. M. Hirschmann (2012). "Calibration of infrared spectroscopy by elastic recoil detection analysis of H in synthetic olivine". In: *Chemical Geology* 334, pp. 92–98. DOI: 10.1016/j.chemgeo.2012.10.002.

Chapter 3

Synopsis

In this chapter, I will highlight the main results of this thesis and their implications for modelling the composition and physical properties of phase assemblages at lower mantle conditions and inferring the origin of its local heterogeneity. Chapter 4 has been published as Criniti et al. (2021) and presents experimental results on the sound velocities and single-crystal elasticity of $MgSiO_3$ single crystals at lower mantle pressures and their implications for the modelling of the depth-dependent sound velocities of a pyrolitic lower mantle assemblage. Chapter 5 has been prepared for publication and describes the pressure-volume-temperature relations of aluminous bridgmanite single crystals, with implications for the stability of oxygen vacancies in bridgmanite as a function of pressure, temperature, and chemical composition. Additionally, in Section 3.3, single-crystal structural refinements of aluminous bridgmanite at high pressure and temperature are reported for the first time, showing a relation between the pressure and temperature dependency of octahedral tilting systems and the stability of the bridgmanite structure. Chapter 6 has been published online as Criniti et al. (2023a, in press) and reports the phase transition and isothermal equation of state of hydrous Al-bearing tetragonal stishovite, as well as the first experimental evidence of a quenchable orthorhombic post-stishovite phase, with implications for the interpretation of seismic scattering anomalies in the shallow lower mantle. Chapter 7 has been accepted for publication as Criniti et al. (2023b, in press) and reports experimental results on the crystal structure, compressibility, and spin crossover of Fe-bearing Al-phase D, with implications for the symmetrisation of H-bonds in hydrous phases in Earth's transition zone and lower mantle.

3.1 Single-Crystal Elasticity of $MgSiO_3$ bridgmanite

High-pressure measurements of the sound velocities of bridgmanite by Brillouin scattering in the diamond anvil cell (DAC) are often impeded by the overlap of the quasi-longitudinal acoustic velocities (v_P) of the sample with the much more intense transverse mode (v_S) of diamond anvils (Jackson et al., 2005; Murakami et al., 2007; Murakami et al., 2012; Kurnosov et al., 2017). Carefully constraining and controlling the reciprocal orientation of diamond anvils and bridgmanite single-crystal platelets is thus of crucial importance to be able to measure experimentally the sound velocities of this mineral at deep lower mantle

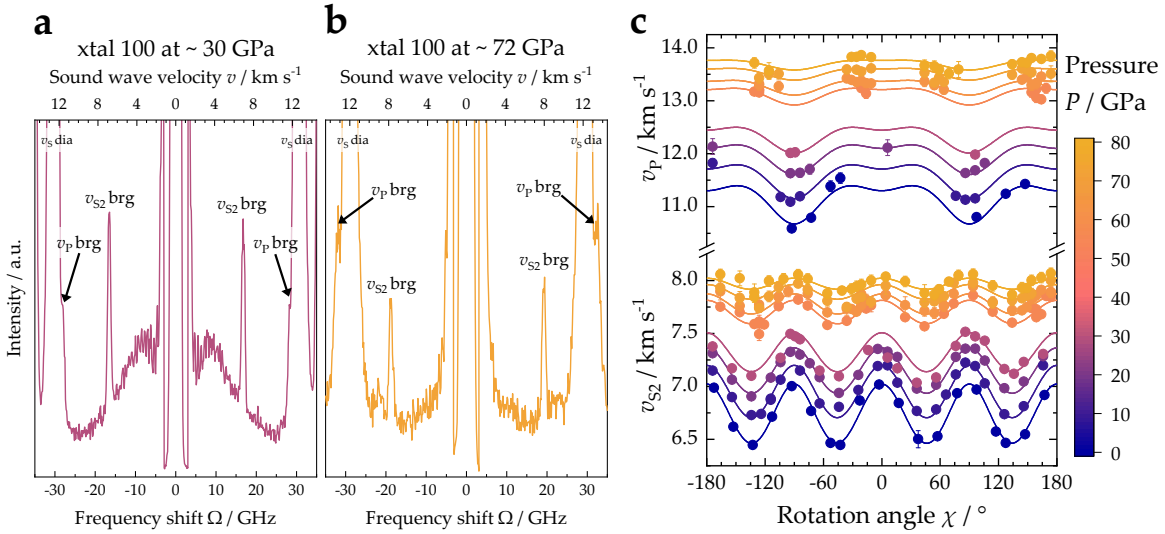

Figure 3.1. (a-b) Brillouin spectra of $MgSiO_3$ bridgmanite collected at pressures of about 30 and 72 GPa, showing the disappearance and reappearance of the v_P of the sample on the low and high-velocity side of the diamond v_S peak. (c) Experimentally determined compressional and shear velocities of $MgSiO_3$ bridgmanite (solid symbols) in the (100) plane as a function of the rotation angle χ and pressure (colour scale), and dispersion curves calculated from the global inversion of sound velocity and density data.

pressures. In Chapter 4, I describe a new protocol for preparing and conducting such high-pressure experiments using single crystals of $MgSiO_3$ bridgmanite and present the first experimental constraints on its elastic tensor at high pressure by inverting high-quality sound velocity datasets and X-ray diffraction data. In experiments performed below 30 GPa, extreme care was adopted in matching the direction of maximum and minimum v_P of two bridgmanite samples with those of maximum shear velocity of diamond. In this way, direct observations of the sample's compressional and shear wave velocities up to about 30 GPa were made possible (Figure 3.1a). At pressures exceeding 50 GPa, on the other hand, the directions of minimum diamond velocities needed to be matched with those of maximum v_P of the two samples, so that it was possible to observe a clear crossover between the two peaks (Figure 3.1b) and constrain the full elastic tensor of bridgmanite at mid-lower mantle pressures for the first time.

The range of quasi-longitudinal acoustic phonon directions in a bridgmanite sample accessible above 50 GPa was unfortunately insufficient to independently refine the elastic tensor of bridgmanite at each pressure point. Instead, a global inversion of sound velocities and density measurements at all pressures was adopted. By combining equations 2.63 and 2.38, I was able to obtain the room-pressure elastic stiffness $c_{ij,0}$ and their pressure derivatives $c'_{ij,0}$ with which to fit simultaneously all the measured velocities (Figure 3.1c). From these parameters, the elastic anisotropy of $MgSiO_3$ bridgmanite was calculated at different pressure points and compared with that reported in previous experimental studies. Results from this thesis at 25-35 GPa were found to be in good agreement with the elastic anisotropy of Fe,Al-bearing bridgmanite reported by Kurnosov et al. (2017) from Brillouin

scattering measurements but were found to be dissimilar from to the results of Fu et al. (2019) based on combined Brillouin scattering and impulsive stimulated light scattering data. Given the internal consistency of the measurements presented here and in the study of Kurnosov et al. (2017), I suggested that extreme care should be used when combining datasets collected from the same sample but using two different setups. From the global inversion procedure, referred as to a global fit in Chapter 4, the pressure dependencies of the elastic moduli K and G in the Reuss and Voigt bound were also obtained using equations 2.13-2.16, 2.29, and 2.39. The calculated aggregate velocities were found to be significantly higher (up to 6%) than those obtained in a previous study that employed a polycrystalline sample (Murakami et al., 2007). As polycrystalline samples are often synthesised in situ, with a typical grain size well below 1 micrometre, care should be used when collecting such data as the contribution from grain boundaries can effectively reduce the sound velocities of the material, as previously shown for MgO (Marquardt et al., 2011).

Some of the previous estimates on the composition of Earth's lower mantle were based on separate shear velocity measurements and static compression experiments of bridgmanite polycrystalline samples (Murakami et al., 2007; Murakami et al., 2012), which I have shown to be biased, likely because of grain size effects. Moreover, in those models, the chemical composition of bridgmanite and ferropericlase was arbitrarily assumed to be independent of pressure, and the appropriate averaging schemes required to model the velocities of polycrystalline aggregates were not adopted (Cottaar et al., 2014). This further invalidates the conclusions on both the lower mantle composition and its convection regime drawn by these studies. Here, the high-pressure sound velocity data obtained in this thesis were combined with previously published velocities collected at high pressure and temperature by ultrasonic interferometry measurements in LVP (Chantel et al., 2012) to reassess the thermoelastic parameters of the $MgSiO_3$ bridgmanite end member. Together with experimental and theoretical results from previous studies on other lower mantle minerals (Kono et al., 2010; Fischer et al., 2011; Stixrude and Lithgow-Bertelloni, 2011; Gréaux et al., 2019) and thermodynamic data describing the partitioning of Fe^{2+} and Mg between bridgmanite and ferropericlase (Nakajima et al., 2012), an internally consistent mineral physical model was built to calculate the sound wave velocities of a simplified pyrolite composition (Mcdonough and Rudnick, 1998) along an adiabatic temperature profile at lower mantle depths. The model is a simplified one, as it neglects the effect of Al and oxygen fugacity on the Fe^{2+}-Mg partitioning and sound velocity calculation due to the lack of thermodynamic data on Al-bearing systems at the time of publication. Nevertheless, the calculated velocities are in excellent agreement with those reported in reference models of Earth's interior (Dziewonski and Anderson, 1981; Kennett et al., 1995), as shown in Figure 4.5, suggesting that the chemical compositions of the upper and lower mantle may not be as dissimilar as previously proposed.

3.2 Thermal equation of state and crystal structure of Al-bearing bridgmanite

In recent years, more and more single-crystal diffraction studies of bridgmanite samples have allowed to put tighter and tighter constraints on the compression behaviour and structural evolution of some of its end member components (e.g., Boffa Ballaran et al., 2012; Ismailova et al., 2016). However, compression studies of Fe-free aluminous bridgmanite performed so far were carried out exclusively on polycrystalline samples, typically synthesised in-situ. To determine quantitatively the effect of the charged-couple (CC) $AlAlO_3$ and oxygen-vacancy (OV) $MgAlO_{2.5}$ substitution mechanisms on the compressibility of aluminous bridgmanite, single crystals were first synthesised at shallow lower mantle conditions in a multi-anvil press. The samples were characterised in-house by electron microprobe and single-crystal X-ray diffraction at ambient conditions. From the analysis of a large number of Al-bearing bridgmanite samples reported here and in the literature (Daniel et al., 2004; Walter et al., 2004; Walter et al., 2006; Jackson et al., 2005; Kojitani et al., 2007; Liu et al., 2019c; Liu et al., 2019b; Liu et al., 2017a; Liu et al., 2017b), the difference in the effects of CC and OV substitutions on the molar volume at ambient conditions seems to be not significant, with trends along the $MgSiO_3$-$AlAlO_3$ and $MgSiO_3$-$MgAlO_{2.5}$ joins being identical within the uncertainties (Figure 3.2a). While the trend for the CC solid solution fits well the molar volumes of samples investigated in previous studies, the $MgSiO_3$-$MgAlO_{2.5}$ join was found to plot well below the trend previously determined by micro-focused powder X-ray diffraction, most likely because of the fitting strategy employed in previous studies.

Three of the four samples synthesised in this study were then employed in high-pressure experiments in the DAC. Single-crystal X-ray diffraction measurements were carried out at the synchrotron beamline P02.2 of PETRA-III (Hamburg, Germany) at ambient temperature up to 80 GPa. Additionally, using the resistively heated DAC setup described in Section 2.3.3, simultaneous high-pressure and high-temperature measurements were performed on two samples with the same bulk Al content but different CC and OV molar fractions. In the most successful run, temperatures as high as 1000 K were generated while collecting high-quality diffraction data at lower mantle pressures. Before fitting the experimental data collected for aluminous bridgmanite samples, a best-fit thermal equation of state of $MgSiO_3$ bridgmanite was calculated from literature data (Katsura et al., 2009; Boffa Ballaran et al., 2012; Tange et al., 2012) using mutually consistent pressure scales (Dorogokupets and Dewaele, 2007; Jacobsen et al., 2008). Some of the thermal parameters obtained with this procedure (i.e., $\theta_{D,0}$ and q_0 as defined in Section 5.4) were then assumed to be the same in aluminous bearing bridgmanite samples to reduce the correlation between fit parameters without affecting the quality of the fit. From the analysis of the elastic and thermoelastic parameters, as well as polyhedral compressibility obtained from structural refinements, it appears that the presence of 5 mol.% OV component, compatible with the concentrations expected in a pyrolitic lower mantle (Huang et al., 2021a), have a negligible

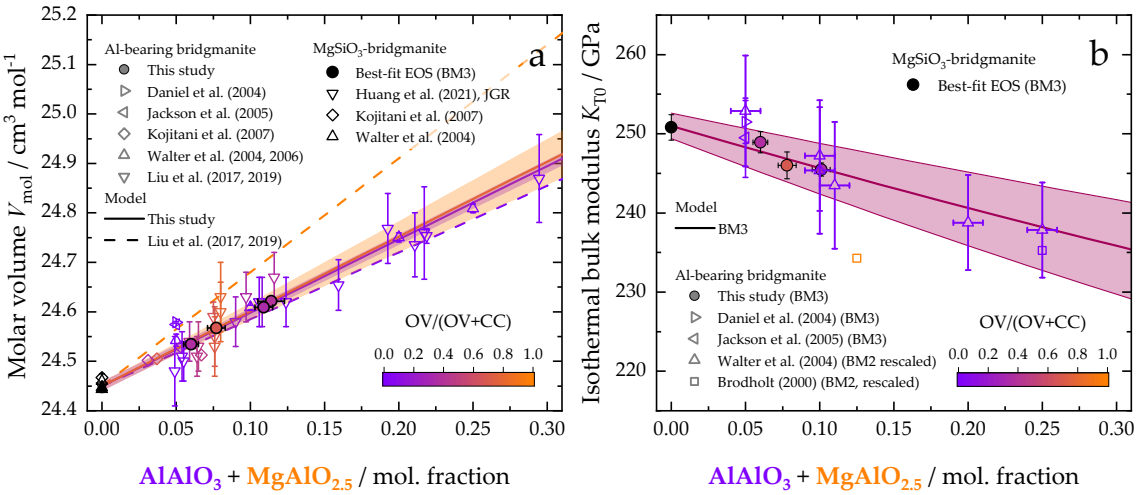

Figure 3.2. (a) Molar volume and (b) isothermal bulk modulus of Al-bearing bridgmanite samples at ambient conditions analysed in this and previous studies as a function of the molar content of CC and OV components. If not shown, error bars are smaller than the symbol. The colour scale indicates the relative abundance of OV and CC substitutions in each sample, i.e., purple for the $MgSiO_3$-CC join and orange for the $MgSiO_3$-OV join. Solid and dashed lines represent the expected volume trend for OV (orange) and CC (purple) joins from this study and Liu et al. (2019c) and Liu et al. (2019b), respectively. Shaded areas represent the estimated uncertainties in the modelled trends.

effect on the high-pressure and high-temperature behaviour of aluminous bridgmanite. In fact, the trend obtained by plotting the isothermal bulk modulus versus CC + OV content seems to be linear and independent of the fraction of CC and OV (Figure 3.2b). Therefore, it seems that the main factor influencing the isothermal bulk modulus of aluminous bridgmanite is the octahedral Al content. The data and trend obtained in Chapter 5 are in good agreement with previous results from isothermal compression and sound velocity measurements under quasi-hydrostatic conditions (Daniel et al., 2004; Jackson et al., 2005). Rescaling of static compression data collected using non-hydrostatic pressure transmitting media (Walter et al., 2004; Walter et al., 2006) relative to K_{T0} from the best-fit equation of state of $MgSiO_3$ bridgmanite also shows a compatible dependence of K_{T0} with the Al content in the B-site.

One application of the experimental results on the thermal equation of state of aluminous bridgmanite involves the extrapolation of the phase relations data in the MgO-$AlO_{1.5}$-SiO_2 system to pressures of the mid lower mantle. As show in Section 2.5.2, a Debye model can be used to compute thermodynamic properties of a given end member component at high pressure and temperature. From experimental data, the molar solubility of the $AlAlO_3$ and $MgAlO_{2.5}$ end members is limited to about 20% and 7%, respectively. Therefore, fictitious components with an intermediate composition can be treated as end members to reduce the magnitude of interaction parameters in the calculations (see Huang et al., 2021a, and section 5.5). From a reanalysis of literature data at 25-27 GPa and 1873-2000 K, I refined the interaction parameter of Si and Al in the B-site of bridgmanite and the standard state

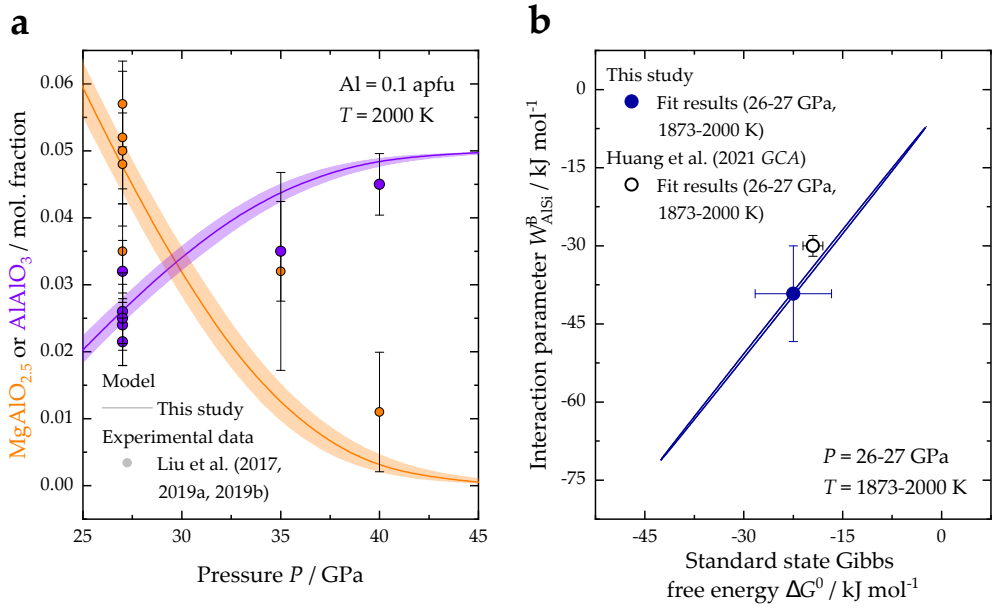

Figure 3.3. (a) Refined Si-Al interaction parameter and Gibbs free energy of reaction at 26-27 GPa and 1873-2000 K from this thesis and Huang et al. (2021a). The error bars and confidence ellipse correspond to 1 estimated standard deviation. (b) Modelled CC and OV molar fractions in bridgmanite containing 0.1 Al per formula unit as a function of pressure at 2000 K. Solid symbols are literature data (Liu et al., 2017a; Liu et al., 2019c; Liu et al., 2019b), solid lines are the modelled CC and OV molar fractions and the shaded areas represent the estimated model uncertainties.

Gibbs free energy of the reaction describing the formation of oxygen vacancies (Figure 3.3a). Extrapolation to higher pressure using the newly determined thermoelastic parameters of aluminous bridgmanite shows a reasonable agreement with experimental data up to 40 GPa (Liu et al., 2017a). Furthermore, it is shown that large molar volume and compressibility differences between the $AlAlO_3$ and $MgAlO_{2.5}$, as proposed by previous studies (Brodholt, 2000), lead to a much steeper decrease of the $MgAlO_{2.5}$ component, which is inconsistent with high-pressure-temperature experiments. When included in more complex models, considering the effect of Fe and oxygen fugacity, the thermoelastic and thermodynamic parameters reported in Chapter 5 will also enable to obtain more reliable estimates for the composition of bridgmanite and coexisting ferropericlase at shallow- to mid-lower mantle conditions.

3.3 Structural distortions of $MgSiO_3$ and aluminous bridgmanite at high pressure and temperature

Structural distortions in minerals are often related to their thermodynamic stability and can be used to infer how their physical and thermal properties change in the proximity of phase transformations (Carpenter et al., 1998). To assess what are the most relevant structural distortions in bridgmanite and how they respond to changes in pressure and temperature

is thus of pivotal importance to understand, for instance, the mechanism that leads to the formation of post-perovskite at the bottom of Earth's lower mantle (Murakami et al., 2004; Oganov and Ono, 2004). Distortions of the perovskite structure are typically calculated with respect to an ideal cubic perovskite (space group $Pm\bar{3}m$), called aristotype. Tilting of octahedra around the unit-cell axes of the aristotype perovskite structure, or pseudo-cubic axes, causes a decrease in the space-group symmetry (Glazer, 1972). A rigorous derivation of octahedral tilt angles can only be achieved by decomposition of the overall structural distortion, obtained from a structural refinement, into simple displacive modes, each complying with a specific set of symmetry operations (Howard and Stokes, 1998). The symmetry of each mode can be described by an irreducible representation (irrep) of the aristotype space group. The irreps amplitude, calculated as the total displacement of O atoms and A-site cation, can then be used to directly assess which structural distortions are more prominent and which are more sensitive to changes in pressure and temperature. In this section, I have derived the amplitude of the irreps related to octahedral tilting in $MgSiO_3$ and aluminous bridgmanite from high-pressure-temperature structural refinements using the web-based computer programs AMPLIMODES and ISODISTORT (Campbell et al., 2006; Orobengoa et al., 2009). Structural refinements of $MgSiO_3$ bridgmanite at high pressure were derived from the dataset published by Boffa Ballaran et al. (2012), while the three datasets of aluminous bridgmanite (CC2OV5, CC4OV2, and CC7OV3, see Table 5.1) are the same presented in Section 3.2 and described more in detail in Chapter 5.

Five displacive modes are required to describe the global distortion of bridgmanite (Huang et al., 2021b). Out of these modes, the irreps R_4^+, M_3^+, and X_5^+ (Miller and Love, 1967; Howard and Stokes, 1998) exhibit the largest amplitudes. These three irreps are related to the out-of-phase tilting of BO_6 octahedra about the pseudo-cubic [110] direction, the in-phase tilting of BO_6 octahedra about the pseudo-cubic [001] direction and the distortion of the A-site, respectively. Previous experimental studies on orthorhombic perovskite analogue materials (Martin et al., 2006) and theoretical studies of $MgSiO_3$ bridgmanite (Tsuchiya et al., 2004; Oganov et al., 2005) proposed that the $Pbnm$ perovskite structure becomes unstable and transforms to $Cmcm$ post-perovskite when inter-octahedral anions become too close to each other due to either shearing or pressure-induced octahedral tilting. Therefore, the post-perovskite transformation must occur when the amplitudes of R_4^+ and/or M_3^+ reach a critical value, which may vary depending on composition. Martin and Parise (2008) analysed the transformation of orthorhombic perovskites to post-perovskites driven by changes in pressure and temperature and proposed that such transition should occur when one of the inter-octahedral distances between anions (i.e., O-O measured across the A-site) becomes equal to the average intra-octahedral anion-anion distance (i.e., measured along the edges of the B-site octahedron). These authors found that the shortest inter-octahedral anion-anion distance driving the post-perovskite transition is aligned along the *c*-axis and is related to the out-of-phase tilting of octahedra (irrep R_4^+) about the [110] direction of the pseudo-cubic aristotype unit cell.

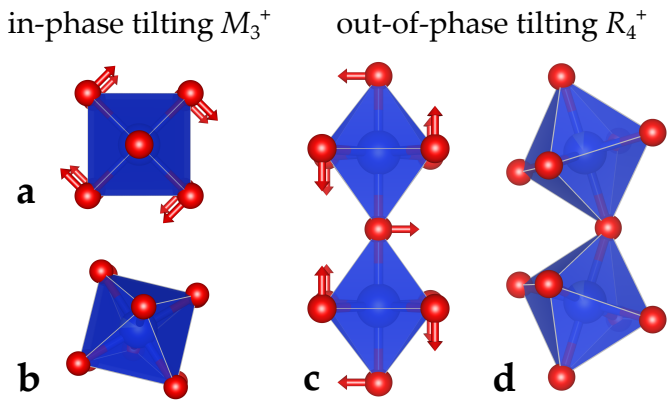

Figure 3.4. Sketch of the two most prominent distortion modes in bridgmanite, related to in-phase (a-b, view along [001]) and out-of-phase (c-d, view along [110]) octahedral tilting. Arrows in (a) and (c) indicate the direction of displacement of O atoms in the undistorted aristotype cubic structure, while (b) and (d) show the resulting overall distortion in the orthorhombic $Pbnm$ structure.

In our datasets, we observed that M_3^+ increases more steeply than R_4^+ with pressure at room temperature, yet R_4^+ remains the most prominent distortion in the pressure and temperature range investigated (Figure 3.5a). Additionally, we found that M_3^+ is basically temperature-independent, while R_4^+ decreases at high temperature (Figure 3.5b). This means that high-temperature conditions reduce the out-of-phase octahedral tilting and that the critical value of R_4^+ for which the post-perovskite transition is triggered shifts to higher pressure. Although this observation is only qualitative and does not allow to predict the exact pressure-temperature conditions of the post-perovskite transition, it is consistent with the positive Clapeyron slope observed for the reaction (e.g., Catalli et al., 2009; Hirose et al., 2006; Murakami et al., 2005). From a more quantitative perspective, it should be noted that the amplitudes of R_4^+ and M_3^+ in Al-bearing bridgmanite are equal to or higher than in the $MgSiO_3$ sample throughout the entire pressure range investigated (Figure 3.5a). If the critical value of R_4^+ is, on a first approximation, independent of composition, our structural data would suggest that Al-bearing bridgmanite should transform to post-perovskite at lower pressure than $MgSiO_3$. Experimental and theoretical studies, however, actually suggest that the opposite is true, i.e., that the bridgmanite to post-perovskite transition in Al-bearing systems should occur at higher pressure (Akber-Knutson et al., 2005; Caracas and Cohen, 2005; Tateno et al., 2005). Given that the pressure dependence of R_4^+ is similar for all the investigated samples (Figure 3.5a), it is hard to imagine that this inconsistency is due to a different temperature-dependency between Al-bearing and $MgSiO_3$ bridgmanite. For instance, by normalising the high-temperature R_4^+ and M_3^+ values for CC2OV5 and CC4OV2 samples to their room temperature values, the same line can be fit to both data sets. An alternative explanation could be that the Si-Al interactions between neighboring octahedral sites that develop at the local scale in Al-bearing bridgmanite might stabilise the perovskite structure to higher degrees of distortion and, thus, to higher pressures than in $MgSiO_3$ bridgmanite. This possibility was not considered by Martin and Parise (2008), who focused only on perovskite end members in their analysis, but may significantly affect the critical value of octahedral tilting for the stability of bridgmanite solid solutions. Single-crystal X-ray diffraction measurements at pressure and temperature conditions of the bottom lower mantle will be needed to further discuss this hypothesis.

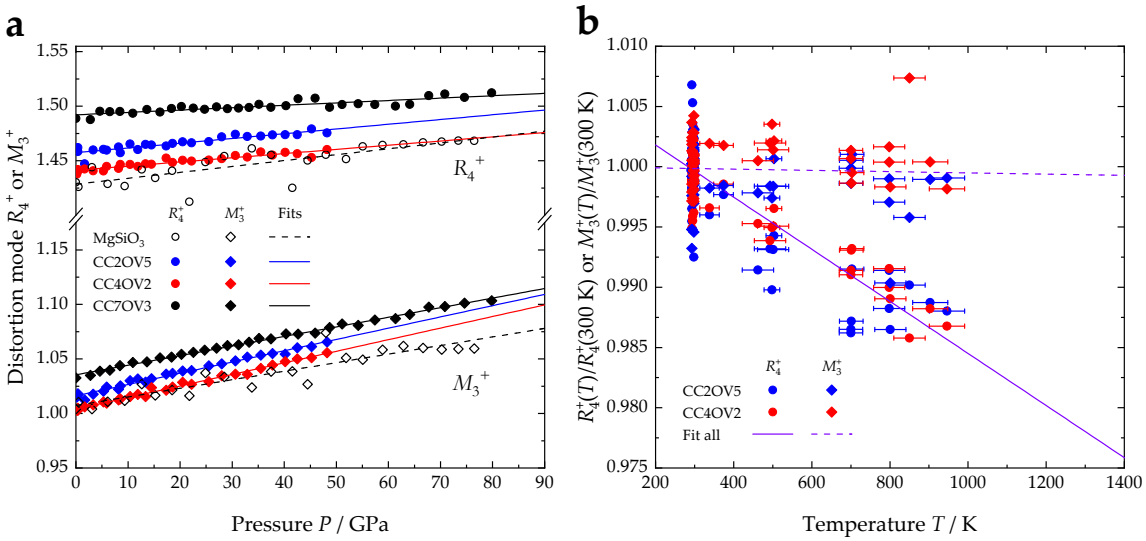

Figure 3.5. (a) Pressure and (b) temperature dependence of octahedral tilting distortion modes R_4^+ and M_3^+ of $MgSiO_3$ and Al-bearing bridgmanite. In (a), room temperature data of the four bridgmanite compositions are shown. In (b) the amplitudes of R_4^+ and M_3^+ of CC2OV5 and CC4OV2 are normalised to their room-temperature value (300 K) and plotted as a function of temperature. Additionally, due to the limited amount of data, the same line (purple) was used to fit to data points of CC2OV5 and CC4VO2.

3.4 High-pressure behaviour of hydrous Al-bearing silica

The phase transformation of tetragonal SiO_2 stishovite to its orthorhombic high-pressure polymorph post-stishovite is known to be influenced by the concentration of chemical impurities, such as Al and H, which shift the transition boundary towards lower pressures (Lakshtanov et al., 2007b; Bolfan-Casanova et al., 2009; Nisr et al., 2017). The post-stishovite transition is of the ferroelastic type (Carpenter et al., 2000) and therefore is accompanied by a reduction of up to 20% of the aggregate shear wave velocity (v_S) (Carpenter et al., 2000; Buchen et al., 2018a; Zhang et al., 2021) and is believed to be seismologically detectable (Kaneshima and Helffrich, 1999). As stishovite is a main constituent of basaltic phase assemblages at lower mantle conditions (Ishii et al., 2022b), understanding the individual and combined effects of Al and H substitution on the transition mechanism and transition pressure yields the potential to infer the position and degree of hydration of fragments of oceanic crustal material in the topmost to mid-lower mantle by interpreting seismic scattering anomalies (Kaneshima, 2019). Additionally, in a recent publication we found that Al-bearing silica not only retains up to 1.1 wt.% H_2O up to 2200 K at 28 GPa but also preserves the $CaCl_2$-type structural modification of post-stishovite upon decompression to ambient conditions (Ishii et al., 2022a). The high water solubility and thermal stability of hydrous Al-bearing silica phases is likely related to the particular incorporation mechanism of H atoms in their crystal structure and possibly the symmetrisation of their H-bond, as observed in the isostructural compound phase δ-AlOOH (Sano-Furukawa et al., 2018).

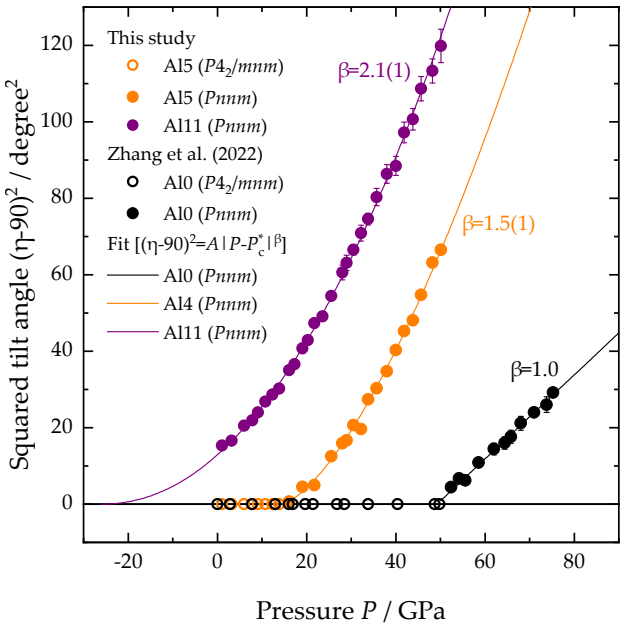

Figure 3.6. Squared tilt angle of $(Si_{1-x}Al_x)O_6$ octahedra in SiO_2 (Zhang et al., 2023) and hydrous Al-bearing silica as a function of pressure. With increasing AlOOH component, the exponent in the power law gradually changes from 1, as in a pseudo-proper ferroelastic transition, to more than 2.

To better understand these relations, in Chapter 6 I present results obtained from single-crystal X-ray diffraction measurements, structural refinements, and Raman spectroscopy measurements at high pressure on two samples of tetragonal $Al_{0.05}Si_{0.95}O_{1.98}H_{0.02}$ (Al5) and orthorhombic $Al_{0.11}Si_{0.89}O_{1.98}H_{0.07}$ (Al11).

Upon compression to about 16 GPa, the symmetry of Al5 changed from tetragonal to orthorhombic, which was evidenced by the splitting of the diagnostic diffraction peaks (e.g., 200, 310) and the consequent divergence of the a and b unit-cell lattice parameters. Across this transformation, the isothermal bulk modulus dropped by about 12%, as observed in some previous static compression studies (e.g., Buchen et al., 2018a). The Al11 sample, on the other hand, presented the orthorhombic modification throughout the entire pressure range investigated, i.e., up to about 50 GPa. From the structural refinements, the pressure dependence of the octahedral tilt angle in the two samples was also extracted, while the deviation of the oxygen position from that expected in the tetragonal structure was used to calculate the amplitude of the Γ_2^+ irrep, which is the one driving the phase transition. A Landau theory expansion for the post-stishovite transition was first proposed by Carpenter et al. (2000) and subsequently employed in other studies (Buchen et al., 2018a; Zhang et al., 2021) to infer the high-pressure evolution of the c_{ij} in the tetragonal and orthorhombic phases. The underlying assumption to these calculations is that the squared order parameter (Q^2) driving the phase transition, which in this case is the squared octahedral tilt angle (η^2) or the squared amplitude of its respective irrep (Γ_2^{+2}), scales linearly with pressure. This behaviour, however, was not observed in Al5, which instead showed a concave evolution with pressure of the mentioned parameters (Figure 3.6). In addition to this, the evolution of the Raman active soft mode associated with the post-stishovite transition also displayed a different behaviour from previously studied SiO_2 and aluminous stishovite samples

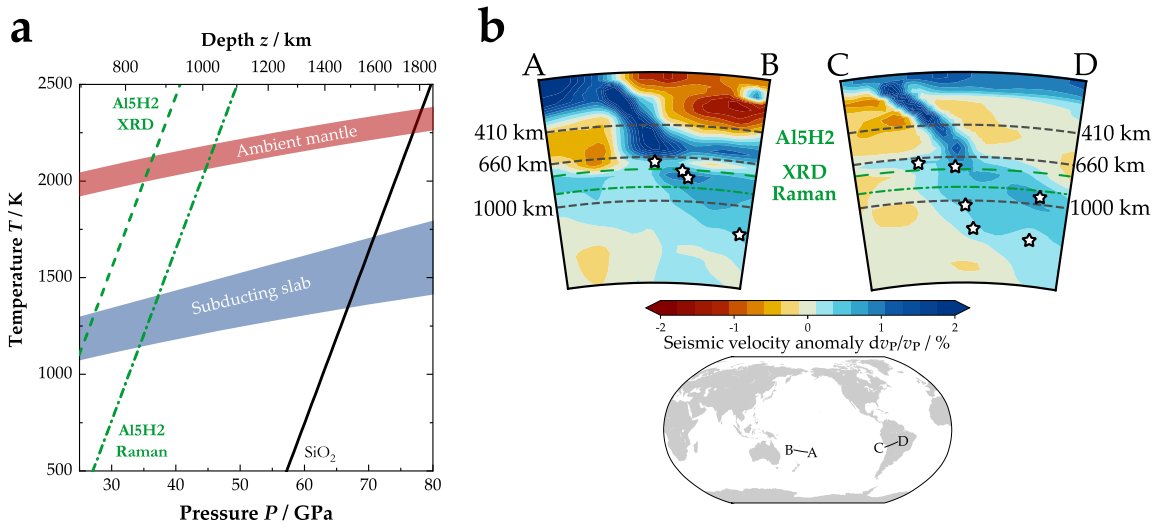

Figure 3.7. (a) Pressure-temperature-depth conditions for the transformation of SiO_2 (black line, Zhang et al., 2021) and $Al_{0.05}Si_{0.95}O_{1.98}H_{0.02}$ (Al5H2, green lines, this study) stishovite to post-stishovite assuming a Clapeyron slope of 89 K/GPa (Nomura et al., 2010), and temperature profiles proposed for the ambient mantle (Katsura et al., 2010) and subducting slabs (Kirby et al., 1996; Eberle et al., 2002). (b) Depth and position of seismic scattering anomalies (Kaneshima, 2019) superimposed to P-wave seismic tomographic sections across the Tonga-Fiji (A-B) and South American (C-D) subduction zones. Green lines represent the expected depth conditions for the post-stishovite transformation of $Al_{0.05}Si_{0.95}O_{1.98}H_{0.02}$, as shown in (a). Seismic tomographic sections were computed from the TX2019slab model (Lu et al., 2019) using the web-based tool SubMachine (Hosseini et al., 2018).

(Kingma et al., 1995; Lakshtanov et al., 2007b; Zhang et al., 2021). Specifically, the squared wavenumber (ω^2) is expected to initially decrease linearly with pressure and abruptly increase after the transition to post-stishovite. In Al5, on the other hand, ω^2 was found to decrease up to 20 GPa, then to remain constant for a pressure interval of about 10 GPa, and to increase only above 30 GPa. A similar plateau was observed in the high-pressure evolution of ω^2 of Al11 from room pressure up to 25 GPa, suggesting that this unexpected behaviour may be related to the high concentration of H in the crystal structure and the symmetrisation of H-bonds.

Combining the transition pressure observed in this and previous studies (Lakshtanov et al., 2005; Lakshtanov et al., 2007b; Zhang et al., 2021), it is possible to model the effect of $AlO_{1.5}$ and AlOOH substitutions in stishovite on the post-stishovite transformation. Note, however, that the effect of the AlOOH component changes significantly depending on the transition pressure used for this sample, i.e., 16 GPa from X-ray diffraction or 25 GPa (midpoint of the plateau region) from Raman spectroscopy. In Figure 3.7a, both scenarios are shown for the Al5 sample, where the extrapolation to higher temperature was obtained assuming a Clapeyron slope of 89 K/GPa, in agreement with experimental data (Nomura et al., 2010). The calculated pressure-temperature conditions for Al5 match those of the

topmost lower mantle along a subduction geotherm, corresponding to depths of about 720 or 860 km depth. In the same depth interval, several seismic scattering bodies were detected in the proximity of subducted slabs (Kaneshima, 2019), for instance beneath the Fiji-Tonga and South American subduction zones (Figure 3.7b). This suggests that water can be effectively stored in subducted metabasalt in the topmost lower mantle even in the absence of nominally hydrous phases such as hydrous phase D or phase δ-(Al,Mg,Si)OOH.

3.5 Structure and compressibility of Fe-bearing Al-phase D

Out of the hydrous phases that have been proposed to carry water in the mantle transition zone and topmost lower mantle, Al-phase D, nominally $Al_2SiO_6H_2$, was found to be the more resistant to high temperatures (Pamato et al., 2015). Such an enhanced thermal resistance seems to be caused by the disordering of Si and Al, which are evenly distributed among the available octahedral sites, and the presence of strong hydrogen bonds (H-bonds), as revealed from the Pauling bond strength of O atoms (i.e., +1.42) that is significantly smaller than in Mg-phase D (i.e., +1.67, Yang et al., 1997a). Additionally, the structural disorder promotes an increase in the space group symmetry from $P\bar{3}1m$ in Mg-phase D to $P6_3/mcm$. In Chapter 7, the first experimental constraints on the crystal structure and high-pressure behaviour of an Fe-bearing Al-phase D are presented. The choice of studying a Fe-bearing sample is motivated by the occurrence of a high-to-low spin crossover in octahedrally coordinated Fe^{3+} at shallow lower mantle pressure, which is known to also affect the physical properties of phase D solid solutions (Chang et al., 2013; Wu et al., 2016; Hsieh et al., 2022). After carefully characterising the sample at ambient conditions by Mössbauer spectroscopy and electron microprobe analysis, the chemical composition was determined to be $Al_{1.53(2)}Fe^{3+}_{0.22(1)}Si_{(0.86(1)}O_6H_{3.33(9)}$. Single-crystal structural refinements showed that the Fe-bearing Al-phase D retains the hexagonal symmetry, as in pure Al-phase D, but loses its center of symmetry due to partial ordering of the cations, resulting in non-equally populated crystallographic sites that are compatible with the space group $P6_322$ (Figure 3.8). Partial ordering of cations at the 2*b* and 2*c* sites of Fe-bearing Al-phase D was further confirmed by the presence of strong diffuse scattering streaks in the collected X-ray frames.

High-pressure X-ray diffraction measurements in diamond anvil cell were also conducted to determine for the first time the compressibility of an Mg-free Al-phase D sample. The sample was compressed to about 52 GPa in two runs and revealed a smooth decrease in the unit-cell volume and lattice parameters up to 38 GPa, after which the observed data points started to progressively deviate from the extrapolation of their respective equations of state. The values of K_{T0} and K'_{T0} obtained for the 3rd-order Birch-Murnaghan fit of the *P-V* data between room pressure and 38 GPa falls toward the higher boundary of the range of values proposed for Mg-phase D (143-186 GPa, Frost and Fei, 1999; Hushur et al., 2011; Rosa et al., 2012; Rosa et al., 2013). No evidence for elastic stiffening due to the

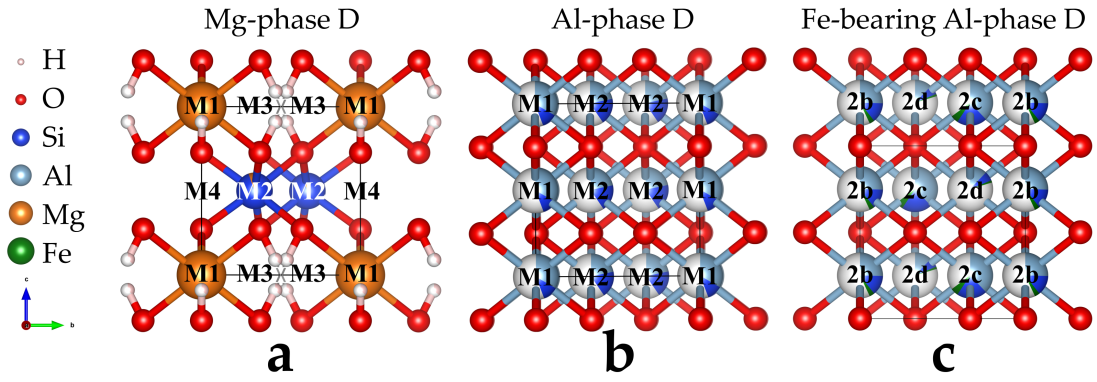

Figure 3.8. Crystal structures of phase D samples having different Mg and Al contents viewed along the a crystallographic axis. The arrows on the bottom left corner show the orientation of the three crystallographic axes. (a) Mg-phase D, nominally $MgSi_2O_6H_2$, space group $P\bar{3}1m$ (Yang et al., 1997a). (b) Al-phase D, nominally $Al_2SiO_6H_2$, space group $P6_3/mcm$ (Pamato et al., 2015). (c) Fe-bearing Al-Phase D, space group $P6_322$ (this study).

symmetrisation of H-bonds was found in this pressure interval. In the same pressure range, recent nuclear magnetic resonance measurements of Fe,Al-bearing Mg-phase D revealed a narrowing of the ^{1}H linewidth, which is related to proton mobility and is diagnostic of the onset of the H-bond symmetrisation (Meier et al., 2022). Given that O···O distances are even shorter in Al-phase D, the symmetrisation would be expected to take place at even lower pressure than in Fe,Al-bearing Mg-phase D. Therefore, I concluded that the strength of H-bonds and their symmetrisation do not seem to affect the elasticity of phase D solid solutions, independently from their chemical composition.

The change in compression behavior observed above 38 GPa is compatible with a spin crossover of Fe^{3+}, which has been reported between 40 and 70 GPa by previous studies (Chang et al., 2013; Wu et al., 2016). The limited number of data points and investigated pressure range after the onset of the spin crossover were insufficient to refine separate EOS parameters for the high- and low-spin states. Instead, a fit of all data points between room pressure and 52 GPa was obtained using a recently-proposed formalism (Buchen, 2021) where the contribution of the spin crossover to the elastic energy (and thus to pressure) is modelled from the volume dependency of crystal-field parameters, which are treated as adjustable parameters. The spin-crossover equation of state provides an excellent fit of the entire dataset, suggesting that the spin crossover region extends between approximately 35 and 65 GPa, in good agreement with X-ray emission spectroscopy data collected on Fe,Al-bearing Mg-phase D (Chang et al., 2013). Therefore, it seems that the substitution of Mg + Si by 2Al has negligible effects on the behavior of phase D across the spin crossover.

The difference in fit parameters reported for phase D samples in the literature can be likely explained by the negative correlation of K_{T0} and K'_{T0} in the equation of state

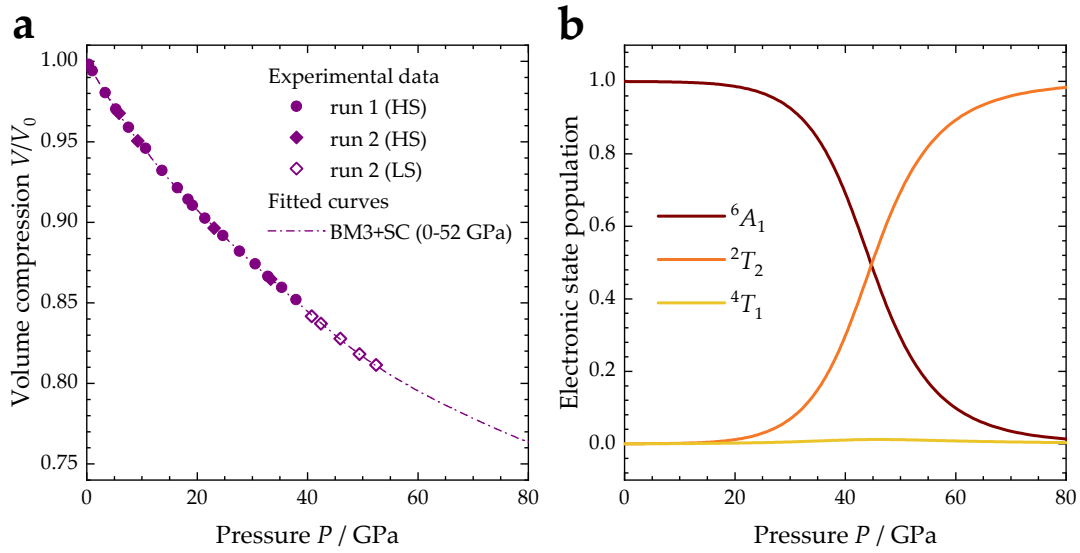

Figure 3.9. (a) Volume compression and (b) high-pressure evolution of the three most populated electronic states in Fe-bearing Al-phase D.

fitting procedure. Due to this tradeoff, K_T values calculated at a pressure of 20-25 GPa, where phase D is expected to be stable (Ghosh and Schmidt, 2014; Liu et al., 2019a), differ from each other by 10-7 GPa at most. Therefore, at mantle transition zone and topmost lower mantle pressures, the bulk modulus of phase D solid solution is expected to be scarcely affected by crystal chemical substitutions. Independently of the phase D chemical composition, its calculated bulk sound velocity in this pressure region results in values that are lower than that of solid solutions of phase δ-AlOOH and $MgSiO_4H_2$ phase H (phase δ-H), for which the disordering and symmetrisation of H-bonds significantly increases the bulk modulus. Therefore, an increase in the bulk sound velocity of hydrous metabasaltic rocks can be expected when phase D converts to phase δ-H at about 25 GPa and 1200 K (Liu et al., 2019a) in the topmost region of Earth's lower mantle.

References

Akber-Knutson, S., G. Steinle-Neumann, and P. D. Asimow (2005). "Effect of Al on the sharpness of the $MgSiO_3$ perovskite to post-perovskite phase transition". In: *Geophysical Research Letters* 32 (14), pp. 1–4. DOI: 10.1029/2005GL023192.

Boffa Ballaran, T., A. Kurnosov, K. Glazyrin, D. J. Frost, M. Merlini, M. Hanfland, and R. Caracas (2012). "Effect of chemistry on the compressibility of silicate perovskite in the lower mantle". In: *Earth and Planetary Science Letters* 333-334, pp. 181–190. DOI: 10.1016/j.epsl.2012.03.029.

Bolfan-Casanova, N., D. Andrault, E. Amiguet, and N. Guignot (2009). "Equation of state and post-stishovite transformation of Al-bearing silica up to 100 GPa and 3000 K". In:

Physics of the Earth and Planetary Interiors 174 (1-4), pp. 70–77. DOI: 10.1016/j.pepi.2008.06.024.

Brodholt, J. P. (2000). "Pressure-induced changes in the compression mechanism of aluminous perovskite in the Earth's mantle". In: *Nature* 407 (6804), pp. 620–622. DOI: 10.1038/35036565.

Buchen, J. (2021). *Seismic Wave Velocities in Earth's Mantle from Mineral Elasticity*, pp. 51–95. DOI: 10.1002/9781119528609.ch3.

Buchen, J., H. Marquardt, K. Schulze, S. Speziale, T. Boffa Ballaran, N. Nishiyama, and M. Hanfland (2018a). "Equation of State of Polycrystalline Stishovite Across the Tetragonal-Orthorhombic Phase Transition". In: *Journal of Geophysical Research: Solid Earth* 123 (9), pp. 7347–7360. DOI: 10.1029/2018JB015835.

Campbell, B. J., H. T. Stokes, D. E. Tanner, and D. M. Hatch (2006). "*ISODISPLACE*: A web-based tool for exploring structural distortions". In: *Journal of Applied Crystallography* 39 (4), pp. 607–614. DOI: 10.1107/S0021889806014075.

Caracas, R. and R. E. Cohen (2005). "Effect of chemistry on the stability and elasticity of the perovskite and post-perovskite phases in the $MgSiO_3$-FeSiO3- Al2O3 system and implications for the lowermost mantle". In: *Geophysical Research Letters* 32 (16), pp. 1–4. DOI: 10.1029/2005GL023164.

Carpenter, M. A., R. J. Hemley, and H. kwang Mao (2000). "High-pressure elasticity of stishovite and the $P4_2/mnm$ - $Pnnm$ phase transition". In: *Journal of Geophysical Research* 105, pp. 807–816.

Carpenter, M. A., E. K. Salje, and A. Graeme-Barber (1998). "Spontaneous strain as a determinant of thermodynamic properties for phase transitions in minerals". In: *European Journal of Mineralogy* 10 (4), pp. 621–691. DOI: 10.1127/ejm/10/4/0621.

Catalli, K., S. H. Shim, and V. Prakapenka (2009). "Thickness and Clapeyron slope of the post-perovskite boundary". In: *Nature* 462 (7274), pp. 782–785. DOI: 10.1038/nature08598.

Chang, Y. Y., S. D. Jacobsen, J. F. Lin, C. R. Bina, S. M. Thomas, J. Wu, G. Shen, Y. Xiao, P. Chow, D. J. Frost, C. A. McCammon, and P. Dera (2013). "Spin transition of Fe^{3+} in Al-bearing phase D: An alternative explanation for small-scale seismic scatterers in the mid-lower mantle". In: *Earth and Planetary Science Letters* 382, pp. 1–9. DOI: 10.1016/j.epsl.2013.08.038.

Chantel, J., D. J. Frost, C. A. McCammon, Z. Jing, and Y. Wang (2012). "Acoustic velocities of pure and iron-bearing magnesium silicate perovskite measured to 25 GPa and 1200 K". In: *Geophysical Research Letters* 39 (19). DOI: 10.1029/2012GL053075.

Cottaar, S., T. Heister, I. Rose, and C. Unterborn (2014). "BurnMan: A lower mantle mineral physics toolkit". In: *Geochemistry, Geophysics, Geosystems* 15, 1164–1179. DOI: doi:10.1002/2013GC005122.

Criniti, G., T. Ishii, A. Kurnosov, K. Glazyrin, and T. B. Ballaran (2023a). "High-pressure phase transition and equation of state of hydrous Al-bearing silica". In: *American Mineralogist* (In press). DOI: 10.2138/am-2022-8546.

Criniti, G., T. Ishii, A. Kurnosov, K. Glazyrin, R. J. Husband, and T. B. Ballaran (2023b). "Structure and compressibility of Fe-bearing Al-phase D". In: *American Mineralogist* (in press). DOI: 10.2138/am-2022-8559.

Criniti, G., A. Kurnosov, T. B. Ballaran, and D. J. Frost (2021). "Single-Crystal Elasticity of $MgSiO_3$ Bridgmanite to Mid-Lower Mantle Pressure". In: *Journal of Geophysical Research: Solid Earth* 126 (5). DOI: 10.1029/2020JB020967.

Daniel, I., J. D. Bass, G. Fiquet, H. Cardon, J. Zhang, and M. Hanfland (2004). "Effect of aluminium on the compressibility of silicate perovskite". In: *Geophysical Research Letters* 31 (15), pp. 3–6. DOI: 10.1029/2004GL020213.

Dorogokupets, P. I. and A. Dewaele (2007). "Equations of state of MgO, Au, Pt, NaCl-B1, and NaCl-B2: Internally consistent high-temperature pressure scales". In: *High Pressure Research* 27 (4), pp. 431–446. DOI: 10.1080/08957950701659700.

Dziewonski, A. M. and D. L. Anderson (1981). "Preliminary reference Earth model". In: *Physics of the Earth and Planetary Interiors* 25 (4), pp. 297–356. DOI: 10.1016/0031-9201(81)90046-7.

Eberle, M. A., O. Grasset, and C. Sotin (2002). "A numerical study of the interaction between the mantle wedge, subducting slab, and overriding plate". In: *Physics of the Earth and Planetary Interiors* 134 (3-4), pp. 191–202. DOI: 10.1016/S0031-9201(02)00157-7.

Fischer, R. A., A. J. Campbell, G. A. Shofner, O. T. Lord, P. Dera, and V. B. Prakapenka (2011). "Equation of state and phase diagram of FeO". In: *Earth and Planetary Science Letters* 304 (3-4), pp. 496–502. DOI: 10.1016/j.epsl.2011.02.025.

Frost, D. J. and Y. Fei (1999). "Static compression of the hydrous magnesium silicate phase D to 30 GPa at room temperature". In: *Physics and Chemistry of Minerals* 26 (5), pp. 415–418. DOI: 10.1007/s002690050202.

Fu, S., J. Yang, N. Tsujino, T. Okuchi, N. Purevjav, and J.-F. F. Lin (2019). "Single-crystal elasticity of (Al,Fe)-bearing bridgmanite and seismic shear wave radial anisotropy at the topmost lower mantle". In: *Earth and Planetary Science Letters* 518, pp. 116–126. DOI: 10.1016/j.epsl.2019.04.023.

Ghosh, S. and M. W. Schmidt (2014). "Melting of phase D in the lower mantle and implications for recycling and storage of H2O in the deep mantle". In: *Geochimica et Cosmochimica Acta* 145, pp. 72–88. DOI: 10.1016/j.gca.2014.06.025.

Glazer, A. M. (1972). "The classification of tilted octahedra in perovskites". In: *Acta Crystallographica Section B Structural Crystallography and Crystal Chemistry* 28 (11), pp. 3384–3392. DOI: 10.1107/s0567740872007976.

Gréaux, S., T. Irifune, Y. Higo, Y. Tange, T. Arimoto, Z. Liu, and A. Yamada (2019). "Sound velocity of $CaSiO_3$ perovskite suggests the presence of basaltic crust in the Earth's lower mantle". In: *Nature* 565 (7738), pp. 218–221. DOI: 10.1038/s41586-018-0816-5.

Hirose, K., R. Sinmyo, N. Sata, and Y. Ohishi (2006). "Determination of post-perovskite phase transition boundary in $MgSiO_3$ using Au and MgO pressure standards". In: *Geophysical Research Letters* 33 (1), pp. 1–5. DOI: 10.1029/2005GL024468.

Hosseini, K., K. J. Matthews, K. Sigloch, G. E. Shephard, M. Domeier, and M. Tsekhmistrenko (2018). "SubMachine: Web-Based Tools for Exploring Seismic Tomography and Other Models of Earth's Deep Interior". In: *Geochemistry, Geophysics, Geosystems* 19 (5), pp. 1464–1483. DOI: 10.1029/2018GC007431.

Howard, C. J. and H. T. Stokes (1998). "Group-theoretical analysis of octahedral tilting in perovskites". In: *Acta Crystallographica Section B: Structural Science* 54, pp. 782–789. DOI: 10.1107/S0108768198004200.

Hsieh, W. P., E. Marzotto, T. Ishii, L. Dubrovinsky, A. A. Aslandukova, G. Criniti, Y. C. Tsao, C. H. Lin, J. Tsuchiya, and E. Ohtani (2022). "Low Thermal Conductivity of Hydrous Phase D Leads to a Self-Preservation Effect Within a Subducting Slab". In: *Journal of Geophysical Research: Solid Earth* 127 (6), pp. 1–11. DOI: 10.1029/2022JB024556.

Huang, R., T. B. Ballaran, C. A. McCammon, N. Miyajima, D. Dolejš, and D. J. Frost (2021a). "The composition and redox state of bridgmanite in the lower mantle as a function of oxygen fugacity". In: *Geochimica et Cosmochimica Acta* 303, pp. 110–136. DOI: 10.1016/J.GCA.2021.02.036.

Huang, R., T. B. Ballaran, C. A. McCammon, N. Miyajima, and D. J. Frost (2021b). "The effect of Fe–Al substitution on the crystal structure of $MgSiO_3$ bridgmanite". In: *Journal of Geophysical Research: Solid Earth*, e2021JB021936. DOI: 10.1029/2021jb021936.

Hushur, A., M. H. Manghnani, J. R. Smyth, Q. Williams, E. Hellebrand, D. Lonappan, Y. Ye, P. Dera, and D. J. Frost (2011). "Hydrogen bond symmetrization and equation of state of phase D". In: *Journal of Geophysical Research: Solid Earth* 116 (6), pp. 1–8. DOI: 10.1029/2010JB008087.

Ishii, T., G. Criniti, E. Ohtani, N. Purevjav, H. Fei, T. Katsura, and H. K. Mao (2022a). "Superhydrous aluminous silica phases as major water hosts in high-temperature lower mantle". In: *Proceedings of the National Academy of Sciences of the United States of America* 119 (44), pp. 1–6. DOI: 10.1073/pnas.2211243119.

Ishii, T., N. Miyajima, G. Criniti, Q. Hu, K. Glazyrin, and T. Katsura (2022b). "High pressure-temperature phase relations of basaltic crust up to mid-mantle conditions". In: *Earth and Planetary Science Letters* 584, p. 117472. DOI: 10.1016/j.epsl.2022.117472.

Ismailova, L., E. Bykova, M. Bykov, V. Cerantola, C. McCammon, T. B. Ballaran, A. Bobrov, R. Sinmyo, N. Dubrovinskaia, K. Glazyrin, H. P. Liermann, I. Kupenko, M. Hanfland, C. Prescher, V. Prakapenka, V. Svitlyk, and L. Dubrovinsky (2016). "Stability of Fe,Al-bearing bridgmanite in the lower mantle and synthesis of pure Fe-bridgmanite". In: *Science Advances* 2 (7). DOI: 10.1126/sciadv.1600427.

Jackson, J. M., J. Zhang, J. Shu, S. V. Sinogeikin, and J. D. Bass (2005). "High-pressure sound velocities and elasticity of aluminous $MgSiO_3$ perovskite to 45 GPa: Implications for lateral heterogeneity in Earth's lower mantle". In: *Geophysical Research Letters* 32 (21), pp. 1–4. DOI: 10.1029/2005GL023522.

Jacobsen, S. D., C. M. Holl, K. A. Adams, R. A. Fischer, E. S. Martin, C. R. Bina, J. F. Lin, V. B. Prakapenka, A. Kubo, and P. Dera (2008). "Compression of single-crystal magnesium oxide to 118 GPa and a ruby pressure gauge for helium pressure media". In: *American Mineralogist* 93 (11-12), pp. 1823–1828. DOI: 10.2138/am.2008.2988.

Kaneshima, S. (2019). "Seismic scatterers in the lower mantle near subduction zones". In: *Geophysical Journal International* 218 (3), pp. 1873–1891. DOI: 10.1093/gji/ggz241.

Kaneshima, S. and G. Helffrich (1999). "Dipping low-velocity layer in the mid-lower mantle: Evidence for geochemical heterogeneity". In: *Science* 283 (5409), pp. 1888–1891. DOI: 10.1126/science.283.5409.1888.

Katsura, T., S. Yokoshi, K. Kawabe, A. Shatskiy, M. A. Manthilake, S. Zhai, H. Fukui, H. A. Hegoda, T. Yoshino, D. Yamazaki, T. Matsuzaki, A. Yoneda, E. Ito, M. Sugita, N. Tomioka, K. Hagiya, A. Nozawa, and K. I. Funakoshi (2009). "*P-V-T* relations of $MgSiO_3$ perovskite determined by in situ X-ray diffraction using a large-volume high-pressure apparatus". In: *Geophysical Research Letters* 36 (1), pp. 2–7. DOI: 10.1029/2008GL035658.

Katsura, T., A. Yoneda, D. Yamazaki, T. Yoshino, E. Ito, D. Suetsugu, C. Bina, T. Inoue, D. Wiens, and M. Jellinek (2010). "Adiabatic temperature profile in the mantle". In: *Physics of the Earth and Planetary Interiors* 183 (1-2), pp. 212–218. DOI: 10.1016/j.pepi.2010.07.001.

Kennett, B. L. N., E. R. Engdahl, and R. Buland (1995). "Constraints on seismic velocities in the Earth from traveltimes". In: *Geophysical Journal International* 122 (1), pp. 108–124. DOI: 10.1111/j.1365-246X.1995.tb03540.x.

Kingma, K. J., R. E. Cohen, R. J. Hemley, and H. K. Mao (1995). "Transformation of stishovite to a denser phase at lower-mantle pressures". In: *Nature* 374 (6519), pp. 243–245. DOI: 10.1038/374243a0.

Kirby, S. H., S. Stein, E. A. Okal, and D. C. Rubie (1996). "Metastable mantle phase transformations and deep earthquakes in subducted oceanic lithosphere". In: *Reviews of Geophysics* 34 (2), pp. 261–306. DOI: 10.1029/96RG01050.

Kojitani, H., T. Katsura, and M. Akaogi (2007). "Aluminum substitution mechanisms in perovskite-type $MgSiO_3$: An investigation by Rietveld analysis". In: *Physics and Chemistry of Minerals* 34 (4), pp. 257–267. DOI: 10.1007/s00269-007-0144-z.

Kono, Y., T. Irifune, Y. Higo, T. Inoue, A. Barnhoorn, D. Suetsugu, C. Bina, T. Inoue, D. Wiens, and M. Jellinek (2010). "*P-V-T* relation of MgO derived by simultaneous elastic wave velocity and in situ X-ray measurements: A new pressure scale for the mantle transition region". In: *Physics of the Earth and Planetary Interiors* 183 (1-2), pp. 196–211. DOI: 10.1016/j.pepi.2010.03.010.

Kurnosov, A., H. Marquardt, D. J. Frost, T. B. Ballaran, and L. Ziberna (2017). "Evidence for a Fe^{3+}-rich pyrolitic lower mantle from (Al,Fe)-bearing bridgmanite elasticity data". In: *Nature* 543, pp. 543–546. DOI: 10.1038/nature21390.

Lakshtanov, D. L., S. V. Sinogeikin, K. D. Litasov, V. B. Prakapenka, H. Hellwig, J. Wang, C. Sanches-Valle, J. P. Perrillat, B. Chen, M. Somayazulu, J. Li, E. Ohtani, and J. D. Bass (2007b). "The post-stishovite phase transition in hydrous alumina-bearing SiO_2 in the lower mantle of the earth". In: *Proceedings of the National Academy of Sciences of the United States of America* 104 (34), pp. 13588–13590. DOI: 10.1073/pnas.0706113104.

Lakshtanov, D. L., C. B. Vanpeteghem, J. M. Jackson, J. D. Bass, G. Shen, V. B. Prakapenka, K. Litasov, and E. Ohtani (2005). "The equation of state of Al,H-bearing SiO 2 stishovite to 58 GPa". In: *Physics and Chemistry of Minerals* 32 (7), pp. 466–470. DOI: 10.1007/s00269-005-0016-3.

Liu, X., K. N. Matsukage, Y. Nishihara, T. Suzuki, and E. Takahashi (2019a). "Stability of the hydrous phases of Al-rich phase D and Al-rich phase H in deep subducted oceanic crust". In: *American Mineralogist* 104 (1), pp. 64–72. DOI: 10.2138/am-2019-6559.

Liu, Z., M. Akaogi, and T. Katsura (2019b). "Increase of the oxygen vacancy component in bridgmanite with temperature". In: *Earth and Planetary Science Letters* 505, pp. 141–151. DOI: 10.1016/j.epsl.2018.10.014.

Liu, Z., T. B. Ballaran, R. Huang, D. J. Frost, and T. Katsura (2019c). "Strong correlation of oxygen vacancies in bridgmanite with Mg/Si ratio". In: *Earth and Planetary Science Letters* 523, p. 115697. DOI: 10.1016/j.epsl.2019.06.037.

Liu, Z., T. Ishii, and T. Katsura (2017a). "Rapid decrease of $MgAlO_{2.5}$ component in bridgmanite with pressure". In: *Geochemical Perspectives Letters* 5, pp. 12–18. DOI: 10.7185/geochemlet.1739.

Liu, Z., M. Nishi, T. Ishii, H. Fei, N. Miyajima, T. B. Ballaran, H. Ohfuji, T. Sakai, L. Wang, S. Shcheka, T. Arimoto, Y. Tange, Y. Higo, T. Irifune, and T. Katsura (2017b). "Phase Relations in the System $MgSiO_3$-Al_2O_3 up to 2300 K at Lower Mantle Pressures". In: *Journal of Geophysical Research: Solid Earth* 122 (10), pp. 7775–7788. DOI: 10.1002/2017JB014579.

Lu, C., S. P. Grand, H. Lai, and E. J. Garnero (2019). "TX2019slab: A New P and S Tomography Model Incorporating Subducting Slabs". In: *Journal of Geophysical Research: Solid Earth* 124 (11), pp. 11549–11567. DOI: 10.1029/2019JB017448.

Marquardt, H., A. Gleason, K. Marquardt, S. Speziale, L. Miyagi, G. Neusser, H. R. Wenk, and R. Jeanloz (2011). "Elastic properties of MgO nanocrystals and grain boundaries at high pressures by Brillouin scattering". In: *Physical Review B - Condensed Matter and Materials Physics* 84 (6), pp. 1–9. DOI: 10.1103/PhysRevB.84.064131.

Martin, C. D., W. A. Crichton, H. Liu, V. Prakapenka, J. Chen, and J. B. Parise (2006). "Rietveld structure refinement of perovskite and post-perovskite phases of $NaMgF_3$ (Neighborite) at high pressures". In: *American Mineralogist* 91 (10), pp. 1703–1706. DOI: 10.2138/am.2006.2308.

Martin, C. D. and J. B. Parise (2008). "Structure constraints and instability leading to the post-perovskite phase transition of $MgSiO_3$". In: *Earth and Planetary Science Letters* 265 (3-4), pp. 630–640. DOI: 10.1016/j.epsl.2007.11.001.

Mcdonough, W. F. and R. L. Rudnick (1998). "Mineralogy and composition of the upper mantle". In: *Reviews in Mineralogy and Geochemistry* (37), pp. 139–164. DOI: 10.1515/9781501509179-006.

Meier, T., F. Trybel, S. Khandarkhaeva, D. Laniel, T. Ishii, A. Aslandukova, N. Dubrovinskaia, and L. Dubrovinsky (2022). "Structural independence of hydrogen-bond symmetrisation dynamics at extreme pressure conditions". In: *Nature Communications* 13.1. DOI: 10.1038/s41467-022-30662-4.

Miller, S. C. and W. F. Love (1967). *Tables of Irreducible Representations of Space Groups and Co-representations of Magnetic Space Groups*. Pruett Press, p. 1095.

Murakami, M., K. Hirose, K. Kawamura, N. Sata, and Y. Ohishi (2004). "Post-Perovskite Phase Transition in $MgSiO_3$". In: *Science* 304, pp. 855–858. DOI: 10.1126/science.1095932.

Murakami, M., K. Hirose, N. Sata, and Y. Ohishi (2005). "Post-perovskite phase transition and mineral chemistry in the pyrolitic lowermost mantle". In: *Geophysical Research Letters* 32 (3), pp. 1–4. DOI: 10.1029/2004GL021956.

Murakami, M., Y. Ohishi, N. Hirao, and K. Hirose (2012). "A perovskitic lower mantle inferred from high-pressure, high-temperature sound velocity data". In: *Nature* 485 (7396), pp. 90–94. DOI: 10.1038/nature11004.

Murakami, M., S. V. Sinogeikin, H. Hellwig, J. D. Bass, and J. Li (2007). "Sound velocity of $MgSiO_3$ perovskite to Mbar pressure". In: *Earth and Planetary Science Letters* 256 (1-2), pp. 47–54. DOI: 10.1016/j.epsl.2007.01.011.

Nakajima, Y., D. J. Frost, and D. C. Rubie (2012). "Ferrous iron partitioning between magnesium silicate perovskite and ferropericlase and the composition of perovskite in the Earth's lower mantle". In: *Journal of Geophysical Research: Solid Earth* 117 (8), pp. 1–12. DOI: 10.1029/2012JB009151.

Nisr, C., K. Leinenweber, V. Prakapenka, C. Prescher, S. Tkachev, and S. H. Shim (2017). "Phase transition and equation of state of dense hydrous silica up to 63 GPa". In: *Journal of Geophysical Research: Solid Earth* 122 (9), pp. 6972–6983. DOI: 10.1002/2017JB014055.

Nomura, R., K. Hirose, N. Sata, Y. Ohishi, D. Suetsugu, C. Bina, T. Inoue, D. Wiens, and M. Jellinek (2010). "Precise determination of post-stishovite phase transition boundary and implications for seismic heterogeneities in the mid-lower mantle". In: *Physics of the Earth and Planetary Interiors* 183 (1-2), pp. 104–109. DOI: 10.1016/j.pepi.2010.08.004.

Oganov, A. R., R. Martoňák, A. Laio, P. Raiteri, and M. Parrinello (2005). "Anisotropy of earth's D" layer and stacking faults in the $MgSiO_3$ post-perovskite phase". In: *Nature* 438 (7071), pp. 1142–1144. DOI: 10.1038/nature04439.

Oganov, A. R. and S. Ono (2004). "Theoretical and experimental evidence for a post-perovskite phase of $MgSiO_3$ in Earth's D" layer". In: *Nature* 430 (6998), pp. 445–448. DOI: 10.1038/nature02701.

Orobengoa, D., C. Capillas, M. I. Aroyo, and J. M. Perez-Mato (2009). "*AMPLIMODES*: Symmetry-mode analysis on the Bilbao Crystallographic Server". In: *Journal of Applied Crystallography* 42 (5), pp. 820–833. DOI: 10.1107/S0021889809028064.

Pamato, M. G., R. Myhill, T. B. Ballaran, D. J. Frost, F. Heidelbach, and N. Miyajima (2015). "Lower-mantle water reservoir implied by the extreme stability of a hydrous aluminosilicate". In: *Nature Geoscience* 8 (1), pp. 75–79. DOI: 10.1038/ngeo2306.

Rosa, A. D., M. Mezouar, G. Garbarino, P. Bouvier, S. Ghosh, A. Rohrbach, and C. Sanchez-Valle (2013). "Single-crystal equation of state of phase D to lower mantle pressures and the effect of hydration on the buoyancy of deep subducted slabs". In: *Journal of Geophysical Research: Solid Earth* 118 (12), pp. 6124–6133. DOI: 10.1002/2013JB010060.

Rosa, A. D., C. Sanchez-Valle, and S. Ghosh (2012). "Elasticity of phase D and implication for the degree of hydration of deep subducted slabs". In: *Geophysical Research Letters* 39 (6), pp. 6–11. DOI: 10.1029/2012GL050927.

Sano-Furukawa, A., T. Hattori, K. Komatsu, H. Kagi, T. Nagai, J. J. Molaison, A. M. dos Santos, and C. A. Tulk (2018). "Direct observation of symmetrization of hydrogen bond

in δ-AlOOH under mantle conditions using neutron diffraction". In: *Scientific Reports* 8 (1), pp. 1–9. DOI: 10.1038/s41598-018-33598-2.

Stixrude, L. and C. Lithgow-Bertelloni (2011). "Thermodynamics of mantle minerals - II. Phase equilibria". In: *Geophysical Journal International* 184 (3), pp. 1180–1213. DOI: 10.1111/j.1365-246X.2010.04890.x.

Tange, Y., Y. Kuwayama, T. Irifune, K. I. Funakoshi, and Y. Ohishi (2012). "*P-V-T* equation of state of $MgSiO_3$ perovskite based on the MgO pressure scale: A comprehensive reference for mineralogy of the lower mantle". In: *Journal of Geophysical Research: Solid Earth* 117 (6), pp. 1–12. DOI: 10.1029/2011JB008988.

Tateno, S., K. Hirose, N. Sata, and Y. Ohishi (2005). "Phase relations in $Mg_3Al_2Si_3O_{12}$ to 180 GPa: Effect of Al on post-perovskite phase transition". In: *Geophysical Research Letters* 32 (15), pp. 10–13. DOI: 10.1029/2005GL023309.

Tsuchiya, T., R. Caracas, and J. Tsuchiya (2004). "First principles determination of the phase boundaries of high-pressure polymorphs of silica". In: *Geophysical Research Letters* 31 (11), pp. 1–4. DOI: 10.1029/2004GL019649.

Walter, M. J., A. Kubo, T. Yoshino, J. P. Brodholt, K. T. Koga, and Y. Ohishi (2004). "Phase relations and equation-of-state of aluminous Mg-silicate perovskite and implications for Earth's lower mantle". In: *Earth and Planetary Science Letters* 222 (2), pp. 501–516. DOI: 10.1016/j.epsl.2004.03.014.

Walter, M. J., R. G. Trønnes, L. S. Armstrong, O. T. Lord, W. A. Caldwell, and S. M. Clark (2006). "Subsolidus phase relations and perovskite compressibility in the system MgO-AlO1.5-SiO_2 with implications for Earth's lower mantle". In: *Earth and Planetary Science Letters* 248 (1-2), pp. 77–89. DOI: 10.1016/j.epsl.2006.05.017.

Wu, X., Y. Wu, J.-F. Lin, J. Liu, Z. Mao, X. Guo, Y. Takashi, C. McCammon, V. B. Prakapenka, and Y. Xiao (2016). "Two-stage spin transition of iron in FeAl-bearing phase D at lower mantle". In: *Journal of Geophysical Research: Solid Earth* 121, 6411–6420. DOI: 10.1002/2016JB013209.

Yang, H., R. T. Downs, L. W. Finger, R. M. Hazen, and C. T. Prewitt (1997a). "Compressibility and crystal structure of kyanite, Al2SiO5, at high pressure". In: *American Mineralogist* 82 (5-6), pp. 467–474. DOI: 10.1007/s002690050084.

Zhang, Y., S. Chariton, J. He, S. Fu, F. Xu, V. B. Prakapenka, and J. F. Lin (2023). "Atomistic insight into the ferroelastic post-stishovite transition by high-pressure single-crystal X-ray diffraction". In: *American Mineralogist* 108 (1), pp. 110–119. DOI: 10.2138/AM-2022-8458.

Zhang, Y., S. Fu, B. Wang, and J. F. Lin (2021). "Elasticity of a Pseudoproper Ferroelastic Transition from Stishovite to Post-Stishovite at High Pressure". In: *Physical Review Letters* 126 (2), p. 25701. DOI: 10.1103/PhysRevLett.126.025701.

Chapter 4

Single-Crystal Elasticity of $MgSiO_3$ Bridgmanite to Mid-Lower Mantle Pressure

Giacomo Criniti[1*], Alexander Kurnosov[1], Tiziana Boffa Ballaran[1], Daniel J. Frost[1]

[1] Bayerisches Geoinstitut, University of Bayreuth, 95440 Bayreuth, Germany

[*] **Corresponding author**: giacomo.criniti@uni-bayreuth.de

This chapter has been published as:
Criniti, G., A. Kurnosov, T. Boffa Ballaran, and D.J. Frost (2021). "Single-crystal elasticity of $MgSiO_3$ bridgmanite to mid-lower mantle pressure". In: *Journal of Geophysical Research: Solid Earth* 126, e2020JB020967. DOI: https://doi.org/10.1029/2020JB020967

Author contributions: G. Criniti selected and oriented the bridgmanite crystals, conducted the high-pressure measurements, analyzed the data, and wrote the manuscript. A. Kurnosov conducted the high-pressure measurements, analyzed the data, and commented on the manuscript. T. Boffa Ballaran conceived and supervised the project, selected and oriented the bridgmanite crystals, conducted the high-pressure measurements, and commented on the manuscript. D.J. Frost conceived and supervised the project, synthesized the bridgmanite crystals, performed the thermodynamic modelling, and commented on the manuscript.

Key Points:

- We measured both compressional and shear wave velocities of $MgSiO_3$ bridgmanite up to mid-lower mantle pressure for the first time.
- The effect of chemistry on the elastic moduli and elastic anisotropy of bridgmanite at lower mantle pressures is discussed.
- We compare the seismic velocities for a simplified primitive upper mantle composition with 1D seismic models of Earth's lower mantle

Abstract

The combination of seismic observations and mineral physics data represents a unique tool to understand the structure and evolution of the deep Earth's interior. However, to date, elasticity data on both compressional (v_P) and shear (v_S) wave velocities of $MgSiO_3$ bridgmanite are limited to shallow mantle conditions, hampering the resolution of mineral physics models. Here, we report the first single-crystal measurements of v_P and v_S of $MgSiO_3$ bridgmanite up to $\sim$ 79 GPa using high-pressure Brillouin scattering and single-crystal X-ray diffraction in a diamond anvil cell. At shallow lower mantle pressures, the elastic anisotropy of $MgSiO_3$ bridgmanite was found to be similar, albeit smaller than that of Fe,Al-bearing bridgmanite of Kurnosov et al. (2017), but differed significantly from that proposed in the recent study of Fu et al. (2019). Using the elastic stiffness components of bridgmanite obtained in this study at different pressures, we calculate the pressure dependence of the adiabatic bulk modulus, K_{S0} = 257.1(6) GPa, K'_{S0} = 3.71(4), and of the shear modulus, G_0 = 175.6(2) GPa, G'_0 = 1.86(1). These elastic parameters are included in a self-consistent thermodynamic model to calculate seismic wave velocities along a lower mantle adiabat for a primitive upper mantle bulk composition in the FeO-CaO-MgO-SiO_2 system, which is currently the most complex system for which sufficient data exist. This preliminary model provides a good match to the v_S and v_P of 1D seismic models, implying that the composition of the lower mantle may be closer to pyrolite, rather than being more bridgmanite rich.

4.1 Introduction

While it is accepted that the lower mantle phase assemblage is comprised primarily of Al- and Fe-bearing $MgSiO_3$ bridgmanite, the exact proportion and the bulk composition of the lower mantle as a whole remain uncertain. The abundance of bridgmanite relative to ferropericlase will be controlled by the bulk Mg/Si ratio. In a pyrolite composition, which is believed to represent the average composition of the upper mantle (Ringwood, 1962), this ratio is approximately 1.3 and a pyrolytic lower mantle assemblage would be comprised of approximately 78 % bridgmanite, 15 % ferropericlase and 7 % calcium perovskite by volume (e.g., Irifune, 1994; Irifune et al., 2010; Ishii et al., 2011). The Earth is frequently proposed to have formed from carbonaceous chondrites, however, which have a Mg/Si ratio much closer to 1.0 (Palme and O'Neill, 2014). Aside from Si potentially entering the Earth's core (e.g., Wänke, 1981; Poirier, 1994), one way to explain the Mg/Si ratio of the upper mantle is if the lower mantle is richer in bridgmanite as a result of fractional crystallization during the magma ocean stage of Earth's history (e.g., Ballmer et al., 2017; Elkins-Tanton, 2012; Tonks and Melosh, 1993). This scenario is supported by shear wave velocity measurements of $MgSiO_3$ and Al-bearing bridgmanite at pressures over 1 Mbar (Murakami et al., 2012), for which comparison with the PREM seismic velocity model indicates a lower mantle

containing at least 93 vol% of bridgmanite.

In the previous studies of Murakami et al. (2007) and Murakami et al. (2012), performed in the DAC using Brillouin scattering measurements, it was not possible to directly measure values of v_P, which were instead estimated using bulk modulus determinations from previous static compression measurements (Fiquet et al., 2000). This potential cause of uncertainty arises in high pressure Brillouin scattering measurements because the v_P signal overlaps with the much more intense v_S signal of the diamond anvils. This effect is particularly pronounced for polycrystalline samples (Murakami et al., 2007; Murakami et al., 2012), where the sample peaks are broad and tend to overlap with diamond even at ambient pressure. To overcome this problem, Fu et al. (2019) combined Brillouin scattering measurements of v_S with impulsive stimulated light scattering (ISLS) measurements for v_P to examine bridgmanite single crystals at 25 and 35 GPa, because ISLS has the advantage that the signal originating from the sample does not overlap with that of the diamond anvils. Fu et al. (2019) studied two bridgmanite samples with different Fe and Al contents. The determined bridgmanite elastic anisotropy is different, however, from that measured by Kurnosov et al. (2017), who performed simultaneous Brillouin scattering and single crystal X-ray diffraction measurements on Fe- and Al-bearing bridgmanite up to 40 GPa. To date, no direct experimental constraints exist on v_P of bridgmanite at pressures of the mid lower mantle and although a number of computational studies have been performed, they partially disagree with one another due to different choices in the potentials and approximations used (Oganov et al., 2001; Wentzcovitch et al., 1998; Wentzcovitch et al., 2004; Zhang et al., 2013). For instance, both compressional and shear wave velocities calculated at high pressure and room temperature by Oganov et al. (2001) are 2-3% faster than those reported by Wentzcovitch et al. (2004). Results from ultrasonic measurements by Chantel et al. (2012) at low pressure seem to agree with the v_P of Wentzcovitch et al. (2004) and the v_S of Oganov et al. (2001), while the v_S of Murakami et al. (2007) are in good agreement with those of Wentzcovitch et al. (2004) .

In this paper we show that single-crystal DAC elasticity measurements can provide some constraints on the v_P of $MgSiO_3$ bridgmanite even at shallow lower mantle pressures, if the in-plane orientation of the crystal is correctly chosen. Because both the diamond anvils and the sample are single crystals, their sound wave velocities depend on the wave propagation direction. If the minimum of the v_P of the sample matches the maximum of the v_S of the diamond, it is possible to observe a portion of the dispersion curve of bridgmanite even at shallow lower mantle pressure ($\sim$ 30 GPa). At higher pressure, the v_P overlaps completely with the diamond v_S, as the sample has higher pressure derivatives of the elastic moduli than diamond. At deep lower mantle pressures, however, a crossover occurs, and the v_P of bridgmanite appears at higher frequency (i.e. velocity) than the v_S of the diamond in the Brillouin spectrum and, therefore, can be observed again. In this study, we have conducted single-crystal X-ray diffraction and Brillouin scattering measurements on four crystals of $MgSiO_3$ bridgmanite in the DAC up to pressures of the middle lower mantle.

Combining all elasticity and density measurements in a global fit (Buchen, 2018), we self-consistently determine, for the first time, the full elastic tensor of $MgSiO_3$ bridgmanite at mid lower mantle pressures. The newly determined values of the elastic moduli and their pressure derivatives are used to update existing mineral physics models and estimate seismic velocities for a lower mantle with a pyrolite bulk composition.

4.2 Materials and Methods

Single crystals of $MgSiO_3$ bridgmanite were synthesized at 25 GPa and 1573 K (Boffa Ballaran et al., 2012) in a multi-anvil large volume press (LVP). Inclusion free bridgmanite crystals were selected for which sharp X-ray diffraction peak profiles (full width half maxima < 0.12°) were obtained in omega-scan rotations. Suitable crystals were then oriented and polished on both sides to platelets with a thickness of 8-10 μm. High-pressure single-crystal X-ray diffraction and Brillouin spectroscopy measurements were performed in a BX90 piston-cylinder type DAC (Kantor et al., 2012). (100)-oriented Boehler-Almax type Ia diamond anvils were combined with Boehler-Almax seats to achieve opening angles larger than 80° (Boehler and Hantsetters, 2004). The diameter of the diamond culets was 400 or 350 μm for measurements up to approximately 35 GPa, and 250 μm for measurements at higher pressure. Before gluing the diamond anvils, Brillouin scattering measurements were performed on the two diamonds to identify the v_S dispersion curves relative to the orientation of each diamond. By rotating one of the two diamonds with respect to the other, it was possible to align their dispersion curves and, therefore, minimize the effective width of the diamond v_S peak in the Brillouin spectra. Re gaskets were indented to a thickness of $\sim$ 60 μm and $\sim$ 35 μm for target pressures of 35 and 80 GPa respectively. Ne or He were loaded as quasi-hydrostatic pressure transmitting media using a gas loading apparatus (Kurnosov et al., 2017).

High-pressure Brillouin scattering experiments conducted in platelet geometry (Speziale et al., 2014; Whitfield et al., 1976) require at least two different platelet orientations in order to solve for the 9 independent elastic stiffness components, c_{ij}, of an orthorhombic crystal such as bridgmanite. This is achieved by combining experimentally measured density and sound wave velocities to fit the Christoffel's equation (e.g., Every, 1980):

$$|c_{ijkl}q_jq_l - \rho v_i^2\delta_{ik}| = 0 \tag{4.1}$$

Where c_{ijkl} are the elastic stiffness components (tensorial notation, see Appendix A.1), qj and ql are direction vectors, ρ is density, vi are the sound wave velocities and δ_{ik} is the Kronecker delta. Three sets of high-pressure experiments (runs) were performed employing two different sets of bridgmanite single-crystal platelets with different orientations. In the first run, crystals with Cartesian indices (0.81, 0.49, 0.31) and (0.35, 0.16, 0.92), were selected based on the low extent of c_{ij} correlation at ambient conditions (for a more detailed

description, see Text S2). These crystals were loaded into two separate DACs and Brillouin scattering and X-ray diffraction measurements were performed up to approximately 35 GPa. At this pressure, even the slowest bridgmanite v_P values overlapped with the v_S of the diamond anvils, leaving many c_{ij} values unconstrained. To overcome this limitation two further runs were performed using a second set of single crystal platelets with orientations chosen to maximize the appearance of the v_P signals on either side of the diamond v_S peak. The platelet orientations were first selected by simulating the velocities for different crystal planes using published c_{ij} values (Sinogeikin et al., 2004). To simulate realistic datasets, synthetic velocities were scattered by randomly adding up to ±40 m/s to v_S and 70 m/s to v_P, which are values comparable to our estimated experimental uncertainties. Platelets with Cartesian indices (0.00, 0.80, 0.55) and (1.00, 0.00, 0.00), which correspond to the (011) and (100) crystallographic planes, were found to be optimal based on the low correlation between the c_{ij}s (Appendix A.2). These orientations also have relatively slow and fast v_P respectively, such that the direction of the v_P maximum in the (100) plane could be aligned with the diamond v_S minimum, while the v_P minimum in the (011) plane could be aligned with the diamond v_S maximum, in order to maximize the pressure interval over which these signals could be visible (Figure 4.1a). In order to load two crystals into the same DAC, while also maximizing their dimensions with respect to the gasket hole dimension, it was necessary to cut them into semi-circular shaped platelets, which meant that both crystals had to be correctly aligned relative to the diamonds and to each other before cutting. Two double-sided-polished but unshaped platelets in the selected planes were, therefore, first placed on a diamond anvil (Figure 4.1b) and the desired orientations relative to the diamonds were then determined for each crystal using single-crystal X-ray diffraction. The two single-crystal platelets were then cut into semi-circles for loading into the DAC (Figure 4.1b) using a FEI Scios focused ion beam (Schulze et al., 2017), while maintaining the required orientations relative to the straight edges. Ion beam cutting was performed using a beam current of 3 nA at an acceleration voltage of 30 kV. According to the target pressure, one or two platelets were loaded into the DAC sample chamber together with a ruby chip for preliminary pressure determination (Figure 4.1c-e). Before gas loading, the bridgmanite crystals were rotated on the diamond culet using a needle, until the desired orientations – determined by means of XRD – relative to the diamond anvils were achieved. The two crystals were loaded together in the same DAC for measurements up to approximately 30 GPa (second run), and in two separate DACs for measurements above 50 GPa (third run).

Brillouin scattering measurements were performed using the system installed at the BGI (Trots et al., 2013). The system employs a Coherent Verdi V2 solid-state Nd:YVO4 laser with a 532 nm single wavelength output and a six-pass Sandercock-type piezoelectrically driven scanning tandem Fabry-Pérot interferometer (Sandercock, 1982) equipped with a single pixel photon counter detector (Hamamatsu C11202-50). A laser power of 100-200 mW was used, which corresponds to 40-80 mW before entering the DAC. The scattering angle between the incident and the analyzed laser beam, equal to 80°, was calibrated using a fused silica glass standard. Further details concerning the system alignment

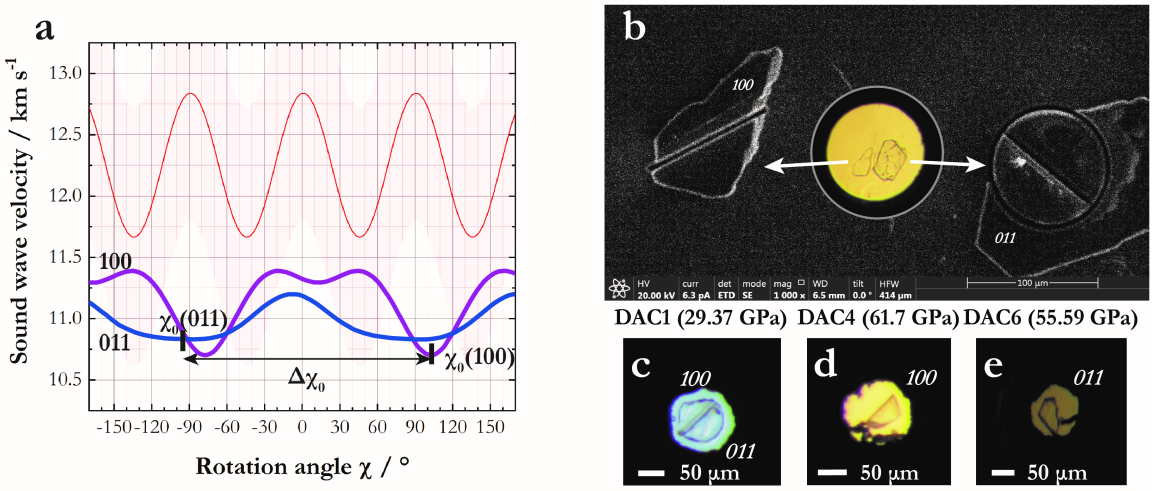

Figure 4.1. a) Schematic representation of the ideal orientation of the v_P of platelets (100) (purple) and (011) (blue) relative to each other and to the diamond v_S (red) at room pressure. The shaded pink area represents the predicted full width of the diamond peak at high pressure (see Text S3), where the v_P of the samples cannot be resolved. Note that the diamonds have been aligned in such a way to produce only one v_S signal at each orientation. The difference in rotation angle ($\Delta\chi_0$) between the g_0 vectors of the two crystal platelets was used together with the UB matrix of the crystals to calculate the desired FIB cutting pattern. b) Photograph of the two platelets 100 and 011 before FIB cutting in a test DAC (middle circular inset) and secondary electron image of the same platelets after FIB cutting. c-e) Photographs of platelets 100 and 011 inside the relevant sample chambers at high pressure, loaded with Ne (c) or He (d,e) gas.

and calibration, as well as a discussion of potential errors related to misalignment, are discussed in Appendix A.2. Simultaneous density measurements were performed on a Huber Eulerian single-crystal diffractometer coupled with an ultra-high intensity rotating anode X-ray source FR-E+ SuperBright from Rigaku equipped with multilayer VaryMax^{TM} focusing optics (MoKα radiation) (Trots et al., 2011). The rotating anode was operated at 45 kV and 55 mA, and the diffractometer was driven by the SINGLE software (Angel and Finger, 2011). Cell parameters were determined and refined with the vector least-squares method (Ralph and Finger, 1982), using up to 15 unique reflections centered in eight positions (King and Finger, 1979) to eliminate the effect of crystal offsets and diffractometer aberrations. In order to reduce the very long counting times required when using a point detector on small crystals at very high pressures, density measurements above 50 GPa were conducted on a Kappa-geometry Oxford Diffraction single-crystal X-ray diffractometer (Xcalibur2) equipped with a Sapphire 2 CCD area detector. The diffractometer uses graphite-monochromatized MoKα radiation (λ = 0.70937 Å) and was operated at 50 kV and 40 mA. At each pressure point, intensity data collections of approximately 24 h with 60 s of exposure time were performed, and lattice parameters were determined from at least 100 reflections.

4.3 Results

4.3.1 Sound wave velocities of $MgSiO_3$ bridgmanite at high pressure

Sound wave velocities of $MgSiO_3$ bridgmanite were measured at 14 pressure points, ranging from ambient pressure to 78.8(5) GPa (Table 4.1) over the three different sets of runs. Typical Brillouin spectra in the low- and high-pressure range (Figure 4.2a) show the progressive overlap between the v_P of bridgmanite and v_S of diamond, with a crossover taking place at pressures above 50 GPa. To our knowledge, these are the first direct measurements of P-wave velocities of $MgSiO_3$ bridgmanite at deep lower mantle pressures, albeit that the v_P of bridgmanite could be observed only in certain ranges of rotation angle (χ) at such high pressures. Usually Equation 4.1 is solved by using the appropriate number of acoustic velocities collected at each individual pressure point, which in the case of an orthorhombic crystal, such as bridgmanite, requires the measurement at the same conditions of at least two differently oriented crystals. This procedure is hereinafter referred to as an individual fit.

Individual fits of the measured sound velocity data from the first run do not converge at pressures higher than 15 GPa because of the limited number of directions where v_P was observed. In the second run, both minima and maxima of the v_P of the two platelets were visible up to 19.40(3) GPa, whereas at higher pressure the maximum of the v_P of both platelets completely overlapped with the diamond peak. It was still possible to obtain an individual fit at a pressure of approximately 30.3 GPa by combining sound velocities collected on 4 different platelets from the first and second run in a small pressure range between 29.37(5) and 31.20(6) GPa (Table 4.1). It is evident that this approach cannot be applied at very high pressure, where some of the c_{ij}s are poorly constrained due to the lack of observations (Appendix A). For this reason, we have used the same approach proposed by Kurnosov et al. (2017) and described in detail in Buchen et al. (2018b), which consists of fitting all sound velocity and density data with finite strain equations of state (EOS) describing the evolution with pressure of each c_{ij}, using the formalism of Stixrude and Lithgow-Bertelloni (2005):

$$c_{ijkl} = (1+2f)^{5/2}\left\{c_{ijkl,0} + \left(3K_0c'_{ijkl,0} - 5c_{ijkl,0}\right)f + \left[6K_0c'_{ijkl,0} - 14c_{ijkl,0} - 3/2K_0\delta^{ij}_{kl}\left(3K'_0 - 16\right)\right]f^2\right\} \quad (4.2)$$

Where c_{ijkl} is the elastic stiffness component (tensorial notation, see Appendix A) at a certain volume, $f = 1/2((V_0/V)^{2/3} - 1)$ is the finite Eulerian strain, $c_{ijkl,0}$ is the elastic stiffness component at ambient conditions and $c'_{ijkl,0}$ its pressure derivative, K_0 is the bulk modulus and K'_0 its pressure derivative, and δ^{kl}_{ij} is -3 for c_{1111}, c_{2222} and c_{3333} and -1 for the other six independent components of the tensor. The coefficients were fitted to the complete velocity dataset using a script implemented in the software package Origin 2019 (OriginLab corporation, Northampton, MA, USA) and described more in detail in Buchen (2018). In our fitting procedure, $c_{ij,0}$ were initially fixed to the values determined independently at ambient conditions, while $c'_{ij,0}$ were refined. Only in the last cycle, the $c_{ij,0}$ were allowed to vary and were therefore refined together with $c'_{ij,0}$. Further details are provided in the

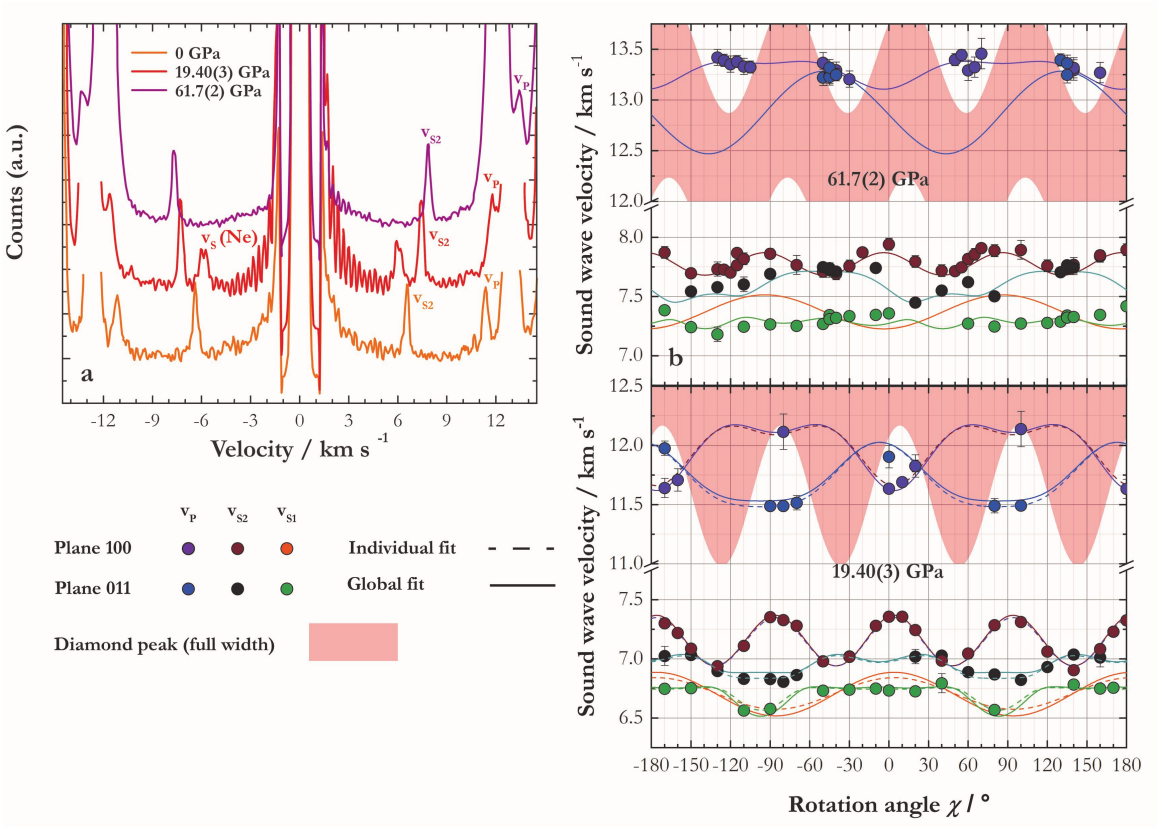

Figure 4.2. a) Selected Brillouin spectra of crystal 100 at different pressures show the progressive overlap of the sample v_P with the v_S of diamond (orange and red lines), with the crossover between the two peaks taking place at pressures above approximately 50 GPa (purple line). b) Data points and dispersion curves (solid lines) obtained from the global fit at low (top) and high (bottom) pressures. The pink shaded area represents the full width of the diamond peak, where the v_P of the sample cannot be measured. At 19.40(3) GPa, the dispersion curves from the individual fit are also plotted (dashed lines), showing excellent agreement between the two fitting procedures.

supplementary information (Appendix A). This approach (hereinafter referred to as a global fit) has the advantage that all velocity data from all pressure points can be used to constrain the c_{ij}, also at those pressures where data are scarce due to the challenging conditions. For instance, c_{22} is not well constrained at 30 GPa, due to the overlap of the v_P of bridgmanite with the v_S of the diamond. However, its pressure evolution is well constrained by the measurements conducted above 50 GPa, i.e. at pressures where v_P can be observed again, at least in some orientations on the other side of the diamond v_S. On the other hand, c_{11} is poorly constrained above 50 GPa, but its high-pressure evolution is very well constrained by measurements on 4 different platelets up to 35 GPa. This approach reduces the number of independent variables from 117 (9 c_{ij} x 13 pressure points) down to 18 (9 $c_{ij,0}$ + 9 pressure derivatives) while having the same number of observables. In this way, it was possible to obtain the elastic tensor of bridgmanite, within reasonable uncertainties, at all pressure points. Measured velocities in the low-pressure range (i.e. less than 30 GPa) constrain well the zero-pressure values of the c_{ij} (i.e. $c_{ijkl,0}$). If we considered only velocities measured in the low-pressure range, data scattering could still bias the

3rd-order fit of the c_{ij}, even when a global fit is employed. This happens because the higher the pressure at which wave velocities are measured, the larger is the constraint they provide on the pressure derivative of the c_{ij} (i.e. $c'_{ij,0}$). Therefore, despite being unable to perform individual fits at pressure points higher than 30 GPa, the measured velocities at mid-lower mantle conditions are of extreme importance in the global fit procedure. Furthermore, we stress that virtually no discrepancies between the c_{ij} calculated from the finite strain EOS and the values determined using the individual fits can be observed, with values typically identical within two standard deviations (Table 4.1, Figure A.1).

A potential downside of the global fit procedure is that we are of course assuming that the c_{ij}s follow a 3rd-order finite strain equation, but this should be a safe assumption given the known high-pressure behavior of $MgSiO_3$ bridgmanite (Boffa Ballaran et al., 2012) where no phase transitions either structural or electronic occur in the pressure range investigated. Although at the highest pressure some c_{ij}s are not as well constrained (e.g. c_{11}) as others in the global fit, the constraints provided by the lower pressure data leave very little room for uncertainty, unless significant anomalous compression behavior occurs. As described in Appendix A, we also tested global fitting using 4th-order EOSs. Although convergence in the refinement was not possible for all c_{ij}s, this led to a slightly poorer agreement with the high-pressure shear velocity data, as shown in Figure A.10 and a 3rd-order fit was, therefore, retained for all c_{ij}s. A detailed assessment of possible errors arising from the deviation of the c_{ij} of bridgmanite from the 3rd order EOS fit is further discussed in section A.2 of the supplementary material.

4.3.2 Aggregate elastic properties of $MgSiO_3$ bridgmanite

At each experimental pressure point, the adiabatic bulk (K_S) and shear moduli (G) have been calculated from the c_{ij} values in the Reuss and Voigt bounds (Appendix AA) and are reported in Table 4.1. The elastic moduli were then fitted with a 3rd-order finite strain EOS (Stixrude and Lithgow-Bertelloni, 2005) to obtain K_{S0}, G_0, K'_{S0} and G'_0 (Table 4.2). While the 3rd-order fits of the Voigt bulk and shear moduli, as well as the Reuss bulk modulus, have only small residuals relative to experimental data points (i.e. typically less than 0.5 GPa), there is a change in the slope of the Reuss bound of the shear modulus (G_R) at $\rho \sim 4.54$ g cm^{-3} (i.e. 35 GPa). This is apparent from the systematic deviations in the fitting residual at both low and high densities (i.e. pressures) (Figure A.2a - inset). This subtle change in the slope of the Reuss shear modulus occurs in the pressure interval where the shear wave anisotropy of $MgSiO_3$ bridgmanite shows a minimum, as already pointed out by Karki et al. (1997), and G_V and G_R tend to converge. At densities higher than 4.54 g cm^{-3}, the two bounds start to diverge again (Figure A.2c) as the shear wave anisotropy of bridgmanite increases. One possible explanation for this behavior is that it results from a change in the response of octahedral tilting and polyhedral distortion of the bridgmanite structure with pressure, i.e. under an isotropic stress environment (Reuss bound), for which corroborating evidence can be found in the evolution of lattice strain components for $MgSiO_3$ bridgmanite. Lattice

Table 4.1. Elastic stiffness components (c_{ij}) and elastic moduli from individual fits and global fit, reported in GPa. The numbers between brackets represent one standard deviation.

P (GPa)	ρ (g cm^{-3})	c_{11}	c_{22}	c_{33}	c_{44}	c_{55}	c_{66}	c_{12}	c_{13}	c_{23}	K_V	G_V	K_R	G_R	K_{VRH}	G_{VRH}
Individual fits																
0.00010(1)	4.1045(10)	482(3)	523(4)	468(3)	202.3(3)	182.8(10)	148.6(14)	122(3)	146(2)	154.3(14)	257.4(13)	176.8(5)	257.0(13)	174.4(5)	257.2(13)	175.6(5)
4.99(1)	4.183(4)	487(9)	580(6)	493(4)	213.3(8)	193.1(17)	160.4(11)	139(4)	149(4)	168(3)	276(2)	187.7(7)	274(2)	185.4(7)	275(2)	186.5(7)
9.32(2)	4.248(4)	535(3)	587(7)	522.5(19)	220.7(3)	198.1(7)	168.8(10)	153(4)	164(2)	170(3)	290.8(15)	194.7(5)	290.2(15)	192.9(5)	290.5(15)	193.8(5)
19.40(3)	4.390(6)	580.0(15)	643.8(8)	597.1(19)	237.1(3)	205.5(4)	189.6(8)	185.0(4)	184.2(17)	196.7(4)	328.1(16)	210.1(5)	327.3(16)	208.8(5)	327.7(16)	209.5(5)
30.3[a]	-	622(3)	697(30)	649(6)	251.7(8)	216.3(5)	208.0(5)	211(13)	199(4)	216(14)	358(5)	224.7(15)	356(6)	223.6(15)	357(5)	224.2(15)
Global fit																
0.00010(1)	4.1045(10)	486.8(20)	524.3(26)	467.7(16)	202.3(2)	180.2(4)	141.9(5)	124.3(18)	140.9(13)	152.6(10)	257.1(8)	175.6(2)	256.7(8)	172.9(2)	256.9(8)	174.2(2)
Set 1																
4.99(1)	4.183(4)	512.7(16)	556(2)	500.3(14)	212.0(2)	187.8(4)	153.4(5)	140.9(16)	151.7(11)	163.4(9)	275.7(7)	184.9(2)	275.2(7)	182.6(2)	275.5(7)	183.7(2)
15.40(3)	4.335(4)	564.0(12)	620(2)	566.5(12)	231.1(2)	202.6(3)	176.9(4)	175.5(13)	173.8(10)	185.3(9)	313.3(5)	203.2(2)	312.6(5)	201.5(2)	313.0(5)	202.4(2)
21.63(4)	4.420(5)	593.4(13)	657(2)	605.1(13)	241.9(2)	210.9(3)	190.8(3)	196.4(13)	186.8(11)	198.2(9)	335.3(5)	213.6(2)	334.5(5)	212.3(2)	334.9(5)	213.0(2)
26.77(5)	4.487(5)	616.8(16)	687(2)	636.4(15)	250.5(2)	217.3(2)	202.0(3)	213.6(14)	197.3(13)	208.6(9)	353.2(6)	222.0(2)	352.3(6)	220.7(2)	352.7(6)	221.4(2)
31.20(6)	4.543(6)	636.5(19)	712(2)	663.1(18)	257.7(2)	222.7(2)	211.7(3)	228.5(16)	206.3(15)	217.4(10)	368.4(7)	229.0(2)	367.4(7)	227.8(2)	367.9(7)	228.4(2)
35.61(7)	4.597(6)	656(2)	737(2)	689(2)	264.8(3)	227.9(2)	221.2(3)	243.3(19)	215.2(18)	226.1(10)	383.4(8)	235.9(2)	382.3(8)	234.7(2)	382.9(8)	235.3(2)
Set 2																
9.32(2)	4.248(4)	533.5(14)	581.8(23)	526.9(13)	219.7(2)	193.9(3)	162.8(4)	154.6(14)	160.6(10)	172.2(9)	290.8(6)	192.3(2)	290.2(6)	190.3(2)	290.5(6)	191.3(2)
19.40(3)	4.390(6)	584.0(12)	645.0(21)	592.7(13)	238.4(2)	208.2(3)	186.3(3)	189.6(13)	182.6(10)	194.0(9)	328.3(5)	210.3(2)	327.5(5)	208.8(2)	327.9(5)	209.6(2)
29.37(5)	4.520(6)	627.3(17)	700.1(22)	650.7(17)	254.4(2)	220.2(2)	207.2(3)	221.5(15)	202.1(14)	213.3(9)	361.3(6)	225.8(2)	360.3(6)	224.5(2)	360.8(6)	225.1(2)
55.59(13)	4.825(6)	738(5)	845(4)	805 (4)	294.7(5)	249.3(4)	263.6(5)	311(3)	254(3)	264.7(15)	449.8(13)	265.4(4)	448.1(13)	263.5(4)	449.0(13)	264.4(4)
61.7(2)	4.89(1)	761(5)	876(4)	839(4)	303.1(6)	255.2(4)	276.1(5)	331(4)	266(4)	275.9(17)	469.1(15)	273.7(4)	467.2(15)	271.4(4)	468.2(15)	272.5(4)
71.5(2)	4.99(1)	800(7)	928(5)	896(5)	317.0(7)	264.7(5)	297.3(7)	367(5)	286(5)	295(2)	502.1(18)	287.6(5)	499.8(18)	284.4(5)	501.0(18)	286.0(5)
78.8(5)	5.06(1)	825(8)	962(5)	933(6)	325.8(8)	270.6(6)	311.1(8)	390(6)	298(5)	307(2)	523 (2)	296.5(5)	521(2)	292.5(5)	522(2)	294.5(5)

[a] combined velocities from pressure points at 29.37 GPa (set 2) and 31.20 GPa (set 1).

Table 4.2. EOS parameters for K and G in the Voigt and Reuss bound. Values of $M_0^{''}$ in italics are implied from 3rd order truncations.

	K_{SV}	G_V	K_{SR}	G_R	G_R	G_R	G_R
Order	3	3	3	3	3	3	4
M_0 (GPa)	257.1(6)	175.6(2)	256.7(4)	173.9(6)	173.0(3)	177.2(12)	172.8(4)
$M_0^{'}$	3.71(4)	1.86(1)	3.70(3)	1.86(4)	1.92(2)	1.81(2)	1.96(2)
$M_0^{''}$ (GPa^{-1})	*-0.014*	*-0.0174*	*-0.014*	*-0.0173*	*-0.0168*	*-0.0179*	-0.0162(8)
P range (GPa)	0-78.8	0-78.8	0-78.8	0-78.8	0-27.0	55.9-78.8	0-78.8

strain components for the orthorhombic perovskite-type structure of bridgmanite can be simply calculated from unit cell parameters and describe the extent of lattice distortion with respect to a cubic perovskite structure, as described in previous studies (Boffa Ballaran et al., 2012; Carpenter et al., 2001; Carpenter, 2007). Of the three strain components, the tetragonal strain (e_{tx}), which is sensitive to both the degree of octahedral tilting and A site distortion, has also been shown to change in slope at approximately 35 GPa (Boffa Ballaran et al., 2012) as shown in Figure A.3. We argue that the change in slope of G_R may, therefore, be detected from the change in the distortion mechanism of the perovskite structure with pressure relative to an undeformed cubic perovskite. It should be noted that this behavior of G_R results from a combination of pressure dependencies of the individual c_{ij}s, through the matrix inversion needed to obtain the compliances (c_{ij}) to calculate the Reuss bound, and does not mean that these dependences are not well described by a 3rd-order finite stain equation. In order to better describe the change in slope of G_R, we fitted a 4th-order EOS to our shear moduli. To do so, we fixed the value of K_{S0}, $K_{S0}^{'}$, as well as $K_{S0}^{''}$ (value implied by a 3rd-order truncation of K, see Appendix A) which can be determined independently from K-V data, and refined only the shear modulus G_0 and its derivatives $G_0^{'}$ and $G_0^{''}$. A similar situation, where a higher truncation order for G is required with respect to K, was observed before in MgO (Zha et al., 2000). Alternatively, it is possible to fit two separate 3rd-order EOS below 30 GPa and above 50 GPa to the same shear moduli dataset (Figure A.2b), assuming two distinct shear mechanisms, as justified by the change in the slope of e_{tx} with pressure (Figure A.3). The two fitting strategies are indistinguishable within uncertainty (Figure A.2b). Fitting parameters of 3rd- and 4th-order EOS are reported in Table 4.2.

4.3.3 Absolute pressure determination

One of the advantages of conducting elasticity and density measurements simultaneously on the same sample is that pressure can be determined without using any secondary pressure scale (e.g. ruby or Sm:YAG). The absolute pressure (P_{abs}) can be determined by integration of the isothermal bulk modulus in the Reuss bound and the volume over a certain volume range:

$$P_{abs} = \int_V^{V_0} \frac{K_{TR}}{V}\, dV = 3K_{TR0} f\,(1+2f)^{5/2}\left[1+\frac{3}{2}\left(K_{TR0}^{'}-4\right)f\right] \tag{4.3}$$

Where K_{TR} is the isothermal bulk modulus, K_{TR0} is its value at ambient conditions and K'TR0 its pressure derivative. Using the relations $K_S = K_T(1 + \alpha\gamma T)$ and $\alpha = \gamma C_V / K_T V$, we converted our experimentally determined K_S into K_T and calculated K_{TR0} and K'_{TR0} by fitting a 3rd-order Birch-Munraghan EOS to our K_T-V data. Thermoelastic parameters used for the conversion of K_S to K_T at high pressure are reported in Table A.2. The absolute pressure was then determined using experimentally measured volumes, and our K_{TR0} = 254.5(4) GPa and K'_{TR0} = 3.73(2). The deviation of P_{abs} from the ruby pressure scale is virtually zero at pressures below 40 GPa and increases to 1 - 5 GPa at the highest pressure achieved (Figure A.4) depending on the employed pressure calibration for the ruby fluorescence (Dewaele et al., 2004; Jacobsen et al., 2008; Mao et al., 1986). The best agreement is found with the pressure scale determination of Jacobsen et al. (2008). For comparison, we also fitted a 3rd-order Birch-Munraghan EOS to the experimental bridgmanite unit cell volumes using pressures determined from the ruby pressure scale of Jacobsen et al. (2008), and the EOSFit software (Angel et al., 2014; Gonzalez-Platas et al., 2016). The obtained fitting parameters of K_{T0} = 255(10) GPa and K'_{T0} = 3.8(2) are in good agreement with the values determined in the K_T-V fit reported above. Pressures calculated with our P-V EOS are in broad agreement, within uncertainty, with those calculated from single-crystal synchrotron X-ray diffraction measurements by Boffa Ballaran et al. (2012), powder diffraction measurements in the LVP by Katsura et al. (2009) and the recent computational study of Zhang et al. (2013) (Figure A.5). On the other hand, powder X-ray diffraction data by Fiquet et al. (1998) and Tange et al. (2012) tend to overestimate pressures by more than 2 GPa already at 50 GPa. Tange et al. (2012) pointed out that the wide range of reported $MgSiO_3$ bridgmanite EOS parameters results from the use of different pressure scales and experimental techniques. Their $MgSiO_3$ bridgmanite EOS employed a primary MgO pressure scale calibrated with data sets where absolute pressure measurements were made Tange et al. (2009a). However, the accuracy of such EOS measurements is reduced by both the error on the primary pressure scale and those on the volume measurements of the pressure marker. Our P_{abs}, on the other hand, is a primary pressure scale and has been derived from volume and elasticity measurements on single-crystals in a quasi-hydrostatic environment, which reduces the sources of systematic errors.

4.4 Discussion

Aggregate velocities of $MgSiO_3$ bridgmanite are computed from the Voigt-Reuss-Hill (VRH) average of the bulk and shear moduli (Hill, 1963) and show excellent agreement between individual fits and the global fit procedure (Figure 4.3a). A comparison of the global fit with previous experimental and computational elasticity studies is shown in Figure 4.3b. Ultrasonic interferometry data collected by Chantel et al. (2012) in a LVP are in good agreement with this study at pressures up to the top of the lower mantle, although the values of K_{S0} and $K_{0'}$, 247(4) GPa and 4.5(2) respectively, would lead to an overestimation of v_P at deeper lower mantle conditions. Shear wave velocity data reported by Murakami et al. (2007) plot below the values determined in this study throughout the whole pressure

range investigated. In order to make a fairer comparison, the v_S data of Murakami et al. (2007) were re-fitted using a consistent 3rd-order truncation of the shear modulus EOS, as proposed by Chantel et al. (2016), rather than that derived from the 4th-order EOS of Davies and Dziewonski (1975), where Murakami et al. (2007) simply assumed that $K_{S0''} = 0$ and $G_{0''} = 0$. Our fit gives $G_0 = 172.1(13)$ GPa and $G_{0'} = 1.70(3)$, instead of $G_0 = 172.9(15)$ GPa and $G_{0'} = 1.56(4)$, only partially lifting the difference in pressure derivatives between Murakami et al. (2007) and this study. The lower $G_{0'}$ compared to our measurements ($G_{0V'} = 1.86(1)$, $G_{0R'} = 1.81(3)$) may be due to the fact that Murakami et al. (2007) used a polycrystalline sample which may be subject to the development of preferred orientation during compression. It is important to note that Murakami et al. (2007) synthesized their polycrystalline bridgmanite sample in situ by laser heating a $MgSiO_3$ gel. In these experiments, it is difficult to control the crystal size of the synthesized products, which rarely exceeds a hundred nanometers. Such small crystallite sizes can potentially trigger non-negligible scattering from grain boundaries, causing sound velocity softening even at high pressure (Marquardt et al., 2011). This effect was reported to be particularly pronounced on the shear modulus of the polycrystalline aggregate, which, in the case of MgO, can be reduced by 1-2% even when the crystal size is 500 nm (Marquardt et al., 2011). A grain size of 100 nm, for example, could therefore potentially explain the 3-4% difference in shear wave velocities observed between our dataset and that of Murakami et al. (2007).

Longitudinal wave velocities obtained in the computational studies of Oganov et al. (2001) and Wentzcovitch et al. (2004) are in reasonable agreement with our data at deep mantle conditions, as well as the shear wave velocities reported by Oganov et al. (2001). On the other hand, shear wave velocities reported by Wentzcovitch et al. (2004) are smaller by more than 3% at deep lower mantle pressure and close to the experimental results of Murakami et al. (2007). Based on their velocity data and previous static compression experiments Murakami et al. (2007) and Murakami et al. (2012) argued that a perovskite-rich (at least 93 volume%) lower mantle is required to match 1D seismic velocity models. Our elasticity data, instead, suggest that the shear modulus of bridgmanite is 3% stiffer than the values reported by Murakami et al. (2007) at mid lower mantle pressures. Therefore, the addition of softer materials (i.e. ferropericlase) is required to explain the slower v_S of the lower mantle assemblage, pointing towards a bulk composition that is more compatible with that of the upper mantle.

4.4.1 Effect of chemistry on the elasticity of bridgmanite

The effect of Fe and Al on the compressional and shear wave velocities of bridgmanite has been investigated in several previous studies by means of Brillouin scattering, impulsive stimulated light scattering (ISLS) and ultrasonic interferometry (Chantel et al., 2012; Fu et al., 2018; Fu et al., 2019; Jackson et al., 2005; Kurnosov et al., 2017). A comparison between velocity data for $MgSiO_3$ bridgmanite from this study with selected previous studies, summarized in Table A.1, is shown in Figure 4.3b. Chantel et al. (2012) reported that

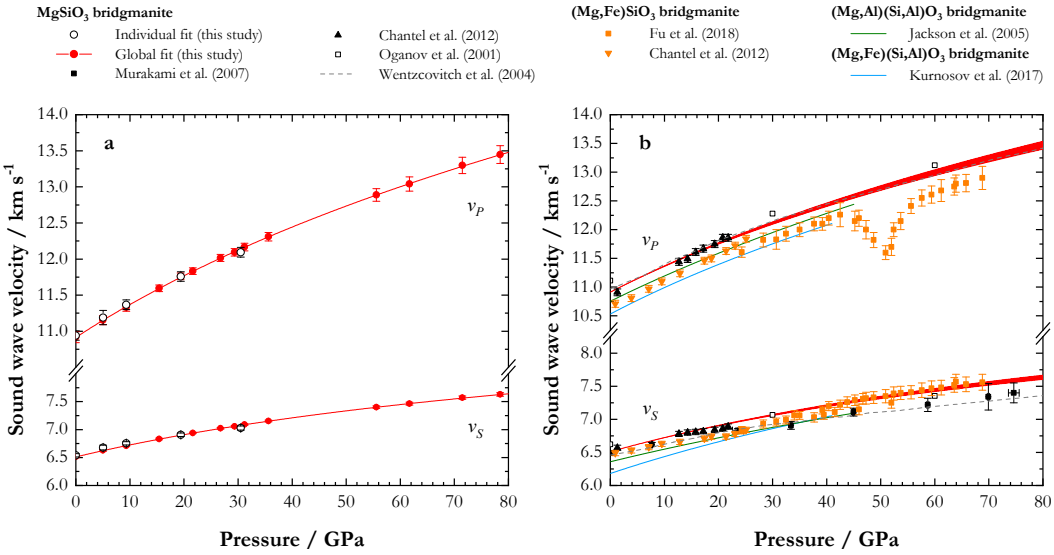

Figure 4.3. a) Aggregate sound wave velocities of $MgSiO_3$ bridgmanite calculated from our single-crystal elasticity data, showing excellent agreement between individual fits (empty circles) and the global fit (red line and symbols). The error bars are calculated by propagating the experimental errors on density and elastic moduli. b) Selected sound wave velocities of bridgmanite as a function of pressure from previous experimental and computational studies compared to the global fit. The shaded area indicates the propagated error on the fitting parameters and density. Murakami et al. (2007): Brillouin scattering on polycrystalline $MgSiO_3$ in DAC; Chantel et al. (2012): ultrasonic interferometry on $MgSiO_3$ and $Mg_{0.95}Fe_{0.05}SiO_3$ in LVP; Oganov et al. (2001): ab initio molecular dynamics on $MgSiO_3$; Wentzcovitch et al. (2004): first principle quasi-harmonic calculations on $MgSiO_3$; Fu et al. (2018): Brillouin scattering (v_S) and ISLS (v_P) on polycrystalline $Mg_{0.96}Fe_{0.05}Si_{0.99}O_3$ in DAC; Jackson et al. (2005): Brillouin scattering on polycrystalline $Mg_{0.95}Al_{0.10}Si_{0.95}O_3$ in DAC; Kurnosov et al. (2017): Brillouin scattering on single crystal $Mg_{0.9}Fe_{0.1}Al_{0.1}Si_{0.9}O_3$ in DAC.

the incorporation of Fe in bridgmanite decreases its sound velocities relative to $MgSiO_3$. Despite showing much larger K_0' (4.7) and lower G_0' (1.56) than values reported here, sound velocities measured by Chantel et al. (2012) plot subparallel to the $MgSiO_3$ bridgmanite samples measured in this study. Recently, Fu et al. (2018) used Brillouin scattering and ISLS to further investigate the sound velocity of $Mg_{0.96}Fe_{0.05}Si_{0.99}O_3$ bridgmanite in DAC up to 70 GPa. The v_P of Fe-bearing bridgmanite is subparallel to the $MgSiO_3$ endmember presented in this study, except between 40 and 60 GPa, where a spin crossover of Fe^{3+} in the B site of bridgmanite is proposed to take place causing a drop in v_P. Note that at the onset of the spin crossover, the slope of the v_S increases and becomes slightly larger than that of $MgSiO_3$. Jackson et al. (2005) studied the effect of the $AlAlO_3$ component on the aggregate acoustic velocities of bridgmanite using Brillouin scattering in a DAC. Incorporation of 0.05 Al atoms in both A and B sites of the bridgmanite structure seems to decrease both v_P and v_S (Jackson et al., 2005), but does not appear to affect their pressure dependence compared to the $MgSiO_3$ endmember reported in this study. On the other hand, the incorporation of the $FeAlO_3$ component decreases acoustic velocities at ambient conditions and causes

an increase in their pressure derivatives (Kurnosov et al., 2017). In particular, the slope of the shear wave velocity for 10 mol% $FeAlO_3$ bridgmanite is considerably higher than that measured for $MgSiO_3$ (Kurnosov et al., 2017). The decrease of both v_P and v_S in Fe-bearing Al-free bridgmanite at ambient conditions can be mainly attributed to the increase in density due to incorporation of Fe in the structure (Fu et al., 2018). On the other hand, Al incorporation in the B-site of bridgmanite increases the volume of the octahedral site causing an increase in its compressibility, which results in a lower bulk elastic moduli for Fe,Al-bearing bridgmanite (Kurnosov et al., 2017).

4.4.2 Elastic anisotropy

The elastic properties of $MgSiO_3$ bridgmanite determined in this study at ambient conditions are in overall good agreement with previously reported values by Sinogeikin et al. (2004) in terms of both elastic anisotropy (Figure A.6) and average properties (Table A.1). The stiffest elastic component of $MgSiO_3$ bridgmanite at all pressures investigated in this study is the c_{22}, while the c_{11} and c_{33} show a crossover at approximately 15 GPa (Figure A.1) with c_{33} becoming stiffer than c_{11}. The off-diagonal components c_{13} and c_{23} have very similar slopes throughout the whole pressure range investigated in this study, while the c_{12} is much steeper (Figure A.1). A similar behavior was observed for $FeAlO_3$-bearing bridgmanite by Kurnosov et al. (2017). Among the shear components, the stiffest is the c_{44}, while the observed crossover in the c_{55} and c_{66} might be related to changes in the compression mechanism of individual Mg-O bonds with increasing pressure, affecting the shear mechanism of the A site of bridgmanite. While the c_{44} and c_{55} of $FeAlO_3$-bearing bridgmanite measured by Kurnosov et al. (2017) are subparallel to $MgSiO_3$ bridgmanite, the slope of c_{66} is considerably higher. Once again, this is probably related to the higher degree of distortion of $FeAlO_3$-bearing bridgmanite relative to the $MgSiO_3$ end member, which is described by the lattice strain term e_{tx} (Figure A.3). Several first principle studies have also calculated the anisotropic elastic properties of $MgSiO_3$ bridgmanite at high pressure (Karki et al., 1997; Oganov et al., 2001; Wentzcovitch et al., 1998; Wentzcovitch et al., 2004) and, in general, they show fairly good agreement with our results. While the diagonal components predicted by computational studies match well the values obtained in this study, the off-diagonal components tend to be more than 10% stiffer than our experimental values at mid-lower mantle pressures.

There are a number of inconsistencies that arise when the elastic stiffness components determined in this study and those determined by Kurnosov et al. (2017) are compared with values reported in the recent study of Fu et al. (2019) for bridgmanite solid solutions along the $MgSiO_3$–$FeAlO_3$ join. The results of Fu et al. (2019) at 25 GPa indicate the relationship $c_{22} > c_{33} > c_{11}$ for a bridgmanite sample with composition $Mg_{0.89}Fe_{0.12}Al_{0.11}Si_{0.89}O_3$ (Fe12Al11), in agreement with this study and that of Kurnosov et al. (2017). However, they also report the relation $c_{33} > c_{22} > c_{11}$ for another bridgmanite sample with the composition $Mg_{0.96}Fe_{0.06}Al_{0.04}Si_{0.96}O_3$ (Fe6Al4). Based on their results, Fu et al. (2019) concluded that

c_{22} increases while c_{11} and c_{33} decreases with increasing $FeAlO_3$ component. However, in determining these trends Fu et al. (2019) appear to have swapped the values of c_{22} and c_{33} calculated for the $MgSiO_3$ end member by Karki et al. (1997), who clearly report a c_{22} larger than c_{33} at all pressures. The trends as a function of $FeAlO_3$ component reported by Fu et al. (2019) appear therefore inconsistent when compared to experimental and theoretical studies reported in the literature (Karki et al., 1997; Kurnosov et al., 2017; Oganov et al., 2001; Wentzcovitch et al., 1998; Wentzcovitch et al., 2004) (Figure A.7). Moreover, the v_P anisotropy determined by Fu et al. (2019) for the Fe6Al4 and Fe12Al11 compositions at 25 GPa is quite different, even though the compositional change is relatively small (Figure 4.4). The v_P anisotropy determined by Kurnosov et al. (2017), on the other hand follows the same general trend as that of the $MgSiO_3$ end member measured in this study and deviates quite strongly from the results of Fu et al. (2019). At 35 GPa, the v_S anisotropy displayed by the Fe6Al4 and Fe12Al11 samples of Fu et al. (2019) becomes more similar (Figure A.8), because of a major change in the anisotropy of the Fe6Al4 sample. This would imply a significant change in the compressibility mechanism for these samples over a pressure interval of only 10 GPa, which seems unlikely. Although the three studies employed Brillouin scattering to probe the v_S of the bridgmanite samples, the v_S anisotropy displayed by the Fe6Al4 and Fe12Al11 samples of Fu et al. (2019) is not always in agreement with that of $MgSiO_3$ bridgmanite and FeAl-bearing bridgmanite samples measured in this study and by Kurnosov et al. (2017) respectively. For instance, at 25 GPa, the v_S of Fe12Al11 between [100] and [010] directions (i.e. (001) plane) looks similar to that of $MgSiO_3$ and Fe6Al4 between [010] and [001] (i.e. (100) plane), as shown in Figure 4.4, suggesting orientation problems. Note that the XRD, ISLS and Brillouin scattering measurements reported by Fu et al. (2019) were performed on three different setups and combined only afterwards. On the other hand, XRD and Brillouin scattering measurements performed in this study and by Kurnosov et al. (2017) were performed on the same setup, without moving the sample. Further investigations on bridgmanite samples with intermediate compositions are therefore required to univocally solve this issue.

Using our high-pressure elastic stiffness components, the axial compressibility of $MgSiO_3$ bridgmanite can also be calculated for comparison purposes. The same relation between axial compressibilities $\beta_a > \beta_c > \beta_b$ (or axial moduli, $M_b > M_c > M_a$) can be observed in $MgSiO_3$ and $FeAlO_3$-bridgmanite through both elasticity and X-ray diffraction measurements independently (Boffa Ballaran et al., 2012; Kurnosov et al., 2017). We have used 3rd-order linear EOS (Angel et al., 2014) to fit the unit cell parameters reported by Boffa Ballaran et al. (2012) for $MgSiO_3$ bridgmanite using the EosFit7-GUI software (Gonzalez-Platas et al., 2016). The axial moduli are calculated from the compliance components, s_{ij}, of $MgSiO_3$ bridgmanite obtained by inverting at each pressure the elastic stiffness tensor reported in this study. The axial moduli calculated in this way are in qualitative agreement with those calculated from the compression data reported in Boffa Ballaran et al. (2012), despite showing a less anisotropic behavior at high pressure and a smaller M_b (Figure A.9). The axial moduli calculated from our elasticity measurements are also in

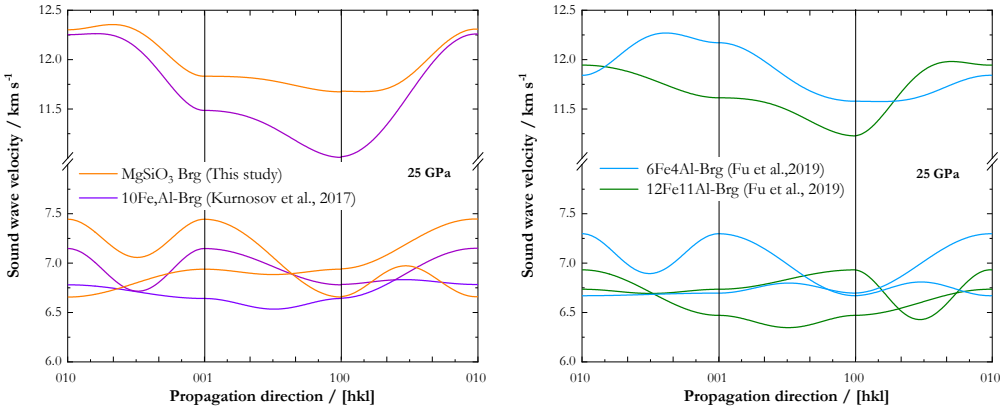

Figure 4.4. Dispersion curves of bridgmanite at 25 GPa. This study: $MgSiO_3$ (orange line) c_{ij} calculated from finite strain 3rd-order EOS; Kurnosov et al. (2017): 10 mol% $FeAlO_3$ (purple line), c_{ij} calculated from finite strain 3rd-order EOS; Fu et al. (2019): Fe6Al4-Brg (cyan line) and Fe12Al11-Brg (green line), c_{ij} at 25 GPa as reported in the mentioned paper.

fair agreement with computational studies (Oganov et al., 2001; Wentzcovitch et al., 1998; Wentzcovitch et al., 2004) which reproduce well the axial compressibility of Boffa Ballaran et al. (2012) (Figure A.9). Larger values of M_b observed at high pressure by Boffa Ballaran et al. (2012) may be explained by the larger calculated K'_{T0} relative to this study, which is most likely due to the different pressure scales employed.

4.5 A mineral physics model for the lower mantle

Using previously published parameters for the thermal EOS of $MgSiO_3$ bridgmanite along with elasticity data for other components of the lower mantle, a mineral physical model can be constructed to predict seismic wave velocities for a given bulk mantle composition, which can then be compared with 1D seismic reference models (Dziewonski and Anderson, 1981; Kennett et al., 1995). Currently such a model can only be preliminary as the phase equilibria and EOS data required to model a complex mantle composition throughout the lower mantle are not available. Without more accurate knowledge, for example, of how the proportions and site occupancies of Fe^{3+} and Al in bridgmanite change with pressure, their inclusion in such a model introduces more uncertainty than they likely resolve. However, as uncertainties rise with the complexity of the model, a comparison with simpler chemical models allows factors to be identified that may be important in a suitably realistic model of the mantle.

Seismic wave velocities were computed as a function of depth for a primitive mantle composition (Mcdonough and Rudnick, 1998) consisting of bridgmanite, ferropericlase and Ca-perovskite in the CaO-MgO-SiO_2 (CMS) and CaO-FeO-MgO-SiO_2 (CFMS) systems.

Mass fractions of Al_2O_3, Cr_2O_3 and TiO_2 were added to SiO_2. Calculations were performed using the formalism of Stixrude and Lithgow-Bertelloni (2005) and Stixrude and Lithgow-Bertelloni (2011) to determine mineral compositions (in the CFMS system), seismic velocities and the adiabatic temperature profile, assuming a temperature of 1960 K at 24 GPa (Katsura et al., 2010). In the light of new experimental results on the elastic properties of $MgSiO_3$ bridgmanite presented in this study, as well as of cubic Ca-perovskite (Gréaux et al., 2019), we decided to update the list of thermoelastic parameters presented in Stixrude and Lithgow-Bertelloni (2011). The complete list of employed parameters is reported in Table A.2. For comparison, the aggregate velocities for the CMFS phase assemblage were also calculated using the original set of thermoelastic parameters reported in Stixrude and Lithgow-Bertelloni (2011). Our calculated v_S are approx. 0.8% (top lower mantle) to 1.7% (bottom lower mantle) faster than those calculated with the parameters of Stixrude and Lithgow-Bertelloni (2011), while v_P ranges from 0.4% faster (top lower mantle) to 1.0% slower (bottom lower mantle). A mass balance was used to determine component fractions and in the CFMS system the proportions of Fe^{2+} and Mg end members were constrained using a thermodynamic description of the distribution coefficient, K_D, defined as:

$$K_D = \frac{X_{Fe}^{Brg}/X_{Mg}^{Brg}}{X_{Fe}^{Fp}/X_{Mg}^{Fp}} \tag{4.4}$$

Where X is the mole fraction of either bridgmanite (Brg) or ferropericlase (Fp) components. To model the effect of Fe-Mg non-ideality of mixing, we used the parameters given by Nakajima et al. (2012). However, we calculate the standard state Gibbs free energy change for equilibrium (4.4) self consistently using the model of Stixrude and Lithgow-Bertelloni (2005) and Stixrude and Lithgow-Bertelloni (2011). The model results in values of K_D which are in excellent agreement with recent multi-anvil studies performed up to approximately 60 GPa (Arimoto et al., 2019; Tange et al., 2009b) and in good agreement with some studies performed in the diamond anvil cell to approximately 100 GPa (e.g. Auzende et al., 2008; Sakai et al., 2009), even though the Fe-Mg partitioning model does not explicitly account for the effect of an electronic spin transition of Fe^{2+} in ferropericlase. Using appropriate mineral component averaging schemes (Cottaar et al., 2014) the aggregate wave velocities in the Voigt and Reuss bound, as well as in Voigt-Reuss-Hill average, were then calculated. We make no allowance for the effects of attenuation in the calculation, which may further lower the calculated velocities (Cottaar et al., 2014) and the effects of iron spin transitions on the elastic properties have not been explicitly considered.

In Figure 4.5 velocities calculated along a mantle adiabat for a primitive mantle composition (Mcdonough and Rudnick, 1998) are compared in different systems with 1D seismic models (Dziewonski and Anderson, 1981; Kennett et al., 1995). Velocities for single phase $MgSiO_3$ bridgmanite and the CMS model are faster than the seismic models; moreover, the CMS velocities also have distinctly steeper slopes, particularly for v_P (Figure 4.5). This arises from the slightly higher $K_0^{'}$ of MgO (Kono et al., 2010) compared to bridgmanite. When Fe^{2+} is included in the CMFS model, however, there is reasonable agreement between

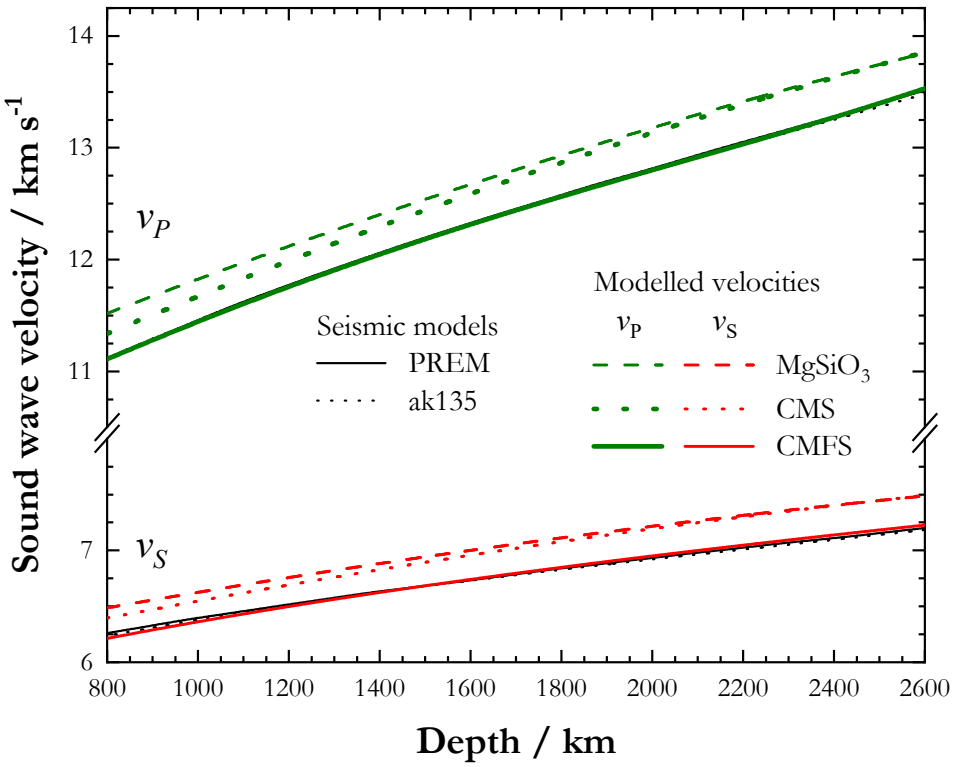

Figure 4.5. P- and S-wave velocities of $MgSiO_3$ bridgmanite (dashed colored lines) and lower mantle assemblages determined for a primitive mantle composition (Mcdonough and Rudnick, 1998) in the CMS (dotted colored lines) and CFMS (solid colored line) systems calculated along an adiabat with a temperature of 1960 K at 660 km (Katsura et al., 2010). The difference between Voigt and Reuss bound of lower mantle assemblages, indicated by the thickness of the line, is about 40-60 m/s for v_P and 20-40 m/s for v_S. 1D seismic models PREM (solid black lines) and ak135 (dotted black lines) are shown for comparison.

the calculated v_S and the seismic models throughout the entire lower mantle, with residuals never exceeding 0.6%. Even more striking agreement exists for v_P, which perfectly overlaps with PREM along the entire modelled depth interval within the Voigt and Reuss bounds. The improved agreement in the slope of v_P compared with the CMS model arises mainly because the Fe^{2+}-Mg K_D decreases with pressure, in line with experimental observations (Nakajima et al., 2012). As the proportion of the FeO endmember of ferropericlase increases, both v_P and v_S decrease. Despite the excellent match between the slope of v_P for the CMFS phase assemblage and that of seismic models, it should be noted that the v_S slope is not in perfect agreement. This difference cannot be attributed to temperature, as it would similarly displace both v_P and v_S. This likely arises because the model does not include potential effects of Al or the spin crossover transition of Fe^{2+} in ferropericlase, which would need to be considered in any meaningful comparison. As far as the spin crossover of Fe^{2+} in ferropericlase is concerned (Kantor et al., 2006; Lin et al., 2005; Valencia-Cardona et al.,

2017; Marquardt et al., 2018, and references therein), its effect on the elastic properties have not been considered at high pressure and temperature, but the CMFS model should at least capture any resulting effects on the Fe-Mg K_D because the available experimental data at pressure above the spin cross over transition are relatively well reproduced by our model. The incorporation of Al in bridgmanite is known to also raise the bridgmanite $Fe^{3+}/\Sigma Fe$ ratio to levels of approximately 0.5 (Frost et al., 2004), at least at conditions of the top of the lower mantle, due to the favorable substitution of an $FeAlO_3$ component. Fe^{3+} is likely produced in the lower mantle through charge disproportionation of Fe^{2+} that also leads to precipitation of Fe-rich alloy. As Al is added to bridgmanite half of the Fe^{2+}, therefore, becomes Fe^{3+}. The effect of adding an $FeAlO_3$ component to bridgmanite is twofold; on the one hand the incorporation of an $FeAlO_3$ component will lower the bulk and shear modulus of bridgmanite (Fu et al., 2019; Kurnosov et al., 2017) to some extent, while on the other hand the replacement of Fe^{2+} for Fe^{3+} will reduce the amount of Fe^{2+} that partitions into ferropericlase, which will tend to raise the bulk and shear modulus. These combined effects may, therefore, tend to cancel out to some extent. However, quantifying this effect by incorporating it into a model for the entire bridgmanite stability field is not currently possible, because the definitive experiments to determine how the proportion of the bridgmanite $FeAlO_3$ component is likely to vary with depth in a primitive mantle composition have not yet been performed. It is quite possible, for example, that at higher pressures the proportion of the $FeAlO_3$ component decreases either due to changes in the Fe^{2+} disproportionation reaction, as proposed recently for silica saturated assemblages (Shim et al., 2017) or due to a raised preference for the $AlAlO_3$ and $FeFeO_3$ bridgmanite components. In addition to these problems, however, there is also a lack of high-pressure elasticity data on the effects of all bridgmanite components other than $MgSiO_3$, as elasticity measurements performed so far on $FeSiO_3$- and $AlAlO_3$-bearing bridgmanite, for example, were conducted only on polycrystalline samples (Chantel et al., 2012; Fu et al., 2018; Jackson et al., 2005; Murakami et al., 2012).

In this study we have shown that self-consistent measurements of X-ray diffraction and Brillouin scattering of single crystals can provide accurate and precise elastic parameters of bridgmanite up to pressures of the mid lower mantle. In order to improve the resolution of mineral physics models, more self-consistent single-crystal elasticity measurements at high-pressure and high-temperature are required to better constrain the effects of these bridgmanite components. Assumed thermal parameters and the effects of attenuation also need to be addressed. Reducing the chemical and thermal uncertainties should eventually allow more reliable complex mineral physics models to be developed through which the average bulk composition of the lower mantle, in addition to the nature of large-scale apparent heterogeneities, can ultimately be constrained.

Acknowledgments

The equipment for this research was supported through the ERC advanced grant number 227893 'DEEP' funded through the EU seventh Framework Programme and by grant INST 91/315-1 FUGG and FR1555/11 from the DFG. We thank R. Njul for sample polishing and N. Miyajima and D. Wiesner for their assistance with the FIB device.

Data Availability Statement

Sound velocity data used for c_{ij} calculation are available at: https://figshare.com/articles/dataset/sound_velocity_data_xlsx/14265176.

References

Angel, R. J. and L. W. Finger (2011). "SINGLE: A program to control single-crystal diffractometers". In: *Journal of Applied Crystallography* 44 (1), pp. 247–251. DOI: 10.1107/S0021889810042305.

Angel, R. J., J. Gonzalez-Platas, and M. Alvaro (2014). "EosFit7c and a Fortran module (library) for equation of state calculations". In: *Zeitschrift fur Kristallographie* 229 (5), pp. 405–419. DOI: 10.1515/zkri-2013-1711.

Arimoto, T., T. Irifune, M. Nishi, Y. Tange, T. Kunimoto, and Z. Liu (2019). "Phase relations of $MgSiO_3$-$FeSiO_3$ system up to 64FIX ME!!!!GPa and 2300FIX ME!!!!K using multianvil apparatus with sintered diamond anvils". In: *Physics of the Earth and Planetary Interiors* 295. DOI: 10.1016/j.pepi.2019.106297.

Auzende, A. L., J. Badro, F. J. Ryerson, P. K. Weber, S. J. Fallon, A. Addad, J. Siebert, and G. Fiquet (2008). "Element partitioning between magnesium silicate perovskite and ferropericlase: New insights into bulk lower-mantle geochemistry". In: *Earth and Planetary Science Letters* 269 (1-2), pp. 164–174. DOI: 10.1016/j.epsl.2008.02.001.

Ballmer, M. D., C. Houser, J. W. Hernlund, R. M. Wentzcovitch, and K. Hirose (2017). "Persistence of strong silica-enriched domains in the Earth's lower mantle". In: *Nature Geoscience* 10 (3), pp. 236–240. DOI: 10.1038/ngeo2898.

Boehler, R. and K. D. Hantsetters (Sept. 2004). "New anvil designs in diamond-cells". In: *High Pressure Research* 24 (3), pp. 391–396. DOI: 10.1080/08957950412331323924.

Boffa Ballaran, T., A. Kurnosov, K. Glazyrin, D. J. Frost, M. Merlini, M. Hanfland, and R. Caracas (2012). "Effect of chemistry on the compressibility of silicate perovskite in the lower mantle". In: *Earth and Planetary Science Letters* 333-334, pp. 181–190. DOI: 10.1016/j.epsl.2012.03.029.

Buchen, J. (2018). "The Elastic Properties of Wadsleyite and Stishovite at High Pressures". URL: https://epub.uni-bayreuth.de/4410/.

Buchen, J., H. Marquardt, S. Speziale, T. Kawazoe, T. B. Ballaran, and A. Kurnosov (2018b). "High-pressure single-crystal elasticity of wadsleyite and the seismic signature of water in the shallow transition zone". In: *Earth and Planetary Science Letters* 498, pp. 77–87. DOI: 10.1016/j.epsl.2018.06.027.

Carpenter, M. A. (2007). "Elastic anomalies accompanying phase transitions in (Ca,Sr)TiO_3 perovskites: Part I. Landau theory and a calibration for SrTiO3". In: *American Mineralogist* 92 (2-3), pp. 309–327. DOI: 10.2138/am.2007.2295.

Carpenter, M. A., A. I. Bacerro, and F. Seifert (2001). "Strain analysis of phase transitions in (Ca,Sr)TiO_3 perovskites". In: *American Mineralogist* 86 (3), pp. 348–363. DOI: 10.2138/am-2001-2-319.

Chantel, J., D. J. Frost, C. A. McCammon, Z. Jing, and Y. Wang (2012). "Acoustic velocities of pure and iron-bearing magnesium silicate perovskite measured to 25 GPa and 1200 K". In: *Geophysical Research Letters* 39 (19). DOI: 10.1029/2012GL053075.

Chantel, J., G. M. Manthilake, D. J. Frost, C. Beyer, T. B. Ballaran, Z. Jing, and Y. Wang (2016). "Elastic wave velocities in polycrystalline $Mg_3Al_2Si_3O_{12}$-pyrope garnet to 24 GPa and 1300 K". In: *American Mineralogist* 101 (4), pp. 991–997. DOI: 10.2138/am-2016-5335.

Cottaar, S., T. Heister, I. Rose, and C. Unterborn (2014). "BurnMan: A lower mantle mineral physics toolkit". In: *Geochemistry, Geophysics, Geosystems* 15, 1164–1179. DOI: doi:10.1002/2013GC005122.

Davies, G. F. and A. M. Dziewonski (1975). "Homogeneity and constitution of the earth's lower mantle and outer core". In: *Physics of the Earth and Planetary Interiors* 10 (4), pp. 336–343. DOI: 10.1016/0031-9201(75)90060-6.

Dewaele, A., P. Loubeyre, and M. Mezouar (2004). "Equations of state of six metals above 94 GPa". In: *Physical Review B - Condensed Matter and Materials Physics* 70 (9), p. 094112. DOI: 10.1103/PhysRevB.70.094112.

Dziewonski, A. M. and D. L. Anderson (1981). "Preliminary reference Earth model". In: *Physics of the Earth and Planetary Interiors* 25 (4), pp. 297–356. DOI: 10.1016/0031-9201(81)90046-7.

Elkins-Tanton, L. T. (2012). "Magma oceans in the inner solar system". In: *Annual Review of Earth and Planetary Sciences* 40, pp. 113–139. DOI: 10.1146/annurev-earth-042711-105503.

Every, A. G. (1980). "General closed-form expressions for acoustic waves in elastically anisotropic solids". In: *Physical Review B* 22 (4), pp. 1746–1760. DOI: 10.1103/PhysRevB.22.1746.

Fiquet, G., D. Andrault, A. Dewaele, T. Charpin, M. Kunz, and D. Haüsermann (1998). "*P-V-T* equation of state of $MgSiO_3$ perovskite". In: *Physics of the Earth and Planetary Interiors* 105 (1-2), pp. 21–31. DOI: 10.1016/S0031-9201(97)00077-0.

Fiquet, G., A. Dewaele, D. Andrault, M. Kunz, and T. L. Bihan (2000). "Thermoelastic properties and crystal structure of $MgSiO_3$ perovskite at lower mantle pressure and temperature conditions". In: *Geophysical Research Letters* 27 (1), pp. 21–24. DOI: 10.1029/1999GL008397.

Frost, D. J., C. Liebske, F. Langenhorst, C. A. McCammon, R. G. Trønnes, and D. C. Rubie (2004). "Experimental evidence for the existence of iron-rich metal in the Earth's lower mantle". In: *Nature* 428, pp. 409–412. DOI: 10.1029/200/JC000964.

Fu, S., J. Yang, N. Tsujino, T. Okuchi, N. Purevjav, and J.-F. F. Lin (2019). "Single-crystal elasticity of (Al,Fe)-bearing bridgmanite and seismic shear wave radial anisotropy at the topmost lower mantle". In: *Earth and Planetary Science Letters* 518, pp. 116–126. DOI: 10.1016/j.epsl.2019.04.023.

Fu, S., J. Yang, Y. Zhang, T. Okuchi, C. McCammon, H. I. Kim, S. K. Lee, and J. F. Lin (2018). "Abnormal Elasticity of Fe-Bearing Bridgmanite in the Earth's Lower Mantle". In: *Geophysical Research Letters* 45 (10), pp. 4725–4732. DOI: 10.1029/2018GL077764.

Gonzalez-Platas, J., M. Alvaro, F. Nestola, and R. J. Angel (2016). "EosFit7-GUI: A new graphical user interface for equation of state calculations, analyses and teaching". In: *Journal of Applied Crystallography* 49 (4), pp. 1377–1382. DOI: 10.1107/S1600576716008050.

Gréaux, S., T. Irifune, Y. Higo, Y. Tange, T. Arimoto, Z. Liu, and A. Yamada (2019). "Sound velocity of $CaSiO_3$ perovskite suggests the presence of basaltic crust in the Earth's lower mantle". In: *Nature* 565 (7738), pp. 218–221. DOI: 10.1038/s41586-018-0816-5.

Hill, R. (1963). "Elastic properties of reinforced solids: Some theoretical principles". In: *Journal of the Mechanics and Physics of Solids* 11 (5), pp. 357–372. DOI: 10.1016/0022-5096(63)90036-X.

Irifune, T. (1994). "Absence of an aluminous phase in the upper part of the Earth's lower mantle". In: *Nature* 370 (6485), pp. 131–133. DOI: 10.1038/370131a0.

Irifune, T., T. Shinmei, C. A. McCammon, N. Miyajima, D. C. Rubie, and D. J. Frost (2010). "Iron Partitioning and Density Changes of Pyrolite in Earth's Lower Mantle". In: *Science* 327 (5962), pp. 193–195. DOI: 10.1126/science.1181443.

Ishii, T., H. Kojitani, and M. Akaogi (2011). "Post-spinel transitions in pyrolite and Mg_2SiO_4 and akimotoite-perovskite transition in $MgSiO_3$: Precise comparison by high-pressure high-temperature experiments with multi-sample cell technique". In: *Earth and Planetary Science Letters* 309 (3-4), pp. 185–197. DOI: 10.1016/j.epsl.2011.06.023.

Jackson, J. M., J. Zhang, J. Shu, S. V. Sinogeikin, and J. D. Bass (2005). "High-pressure sound velocities and elasticity of aluminous $MgSiO_3$ perovskite to 45 GPa: Implications for lateral heterogeneity in Earth's lower mantle". In: *Geophysical Research Letters* 32 (21), pp. 1–4. DOI: 10.1029/2005GL023522.

Jacobsen, S. D., C. M. Holl, K. A. Adams, R. A. Fischer, E. S. Martin, C. R. Bina, J. F. Lin, V. B. Prakapenka, A. Kubo, and P. Dera (2008). "Compression of single-crystal magnesium oxide to 118 GPa and a ruby pressure gauge for helium pressure media". In: *American Mineralogist* 93 (11-12), pp. 1823–1828. DOI: 10.2138/am.2008.2988.

Kantor, I., V. Prakapenka, A. Kantor, P. Dera, A. Kurnosov, S. Sinogeikin, N. Dubrovinskaia, and L. Dubrovinsky (2012). "BX90: A new diamond anvil cell design for X-ray diffraction and optical measurements". In: *Review of Scientific Instruments* 83 (12), p. 125102. DOI: 10.1063/1.4768541.

Kantor, I. Y., L. S. Dubrovinsky, and C. A. McCammon (2006). "Spin crossover in (Mg,Fe)O: A Mössbauer effect study with an alternative interpretation of x-ray emission spectroscopy data". In: *Physical Review B* 73 (10), p. 100101. DOI: 10.1103/PhysRevB.73.100101.

Karki, B. B., L. Stixrude, S. J. Clark, M. C. Warren, G. J. Ackland, and J. Crain (1997). "Elastic properties of orthorhombic $MgSiO_3$ perovskite at lower mantle pressures". In: *American Mineralogist* 82 (5-6), pp. 635–638. DOI: 10.2138/am-1997-5-623.

Katsura, T., S. Yokoshi, K. Kawabe, A. Shatskiy, M. A. Manthilake, S. Zhai, H. Fukui, H. A. Hegoda, T. Yoshino, D. Yamazaki, T. Matsuzaki, A. Yoneda, E. Ito, M. Sugita, N. Tomioka, K. Hagiya, A. Nozawa, and K. I. Funakoshi (2009). "*P-V-T* relations of $MgSiO_3$ perovskite determined by in situ X-ray diffraction using a large-volume high-pressure apparatus". In: *Geophysical Research Letters* 36 (1), pp. 2–7. DOI: 10.1029/2008GL035658.

Katsura, T., A. Yoneda, D. Yamazaki, T. Yoshino, E. Ito, D. Suetsugu, C. Bina, T. Inoue, D. Wiens, and M. Jellinek (2010). "Adiabatic temperature profile in the mantle". In: *Physics of the Earth and Planetary Interiors* 183 (1-2), pp. 212–218. DOI: 10.1016/j.pepi.2010.07.001.

Kennett, B. L. N., E. R. Engdahl, and R. Buland (1995). "Constraints on seismic velocities in the Earth from traveltimes". In: *Geophysical Journal International* 122 (1), pp. 108–124. DOI: 10.1111/j.1365-246X.1995.tb03540.x.

King, H. E. and L. W. Finger (1979). "Diffracted beam crystal centering and its application to high-pressure crystallography". In: *Journal of Applied Crystallography* 12 (4), pp. 374–378. DOI: 10.1107/S0021889879012723.

Kono, Y., T. Irifune, Y. Higo, T. Inoue, A. Barnhoorn, D. Suetsugu, C. Bina, T. Inoue, D. Wiens, and M. Jellinek (2010). "*P-V-T* relation of MgO derived by simultaneous elastic wave velocity and in situ X-ray measurements: A new pressure scale for the mantle transition region". In: *Physics of the Earth and Planetary Interiors* 183 (1-2), pp. 196–211. DOI: 10.1016/j.pepi.2010.03.010.

Kurnosov, A., H. Marquardt, D. J. Frost, T. B. Ballaran, and L. Ziberna (2017). "Evidence for a Fe^{3+}-rich pyrolitic lower mantle from (Al,Fe)-bearing bridgmanite elasticity data". In: *Nature* 543, pp. 543–546. DOI: 10.1038/nature21390.

Lin, J. F., V. V. Struzhkin, S. D. Jacobsen, G. Shen, V. B. Prakapenka, H. K. Mao, and R. J. Hemley (2005). "X-ray emission spectroscopy with a laser-heated diamond anvil cell: A new experimental probe of the spin state of iron in the Earth's interior". In: vol. 12. International Union of Crystallography, pp. 637–641. DOI: 10.1107/S0909049505020741.

Mao, H. K., J. Xu, and P. M. Bell (1986). "Calibration of the ruby pressure gauge to 800 kbar under quasi-hydrostatic conditions". In: *Journal of Geophysical Research* 91 (B5), p. 4673. DOI: 10.1029/jb091ib05p04673.

Marquardt, H., J. Buchen, A. S. Mendez, A. Kurnosov, M. Wendt, A. Rothkirch, D. Pennicard, and H. P. Liermann (2018). "Elastic Softening of (Mg0.8Fe0.2)O Ferropericlase Across the Iron Spin Crossover Measured at Seismic Frequencies". In: *Geophysical Research Letters* 45 (14), pp. 6862–6868. DOI: 10.1029/2018GL077982.

Marquardt, H., A. Gleason, K. Marquardt, S. Speziale, L. Miyagi, G. Neusser, H. R. Wenk, and R. Jeanloz (2011). "Elastic properties of MgO nanocrystals and grain boundaries

at high pressures by Brillouin scattering". In: *Physical Review B - Condensed Matter and Materials Physics* 84 (6), pp. 1–9. DOI: 10.1103/PhysRevB.84.064131.

Mcdonough, W. F. and R. L. Rudnick (1998). "Mineralogy and composition of the upper mantle". In: *Reviews in Mineralogy and Geochemistry* (37), pp. 139–164. DOI: 10.1515/9781501509179-006.

Murakami, M., Y. Ohishi, N. Hirao, and K. Hirose (2012). "A perovskitic lower mantle inferred from high-pressure, high-temperature sound velocity data". In: *Nature* 485 (7396), pp. 90–94. DOI: 10.1038/nature11004.

Murakami, M., S. V. Sinogeikin, H. Hellwig, J. D. Bass, and J. Li (2007). "Sound velocity of $MgSiO_3$ perovskite to Mbar pressure". In: *Earth and Planetary Science Letters* 256 (1-2), pp. 47–54. DOI: 10.1016/j.epsl.2007.01.011.

Nakajima, Y., D. J. Frost, and D. C. Rubie (2012). "Ferrous iron partitioning between magnesium silicate perovskite and ferropericlase and the composition of perovskite in the Earth's lower mantle". In: *Journal of Geophysical Research: Solid Earth* 117 (8), pp. 1–12. DOI: 10.1029/2012JB009151.

Oganov, A. R., J. P. Brodholt, and G. D. Price (2001). "Ab initio elasticity and thermal equation of state of $MgSiO_3$ perovskite". In: *Earth and Planetary Science Letters* 184 (3-4), pp. 555–560. DOI: 10.1016/S0012-821X(00)00363-0.

Palme, H and H. O'Neill (2014). "Cosmochemical Estimates of Mantle Composition". In: *Treatise on Geochemistry: Second Edition* 3, pp. 1–39. DOI: 10.1016/B978-0-08-095975-7.00201-1.

Poirier, J. P. (1994). "Light elements in the Earth's outer core: A critical review". In: *Physics of the Earth and Planetary Interiors* 85 (3-4), pp. 319–337. DOI: 10.1016/0031-9201(94)90120-1.

Ralph, R. L. and L. W. Finger (1982). "A Computer-Program for Refinement of Crystal Orientation Matrix and Lattice-Constants from Diffractometer Data with Lattice Symmetry Constraints". In: *Journal of Applied Crystallography* 15 (10), pp. 537–539. DOI: 10.1107/S0021889882012539.

Ringwood, A. E. (1962). "A model for the upper mantle: 2." In: *Journal of Geophysical Research* 67 (11), pp. 4473–4478. DOI: 10.1029/jz067i011p04473.

Sakai, T., E. Ohtani, H. Terasaki, N. Sawada, Y. Kobayashi, M. Miyahara, M. Nishijima, N. Hirao, Y. Ohishi, and T. Kikegawa (2009). "Fe-Mg partitioning between perovskite and ferropericlase in the lower mantle". In: *American Mineralogist* 94 (7), pp. 921–925. DOI: 10.2138/am.2009.3123.

Sandercock, J. R. (1982). "Trends in brillouin scattering: Studies of opaque materials, supported films, and central modes". In: *Light Scattering in Solids III*, pp. 173–206. DOI: 10.1007/3540115137_6.

Schulze, K., J. Buchen, K. Marquardt, and H. Marquardt (2017). "Multi-sample loading technique for comparative physical property measurements in the diamond-anvil cell". In: *High Pressure Research* 37 (2), pp. 159–169. DOI: 10.1080/08957959.2017.1299719.

Shim, S. H., B. Grocholski, Y. Ye, E. E. Alp, S. Xu, D. Morgan, Y. Meng, and V. B. Prakapenka (2017). "Stability of ferrous-iron-rich bridgmanite under reducing midmantle conditions". In: *Proceedings of the National Academy of Sciences of the United States of America* 114 (25), pp. 6468–6473. DOI: 10.1073/pnas.1614036114.

Sinogeikin, S. V., J. Zhang, and J. D. Bass (2004). "Elasticity of single crystal and polycrystalline $MgSiO_3$ perovskite by Brillouin spectroscopy". In: *Geophysical Research Letters* 31 (6). DOI: 10.1029/2004gl019559.

Speziale, S., H. Marquardt, and T. S. Duffy (2014). "Brillouin scattering and its application in geosciences". In: *Reviews in Mineralogy and Geochemistry* 78 (1), pp. 543–603. DOI: 10.2138/rmg.2014.78.14.

Stixrude, L. and C. Lithgow-Bertelloni (2005). "Thermodynamics of mantle minerals - I. Physical properties". In: *Geophysical Journal International* 162 (2), pp. 610–632. DOI: 10.1111/j.1365-246X.2005.02642.x.

— (2011). "Thermodynamics of mantle minerals - II. Phase equilibria". In: *Geophysical Journal International* 184 (3), pp. 1180–1213. DOI: 10.1111/j.1365-246X.2010.04890.x.

Tange, Y., Y. Kuwayama, T. Irifune, K. I. Funakoshi, and Y. Ohishi (2012). "*P-V-T* equation of state of $MgSiO_3$ perovskite based on the MgO pressure scale: A comprehensive reference for mineralogy of the lower mantle". In: *Journal of Geophysical Research: Solid Earth* 117 (6), pp. 1–12. DOI: 10.1029/2011JB008988.

Tange, Y., Y. Nishihara, and T. Tsuchiya (2009a). "Unified analyses for *P-V-T* equation of state of MgO: A solution for pressure-scale problems in high *P-T* experiments". In: *Journal of Geophysical Research* 114 (B3), B03208. DOI: 10.1029/2008JB005813.

Tange, Y., E. Takahashi, Y. Nishihara, K. I. Funakoshi, and N. Sata (2009b). "Phase relations in the system MgO-FeO-SiO_2 to 50 GPa and 2000°C: An application of experimental techniques using multianvil apparatus with sintered diamond anvils". In: *Journal of Geophysical Research: Solid Earth* 114 (2), pp. 1–12. DOI: 10.1029/2008JB005891.

Tonks, W. B. and H. J. Melosh (1993). "Magma ocean formation due to giant impacts". In: *Journal of Geophysical Research* 98 (E3), pp. 5319–5333. DOI: 10.1029/92JE02726.

Trots, D. M., A. Kurnosov, T. B. Ballaran, S. Tkachev, K. Zhuravlev, V. Prakapenka, M. Berkowski, and D. J. Frost (2013). "The Sm:YAG primary fluorescence pressure scale". In: *Journal of Geophysical Research: Solid Earth* 118 (11), pp. 5805–5813. DOI: 10.1002/2013JB010519.

Trots, D. M., A. Kurnosov, L. Vasylechko, M. Berkowski, T. B. Ballaran, and D. J. Frost (2011). "Elasticity and equation of state of $Li_2B_4O_7$". In: *Physics and Chemistry of Minerals* 38 (7), pp. 561–567. DOI: 10.1007/s00269-011-0428-1.

Valencia-Cardona, J. J., G. Shukla, Z. Wu, C. Houser, D. A. Yuen, and R. M. Wentzcovitch (2017). "Influence of the iron spin crossover in ferropericlase on the lower mantle geotherm". In: *Geophysical Research Letters* 44 (10), pp. 4863–4871. DOI: 10.1002/2017GL073294.

Wentzcovitch, R. M., B. B. Karki, M. Cococcioni, and S. de Gironcoli (2004). "Thermoelastic Properties of $MgSiO_3$-Perovskite: Insights on the Nature of the Earth's Lower Mantle". In: *Physical Review Letters* 92 (1). DOI: 10.1103/PhysRevLett.92.018501.

Wentzcovitch, R. M., B. B. Karki, S. Karato, and C. R. S. D. Silva (1998). "High pressure elastic anisotropy of $MgSiO_3$ perovskite and geophysical implications". In: *Earth and Planetary Science Letters* 164 (1-2), pp. 371–378. DOI: 10.1016/S0012-821X(98)00230-1.

Whitfield, C. H., E. M. Brody, and W. A. Bassett (1976). "Elastic moduli of NaCl by Brillouin scattering at high pressure in a diamond anvil cell". In: *Review of Scientific Instruments* 47 (8), pp. 942–947. DOI: 10.1063/1.1134778.

Wänke, H. (1981). "Constitution of terrestrial planets". In: *Philosophical Transactions of the Royal Society of London. Series A, Mathematical and Physical Sciences* 303 (1477), pp. 287–302. DOI: 10.1098/rsta.1981.0203.

Zha, C. S., H. K. Mao, and R. J. Hemley (2000). "Elasticity of MgO and a primary pressure to 55 GPa". In: *Proceedings of the National Academy of Sciences of the United States of America* 97 (25), pp. 13494–13499. DOI: 10.1073/pnas.240466697.

Zhang, Z., L. Stixrude, and J. Brodholt (2013). "Elastic properties of $MgSiO_3$-perovskite under lower mantle conditions and the composition of the deep Earth". In: *Earth and Planetary Science Letters* 379, pp. 1–12. DOI: 10.1016/j.epsl.2013.07.034.

Chapter 5

Thermal equation of state and structural evolution of Al-bearing bridgmanite

Giacomo Criniti[1*], Tiziana Boffa Ballaran[1], Alexander Kurnosov[1], Zhaodong Liu[2], Konstantin Glazyrin[3], Marco Merlini[4], Michael Hanfland[5], Daniel J. Frost[1]

[1] Bayerisches Geoinstitut, University of Bayreuth, 95440 Bayreuth, Germany

[2] State Key Laboratory of Superhard Materials, Jilin University, 130012 Changchun, People's Republic of China

[3] Deutsches Elektronen-Synchrotron DESY, Notkestraße 85, 22607 Hamburg, Germany

[4] Dipartimento di Scienze della Terra, Università degli Studi di Milano, Via Botticelli 23, 20133 Milano, Italy

[5] ESRF - European Synchrotron Radiation Facility, 71 Avenue des Martyrs, CS40220, 38043 Grenoble Cedex, France

[*] **Corresponding author**: giacomo.criniti@uni-bayreuth.de

This chapter has been prepared for submission to: *Journal of Geophysical Research: Solid Earth*

Author contributions: G. Criniti conceived the project, synthesized and characterized the bridgmanite samples, conducted the synchrotron experiments, analyzed the data, performed the thermodynamic calculations, and wrote the manuscript. T. Boffa Ballaran conceived and supervised the project, conducted the synchrotron experiments, and commented on the manuscript. A. Kurnosov conducted the synchrotron experiments and commented on the manuscript. Z. Liu synthesized and characterized the bridgmanite samples, and commented on the manuscript. K. Glazyrin provided assistance during the synchrotron experiments and commented on the manuscript. M. Merlini provided assistance during the synchrotron experiments and commented on the manuscript. M. Hanfland provided assistance during the synchrotron experiments and commented on the manuscript. D.J. Frost conceived and supervised the project, and commented on the manuscript.

Key Points:

- We determined the thermal equation of state of Al-bearing bridgmanite single-crystals for the first time.
- We show that the bulk compressibility of Al-bearing bridgmanite is mostly controlled by Al-Si substitution in the octahedral site.
- Using the obtained equation of state parameters, we modeled the pressure dependency of oxygen vacancies in bridgmanite in MgO-SiO_2-Al_2O_3.

Abstract

(Mg,Fe,Al)(Si,Al)O_3 bridgmanite is the most abundant mineral of Earth's lower mantle. Al is incorporated in the crystal structure of bridgmanite through the $Fe^{3+}AlO_3$ and $AlAlO_3$ charge coupled (CC) mechanisms, and through the $MgAlO_{2.5}$ oxygen vacancy (OV) mechanism. It is believed that the presence of oxygen vacancies causes a substantial decrease of the bulk modulus of aluminous bridgmanite based on first-principles calculations on the $MgAlO_{2.5}$ end member. However, there is no conclusive experimental evidence supporting this idea due to the uncertainties on the chemical composition, crystal chemistry, and/or high-pressure behavior of samples analyzed in previous studies. Here, we synthesized high-quality single crystals of bridgmanite in the MgO-$AlO_{1.5}$-SiO_2 system with different bulk Al contents and degrees of CC and OV substitutions. Suitable crystals with different compositions were loaded in resistively-heated diamond anvil cells and analyzed by synchrotron X-ray diffraction at pressures up to approximately 80 GPa at room temperature and 35 GPa at temperatures up to 1000 K. By performing single-crystal structural refinements at high pressure, we show that the compressibility of bridgmanite is mainly controlled by Al-Si substitution in the octahedral site. Together with a re-analysis of literature data on $MgSiO_3$ bridgmanite, we found that oxygen vacancies in bridgmanite have no detectable effect on the bulk modulus in the compositional range investigated here, which is that relevant to a pyrolytic lower mantle. The determined thermoelastic parameters of Al-bearing bridgmanite are employed to calculate the proportion of oxygen vacancies in bridgmanite within the top 1250 km of the lower mantle.

Plain Language Summary

Earth's lower mantle, spanning from about 660 to 2890 km depth, is mainly composed of bridgmanite, (Mg,Fe,Al)(Si,Al)O_3 with a distorted perovskite-type structure. Al is typically incorporated in bridgmanite through the charge-coupled substitution of the $MgSiO_3$ component by $Fe^{3+}AlO_3$ and $AlAlO_3$. However, in the topmost 500 km of the lower mantle, experiments showed that the oxygen vacancy component $MgAlO_{2.5}$ also needs to be considered. The effect of oxygen vacancies on the thermoelastic properties of bridgmanite is still not well constrained. These parameters are of crucial importance not only to model the thermodynamic stability of bridgmanite components but also to calculate

the physical properties of lower mantle rocks. Here, we have determined the high-pressure and high-pressure-temperature equations of state of three bridgmanite samples having different concentrations of Al and oxygen vacancies using X-ray diffraction in diamond anvil cells. Additionally, the crystal structure of our samples and that of the $MgSiO_3$ end member were refined at high-pressure conditions to understand how the substitution of Al in each crystallographic site of bridgmanite affects its compressibility. From these analyses, we found that oxygen vacancies likely have a minor effect on the elastic properties of bridgmanite at concentrations relevant for the lower mantle, while the main factor affecting its compressibility is the substitution of Si by Al in the octahedral site. Combining our results with experimental data on the stability of bridgmanite in the MgO-$AlO_{1.5}$-SiO_2 system, we have modeled the thermodynamic stability of the $MgAlO_{2.5}$ component as a function of pressure and bulk Al content. These data can then be incorporated in more complex models of Earth's lower mantle to determine the density and elastic properties of candidate lower mantle rocks and compare them with geophysical observations.

5.1 Introduction

Bridgmanite, $MgSiO_3$ with a distorted perovskite structure, is the most abundant mineral phase in Earth's interior and constitutes approximately 80 vol.% of the lower mantle (Irifune et al., 2010; Kurnosov et al., 2017). The structure of bridgmanite comprises a framework of corner-sharing SiO_6 octahedra (B site), which forms large 12-fold coordinated cavities that are filled by Mg (A site). High-pressure experiments indicate that Al and Fe account for the main chemical substitutions in bridgmanite at lower mantle conditions and their incorporation mechanism depends on pressure, temperature, oxygen fugacity, and the bulk chemical composition of the system (e.g., Huang et al., 2021a). Al can substitute for both Si and Mg in the B and A sites, respectively, via the charge-coupled (CC) substitution of the components $AlAlO_3$ and $Fe^{3+}AlO_3$, and the oxygen vacancy (OV) substitution of the component $MgAlO_{2.5}$ (e.g., Navrotsky et al., 2003; Vanpeteghem et al., 2006). The concentration of the OV component in bridgmanite was found to reach a maximum at topmost lower mantle conditions in MgO saturated systems and to rapidly decay with increasing pressure and Al_2O_3 content (Liu et al., 2019c; Liu et al., 2017a). The near absence of oxygen vacancies around 40 GPa was argued to affect not only the elastic properties but also the transport properties of bridgmanite (Liu et al., 2017a), which may account for a possible increase in viscosity of the mid-mantle, proposed to occur at approximately 1000 km depth (Rudolph et al., 2015). It follows that being able to model the crystal chemistry of bridgmanite as a function of pressure, temperature and composition is of pivotal importance for understanding mantle dynamics and building internally consistent thermodynamic and mineral physical models for comparison with geophysical observations (e.g., Criniti et al., 2021; Kurnosov et al., 2017). To date, however, the resolution of such models of the lower mantle is limited by the lack of experimental data on the thermoelastic parameters of bridgmanite and by uncertainties on thermodynamic parameters that describe its pressure-

and temperature-dependent element partitioning. For instance, the effect of CC and OV Al-substitutions on the thermoelastic parameters of bridgmanite is still controversial. A previous computational study suggested the OV component to be much softer than $MgSiO_3$ (Brodholt, 2000). This could explain some observations on the compressibility of Al-bearing bridgmanite made using powder X-ray diffraction measurements in the diamond anvil cell (DAC) (Daniel et al., 2001; Yagi et al., 2004; Zhang and Weidner, 1999). Other DAC studies, on the other hand, found that Al has a much milder effect on the compressibility of bridgmanite, which was found to be either slightly higher or slightly lower than that of the $MgSiO_3$ end member (Andrault et al., 2001; Andrault et al., 2007; Daniel et al., 2004; Jackson et al., 2005; Walter et al., 2004; Walter et al., 2006). The contrasting results presented in previous studies arise in part from the poor chemical characterization of the samples, which were often synthesized and compressed in the same diamond anvil cell run (Andrault et al., 2001; Andrault et al., 2007; Walter et al., 2004; Walter et al., 2006), in part from the limited and sometimes discontinuous pressure range investigated (Andrault et al., 2001; Andrault et al., 2007; Yagi et al., 2004; Walter et al., 2004), which in some instances did not even reach pressures of the bridgmanite stability field (Walter et al., 2006; Zhang and Weidner, 1999). As a result, the thermoelastic parameters of Al-bearing bridgmanite remain largely unconstrained, hampering our ability to model the stability of the CC and OV components in the lower mantle, as well as their effect on the seismic properties of the bridgmanite solid solution.

Single-crystal X-ray diffraction is a powerful tool for determining the thermal equation of state of materials in the DAC. This technique allows not only high-quality unit-cell lattice parameters of materials at high pressure and high temperature to be obtained, but enables as well unique information on their crystal structures to be retrieved with higher accuracy and precision than powder diffraction measurements. This opens the possibility of determining the individual effects of different Al-substitutions through a detailed examination of the relationship between crystal chemistry, structural evolution, and compressibility of bridgmanite. Here, we report the thermal equation of state of Fe-free Al-bearing bridgmanite determined by single-crystal X-ray diffraction at high pressure and high temperature using externally-heated DACs. Each of the studied samples was synthesized in a multi-anvil apparatus and its composition was accurately determined in terms of CC and OV substitutions prior to the compression experiments. From the refinement of more than 100 crystal structures of Al-bearing bridgmanite and $MgSiO_3$ bridgmanite (original dataset collected by Boffa Ballaran et al., 2012) at high-pressure conditions, we then derived the relation between Al-substitution, polyhedral compressibility, and bulk compressibility. Equation of state parameters obtained in this study were then used to define the solid solution behavior between $MgSiO_3$, $AlAlO_3$, and $MgAlO_{2.5}$ bridgmanite components and model the stability of oxygen vacancies in the MgO-$AlO_{1.5}$-SiO_2 system as a function of pressure, temperature, and composition.

5.2 Experimental Methods

5.2.1 Sample Synthesis and Characterization

Single crystals of Fe-free Al-bearing bridgmanite were synthesized at 24 GPa and 1800-2000 K (Table 5.1) using a 1200-tonne split-sphere-type multi-anvil apparatus installed at the Bayerisches Geoinstitut, University of Bayreuth (Keppler and Frost, 2005). The starting material consisted of finely ground mixtures of synthetic $MgSiO_3$ enstatite and reagent grade Al_2O_3 corundum in different molar ratios (Table 5.1). To synthesize the $MgSiO_3$ enstatite powder, a glass with the same composition was obtained by heating a stoichiometric mixture of reagent grade SiO_2 and MgO at 1873 K in a furnace for 6 h. The $MgSiO_3$ glass was then ground for 1 h in an agate mortar under ethanol and then heated in a furnace at 1473 K for 5 h. To confirm that the glass had converted to enstatite, a powder X-ray diffraction pattern of the recovered material was collected on a Philips X'Pert Pro diffractometer equipped with CoKα_1 radiation operated at 40 kV and 40 mA monochromatized with a curved Johansson Ge(111) crystal and a Philips X'celerator detector. The $MgSiO_3$-Al_2O_3 mixtures were loaded in 2 mm long Pt-tube capsules together with about 10-20 vol.% of reagent grade $MgCl_2$ that served as flux material to facilitate crystal growth at high pressure and temperature conditions. As $MgCl_2$ is highly hygroscopic, it was stored in an oven at 423 K for at least 12 h before being used and was loaded in the Pt-capsule while still warm. Each capsule was then immediately closed with Pt-lids and sealed using an arc welder to prevent $MgCl_2$ from adsorbing water from air moisture. To generate high-pressure and high-temperature conditions, WC (7 wt.% Co content) cubes with 3 mm corner truncations were used with a 7 mm edge-length octahedral Cr_2O_3-doped MgO pressure medium (7/3 assembly) that contained a cylindrical $LaCrO_3$ heater. The capsule was then enclosed in an MgO sleeve to avoid contact with the $LaCrO_3$ heater and placed at the center of the octahedral pressure medium. The cell assembly was first compressed to the desired press load and then heated at a rate of 100 K per minute until the target temperature was reached. The temperature was estimated based on the power generated by the $LaCrO_3$ heater, which had been calibrated in previous runs. Experimental conditions are reported in Table 5.1. After heating, the experiment was quenched by cutting the electrical power and slowly decompressed to ambient conditions over 15 h. One additional experimental run (I701) was performed at 28 GPa in the 15-MN Kawai-type multi-anvil press IRIS15 (Ishii et al., 2016; Ishii et al., 2019c; Liu et al., 2017b) installed at the Bayerisches Geoinstitut, University of Bayreuth. In this run, harder WC anvils were used (grade TF05, Fuji Die Co. Ltd) with the same type of 7/3 assembly. The starting material for this experiment consisted of a mixture of $MgSiO_3$ enstatite, Al_2O_3 corundum and $Mg(OH)_2$ brucite (Table 5.1). The temperature was also estimated based on the power supplied to the $LaCrO_3$ heater, which was calibrated in previous runs.

The recovered samples were observed under an optical microscope and consisted of mixtures of Al-bearing bridgmanite crystals up to 100 μm in size and quenched Cl-rich

Table 5.1. Synthesis conditions and chemical compositions of Al-bearing bridgmanite samples. Brg, bridgmanite; Hym, hydrous melt; Clm, Cl-rich melt; Grt, garnet (traces).

Run	Starting material	Flux	P (GPa)	T (K)	t (h)	Run products	Brg composition CC	Brg composition OV	Label
I701	En95-Cor5	$Mg(OH)_2$	28	1973	6	Brg+Hym	0.038(6)	0.022(11)	CC4OV2
S7412	En90-Cor10	$MgCl_2$	24	1873	4	Brg+Clm±Grt	0.068(9)	0.046(14)	CC7OV5
S7464	En95-Cor5	$MgCl_2$	24	1973	3	Brg+Clm	0.025(7)	0.053(11)	CC2OV5
S7585	En85-Cor15	$MgCl_2$	24	1773	8	Brg+Clm±Grt	0.067(6)	0.034(9)	CC7OV3

(S7412, S7464, S7585) or hydrous melt (I701). In experimental runs at 24 GPa with a relatively Al_2O_3-rich starting composition (i.e., S7412, S7585), minor amounts of garnet were also found in the run products. Inclusion-free single crystals of Al-bearing bridgmanite larger than 60 μm were selected from each crystal batch and mounted on glass fibers for single-crystal X-ray diffraction analyses at ambient conditions. Several crystals were tested on a kappa-geometry Xcalibur single-crystal diffractometer equipped with a Sapphire2 CCD detector and graphite-monochromatized MoKα radiation operated at 40 kV and 50 mA. For each batch, the single crystal displaying the sharpest peak profiles was then analyzed on a Eulerian-geometry Huber diffractometer equipped with a point detector and using MoKα radiation operated at 40 kV and 50 mA, and driven by the software SINGLE (Angel and Finger, 2011). The peaks full width half maxima measured upon ω-scan rotations typically ranged between 0.07° and 0.11°. The unit-cell lattice parameters, reported in Table B.1, were accurately and precisely determined by a least square inversion of 16 to 32 reflections measured at eight equivalent positions (King and Finger, 1979; Ralph and Finger, 1982). The chemical compositions of several selected single crystals (Table B.2) were measured using a JEOL JXA-8200 electron probe microanalyzer (EPMA) operated in wavelength dispersive mode. Spectra were acquired for 10 s using an acceleration voltage and beam current of 15 kV and 5 nA, respectively. $MgSiO_3$ enstatite was used as a standard for Si and Mg, Al_2O_3 corundum for Al, and $Pb_5(VO_4)_3Cl$ vanadinite for Cl. The Cl content in the samples synthesized using a $MgCl_2$ flux was below the detection level (<0.001 atoms per formula unit) and thus is not reported in Table B.2. The water content of the sample recovered from 28 GPa was not directly measured but was assumed to be negligible (i.e., less than 50 ppm wt.) based on Fourier transform infrared spectroscopy measurements of bridgmanite single crystals previously synthesized using the same conditions and strategy (Liu et al., 2021). The composition of Al-bearing bridgmanite samples in terms of their end member components $MgSiO_3$, $AlAlO_3$ (CC) and $MgAlO_{2.5}$ (OV) were determined according to Liu et al. (2019b) and are listed in Table 5.1.

5.2.2 High-pressure and high-temperature X-ray diffraction measurements

Al-bearing bridgmanite samples with compositions CC4OV2, CC2OV5 and CC7OV3 (see Table 5.1) were employed in high-pressure DAC experiments aimed at constraining their isothermal and/or thermal equation of state. Single-crystal X-ray diffraction measurements at high pressure and temperature were carried out during several runs (Table 5.2) at the

Extreme Conditions Beamline (ECB) P02.2 of the PETRA-III synchrotron facility (Hamburg, Germany) using an X-ray beam of 42.7 keV ($\lambda \sim 0.29$ Å) focused to either 2 x 2 or 8 x 3 μm^2 (full width at half maximum) and a Perkin-Elmer 1621 flat panel detector (Liermann et al., 2015). The sample to detector distance and detector parameters for single-crystal diffraction were calibrated using polycrystalline CeO_2 and a single crystal of natural enstatite, respectively. To generate high-pressure conditions, we employed BX-90 DACs (Kantor et al., 2012) in combination with Almax-Boehler-type diamond anvils and WC seats (Boehler and Hantsetters, 2004), which allowed effective X-ray opening angles of approximately 75-80°. Al-bearing bridgmanite single-crystals with lengths of 10-20 μm and less than 10 μm thick were tested at ambient conditions at the ECB P02.2 and selected based on their sharp diffraction peak profiles. Suitable crystals were then loaded in the DACs for high-pressure measurements. For room temperature runs (RT1-RT3), a Re gasket was indented between diamond anvils with culets of 350 or 250 μm (Table 5.2) to a final thickness of approximately 60 or 45 μm, respectively. To create the sample chamber, an infrared laser was used to drill a hole of 200 or 150 μm diameter, respectively, in the center of the indented area of the Re gasket. One (CC7OV3, run RT3) or two (CC2OV4 and CC2OV5, run RT1 and RT2) bridgmanite crystals were loaded into the sample chamber together with a ruby sphere for pressure determination and a piece of Au or W, whose absorption profiles were used to finely align the cell using the X-ray beam (Table 5.2). He or Ne gas (Table 5.2) were loaded into the sample chamber at 0.13 GPa using the gas loading system installed at the Bayerisches Geoinstitut, University of Bayreuth (Kurnosov et al., 2008) or at PETRA-III. The samples were compressed on line at room temperature using a gas-driven membrane up to 50 (CC2OV4, CC2OV5) or 80 GPa (CC7OV3) with typical steps of 1-3 GPa. At each pressure point, step scans were collected upon continuous ω-rotation of the DAC between ± 35° with steps of 0.5° and an exposure time of 0.5-1 s.

High-temperature measurements were carried out in several runs (Table 5.2) using BX-90-type DACs equipped with external resistive heaters consisting of a Pt-wire wrapped around a MACOR® (Corning Inc.) ceramic disk. Almax-Boehler diamond anvils with 350 or 400 μm culets were employed to generate high-pressure conditions. The ceramic disk and Pt-wire heater were placed around the WC seat in the BX-90 piston and fixed using cement. In order to prevent the heater from touching the BX-90 cylinder, a thin layer of mica was placed on top of the ceramic ring and acted as an electrical insulator. The Pt-wire was then connected to a Type 6674A DC power supply from Agilent Technology, capable of generating up to 35 A at 60 V (Liermann et al., 2015). Temperature was monitored using a Pt/Pt-10%Rh (Type S) thermocouple that was passed through a hole drilled in the ceramic ring and placed as close as possible to the sample chamber. A Re gasket was indented to 45-50 μm thickness and a 150 μm hole was laser-drilled in the center of the indented region to obtain the sample chamber. Two selected Al-bearing bridgmanite crystals with compositions CC2OV4 and CC2OV5 were loaded in each sample chamber together with a ruby sphere, Au powder and a piece of W that were used as pressure standards (Table 5.2). Pre-compressed Ne gas at 0.13 GPa was loaded in the sample chamber using the gas

loading system installed at PETRA-III. Resistively-heated DACs (RHDACs) were inserted into a membrane cup and pressure was increased on line using a gas-driven membrane. In addition, to prevent the oxidation of the heater components, diamond anvils and Re gasket, an Ar-H_2 gas mixture was flushed inside the RHDAC through an aperture drilled on one side of the membrane cup. The RHDAC was then placed in a custom-designed holder consisting of a water-cooled lower metallic body, a central ceramic insulator and a top metallic body where the membrane cup was fixed (Figure B.1). In this way, the efficiency of the heater is enhanced, and higher temperatures can be generated. At each pressure-temperature point, step scans were collected upon continuous ω-rotation of the DAC between ± 32°, following the same procedure described above for room temperature measurements. Additional wide-scan images of single-crystal W between ω = ± 20° or still frames of polycrystalline Au were acquired to determine the pressure conditions in the sample chamber through their thermal equations of state (Dorogokupets and Dewaele, 2007; Litasov et al., 2013). 2D images were integrated into 1D patterns using the software DIOPTAS (Prescher and Prakapenka, 2015) and the lattice parameters of Au and W were obtained from full-profile Le Bail refinements performed in JANA2006 (Petrícek et al., 2014). The high-temperature correction of Datchi et al. (2007) to the room-temperature ruby fluorescence scale was also used to determine pressure at temperatures below 500 K, where the ruby R1 and R2 fluorescence lines were intense and sufficiently well-resolved (Figure B.2). In runs HT1 and HT4, the temperature readout of the thermocouple was found to be several hundred K higher than what we expected from the power generated by the Pt-wire heater. Such inconsistent temperature values likely originated from contact between the thermocouple wires as they passed through the hole drilled in the ceramic ring, which is at higher temperature than the sample chamber. However, since several pressure standards were placed in the sample chamber during each run, it was still possible to estimate the pressure-temperature conditions of the sample using a cross-correlation function between ruby and Au or ruby, Au and W (Table 5.2). As stated above, this method could be applied only at temperatures of 500 K or below, where the ruby fluorescence spectra are still of sufficiently high quality (Figure B.2). To account for potential systematic deviations that may be caused by using a cross-correlation function instead of the thermocouple, the temperature and pressure uncertainties in the two mentioned runs were rescaled to have smaller weights in the EOS fitting procedure.

5.2.3 Single-Crystal Structural Refinements

Single-crystal X-ray diffraction step-scans were analyzed using *CrysAlisPro* (Rigaku, Oxford Diffraction) to extract Al-bearing bridgmanite unit-cell lattice parameters from high-pressure conditions. Data analysis included peak search and indexing, background subtraction, integration of intensities and correction for Lorentz and polarization factors. Frame scaling and empirical absorption correction based on spherical harmonics were carried out using the SCALE3 ABSPACK scaling algorithm implemented in *CrysAlisPro*. We then employed the dual space algorithm *SHELXT* (Sheldrick, 2015b) to solve the

Table 5.2. Conditions of the high-pressure room-temperature (RT) and high-pressure, high-temperature (HT) runs. TC, thermocouple; *P*, pressure; *T*, temperature.

Run	Sample(s)	Pressure medium	Culet size (μm)	*P* sensor(s)	*P* range (GPa)	*T* range (K)	*P-T* determination
RT1	CC2OV5, CC4OV2	He	350	ruby, Au	0-22	300	-
RT2	CC2OV5, CC4OV2	He	350	ruby, Au	0-50	300	-
RT3	CC7OV3	He	250	ruby, W	0-80	300	-
HT1	CC2OV5, CC4OV2	Ne	350	ruby, Au, W	0-26	300-500	Au + W + ruby[a]
HT2	CC2OV5, CC4OV2	Ne	400	ruby, Au, W	0-29	300-700	Au + TC
HT4	CC2OV5, CC4OV2	Ne	400	ruby, Au	0-21	300-460	Au + ruby[a]
HT5	CC2OV5, CC4OV2	Ne	350	ruby, Au, W	0-35	300-1000	Au + TC

[a] Due to an inaccurate TC readout, a cross correlation of ruby and Au sensors or ruby, Au, and W sensors was used to determine *P* and *T*.

structures of Al-bearing bridgmanite crystals and performed structural refinements against F^2 using *SHELXL* in the *Shelxle* GUI (Sheldrick, 2015a; Hübschle et al., 2011). In the refinement procedure, atomic scattering factors were used for all atoms, while the site occupancy factors for Mg, Al and Si cations in the A and B sites were fixed according to the abundancies of the bridgmanite end member components determined by EPMA (Table 5.1, Table B.2). Given that the number of unique reflections typically exceeded 250, anisotropic displacement parameters (ADPs) were used for all atoms, resulting in a total of 29 refined parameters. When the number of unique reflections dropped below 210 or one of the ADPs showed negative values, isotropic displacement parameters were used instead. In the last cycle of each refinement, the crystallographic *R1* factors were typically between 2% and 3% and rarely exceeded 4%, highlighting the high quality of the datasets and the robustness of the structural models. In addition, structural refinements at high pressure and room temperature for $MgSiO_3$ bridgmanite were obtained using the datasets reported and described by Boffa Ballaran et al. (2012), by applying the same refinement procedure described above. Given the longer wavelength employed by Boffa Ballaran et al. (2012) (λ = 0.41474 Å), the number of observed and unique reflections for $MgSiO_3$ bridgmanite was smaller than for measurements performed in this study ($\lambda \sim 0.29$ Å). Therefore, isotropic displacement parameters were used for all atoms in the structural refinements of $MgSiO_3$ bridgmanite. Further details can be found in the deposited crystallographic information files (CIFs).

5.3 Isothermal Equation of State of Al-Bearing Bridgmanite

5.3.1 Volume and Axial Compressibility

The unit-cell volume and lattice parameters of Al-bearing bridgmanite samples (Tables A.3-A.5) were found to decrease smoothly with increasing pressure (Figure 5.1). We used 3rd-order Birch-Murnaghan (BM3) equations of state (EOS) to fit the pressure-volume datasets (Angel et al., 2014; Birch, 1947):

$$P = \frac{3}{2}K_{T0}\left[\left(\frac{V_0}{V}\right)^{\frac{7}{3}} - \left(\frac{V_0}{V}\right)^{\frac{5}{3}}\right]\left\{1 + \frac{3}{4}\left(K'_{T0} - 4\right)\left[\left(\frac{V_0}{V}\right)^{\frac{2}{3}} - 1\right]\right\} \tag{5.1}$$

Where V_0, K_{T0} and K'_{T0} are the room-pressure and room-temperature unit-cell volume, the isothermal bulk modulus, and its pressure derivative. Fits were performed using a script implemented in OriginPro2021 (OriginLab corporation, Northampton, MA, USA) that was previously benchmarked with the EosFit7-GUI software (Angel et al., 2014; Gonzalez-Platas et al., 2016). Fit results are reported in Table 5.3. Despite showing small differences in K_{T0} and K'_{T0}, the EOSs of the three samples are relatively similar to each other, owing to the negative correlation coefficient between these two fit parameters (Figure B.3). Since the refined K'_{T0} values for the three Al-bearing bridgmanite samples are close to 4, a 2nd-order Birch-Murnaghan EOS was also used to fit the three datasets (Table 5.3). The BM2 K_{T0} values of the CC2OV5 and CC7OV3 samples are identical to their respective BM3 values within the uncertainties, while for the CC4OV2 sample the BM2 K_{T0} value is about 3 GPa lower than its BM3 counterpart due to the fact that this sample has a smaller BM3 K'_{T0} (Table 5.3). As discussed later, these subtle variations in K_{T0} seem to be correlated with the Al-Si substitution in the B site, which influences its compressibility.

The axial compression of the three Al-bearing bridgmanite samples was described using a linearized BM3 EOS (Angel, 2000; Angel et al., 2014), which was originally derived for cubic and isotropic materials by considering that $V = a^3$ and $\beta_V = 3\beta_a$, with β_V and β_a being the volume and a-axis compressibility, respectively. This notation can be generalized for lower-symmetry materials by replacing the fit parameters V_0, K_{T0} and K'_{T0} with the cubed unit cell edge length ${l_0}^3$, the axial modulus $M_0/3$ and its pressure derivative $M_0/3$ (Angel et al., 2014):

$$P = \frac{1}{2}M_{l,0}\left[\left(\frac{l_0}{l}\right)^{7} - \left(\frac{l_0}{l}\right)^{5}\right]\left\{1 + \frac{1}{4}\left(M'_{l,0} - 12\right)\left[\left(\frac{l_0}{l}\right)^{2} - 1\right]\right\} \tag{5.2}$$

Fit parameters for the three Al-bearing samples measured in this study, as well as for $MgSiO_3$ bridgmanite by Boffa Ballaran et al. (2012), are reported in Table 5.3. It can be seen that the *b*-axis is the most incompressible direction, while the *a*-axis is slightly more compressible than the *c*-axis for all samples. These observations are in agreement with previous static compression (Boffa Ballaran et al., 2012) and elasticity measurements (Criniti et al., 2021; Sinogeikin et al., 2004) of single-crystal $MgSiO_3$ bridgmanite. In agreement

Table 5.3. Isothermal EOS parameters for single-crystal Al-bearing bridgmanite and $MgSiO_3$ bridgmanite from Boffa Ballaran et al. (2012).

	CC2OV5	CC4OV2	CC7OV3	$MgSiO_3$[a]
			BM3	
V_0 (Å^3)	163.14(2)	162.95(2)	163.53(2)	162.36(4)
K_{T0} (GPa)	246.3(14)	249.0(16)	245.4(8)	251(2)
K'_{T0}	3.96(7)	3.85(9)	3.91(3)	4.11(7)
a_0 (Å)	4.7762(4)	4.7798(3)	4.7737(3)	4.7757(3)
$M_{a,0}$ (GPa)	708(7)	693(5)	688(4)	715(4)
$M'_{a,0}$	8.9(3)	10.1(3)	9.81(13)	9.2(2)
b_0 (Å)	4.9362(3)	4.9333(3)	4.9388(4)	4.9285(5)
$M_{b,0}$ (GPa)	840(9)	865(10)	836(8)	848(13)
$M'_{b,0}$	16.6(5)	13.7(6)	15.6(3)	16.7(7)
c_0 (Å)	6.9199(6)	6.9106(3)	6.9364(12)	6.8970(3)
$M_{c,0}$ (GPa)	685(7)	703(5)	690(9)	721(4)
$M'_{c,0}$	12.0(4)	11.6(3)	11.7(3)	12.7(2)
			BM2	
V_0 (Å^3)	163.14(2)	162.97(2)	163.57(2)	162.31(3)
K_{T0} (GPa)	245.6(3)	246.3(4)	243.2(3)	254.5(6)

[a] Axial compressibility parameters of $MgSiO_3$ bridgmanite were obtained by refitted the data reported by Boffa Ballaran et al. (2012)

with that found for the $Fe^{3+}AlO_3$ substitution mechanism, the compressibility of the *c*-axis is higher than in $MgSiO_3$, confirming that it is likely related to the Al-Si substitution in the B-site, as proposed by Boffa Ballaran et al. (2012).

5.3.2 Polyhedral and Bond Length Compressibility

By refining the crystal structure of Al-bearing and $MgSiO_3$ bridgmanite at high pressure and room temperature, the pressure evolution of the individual B-O and A-O bond lengths, as well as the polyhedral volumes, can be derived. It has been suggested that the compression behavior of bridgmanite is mainly determined by the compressibility of B-site octahedra and by the distortion of the octahedral framework (Huang et al., 2021b). To describe the compression behavior of the octahedral volume V_B (Figure 5.2) and interatomic distances B-O (Figure B.4), we use equations 5.1 and 5.2 respectively. The obtained fit parameters (Table B.3) can be used to quantitatively describe the influence of the Si-Al substitution on the B-site volume, as well as on the compressibility in bridgmanite solid solutions, and to compare them, when possible, with previous studies. At ambient conditions, the B-O1 distance, connecting octahedra along the *c*-axis, has been shown to be the largest distance in both $MgSiO_3$ and Fe,Al-bearing bridgmanite (Huang et al., 2021b). At high-pressure, however, the compressibility of the B-O1 bond is higher than the two B-O2 bonds in all

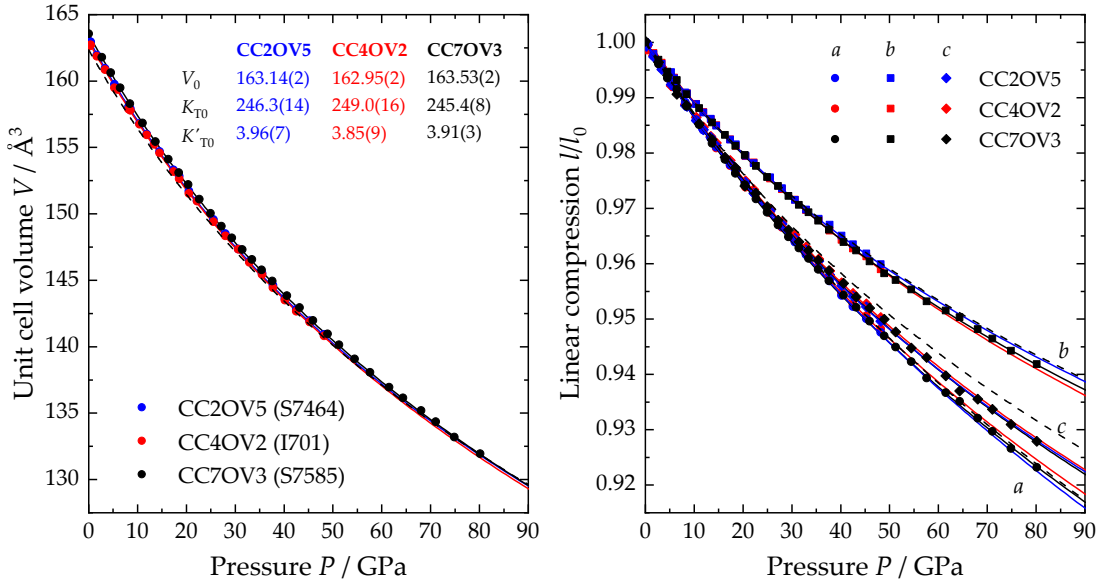

Figure 5.1. (a) Volume and (b) linear compression of Al-bearing bridgmanite samples at room temperature. Error bars are smaller than the symbol when they are not shown. Solid lines indicate BM3 fits to the experimental pressure-volume datasets of CC2OV5 (blue), CC4OV2 (red) and CC7OV3 (black). Dashed black lines indicate BM3 fits to the pressure-volume dataset of $MgSiO_3$ bridgmanite reported by Boffa Ballaran et al. (2012).

samples (Figure B.4), which causes the octahedral distortion to progressively decrease. We observe that the overall B-O compression anisotropy of the four samples considered in our analysis is relatively similar (Figure B.4), although the SiO_6 octahedra in $MgSiO_3$ bridgmanite appear to be less compressible than the (Si,Al)O_6 octahedra of the more Al-rich bridgmanites (Figure 5.2). The CC7OV3 sample, which has the highest B-site Al content, has the most compressible octahedra, while the octahedra of the CC2OV5 and CC4OV2 samples have very similar moduli (Table B.3). This observation is consistent with Al-bearing samples being slightly more compressible than the end member $MgSiO_3$ bridgmanite (Figure 5.1, Figure B.3) and supports the idea that a tight relation exists between octahedral and bulk compressibility of perovskite structures. The variation of the octahedral incompressibility ${K_0}^B$ with the octahedral volume ${V_0}^B$ (Figure 5.3a) suggests that the OV substitution may give rise to a more compressible octahedron than the CC substitution in agreement with computational results (Brodholt, 2000). However, given the uncertainties, we found that linear fits can suitably describe the dependency of the octahedral incompressibility, ${K_0}^B$, both with the octahedral volume, ${V_0}^B$, and with the Al content in the B site (Figure 5.3). The difference between OV-rich and CC-rich samples is not clearly observed in the compression data, likely due to the low concentration of the OV concentration component (i.e., 5 mol.% at most) but also probably due to there being only a small difference in the effects of the OV and CC components on the compressibility. The effect of oxygen vacancies on ${K_0}^B$, and thus on K_{T0}, of Al-bearing bridgmanite is likely to become more prominent at higher OV component contents, where higher defect concentrations can lead to the ordering and clustering of oxygen vacancies (Grüninger et al., 2019), as occurs in the brownmillerite-type

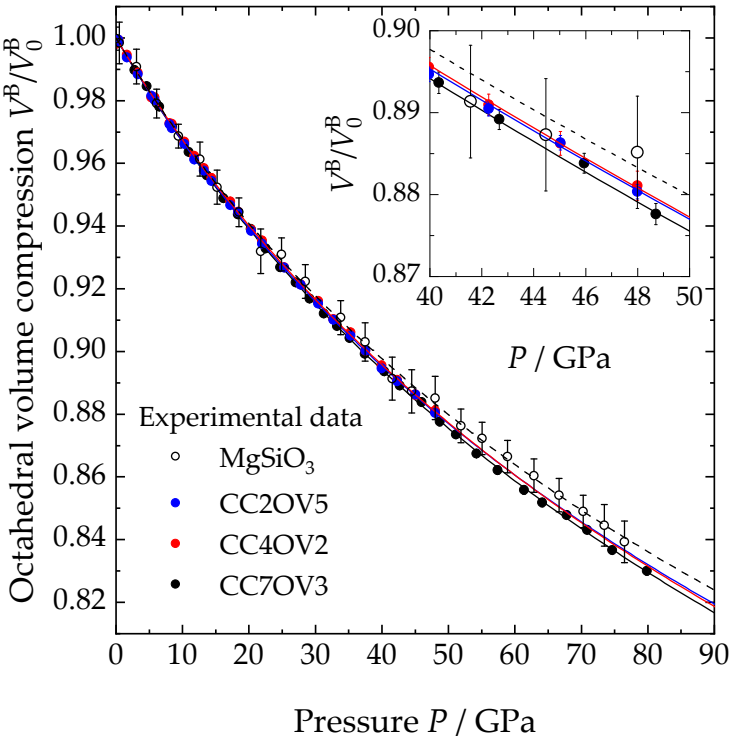

Figure 5.2. Compression behavior of the octahedral volume (V^B) in $MgSiO_3$ (empty symbols) and Al-bearing (solid symbols) bridgmanite. A BM3 EOS was used to fit to each dataset and is shown as dashed ($MgSiO_3$) or solid line (Al-bearing). When not shown, error bars are smaller than the symbols. In the inset, a magnification of the range between 40 and 50 GPa is shown for clarity.

structure (Brodholt, 2000). Such high OV contents are, however, unlikely to match the composition of bridgmanite in a pyrolitic phase assemblage at topmost lower mantle conditions (Huang et al., 2021a).

The A-site volume (V^{A12}), defined as $V^{A12} = V/4 - V^B$ (e.g., Huang et al., 2021b; Martin et al., 2006), depends mainly on the volume of the B site and on the tilting of the octahedral framework. In fact the room-pressure ${V_0}^{A12}$ increases with increasing Al content (Figure B.5) in spite of the A-site substitution of Mg^{2+} by Al^{3+},which has a much smaller ionic radius (Shannon, 1976). The same trend is observed for Fe,Al-bearing bridgmanites (Huang et al., 2021a), although the latter samples have a more pronounced slope (Figure B.5). Since Fe^{3+} has a larger ionic radius than Al^{3+}, the slightly different slopes between the Fe-bearing and Fe-free trends may indicate that the size of the A-site cation has only a limited effect on ${V_0}^{A12}$ and is less prominent than that of Al-Si substitution in the B-site. Note also that the refined A-site incompressibility values (${K_0}^{A12}$) are found to decrease linearly as a function of both ${V_0}^{A12}$ and the Al content in the B site (Figure B.6), although Al^{3+}, being smaller than Mg^{2+}, would be generally expected to make the MgO_{12} polyhedra smaller and less compressible. Moreover, the ratio between polyhedral moduli ${K_0}^{A12}/{K_0}^{B}$ for $MgSiO_3$ and

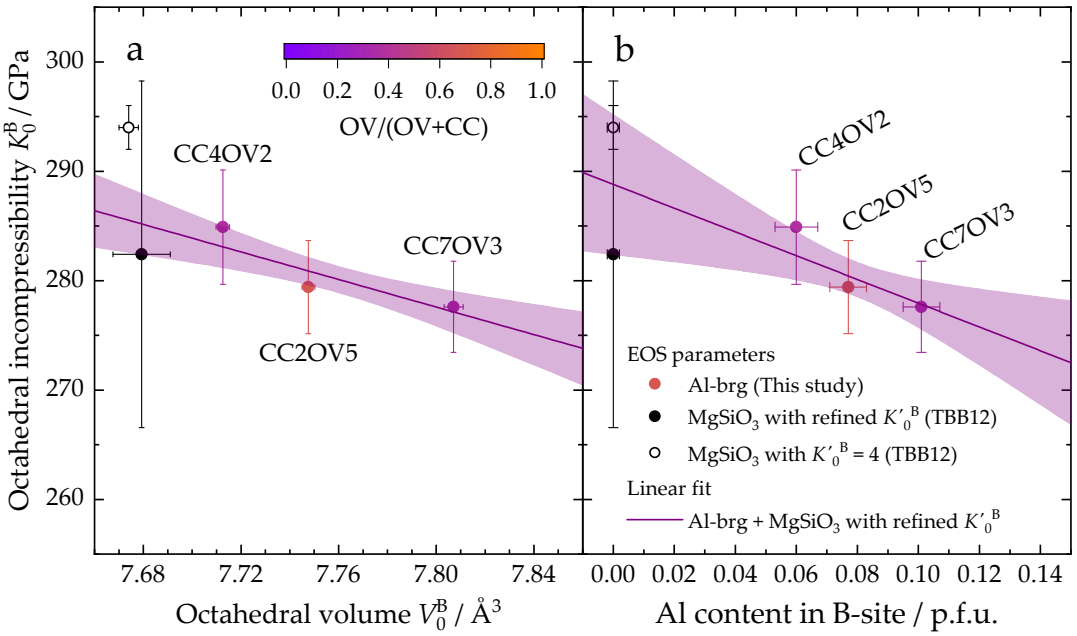

Figure 5.3. Octahedral incompressibility of $MgSiO_3$ and Al-bearing bridgmanite as a function of (a) the octahedral volume and (b) the Al content in the B site. The color scale indicates the fraction of OV component. Linear fits and their 68% confidence intervals are represented by the purple lines and shaded areas, respectively.

Al-bearing bridgmanite ranges between 0.85(2) and 0.87(5) (Table B.3). These values are identical within uncertainties and show no obvious systematic change as a function of composition (Figure B.7), suggesting that Al incorporation in the B site similarly decreases both $K_0{}^{A12}$ and $K_0{}^B$. As Al is incorporated in B site of bridgmanite through both the CC and OV substitution mechanisms, their effect on the compressibility of bridgmanite seems to be indistinguishable in the compositional range investigated in this study, which is that relevant to a pyrolitic lower mantle. Therefore, it is likely that the presence of limited amounts of oxygen vacancies does not greatly affect the polyhedral and bulk compression behavior of bridgmanite.

5.4 Thermal Equation of State of Bridgmanite

To determine the thermal EOS of Al-bearing bridgmanite, pressure-volume-temperature (*PVT*) data were collected over four runs between 0 and 35 GPa and up to 1000 K (Table 5.4). As described above, in each run a crystal of CC2OV5 and one of CC4OV2 were loaded in the same pressure chamber so that a direct comparison could be made between samples with the same bulk Al content but different degrees of CC and OV substitution. We employed the thermal equation of state formalism proposed by Stixrude and Lithgow-Bertelloni (2005), which is based on a Debye model where the Debye temperature (θ_D), the Grüneisen parameter (γ), and its logarithmic derivative (q) are expressed as functions of the Eulerian

finite strain (see Appendix B). Note that a meaningful comparison between the thermoelastic parameters of $MgSiO_3$ and Al-bearing bridgmanite can be made only if consistent pressure scales are used to fit all datasets. Therefore, we first derived a best-fit thermal EOS of $MgSiO_3$ bridgmanite by reanalyzing published data using pressure scales that are consistent with one another (Appendix B). As the fit parameters θ_{D0}, γ_0, and q_0 (i.e., the room-pressure room-temperature values of θ_D, γ, and q) are typically highly correlated, we then employed the θ_{D0} and q_0 values determined for $MgSiO_3$ bridgmanite in the fit of the thermal EOSs of Al-bearing bridgmanite. The refined fit parameters V_0, K_{T0}, K'_{T0}, and γ_0 are reported in Table 5.4. For comparison, we also used a conventional Mie-Grüneisen-Debye (MGD) formalism (see Appendix B and B) to fit the $MgSiO_3$ and Al-bearing bridgmanite *PVT* data, which yielded consistent results (Table B.4, Figures B.8 and B.9). Therefore, only results from the finite-strain-based formalism of Stixrude and Lithgow-Bertelloni (2005) will be discussed here.

The γ_0 values for the CC2OV5 and CC4OV2 samples are identical to each other within uncertainty and about 30% larger than γ_0 determined for $MgSiO_3$ bridgmanite by our best-fit EOS (Table 5.4). An attempt was made to also refine q_0 but resulted in extremely high correlation coefficients between q_0 and γ_0, as well as in unrealistic uncertainties on q_0 (e.g. $q_0 = 1 \pm 6$) and no visible increase in the quality of the fit. Although the quality of the fit is not strongly dependent on the absolute value of q_0, it is important to be able to evaluate the uncertainty of fixing q_0 when extrapolating the fitted model, particularly in temperature. To do so, we calculated isotherms using the fit parameters reported in Table 5.4 and varying q_0 by ±1 (Figure B.10). The resulting change in thermal pressure at 2000 K is approximately ± 0.5 and ± 1.5 GPa at 20 and 50 GPa, respectively (Figure B.10). Note, however, that γ_0 and q_0 are typically highly correlated, meaning that if, for instance, q decreases as a function of Al-incorporation, then γ_0 will also be smaller than the values refined in this study. This becomes relevant, for example, if our EOSs are used to calculate the thermodynamic properties and stability of the CC end member component at deeper lower mantle conditions, where the CC mole fraction has been argued to increase at the expense of that of the $FeAlO_3$ component in both pyrolite and MORB (Irifune et al., 2010; Ishii et al., 2022b). For this purpose, further high-pressure and high-temperature measurements on CC-rich bridgmanite samples at deep lower mantle conditions will help to more tightly constrain its thermal EOS and model the crystal chemistry and composition of bridgmanite in complex chemical systems at mid- and bottom-lower mantle conditions.

5.5 Solid solution behavior of $MgSiO_3$-$AlAlO_3$-$MgAlO_{2.5}$

Constraining the solid solution behavior of bridgmanite in the $MgSiO_3$-$AlAlO_3$-$MgAlO_{2.5}$ system is of great importance for modeling the thermodynamic and physical properties of lower mantle phase assemblages. In our modelling strategy, V_{mol} was assumed to be linear along the $MgSiO_3$-$AlAlO_3$ and the $MgSiO_3$-$MgAlO_{2.5}$ joins within the considered compositional range, in agreement with experimental data (Figure 5.5a). Since the $AlAlO_3$ and

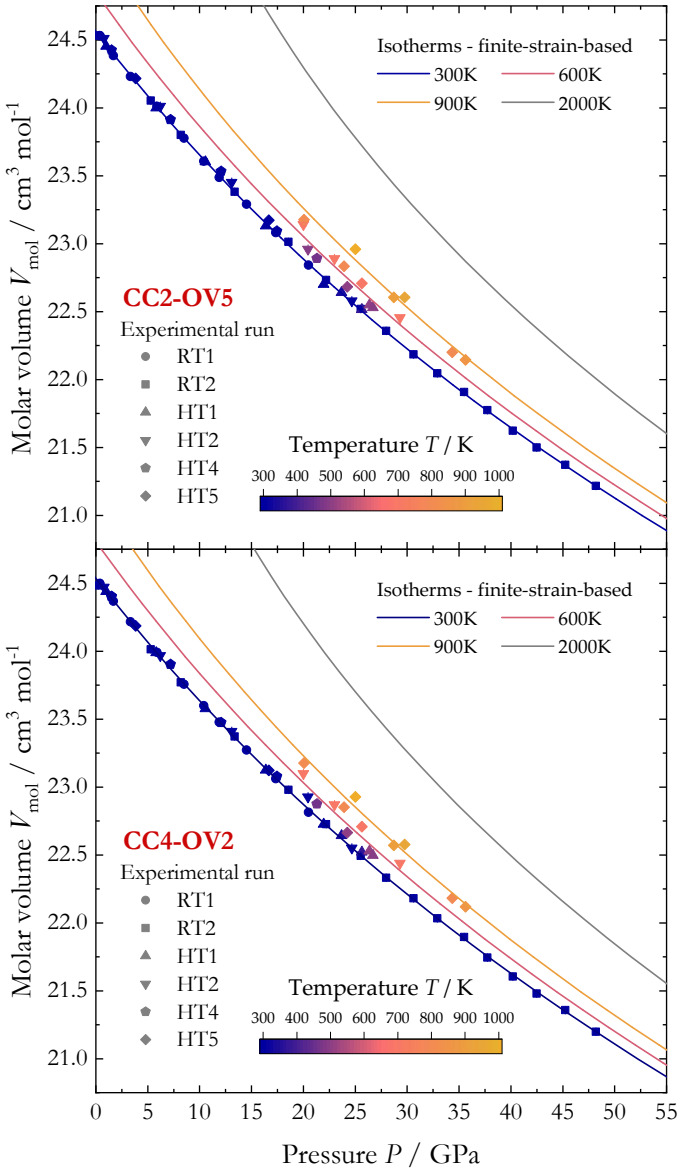

Figure 5.4. *PVT* relations of CC2OV5 and CC4OV2 Al-bearing bridgmanite single-crystals collected over several experimental runs. Solid lines were calculated using the finite-strain-based formalism and parameters reported in Table 5.4. Experimental temperatures and calculated isotherms (300-900 K) are expressed as a color scale. Additional isotherms at 2000 K (gray lines) are also plotted to show the model extrapolation to temperatures relevant to the lower mantle.

$MgAlO_{2.5}$ bridgmanite end members are unstable, however, their V_{mol} cannot be directly constrained. Moreover, given that mixing of the $AlAlO_3$ and $MgAlO_{2.5}$ components in $MgSiO_3$-bridgmanite is strongly non-ideal (Huang et al., 2021a), it very likely that molar volumes of mixing involving these components are also non-linear over wide ranges of composition. A linear volume of mixing can be safely assumed, however, by selecting an end member composition that is close to the limit of the experimental compositional range (Huang et al., 2021a; Siersch et al., 2023). If experimental data on the molar volume of solid

Table 5.4. Thermal EOS fit parameters for $MgSiO_3$ (best-fit) and Al-bearing bridgmanite (this study) using the finite strain-based formalism of Stixrude and Lithgow-Bertelloni (2005). n is the number of atoms per formula unit. Numbers in italics were fixed during the fitting procedure.

	$MgSiO_3$ best-fit	CC4OV2	CC2OV5
P scale	MgO[a], ruby[b]	Au[a], ruby[b]	Au[a], ruby[b]
V_{mol0} (cm^3/mol)	24.455(8)	24.536(3)	24.562(4)
T_0 (K)	*298*	*298*	*298*
K_{T0} (GPa)	251(2)	248.9(1.3)	246(2)
K'_{T0}	4.08(5)	3.84(7)	3.97(9)
γ_0	1.64(3)	2.12(12)	2.21(14)
q_0	3.1(2)	*3.1*	*3.1*
θ_{D0} (K)	*912*	*912*	*912*
n	*5*	*5*	*5*
reduced χ^2	1.56	2.86	3.47

[a] Dorogokupets and Dewaele (2007)
[b] Jacobsen et al. (2008)

solutions exist also at high pressure, it is then possible to refine K_{T0} and K'_{T0} for the intermediate reference composition, which will compensate for the pressure-induced change in excess molar volume. Under these assumptions, we define a linear mixing behavior of the molar volume between two or more end members or intermediate components (i) as:

$$V_{mol} = \sum_i n_i V_i \tag{5.3}$$

where n_i is the molar fraction of component i in the solid solution and V_i is its molar volume. Following the approach of Stixrude and Lithgow-Bertelloni (2011), by differentiating once and twice with respect to pressure both sides of equation 5.3, we derived the solid solution behavior of K_{T0} and K'_{T0}, respectively, under hydrostatic stress conditions (Reuss bound):

$$\frac{V_{mol}}{K_{T0}} = \sum_i n_i \frac{V_i}{K_i} \tag{5.4}$$

$$\frac{V_{mol}\,(1 + K'_{T0})}{K_{T0}^2} = \sum_i n_i \frac{V_i\,(1 + K_i')}{K_i^2} \tag{5.5}$$

where K_i and K'_i are the ambient-pressure bulk modulus and pressure derivative of the end member component i.

The molar volume of the $AlAlO_3$ and $MgAlO_{2.5}$ components was refined using experimental data from this and previous studies (Daniel et al., 2004; Huang et al., 2021b; Jackson et al., 2005; Kojitani et al., 2007; Liu et al., 2019c; Liu et al., 2019b; Boffa Ballaran et al., 2012; Walter et al., 2004; Walter et al., 2006). To allow for a better comparison with previous

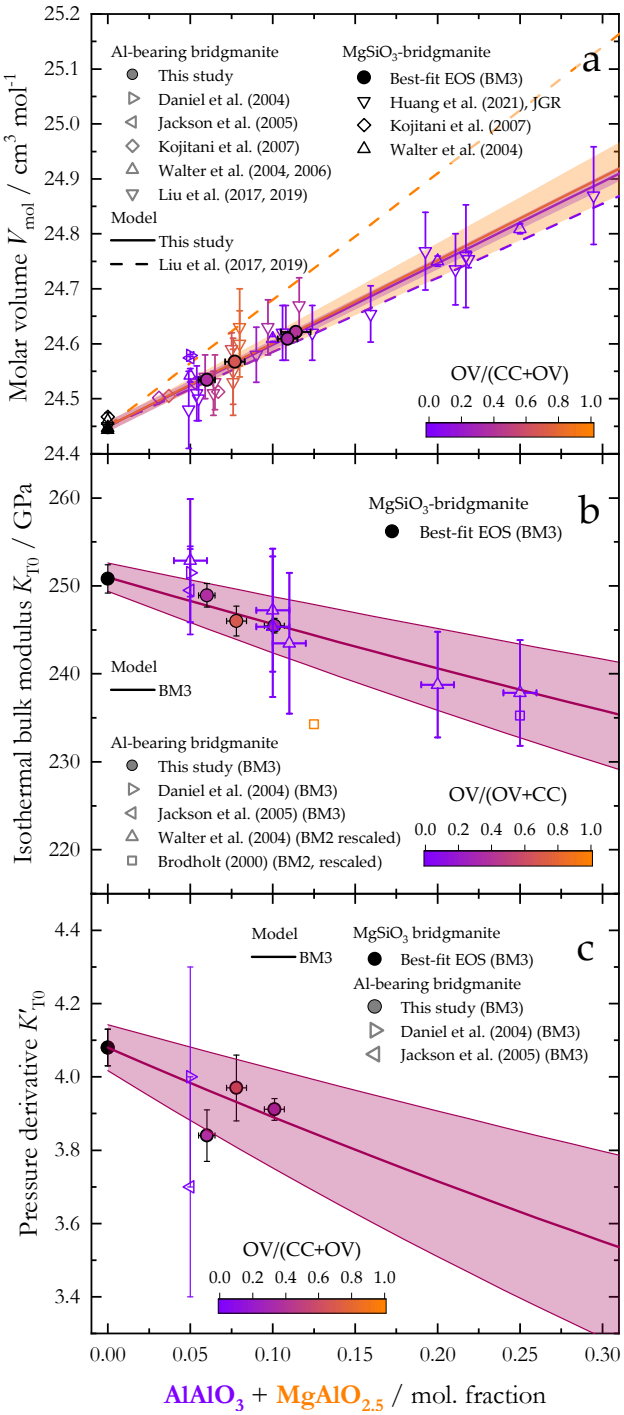

Figure 5.5. The compositional dependence of (a) molar volume, (b) isothermal bulk modulus and (c) its pressure derivative (c) at ambient conditions for Al-bearing bridgmanite. The color scale indicates the degree of CC and OV substitution for each sample and trendline. In (a), solid lines and shaded areas represent trends and estimated uncertainties for the $MgSiO_3$-$AlAlO_3$ and $MgSiO_3$-$MgAlO_{2.5}$ joins determined in this study, while dashed lines are trends proposed in previous studies. In (b) and (c) lines and shaded areas represent trends and estimated uncertainties for the $MgSiO_3$-$AlAlO_3$ and $MgSiO_3$-$MgAlO_{2.5}$ joins, under the assumption that $K_{AlAlO_3} = K_{MgAlO_{2.5}}$ and $K'_{AlAlO_3} = K'_{MgAlO_{2.5}}$.

Table 5.5. Modelled equation of state parameters for the bridgmanite end members in the $MgSiO_3$-$AlAlO_3$-$MgAlO_{2.5}$ system. Numbers between brackets represent one standard deviation on the last digit(s). The equation of state parameters for $(Mg_{3/4}Al_{1/4})(Al_{1/4}Si_{3/4})O_2O_1$ and $Mg(Al_{1/8}Si_{7/8})O_2O_{15/16}$ were calculated using equations 5.3-5.5 (italics) or assumed to be the same as in Table 5.4 (bold).

	Best-fit EOS	Refined end members		End members for thermodynamic modelling	
	$MgSiO_3$	$AlAlO_3$	$MgAlO_{2.5}$	$(Mg_{3/4}Al_{1/4})(Al_{1/4}Si_{3/4})O_2O_1$	$Mg(Al_{1/8}Si_{7/8})O_2O_{15/16}$
V_{mol0} (cm^3/mol)	24.455(8)	25.93(4)	25.96(15)	*24.82(1)*	*24.64(2)*
K_{T0} (GPa) - BM3	251(2)	209(11)	209(11)	*238(5)*	*244(4)*
K'_{T0} - BM3	4.08(5)	2.7(4)	2.7(4)	*3.6(2)*	*3.85(15)*
K_{T0} (GPa) - BM2	251.6(5)	189(3)	189(3)	*231.9(17)*	*241.3(11)*
γ_0	1.63(3)	-	-	**2.1**	**2.1**
q_0	3.1(2)	-	-	**3.1**	**3.1**
θ_{D0} (K)	912	-	-	**912**	**912**

studies, we first employed a three end member model (i.e., $MgSiO_3$-$AlAlO_3$-$MgAlO_{2.5}$) to fit the data reported in Figure 5.5a using equation 5.3, thus simultaneously refining V_{MgSiO_3}, V_{AlAlO_3} and $V_{MgAlO_{2.5}}$. Then, we calculated the molar volumes of CC and OV intermediate end members, which will then be used for the thermodynamic modelling, as 25 mol.% $AlAlO_3$-75 mol.% $MgSiO_3$ and 12.5 mol.% $MgAlO_{2.5}$-87.5 mol.% $MgSiO_3$, respectively. From our analysis, we found V_{AlAlO_3} and $V_{MgAlO_{2.5}}$ to be identical to each other within uncertainty (Table 5). On the one hand, this could be an effect of the large estimated uncertainties on Vmol reported in most studies. On the other hand, our results are supported by the fact that volume data obtained by single-crystal X-ray diffraction (this study) and Rietveld refinements (Kojitani et al., 2007), which are supposedly the most accurate and precise techniques, plot basically on the same line despite having different degrees of CC and OV substitution. Liu et al. (2019c) proposed that $V_{MgAlO_{2.5}} > V_{AlAlO_3}$ by fitting data along the $MgSiO_3$-$AlAlO_3$ join first, and then fixing the obtained V_{MgSiO_3} and V_{AlAlO_3} to constrain $V_{MgAlO_{2.5}}$ from the analysis of OV-bearing samples, thus neglecting the potential correlation between V_{AlAlO_3} and $V_{MgAlO_{2.5}}$. Note, however, that microfocussed X-ray diffraction data of OV-rich samples by Liu et al. (2019c) are in agreement with our model within mutual uncertainties. Our findings support the idea that, at least for small concentrations of OV component, the molar volume of bridgmanite is mainly controlled by substitution of Al in the B-site, due to its greater influence on the octahedral volume than the creation of oxygen vacancies themselves or the Mg-Al substitution in the A-site.

Experimental studies on the compressibility of Al-bearing bridgmanite conducted so far have only employed powdered samples, often synthesized in situ inside a DAC (e.g., Andrault et al., 2001; Daniel et al., 2001; Walter et al., 2004; Walter et al., 2006). The range of values obtained for K_{T0} and K'_{T0} of these samples is considerably large, and results are often in contrast with one another. For instance, Andrault et al. (2001) and Walter et al. (2004) and Walter et al. (2006) conducted similar experiments to determine the compressibility of bridgmanite solid solutions with different Al content, where samples were synthesized in the DAC by laser heating and their EOSs were measured upon further compression or decompression. While Andrault et al. (2001) suggested that K_{T0} increases along the

$MgSiO_3$-$AlAlO_3$ join, Walter et al. (2004) and Walter et al. (2006) reported an opposite trend, with K_{T0} linearly decreasing with increasing CC substitution. Other studies reported K_{T0} values as low as 240 and 220 GPa for bridgmanite samples with $AlAlO_3$ concentrations of 1.2 and 7.7 mol.%, respectively, which seem unrealistically low given the relatively small difference in chemical composition with the $MgSiO_3$ end member (Daniel et al., 2001; Yagi et al., 2004). Such low K_{T0} values were argued to be related to the presence of oxygen vacancies in the investigated bridgmanite samples. However, our data indicate that this effect is not significantly different from $AlAlO_3$ substitution, even for concentrations of $MgAlO_{2.5}$ as high as 5 mol.%. The broad disagreement between previous experimental studies prevents us from applying the same strategy described for the molar volume, i.e., to consider all literature data to refine K_{AlAlO_3} and $K_{MgAlO_{2.5}}$. Instead, we decided to use equations 5.4 and 5.5 to fit our single-crystal dataset alone and then compare the refined trends with previous studies. As stated in section 3.2, the bulk compressibility of Al-bearing bridgmanite seems to be controlled mainly by the compression of octahedra, at least for limited amounts of OV component. Therefore, we constrained K_{AlAlO_3} and $K_{MgAlO_{2.5}}$, as well as K'_{AlAlO_3} and $K'_{MgAlO_{2.5}}$, to be equal to each other in the fitting procedure. To reduce the number of parameters, we fixed K_{MgSiO_3} and K'_{MgSiO_3} to the value obtained from our best-fit EOS (Table 5.4). In this way, we obtained $K_{AlAlO_3} = K_{MgAlO_{2.5}} = 208(11)$ GPa and $K'_{AlAlO_3} = K'_{MgAlO_{2.5}} = 2.7(4)$ based on BM3 fit parameters, and $K_{AlAlO_3} = K_{MgAlO_{2.5}} = 190(3)$ GPa based on BM2 fit parameters. Results on the molar volume and BM3 fits are plotted in Figure 5.5b-c together with 68% confidence bands (i.e., one standard deviation) represented by shaded areas. The solid solution model constructed using the BM3 EOS parameters interpolates well the refined K_{T0} data points from this study. The trend is also in good agreement with experimental data for a 5 mol.% $AlAlO_3$-bearing sample that was analyzed by both powder X-ray diffraction and Brillouin scattering up to about 40 GPa (Daniel et al., 2004; Jackson et al., 2005). The K_{T0} data from Walter et al. (2004) and Walter et al. (2006) renormalized with respect to the K_{MgSiO_3} determined by Walter et al. (2004) and multiplied by K_{MgSiO_3} of our best-fit EOS are in good agreement with our data. Following the same approach, a good agreement with our model is also found for the rescaled K_{T0} value of bridgmanite with pyrope composition from the computational study of Brodholt (2000). To compare our trends with the results of from Brodholt (2000) on $MgAlO_{2.5}$, we show in Figure 5.5b the bulk modulus (calculated through equation 5.4) for a solid solution of 87.5 mol.% $MgSiO_3$-12.5 mol.% $MgAlO_{2.5}$, that is the composition of intermediate end member that we will later use for thermodynamic modeling. The resulting K value plots 14 GPa below our trend and 7 GPa below the lower confidence band. Again, this could either be an effect of non-ideality along the $MgSiO_3$-$MgAlO_{2.5}$ join at higher $MgAlO_{2.5}$ content or could result from the ordered oxygen vacancies distribution in the brownmillerite-type structure employed by Brodholt (2000). Similar considerations apply to the BM2 K_{T0} which are reported in the Appendix (Figure B.11). K'_{T0} values for the BM3 solid solution model are in slightly poorer agreement due to the relatively low refined value for CC4OV2 (Table 5.3), but still consistent with the refined model within mutual uncertainties. The proposed trend is also in excellent agreement with static compression data by Daniel et al. (2004) and in

good agreement with high-pressure elasticity measurements by Jackson et al. (2005).

5.6 Implications for the stability of the oxygen vacancy component in Al-bearing bridgmanite

The presence of defects in the crystal structure of lower mantle minerals has the potential to greatly affect the transport properties of lower mantle rocks, such as their viscosity. For instance, the pressure dependence of defects could contribute to enhance mantle viscosity at depths greater than 1000 km (Rudolph et al., 2015), which in turn was linked to slab stagnation (Fukao and Obayashi, 2013) and plume deflection (French and Romanowicz, 2015) in the same depth interval. This has motivated a number of previous studies to investigate and model the stability of the bridgmanite OV components $MgAlO_{2.5}$ and $MgFe^{3+}O_{2.5}$ as a function of pressure (Fei et al., 2021; Huang et al., 2021a; Liu et al., 2017a). The main limitation of the models proposed so far is that the thermoelastic parameters of the $AlAlO_3$ and $MgAlO_{2.5}$ bridgmanite end members, which are required to model the stability of oxygen vacancies as a function of pressure, were assumed to be equal to $MgSiO_3$ or derived from crystallographic observations at ambient conditions (Huang et al., 2021b; Huang et al., 2021a). Here, we have combined the thermodynamic formalism proposed in these previous studies with the thermal equation of state parameters for $MgSiO_3$ and Al-bearing bridgmanite end members determined in this study (Table 5.5). In order to model the stability of oxygen vacancies in bridgmanite in the MgO-$AlO_{1.5}$-SiO_2 system, we assumed the following equilibrium:

$$\underset{\text{OV}}{\mathrm{MgAl_{1/8}Si_{7/8}O_2O_{15/16}}}(brg) = \\ = \frac{1}{4}\mathrm{Mg_{3/4}Al_{1/4}}\underset{\text{CC}}{\mathrm{Al_{1/4}Si_{3/4}O_3}}(brg) + \frac{11}{16}\mathrm{MgSiO_3}(brg) + \frac{1}{8}\mathrm{MgO}(fp) \quad (5.6)$$

where *brg* and *fp* indicate the a given components belongs to bridgmanite and ferropericlase, respectively. Note that the $AlAlO_3$ and $MgAlO_{2.5}$ end member components have been replaced by the intermediate composition end members introduced in the previous section, which will be referred to as CC and OV hereinafter. The equilibrium constant for the reaction 5.6 is related to the standard state (pure phases at the P and T of interest) Gibbs free energy ($\Delta\mathcal{G}^0$) by:

$$\Delta\mathcal{G}^0 = -RTln\frac{(a^{brg}_{\text{CC}})^{1/4}(a^{brg}_{\text{MgSiO}_3})^{11/16}(a_{\text{MgO}^{fp}})^{1/8}}{a^{brg}_{OV}} \quad (5.7)$$

where a_i^α is the activity of the component i in the phase α, R is the gas constant and T is temperature. The activity of the component i in the phase α is calculated as $a_i^\alpha = x_i^\alpha\gamma_i^\alpha$, where x is the ideal mixing activity and γ is the activity coefficient accounting for non-ideal mixing. In the MgO-$AlO_{1.5}$-SiO_2 system, ferropericlase (*fp*) is pure MgO and, thus, its activity is 1. Following Huang et al. (2021a), we arbitrarily assumed that the oxygen vacancies are

localized in the O1 site of bridgmanite. Previous DFT calculation proposed $MgAlO_{2.5}$ with brownmillerite-type structure to be the OV end member of bridgmanite (Brodholt, 2000), with oxygen vacancies being ordered and localized at the O2 site in alternate layers perpendicular to the *c*-axis. In this structural type, Al occupies either tetrahedral or octahedral sites, while recent ^{27}Al MAS NMR showed evidence also for 5-fold coordinated Al (Grüninger et al., 2019), which is in principle compatible with both O1 and O2 vacancies. However, as we will discuss later, the choice of the specific site where oxygen vacancies are located does not affect our thermodynamic model as the dominant interaction parameter in the nearest-neighbor model is related to Si-Al substitution in the B site. Under these assumptions, the ideal mixing activity of bridgmanite components is calculated as follows:

$$x^{brg}_{MgSiO_3} = (x^{A}_{Mg})(x^{B}_{Si})(x^{O1}_{O}) \tag{5.8}$$

$$x^{brg}_{CC} = 3.0792(x^{A}_{Mg})^{3/4}(x^{A}_{Al})^{1/4}(x^{B}_{Si})^{3/4}(x^{B}_{Al})^{1/4}(x^{O1}_{O}) \tag{5.9}$$

$$x^{brg}_{OV} = 1.8415(x^{A}_{Mg})(x^{B}_{Si})^{7/8}(x^{B}_{Al})^{1/8}(x^{O1}_{O})^{15/16}(x^{O1}_{V})^{1/16} \tag{5.10}$$

where *x* is the concentration of Mg, Si, Al, O or vacancies (V) in the A, B or O1 crystallographic site of the bridgmanite structure. The coefficients 3.0792 and 1.8415 were obtained by substituting each ideal mixing activity *x* with its exponent in 5.9 and 5.10, which is required in order to have an activity of 1 when the composition of bridgmanite is $(Mg_{3/4}Al_{1/4})(Al_{1/4}Si_{3/4})O_2O_1$ or $Mg(Al_{1/8}Si_{7/8})O_2O_{15/16}$, respectively. The activity coefficients for non-ideal mixing are calculated assuming a nearest-neighbor binary symmetric model:

$$RTln\gamma^{brg}_{CC} = W^{A}_{MgAl}\left(1 - x^{A}_{Al}\right)^2 + W^{B}_{AlSi}\left(1 - x^{B}_{Al}\right)^2 + W^{O1}_{OV}\left(1 - x^{O1}_{O}\right)^2 \tag{5.11}$$

$$RTln\gamma^{brg}_{MgSiO_3} = W^{A}_{MgAl}\left(1 - x^{A}_{Mg}\right)^2 + W^{B}_{AlSi}\left(1 - x^{B}_{Si}\right)^2 + W^{O1}_{OV}\left(1 - x^{O1}_{O}\right)^2 \tag{5.12}$$

$$RTln\gamma^{brg}_{MgSiO_3} = W^{A}_{MgAl}\left(1 - x^{A}_{Mg}\right)^2 + W^{B}_{AlSi}\left(1 - x^{B}_{Si}\right)^2 + W^{O1}_{OV}\left(1 - x^{O1}_{O}\right)^2 \tag{5.13}$$

where *W* are Margules interaction parameters describing the interaction of Mg-Al in the A site, Al-Si in the B site or O-V in the O1 site. By assuming $W^{A}_{MgAl} = W^{O1}_{OV} = 0$ (Huang et al., 2021a) and substituting equations 5.8-5.13, we can rewrite equation 5.7 explicitly as a function of composition:

$$\Delta\mathcal{G}^0 = -RTln\frac{(x^{brg}_{CC})^{1/4}(x^{brg}_{MgSiO_3})^{11/16}}{a^{brg}_{OV}} - W^{B}_{AlSi}\left[\frac{1}{4}\left(x^{B}_{Si}\right)^2 + \frac{11}{16}\left(x^{B}_{Si}\right)^2 - \left(x^{B}_{Si}\right)^2\right] \tag{5.14}$$

Equivalent expressions were also calculated assuming the dominant interaction parameter to be W^{A}_{MgAl} or W^{O1}_{OV}. However, the fit did not reach convergence in these cases, supporting the choice of W^{B}_{Si} as the most relevant interaction parameter.

Since most of the experimental studies on the phase relations of OV-bearing bridgmanite in the MgO-$AlO_{1.5}$-SiO_2 system were conducted at 26-27 GPa and 1873-2000 K (Grüninger et al., 2019; Kojitani et al., 2007; Liu et al., 2019c; Liu et al., 2019b; Navrotsky et al., 2003), these were assumed as standard conditions in our calculations. We used OriginPro2021

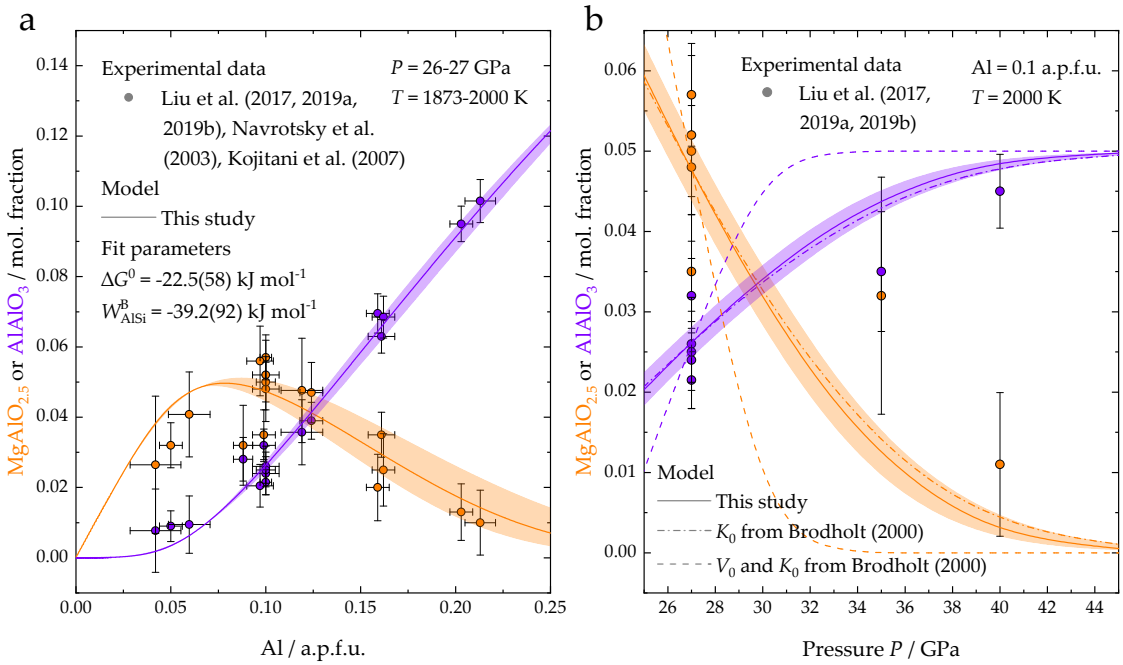

Figure 5.6. Concentration of AlAlO3 (CC) and MgAlO2.5 (OV) components in bridgmanite (a) as a function of the bulk Al content at 26-27 GPa and 1873-2000 K, and (b) as a function of pressure at 0.1 Al a.p.f.u. and 2000 K. The shaded areas represent our estimated uncertainties and take into account (a,b) the correlation between ΔG^0 and $W^{\mathrm{B}}_{\mathrm{Si}}$ (Figure B.12) and (b) the uncertainty on the equation of state parameters (Table 5.5).

(OriginLab corporation, Northampton, MA, USA) to fit the compositional data for bridgmanite synthesized under MgO-saturated conditions. The analytical uncertainties on EPMA data were propagated to the fit parameters $\Delta\mathcal{G}^0$ and $W^{\mathrm{B}}_{\mathrm{Si}}$ using an orthogonal regression scheme. The obtained model interpolates well the experimental data points (Figure 5.6a). From our fit, we found $\Delta\mathcal{G}^0$ = -22(6) kJ mol^{-1} and $W^{\mathrm{B}}_{\mathrm{Si}}$ = -39(9) kJ mol^{-1}, which are in agreement with previous results within mutual uncertainties (Huang et al., 2021a). As suggested by these authors, the correlation between the two fit parameters is extremely high (Figure B.12), which in turn is responsible for the large estimated errors on the parameters of our fit.

Using the thermal EOS parameters for the three end members $MgSiO_3$, $(Mg_{3/4}Al_{1/4})(Al_{1/4}Si_{3/4})O_2O_1$, and $Mg(Al_{1/8}Si_{7/8})O_2O_{15/16}$, we can evaluate how the standard Gibbs free energy expressed by equation 5.14 evolves with pressure. We can express ΔG^0 as a function of the Helmholtz free energy F:

$$\Delta\mathcal{G}^0_{PT} = \Delta U + P\Delta V - T\Delta S = \Delta\mathcal{F}_{PT} + P\Delta V = \Delta\mathcal{F}_0 + \Delta\mathcal{F}_c + \Delta\mathcal{F}_{th} + P\Delta V \qquad (5.15)$$

where $\Delta\mathcal{G}^0_{PT}$ is the standard state Gibbs free energy at given pressure and temperature conditions, ΔU is the change in internal energy of the reaction, S is entropy, $\Delta\mathcal{F}_{PT}$ is the reaction Helmholtz free energy at a given pressure and temperature, $\Delta\mathcal{F}_0$ is the reaction Helmholtz

free energy at room pressure and temperature, $\Delta\mathcal{F}_c$ is the change in Helmholtz free energy upon compression at room temperature and $\Delta\mathcal{F}_{th}$ is the change in Helmholtz free energy upon heating at constant volume. All the parameters on the right hand side of 5.15, except for $\Delta\mathcal{F}_0$, are directly derived from the thermal EOSs of the three bridgmanite end member components (Table 5.5) and of MgO (Kono et al., 2010). $\Delta\mathcal{F}_0$ can be further expanded as:

$$\Delta\mathcal{F}_0 = \frac{1}{4}\mathcal{F}_{0,\mathrm{CC}} + \frac{11}{16}\mathcal{F}_{0,\mathrm{MgSiO_3}} + \frac{1}{8}\mathcal{F}_{0,\mathrm{MgO}} - \mathcal{F}_{0,\mathrm{OV}} \tag{5.16}$$

Where $\mathcal{F}_{0,\mathrm{MgO}}$ and $\mathcal{F}_{0,\mathrm{MgSiO_3}}$ are tabulated values for the Helmholtz free energy of MgO and $MgSiO_3$ bridgmanite at ambient conditions (Stixrude and Lithgow-Bertelloni, 2011), while $\mathcal{F}_{0,\mathrm{CC}}$ and $\mathcal{F}_{0,\mathrm{OV}}$ are unknown. Note, however, that the exact value of these two parameters is not necessary for our thermodynamic calculations and only the term $1/4\mathcal{F}_{0,\mathrm{CC}} - \mathcal{F}_{0,\mathrm{OV}}$ is needed. This term can be calculated through 5.15 knowing that $\Delta\mathcal{G}^0$ = -22 kJ mol^{-1} at 27 GPa and 2000 K, yielding $1/4\mathcal{F}_{0,\mathrm{CC}} - \mathcal{F}_{0,\mathrm{OV}} = 996$ kJ mol^{-1}. This now allows to calculate $\Delta\mathcal{G}^0$ at any pressure and temperature conditions. Using this information, we calculated the composition of bridgmanite in the MgO-$AlO_{1.5}$-SiO_2 under MgO saturating conditions as a function of pressure (Figure 5.6b). The main factor controlling how pressure affects the OV concentration in bridgmanite is the term $P\Delta V$ in equation 5.15. As the ΔV term for the equilibrium 5.6 is negative, the concentration of the OV component will decrease with increasing pressure. To evaluate the effect of the EOS fit parameters on the model, we added or subtracted the estimated uncertainties on V_0, K_0, and K'_0 for the OV and CC end members (Table 5.5) in a way to maximize or minimize the ΔV term. We found the contribution to overall uncertainties on the CC and OV concentration to be much smaller than that arising from data scattering at 26-27 GPa and 1873-2000 K (Figure 5.6a). The experimental data of Liu et al. (2017a) at 2000 K and 27-40 GPa exhibit a similarly decreasing trend for the concentration of the OV component, although with a slightly milder slope (Figure 5.6b). This difference is significant especially for the data point at 35 GPa, where the experimentally determined OV concentration and that determined from our model do not overlap even within their mutual uncertainties. As this could be related to the choice of EOS parameters used to extrapolate the model to higher pressures, we further tested the sensitivity of the model to the input EOS parameters for the CC and OV end members by employing a combination of V_0 from this study and K_0 from Brodholt (2000), as well as V_0 and K_0 from Brodholt (2000). In the former case, despite the larger difference between $K_{\mathrm{AlAlO_3}}$ and $K_{\mathrm{MgAlO_{2.5}}}$, the change in concentration of the two end members as a function of pressure falls withing the estimated uncertainties of our model. In the latter case, owing to the much larger difference between $V_{\mathrm{MgAlO_{2.5}}}$ and $V_{\mathrm{AlAlO_3}}$, the variation in the OV concentration is unrealistically sharp and does not fit the experimental data at pressure higher than 27 GPa. Therefore, we consider the observed misfit to be more likely due to the scatter of the experimental data points, similarly to the case of the 26-27 GPa and 1873-2000 K data (Figure 5.6a).

Huang et al. (2021a) predicted that the concentration of the $Fe^{3+}Fe^{3+}O_3$ component in

bridgmanite could increase with pressure and become relevant for a pyrolytic lower mantle composition. The presence of such a component could have important implications for the electronic and elastic properties of bridgmanite Liu et al. (e.g., 2018) and Mao et al. (2015), which need to be constrained to produce meaningful thermodynamic and mineral physical models of Earth's lower mantle. Recent experimental data showed that both the $Fe^{3+}Fe^{3+}O_3$ and $MgFe^{3+}O_{2.5}$ end members are stabilized under oxidizing conditions in Al-free systems and that the concentration of the $MgFe^{3+}O_{2.5}$ component decreases with pressure (Fei et al., 2020; Fei et al., 2021). In these experiments, bridgmanite was found to coexist with a post-spinel phase of $MgFe_2O_4$ and/or ferropericlase. As phase assemblages becomes more complex with the addition of Fe, constraining the thermal equation of state of $Fe^{3+}Fe^{3+}O_3$-bearing and $MgFe^{3+}O_{2.5}$-bearing bridgmanite is of crucial importance to model the phase equilibria of Fe-bearing systems, such as candidate rock compositions for the lower mantle like pyrolite and basalt. As EOSs of different components become more and more accurate, our ability to build more complete thermodynamic models will also improve, allowing us to predict the stability of bridgmanite components and calculate their physical properties in a wider pressure, temperature and compositional range than it is currently possible.

Acknowledgements

We would like to thank Raphael Njul for preparing the samples for EPMA and Detlef Krauße for his assistance with the acquisition of EPMA data. This study was supported by DFG grant FR1555/11. We acknowledge DESY (Hamburg, Germany), a member of the Helmholtz Association HGF, for the provision of experimental facilities. Parts of this research were carried out at the Extreme Conditions Beamline P02.2, PETRA-III.

Data Availability Statement

Crystallographic Information Files (CIFs) are available at: https://figshare.com/s/ce5a9194e4e3a235e7bb.

References

Andrault, D., N. Bolfan-Casanova, M. A. Bouhifd, N. Guignot, and T. Kawamoto (2007). "The role of Al-defects on the equation of state of Al-(Mg,Fe)SiO3 perovskite". In: *Earth and Planetary Science Letters* 263 (3-4), pp. 167–179. DOI: 10.1016/j.epsl.2007.08.012.

Andrault, D., N. Bolfan-Casanova, and N. Guignot (2001). "Equation of state of lower mantle (Al,Fe)-$MgSiO_3$ perovskite". In: *Earth and Planetary Science Letters* 193 (3-4), pp. 501–508. DOI: 10.1016/S0012-821X(01)00506-4.

Angel, R. J. (2000). "Equations of State". In: *Reviews in Mineralogy and Geochemistry* 41 (1), pp. 35–59. DOI: 10.2138/rmg.2000.41.2.

Angel, R. J. and L. W. Finger (2011). "SINGLE: A program to control single-crystal diffractometers". In: *Journal of Applied Crystallography* 44 (1), pp. 247–251. DOI: 10.1107/S0021889810042305.

Angel, R. J., J. Gonzalez-Platas, and M. Alvaro (2014). "EosFit7c and a Fortran module (library) for equation of state calculations". In: *Zeitschrift fur Kristallographie* 229 (5), pp. 405–419. DOI: 10.1515/zkri-2013-1711.

Birch, F. (1947). "Finite elastic strain of cubic crystals". In: *Physical Review* 71 (11), pp. 809–824. DOI: 10.1103/PhysRev.71.809.

Boehler, R. and K. D. Hantsetters (Sept. 2004). "New anvil designs in diamond-cells". In: *High Pressure Research* 24 (3), pp. 391–396. DOI: 10.1080/08957950412331323924.

Boffa Ballaran, T., A. Kurnosov, K. Glazyrin, D. J. Frost, M. Merlini, M. Hanfland, and R. Caracas (2012). "Effect of chemistry on the compressibility of silicate perovskite in the lower mantle". In: *Earth and Planetary Science Letters* 333-334, pp. 181–190. DOI: 10.1016/j.epsl.2012.03.029.

Brodholt, J. P. (2000). "Pressure-induced changes in the compression mechanism of aluminous perovskite in the Earth's mantle". In: *Nature* 407 (6804), pp. 620–622. DOI: 10.1038/35036565.

Criniti, G., A. Kurnosov, T. B. Ballaran, and D. J. Frost (2021). "Single-Crystal Elasticity of $MgSiO_3$ Bridgmanite to Mid-Lower Mantle Pressure". In: *Journal of Geophysical Research: Solid Earth* 126 (5). DOI: 10.1029/2020JB020967.

Daniel, I., J. D. Bass, G. Fiquet, H. Cardon, J. Zhang, and M. Hanfland (2004). "Effect of aluminium on the compressibility of silicate perovskite". In: *Geophysical Research Letters* 31 (15), pp. 3–6. DOI: 10.1029/2004GL020213.

Daniel, I., H. Cardon, G. Fiquet, F. Guyot, and M. Mezoaur (2001). "Equation of State of Al-bearing Perovskite to Lower Mantle Pressure Conditions". In: *Geophysical Research Letters* 28 (19), pp. 3789–3792.

Datchi, F., A. Dewaele, P. Loubeyre, R. Letoullec, Y. L. Godec, and B. Canny (2007). "Optical pressure sensors for high-pressure–high-temperature studies in a diamond anvil cell". In: *High Pressure Research* 27 (4), pp. 447–463. DOI: 10.1080/08957950701659593.

Dorogokupets, P. I. and A. Dewaele (2007). "Equations of state of MgO, Au, Pt, NaCl-B1, and NaCl-B2: Internally consistent high-temperature pressure scales". In: *High Pressure Research* 27 (4), pp. 431–446. DOI: 10.1080/08957950701659700.

Fei, H., Z. Liu, R. Huang, S. Kamada, N. Hirao, S. Kawaguchi, C. McCammon, and T. Katsura (2021). "Pressure Destabilizes Oxygen Vacancies in Bridgmanite". In: *Journal of Geophysical Research: Solid Earth* 126 (12), pp. 1–18. DOI: 10.1029/2021JB022437.

Fei, H., Z. Liu, C. McCammon, and T. Katsura (2020). "Oxygen Vacancy Substitution Linked to Ferric Iron in Bridgmanite at 27 GPa". In: *Geophysical Research Letters* 47 (6), pp. 1–9. DOI: 10.1029/2019GL086296.

French, S. W. and B. Romanowicz (2015). "Broad plumes rooted at the base of the Earth's mantle beneath major hotspots". In: *Nature* 525 (7567), pp. 95–99. DOI: 10.1038/nature14876.

Fukao, Y. and M. Obayashi (2013). "Subducted slabs stagnant above, penetrating through, and trapped below the 660 km discontinuity". In: *Journal of Geophysical Research: Solid Earth* 118 (11), pp. 5920–5938. DOI: 10.1002/2013JB010466.

Gonzalez-Platas, J., M. Alvaro, F. Nestola, and R. J. Angel (2016). "EosFit7-GUI: A new graphical user interface for equation of state calculations, analyses and teaching". In: *Journal of Applied Crystallography* 49 (4), pp. 1377–1382. DOI: 10.1107/S1600576716008050.

Grüninger, H., Z. Liu, R. Siegel, T. B. Ballaran, T. Katsura, J. Senker, and D. J. Frost (2019). "Oxygen Vacancy Ordering in Aluminous Bridgmanite in the Earth's Lower Mantle". In: *Geophysical Research Letters* 46 (15), pp. 8731–8740. DOI: 10.1029/2019GL083613.

Huang, R., T. B. Ballaran, C. A. McCammon, N. Miyajima, D. Dolejš, and D. J. Frost (2021a). "The composition and redox state of bridgmanite in the lower mantle as a function of oxygen fugacity". In: *Geochimica et Cosmochimica Acta* 303, pp. 110–136. DOI: 10.1016/J.GCA.2021.02.036.

Huang, R., T. B. Ballaran, C. A. McCammon, N. Miyajima, and D. J. Frost (2021b). "The effect of Fe–Al substitution on the crystal structure of $MgSiO_3$ bridgmanite". In: *Journal of Geophysical Research: Solid Earth*, e2021JB021936. DOI: 10.1029/2021jb021936.

Hübschle, C. B., G. M. Sheldrick, and B. Dittrich (2011). "ShelXle: A Qt graphical user interface for SHELXL". In: *Journal of Applied Crystallography* 44 (6), pp. 1281–1284. DOI: 10.1107/S0021889811043202.

Irifune, T., T. Shinmei, C. A. McCammon, N. Miyajima, D. C. Rubie, and D. J. Frost (2010). "Iron Partitioning and Density Changes of Pyrolite in Earth's Lower Mantle". In: *Science* 327 (5962), pp. 193–195. DOI: 10.1126/science.1181443.

Ishii, T., Z. Liu, and T. Katsura (2019c). "A Breakthrough in Pressure Generation by a Kawai-Type Multi-Anvil Apparatus with Tungsten Carbide Anvils". In: *Engineering* 5 (3), pp. 434–440. DOI: 10.1016/j.eng.2019.01.013.

Ishii, T., N. Miyajima, G. Criniti, Q. Hu, K. Glazyrin, and T. Katsura (2022b). "High pressure-temperature phase relations of basaltic crust up to mid-mantle conditions". In: *Earth and Planetary Science Letters* 584, p. 117472. DOI: 10.1016/j.epsl.2022.117472.

Ishii, T., L. Shi, R. Huang, N. Tsujino, D. Druzhbin, R. Myhill, Y. Li, L. Wang, T. Yamamoto, N. Miyajima, T. Kawazoe, N. Nishiyama, Y. Higo, Y. Tange, and T. Katsura (2016). "Generation of pressures over 40 GPa using Kawai-type multi-anvil press with tungsten carbide anvils". In: *Review of Scientific Instruments* 87 (2). DOI: 10.1063/1.4941716.

Jackson, J. M., J. Zhang, J. Shu, S. V. Sinogeikin, and J. D. Bass (2005). "High-pressure sound velocities and elasticity of aluminous $MgSiO_3$ perovskite to 45 GPa: Implications for lateral heterogeneity in Earth's lower mantle". In: *Geophysical Research Letters* 32 (21), pp. 1–4. DOI: 10.1029/2005GL023522.

Jacobsen, S. D., C. M. Holl, K. A. Adams, R. A. Fischer, E. S. Martin, C. R. Bina, J. F. Lin, V. B. Prakapenka, A. Kubo, and P. Dera (2008). "Compression of single-crystal magnesium

oxide to 118 GPa and a ruby pressure gauge for helium pressure media". In: *American Mineralogist* 93 (11-12), pp. 1823–1828. DOI: 10.2138/am.2008.2988.

Kantor, I., V. Prakapenka, A. Kantor, P. Dera, A. Kurnosov, S. Sinogeikin, N. Dubrovinskaia, and L. Dubrovinsky (2012). "BX90: A new diamond anvil cell design for X-ray diffraction and optical measurements". In: *Review of Scientific Instruments* 83 (12), p. 125102. DOI: 10.1063/1.4768541.

Keppler, H. and D. J. Frost (2005). "Introduction to minerals under extreme conditions". In: *EMU notes in Mineralogy*, pp. 1–30. DOI: 10.1180/emu-notes.7.1.

King, H. E. and L. W. Finger (1979). "Diffracted beam crystal centering and its application to high-pressure crystallography". In: *Journal of Applied Crystallography* 12 (4), pp. 374–378. DOI: 10.1107/S0021889879012723.

Kojitani, H., T. Katsura, and M. Akaogi (2007). "Aluminum substitution mechanisms in perovskite-type $MgSiO_3$: An investigation by Rietveld analysis". In: *Physics and Chemistry of Minerals* 34 (4), pp. 257–267. DOI: 10.1007/s00269-007-0144-z.

Kono, Y., T. Irifune, Y. Higo, T. Inoue, A. Barnhoorn, D. Suetsugu, C. Bina, T. Inoue, D. Wiens, and M. Jellinek (2010). "*P-V-T* relation of MgO derived by simultaneous elastic wave velocity and in situ X-ray measurements: A new pressure scale for the mantle transition region". In: *Physics of the Earth and Planetary Interiors* 183 (1-2), pp. 196–211. DOI: 10.1016/j.pepi.2010.03.010.

Kurnosov, A., I. Kantor, T. Boffa-Ballaran, S. Lindhardt, L. Dubrovinsky, A. Kuznetsov, and B. H. Zehnder (2008). "A novel gas-loading system for mechanically closing of various types of diamond anvil cells". In: *Review of Scientific Instruments* 79 (4). DOI: 10.1063/1.2902506.

Kurnosov, A., H. Marquardt, D. J. Frost, T. B. Ballaran, and L. Ziberna (2017). "Evidence for a Fe^{3+}-rich pyrolitic lower mantle from (Al,Fe)-bearing bridgmanite elasticity data". In: *Nature* 543, pp. 543–546. DOI: 10.1038/nature21390.

Liermann, H. P., Z. Konôpková, W. Morgenroth, K. Glazyrin, J. Bednarčik, E. E. McBride, S. Petitgirard, J. T. Delitz, M. Wendt, Y. Bican, A. Ehnes, I. Schwark, A. Rothkirch, M. Tischer, J. Heuer, H. Schulte-Schrepping, T. Kracht, and H. Franz (2015). "The Extreme Conditions Beamline P02.2 and the Extreme Conditions Science Infrastructure at PETRA III". In: *Journal of Synchrotron Radiation* 22, pp. 908–924. DOI: 10.1107/S1600577515005937.

Litasov, K. D., P. N. Gavryushkin, P. I. Dorogokupets, I. S. Sharygin, A. Shatskiy, Y. Fei, S. V. Rashchenko, Y. V. Seryotkin, Y. Higo, K. Funakoshi, and E. Ohtani (2013). "Thermal equation of state to 33.5 GPa and 1673 K and thermodynamic properties of tungsten". In: *Journal of Applied Physics* 113 (13). DOI: 10.1063/1.4799018.

Liu, J., S. M. Dorfman, F. Zhu, J. Li, Y. Wang, D. Zhang, Y. Xiao, W. Bi, and E. E. Alp (2018). "Valence and spin states of iron are invisible in Earth's lower mantle". In: *Nature Communications* 9 (1), pp. 1–9. DOI: 10.1038/s41467-018-03671-5.

Liu, Z., M. Akaogi, and T. Katsura (2019b). "Increase of the oxygen vacancy component in bridgmanite with temperature". In: *Earth and Planetary Science Letters* 505, pp. 141–151. DOI: 10.1016/j.epsl.2018.10.014.

Liu, Z., T. B. Ballaran, R. Huang, D. J. Frost, and T. Katsura (2019c). "Strong correlation of oxygen vacancies in bridgmanite with Mg/Si ratio". In: *Earth and Planetary Science Letters* 523, p. 115697. DOI: 10.1016/j.epsl.2019.06.037.

Liu, Z., H. Fei, L. Chen, C. McCammon, L. Wang, R. Liu, F. Wang, B. Liu, and T. Katsura (2021). "Bridgmanite is nearly dry at the top of the lower mantle". In: *Earth and Planetary Science Letters* 570, p. 117088. DOI: 10.1016/j.epsl.2021.117088.

Liu, Z., T. Ishii, and T. Katsura (2017a). "Rapid decrease of $MgAlO_{2.5}$ component in bridgmanite with pressure". In: *Geochemical Perspectives Letters* 5, pp. 12–18. DOI: 10.7185/geochemlet.1739.

Liu, Z., M. Nishi, T. Ishii, H. Fei, N. Miyajima, T. B. Ballaran, H. Ohfuji, T. Sakai, L. Wang, S. Shcheka, T. Arimoto, Y. Tange, Y. Higo, T. Irifune, and T. Katsura (2017b). "Phase Relations in the System $MgSiO_3$-Al_2O_3 up to 2300 K at Lower Mantle Pressures". In: *Journal of Geophysical Research: Solid Earth* 122 (10), pp. 7775–7788. DOI: 10.1002/2017JB014579.

Mao, Z., J. F. Lin, J. Yang, T. Inoue, and V. B. Prakapenka (2015). "Effects of the Fe^{3+} spin transition on the equation of state of bridgmanite". In: *Geophysical Research Letters* 42 (11), pp. 4335–4342. DOI: 10.1002/2015GL064400.

Martin, C. D., W. A. Crichton, H. Liu, V. Prakapenka, J. Chen, and J. B. Parise (2006). "Rietveld structure refinement of perovskite and post-perovskite phases of $NaMgF_3$ (Neighborite) at high pressures". In: *American Mineralogist* 91 (10), pp. 1703–1706. DOI: 10.2138/am.2006.2308.

Navrotsky, A., M. Schoenitz, H. Kojitani, H. Xu, J. Zhang, D. J. Weidner, and R. Jeanloz (2003). "Aluminum in magnesium silicate perovskite: Formation, structure, and energetics of magnesium-rich defect solid solutions". In: *Journal of Geophysical Research: Solid Earth* 108 (B7). DOI: 10.1029/2002jb002055.

Petrícek, V., M. Dušek, and L. Palatinus (2014). "Crystallographic computing system JANA2006: General features". In: *Zeitschrift fur Kristallographie* 229 (5), pp. 345–352. DOI: 10.1515/zkri-2014-1737.

Prescher, C. and V. B. Prakapenka (2015). "DIOPTAS: A program for reduction of two-dimensional X-ray diffraction data and data exploration". In: *High Pressure Research* 35 (3), pp. 223–230. DOI: 10.1080/08957959.2015.1059835.

Ralph, R. L. and L. W. Finger (1982). "A Computer-Program for Refinement of Crystal Orientation Matrix and Lattice-Constants from Diffractometer Data with Lattice Symmetry Constraints". In: *Journal of Applied Crystallography* 15 (10), pp. 537–539. DOI: 10.1107/S0021889882012539.

Rudolph, M. L., V. Lekić, and C. Lithgow-Bertelloni (2015). "Viscosity jump in Earth's mid-mantle". In: *Science* 350 (6266), pp. 1349–1352. DOI: 10.1126/science.aad1929.

Shannon, R. D. (1976). "Revised effective ionic radii and systematic studies of interatomic distances in halides and chalcogenides". In: *Acta Crystallographica Section A* 32 (5), pp. 751–767. DOI: 10.1107/S0567739476001551.

Sheldrick, G. M. (2015a). "Crystal structure refinement with *SHELXL*". In: *Acta Crystallographica Section C: Structural Chemistry* 71, pp. 3–8. DOI: 10.1107/S2053229614024218.

Sheldrick, G. M. (2015b). "Foundations and Advances *SHELXT*-Integrated space-group and crystal-structure determination". In: *Acta Cryst* 71, pp. 3–8. DOI: 10.1107/S2053273314026370.

Siersch, N. C., G. Criniti, A. Kurnosov, T. B. Ballaran, Z. Liu, T. Ishii, D. J. Frost, T. Yu, and Y. Wang (2023). "The influence of Al_2O_3 on the structural properties of $MgSiO_3$ akimotoite". In: *American Mineralogist* 108 (1), pp. 100–109. DOI: 10.2138/am-2022-8257.

Sinogeikin, S. V., J. Zhang, and J. D. Bass (2004). "Elasticity of single crystal and polycrystalline $MgSiO_3$ perovskite by Brillouin spectroscopy". In: *Geophysical Research Letters* 31 (6). DOI: 10.1029/2004gl019559.

Stixrude, L. and C. Lithgow-Bertelloni (2005). "Thermodynamics of mantle minerals - I. Physical properties". In: *Geophysical Journal International* 162 (2), pp. 610–632. DOI: 10.1111/j.1365-246X.2005.02642.x.

— (2011). "Thermodynamics of mantle minerals - II. Phase equilibria". In: *Geophysical Journal International* 184 (3), pp. 1180–1213. DOI: 10.1111/j.1365-246X.2010.04890.x.

Vanpeteghem, C. B., J. Zhao, R. J. Angel, N. L. Ross, and N. Bolfan-Casanova (2006). "Crystal structure and equation of state of $MgSiO_3$ perovskite". In: *Geophysical Research Letters* 33 (3), pp. 10–13. DOI: 10.1029/2005GL024955.

Walter, M. J., A. Kubo, T. Yoshino, J. P. Brodholt, K. T. Koga, and Y. Ohishi (2004). "Phase relations and equation-of-state of aluminous Mg-silicate perovskite and implications for Earth's lower mantle". In: *Earth and Planetary Science Letters* 222 (2), pp. 501–516. DOI: 10.1016/j.epsl.2004.03.014.

Walter, M. J., R. G. Trønnes, L. S. Armstrong, O. T. Lord, W. A. Caldwell, and S. M. Clark (2006). "Subsolidus phase relations and perovskite compressibility in the system MgO-AlO1.5-SiO_2 with implications for Earth's lower mantle". In: *Earth and Planetary Science Letters* 248 (1-2), pp. 77–89. DOI: 10.1016/j.epsl.2006.05.017.

Yagi, T., K. Okabe, N. Nishiyama, A. Kubo, and T. Kikegawa (2004). "Complicated effects of aluminum on the compressibility of silicate perovskite". In: *Physics of the Earth and Planetary Interiors* 143 (1-2), pp. 81–91. DOI: 10.1016/j.pepi.2003.07.020.

Zhang, J. and D. J. Weidner (1999). "Thermal equation of state of aluminum-enriched silicate perovskite". In: *Science* 284 (5415), pp. 782–784. DOI: 10.1126/science.284.5415.782.

Chapter 6

High-pressure phase transition and equation of state of hydrous Al-bearing silica

Giacomo Criniti[1*], Takayuki Ishii[2†], Alexander Kurnosov[1], Konstantin Glazyrin[3] Tiziana Boffa Ballaran[1],

[1] Bayerisches Geoinstitut, University of Bayreuth, 95440 Bayreuth, Germany

[2] Center for High Pressure Science and Technology Advanced Research, 100094 Beijing, China

[3] Deutsches Elektronen-Synchrotron, 22603 Hamburg, Germany

[*] **Corresponding author**: giacomo.criniti@uni-bayreuth.de

[†] Present address: Institute for Planetary Materials, Okayama University, Misasa, Japan.

This chapter has been published as:
Criniti, G., T. Ishii, A. Kurnosov, K. Glazyrin, and T. Boffa Ballaran (2023). "High-pressure phase transition and equation of state of hydrous Al-bearing silica". In: *American Mineralogist 108(8)*, 1558-1568. DOI: https://doi.org/10.2138/am-2022-8546

Author contributions: G. Criniti conceived the project, characterized the hydrous Al-bearing silica samples, conducted the Raman and synchrotron measurements, analyzed the data, and wrote the manuscript. T. Ishii conceived the project, synthesized and characterized the hydrous Al-bearing silica samples, and commented on the manuscript. A. Kurnosov conducted the Raman and synchrotron measurements, and commented on the manuscript. K. Glazyrin provided assistance during the synchrotron measurements and commented on the manuscript. T. Boffa Ballaran conceived and supervised the project, conducted the synchrotron measurements, and commented on the manuscript.

Abstract

Stishovite, a rutile-structured polymorph of SiO_2, is a main component of subducted basaltic lithologies in the lower mantle. At mid lower-mantle depths, a second-order ferroelastic transition to orthorhombic $CaCl_2$-type (post-stishovite) structure occurs, causing extensive elastic shear softening. Previous studies showed that Al incorporation can decrease the transition pressure, while it is still debated whether H has a similar effect. Here we report the equations of state, structural evolution and phase transformation of $Si_{0.948(6)}Al_{0.052(2)}O_{1.983}H_{0.018(5)}$ (Al5) stishovite and $Si_{0.886(4)}Al_{0.114(2)}O_{1.980}H_{0.07(3)}$ (Al11) post-stishovite samples using diamond anvil cells in combination with synchrotron X-ray diffraction and Raman spectroscopy. The Al5 sample transformed to the orthorhombic polymorph upon compression to 16 GPa, displaying a drop of $\sim$ 12% in its bulk modulus across the transformation. The Al11 sample did not undergo any phase transition in the pressure range investigated. Single-crystal structural refinements and Raman spectroscopy measurements on the Al5 sample show that the soft optic mode B_{1g} is decoupled from the structural tetragonal-to-orthorhombic transformation and shows a plateau in the stability field of post-stishovite, between 20 and 30 GPa. This observation indicates that the transformation is not pseudo-proper ferroelastic as in SiO_2 stishovite and that existing Landau expansions are likely not applicable to H-rich Al-bearing silica samples. Using the equation of state parameters of orthorhombic Al5 and Al11 and literature data on SiO_2 post-stishovite we then discuss the possibility of non-ideal mixing along the SiO_2-AlOOH join.

6.1 Introduction

Stishovite is a high-pressure polymorph of SiO_2 with rutile-type structure (space group $P4_2/mnm$) that constitutes up to 25 vol.% of metabasaltic phase assemblages at lower mantle depths (e.g., Irifune and Ringwood, 1993; Ishii et al., 2019b; Ishii et al., 2022b). At approximately 50 GPa and room temperature, SiO_2-stishovite was found to undergo a second-order ferroelastic phase transition to a post-stishovite phase having $CaCl_2$-type structure (space group $Pnnm$), with a decrease from tetragonal to orthorhombic symmetry (Kingma et al., 1995; Andrault et al., 1998). Stishovite experiences extensive elastic softening across the post-stishovite transition, where its aggregate shear wave velocity (vS) is expected to drop by approximately 20% (Carpenter et al., 2000). In the last few decades, seismological studies have detected a number of plate-like seismic scattering bodies having negative shear wave velocity anomalies (-4% < dv_S < -12%), but positive density anomalies (+2% < $d\rho$ < +6%) compared to the surrounding mantle at approximately 1600-1800 km depth (e.g., Kaneshima and Helffrich, 1999; Niu, 2014). Temperature anomalies alone cannot explain such a drastic change in the elastic properties and density of the scatterers, which were therefore argued to represent chemically heterogeneous layers of dense subducted basalt (Kaneshima and Helffrich, 1999). In addition, the shear elastic softening that characterizes the post-stishovite transition in subducted basalt matches well the elastic anomalies proposed for the scatterers (Kaneshima, 2019), providing evidence for

the recycling of subducted oceanic plates down to the mid-lower mantle.

More recently, scattering bodies displaying similar features have been detected in the proximity of subducted oceanic plates sinking or stagnating in the topmost lower mantle (Kaneshima, 2019). These conditions are too shallow to be reconciled with the pressure and temperature conditions of the post-stishovite transition in SiO_2. In a dry mid-ocean ridge basalt (MORB) phase assemblage, however, stishovite is not pure SiO_2 and can host up to 4 mol% of $AlO_{1.5}$ component between 25 and 60 GPa (Ono et al., 2001; Hirose et al., 2005; Ricolleau et al., 2010; Ishii et al., 2019b; Ishii et al., 2022b). In the presence of water, the solubility of Al is even higher and reaches 7 mol% $AlO_{1.5}$ component, corresponding to approximately 6 wt.% Al_2O_3 (Litasov et al., 2007a). It was shown that Al-enriched stishovite samples transformed to the post-stishovite phase at lower pressures compared to pure SiO_2 (Lakshtanov et al., 2005; Lakshtanov et al., 2007b; Bolfan-Casanova et al., 2009). In the previous study by Lakshtanov et al. (2007b), the soft optic (B_{1g}) and acoustic modes (v_S along the [110] direction) of a stishovite sample with composition $Al_{0.07}Si_{0.93}O_{1.97}H_{0.016}$ showed evidence for elastic softening around 25 GPa at room temperature. At the same pressure, splitting of Bragg reflections of the tetragonal phase was also observed, confirming that the sample had transformed to orthorhombic post-stishovite (Lakshtanov et al., 2007b). While these findings suggest that Al-bearing stishovite can be responsible for seismic scattering in the topmost lower mantle, the Al concentration in the sample of Lakshtanov et al. (2007b) is much higher than determined in phase relations studies of hydrous MORB (Litasov and Ohtani, 2005). More recent studies showed that also H-bearing Al-free stishovite exhibits lower transition pressure relative to SiO_2 (Nisr et al., 2017; Nisr et al., 2020), suggesting that both Al and H can play a critical role in stabilizing the orthorhombic phase at lower pressures. Additionally, to date, the high-pressure structure and equation of state of hydrous Al-bearing stishovite and post-stishovite phases have been scarcely characterized, hampering our understanding of what are the individual effects of H and Al on their elastic properties and transition mechanism. In order to better understand whether the effect of Al and H on the phase transformation of stishovite to its $CaCl_2$-type polymorph can also be reconciled with the seismic scattering anomalies detected in the topmost lower mantle, samples with lower Al/H ratios need to be studied. For these reasons, in this study we report the high-pressure behavior of tetragonal $Si_{0.948(6)}Al_{0.052(2)}O_{1.983}H_{0.018(5)}$ (Al5) and orthorhombic $Si_{0.886(4)}Al_{0.114(2)}O_{1.980}H_{0.07(3)}$ (Al11) silica samples analyzed by means of single-crystal X-ray diffraction (XRD) and Raman spectroscopy in diamond anvil cell (DAC).

6.2 Materials and Methods

6.2.1 Sample synthesis and characterization

Single crystals of hydrous Al-bearing silica were synthesized at high pressure and high temperature in the 15-MN Kawai-type multi-anvil apparatus with Osugi-type

(DIA) guide block system installed at Bayerisches Geoinstitut, University of Bayreuth (Ishii et al., 2016; Ishii et al., 2019c). The starting materials consisted of mixtures of SiO_2 and AlOOH-boehmite in molar ratios 95:5 (run I1072) and 8:2 (run I1063). Each mixture was ground in an agate mortar before being loaded in a Pt-tube capsule which was then sealed by welding. Tungsten carbide cubes with 3 mm truncated edge length were combined with a 7 mm Cr-doped MgO octahedral pressure medium and a $LaCrO_3$ heater. Temperature was monitored using a W97/Re3–W75/Re25 thermocouple. In both runs, the sample was first compressed to a target press load corresponding to 28 GPa (Liu et al., 2017b) and then heated for 3-4 h at 1973 K (I1072) or 2173 K (I1063). Finally, the assembly was quenched by cutting the electrical power supply and slowly decompressed to ambient conditions. The chemical composition of the run products was analyzed using a JEOL JXA-8200 electron probe microanalyzer (EPMA) operated at an acceleration voltage of 15 kV and a beam current of 5 nA using $MgSiO_3$ enstatite and Al_2O_3 corundum as standards for Si and Al, respectively. Chemical analysis revealed that the run products are chemically homogeneous throughout the entire length of each capsule based on the average of 15 data points per sample.The calculated oxide abundancies and estimated standard deviations (between parentheses) resulted to be SiO_2 = 94.32(56) wt.%, Al_2O_3 = 4.36(19) wt.% for I1072 and SiO_2 = 87.73(43) wt.%, Al_2O_3 = 9.54(14) wt.% for I1063. In order to quantify the water content of the two samples, inclusion-free single crystals were hand-picked and polished on both sides to obtain platelets approximately 15 μm thick. Fourier transform infrared (FTIR) spectra were collected between 2000 and 10000 cm^{-1} with a spectral resolution of 4 cm^{-1} by averaging of 100-200 scans. In order to make a direct comparison with the sample of Lakshtanov et al. (2007b), H concentrations were determined using the calibration of Paterson (1982). Unpolarized FTIR measurements were conducted on randomly oriented crystals for run I1063, while polarized FTIR measurements were performed on the (100) crystallographic plane of a single crystal from run I1072. Although the FTIR measurements were conducted on different crystals than those employed in high-pressure experiments, we expect the water concentration to be homogeneous in the run products, similarly to what we found for the Al and Si content in our EPMA analyses. We found that water contents of I1063 and I1072 samples were 1.1(5) wt.% and 0.27(8) wt.%, respectively, where the number between parenthesis represent either the standard deviation calculated from different unpolarized measurements (I1063) or the effect of using different baseline subtraction strategies (I1072). Further details approximately the analytical procedure and water content determination have been reported in a separate publication (Ishii et al., 2022a). The overall compositions of the two samples resulted to be $Si_{0.886(4)}Al_{0.114(2)}O_{1.980}H_{0.07(3)}$ (Al11) and $Si_{0.948(6)}Al_{0.052(2)}O_{1.983}H_{0.018(5)}$ (Al5). Preliminary in-house single-crystal X-ray diffraction (XRD) measurements were performed on a Huber diffractometer equipped with MoKα radiation and a point detector and driven by the software SINGLE (Angel and Finger, 2011). Al5 displayed tetragonal symmetry, like Al-rich stishovite samples reported in a previous study (Litasov et al., 2007a), with unit-cell lattice parameters a = 4.1988(1) Å, c = 2.6730(1) Å and V = 47.125(3) $Å^3$. Al11, on the other hand, exhibited the high-pressure orthorhombic

$CaCl_2$-type structure of post-stishovite, with unit-cell lattice parameters a = 4.2597(2) Å, b = 4.1831(4) Å, c = 2.6829(1) Å and V = 47.806(6) $Å^3$.

6.2.2 High-pressure X-ray diffraction measurements

Single crystals of Al5 (15x15x10 μm^3) and Al11 (20x10x10 μm^3) were loaded in a BX90-type DAC (Kantor et al., 2012) equipped with Almax-Boehler diamonds (Boehler and Hantsetters, 2004) having culets of 350 μm in diameter (Table C.1). A 200 μm-thick Re foil was indented to 51(1) μm and drilled using an infrared laser to obtain the sample chamber. The Al5 and Al11 samples were loaded in the same sample chamber together with a ruby sphere for pressure determination (Shen et al., 2020) and a piece of Au. Pre-compressed He gas at 1.3 kbar was loaded as quasi-hydrostatic pressure transmitting medium using the gas loading system installed at the Bayerishces Geoinstitut, University of Bayreuth (Kurnosov et al., 2008).

High-pressure XRD measurements were conducted at the Extreme Conditions Beamline P02.2 of PETRA III (DESY, Hamburg, Germany) using a 2x2 μm2 X-ray beam of 42.7 keV and a Perkin-Elmer XRD 1621 flat panel detector (Liermann et al., 2015). Polycrystalline CeO)2 and a single crystal of natural enstatite were measured to calibrate the sample-detector distance and instrument parameters for single-crystal XRD, respectively. Pressure was increased online using a gas-driven membrane up to $\sim$ 50 GPa at steps of 1-2 GPa. As it is commonly observed for ferroelastic phases (e.g., Salje, 1991), twin structures develop in hydrous Al-bearing stishovite upon transformation to the $CaCl_2$-type phase (Lakshtanov et al., 2007b), where the twin law consists of a reflection of the two lattices by the {110} planes. The Al11 sample displayed the same type of twinning already at ambient conditions, despite being recovered in the orthorhombic phase, suggesting that the same type of twinning can occur as well during crystal growth in the stability field of the $CaCl_2$-type phase. The Al5 sample was not twinned at ambient conditions, but ferroelastic twin domains developed at the onset of the phase transition to $CaCl_2$-type phase. In the proximity of the phase transition, when the orientations of the twin components are too close to each other, peaks at low 2θ values are difficult to distinguish in single-crystal diffraction step scans. Although this problem was observed only in the Al5 sample and only in a limited pressure range, we decided to determine the unit cell parameters of both Al5 and Al11 (Table C.2 and C.3) by fitting 1D profiles to avoid systematic differences that could arise due to the proximity and/or overlapping of reflections between the two twin components at different pressures. For this purpose, wide-scan images were collected upon continuous rotation of the DAC between -20° and +20° and integrated to 1D patterns using *DIOPTAS* (Prescher and Prakapenka, 2015). Full profile Le Bail fits were then obtained using *JANA2006* (Petrícek et al., 2014).

Step scans were also acquired at each pressure point upon continuous rotation of the DAC between -35° and +35° and processed using *CrisAlysPro* (Agilent Technologies Ltd.,

Yarton, Oxfordshire, UK). Data processing included peak search and indexing, background subtraction, intensity integration, Lorentz and polarization corrections, frame scaling and empirical absorption correction based on spherical harmonics. For the Al11 sample, the orientation matrices of the two twin components were sufficiently different from each other. Therefore, the intensity data from the two twin domains were simultaneously integrated and then merged in a single reflection file that was used for structural refinements. For the Al5 sample, this strategy could not be applied in the proximity of the phase transformation where the reflections of the two twin components were too close to each other at low 2θ angles. For internal consistence, we decided instead to use a small mask and integrate only the most intense of the two domains at all pressure points, excluding reflections that would overlap with the other twin component. A comparison of the two integration strategies for the Al5 sample at the highest pressures, where the orientations of the two twin components were sufficiently different, yielded very consistent results, with structural parameters being almost identical within their mutual uncertainties, confirming the robustness of our approach. The structures of the two phases were solved using the dual space algorithm *SHELXT* (Sheldrick, 2015b) and refinements against F^2 were performed with *SHELXL* in the *Shelxle* GUI (Hübschle et al., 2011; Sheldrick, 2015a). Atomic scattering factors were used in all refinements and site occupancies at the cation site were fixed to Si = 0.95 and Al = 0.05 for Al5 and Si = 0.89 and Al = 0.11 for Al11, as determined from chemical analyses. H atoms could not be located in the structure because of their low concentration and extremely weak scattering factor. Anisotropic displacement parameters were employed for all atoms, except for data collected at 21.75(3) and 32.21(4) GPa on Al5, where isotropic parameters were used due to the lower number of observed reflections. R-factors obtained for structural refinements were typically between 3% and 5% for both samples, proving the high quality of our structural models. Further information can be found in the deposited Crystallographic Information File (CIF).

6.2.3 High-pressure Raman Spectroscopy

Two crystals with Al5 and Al11 compositions were further analyzed at high-pressure and room temperature in DACs by means of Raman spectroscopy. Several runs were performed employing BX-90 DACs with Almax-Boehler diamonds having culet diameters of 400 or 250 μm, Re as gasket material and He or Ne as pressure transmitting media (Table C.1). A ruby sphere was loaded in each DAC as pressure standard (Shen et al., 2020). Pressure was increased manually by mechanically tightening the screws of the DACs up to approximately 40 or 44 GPa at steps of 0.5 - 3 GPa. Raman spectroscopy measurements were performed on a Dilor XY Spectrometer equipped with a 50x microscope objective and a 1800 groove/mm diffraction grating. The spectrometer employed a 532 nm ventus532 laser from Laser Quantum and a TE cooled SynapseTM CCD detector (1024x256 resolution) from HORIBA Jobin Yvon, and was driven by LABRAM 5 software. Raman spectra were acquired using a laser power of 200-800 mW between 150 and 500 cm^{-1} with a resolution of 2 cm^{-1}. To analyze

the high-pressure Raman spectra of Al5 and Al11 samples, background was manually subtracted from each spectrum and peaks were fitted using pseudo-Voigt functions using the software package Origin2019 (OriginLab corporation, Northampton, MA, USA). Peak positions and their estimated standard deviations for Al5 and Al11 samples are reported as supplementary material (Tables C.4 and C.5).

6.3 Results and discussion

6.3.1 Equation of state of hydrous Al-bearing silica

The pressure evolution of the unit-cell parameters of Al5 and Al11 samples is shown in Figure 1. The Al5 sample retained its tetragonal symmetry up to 13.83(3) GPa, after which transformed to the orthorhombic $CaCl_2$-type phase, as observed by the divergence of the a and b unit-cell parameters (Figure 6.1b). The Al11 sample exhibited the $CaCl_2$-type structure of post-stishovite already at ambient conditions, suggesting that such structural modification is quenchable as long as a sufficient amount of Al and H is present in the stishovite crystal structure (Ishii et al., 2022a). The orthorhombic symmetry of Al11 was retained upon compression to 50.13(4) GPa and no phase transformations were detected in the pressure range investigated. EOSFit7c in the EOSFit GUI software (Angel et al., 2014; Gonzalez-Platas et al., 2016) was used to fit 3rd-order Birch-Murnaghan (BM3) equations of state (EOS) to our *P*-*V* datasets (Angel et al., 2014; Birch, 1947):

$$P = \frac{3}{2}K_{T0}\left[\left(\frac{V_0}{V}\right)^{\frac{7}{3}} - \left(\frac{V_0}{V}\right)^{\frac{5}{3}}\right]\left\{1 + \frac{3}{4}\left(K'_{T0} - 4\right)\left[\left(\frac{V_0}{V}\right)^{\frac{2}{3}} - 1\right]\right\} \quad (6.1)$$

Where V_0 is the ambient pressure unit-cell volume, K_{T0} the isothermal bulk modulus at ambient conditions and K'_{T0} is its pressure derivative. Due to the limited pressure interval in which the tetragonal polymorph of Al5 is stable, its K'_{T0} was fixed to 4.8, as reported by Zhang et al. (2021) for SiO_2 stishovite based on single-crystal XRD measurements. The refined EOS parameters are consistent with the analysis of the *F*-f_E plots of boths samples, as reported shown in Figure C.1. Static compression and elasticity measurements on SiO_2 reported, on average, a bulk modulus of 310 GPa for stishovite at ambient conditions (Weidner et al., 1982; Andrault et al., 2003; Jiang et al., 2009; Zhang et al., 2021). The K_{T0} value of our tetragonal sample Al5, i.e. 299(2) GPa, is smaller than that of SiO_2 stishovite, but larger than that of other Al-bearing samples investigated in previous studies (Figure 6.2). $AlO_{1.5}$ incorporation in dry stishovite (Bolfan-Casanova et al., 2009) seems to induce a more pronounced reduction of the bulk modulus than that observed for Al,H-bearing samples (Figure 6.2), possibly due to higher concentration of oxygen vacancies related to the substitution of the $AlO_{1.5}$ component. H-poor Al-bearing stishovite samples were also previously analyzed by Brillouin scattering (Lakshtanov et al., 2007a), showing values of the adiabatic bulk modulus, K_{S0}, similar to those of K_{T0} determined in our study (Figure 6.2). Since K_{T0} at ambient conditions is usually only 1-2% larger than K_{T0}, the data of Lakshtanov et al. (2007a) support the observation that increasing the H content for a given Al concentration

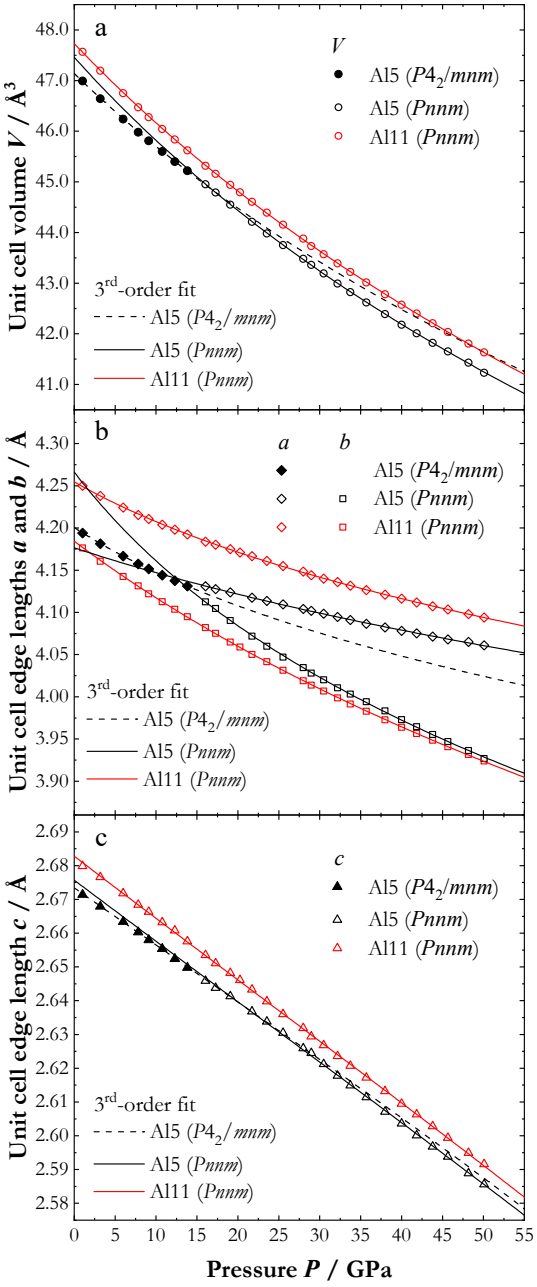

Figure 6.1. Pressure evolution of the unit-cell volume (a) and the unit-cell lattice parameters (b,c) of samples Al5 and Al11 investigated in this study. Error bars are smaller than the symbols and thus are not shown in the figures. Splitting of the *a* and *b* unit-cell parameters of Al5, indicating the tetragonal to orthorhombic phase transition, is observed at 16.09(2) GPa. Solid black symbols are tetragonal Al5; empty black symbols are orthorhombic Al5; empty red symbols are orthorhombic Al11. Dashed black lines are BM3 fits of tetragonal Al5; solid black lines are BM3 fits of orthorhombic Al5; solid red lines are BM3 fits of orthorhombic Al11.

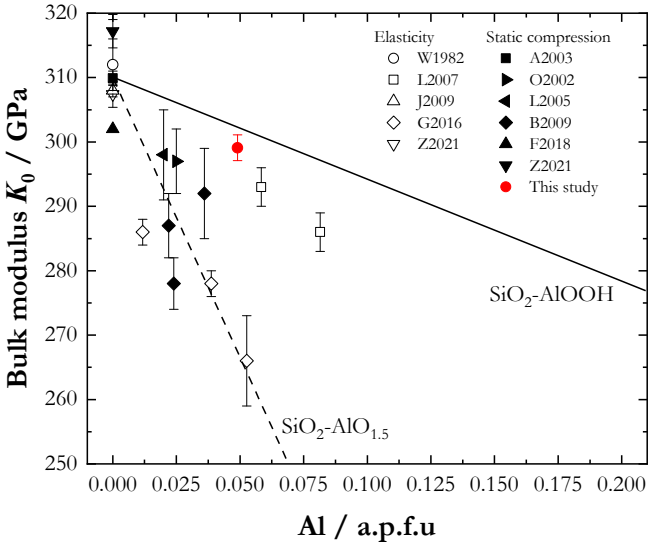

Figure 6.2. Comparison of the isothermal bulk moduli of tetragonal Al5 at ambient conditions with isothermal (static compression) and adiabatic bulk moduli (elasticity) from previous studies on SiO_2 and aluminous stishovite. W1982: Weidner et al. (1982), Brillouin scattering (BS) measurements at room pressure. L2007: Lakshtanov et al. (2007a), BS measurements at room pressure. J2009: Jiang et al. (2009), BS measurements in DAC. G2006: Gréaux et al. (2016), ultrasonic interferometry (UI) measurements in large volume press (LVP). Z2021: Zhang et al. (2021), BS measurements at room and high pressure. A2003: Andrault et al. (2003), powder and single crystal XRD in DAC. Ono et al. (2002), powder XRD in DAC. L2005: Lakshtanov et al. (2005), powder XRD in DAC. B2009: Bolfan-Casanova et al. (2009), powder XRD in DAC. F2018: Fischer et al. (2018), powder XRD in DAC. Z2021: Zhang et al. (2021), single crystal XRD in DAC. Relatively dry Al-bearing samples (G2016, B2009) seem to show a steeper decrease in K_0 with increasing Al content with respect to more H-rich samples (this study, L2007). Note that the solid and dashed line representing the SiO_2-AlOOH and SiO_2-$AlO_{1.5}$ substitution mechanisms are meant to be just a guide to the eye.

in stishovite increases the bulk modulus. At pressure higher than 16 GPa, after the tetragonal to orthorhombic transition in Al5, K_T of the sample decreases by $\sim 12\%$ and becomes identical to that of Al11 within uncertainty (Figure C.2), albeit with a slightly steeper slope due to its larger K'_{T0} (Table 6.1).

6.3.2 Axial compressibility of hydrous Al-bearing silica

Following the approach of Angel (2000) and Angel et al. (2014), we used a linearized BM3 EOS to describe the pressure evolution of the unit-cell parameters (l) by substituting V with l, $3K_{T0}$ with M_0 and $3K'_{T0}$ with M'_0:

$$P = \frac{1}{2} M_{l,0} \left[\left(\frac{l_0}{l} \right)^7 - \left(\frac{l_0}{l} \right)^5 \right] \left\{ 1 + \frac{1}{4} \left(M'_{l,0} - 12 \right) \left[\left(\frac{l_0}{l} \right)^2 - 1 \right] \right\} \tag{6.2}$$

Due to the little sensitivity of our dataset to the $M'_{c,0}$ of Al5, its value was fixed to 0 in the tetragonal phase (i.e. the compression of the c-axis was assumed to be linear up to 16 GPa) and to 1.3 in the orthorhombic phase, the latter of which is the value determined for the Al11 sample, given that the evolution with pressure of the orthorhombic c-axis seems identical for the two samples. A complete list of the refined EOS parameters is provided in Table 6.1. The *c*-axis is the most incompressible direction in both samples and seems to be not much affected by changes in the chemical composition and crystal structure of hydrous Al-bearing SiO_2. By comparing the linear equations of state of tetragonal and orthorhombic Al5, only a very subtle softening of the *c*-axis was detected across the phase transition (Figure 6.1), consistently with previous observations on SiO_2 stishovite (e.g., Andrault et al., 2003). The a and b lattice parameters of Al5 quickly diverged upon transformation to the $CaCl_2$-type-type phase (Figure 6.1b), although their EOSs became practically subparallel to those of Al11 at approximately 50 GPa. The resulting axial compressibility for tetragonal Al5 and for orthorhombic Al5 and Al11 followed the schemes $\beta_a > \beta_c$ and $\beta_b > \beta_a > \beta_c$, respectively.

Table 6.1. 3rd-order Birch-Murnaghan equation of state parameters of tetragonal ($P4_2/mnm$) and orthorhombic ($Pnnm$) Al5 and orthorhombic ($Pnnm$) Al11. Numbers in parentheses represent one standard deviation on the last digits. K'_{T0} of tetragonal Al5 was fixed to the value reported by Zhang et al. (2021) for SiO_2 stishovite. $M'_{c,0}$ of tetragonal Al5 was fixed to 0, while that of orthorhombic Al5 was fixed to the same $M'_{c,0}$ value of Al11.

	Al5		**Al11**
	$P4_2/mnm$	$Pnnm$	$Pnnm$
V_0	47.163(6)	47.44(3)	47.731(7)
K_{T0}	299.3(2.0)	266(4)	280.8(1.3)
K'_{T0}	4.8 (fixed)	4.23(13)	3.89(5)
a_0	4.2006(2)	4.175(2)	4.2546(1)
$M_{a,0}$	659(10)	1357(98)	760(5)
$M'_{a,0}$	28.4(1.8)	20.2(3.7)	30.0(5)
b_0		4.269(6)	4.1843(4)
$M_{b,0}$		327(20)	573(4)
$M'_{b,0}$		14.6(9)	9.73(15)
c_0	2.6734(5)	2.6757(4)	2.6828(2)
$M_{c,0}$	1578(16)	1468(8)	1447(14)
$M'_{c,0}$	0 (fixed)	1.3 (fixed)	1.3(4)

6.3.3 Spontaneous strains and structural distortion analysis

In a ferroelastic transition, such as that of SiO_2 stishovite, the pressure evolution of the spontaneous strains in the low-symmetry orthorhombic phase (i.e. the fractional change in the unit-cell parameters relative to the high symmetry phase) yields important information approximately the anisotropic elastic properties of that material (Carpenter et al., 2000;

Buchen et al., 2018a; Zhang et al., 2021). These strains can be defined as $e_1 = (a - a_t)/a_1$ and $e_2 = (b - a_t)/a_t$ where a and b are the unit-cell lattice parameters of the low symmetry $CaCl_2$-type phase at a given pressure and a_t is the a lattice parameter that the high symmetry phase would have at the same pressure. When the phase transition to the low symmetry orthorhombic phase occurs, a and b become free to vary and diverge from the value that they would have in the high symmetry tetragonal phase. A symmetry breaking strain that quantifies the distortion of the low-symmetry phase relative to the high symmetry phase can then be defined as the difference between e_1 and e_2.

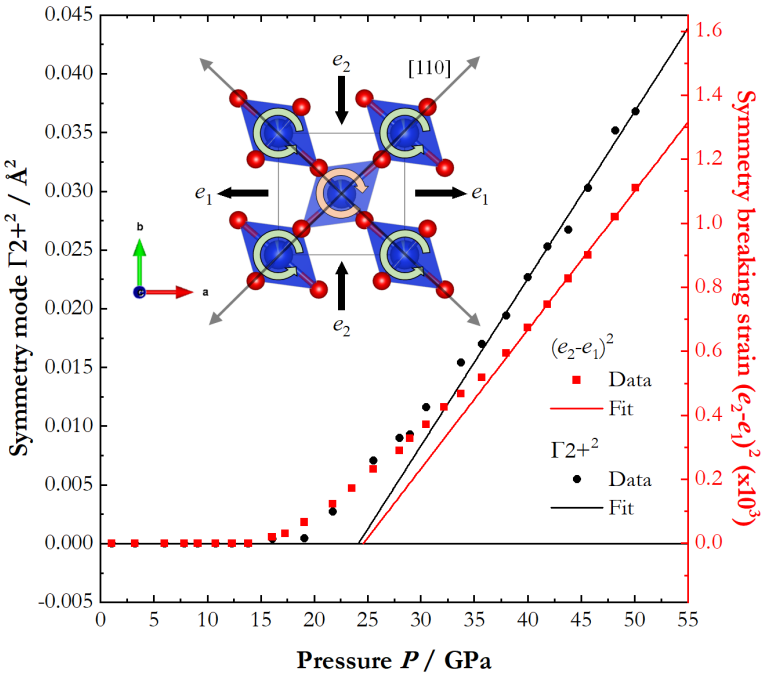

Figure 6.3. Pressure evolution of structural parameters related to the tetragonal-to-orthorhombic phase transition in Al5 stishovite. The inset shows the direction of shortening and lengthening of the unit-cell of post-stishovite, indicated by the spontaneous strains e_1 and e_2 (thick black arrows), as well as the direction of elastic shear softening (thin gray arrows). Green and orange curved arrows indicate the rotation of $(Si,Al)O_6$ octahedra approximately the c-axis, showing the effect of the Γ_{2+} distortion. The squared difference of symmetry breaking strains e_1 and e_2 (red squares) is non-zero above 16 GPa, but becomes linear only after 35 GPa, with a predicted transition pressure of 24.7(1.1) GPa (red line). The squared amplitude of the Γ_{2+} distortion, on the other hand, starts to increase significantly only above 20 GPa. In this case, a linear fit above 35 GPa yields a predicted transition pressure of 24.1(1.9) GPa.

Symmetry breaking strains are typically used in the Landau theory of phase transitions, where ferroelastic transitions are described in terms of coupling between an order parameter (Q) driving the phase transition and a soft optic mode (Carpenter and Salje, 1998). Unlike the spontaneous strains, which are related simply to the unit-cell lattice parameters, the order parameter is in general represented by the magnitude or amplitude of a given

structural feature (e.g., atomic displacement, tilt angle, etc.). Q is, by definition, zero in the high symmetry phase and free to vary in the low symmetry phase. The transformation of SiO_2 stishovite to $CaCl_2$-type phase is a pseudo-proper ferroelastic one, meaning that the spontaneous strains and Q are also coupled to one another. This coupling causes a violation of the Born stability criterion $c_{11} - c_{12} > 0$, which approaches zero in the proximity of the phase transformation and causes elastic instability and shear softening along the [110] direction (Carpenter et al., 2000). According to Landau theory, the square of the order parameter (Q^2) that drives the pseudo-proper ferroelastic transition of SiO_2 stishovite to post-stishovite couples linearly with the square of the symmetry breaking strain $(e_1 - e_2)^2$. For Al5, the values of e_1 and e_2 were calculated according to the relations reported above from the measured unit-cell lattice parameters of the low-symmetry phase at a given pressure and the unit-cell lattice parameters of the high-symmetry phase extrapolated to the same pressure using the linear EOS parameters reported in Table 6.1. When $(e_1 - e_2)^2$ is plotted against pressure for SiO_2 stishovite, a linear fit of the squared symmetry breaking strain yields the transition pressure (P_c^*), at which elastic softening is most extensive (Carpenter et al., 2000). Spontaneous strains calculated for Al5 (Figure 6.3), however, show a concave trend up to 35 GPa. A linear fit of the data was only possible above this pressure and yielded P_c^* = 24.7(1.1) GPa, which is much higher than the observed transition pressure of approximately 16 GPa for the tetragonal-to-orthorhombic transition.

Further insights on the nature of the phase transition of Al5 may be obtained by considering the relationship between the crystal structures of Al-bearing stishovite and post-stishovite. According to group theory, the space group of post-stishovite (*Pnnm*) has the same symmetry elements as the space group of stishovite ($P4_2/mnm$) apart from the 4-fold symmetry axis. Therefore, *Pnnm* is called a subgroup of $P4_2/mnm$. Note, however, that the differences between the *Pnnm* and $P4_2/mnm$ structures of silica are not only in the point group symmetry, which affects the length of the a and b unit-cell edges, but also in the position of atoms in the unit-cells of the two phases. In the case of stishovite, the point symmetry at the oxygen position across the $P4_2/mnm$ to *Pnnm* transition changes from *m.2m* (x,-x,0) to *..m* (x,y,0) and therefore acquires one degree of freedom. As a result, the y fractional coordinate of oxygen in the orthorhombic phase (Table C.4) deviates from the value that it would have in the tetragonal phase (i.e. -x), causing the SiO_6 octahedra in the a-b plane of the orthorhombic phase to rotate. This is shown in Figure 6.4, where the pressure evolution the octahedral tilting angles (η) is shown for the Al5 and Al11 samples. In the Al5 sample, this angle is 90° due to symmetry constraints in the tetragonal phase and deviates from such value after transformation to the orthorhombic phase. The evolution of η with pressure becomes linear above 25 GPa. The octahedral tilting in the Al11 sample, on the other hand, shows a linear trend throughout the entire pressure range investigated (Figure 6.4).

The movement of oxygen away from the (x,-x,0) position, and thus the degree of octahedral tilting, can be quantified by the irreducible representation (irrep) Γ_{2+} of the

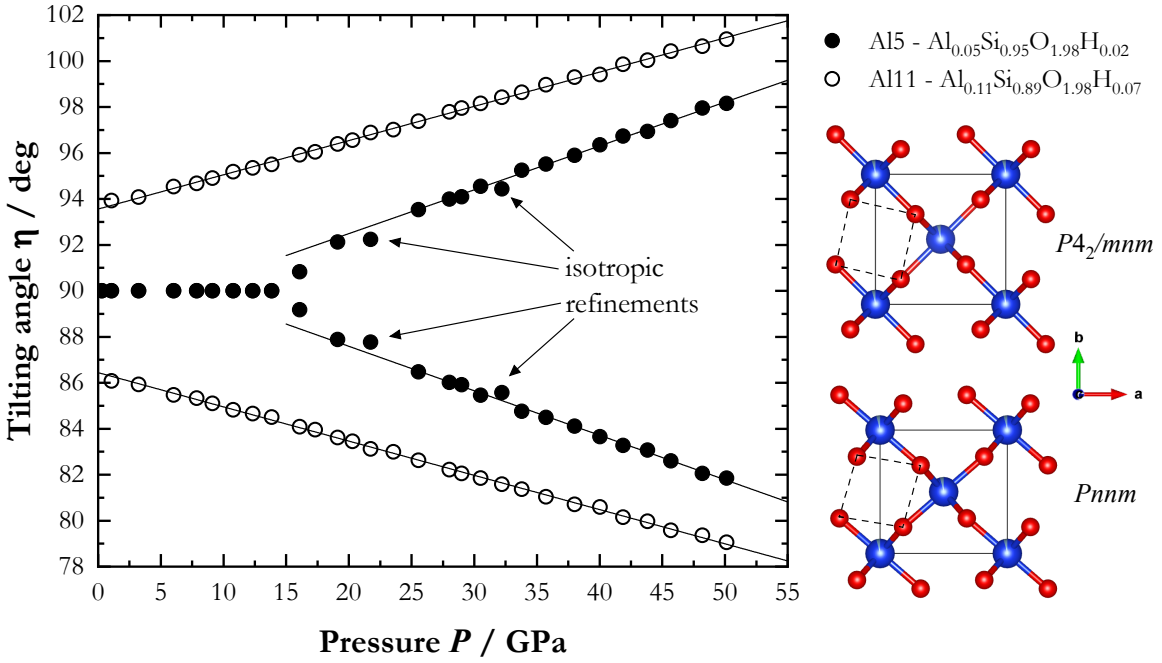

Figure 6.4. Pressure evolution of octahedral tilting angles (η) in Al5 (solid circles) and Al11 (empty circles). Solid lines represent linear fits to the datapoints between 0 (Al11) or 25 (Al5) and 50 GPa. Error bars are not shown as they are smaller than the symbols.η angles are defined by dashed lines superimposed to the crystal structures of stishovite (space group $P4_2/mnm$) and post-stishovite ($Pnnm$) at the right of the graph.

space group $P4_2/mnm$ (Miller and Love, 1967), which coincides with the order parameter Q and has the same point group symmetry as the optic soft mode B_{1g}. In SiO_2 stishovite, the tilting of the SiO_6 octahedra is coupled with the soft optic mode B_{1g} in the tetragonal phase and is responsible for the elastic softening that has been observed in the [110] direction prior to and across the phase transition (Zhang et al., 2021). In order to determine the variation of Γ_{2+} and thus quantify the order parameter variation as a function of pressure, a symmetry-mode decomposition analysis for the Al5 sample was performed using the computer program AMPLIMODES (Orobengoa et al., 2009). The input files required for calculating the amplitude of the irrep Γ_{2+} are the unit-cell parameters and atomic coordinates of the high- and low-symmetry phases at the same pressure conditions. As far as the orthorhombic phase is concerned, these quantities were directly derived from the analysis of diffraction patterns and single-crystal structural refinements, as described above. For the high-symmetry phase, on the other hand, the unit-cell parameters and the atomic coordinates of the Si and O sites needed to be extrapolated to the pressure range where the orthorhombic phase is stable. The unit-cell parameters of the tetragonal phase above 16 GPa were easily obtained by extrapolating the linear EOS (6.2) of the a and c lattice parameters determined below 16 GPa (Table 6.1). The x atomic coordinate of the O atom, on the other hand, was found to be basically pressure-independent between 0 and 16 GPa, having an average value of 0.3054 (Figure C.3, Table refat3-tab6) and therefore

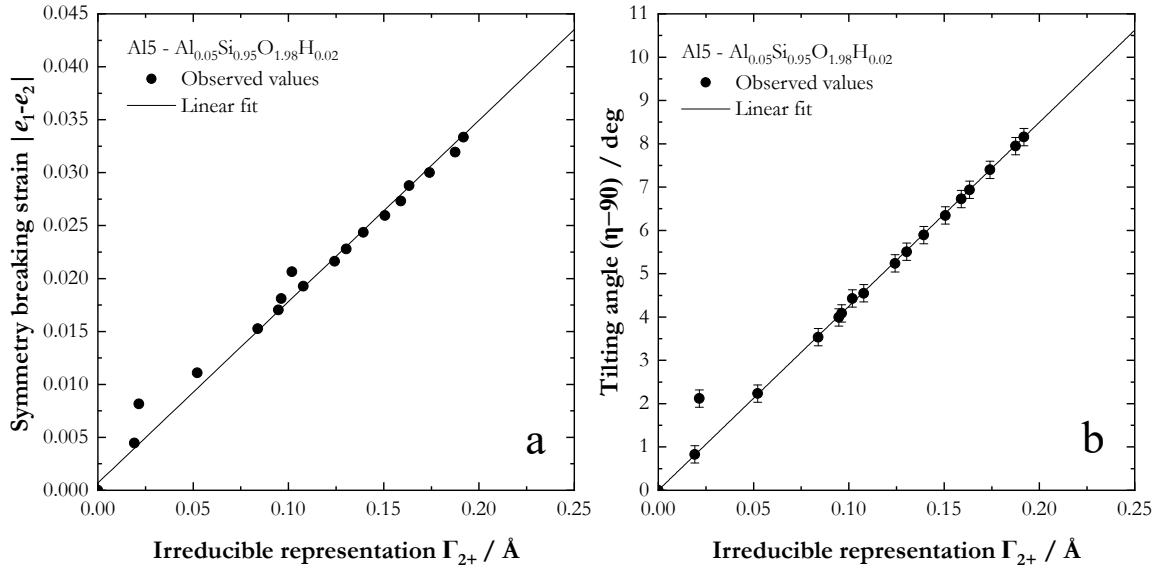

Figure 6.5. Linear coupling between the squared amplitude of the irrep Γ_{2+} and (a) the square of symmetry breaking strain and (b) the octahedral tilting angle. When not shown, errors are smaller than the symbols.

this value well describes the tetragonal oxygen position at all pressures. The position of Si is (0,0,0) in both phases. When the square of the tilt angle (η - 90°) and of the symmetry breaking strain (e_1 - e_2) are plotted against the square of Γ_{2+}, a linear relationship is found (Figure 6.5). While such a linear relationship is expected for a pseudo-proper ferroelastic transition, it is not necessarily a diagnostic factor. In fact the evolution of ${\Gamma_{2+}}^2$ vs P , which is supposed to be linear in SiO_2 stishovite, was found to be concave in the proximity of the phase transition, similarly to the case of the symmetry breaking strain, and a linear fit is only possible above 35 GPa (Figure 6.3). The resulting transition pressure would be P_c^* = 24.1(1.9) GPa, which is consistent with the value obtained from the fit of $(e_1 - e_2)^2$ but much larger than the actual transition pressure observed by XRD.

6.3.4 High-pressure evolution of the optic soft mode

The low wavenumber region of the Raman spectra, where the B_{1g} and A_g lattice modes can be observed, is shown for Al5 (180 $\sim$ 250 cm^{-1}) and Al11 (180 $\sim$ 330 cm^{-1}) in Figure 6.6a and 6.6b, respectively. By analyzing the full width at half maximum (FWHM) of the measured Raman peaks, we observed that the peak widths remained almost constant between 0 and 20 GPa (FWHM $\sim$ 6 cm^{-1}) for data collected for Al5, while slight broadening was detected between 20 and 30 GPa for Al5 (FWHM $\sim$ 8 cm^{-1}) and between 0 and 25 GPa for Al11 (FWHM $\sim$ 8-14 cm^{-1}), where the Raman shifts of the optic modes of the two samples seem to be pressure-independent (Figure 6.6c). Further broadening of the peaks occurred above 30 GPa for Al5 and above 25 GPa for Al11, where the Raman signals could be fitted as a doublet peak. Note that, for Al5, the intensity of the peak at lower wavenumber progressively decreased at higher pressures and it is only a small shoulder at 38 GPa

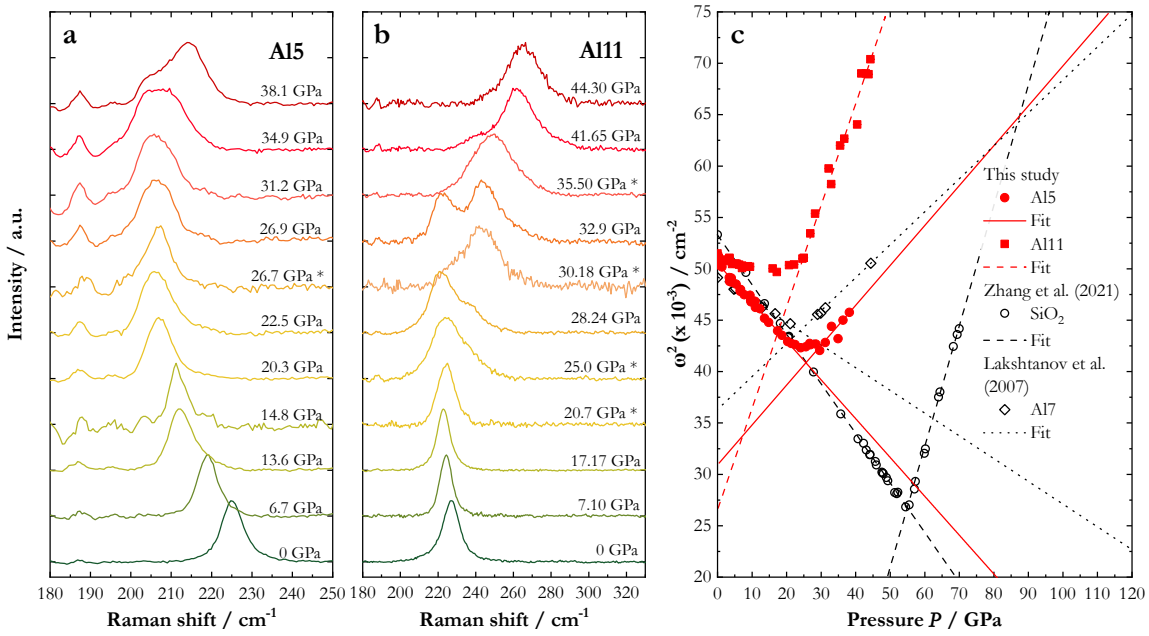

Figure 6.6. Stacked Raman spectra of (a) Al5 and (b) Al11 show the pressure evolution of the soft optic mode B_{1g} (tetragonal symmetry) and the optic mode A_g (orthorhombic symmetry). Pressures marked with an asterisk denote points collected upon decompression. The Raman shift of the B_{1g} and A_g mode of Al5 (a) keep decreasing even after Al5 became orthorhombic ($\sim$ 16 GPa) up to 20 GPa and remains almost constant between 20 and 30 GPa. Only above this pressure, the Raman shift starts to increase. In the Al11 sample (b), splitting of A_g mode occurs above 25 GPa upon compression with the peak at lower wavenumber becoming progressively less intense with increasing pressure. Upon decompression, only small shoulders, but no clear splitting, are observed in the same pressure interval, as shown by spectra collected at 35.50, 30.18 and 25.0 GPa. In (c), the squared Raman shifts of the optic modes of Al5 (red circles and solid lines) and Al11 (red squares and dashed line) are plotted against pressure and compared to the same optic mode of SiO_2 (Zhang et al., 2021, empty circles, dashed black lines) and Al,H-bearing stishovite (Lakshtanov et al., 2007b, empty diamonds, dotted black lines). A plateau between 20 and 35 GPa (Al5) and between 0 and 25 GPa (Al11) appears only in our AlOOH-rich compositions. This corroborates our hypothesis that the evolution of the optic mode is not only affected by octahedral tilting, but also by the concentration and bonding of the H atoms.

(Figure 6.6a). A similar behavior was observed for Al11 above 25 GPa (Figure 6.6b). At first, a small shoulder appeared at higher wavenumber to the main peak, then it rapidly evolved into a doublet of peaks having similar intensity, with the linewidth of the peak at higher wavenumber being approximately 1.5-2 times larger than that of the peak at lower wavenumber. Within a few GPa interval, the intensity of the peak at higher wavenumber rapidly increased while the peak at lower wavenumber disappeared (Figure 6.6b, Figure C.4). Peak splitting across the post-stishovite transformation was previously reported for SiO_2 stishovite upon compression under non-hydrostatic conditions (Kingma et al., 1995), but was not visible in a more recent study where Ne was employed as pressure transmitting medium (Zhang et al., 2021). In this study, Raman spectroscopy measurements

at the highest pressures were conducted using He as pressure transmitting medium (Table C.1), which is known to provide an even more hydrostatic environment than Ne in the pressure interval investigated in this study. In addition, single crystals used for Raman spectroscopy measurements were as thin as 10 μm. Therefore, we exclude that the observed splitting of the Raman peaks of Al5 and Al11 at pressures higher than 25 GPa is related to non-hydrostatic conditions in our DACs or bridging between diamond anvils and the samples. Moreover, in the case of Al11, the shoulder completely disappeared at higher pressure without thermally annealing the sample (Figure 6.6b, Figure C.4). We therefore suggest that the presence of two peaks in the Raman spectra is due to fluctuations of the order parameter associated with octahedral tilting. i.e. by differences in the magnitude of the order parameter between adjacent unit-cells due to their different crystal or defect chemistry. Fluctuations are invisible to XRD techniques, which provide information only on the long-range order of the crystal structure, while Raman spectroscopy probes interactions taking place at a much shorter scale and therefore is sensitive to the different local environments arising from the substitution of Si^{4+} by Al^{3+} and H^{+} or from the presence of oxygen vacancies. Since Al and H occupy only a relatively small number of unit-cells (i.e., 10% in Al5 and 22% in Al11), we can expect a distribution of unit-cells displaying different tilting at the local scale. According to our interpretation, the peak at higher wavenumber would represent more distorted environments, where the structure is more affected by the substitution of Si by Al and H, while the shoulder or peak at lower wavenumber indicates regions of the sample with a smaller degree of distortion.

Following Carpenter et al. (2000), the square of wavenumber (ω^2) of the soft optic mode of tetragonal stishovite (B_{1g}) as well as that of the A_g optic mode of orthorhombic post-stishovite have been plotted as a function of pressure for Al5 and Al11 (Figure 6.6c). In the figure, we have reported only the peak at higher wavenumber because (i) it was the most intense peak at the highest pressures and (ii) it was the dominant feature in the Raman spectra collected upon decompression (Figure 6.6a,b). It is known that some fluctuations are time-dependent and the disappearance of the shoulder with increasing pressure further supports the fluctuations hypothesis. As expected, ω^2 decreases linearly for the high-symmetry phase of Al5, as observed for pure stishovite and poorly hydrated Al-bearing stishovite (Figure 6.6c). However, after the transformation of Al5 to orthorhombic symmetry above 16 GPa, the optic mode continues to decrease following the same trend up to $\sim$ 20 GPa, then flattens and stays constant up to $\sim$ 30 GPa. Only above 30 GPa, the Raman shifts starts to increase with a slope similar in magnitude to that shown by the decreasing B_{1g} mode (Figure 6.6c). For Al11, a similar plateau in the high-pressure evolution of $\omega^2 2$ for the optic mode A_g is observed between 0 and 25 GPa (Figure 6.6c), despite the sample showing no evidence of structural phase transition in the investigate pressure range. Above this pressure, ω^2 increases linearly with a steeper slope than that shown by Al5 above 30 GPa.

6.3.5 Effect of H on the post-stishovite transition mechanism

From the combination of XRD, structural and Raman spectroscopy data, it is evident that the tetragonal-to-orthorhombic transition observed in Al5 at $\sim$ 16 GPa and the optic mode plateau between 20 and 30 GPa result from a different transformation mechanism than that of the ferroelastic transition of SiO_2 and H-poor Al-bearing stishovite. While it appears that a higher H content than reported by (Lakshtanov et al., 2007b) can further reduces the transition pressure of Al-bearing stishovite, the decoupling of the structural phase transition from the soft optic mode behavior prevents us from making a more quantitative comparison with samples investigated in previous studies. In these latter compounds, in fact, the splitting of Bragg reflections denoting the transition to the orthorhombic structure was observed at the same pressure where the trends of soft optic mode, as well as those of the soft acoustic mode, for the high-symmetry and low-symmetry phases met (Lakshtanov et al., 2007b; Zhang et al., 2021). It follows that the decoupling between the order parameter and the soft optic mode observed in this study prevents us from applying published Landau expansions for the ferroelastic transition of SiO_2 to our Al5 sample.

One possible explanation for the observed behavior could lie in the different Al/H ratios of Al-bearing silica samples investigated here (Al/H $\sim$ 2) and in the previous study of Lakshtanov et al. (2007b) (Al/H $\sim$ 4). The XRD data collected for Al5 do not allow to refine the H position in this sample, due to the fact that only $\sim$ 0.02 hydrogen atoms per formula unit are present. Given the strong anisotropy of polarized FTIR spectra observed in hydrous Al-bearing stishovite (Pawley et al., 1993; Litasov et al., 2007b; Thomas et al., 2009; Ishii et al., 2022a), the O-H vectors have been proposed to lie perpendicular to the c-axis. Based on neutron diffraction measurements on isostructural H-bearing rutile, Smyth et al. (1995) proposed that H atoms in stishovite have fractional coordinates (0.5,0.42,0). The related O$\cdots$O vectors, however, measure approximately 2.3 Å in Al-bearing silica and constitute the shortest intra-octahedral distances, corresponding to the shared edge of (Si,Al)O_6 octahedra perpendicular to the c-axis. More recent first principle calculations suggested that H atoms are bonded either to the apical (H1) or the equatorial (H2) oxygens of the octahedra that host the Al impurities, with O-H vectors actually pointing towards the empty channels of the stishovite structure (Umemoto et al., 2016). The H1 position, located in the proximity of (0.5,0,0), corresponds to the position of hydrogen in δ-AlOOH (Sano-Furukawa et al., 2018) and was found to be energetically more stable than H2 (Umemoto et al., 2016). Therefore, we argue that H atoms in the hydrous Al-bearing samples analyzed in this study are incorporated as in the isostructural compound δ-AlOOH.

In this scenario, the strain field induced by H incorporation in the structure of Al-bearing silica propagates at the local scale through the displacements of O atoms towards or away from H, causing a tilt of (Si,Al)O_6 octahedral units. If the concentration of oxygen vacancies is large enough, H atoms might not "see" each other's strain fields as some of the O atoms through which the strain field propagates are actually missing. As a consequence, the effect of H on the post-stishovite transition might be negligible in samples with a

sufficiently large Al/H ratio and the transition mechanism would result similar to that of SiO_2 stishovite (Lakshtanov et al., 2007b). The delayed response of the soft optic mode to the post-stishovite transition and the plateau of the vibrational frequencies observed in our samples would suggest that there may be two different transformations, both involving the tilting of octahedra, that take place in a relatively narrow pressure interval. Despite never being observed in stishovite samples before, a plateau of the vibrational frequencies in ferroic materials is in fact not unusual. For instance, recent resonant ultrasound spectroscopy (RUS) measurements of Co-doped Fe-pnictide at low temperature highlighted similar features, which were explained as the effect of interacting parameters driving different structural transition in a narrow temperature interval (Carpenter et al., 2019). In the light of all the above-mentioned considerations, the post-stishovite transition in H-rich Al-bearing silica cannot be regarded as a pure second-order ferroelastic transformation and further measurements of its elasticity and H-bond evolution at high pressure are required to quantitatively constrain the extent of its elastic shear softening and the involved transformation mechanism. If the observed decoupling of optic mode and structural phase transitions arises from the interaction of two order parameters related to different phase transformation, a similar behavior may be expected for H-bearing davemaoite, i.e., $CaSiO_3$ with perovskite structure. This mineral is expected to undergo a second-order ferroelastic transition from tetragonal to cubic symmetry with increasing temperature driven by octahedral tilting (e.g., Komabayashi et al., 2007; Stixrude et al., 2007). Additionally, recent in-situ IR measurements showed that the O-H stretching frequency of H-bearing $CaSiO_3$ davemaoite decreases with increasing pressure, suggesting that a H-bond symmetrization may occur at pressures of the lower mantle (Chen et al., 2020). Further investigations on the H-bond evolution and transition mechanism of H-bearing $CaSiO_3$ davemaoite may also help to understand whether the behavior observed in this study is unique to stishovite or is shared with other lower mantle mineral phases.

6.4 Implications

As discussed above, the decoupling between the soft optic mode and the structural phase transition of hydrous Al-bearing stishovite can affect the pressure interval where elastic softening associated with the ferroelastic transition occurs. The Clapeyron slope of the post stishovite transition is positive (e.g. Nomura et al. 2010; Fischer et al. 2018), meaning that the transition pressure increases with increasing temperature. We can think of two possible scenarios where the soft acoustic mode (i.e. the v_S of stishovite along the [110] direction) would be coupled either with the soft optic mode or with the octahedral tilting. In the former case, elastic softening at room temperature would be observed in pressure range of the plateau region of the soft optic mode (i.e., around 20-30 GPa) which overlaps with the transition pressure of approximately 25 GPa reported by Lakshtanov et al. (2007b). Extrapolation to subducting slab temperatures (Kirby et al., 1996; Eberle et al., 2002) would move the boundary up by approximately 10 GPa (Nomura et al., 2010) corresponding to

the pressure range where seismic scattering anomalies have been located by seismological methods in the proximity of subducting slabs (Kaneshima, 2019). In the latter case, acoustic softening would be observed in the proximity of the structural transformation (i.e., around 15 GPa) at room temperature and extrapolation to high temperature would yield a transition pressure corresponding to the very top portion of the lower mantle, where only few seismic scatterers have been observed so far. Based on our results and on previous observations, we have suggested that not only the H content but also the Al/H ratio is a critical factor in lowering the transition pressure of hydrous Al-bearing stishovite to post-stishovite. Therefore, negative dv_S anomalies associated with seismic scattering could be explained by the presence of hydrous stishovite with lower Al contents than our samples, but with similar or even lower Al/H ratios, thus closer to the SiO_2-AlOOH join. Slightly lower Al content would then be in good agreement with previous experimental phase relations studies at topmost lower mantle conditions (Ono et al., 2001; Litasov and Ohtani, 2005; Ishii et al., 2019b; Ishii et al., 2022b). Further elasticity measurements across the structural phase transformation of hydrous Al-bearing silica will allow to pinpoint the pressure range and the extent of its elastic shear softening, enabling us to evaluate its actual geophysical relevance.

Accurate EOS parameters for hydrous Al-bearing silica are also important to understand the seismic signature of Al-bearing post-stishovite and its solid solution behavior with $CaCl_2$-type AlOOH. In Figure 6.7, we compare the high-pressure evolution of K_T of our samples with those of isostructural SiO_2 and AlOOH obtained in previous studies by isothermal compression and elasticity measurements (Andrault et al., 2003; Sano-Furukawa et al., 2009; Buchen et al., 2018a; Fischer et al., 2018; Zhang et al., 2021). There is clearly a large variation in the K_T behavior among the different studies. However, when we compare our data with measurements performed under quasi-hydrostatic conditions (i.e., Zhang et al., 2021) for post-stishovite and δ-AlOOH (Sano-Furukawa et al., 2009), the K_T curves for our Al-bearing $CaCl_2$-type samples appears above both SiO_2 post-stishovite and δ-AlOOH. Note that the K_T curve of Zhang et al. (2021) is in excellent agreement with the K_S values determined for the Reuss bound (isotropic stress) in the same study using Brillouin scattering. The previous study of Buchen et al. (2018a) employed a sintered polycrystalline sample compressed in a Ne pressure medium, which was argued to represent the Voigt bound of the material (i.e., isotropic strain conditions) as the grain boundaries of the polycrystalline aggregate were locked together. This hypothesis is consistent with the fact that the KT values obtained by Buchen et al. (2018a) are in agreement with the Voigt bound of K_S calculated from the Brillouin scattering data reported by Zhang et al. (2021), although the two trends still diverge owing again to differences in $K_0^{'}$ (Figure 6.7). The K_T values predicted by Andrault et al. (2003) and Fischer et al. (2018), on the other hand, deviate more significantly from the trends observed in this study and in Zhang et al. (2021), possibly because of the use of solid pressure media (KBr, NaCl) or no pressure medium at all that can induce non-hydrostatic stress in the sample, even when thermal annealing is performed. This highlights the importance of using highly hydrostatic pressure media such

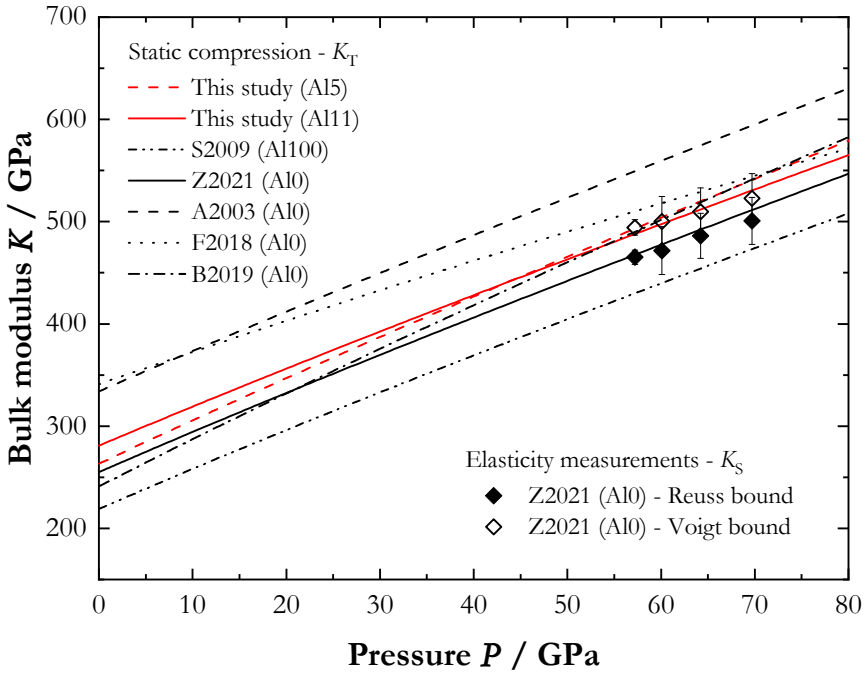

Figure 6.7. High-pressure evolution of the isothermal bulk modulus of $CaCl_2$-type pure and Al,H-bearing SiO_2, and AlOOH from this and previous studies. Z2021: Zhang et al. (2021), single-crystal XRD in DAC. A2003: Andrault et al. (2003), powder and single crystal XRD in DAC. F2018: Fischer et al. (2018), powder XRD in DAC. B2018: Buchen et al. (2018a), powder XRD in DAC. S2009: Sano-Furukawa et al. (2009), powder XRD in DAC. Labels between brackets show the Al content as Al/(Al+Si). Adiabatic bulk moduli in the Reuss (solid symbols) and Voigt (empty symbols) bounds calculated from single-crystal BS measurements of Zhang et al. (2021) are shown for comparison.

as Ne and He in compressibility and elasticity studies, especially at such high-pressure conditions. For this reason, it is difficult to accurately quantify the individual effect of Al and H substitution on the compressibility of stishovite. If we restrict our comparison to the previous studies of Zhang et al. (2021) and Sano-Furukawa et al. (2009), our results suggest that the bulk modulus behavior along the solid solution between $CaCl_2$-type SiO_2 and AlOOH is not linear since the K_T values determined for Al5 and Al11 do not plot between those of the two end-members. Therefore, we argue that excess molar properties may be non-negligible when modelling the thermodynamic stability and elastic properties of the SiO_2-AlOOH solid solutions with $CaCl_2$-type structure at lower mantle conditions.

Acknowledgments

We thank Raphael Njul and Detlef Krauße for their help with the sample preparation and assistance with electron microprobe analyses. We also thank two anonymous reviewers and a technical editor for their constructive comments that helped us to improve the manuscript.

This study was supported by DFG grant FR1555/11. We acknowledge DESY (Hamburg, Germany), a member of the Helmholtz Association HGF, for the provision of experimental facilities. Parts of this research were carried out at the Extreme Conditions Beamline P02.2, PETRA-III.

Data Availability Statement

The deposited Crystallographic Information Files (CIFs) are available at: https://figshare.com/s/b98b413187f434ab55e9.

References

Andrault, D., R. J. Angel, J. L. Mosenfelder, and T. L. Bihan (2003). "Equation of state of stishovite to lower mantle pressures". In: *American Mineralogist* 88 (2-3), pp. 301–307. DOI: 10.2138/am-2003-2-307.

Andrault, D., G. Fiquet, F. Guyot, and M. Hanfland (1998). "Pressure-induced Landau-type transition in stishovite". In: *Science* 282 (5389), pp. 720–724. DOI: 10.1126/science.282.5389.720.

Angel, R. J. (2000). "Equations of State". In: *Reviews in Mineralogy and Geochemistry* 41 (1), pp. 35–59. DOI: 10.2138/rmg.2000.41.2.

Angel, R. J. and L. W. Finger (2011). "SINGLE: A program to control single-crystal diffractometers". In: *Journal of Applied Crystallography* 44 (1), pp. 247–251. DOI: 10.1107/S0021889810042305.

Angel, R. J., J. Gonzalez-Platas, and M. Alvaro (2014). "EosFit7c and a Fortran module (library) for equation of state calculations". In: *Zeitschrift fur Kristallographie* 229 (5), pp. 405–419. DOI: 10.1515/zkri-2013-1711.

Birch, F. (1947). "Finite elastic strain of cubic crystals". In: *Physical Review* 71 (11), pp. 809–824. DOI: 10.1103/PhysRev.71.809.

Boehler, R. and K. D. Hantsetters (Sept. 2004). "New anvil designs in diamond-cells". In: *High Pressure Research* 24 (3), pp. 391–396. DOI: 10.1080/08957950412331323924.

Bolfan-Casanova, N., D. Andrault, E. Amiguet, and N. Guignot (2009). "Equation of state and post-stishovite transformation of Al-bearing silica up to 100 GPa and 3000 K". In: *Physics of the Earth and Planetary Interiors* 174 (1-4), pp. 70–77. DOI: 10.1016/j.pepi.2008.06.024.

Buchen, J., H. Marquardt, K. Schulze, S. Speziale, T. Boffa Ballaran, N. Nishiyama, and M. Hanfland (2018a). "Equation of State of Polycrystalline Stishovite Across the Tetragonal-Orthorhombic Phase Transition". In: *Journal of Geophysical Research: Solid Earth* 123 (9), pp. 7347–7360. DOI: 10.1029/2018JB015835.

Carpenter, M. A., D. M. Evans, J. A. Schiemer, T. Wolf, P. Adelmann, A. E. Böhmer, C. Meingast, S. E. Dutton, P. Mukherjee, and C. J. Howard (2019). "Ferroelasticity, anelasticity and magnetoelastic relaxation in Co-doped iron pnictide: $Ba(Fe_{0.957}Co_{0.043})_2As_2$". In: *Journal of Physics Condensed Matter* 31 (15). DOI: 10.1088/1361-648X/aafe29.

Carpenter, M. A., R. J. Hemley, and H. kwang Mao (2000). "High-pressure elasticity of stishovite and the $P4_2/mnm$ - *Pnnm* phase transition". In: *Journal of Geophysical Research* 105, pp. 807–816.

Carpenter, M. A. and E. K. Salje (1998). "Elastic anomalies in minerals due to structural phase transitions". In: *European Journal of Mineralogy* 10 (4), pp. 693–812. DOI: 10.1127/ejm/10/4/0693.

Chen, H., K. Leinenweber, V. Prakapenka, C. Prescher, Y. Meng, H. Bechtel, M. Kunz, and S.-H. Shim (2020). "Possible H_2O storage in the crystal structure of $CaSiO_3$ perovskite". In: *Physics of the Earth and Planetary Interiors* 299, p. 106412. DOI: 10.1016/j.pepi.2019.106412.

Eberle, M. A., O. Grasset, and C. Sotin (2002). "A numerical study of the interaction between the mantle wedge, subducting slab, and overriding plate". In: *Physics of the Earth and Planetary Interiors* 134 (3-4), pp. 191–202. DOI: 10.1016/S0031-9201(02)00157-7.

Fischer, R. A., A. J. Campbell, B. A. Chidester, D. M. Reaman, E. C. Thompson, J. S. Pigott, V. B. Prakapenka, and J. S. Smith (2018). "Equations of state and phase boundary for stishovite and $CaCl_2$-type SiO_2". In: *American Mineralogist* 103 (5), pp. 792–802. DOI: 10.2138/am-2018-6267.

Gonzalez-Platas, J., M. Alvaro, F. Nestola, and R. J. Angel (2016). "EosFit7-GUI: A new graphical user interface for equation of state calculations, analyses and teaching". In: *Journal of Applied Crystallography* 49 (4), pp. 1377–1382. DOI: 10.1107/S1600576716008050.

Gréaux, S., Y. Kono, Y. Wang, A. Yamada, C. Zhou, Z. Jing, T. Inoue, Y. Higo, T. Irifune, N. Sakamoto, and H. Yurimoto (2016). "Sound velocities of aluminum-bearing stishovite in the mantle transition zone". In: *Geophysical Research Letters* 43 (9), pp. 4239–4246. DOI: 10.1002/2016GL068377.

Hirose, K., N. Takafuji, N. Sata, and Y. Ohishi (2005). "Phase transition and density of subducted MORB crust in the lower mantle". In: *Earth and Planetary Science Letters* 237 (1-2), pp. 239–251. DOI: 10.1016/j.epsl.2005.06.035.

Hübschle, C. B., G. M. Sheldrick, and B. Dittrich (2011). "ShelXle: A Qt graphical user interface for SHELXL". In: *Journal of Applied Crystallography* 44 (6), pp. 1281–1284. DOI: 10.1107/S0021889811043202.

Irifune, T. and A. E. Ringwood (1993). "Phase transformations in subducted oceanic crust and buoyancy relationships at depths of 600-800 km in the mantle". In: *Earth and Planetary Science Letters* 117 (1-2), pp. 101–110. DOI: 10.1016/0012-821X(93)90120-X.

Ishii, T., G. Criniti, E. Ohtani, N. Purevjav, H. Fei, T. Katsura, and H. K. Mao (2022a). "Superhydrous aluminous silica phases as major water hosts in high-temperature lower mantle". In: *Proceedings of the National Academy of Sciences of the United States of America* 119 (44), pp. 1–6. DOI: 10.1073/pnas.2211243119.

Ishii, T., H. Kojitani, and M. Akaogi (2019b). "Phase Relations of Harzburgite and MORB up to the Uppermost Lower Mantle Conditions: Precise Comparison With Pyrolite by Multisample Cell High-Pressure Experiments With Implication to Dynamics of Subducted Slabs". In: *Journal of Geophysical Research: Solid Earth* 124 (4), pp. 3491–3507. DOI: 10.1029/2018JB016749.

Ishii, T., Z. Liu, and T. Katsura (2019c). "A Breakthrough in Pressure Generation by a Kawai-Type Multi-Anvil Apparatus with Tungsten Carbide Anvils". In: *Engineering* 5 (3), pp. 434–440. DOI: 10.1016/j.eng.2019.01.013.

Ishii, T., N. Miyajima, G. Criniti, Q. Hu, K. Glazyrin, and T. Katsura (2022b). "High pressure-temperature phase relations of basaltic crust up to mid-mantle conditions". In: *Earth and Planetary Science Letters* 584, p. 117472. DOI: 10.1016/j.epsl.2022.117472.

Ishii, T., L. Shi, R. Huang, N. Tsujino, D. Druzhbin, R. Myhill, Y. Li, L. Wang, T. Yamamoto, N. Miyajima, T. Kawazoe, N. Nishiyama, Y. Higo, Y. Tange, and T. Katsura (2016). "Generation of pressures over 40 GPa using Kawai-type multi-anvil press with tungsten carbide anvils". In: *Review of Scientific Instruments* 87 (2). DOI: 10.1063/1.4941716.

Jiang, F., G. D. Gwanmesia, T. I. Dyuzheva, and T. S. Duffy (2009). "Elasticity of stishovite and acoustic mode softening under high pressure by Brillouin scattering". In: *Physics of the Earth and Planetary Interiors* 172 (3-4), pp. 235–240. DOI: 10.1016/j.pepi.2008.09.017.

Kaneshima, S. (2019). "Seismic scatterers in the lower mantle near subduction zones". In: *Geophysical Journal International* 218 (3), pp. 1873–1891. DOI: 10.1093/gji/ggz241.

Kaneshima, S. and G. Helffrich (1999). "Dipping low-velocity layer in the mid-lower mantle: Evidence for geochemical heterogeneity". In: *Science* 283 (5409), pp. 1888–1891. DOI: 10.1126/science.283.5409.1888.

Kantor, I., V. Prakapenka, A. Kantor, P. Dera, A. Kurnosov, S. Sinogeikin, N. Dubrovinskaia, and L. Dubrovinsky (2012). "BX90: A new diamond anvil cell design for X-ray diffraction and optical measurements". In: *Review of Scientific Instruments* 83 (12), p. 125102. DOI: 10.1063/1.4768541.

Kingma, K. J., R. E. Cohen, R. J. Hemley, and H. K. Mao (1995). "Transformation of stishovite to a denser phase at lower-mantle pressures". In: *Nature* 374 (6519), pp. 243–245. DOI: 10.1038/374243a0.

Kirby, S. H., S. Stein, E. A. Okal, and D. C. Rubie (1996). "Metastable mantle phase transformations and deep earthquakes in subducted oceanic lithosphere". In: *Reviews of Geophysics* 34 (2), pp. 261–306. DOI: 10.1029/96RG01050.

Komabayashi, T., K. Hirose, N. Sata, Y. Ohishi, and L. S. Dubrovinsky (2007). "Phase transition in CaSiO3 perovskite". In: *Earth and Planetary Science Letters* 260 (3-4), pp. 564–569. DOI: 10.1016/j.epsl.2007.06.015.

Kurnosov, A., I. Kantor, T. Boffa-Ballaran, S. Lindhardt, L. Dubrovinsky, A. Kuznetsov, and B. H. Zehnder (2008). "A novel gas-loading system for mechanically closing of various types of diamond anvil cells". In: *Review of Scientific Instruments* 79 (4). DOI: 10.1063/1.2902506.

Lakshtanov, D. L., K. D. Litasov, S. V. Sinogeikin, H. Hellwig, J. Li, E. Ohtani, and J. D. Bass (2007a). "Effect of Al^{3+} and H^{+} on the elastic properties of stishovite". In: *American Mineralogist* 92 (7), pp. 1026–1030. DOI: 10.2138/am.2007.2294.

Lakshtanov, D. L., S. V. Sinogeikin, K. D. Litasov, V. B. Prakapenka, H. Hellwig, J. Wang, C. Sanches-Valle, J. P. Perrillat, B. Chen, M. Somayazulu, J. Li, E. Ohtani, and J. D. Bass (2007b). "The post-stishovite phase transition in hydrous alumina-bearing SiO_2 in the

lower mantle of the earth". In: *Proceedings of the National Academy of Sciences of the United States of America* 104 (34), pp. 13588–13590. DOI: 10.1073/pnas.0706113104.

Lakshtanov, D. L., C. B. Vanpeteghem, J. M. Jackson, J. D. Bass, G. Shen, V. B. Prakapenka, K. Litasov, and E. Ohtani (2005). "The equation of state of Al,H-bearing SiO 2 stishovite to 58 GPa". In: *Physics and Chemistry of Minerals* 32 (7), pp. 466–470. DOI: 10.1007/s00269-005-0016-3.

Liermann, H. P., Z. Konôpková, W. Morgenroth, K. Glazyrin, J. Bednarčik, E. E. McBride, S. Petitgirard, J. T. Delitz, M. Wendt, Y. Bican, A. Ehnes, I. Schwark, A. Rothkirch, M. Tischer, J. Heuer, H. Schulte-Schrepping, T. Kracht, and H. Franz (2015). "The Extreme Conditions Beamline P02.2 and the Extreme Conditions Science Infrastructure at PETRA III". In: *Journal of Synchrotron Radiation* 22, pp. 908–924. DOI: 10.1107/S1600577515005937.

Litasov, K. D., H. Kagi, A. Shatskiy, E. Ohtani, D. L. Lakshtanov, J. D. Bass, and E. Ito (2007a). "High hydrogen solubility in Al-rich stishovite and water transport in the lower mantle". In: *Earth and Planetary Science Letters* 262 (3-4), pp. 620–634. DOI: 10.1016/j.epsl.2007.08.015.

Litasov, K. D. and E. Ohtani (2005). "Phase relations in hydrous MORB at 18-28 GPa: Implications for heterogeneity of the lower mantle". In: *Physics of the Earth and Planetary Interiors* 150 (4), pp. 239–263. DOI: 10.1016/j.pepi.2004.10.010.

Litasov, K. D., E. Ohtani, A. Suzuki, and K. Funakoshi (2007b). "The compressibility of Fe- and Al-bearing phase D to 30 GPa". In: *Physics and Chemistry of Minerals* 34 (3), pp. 159–167. DOI: 10.1007/s00269-006-0136-4.

Liu, Z., M. Nishi, T. Ishii, H. Fei, N. Miyajima, T. B. Ballaran, H. Ohfuji, T. Sakai, L. Wang, S. Shcheka, T. Arimoto, Y. Tange, Y. Higo, T. Irifune, and T. Katsura (2017b). "Phase Relations in the System $MgSiO_3$-Al_2O_3 up to 2300 K at Lower Mantle Pressures". In: *Journal of Geophysical Research: Solid Earth* 122 (10), pp. 7775–7788. DOI: 10.1002/2017JB014579.

Miller, S. C. and W. F. Love (1967). *Tables of Irreducible Representations of Space Groups and Co-representations of Magnetic Space Groups*. Pruett Press, p. 1095.

Nisr, C., K. Leinenweber, V. Prakapenka, C. Prescher, S. Tkachev, and S. H. Shim (2017). "Phase transition and equation of state of dense hydrous silica up to 63 GPa". In: *Journal of Geophysical Research: Solid Earth* 122 (9), pp. 6972–6983. DOI: 10.1002/2017JB014055.

Nisr, C., H. Chen, K. Leinenweber, A. Chizmeshya, V. B. Prakapenka, C. Prescher, S. N. Tkachev, Y. Meng, Z. Liu, and S. H. Shim (2020). "Large H_2O solubility in dense silica and its implications for the interiors of water-rich planets". In: *Proceedings of the National Academy of Sciences of the United States of America* 117 (18), pp. 9747–9754. DOI: 10.1073/pnas.1917448117.

Niu, F. (2014). "Distinct compositional thin layers at mid-mantle depths beneath northeast China revealed by the USArray". In: *Earth and Planetary Science Letters* 402 (C), pp. 305–312. DOI: 10.1016/j.epsl.2013.02.015.

Nomura, R., K. Hirose, N. Sata, Y. Ohishi, D. Suetsugu, C. Bina, T. Inoue, D. Wiens, and M. Jellinek (2010). "Precise determination of post-stishovite phase transition boundary and implications for seismic heterogeneities in the mid-lower mantle". In: *Physics of the Earth and Planetary Interiors* 183 (1-2), pp. 104–109. DOI: 10.1016/j.pepi.2010.08.004.

Ono, S., K. Hirose, M. Murakami, and M. Isshiki (2002). "Post-stishovite phase boundary in SiO_2 determined by in situ X-ray observations". In: *Earth and Planetary Science Letters* 197 (3-4), pp. 187–192. DOI: 10.1016/S0012-821X(02)00479-X.

Ono, S., E. Ito, and T. Katsura (2001). "Mineralogy of subducted basaltic crust (MORB) from 25 to 37 GPa, and chemical heterogeneity of the lower mantle". In: *Earth and Planetary Science Letters* 190 (1-2), pp. 57–63. DOI: 10.1016/S0012-821X(01)00375-2.

Orobengoa, D., C. Capillas, M. I. Aroyo, and J. M. Perez-Mato (2009). "*AMPLIMODES*: Symmetry-mode analysis on the Bilbao Crystallographic Server". In: *Journal of Applied Crystallography* 42 (5), pp. 820–833. DOI: 10.1107/S0021889809028064.

Paterson, M. S. (1982). "The determination of hydroxyl by infrared adsorption in quartz, silicate glasses and similar materials." In: *Bulletin de Mineralogie* 105 (1), pp. 20–29. DOI: 10.3406/bulmi.1982.7582.

Pawley, A. R., P. F. McMillan, and J. R. Holloway (1993). "Hydrogen in stishovite, with implications for mantle water content". In: *Science* 261 (5124), pp. 1024–1026. DOI: 10.1126/science.261.5124.1024.

Petrícek, V., M. Dušek, and L. Palatinus (2014). "Crystallographic computing system JANA2006: General features". In: *Zeitschrift fur Kristallographie* 229 (5), pp. 345–352. DOI: 10.1515/zkri-2014-1737.

Prescher, C. and V. B. Prakapenka (2015). "DIOPTAS: A program for reduction of two-dimensional X-ray diffraction data and data exploration". In: *High Pressure Research* 35 (3), pp. 223–230. DOI: 10.1080/08957959.2015.1059835.

Ricolleau, A., J. P. Perrillat, G. Fiquet, I. Daniel, J. Matas, A. Addad, N. Menguy, H. Cardon, M. Mezouar, and N. Guignot (2010). "Phase relations and equation of state of a natural MORB: Implications for the density profile of subducted oceanic crust in the Earth's lower mantle". In: *Journal of Geophysical Research: Solid Earth* 115 (8). DOI: 10.1029/2009JB006709.

Salje, E. K. (1991). *Phase Transitions in Ferroelastic and Co-elastic Crystals*. Cambridge University Press. DOI: 10.1017/cbo9780511586460.

Sano-Furukawa, A., T. Hattori, K. Komatsu, H. Kagi, T. Nagai, J. J. Molaison, A. M. dos Santos, and C. A. Tulk (2018). "Direct observation of symmetrization of hydrogen bond in δ-AlOOH under mantle conditions using neutron diffraction". In: *Scientific Reports* 8 (1), pp. 1–9. DOI: 10.1038/s41598-018-33598-2.

Sano-Furukawa, A., H. Kagi, T. Nagai, S. Nakano, S. Fukura, D. Ushijima, R. Iizuka, E. Ohtahtahtani, and T. Yagi (2009). "Change in compressibility of δ-AlOOH and δ-AlOOD at high pressure: A study of isotope effect and hydrogen-bond symmetrization". In: *American Mineralogist* 94 (8-9), pp. 1255–1261. DOI: 10.2138/am.2009.3109.

Sheldrick, G. M. (2015a). "Crystal structure refinement with *SHELXL*". In: *Acta Crystallographica Section C: Structural Chemistry* 71, pp. 3–8. DOI: 10.1107/S2053229614024218.

— (2015b). "Foundations and Advances *SHELXT*-Integrated space-group and crystal-structure determination". In: *Acta Cryst* 71, pp. 3–8. DOI: 10.1107/S2053273314026370.

Shen, G., Y. Wang, A. Dewaele, C. Wu, D. E. Fratanduono, J. Eggert, S. Klotz, K. F. Dziubek, P. Loubeyre, O. V. Fat'yanov, P. D. Asimow, T. Mashimo, and R. M. Wentzcovitch (2020).

"Toward an international practical pressure scale: A proposal for an IPPS ruby gauge (IPPS-Ruby2020)". In: *High Pressure Research*, pp. 1–16. DOI: 10.1080/08957959.2020.1791107.

Smyth, J. R., R. J. Swope, and A. R. Pawley (1995). "H in rutile-type compounds: II. Crystal chemistry of Al substitution in H-bearing stishovite". In: *American Mineralogist* 80 (5-6), pp. 454–456. DOI: 10.2138/am-1995-5-605.

Stixrude, L., C. Lithgow-Bertelloni, B. Kiefer, and P. Fumagalli (2007). "Phase stability and shear softening in $CaSiO_3$ perovskite at high pressure". In: *Physical Review B - Condensed Matter and Materials Physics* 75 (2), pp. 1–10. DOI: 10.1103/PhysRevB.75.024108.

Thomas, S. M., M. Koch-Müller, P. Reichart, D. Rhede, R. Thomas, R. Wirth, and S. Matsyuk (2009). "IR calibrations for water determination in olivine, r-GeO2, and SiO_2 polymorphs". In: *Physics and Chemistry of Minerals* 36 (9), pp. 489–509. DOI: 10.1007/s00269-009-0295-1.

Umemoto, K., K. Kawamura, K. Hirose, and R. M. Wentzcovitch (2016). "Post-stishovite transition in hydrous aluminous SiO_2". In: *Physics of the Earth and Planetary Interiors* 255, pp. 18–26. DOI: 10.1016/j.pepi.2016.03.008.

Weidner, D. J., J. D. Bass, A. E. Ringwood, and W. Sinclair (1982). "The single-crystal elastic moduli of stishovite." In: *Journal of Geophysical Research* 87 (B6), pp. 4740–4746. DOI: 10.1029/JB087iB06p04740.

Zhang, Y., S. Fu, B. Wang, and J. F. Lin (2021). "Elasticity of a Pseudoproper Ferroelastic Transition from Stishovite to Post-Stishovite at High Pressure". In: *Physical Review Letters* 126 (2), p. 25701. DOI: 10.1103/PhysRevLett.126.025701.

Chapter 7

Structure and Compressibility of Fe-Bearing Al-Phase D

Giacomo Criniti[1*], Takayuki Ishii[2†], Alexander Kurnosov[1], , Konstantin Glazyrin[3], Rachel J. Husband[3], Tiziana Boffa Ballaran[1]

[1] Bayerisches Geoinstitut, University of Bayreuth, 95440 Bayreuth, Germany

[2] Center for High Pressure Science and Technology Advanced Research, 100094 Beijing, China

[3] Deutsches Elektronen-Synchrotron, 22603 Hamburg, Germany

* **Corresponding author**: giacomo.criniti@uni-bayreuth.de

† Present address: Institute for Planetary Materials, Okayama University, Misasa, Japan.

This chapter has been published as:
Criniti, G., T. Ishii, A. Kurnosov, K. Glazyrin, R. J. Husband, and T. Boffa Ballaran (2023). "Structure and Compressibility of Fe-Bearing Al-Phase D". In: *American Mineralogist 108(9)*, 1764-1772. DOI: https://doi.org/10.2138/am-2022-8559

Author contributions: G. Criniti conceived the project, characterized the Al-phase D crystals, conducted the synchrotron experiments, analyzed the data, and wrote the manuscript. T. Ishii synthesized and characterized the Al-phase D crystals, conducted the synchrotron experiments, and commented on the manuscript. A. Kurnosov conducted the synchrotron experiments and commented on the manuscript. K. Glazyrin provided assistance during the synchrotron experiments and commented on the manuscript. R.J. Husband provided assistance during the synchrotron experiments and commented on the manuscript. T. Boffa Ballaran conceived and supervised the project, conducted the synchrotron experiments, and commented on the manuscript.

Abstract

Due to its large thermal stability, Al-phase D, the $(Al,Fe^{3+})_2SiO_6H_2$ member of the dense hydrous magnesium silicate (DHMS) phase D, may survive along hot subduction geotherms or

even at ambient mantle temperatures in the Earth's transition zone and lower mantle, playing therefore a major role as water reservoir and carrier in the Earth's interior. We have investigated the crystal structure and high-pressure behavior of Fe-bearing Al-phase D with a composition of $Al_{1.53(2)}Fe_{0.22(1)}Si_{0.86(1)}O_6H_{3.33(9)}$ by means of single-crystal X-ray diffraction. While the structure of pure Al-phase D ($Al_2SiO_6H_2$) has space group $P6_3/mcm$ and consists of equally populated and half-occupied (Al,Si)O_6 octahedra, Fe-incorporation in Al-phase D seems to induce partial ordering of the cations over the octahedral sites, resulting in a change of the space group symmetry from $P6_3/mcm$ to $P6_322$ and in well-resolved diffuse scattering streaks observed in X-ray images. The evolution of the unit-cell volume of Fe-bearing Al-phase D between room pressure and 38 GPa, determined by means of synchrotron X-ray diffraction in a diamond anvil cell, is well described by a 3rd-order Birch-Murnaghan equation of state having isothermal bulk modulus K_{T0} = 166.3(15) GPa and first pressure derivative K'_{T0} = 4.46(12). Above 38 GPa, a change in the compression behavior is observed, likely related to the high-to-low spin crossover of octahedrally coordinated Fe^{3+}. The evolution of the unit-cell volume across the spin crossover was modelled using a recently proposed formalism based on crystal-field theory, which shows that the spin crossover region extends from approximately 30 to 65 GPa. Given the absence of abrupt changes in the compression mechanism of Fe-bearing Al-phase D before the spin crossover, we show that the strength of H-bonds and likely their symmetrization do not greatly affect the elastic properties of phase D solid solutions, independently of their compositions.

7.1 Introduction

The stability of dense hydrous magnesium silicates (DHMS) at high-pressure and high-temperature conditions has been extensively studied for more than 20 years as these phases yield the potential to carry and recycle water from Earth's surface to its deep interior (e.g., Frost, 2006; Nishi et al., 2014; Ohtani et al., 2014). The crystal structure of DHMS generally consists of hexagonal closest-packed (hcp) layers of O atoms with Mg and Si occupying interstitial octahedral and tetrahedral sites, respectively. However, in phase D and phase H, which are stable under mantle transition zone and lower mantle conditions, Si displays octahedral coordination, allowing partial (Yang et al., 1997b) or complete (Bindi et al., 2014) mixing with Mg to take place. Al incorporation in the crystal structures of these two phases further promotes cation mixing at octahedral sites and enhances their thermal stability, allowing Al-bearing phase D and phase H to potentially survive along hot subduction geotherms or even at ambient mantle temperatures in the transition zone and lower mantle (Ohira et al., 2014; Pamato et al., 2015).

In the end member Mg-phase D (space group $P\bar{3}1m$), with nominal composition $MgSi_2O_6H_2$, Mg and Si occupy distinct octahedral sites, named M1 and M2, respectively, located on alternated interstitial layers of the oxygen *hcp* sublattice (Yang et al., 1997b). M2 octahedra are connected with one another through one edge and to M1 octahedra through vertices, while M1 octahedra are separated from one another and share vertices with M2

octahedra (D.1a). The remaining two octahedral sites, i.e., M3 and M4, share faces with M2 and M1, respectively, and are nominally vacant in Mg-phase D. Previous studies showed that the crystal structure of phase D becomes progressively disordered in the proximity of its Al-end member (Boffa Ballaran et al., 2010; Pamato et al., 2015). As Al is incorporated in the structure of phase D via the $Mg^{2+} + Si^{4+} = 2Al^{3+}$ substitution, not only this cation substitutes in both M1 and M2, but also causes a partial redistribution of the cations in the M3 and M4 sites. In an Al-rich phase D sample having Mg + Fe = 0.3 atoms per formula unit, cation disordering was observed in the form of partially occupied, but not equally populated M2 and M3 sites, while M1 showed full occupancy and M4 appeared vacant (Boffa Ballaran et al., 2010). In Mg- and Fe-free Al-phase D (D.1b), nominally $Al_2SiO_6H_2$, the distribution of Al and Si over the cation sites is completely random (Pamato et al., 2015) and, as a consequence, the space group symmetry increases from $P\bar{3}1m$ to $P6_3/mcm$. From the structural refinement of Al-phase D, it was also found that the Pauling bond strength of O atoms is +1.42, which is significantly smaller than in Mg-phase D (i.e., +1.67) and suggests that stronger covalent bonds O–H and hydrogen bonds (or H-bonds) O$\cdots$H are formed as a result of Al substitution and cation disordering.

In a recent publication, the pressure induced symmetrization of H-bonds was reported in $CaCl_2$-structured δ-AlOOH (Sano-Furukawa et al., 2018). Phase δ is stable in hydrous basaltic systems at lower mantle pressures, where it forms solid solutions with $MgSiO_4H_2$ phase H (Ohira et al., 2014; Liu et al., 2019a). Owing to its strong symmetric H-bonds, the bulk modulus of δ-AlOOH was found to substantially increase across the symmetrization (Sano-Furukawa et al., 2009; Satta et al., 2021), to the point that the presence of δ-H solid solutions in hydrous subducted basalt can produce a 1.5% increase in its seismic velocities with respect to dry basalt at topmost lower mantle pressures (Satta et al., 2021). While it is still controversial whether a pressure induced H-bond symmetrization takes place in Mg-phase D and whether it affects its elastic properties (Hushur et al., 2011; Rosa et al., 2013), H-bonds in Al-phase D are known to be stronger than in Mg-phase D already at ambient conditions (Pamato et al., 2015). However, previous experimental studies on the compressibility of phase D were conducted only on samples rich in Mg, hampering our understanding of how strongly the H-bonds affect the bulk modulus systematics of phase D solid solutions and whether the H-bond symmetrization influences the high-pressure structural evolution of phase D, similarly to what has been observed for phase δ-H. To assess this possibility, we investigated the crystal structure of single-crystal Fe-bearing Al-phase D at ambient conditions using X-ray diffraction, with particular emphasis on the relation between cation disordering and strength of H-bonds. Additionally, the high-pressure behavior of Fe-bearing Al-phase D was determined for the first time using diamond anvil cells (DACs) and synchrotron X-ray diffraction, providing insights on the relation between H-bond symmetrization, spin state of Fe, and elasticity of phase D solid solutions at high pressure.

7.2 Experimental Methods

7.2.1 Sample synthesis and characterization

Fe-bearing Al-Phase D was synthesized at 27 GPa and 1673 K in the 15-MN Kawai-type multi-anvil apparatus with the Osugi-type (DIA) guide block system, IRIS-15, installed at the Bayerisches Geoinstitut, University of Bayreuth (Ishii et al., 2016; Ishii et al., 2019c; Liu et al., 2017b). The starting material, consisting of a finely ground mixture of SiO_2, $Al(OH)_3$ and Fe_2O_3 in molar proportion 2:6:1, was loaded in a Pt tube capsule that was then sealed by welding. A $LaCrO_3$ heater was inserted in a Cr_2O_3-doped MgO octahedron with 7 mm edge length, which served as pressure medium. WC cubes having 3 mm truncated edge length were employed for high pressure generation and compressed to a load of 13 MN. The sample was heated for 3 h, quenched by cutting the electric power supply and slowly decompressed to ambient conditions in 12 h. The recovered sample consisted of coexisting Fe-bearing Al-phase D (light brown color and up to approximately 150 μm in their longest directions) and δ-(Al,Si,Fe)OOH (brown-blue pleochroism under polarized light and up to 200 μm in size), identified by single-crystal X-ray diffraction.

Inclusion free samples of Fe-bearing Al-phase D were embedded in epoxy for textural and chemical analyses. Backscattered electron (BSE) images were acquired using a LEO Gemini 1530 scanning electron microscope (SEM) and showed that the samples are chemically homogeneous. The chemical compositions of several phase D crystals were determined using a JEOL JXA-8200 electron probe microanalyzer (EPMA) operated at

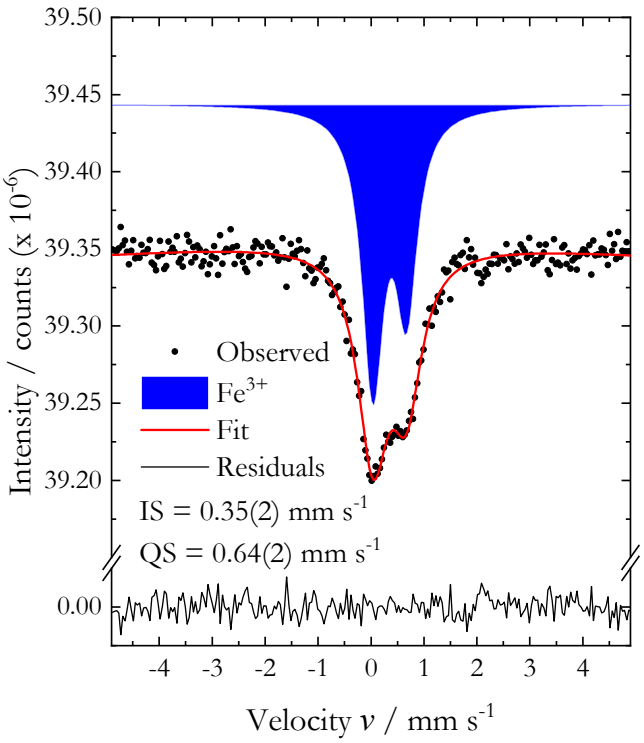

Figure 7.1. Mössbauer spectrum of Fe-bearing Al-phase D. The spectrum was fit to a single Lorentzian doublet that was assigned to octahedrally coordinated Fe^{3+} (blue area). The asymmetry of the doublet likely arises from the fact that the sample consisted of a mosaic of few single crystals, rather than a fine powder with completely randomly oriented crystallites. Although the candidate $P6_322$ and $P\bar{3}1m$ space groups have multiple octahedral sites occupied by Fe^{3+}, we used a single Lorentzian doublet to fit the transmission spectrum due to the non-distorted shape and very similar volumes of octahedra (similar crystal field).

an acceleration voltage of 15 kV and a beam current of 5 nA. Enstatite was used as a standard for Si, corundum for Al and metal iron for Fe, while the H_2O concentration was determined as the difference between 100% and the observed EPMA totals. The average composition was calculated from a total of 51 measurements on 6 different crystals and resulted to be $Al_{1.53(2)}Fe_{0.22(1)}Si_{0.86(1)}O_6H_{3.33(9)}$, where the numbers between parentheses indicate one standard deviation on the last digit. To determine the valence of Fe in the sample, Mössbauer spectroscopy (MS) measurements were performed on a mosaic of several hand-picked single crystals of Fe-bearing Al-phase D using a constant acceleration spectrometer in combination with a point ^{57}Co source (McCammon, 1994). A Ta mask with a 500 μm hole was applied in front of the sample because of the limited amount of material available. The Mössbauer spectrum of Fe-bearing Al-phase D (Figure 7.1) was collected over 7 days and fitted with one asymmetric Lorentzian doublet using *MossA* (Prescher et al., 2012). The determined isomer shift (*IS*) of 0.34(2) mm/s and quadrupole splitting (*QS*) of 0.63(2) mm/s are consistent with those of Fe^{3+} found in previous studies for Fe-Al-bearing Mg-phase D samples (Chang et al., 2013; Wu et al., 2016).

7.2.2 Single-Crystal X-Ray Diffraction at Ambient Conditions

Single crystals of Fe-bearing Al-phase D were observed under a polarizing microscope and selected for X-ray diffraction measurements based on their sharp optical extinction and the absence of visible twinning and inclusions. A crystal with dimensions 120 x 70 x 60 μm^3 was analyzed at ambient conditions using a Huber single-crystal diffractometer equipped with a point detector and operated by the *SINGLE* software (Angel and Finger, 2011) for precise and accurate lattice parameters determination. The diffractometer employed a Mo$K\alpha$ tube operated at 50 kV and 40 mA. Typical diffraction profiles measured upon ω-scan rotations showed full width half maxima (FWHM) ranging between 0.05° and 0.08°. The unit-cell lattice parameters were determined by vector least-square fitting of 22 reflections, each centered in 8-positions (King and Finger, 1979; Ralph and Finger, 1982) yielding a = 4.74653(13) Å, c = 4.29002(19) Å and V = 83.703(6) Å^3. Intensity data for the same crystal were collected on a Xcalibur diffractometer (Rigaku, Oxford Diffraction) equipped with a Sapphire2 CCD detector and graphite-monochromatized Mo$K\alpha$ radiation operated at 50 kV and 40 mA. X-ray scans were acquired upon ω-rotations of the crystal up to $2\theta_{max}$ = 90° with exposure times of 5 s or 15 s at low and high 2θ, respectively. *CrisAlysPro* (Rigaku, Oxford Diffraction) was used for data processing, which included integration of intensities, correction for Lorentz and polarization factors, frame scaling and empirical absorption correction based on spherical harmonics. The obtained average redundancy of unique reflections was 6.2 in the Laue class $\bar{3}m$. The space groups $P6_3$, $P6_3/m$ and $P6_322$ resulted compatible with the analysis of systematic absences. In addition, we also tested a structural model having space group $P\bar{3}1m$, i.e., the same as Mg-Phase D. No evidence for polytypism along the c* axis was found through the analysis of unwarp images of reciprocal planes $h0l$ and $h1l$. However, strong diffuse scattering was observed in the $hk1$, $hk3$, etc. reciprocal planes (Figure 7.2), as discussed later. For the hexagonal space groups, structure solutions were performed

using the dual-space algorithm *SHELXT* (Sheldrick, 2015b) and each structural model was refined against F^2 using *SHELXL* (Sheldrick, 2015a) in the *ShelXle* GUI (Hübschle et al., 2011). As Al-phase D has only partially occupied cationic sites, in our structural refinement we assumed Al, Si and Fe to be completely disordered in each site and their cation fractions to be $X_{Al} : X_{Si} : X_{Fe} = 0.59 : 0.33 : 0.08$, as determined by EPMA. The total occupancy of each site was then refined independently. Mean atomic numbers (m.a.n.) for each site were finally calculated by multiplying the site occupancy factors obtained in our structural models by the fraction X_i of each cation (i = Al, Si, Fe) and its atomic number. In their final cycles, structural refinements for all space groups resulted in discrepancy factors ($R1$) not exceeding 5.1%, with the exception of $P6_3/m$ ($R1 > 20\%$). Further details on the structural models with space groups $P6_322$ and $P\bar{3}1m$ are provided in the deposited Crystallographic Information File (CIF). An attempt was also made for the $P6_322$ space group to refine the distribution of cations among the different crystallographic sites without constraining the cation fraction but simply using restraints on the chemical composition, in order to shed light on potential order of Fe vs Al + Si. However, due to the lack of information on the total occupancy of the sites, which are only partially occupied, the resulting model was less stable than the one described above, showing an increased $R1 = 8.6\%$ and negative occupancy factors for some of the sites. Therefore, this structural model was discarded.

7.2.3 Single-Crystal X-Ray Diffraction at High Pressure

In order to study the compressibility of Fe-bearing Al-phase D, we performed single-crystal X-ray diffraction measurements in a DAC up to $\sim$ 52 GPa at the Extreme Conditions Beamline (ECB) P02.2 of PETRA-III (Hamburg, Germany). Two runs were performed using either 8 x 3 μm^2 or 2 x 2 μm^2 (FWHM) X-ray beams of 25.6 and 42.7 keV respectively, and a Perkin-Elmer XRD 1621 flat panel detector (Liermann et al., 2015). The sample-detector distance was calibrated using polycrystalline CeO_2 and the instrument parameters for single-crystal X-ray diffraction were refined using a natural enstatite standard. To generate high pressures, BX-90 type DACs capable to provide opening angles of up to 90° (Kantor et al., 2012) were employed together with Almax-Boehler diamonds (Boehler and Hantsetters, 2004) having culets of 350 μm (run 1) or 250 μm (run 2) in diameter and WC seats with large ($\sim$ 80°) opening angle. According to the target pressure of each run, i.e., $\sim$ 38 GPa in run 1 and 52 GPa in run 2, a Re gasket was indented to 53 or 35 μm, respectively, and laser-drilled to create the sample chamber. The same high-quality single-crystal of Fe-bearing Al-phase D of approximately 20 x 10 x 10 μm^3 was employed for both runs. A ruby sphere serving as the pressure standard (Shen et al., 2020) and a piece of Au for fine alignment of the DAC under the X-ray beam were also placed in the sample chambers next to the crystal. Pre-compressed He at 0.13 GPa was loaded as quasi-hydrostatic pressure transmitting medium in both runs using the gas loading system installed at the Bayerisches Geoinstitut, University of Bayreuth (Kurnosov et al., 2008). Pressure was increased online using a gas-driven membrane up to approximately 38 GPa (run 1) and 52 GPa (run 2) with steps of 2-4 GPa. X-ray scans were collected upon continuous ω rotation of the DAC

between -35° and +35°, with steps of 0.5° and an exposure time of 1 s. Data analysis was performed using *CrisAlysPro* (Rigaku, Oxford Diffraction) following the same procedure described for *in-house* measurements at room pressure. In addition to high-pressure measurements, another single-crystal grain with a diameter of less than 20 μm was also measured at ambient conditions at the same beamline to analyze its crystal structure. To do so, the crystal was placed on the culet of a DAC without loading (i.e., the crystal was still at room pressure) and intensity data were collected following the same procedure employed for high-pressure measurements and described above. The measured unit-cell lattice parameters for this crystal are a = 4.7469(4) Å, c = 4.2891(6) Å, and V = 83.698(17) Å^3, in very good agreement with in-house measurements. Further information can be found in the deposited CIF.

7.3 Results and discussion

7.3.1 Crystal Structure of Fe-Bearing Al-Phase D

Three of the four structural models that were tested in this study, i.e. $P\bar{3}1m$, $P6_3$ and $P6_322$, yielded discrepancy factors ($R1$) of 5% or less. Models having $P6_3$ and $P6_322$ space groups resulted in identical structural parameters (atomic positions and site occupancy factors) within uncertainties. Therefore, only the higher symmetry space group $P6_322$ will be discussed as it employs a smaller number of refined parameters. In Mg-bearing Al-phase D ($P\bar{3}1m$ space group) analyzed by Boffa Ballaran et al. (2010), mean atomic numbers (m.a.n.) were calculated by allowing the site occupancy factor (s.o.f.) of a given site to be refined and subsequently multiplying the s.o.f. by the number of electrons of the scattering factors (for Si or Al) used to refine the occupancy at a given site. In this way, it was possible to quantify the amount of charge present in the M1, M2, and M3 sites of their phase D sample independently of the atomic species (i.e., Mg, Al, Si, or Fe) which were actually present at that site. Boffa Ballaran et al. (2010) found in that way that the m.a.n. of M2 is larger than that of M3, i.e., the adjacent octahedral site that shares faces with M2 perpendicular to the c-axis (Figure D.1a). The cation distribution in their sample indicates that within a given unit cell there is a higher probability that Si and Al atoms occupy edge sharing octahedra on the same interstitial layer rather than face-sharing sites on adjacent layers. This arrangement seems to change, however, in the Fe-bearing Al-phase D sample analyzed in this study, as in both the $P\bar{3}1m$ and $P6_322$ space groups, all the cationic sites were found to be partially occupied and with different m.a.n. It follows that Fe-bearing Al-phase D (Figure D.1c) represents an intermediate configuration between those of Mg-bearing (Figure D.1a) and Fe-free Al-phase D (Figure D.1b), where all sites are equally populated and with almost identical m.a.n.

The main differences between the $P\bar{3}1m$ and $P6_322$ models analyzed here consist of: (i) a shift in the origin of the unit cell of the $P6_322$ model by (1/3, 1/3, 1/4) with respect to that of the $P\bar{3}1m$ model and (ii) an apparently different distribution of the cations over the

four crystallographic sites, resulting from different site occupancy factors and point group symmetry at the cation sites. In the trigonal model, the face-sharing octahedral sites M2 and M3 (Figure D.1a) exhibit m.a.n. of 8.10(7) and 4.27(5) respectively, while M1 and M4, which are also face-sharing, have m.a.n. equal to 9.71(8) and 2.50(7). In the space group $P6_322$, on the other hand, only three distinct cation sites exist (Figure D.1c). The first site has Wyckoff position 2b and its symmetry-equivalent coordinates are (0, 0, 1/4) and (0, 0, 3/4), resulting in a chain of equivalent face-sharing octahedra aligned along the *c*-axis (Figure D.1c). The m.a.n. of the 2b site is 6.23(7), meaning that its occupancy factor is approximately 43%. The other two sites have Wyckoff positions 2c and 2d and occupy the two remaining octahedral sites. These two sites lie at $x = 1/3$, $y = 2/3$ and $x = 2/3$, $y = 1/3$ of each interstitial layer, with their x and y coordinates swapping every interstitial layer. This means that in the first layer, where $z = 1/4$, 2c lies at (1/3, 2/3, 1/4) and 2d at (2/3, 1/3, 1/4), while in the second layer, having $z = 3/4$, 2c is located at (2/3, 1/3, 3/4) and 2d at (1/3, 2/3, 3/4). In other words, 2c octahedra share edges with 2d octahedra that are in the same interstitial layer and share faces with 2d octahedra lying on adjacent layers, and vice versa (Figure D.1c). The m.a.n. refined for the 2c and 2d sites are 2.99(8) and 9.33(9), respectively, which correspond to site occupancy factors of approximately 21% and 65%, respectively. This configuration differs from that of Mg-bearing Al-phase D (Boffa Ballaran et al., 2010), where M2 and M3 sites are located on different interstitial layers (Figure D.1a) and may occur because of the smaller ionic radius of Fe^{3+} relative to Mg^{2+}, which favors cation mixing. For comparison, we determined the m.a.n. of the cation sites in the space group $P6_322$ for the sample measured at ambient conditions at the ECB P02.2 and obtained values of 6.36(7), 3.58(7) and 9.19(12) for 2b, 2c and 2d, respectively, which are in fair agreement with those determined from in-house measurements. The total number of Al, Si and Fe cations for 6 oxygens calculated from the site occupancy factors determined from in-house and synchrotron data falls within a ±2% interval relative to that determined by EPMA. The m.a.n. of the 2b and 2d sites in the two samples are the same within mutual uncertainties, while that of 2c is higher in the sample measured at the ECB P02.2. This could indicate, for instance, that the degree of cation disordering in the two samples is slightly different.

Hamilton (1965) proposed a statistical test to assess whether the increase in the number of parameters between similar structural models produces a statistically significant improvement in the quality of the structural refinement. One condition to apply Hamilton's test is that the number of unique reflections in the two structural models is the same. This condition is not fulfilled by the space groups $P6_322$ and $P\bar{3}1m$ since they belong to different Laue classes and thus have different averaging rules. If the test is conducted while neglecting this condition, the hypothesis that the hexagonal model better represents the actual atomic configuration is rejected at a 0.005 significance level, meaning that the trigonal model should be used. A way to properly apply Hamilton's test would be to compare the hexagonal and trigonal structural models refined against non-merged datasets. In this case, the number of reflections is the same by definition as long as the reflection file in the two refinements is the same. This procedure yielded a slightly larger weighted R factor for the

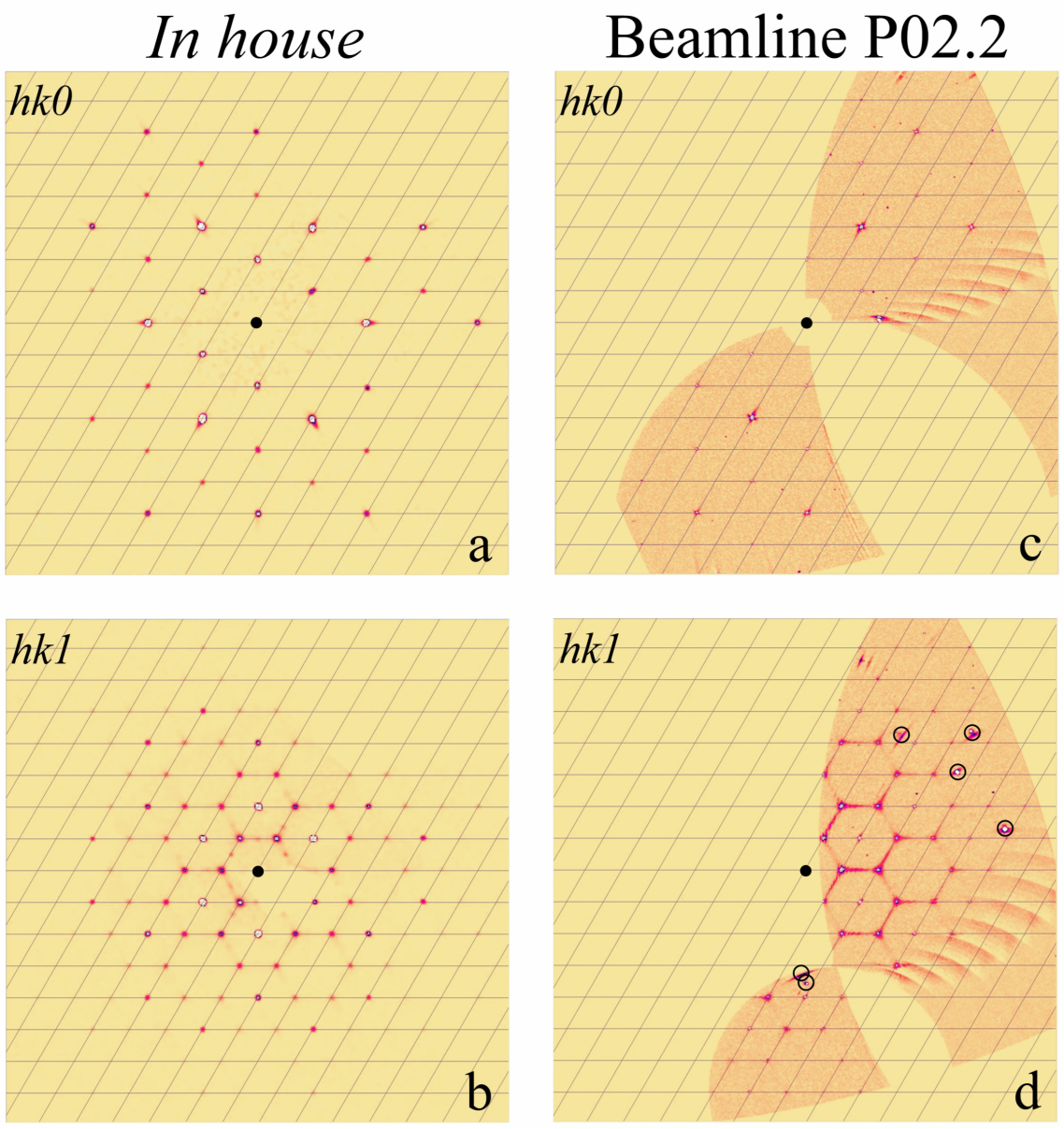

Figure 7.2. Unwarp images of the reciprocal space of Fe-bearing Al-phase D samples obtained from single-crystal X-ray diffraction measurements in-house (a,b) and at the ECB P02.2 in Hamburg (c,d). When l = 2n (e.g., $hk0$ in a and c), no diffuse scattering is observed between neighboring reflections. When l = 2n + 1 (e.g., $hk1$ in b and d) diffuse scattering streaks are observed between neighboring reflection for which $h - k \neq 3n$. The black dot at the center of each image denotes the origin of the plane in reciprocal space. Black circles in (d) denote reflections from the diamond anvil where the crystal was placed in order to be measured at the ECB P02.2.

$P\bar{3}1m$ model relatively to the $P6_322$ model. Therefore, in the case of non-merged intensities, the hypothesis that the hexagonal model better represents the actual atomic configuration cannot be rejected. The apparent contradiction between the two approaches to Hamilton's test prevents us from drawing any conclusion on which model is the most suitable to describe the structure of Fe-bearing Al-phase D.

Like previously analyzed Al-rich phase D samples, we observed no long-range octahedral distortion, with M-O distances being all identical to each other within uncertainties. As pointed out by Boffa Ballaran et al. (2010), this does not exclude that distortions can arise at the local scale due to the fact that in each given unit cell only three of the six cationic sites must be occupied so that charge balance is preserved. Boffa Ballaran et al. (2010) ruled out the possibility of cation ordering in their Mg-bearing Al-phase D sample due to absence of additional peaks in the X-ray diffraction scans that would indicate the presence of a superstructure. However, weak diffuse scattering was observed in electron diffraction images, suggesting that short range ordering of the cations might exist at the nanoscale. Our Fe-bearing Al-phase D sample, on the other hand, shows much stronger diffuse scattering streaks that are well visible in X-ray diffraction images. Unwarps obtained by integration of X-ray scans collected both in-house and at the beamline P02.2 show that diffuse scattering is localized in reciprocal planes having odd l indices and only between reflections that satisfy the conditions h - k = 3n + 1 or h - k = 3n + 2, where n is an integer number (Figure 7.2). If we consider the space group $P6_322$, the first condition rules out any influence of the cation site 2b, for which the reflection condition of any hkl reflection is l = 2n. When h - k = 3n and l = 2n + 1, i.e., when the contribution of Wyckoff positions 2c and 2d to the structure factor is null, no diffuse scattering streaks are observed around the peaks. Therefore, diffuse scattering must originate from the short-range ordering of cations in 2c and 2d. On the other hand, in the trigonal space group $P\bar{3}1m$, there is no extinction rule for any atomic position due to the absence of additional translational symmetry. Therefore, it would be difficult to reconcile such a peculiar type of diffuse scattering with partial ordering of cations over the four available octahedral sites of the trigonal structure. Our analysis of diffuse scattering thus suggests that the hexagonal space group is more suitable to describe the crystal structure and partial ordering of Fe-bearing Al-phase D. Owing to the difference in wavelength between in-house and synchrotron experiments, the types of diffuse scattering observed in the diffraction patterns have slightly different features, as short wavelengths can probe displacements at higher resolution. In fact, in the unwarps from synchrotron measurements, homogeneous streaks are found to connect the main reflections (Figure 2d), while weak additional peaks appear at 1/2 or 1/3 fractional positions between the main reflections in the unwarps obtained from in-house measurements (Figure 2b).

From our structural model, the bond valence analysis of oxygen atoms can also be performed following the example of Pamato et al. (2015). We employed the computer software SPuDS (Lufaso and Woodward, 2001) to compute the effective charge of each bond using the interatomic distances and site occupancy factors for each cation site that were

obtained from our structural models. Note that because Al, Si and Fe coexist in the same crystallographic sites, the contribution of each cation to the bond valence was weighted by their abundances, X_i, with i = Al, Si, Fe. We obtained an effective Pauling bond strength of +1.42 from both the $P\bar{3}1m$ and $P6_322$ models, which is identical to that determined for Al-phase D (Pamato et al., 2015) and larger than Mg-rich compositions (Yang et al., 1997b; Boffa Ballaran et al., 2010), supporting the hypothesis that cation disordering seems to induce stronger H bonds. In Mg-phase D, H-bonds are oriented along the edges of the vacant octahedral sites M3 and M4 (Figure D.1a) and their respective O$\cdots$O distance is 2.675 Å (Yang et al. 1997). The O$\cdots$O distance measured along the edges of octahedra of pure Al-phase D is 2.655(3) Å (Pamato et al., 2015), while for Fe-bearing Al-phase D it is 2.665(1) Å, which are both smaller than in Mg-phase D since the spacing between O layer stacked perpendicular to the c-axis is also smaller. For comparison, O$\cdots$O distances at ambient conditions in phase H and phase δ-AlOOH are 2.461(4) and 2.5479(12) Å, respectively. Phase δ is known to undergo H-bond disordering, followed by symmetrization, only when the O$\cdots$O distances drop below the critical value of 2.443 Å (Meier et al. 2022). Therefore, it is unlikely that H-bonds in Al-phase D samples are symmetric, as they are approximately 4% larger than in phase δ and 9% larger than the critical value of 2.443 Å.

7.3.2 Equation of State of Fe-Bearing Al-Phase D

The evolution of the unit-cell volume and lattice parameters of Fe-bearing Al-phase D (Table 7.1) is displayed in Figure 7.3. A slight change in slope of the volume variation with pressure is observed above 38 GPa. For this reason the volume compression of Fe-bearing Al-phase D has been first modeled between room pressure and 38 GPa by fitting the pressure-volume (P-V) data set to both a 3$^{\text{rd}}$-order Birch-Murnaghan (BM3) (Birch, 1947) and a Vinet (Vinet et al., 1989) equation of state (EOS). Following a similar approach, we use linearized BM3 and Vinet equations of state to fit the pressure evolution of individual unit-cell parameters (l) of Fe-bearing Al-phase D, where V was substituted by the cube of the unit cell parameters (l^3), $3K_{\text{T0}}$ by the axial modulus M_{l0} and $3K'_{\text{T0}}$ by the axial modulus pressure derivative M'_{l0} (Angel, 2000; Angel et al., 2014). Fitting was performed using the *EosFit7c* library implemented in *EosFit7*-GUI (Angel et al., 2014; Gonzalez-Platas et al., 2016) and fitting parameters are reported in Table 7.2. The EOS parameters values obtained from the two equation of states formalisms are identical within their mutual uncertainties (Table 7.2) resulting in volume and linear EOSs perfectly overlapping in the pressure range considered (i.e., 0.0001-38 GPa). Therefore, for clarity, only the curves derived from the BM3 fits are shown in Figure 7.3. The fitted V_0 is in very good agreement (i.e., within one standard deviation) with the unit-cell volume measured in-house and at the beamline P02.2 at room pressure. Alternative fits where the unit-cell volume and lattice parameters were fixed to the values measured at ambient conditions are also provided in Table 7.2, showing only slight variations in the refined moduli and pressure derivatives, typically identical within their mutual uncertainties. Consistently with previous observations on Mg-rich phase D in this pressure range, we observe that the a-axis is more compressible than the

Table 7.1. Unit-cell lattice parameters of Fe-bearing Al-phase D as a function of pressure. P was calculated as the mean between values measured before and after XRD measurements using the ruby fluorescence shift (Shen et al., 2020), with σP being their semi-difference.

Run number	P (GPa)	σP (GPa)	a (Å)	σa (Å)	c (Å)	σc (A)	V (Å^3)	σV (Å^3)
1	0.35	0.02	4.7430	0.0005	4.2873	0.0003	83.525	0.017
1	1.02	0.02	4.7376	0.0004	4.2797	0.0005	83.186	0.015
1	3.35	0.08	4.7172	0.0004	4.2577	0.0004	82.050	0.015
1	5.25	0.07	4.7020	0.0006	4.2408	0.0005	81.196	0.016
1	7.56	0.08	4.6850	0.0004	4.2215	0.0003	80.247	0.016
1	10.66	0.08	4.6653	0.0004	4.2000	0.0003	79.165	0.016
1	13.64	0.16	4.6435	0.0004	4.1774	0.0003	78.007	0.012
1	16.44	0.04	4.6263	0.0006	4.1604	0.0004	77.112	0.016
1	18.36	0.09	4.6148	0.0004	4.1482	0.0003	76.506	0.011
1	19.16	0.08	4.6088	0.0004	4.1427	0.0003	76.205	0.012
1	21.41	0.08	4.5958	0.0004	4.1294	0.0003	75.535	0.011
1	24.66	0.23	4.5779	0.0005	4.1120	0.0003	74.631	0.013
1	27.66	0.11	4.5617	0.0005	4.0964	0.0004	73.821	0.014
1	30.50	0.12	4.5481	0.0007	4.0835	0.0004	73.152	0.017
1	32.79	0.09	4.5346	0.0006	4.0717	0.0004	72.509	0.015
1	35.32	0.10	4.5234	0.0007	4.0595	0.0005	71.935	0.017
1	37.92	0.09	4.5101	0.0007	4.0475	0.0005	71.302	0.018
2	5.84	0.02	4.6985	0.0002	4.2356	0.0013	80.98	0.02
2	9.23	0.02	4.6715	0.0002	4.2093	0.0013	79.55	0.02
2	23.07	0.04	4.5852	0.0003	4.1200	0.0020	75.01	0.04
2	33.30	0.05	4.5295	0.0005	4.0715	0.0018	72.36	0.03
2	40.75	0.05	4.4912	0.0006	4.0300	0.0020	70.43	0.04
2	42.42	0.05	4.4840	0.0007	4.0215	0.0020	70.05	0.04
2	45.96	0.05	4.4677	0.0006	4.0060	0.0020	69.27	0.03
2	49.41	0.08	4.4509	0.0006	3.9890	0.0020	68.47	0.04
2	52.41	0.05	4.4372	0.0006	3.9780	0.0030	67.91	0.05

c-axis (Table 2), despite the difference between the two axial moduli (M_{a0} = 539 GPa and M_{c0} = 421 GPa) being smaller than in Mg-phase D (M_{a0} = 546-669 GPa and M_{c0} = 322-326 GPa) (Rosa et al., 2013; Wu et al., 2016) and Fe,Al-bearing Mg-phase D (M_{a0} = 545-634 GPa and M_{c0} = 216-326 GPa) (Chang et al., 2013; Wu et al., 2016). In fact, although the room pressure value of the c/a ratio for Fe-bearing Al-phase D is similar to those reported in previous studies for Fe-bearing Mg-phase D samples, this changes by only 0.8% upon compression from room pressure to 38 GPa (0.904 to 0.897), which is much less than values of 2.2% and 3.3% determined for pure and Fe-bearing Mg-phase D, respectively (Frost and Fei, 1999; Litasov et al., 2008; Hushur et al., 2011; Chang et al., 2013; Rosa et al., 2013; Wu et al., 2016). A possible reason for these two different behaviors is that all cation sites in Al-phase D are at least partially occupied and are geometrically more regular than in Mg-phase D (Figure D.1b-c), which can lead to a less anisotropic compression mechanism of the two interstitial layers relative to Mg-rich compositions, where nominally vacant sites exist, and

Mg and Si cations occupy different layers (Figure D.1a).

A large number of experimental studies were aimed at constraining the compression behavior of pure and Fe,Al-bearing Mg-phase D (Table 7.3, Figure D.2). Our results show that the bulk modulus of Fe-bearing Al-phase D falls toward the higher boundary of the range of values proposed for Mg-phase D (143-168 GPa, Frost and Fei, 1999; Hushur et al., 2011; Rosa et al., 2012; Rosa et al., 2013). Only one study (Wu et al., 2016) reports a much higher bulk modulus of 179(1) GPa, which is likely related to the use of a 2nd-order BM EOS (i.e. K'_{T0} = 4) to fit the data. In contrast, all other studies suggest that Mg-phase D, as well as Fe-bearing Mg-phase D have a first pressure derivative larger than 4. The lower values of K_{T0} for Mg-phase D are confirmed by a single crystal X-ray diffraction study (Rosa et al., 2013) and a single-crystal Brillouin scattering study (Rosa et al., 2012) on Mg-Phase D samples with very similar compositions that reported consistent values of K_{T0} =151(1) and K_{T0} =149(3) GPa, respectively. Xu et al. (2020) recently determined the pressure and temperature dependence of the sound velocities of Al-bearing Mg-phase D by ultrasonic interferometry and synchrotron X-ray powder diffraction, suggesting that Al incorporation in phase D decreases the bulk modulus of Mg-phase D at ambient conditions. Note, however, that when the tradeoff between K_{T0} and K'_{T0} is taken into account, the range of values determined for phase D in previous studies (Litasov et al., 2007b; Litasov et al.,

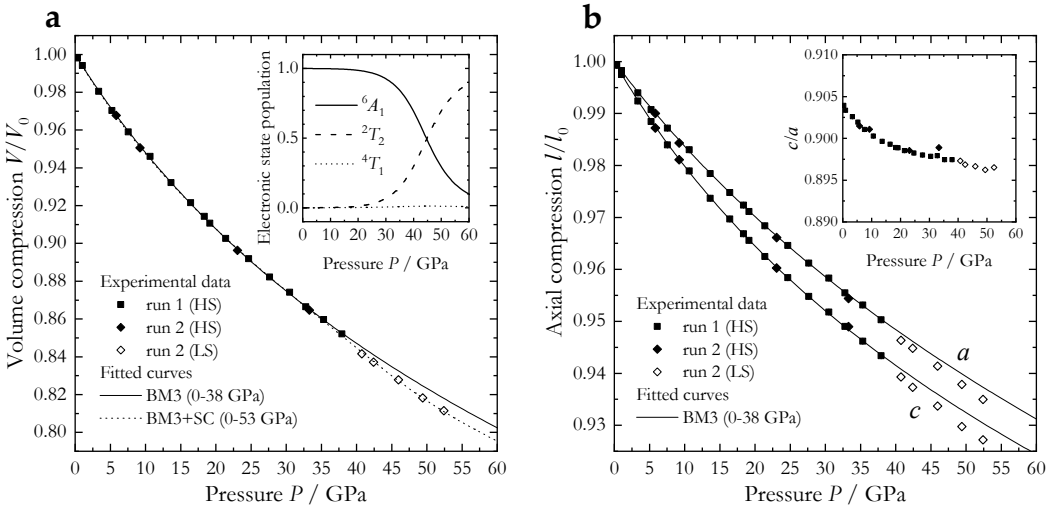

Figure 7.3. Volume (a) and axial (b) compression data of Fe-bearing Al-phase D collected over two separate runs. Solid squares and diamonds represent the high spin phase, while open diamonds represent the low spin phase. Error bars are not shown as they are smaller than the symbols. Solid lines represent 3rd-order Birch-Murnaghan (BM3) equations of state (EOS) fits between 0 and 38 GPa, while the dashed line in (a) indicates the modified BM3 EOS fit of all data accounting for the spin-crossover of Fe^{3+}. In the inset in (a), the population of the three most relevant electronic states is modelled as a function of pressure based on the crystal field parameters used to fit the P-V data. The inset in (b) shows that the c/a ratio of Fe-bearing Al-phase D only slightly decreases with pressure and is barely affected by the onset of the spin crossover.

Table 7.2. Fit parameters of 3rd-order Birch-Murnaghan (BM3), Vinet, and spin-crossover equations of state for Fe-bearing Al-phase D. Values in italics were fixed in the fit.

Low-spin state EOS										
EOS type	P range (GPa)	V_0 (Å^3)	K_{T0} (GPa)	K'_{T0}	a_0 (Å)	M_{a0} (GPa)	M'_{a0}	c_0 (Å)	M_{c0} (GPa)	M'_{c0}
BM3	0-38	83.68(2)	166.3(15)	4.46(12)	4.7460(9)	539(10)	12.6(7)	4.2904(3)	421(4)	15.1(3)
BM3	0-38	*83.689*[a]	165.8(10)	4.49(9)	*4.7469*[a]	531(6)	12.5(6)	*4.2891*[a]	431(4)	14.5(4)
BM3	0-38	*83.703*[b]	164.9(10)	4.53(10)	*4.7465*[b]	536(6)	12.3(6)	*4.2900*[b]	424(3)	14.9(4)
Vinet	0-38	83.68(2)	165.5(15)	4.62(12)	4.7460(8)	537(10)	13.0(7)	4.2905(3)	418(3)	15.7(3)
Vinet	0-38	*83.689*[a]	165.2(10)	4.64(9)	*4.7469*[a]	530(7)	12.9(7)	*4.2891*[a]	428(4)	15.1(4)
Vinet	0-38	*83.703*[b]	164.3(10)	4.69(10)	*4.7465*[b]	534(7)	12.6(7)	*4.2900*[b]	422(3)	15.5(4)
Spin-crossover EOS										
EOS type	P range (GPa)	V_0 (Å^3)	K_{T0} (GPa)	K'_{T0}	Δ_0	B_0	δ	b=c	C/B	
BM3+SC	0-53	83.71(2)	161(2)	5.2(2)	*14750*	627(6)	2.5(2)	*-2*	*4.73*	
BM3+SC	0-53	*83.689*[a]	161.0(12)	5.23(18)	*14750*	627(6)	2.53(14)	*-2*	*4.73*	
BM3+SC	0-53	*83.703*[b]	161.0(13)	5.15(18)	*14750*	626(5)	2.50(14)	*-2*	*4.73*	

[a] Fixed to the value determined at room pressure at the beamline P02.2.
[b] Fixed to the value determined at room pressure *in-house* using the 8-position centering method.

2008; Chang et al., 2013; Rosa et al., 2013; Wu et al., 2016; Xu et al., 2020) falls in a relatively narrow range (Figure D.2). As a consequence, the range of K_T values becomes inevitably smaller with increasing pressure and results in a much weaker compositional effect on the elasticity of phase D solid solutions at mantle transition zone and lower mantle pressures.

7.3.3 Spin-Crossover in Fe-Bearing Al-Phase D

When Fe^{2+} and/or Fe^{3+} are incorporated in phase D, they are known to undergo a high-spin (HS) to low-spin (LS) crossover in the pressure interval ranging between approximately 40 and 70 GPa, as revealed by X-ray emission spectroscopy (XES) (Chang et al., 2013) and synchrotron Mössbauer spectroscopy (SMS) (Wu et al., 2016) observations. Wu et al. (2016) determined that the fraction of Fe^{2+} present in their sample is approximately 60%, corresponding to 0.07 Fe^{2+} atoms per formula unit, which is believed to induce the sharp volume collapse of 1.7% observed by X-ray diffraction in a few GPa interval at approximately 40 GPa. A second drop in the unit-cell volume (2%) at approximately 65 GPa was linked to the spin crossover of Fe^{3+}, which was also present in the sample. On the other hand, Chang et al. (2013) analyzed a phase D sample having less than 0.01 Fe^{2+} per formula unit and observed a smooth continuous decrease both in the unit-cell volume by X-ray diffraction and in the Fe^{3+} high-spin component by XES from 40 to 70 GPa. In this study, we observed a smooth and progressive deviation of the unit-cell volume, V, and lattice parameters a and c from the extrapolation of their respective equations of state determined using the data up to 38 GPa, i.e., below the region at which the spin crossover may occur. Owing to the similar $Fe^{3+}/\Sigma Fe$ ratio of our Fe-bearing Al-phase D with that of the sample studied by Chang et al. (2013), we also interpret the volume decrease above 38 GPa as the onset of Fe^{3+} spin crossover, suggesting that the $Mg^{2+} + Si^{4+} = 2Al^{3+}$ substitution has little to no effect on the spin crossover pressure of Fe^{3+} in phase D.

The number of data points collected after the onset of the spin crossover (i.e., above 38 GPa) is limited and does not allow for the refinement of separate EOS parameters for the Fe-bearing Al-phase D sample in the high- and low-spin states. However, a fit of all data points (i.e., before and across the spin crossover) can be obtained using a new semi-empirical formalism that has been recently proposed by (Buchen, 2021). In this formalism, the contribution of the spin crossover to the elastic energy (and thus to pressure) is obtained from the volume dependency of crystal-field parameters such as the crystal-field splitting Δ and the Racah parameters B and C:

$$\Delta = \Delta_0 \left(\frac{V_0}{V}\right)^{\frac{\delta}{3}}, B = B_0 \left(\frac{V_0}{V}\right)^{\frac{b}{3}}, C = C_0 \left(\frac{V_0}{V}\right)^{\frac{c}{3}} \tag{7.1}$$

where the zero in the subscript denotes parameters at room pressure. The total Helmholtz free energy ($\mathcal{F}$) at a given volume is then calculated by summing the elastic energy obtained from the finite strain equation (i.e., BM3 EOS in this case), the energies associated with the three most populated electronic states (i.e., $^6A_1$, $^2T_2$, and $^4T_1$ for Fe^{3+}) according to the equations proposed by Tanabe and Sugano (1954), and a term accounting for configurational entropy, spin multiplicity and degeneracy of the electronic states (Buchen, 2021). Finally, pressure is calculated by differentiating the total Helmholtz free energy relative to volume as $P = -(\partial\mathcal{F}/\partial V)_T$. This strategy has the advantage that only one set of V_0, K_{T0}, and K'_{T0} needs to be determined for the high-spin state, the low-spin state, and the mixed-spin region, while the electronic contribution to the spin-crossover equation is calculated separately. Buchen (2021) further showed that a good fit to the experimentally measured P-V data can be obtained even when most of these parameters, such as Δ_0, b, and c, are fixed to values determined by previous studies for octahedrally coordinated Fe^{2+} and Fe^{3+} cations in other compounds, while only B_0 and δ are refined. Following the examples provided by Buchen (2021), we assumed C/B to be constant and equal to 4.73, which implies $c = b$, with b = -2 (as Fe^{3+} in CF-type aluminous phase, Buchen, 2021) and Δ_0 = 14750 cm^{-1} (as Fe^{3+} in corundum, Lehmann and Harder, 1970; Krebs and Maisch, 1971), while B_0 and δ were refined. The resulting fit parameters are reported in Table7.2 and the fit to the experimental data points is shown in Figure 7.3a. The EOS curve interpolates well the data points in both the high-spin state region and across the spin crossover, while the population density of the high-spin and low-spin electronic states, shown in the inset of Figure 7.3a, confirms that the transition is broad and takes place over a pressure interval of more than 30 GPa, as was previously observed by Chang et al. (2013). Note also that the room pressure values V_0, K_{T0}, and K'_{T0} obtained from this fit are in agreement with the values obtained fitting the P-V data only up to 38 GPa (Table 7.2) once the tradeoff between K_{T0} and K'_{T0} is taken into account, confirming the validity of the formalism used.

In Fe-bearing Mg-phase D, the volume drop at the spin crossover is mainly driven by a shrinking of the c lattice parameter, whereas the a lattice parameter remains almost unaffected (Chang et al., 2013; Wu et al., 2016). In Fe-bearing Al-phase D, on the other hand, we observe a smooth decrease of both the a and c axes, with the c/a ratio remaining almost

Table 7.3. Fit parameters of 3rd-order Birch-Murnaghan (BM3), Vinet, and spin-crossover equations of state for Fe-bearing Al-phase D. Values in italics were fixed in the fit.

Composition	V_0 (Å^3)	K_{T0} (GPa)	K'_{T0}	P range (GPa)	Method	Reference
$Mg_{1.11}Si_{1.6}O_6H_{3.6}$	85.66(1)	166(3)	4.1(3)	0-30	XRPD in DAC	Frost and Fei (1999)
$Mg_{1.0}Si_{1.7}O_6H_{3.0}$	85.1(2)	168(9)	4.3(5)	0-56	XRPD in DAC	Hushur et al. (2011)
$Mg_{1.0}Si_{1.7}O_6H_{3.0}$	85.4(3)	150(9)	5.5(4)	0-30	XRPD in DAC	Hushur et al. (2011)
$Mg_{1.1}Si_{1.9}O_6H_{2.4}$	85.6(2)	149(3)	-	0	BS	Rosa et al. (2012)
$Mg_{1.00}Fe_{0.11}Al_{0.03}Si_{1.90}O_6H_{2.50}$	85.1(2)	153(4)	-	0	BS	Rosa et al. (2012)
$Mg_{0.89}Fe_{0.14}Al_{0.25}Si_{1.56}O_6H_{2.93}$	86.10(5)	137(3)	6.3(3)	0-30	XRPD in LVP	Litasov et al. (2007b)
$Mg_{0.99}Fe_{0.12}Al_{0.09}Si_{1.75}O_6H_{2.51}$	85.32 (2)	142(3)	6.2(4)	0-20	XRPD in LVP	Litasov et al. (2008)
$Mg_{1.1}Si_{1.8}O_6H_{2.5}$	85.80(5)	151.4(1.2)	4.89(8)	0-65	SCXRD in DAC	Rosa et al. (2013)
$Mg_{1.00}Fe_{0.15}Al_{0.09}Si_{1.75}O_6H_{2.51}$	86.14(3)	147(2)	6.3(3)	0-40	SCXRD in DAC	Chang et al. (2013)
$Mg_{1.14}Si_{1.73}O_6H_{2.81}$	85.07(4)	179(1)	4	0-80	SCXRD in DAC	Wu et al. (2016)
$Mg_{0.89}Fe_{0.11}Al_{0.37}Si_{1.55}O_6H_{2.65}$	85.7(1)	169(2)	4	0-37	SCXRD in DAC	Wu et al. (2016)
$Mg_{0.83}Al_{0.60}Si_{1.20}O_6H_{2.89}$	86.71	143(4)	5.8(7)	0-25	XRPD in LVP	Xu et al. (2020)
$Mg_{0.83}Al_{0.60}Si_{1.20}O_6H_{2.89}$	86.71	144(5)	5.5(7)	0-25	UI in LVP	Xu et al. (2020)
$Fe_{0.22}Al_{1.53}Si_{0.86}O_6H_{3.33}$	83.68(2)	166.3(1.5)	4.46(12)	0-38	SCXRD in DAC	This study (BM3)

constant across the spin crossover (Figure 7.3b). The reason behind the different behavior shown by our sample relative to previous studies could be that, in Mg-phase D, ferric and ferrous Fe likely substitute Mg in the M1 site and not Si in the M2 site. As described above, in Mg-phase D the distance between oxygen atoms across the interstitial layer hosting M1 is larger than that across M2, owing to the larger radius of Mg relative to Si (Figure D.1a). In order to accommodate the difference in size of the two cations, the z coordinates of O in Mg-Phase D (Wyckoff position 6k: x,0,z) are either larger than 1/4 or smaller than 3/4, making the Si layer thinner than the Mg layer (Figure D.1a). At the spin crossover, the ionic radius of Fe decreases and thus the octahedral volume of M1 in Mg-phase D must decrease as well. This means that in order for M1 to be reduced in size while leaving M2 unaffected, the c lattice parameter must shrink while the z coordinates of O approaches the value 1/4 or 3/4. In Fe-bearing Al-phase D, this cannot happen when the hexagonal space group is considered, since the z coordinate of the oxygen atoms is constrained by symmetry (Wyckoff position 6g: x,x,1/2) and the two interstitial layers perpendicular to the c-axis have the same thickness. This is likely the consequence of Al, Si and Fe^{3+} being more or less randomly distributed in Fe-bearing Al-phase D (Figure D.1c). Therefore, the octahedral volumes of the three cation sites must collapse simultaneously while the atomic coordinates of all atoms are likely to remain unchanged. The fact that we observed a simultaneous decrease of the a and c lattice parameters above 38 GPa seems to confirm indeed the hypothesis of a hexagonal space group for our sample.

Recently, Meier et al. (2022) analyzed the possible correlations between H-bond symmetrization and high-to-low spin crossover in Fe-bearing phase δ and Fe,Al-bearing Mg-phase D by means of nuclear magnetic resonance spectroscopy (NMR), synchrotron Mössbauer spectroscopy, and X-ray diffraction. In all the samples studied by Meier et al. (2022), including the one of Fe,Al-bearing Mg-phase D, the H-bond symmetrization was found not to affect the resonance frequency of the ^{1}H nuclei, but only the width of the peak, which is related to the proton mobility. The spin crossover of Fe^{3+}, on the other hand, was found to

significantly change the resonance frequency of the ^{1}H, while leaving the width of the NMR signal unaffected. These two phenomena were observed at different pressures in all the hydrous phases investigated by Meier et al. (2022), suggesting that they are not correlated. The H-bond symmetrization in the phase D sample was observed at 23(2) GPa, while the spin crossover of Fe^{3+} was observed above 36 GPa, which is in good agreement with both our observations and the previous study of Chang et al. (2013). As the strength of H-bonds in Al-phase D samples is higher than in Mg-phase D samples (Yang et al., 1997b; Boffa Ballaran et al., 2010; Pamato et al., 2015), it is reasonable to expect that the symmetrization of H-bond in Al-phase D will take place at lower pressure than in Mg-phase D. Therefore, we expect that the H-bond symmetrization and spin crossover of Fe^{3+} in Fe-bearing Al-phase D are uncorrelated, similarly to what was observed in Fe,Al-bearing Mg-phase D by Meier et al. (2022).

7.4 Implications

Previous experimental studies have shown that the wide *P-T* stability field of phase D makes it a suitable host for water in the Earth's mantle transition zone and lower mantle (Nishi et al., 2014; Pamato et al., 2015; Liu et al., 2019a). As Al is incorporated in its crystal structure, phase D can survive even at temperatures of the ambient mantle within MgO-poor Al-rich subducted basaltic crust, where water can be delivered by hydrous melts upwelling from dehydrating ultramafic lithologies within the slab (Pamato et al., 2015). Al-rich phase D was also reported to be stable in MgO-rich basaltic crust between 20 and 25 GPa (Liu et al., 2019a) and to transform to a solid solution of δ-AlOOH and DHMS phase H ($MgSiO_4H_2$) above 25 GPa. It was recently proposed that solid solutions between phase H and δ-AlOOH contribute to make the sound velocities of hydrous mid-ocean ridge basalt (MORB) faster than those of dry MORB at shallow lower mantle pressures, owing to their high bulk modulus and relative low density after the H-bond symmetrization (Satta et al., 2021). These findings are particularly interesting as they suggest an intimate relationship between H-bond symmetrization and elastic stiffening of $CaCl_2$-type oxyhydroxides at high pressure. Based on the analysis of bond valences and Pauling bond strength of our sample and that studied by Pamato et al. (2015), it seems that the H-bonds of Al-Phase D are stronger than those of Mg-phase D. Nuclear magnetic resonance (NMR) spectroscopy and single-crystal diffraction measurements on a Fe,Al-bearing Mg-phase D sample, however, showed no evidence for a shift in the resonance frequency and a change in compressibility across the H-bond symmetrization (Meier et al., 2022). Given that the H-bonds in Al-phase D and Fe-bearing Al-phase D are stronger than in Mg-phase D samples, it is reasonable to expect the H-bond symmetrization to take place below 23 GPa. However, no change in the volume and axial compressibility was observed in Fe-bearing Al-phase D between room pressure and 38 GPa. Therefore, we conclude that the strength of H-bonds alone cannot be responsible for an increase in the bulk modulus of phase D and other H-bearing minerals, but additional features, such as a change in the space group symmetry, must also occur across

the H-bond symmetrization, as it was observed in the case of pure and Fe-bearing phase δ (Sano-Furukawa et al., 2018; Ohira et al., 2019; Satta et al., 2021).

Acknowledgments

We would like to thank Raphael Njul for preparing the samples for EPMA and Detlef Krauße for his assistance with EPMA measurements. Johannes Buchen is acknowledged for fruitful discussion on the spin-crossover equation of state and for sharing the script to fit the P-V data. We also thank Oliver Tschauner, Angelika D. Rosa, an anonymous reviewer, and the technical editor for their constructive comments that helped us improving the manuscript. This study was supported by DFG grant FR1555/11. We acknowledge DESY (Hamburg, Germany), a member of the Helmholtz Association HGF, for the provision of experimental facilities. Parts of this research were carried out at the Extreme Conditions Beamline P02.2, PETRA-III.

Data Availability Statement

The deposited Crystallographic Information Files (CIFs) are available at: https://figshare.com/s/57ea586081085cf9b9ac.

References

Angel, R. J. (2000). "Equations of State". In: *Reviews in Mineralogy and Geochemistry* 41 (1), pp. 35–59. DOI: 10.2138/rmg.2000.41.2.

Angel, R. J. and L. W. Finger (2011). "SINGLE: A program to control single-crystal diffractometers". In: *Journal of Applied Crystallography* 44 (1), pp. 247–251. DOI: 10.1107/S0021889810042305.

Angel, R. J., J. Gonzalez-Platas, and M. Alvaro (2014). "EosFit7c and a Fortran module (library) for equation of state calculations". In: *Zeitschrift fur Kristallographie* 229 (5), pp. 405–419. DOI: 10.1515/zkri-2013-1711.

Bindi, L., M. Nishi, J. Tsuchiya, and T. Irifune (2014). "Crystal chemistry of dense hydrous magnesium silicates : The structure of phase H ," in: 99 (8-9), pp. 1802–1805.

Birch, F. (1947). "Finite elastic strain of cubic crystals". In: *Physical Review* 71 (11), pp. 809–824. DOI: 10.1103/PhysRev.71.809.

Boehler, R. and K. D. Hantsetters (Sept. 2004). "New anvil designs in diamond-cells". In: *High Pressure Research* 24 (3), pp. 391–396. DOI: 10.1080/08957950412331323924.

Boffa Ballaran, T., D. J. Frost, N. Miyajima, and F. Heidelblbach (2010). "The structure of a super-aluminous version of the dense hydrous-magnesium silicate phase D". In: *American Mineralogist* 95 (7), pp. 1113–1116. DOI: 10.2138/am.2010.3462.

Buchen, J. (2021). *Seismic Wave Velocities in Earth's Mantle from Mineral Elasticity*, pp. 51–95. DOI: 10.1002/9781119528609.ch3.

Chang, Y. Y., S. D. Jacobsen, J. F. Lin, C. R. Bina, S. M. Thomas, J. Wu, G. Shen, Y. Xiao, P. Chow, D. J. Frost, C. A. McCammon, and P. Dera (2013). "Spin transition of Fe^{3+} in Al-bearing phase D: An alternative explanation for small-scale seismic scatterers in the mid-lower mantle". In: *Earth and Planetary Science Letters* 382, pp. 1–9. DOI: 10.1016/j.epsl.2013.08.038.

Frost, D. J. (2006). "The Stability of Hydrous Mantle Phases". In: *Reviews in Mineralogy and Geochemistry* 62, pp. 243–271. DOI: 10.2138/RMG.2006.62.11.

Frost, D. J. and Y. Fei (1999). "Static compression of the hydrous magnesium silicate phase D to 30 GPa at room temperature". In: *Physics and Chemistry of Minerals* 26 (5), pp. 415–418. DOI: 10.1007/s002690050202.

Gonzalez-Platas, J., M. Alvaro, F. Nestola, and R. J. Angel (2016). "EosFit7-GUI: A new graphical user interface for equation of state calculations, analyses and teaching". In: *Journal of Applied Crystallography* 49 (4), pp. 1377–1382. DOI: 10.1107/S1600576716008050.

Hamilton, W. C. (1965). "Significance tests on the crystallographic *R* factor". In: *Acta Crystallographica* 18 (3), pp. 502–510. DOI: 10.1107/s0365110x65001081.

Hushur, A., M. H. Manghnani, J. R. Smyth, Q. Williams, E. Hellebrand, D. Lonappan, Y. Ye, P. Dera, and D. J. Frost (2011). "Hydrogen bond symmetrization and equation of state of phase D". In: *Journal of Geophysical Research: Solid Earth* 116 (6), pp. 1–8. DOI: 10.1029/2010JB008087.

Hübschle, C. B., G. M. Sheldrick, and B. Dittrich (2011). "ShelXle: A Qt graphical user interface for SHELXL". In: *Journal of Applied Crystallography* 44 (6), pp. 1281–1284. DOI: 10.1107/S0021889811043202.

Ishii, T., Z. Liu, and T. Katsura (2019c). "A Breakthrough in Pressure Generation by a Kawai-Type Multi-Anvil Apparatus with Tungsten Carbide Anvils". In: *Engineering* 5 (3), pp. 434–440. DOI: 10.1016/j.eng.2019.01.013.

Ishii, T., L. Shi, R. Huang, N. Tsujino, D. Druzhbin, R. Myhill, Y. Li, L. Wang, T. Yamamoto, N. Miyajima, T. Kawazoe, N. Nishiyama, Y. Higo, Y. Tange, and T. Katsura (2016). "Generation of pressures over 40 GPa using Kawai-type multi-anvil press with tungsten carbide anvils". In: *Review of Scientific Instruments* 87 (2). DOI: 10.1063/1.4941716.

Kantor, I., V. Prakapenka, A. Kantor, P. Dera, A. Kurnosov, S. Sinogeikin, N. Dubrovinskaia, and L. Dubrovinsky (2012). "BX90: A new diamond anvil cell design for X-ray diffraction and optical measurements". In: *Review of Scientific Instruments* 83 (12), p. 125102. DOI: 10.1063/1.4768541.

King, H. E. and L. W. Finger (1979). "Diffracted beam crystal centering and its application to high-pressure crystallography". In: *Journal of Applied Crystallography* 12 (4), pp. 374–378. DOI: 10.1107/S0021889879012723.

Krebs, J. J. and W. G. Maisch (1971). "Study of pure and doped cobaltous and nickelous oxide". In: *Physical Review B* 4 (3), pp. 750–757. DOI: 10.1103/PhysRevB.4.750.

Kurnosov, A., I. Kantor, T. Boffa-Ballaran, S. Lindhardt, L. Dubrovinsky, A. Kuznetsov, and B. H. Zehnder (2008). "A novel gas-loading system for mechanically closing of various types of diamond anvil cells". In: *Review of Scientific Instruments* 79 (4). DOI: 10.1063/1.2902506.

Lehmann, G. and H. Harder (1970). "Optical Spectra of Di-and Trivalent Iron in Corundum". In: *American Mineralogist* 55 (1-2), pp. 98–105.

Liermann, H. P., Z. Konôpková, W. Morgenroth, K. Glazyrin, J. Bednarčik, E. E. McBride, S. Petitgirard, J. T. Delitz, M. Wendt, Y. Bican, A. Ehnes, I. Schwark, A. Rothkirch, M. Tischer, J. Heuer, H. Schulte-Schrepping, T. Kracht, and H. Franz (2015). "The Extreme Conditions Beamline P02.2 and the Extreme Conditions Science Infrastructure at PETRA III". In: *Journal of Synchrotron Radiation* 22, pp. 908–924. DOI: 10.1107/S1600577515005937.

Litasov, K. D., E. Ohtani, Y. Nishihara, A. Suzuki, and K. Funakoshi (2008). "Thermal equation of state of Al- and Fe-bearing phase D". In: *Journal of Geophysical Research: Solid Earth* 113 (8), pp. 1–13. DOI: 10.1029/2007JB004937.

Litasov, K. D., E. Ohtani, A. Suzuki, and K. Funakoshi (2007b). "The compressibility of Fe- and Al-bearing phase D to 30 GPa". In: *Physics and Chemistry of Minerals* 34 (3), pp. 159–167. DOI: 10.1007/s00269-006-0136-4.

Liu, X., K. N. Matsukage, Y. Nishihara, T. Suzuki, and E. Takahashi (2019a). "Stability of the hydrous phases of Al-rich phase D and Al-rich phase H in deep subducted oceanic crust". In: *American Mineralogist* 104 (1), pp. 64–72. DOI: 10.2138/am-2019-6559.

Liu, Z., M. Nishi, T. Ishii, H. Fei, N. Miyajima, T. B. Ballaran, H. Ohfuji, T. Sakai, L. Wang, S. Shcheka, T. Arimoto, Y. Tange, Y. Higo, T. Irifune, and T. Katsura (2017b). "Phase Relations in the System $MgSiO_3$-Al_2O_3 up to 2300 K at Lower Mantle Pressures". In: *Journal of Geophysical Research: Solid Earth* 122 (10), pp. 7775–7788. DOI: 10.1002/2017JB014579.

Lufaso, M. W. and P. M. Woodward (2001). "Prediction of the crystal structures of perovskites using the software program SPuDS". In: *Acta Crystallographica Section B: Structural Science* 57 (6), pp. 725–738. DOI: 10.1107/S0108768101015282.

McCammon, C. A. (1994). "A Mössbauer milliprobe: Practical considerations". In: *Hyperfine Interactions* 92 (1), pp. 1235–1239. DOI: 10.1007/BF02065761.

Meier, T., F. Trybel, S. Khandarkhaeva, D. Laniel, T. Ishii, A. Aslandukova, N. Dubrovinskaia, and L. Dubrovinsky (2022). "Structural independence of hydrogen-bond symmetrisation dynamics at extreme pressure conditions". In: *Nature Communications* 13.1. DOI: 10.1038/s41467-022-30662-4.

Nishi, M., T. Irifune, J. Tsuchiya, Y. Tange, Y. Nishihara, K. Fujino, and Y. Higo (2014). "Stability of hydrous silicate at high pressures and water transport to the deep lower mantle". In: *Nature Geoscience* 7 (3), pp. 224–227. DOI: 10.1038/ngeo2074.

Ohira, I., J. M. Jackson, N. V. Solomatova, W. Sturhahn, G. J. Finkelstein, S. Kamada, T. Kawazoe, F. Maeda, N. Hirao, S. Nakano, T. S. Toellner, A. Suzuki, and E. Ohtani (2019). "Compressional behavior and spin state of δ-(Al,Fe)OOH at high pressures". In: *American Mineralogist* 104 (9), pp. 1273–1284. DOI: 10.2138/am-2019-6913.

Ohira, I., E. Ohtani, T. Sakai, M. Miyahara, N. Hirao, Y. Ohishi, and M. Nishijima (2014). "Stability of a hydrous δ-phase, AlOOH-$MgSiO_2(OH)_2$, and a mechanism for water transport into the base of lower mantle". In: *Earth and Planetary Science Letters* 401, pp. 12–17. DOI: 10.1016/j.epsl.2014.05.059.

Ohtani, E., Y. Amaike, S. Kamada, T. Sakamaki, and N. Hirao (2014). "Stability of hydrous phase H $MgSiO_4H_2$ under lower mantle conditions". In: *Geophysical Research Letters* 41 (23), pp. 8283–8287. DOI: 10.1002/2014GL061690.

Pamato, M. G., R. Myhill, T. B. Ballaran, D. J. Frost, F. Heidelbach, and N. Miyajima (2015). "Lower-mantle water reservoir implied by the extreme stability of a hydrous aluminosilicate". In: *Nature Geoscience* 8 (1), pp. 75–79. DOI: 10.1038/ngeo2306.

Prescher, C., C. McCammon, and L. Dubrovinsky (2012). "MossA : a program for analyzing energy-domain Mössbauer spectra from conventional and synchrotron sources". In: *Journal of Applied Crystallography* 45 (2), pp. 329–331. DOI: 10.1107/S0021889812004979.

Ralph, R. L. and L. W. Finger (1982). "A Computer-Program for Refinement of Crystal Orientation Matrix and Lattice-Constants from Diffractometer Data with Lattice Symmetry Constraints". In: *Journal of Applied Crystallography* 15 (10), pp. 537–539. DOI: 10.1107/S0021889882012539.

Rosa, A. D., M. Mezouar, G. Garbarino, P. Bouvier, S. Ghosh, A. Rohrbach, and C. Sanchez-Valle (2013). "Single-crystal equation of state of phase D to lower mantle pressures and the effect of hydration on the buoyancy of deep subducted slabs". In: *Journal of Geophysical Research: Solid Earth* 118 (12), pp. 6124–6133. DOI: 10.1002/2013JB010060.

Rosa, A. D., C. Sanchez-Valle, and S. Ghosh (2012). "Elasticity of phase D and implication for the degree of hydration of deep subducted slabs". In: *Geophysical Research Letters* 39 (6), pp. 6–11. DOI: 10.1029/2012GL050927.

Sano-Furukawa, A., T. Hattori, K. Komatsu, H. Kagi, T. Nagai, J. J. Molaison, A. M. dos Santos, and C. A. Tulk (2018). "Direct observation of symmetrization of hydrogen bond in δ-AlOOH under mantle conditions using neutron diffraction". In: *Scientific Reports* 8 (1), pp. 1–9. DOI: 10.1038/s41598-018-33598-2.

Sano-Furukawa, A., H. Kagi, T. Nagai, S. Nakano, S. Fukura, D. Ushijima, R. Iizuka, E. Ohtahtahtani, and T. Yagi (2009). "Change in compressibility of δ-AlOOH and δ-AlOOD at high pressure: A study of isotope effect and hydrogen-bond symmetrization". In: *American Mineralogist* 94 (8-9), pp. 1255–1261. DOI: 10.2138/am.2009.3109.

Satta, N., G. Criniti, A. Kurnosov, T. B. Ballaran, T. Ishii, and H. Marquardt (2021). "High-Pressure Elasticity of δ-(Al,Fe)OOH Single Crystals and Seismic Detectability of Hydrous MORB in the Shallow Lower Mantle". In: *Geophysical Research Letters* 48 (23). DOI: 10.1029/2021GL094185.

Sheldrick, G. M. (2015a). "Crystal structure refinement with *SHELXL*". In: *Acta Crystallographica Section C: Structural Chemistry* 71, pp. 3–8. DOI: 10.1107/S2053229614024218.

— (2015b). "Foundations and Advances *SHELXT*-Integrated space-group and crystal-structure determination". In: *Acta Cryst* 71, pp. 3–8. DOI: 10.1107/S2053273314026370.

Shen, G., Y. Wang, A. Dewaele, C. Wu, D. E. Fratanduono, J. Eggert, S. Klotz, K. F. Dziubek, P. Loubeyre, O. V. Fat'yanov, P. D. Asimow, T. Mashimo, and R. M. Wentzcovitch (2020). "Toward an international practical pressure scale: A proposal for an IPPS ruby gauge (IPPS-Ruby2020)". In: *High Pressure Research*, pp. 1–16. DOI: 10.1080/08957959.2020.1791107.

Tanabe, Y. and S. Sugano (1954). “On the Absorption Spectra of Complex Ions. I”. In: *Journal of the Physical Society of Japan* 9, pp. 753–766. DOI: 10.1143/JPSJ.9.753.

Vinet, P., J. H. Rose, J. Ferrante, and J. R. Smith (1989). “Universal features of the equation of state of solids”. In: *Journal of Physics: Condensed Matter* 1 (11), pp. 1941–1963. DOI: 10.1088/0953-8984/1/11/002.

Wu, X., Y. Wu, J.-F. Lin, J. Liu, Z. Mao, X. Guo, Y. Takashi, C. McCammon, V. B. Prakapenka, and Y. Xiao (2016). “Two-stage spin transition of iron in FeAl-bearing phase D at lower mantle”. In: *Journal of Geophysical Research: Solid Earth* 121, 6411–6420. DOI: 10.1002/2016JB013209.

Xu, C., S. Gréaux, T. Inoue, M. Noda, W. Sun, H. Kuwahara, and Y. Higo (2020). “Sound Velocities of Al-Bearing Phase D up to 22 GPa and 1300 K”. In: *Geophysical Research Letters* 47 (18), pp. 1–10. DOI: 10.1029/2020GL088877.

Yang, H., C. T. Prewitt, and D. J. Frost (1997b). “Crystal structure of the dense hydrous magnesium silicate, phase D”. In: *American Mineralogist* 82 (5-6), pp. 651–654. DOI: 10.2138/am-1997-5-627.

Appendix A

Supporting information to: Single-Crystal Elasticity of $MgSiO_3$ Bridgmanite to Mid-Lower Mantle Pressure

Introduction

The following supporting information contains additional details on notations used to describe the anisotropic elastic properties of bridgmanite, as well as the equations used to convert and fit the elastic moduli (Appendix A). In Appendix A we thoroughly describe possible sources of errors in sound velocity measurements and data processing arising from the Brillouin scattering geometry and the correlation of the elastic stiffness tensor components (c_{ij}) at room and high pressure. Further details on the experimental setup and the estimate made for the width of diamond peaks are presented in Appendix A. In Figure A.1 we show the pressure dependence of the c_{ij}s derived from the individual fits and the global fit. After calculating the elastic moduli from the c_{ij}s, in Figure A.2 the elastic moduli are fit to finite strain equations of state, showing that either a 4^{th}-order truncation or two separate EOSs are required to properly fit the sear modulus (G) in the Reuss bound. The dependence of the shear modulus with pressure (G') is linked to the pressure evolution of the lattice strain e_{tx} (tetragonal shear strain) in Figure A.3, which implies that G and G' in the Reuss bound may be correlated to the structural response of bridgmanite to pressure. Using different ruby fluorescence pressure scales, we assess the validity of the existing ruby calibrations in Figure A.4. In Figure A.5, the pressure calculated from the EOSs derived from our P-V (ruby scale) and K_T-V (absolute pressure) data is compared with previous compressibility studies. The dispersion curves of $MgSiO_3$ bridgmanite at ambient conditions are shown in Figure A.6. In Figure A.7 we show the effect of chemical composition on the c_{ij} and the aggregate elastic moduli of bridgmanite at 25 GPa. The elastic anisotropy of bridgmanite as a function of chemistry is displayed for 4 different compositions at 35 GPa in Figure A.8. Figure A.9 describes the axial moduli of our $MgSiO_3$ bridgmanite sample compared to previous experimental and computational studies. Figure A.10 shows a comparison of the v_P and v_S dispersion curves at 78.8 GPa calculated for platelet 011 using 3^{rd}-order and 4^{th}-order

EOSs. Table A.1 summarizes experimentally and computationally determined elastic moduli of bridgmanite and their pressure derivatives determined in previous studies. Table A.2 reports the thermodynamic parameters used in the mineral physics model. In Table A.3 and Table A.4 we report the results of inversion tests on synthetic and real velocity data sets to assess correlations between c_{ij} and to understand their effect on the estimated standard deviations. Table A.5 shows a comparison of RMS errors arising from the use of 3rd-order and 4th-order EOSs in the global fitting procedure.

Supplementary Text A.1

In elasticity calculations, the tensorial and Voigt notations are used to describe the elastic stiffness of a material. As the elastic stiffness is a 4th-rank tensor, 4 indices (i.e. i, j, k, l = 1, 2, 3) are necessary to describe each individual component of the tensor (c_{ijkl}). For symmetry reasons, the elastic tensor of an orthorhombic crystal has 9 independent components: c_{1111}, c_{2222}, c_{3333}, c_{1122}, c_{1133}, c_{2233}, c_{1212}, c_{1313}, c_{2323} (Nye, 1985). However, for computational reasons, it is often easier to work with matrices (i.e. 2nd-rank tensors) instead of 4th-rank tensors and, therefore, the Voigt notation is used. In the Voigt notation, the elastic stiffness is described by a squared matrix of order 6. The conversions between individual tensorial and Voigt components are:

$$c_{1111} = c_{11} \tag{A.1}$$

$$c_{2222} = c_{22} \tag{A.2}$$

$$c_{3333} = c_{33} \tag{A.3}$$

$$c_{1122} = c_{12} \tag{A.4}$$

$$c_{1133} = c_{13} \tag{A.5}$$

$$c_{2233} = c_{23} \tag{A.6}$$

$$c_{2323} = c_{44} \tag{A.7}$$

$$c_{1313} = c_{55} \tag{A.8}$$

$$c_{1212} = c_{66} \tag{A.9}$$

The bulk modulus of a material can be calculated in the ideal conditions of equal stress (Reuss bound) and equal strain (Voigt bound) from the elastic compliance (s_{ij}) and elastic stiffness (c_{ij}) matrices respectively.
The Voigt bound (K_V, G_V) is calculated directly from the c_{ij}s that are obtain by fitting the Christoffel's equation to the measured acoustic velocities:

$$K_V = \frac{c_{11} + c_{22} + c_{33} + 2(c_{12} + c_{13} + c_{23})}{9} \tag{A.10}$$

$$G_V = \frac{(c_{11} + c_{22} + c_{33}) - (c_{12} + c_{13} + c_{23}) + 3(c_{44} + c_{55} + c_{66})}{9} \tag{A.11}$$

The Reuss bound is calculated from the sijs, which can be obtained by inverting the elastic stiffness matrix:

$$s_{ij} = c_{ij}^{-1} \tag{A.12}$$

The elastic moduli (K_R, G_R) in the Reuss bound are then calculated:

$$K_R = \frac{1}{s_{11} + s_{22} + s_{33} + 2(s_{12} + s_{13} + s_{23})} \tag{A.13}$$

$$G_R = \frac{15}{4(s_{11} + s_{22} + s_{33}) - 4(s_{12} + s_{13} + s_{23}) + 3(s_{44} + s_{55} + s_{66})} \tag{A.14}$$

Because the Reuss and Voigt bounds are not equivalent in elastically anisotropic materials, Hill (1963) proposed an average of these two bounds to describe the elastic behavior of crystalline aggregates with random orientation of crystallites. Such average properties are often used to compare mineral-physics based wave velocities with seismic velocities and are called the Voigt-Reuss-Hill average (K_{VRH}, G_{VRH}):

$$K_{VRH} = \frac{K_V + K_R}{2} \tag{A.15}$$

$$G_{VRH} = \frac{G_V + G_R}{2} \tag{A.16}$$

The elastic moduli obtained in this study have been fitted with 3rd-order finite strain equations of state using the formalism of Stixrude and Lithgow-Bertelloni (2005):

$$K = (1 + 2f)^{5/2} \left[K_0 + (3G_0K_0' - 5K_0)f + \frac{27}{2} \left[K_0K_0' - 4K_0 \right) f^2 \right] \tag{A.17}$$

$$G = (1 + 2f)^{5/2} \left[G_0 + \left(3K_0G_0' - 5G_0 \right) f + \left(6K_0G_0' - 24K_0 - 14G_0 + \frac{9}{2}K_0K_0' \right) f^2 \right] \tag{A.18}$$

Where K_0 and G_0 are the elastic moduli at ambient conditions, f is the Eulerian finite strain:

$$f = \frac{1}{2} \left[\left(\frac{V}{V_0} \right)^{-\frac{2}{3}} - 1 \right] = \frac{1}{2} \left[\left(\frac{\rho}{\rho_0} \right)^{\frac{2}{3}} - 1 \right] \tag{A.19}$$

And K_0' and G_0' are the pressure derivative at ambient conditions of the bulk and shear moduli:

$$K_0' = \left(\frac{\partial K}{\partial P} \right)_{P=0,T} \tag{A.20}$$

$$G_0' = \left(\frac{\partial G}{\partial P} \right)_{P=0,T} \tag{A.21}$$

$$\tag{A.22}$$

The 4th-order truncation of the EOS of the shear modulus can be derived from the 4th-order truncation of the c_{ij} (Melinger-Cohen and Jeanloz, 2019; Stixrude and Lithgow-Bertelloni,

2005):

$$G = (1+2f)^{5/2}\left[G_0 + \left(3K_0G_0^{'} - 5G_0\right)f + \frac{1}{2}\left(35G_0 - 36K_0G_0^{'} + 9K_0^2G_0^{''} - 9K_0K_0^{'}K_0^{'}\right)f^2 + \frac{1}{2}\left(126G_0 + 239K_0 + 18K_0^2G_0^{''} + 18K_0K_0^{'}G_0^{'} - 81K_0K_0^{'} - 96K_0G_0^{'} + 9K_0^2K_0^{''} + 9K_0{K_0^{'}}^2\right)f^3\right] \quad \text{(A.23)}$$

Where

$$K_0^{''} = \left(\frac{\partial^2 K}{\partial P^2}\right)_{P=0,T} \quad \text{(A.24)}$$

$$G_0^{''} = \left(\frac{\partial^2 G}{\partial P^2}\right)_{P=0,T} \quad \text{(A.25)}$$

This expression has been used to fit the shear modulus obtained in this study for the Reuss bound, however because the evolution of K with pressure is well described by a 3rd-order EOS, the value of $K_0^{''}$ used in the shear modulus fit is that implied by a 3rd-order truncation.

Supplementary Text A.2

In this section we analyze potential sources of errors and estimated uncertainties in the collection of Brillouin spectra and inversion of sound velocity data to obtain the elastic stiffness coefficients (c_{ij}) of bridgmanite. Since in our experiments the normalized indices of each crystal platelet, as well as the initial phase of the dispersion curves (i.e. χ_0) are accurately calculated from X-ray diffraction measurements at each pressure point, we consider as major sources of error: (i) deviations from the ideal geometry of the Brillouin system (e.g. scattering angle); (ii) tilting of diamond anvils and/or crystal platelet; (iii) correlation between c_{ij}s calculated by inversion of a given velocity data set. Potential errors arising from the conditions (i) and (ii) have been previously described and discussed (i.e. Sinogeikin and Bass, 2000; Zha et al., 1996). In this study, we have performed measurements in forward scattering (or platelet) geometry (Speziale et al., 2014; Whitfield et al., 1976) where the sound wave velocities (v_i) are related to the observed frequency shift (Ω) by the relation:

$$v_i = \frac{\Omega\lambda_0}{2sin\left(\theta^*/2\right)} \quad \text{(A.26)}$$

Where λ_0 = 532 nm is the wavelength of the laser and θ^* = 80° is the external scattering angle between incident and analyzed beams. θ^* was calibrated using a double-polished fused silica glass standard which was previously measured by means of GHz-ultrasonic interferometry. After careful optical alignment of the silica glass platelet on the 4-circle Eulerian cradle of our Brillouin system (Trots et al., 2011; Trots et al., 2013) we aligned the scattering angle of our system using the reflection of the laser beam from the mirror-like surface of the silica glass platelet. This is relatively easily done since the glass plate lies

at the center of rotation of the diffractometer and serves as a fixed point in the alignment procedure. We first aligned the silica glass platelet at χ = 90° and ϕ = 90° using a bubble level, so that the reflecting surface is perfectly vertical. Afterwards, we mounted irises on the focusing and collecting lenses and we adjusted the position of the lenses at χ = 40° and χ = 140°. We then substituted the irises with lenses and checked that the incident and reflected laser beams coincide. Periodic measurements of the glass standard show that the deviation from the 80° ideal geometry is less than 0.2°, which corresponds to a difference of at most 0.2% in the calculated velocities. Our estimated uncertainties on the calculated velocities from Brillouin spectra are of the order of 0.15-1% (see data repository). Therefore, the small differences from θ^* = 80° used to convert Brillouin shifts into sound wave velocities are considered to be within the uncertainties.

The second source of error that we consider is the tilting of diamonds and/or crystal platelets with respect to the bisecting direction of the incident and measured beams. Such contributions to the observed velocities are easily detected as they have the same magnitude, but different sign for phonon directions that differ by 180°. Therefore, they result in an additional modulation of the dispersion curves with a period equal to 360°. To overcome this problem, it is good practice to measure redundant orientations at e.g. ϕ = 0° and ϕ = 180° and calculate the average of the two measurements. In this study, we used a complementary approach that consists in measuring samples over a 360° range of rotation angles and whenever needed, applying a tilting correction as a sinusoidal function whose phase and amplitude are used as variables in fitting the dispersion curve velocities. This correction has been already implemented in Kurnosov et al. (2017), although it was subsequently ignored by Lin et al. (2018) when inverting the sound velocity data published by Kurnosov et al. (2017). As a result, the dispersion curves obtained by Lin et al. (2018) clearly do not fit well the Kurnosov et al. (2017) data citep[see the large residuals displayed in Extended Data Fig. 2 and 3 of Lin et al. (2018) giving rise to slightly different c_{ij}s. As the estimated standard deviation (esd) mainly depends on the magnitude of the residuals between observed and calculated velocities, the larger uncertainties reported by Lin et al. (2018) can be at least partially attributed to their neglection of the tilting correction.

Lastly, it is critical that the set of crystal platelets used for Brillouin scattering measurements contains sufficient information to constrain all the elastic stiffness coefficients of bridgmanite through the Christoffel's equation. This requires a practical verification of whether the velocity data obtained from a specific set of platelets can be inverted to refine elastic stiffness coefficients (c_{ij}) with low uncertainties. If the c_{ij}s obtained in the inversion of sound velocity data show large esd, it typically means that the c_{ij}s are not sensitive enough to the sampled phonon directions and therefore the c_{ij}s will show high correlations between each other. Correlation analysis is automatically taken into account by the fitting routines implemented in OriginLab and used in this and previous studies (Kurnosov et al., 2017). Here we show the results of the initial tests that were used to assess the sensitivity of our second set of platelets (i.e. 100 and 011) and the results of some further tests used to assess

correlations between c_{ij}s at high pressure when using the global fit procedure. For the initial tests, we simulated dispersion curves at ambient conditions using the elastic stiffness tensor of $MgSiO_3$ bridgmanite reported in Sinogeikin et al. (2004). 19 different phonon directions per crystal platelet were generated and then scattered by adding random quantities between ±0.04 km/s and ±0.07 km/s for shear and compressional velocities respectively. In the first test, all 114 generated velocities were used in the inversion procedure. Using this approach, the magnitude of the correlation between the c_{ij}s did not exceed ±0.35 (Table A.3). This test is equivalent to the sensitivity test proposed by Lin et al. (2018) and Fu et al. (2019) and can be helpful only for a very rough estimation of sensitivity, because in real datasets it is rare to observe all three velocities in a given phonon direction, due to scarce photon-phonon coupling or overlapping of sample peaks with those of pressure medium or diamond anvils. Therefore, these tests yield the maximum sensitivity (or minimum correlation), they represent the most ideal and simplistic case and are rarely applicable.

To simulate the sensitivity of more realistic datasets, we tested three more cases in which we subtracted some of the generated velocities from each data set, so that the number of measured phonon directions does not change, but the overall number of observed velocities decreases. In this second test we, therefore, removed one velocity (either v_{S1}, v_{S2} or v_P) per phonon direction (i.e. 76 total synthetic velocities) while keeping constant the ratio of observed v_S over observed v_P n_P/n_P = 2. We can see that this does not affect much the correlations, as well as the refined c_{ij}s and their esd. This means that even when only two velocities are measured per phonon direction, we see no difference from the ideal case (Table A.3). The third test was performed on a dataset from which we subtracted preferentially compressional velocities ($n_P/n_P \sim 3.5$) to mimic the single-crystal measurements at high pressures where the compressional velocities in many directions disappear under the signal of the diamond. The few v_P left, however, were located preferentially in the proximity of the main crystallographic directions [100], [010] and [001], which have maximum sensitivity to c_{11}, c_{22} and c_{33}. This case is similar to the data set reported in Figure 4.2b in the main text, where only the maxima and minima of both v_P are visible. We do not observe any remarkable increase in correlations and in the esd with respect to the first and second tests, whereas the deviation of the refined c_{ij} from the initial values never exceeds 1%. In the fourth test we removed completely one v_P from one platelet and one v_S from the other platelet. The number of synthetic velocities is still 76 and the ratio $n_P/n_P \sim 3.5$, like the third test, but in this case part of the information on the elastic anisotropy is systematically missing. This is the case, for example, for the Fe6Al4-Bgm sample measured by Fu et al. (2019), where v_P were measured only on platelet 1 and not for platelet 2, and only one v_S per orientation was observed in both platelets 1 and 2, so that only 3 of the 6 dispersion curves were actually measured. This test results in high correlation coefficients (i.e. larger than ±0.95), high esd and larger deviations from the initial values (Table refat1-tab3), in spite of the high sensitivity of the platelets to all c_{ij}s as demonstrated in the first test. This effect is more pronounced in compressional and off-diagonal components, while the three shear components are almost unaffected. This test example highlights the poor reliability of the

sensitivity test proposed by Lin et al. (2018) and Fu et al. (2019) when applied to datasets that are systematically missing velocities in all measured phonon directions (e.g. Fu et al., 2019). It appears, therefore, that careful choice of crystal platelets with high sensitivity to c_{11}, c_{22} and c_{33}, together with careful in-plane alignment of the platelets with respect to the diamond anvils can provide reliable values of the elastic coefficients even when the data sets comprise few phonon directions where v_P is observed.

We also performed another set of tests using our global fit model to assess the effect of the number of pressure points and of the pressure interval on the derivatives of the c_{ij}s (i.e. $c'_{ij,0}$). Because in the global fit model the esd of the c_{ij}s refined at each pressure point depend only on the esd of c_{ij},0 and $c'_{ij,0}$, this test represents a good tool to check that the quality of the fit is actually increasing with increasing number of observed velocities. Similar tests were performed on synthetic datasets by Buchen (2018), showing consistency between calculated and original c_{ij}s. Here, we present similar tests applied to real velocity datasets collected in this study. Our point is to demonstrate that measuring even just a portion of the dispersion curves of bridgmanite at pressures higher than 50 GPa can decrease the esd on values of $c'_{ij,0}$, therefore increasing both accuracy and precision of the c_{ij} calculated in spite of conventional individual fits not being possible. We performed inversion of 4 datasets consisting of: (i) platelets 100 and 011 up to 29.4 GPa; (ii) all 4 platelets up to 35.6 GPa; (iii) all platelets up to 61.7 GPa; (iv) all platelets up to the maximum pressure achieved. The sets of elastic stiffness coefficient at ambient conditions ($c_{ij,0}$) and their pressure derivatives ($c'_{ij,0}$) obtained in each test are reported in Table A.4. Note that the values obtained in test iv are the ones used in the calculation of c_{ij}s reported in Table 4.1 of the main text. It can be seen that adding more pressure points at very high pressure to the data has the effect of increasing the values of $c'_{22,0}$, $c'_{12,0}$ and $c'_{23,0}$, reducing their esd, while not affecting much the values of $c_{ij,0}$ because they are very well constrained by the lower pressure data sets. $c_{11,0}$ and $c'_{11,0}$, instead, show only little variations in the four inversion tests, thanks to tight constraints obtained on the [100] direction below 29.4 GPa. Lin et al. (2018) argued that the global fit procedure presented by Kurnosov et al. (2017) and used in this study underestimates the uncertainties on the c_{ij}. Despite this point was already addressed in the reply of Kurnosov et al. (2018), we stress once again that the uncertainties on the c_{ij} are calculated by propagating the esd on $c_{ij,0}$ and $c'_{ij,0}$, which depend on correlations, data scattering and pressure range investigated. These contributions to the final esd of the fitting parameters (i.e. $c_{ij,0}$ and $c'_{ij,0}$) are all taken into account in the fitting procedure. Consistent with what one would expect, uncertainties are smaller at low pressure and gradually increase at high pressure. Unlike the study of Kurnosov et al. (2017), where sound velocities were measured up to about 40 GPa, in this study we constrained most of the elastic tensor up to 78.8 GPa, which contributes to a further decrease of the uncertainties on some of the fitting parameters. Note that the relatively low constraints on the c_{11} at high pressure is reflected by the larger relative uncertainty (1 esd $\sim$ 1%) with respect to c_{22} and c_{33} (1 esd $\sim$ 0.5 and $\sim$ 0.65%). Therefore, we consider that the esd obtained by the global fit procedure are representative of real uncertainties and reflect different degrees of constraints on different c_{ij}.

Uncertainties calculated with the abovementioned procedure should also include differences between the real value of e.g. c_{11} and the value predicted by our 3rd order EOS in the case that small changes in the compression mechanism occur. Such changes might require a 4th order truncation of the finite strain EOS to properly fit the data. However, employment of higher order truncations should always be justified by observations in the experimental data sets and should not be applied because the c_{ij} are assumed to follow a 3rd or a 4th order EOS. This is because finite strain EOS are empirical functions and not based on thermodynamic principles. Here we lack the resolution for discussing whether some c_{ij}s are better fitted by 3rd or 4th order truncations. Such consideration will be made when datasets constraining the full elasticity of bridgmanite will be available at pressures of e.g. 100 GPa. We did explore the possibility of a subtle change in the high-pressure evolution of the c_{ij}s by using a global fitting combined with a 4th order EOS for all c_{ij}s. Some c_{ij}s did not converge, however, even when the $c_{ij,0}$ were fixed to the values obtained at room pressure using the individual fitting procedure, most likely because of the extremely high correlation between the pressure derivatives of at least some of the c_{ij}s. We performed an additional test as follows: the shear components of the elastic stiffness tensor (i.e. c_{44}, c_{55} and c_{66}), for which strong constraints are provided by the large number of v_S measured at each pressure point, were fitted with a 4th-order EOS, while a 3rd-order EOS were used for the longitudinal and off-diagonal components (test v). The statistical error on the fitting parameters is comparable with that of test iv (Tabe A.4), but correlation between the fitting parameters of the shear components is larger because an additional term (i.e. $c''_{ij,0}$) is refined. We decided to compare also the root mean square (RMS) deviations between observed and calculated velocities to see whether the two fitting strategies agree at high pressure (Table refat1-tab5), which is the region of greatest interest in this study. It can be seen that the RMS errors in test v, where 4th-order equations are used for the shear components, are smaller at ambient pressure, but larger at 78.8 GPa with respect to test iv, where only 3rd-order EOSs were used. A comparison of the calculated dispersion curves shows that the main difference lies in the v_{S1} of platelet 011 (Figure A.10), where the 4th-order EOSs predict systematically faster velocities. This indicates that employing higher order equations of state does not, in this case, increase the overall quality of the fit, for which reason we decided to use 3rd-order EOS also for the shear components of the elastic stiffness tensor. Therefore, c_{ij},0 and $c'_{ij,0}$ of test iv have been used to calculate the c_{ij}s shown in Table 4.1 and Figure A.1.

Supplementary Text A.3

The diamond full width at ambient conditions will mainly depend on the characteristics of the experimental setup. In the Brillouin system installed at BGI, we employed focusing and collecting lenses with a 25.4 mm diameter and 100 mm focal length. An optical mask behind the collecting lens measuring 25(H) x 6(V) mm^2 is used to reduce the intensity of the signal coming from the diamond anvil. The laser beam has a diameter of 0.7 mm and no

beam expander is used. The experimental setup was the same in all runs. The full width at half maximum (FWHM) of the diamond peak at ambient conditions is of the order of 800 m/s. However, in a DAC there are two anvils that in general have different orientations. This is a major problem, because if the dispersion curves of diamond anvils are shifted with respect to each other, the cumulative width of the diamond peaks will be much larger than 800 m/s, reducing the range where it is possible to measure the v_P of the sample. For this reason, before gluing the two diamonds anvils, we carefully rotated one until perfect match between the two dispersion curves was obtained. In this way, at room pressure, we were able to observe peaks from the sample v_P that were located at about 700-800 m/s from the central position of the v_S peak of diamond. By full width (FW) of the diamond peak, we mean twice the minimum distance from the center of the peak at which the v_P signal from the sample can be measured (i.e. FW = 1400-1600 m/s at ambient conditions). With increasing pressure, a stress gradient develops in the diamond anvil, which is partly reflected in the Brillouin spectra. In fact, we see that the shape of the diamond peaks became asymmetric at high pressure and for this reason the FW of the diamond peak increased to 1600-2000 m/s, which is the width of the shaded pink area reported in Figure 4.1a.

Supplementary Figures and Tables

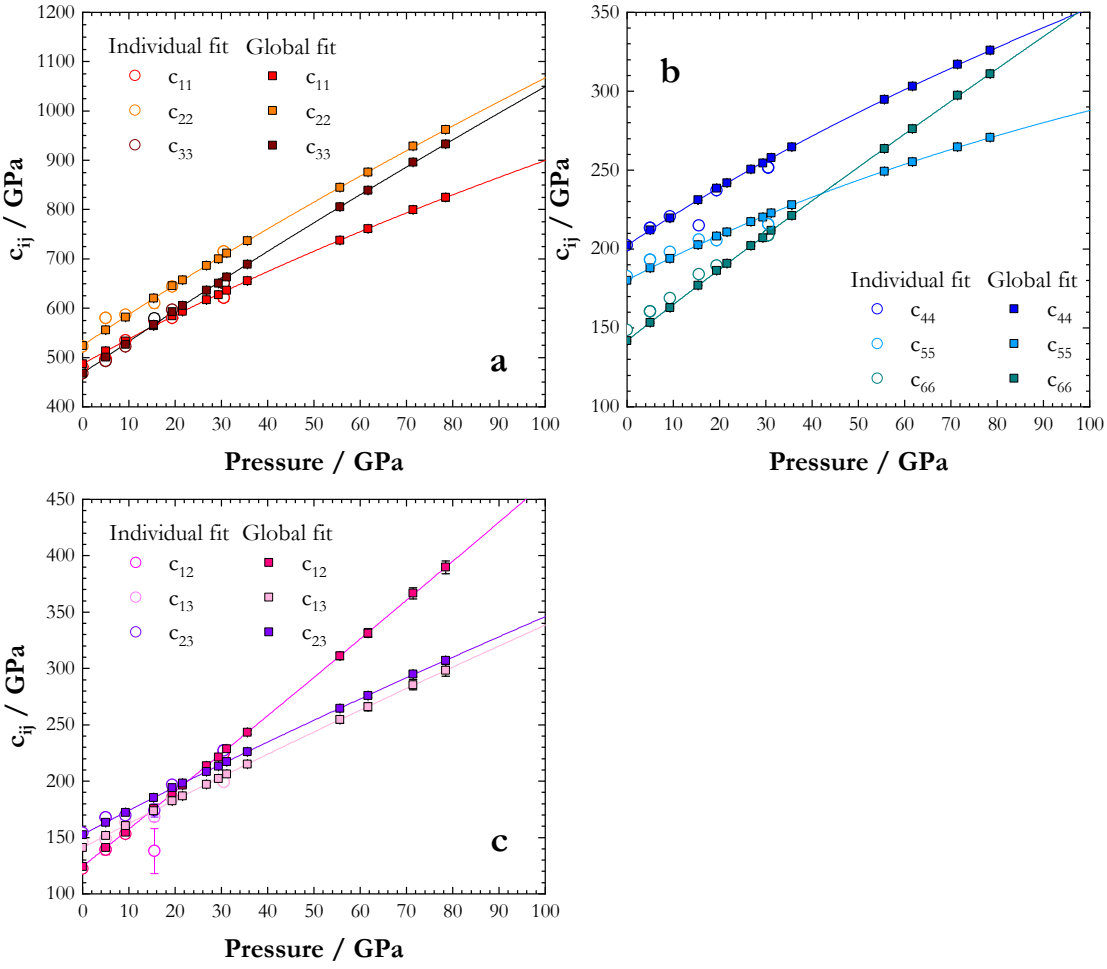

Figure A.1. Comparison of global (solid squares) and individual (open circles) fits of c_{ij}. The solid lines represent 3rd order EoS fits of each c_{ij}. At ambient conditions, the c_{ij} refined using individual ad global fit procedures are always almost identical within mutual uncertainties.

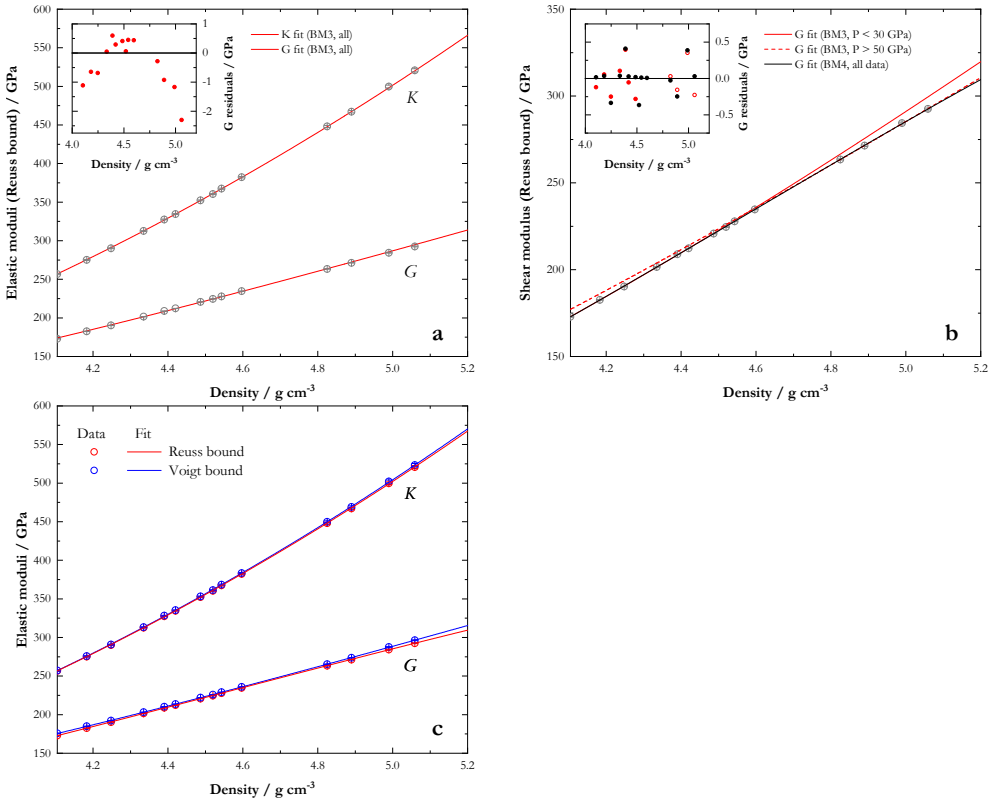

Figure A.2. Fit of experimentally determined adiabatic bulk and shear moduli as a function of density. a) K and G in the Reuss bound (empty grey circles) are fitted individually to 3rd order finite strain EOS (red lines); the deviation of G from experimental data is larger than 2 GPa at high density (pressure), as shown by the residuals plot (red circles). b) A great improvement of the fit can be achieved by using either a 4th order finite strain EOS or two 3rd order equations for data below 30 GPa and above 50 GPa. 3rd order EOS below 30 GPa: solid red line, solid circles; 3rd order EOS above 50 GPa: dashed red line, empty circles; 4th order EOS: solid black line, solid circles. c) Comparison of calculated elastic moduli and finite strain EOSs of $MgSiO_3$ bridgmanite in the Reuss (red) and Voigt (blue) bounds. K bounds differ by less than 0.5%, while G bounds initially converge up to $\rho \sim 4.54$ g cm^{-3}, then diverge up the maximum pressure investigated. The difference between G bounds at the highest pressure investigated is about 1%.

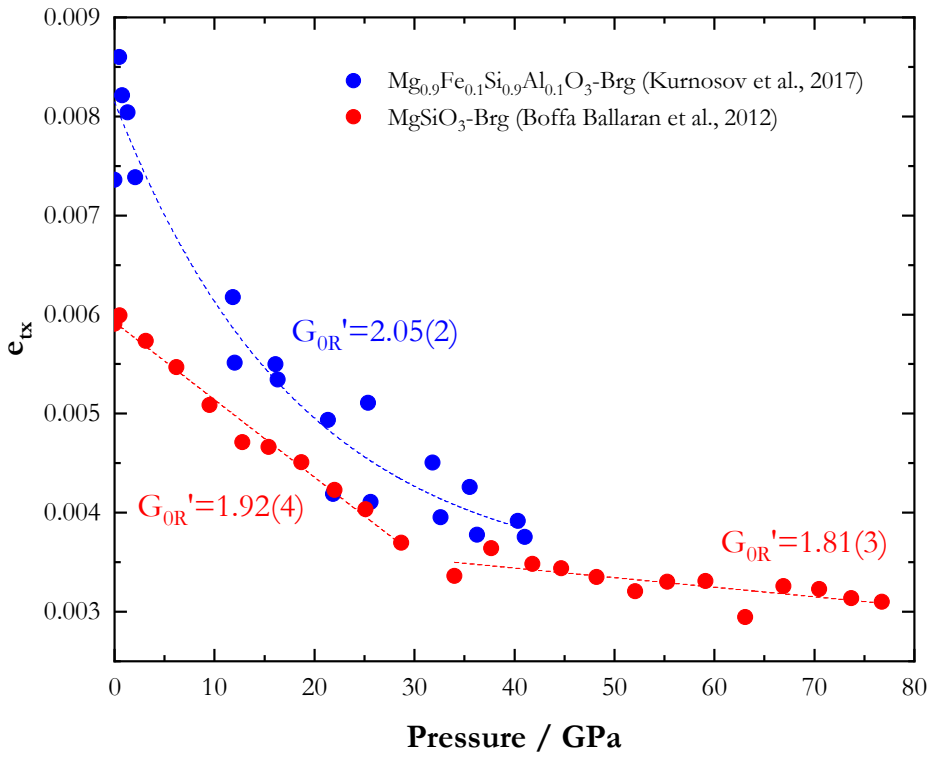

Figure A.3. Lattice strain etx of $MgSiO_3$ (red) and $MgSiO_3$ with 10 mol% $FeAlO_3$ (blue) bridgmanites from previous studies (Boffa Ballaran et al., 2012; Kurnosov et al., 2017, personal communication, reported in the data repository of this study). Dashed lines indicate qualitative trends in e_{tx} that may be correlated with distinct shear mechanisms that correspond to different values of the pressure derivative of the shear modulus (G_0'). It can be seen that the steeper the curve, the higher is the derivative of the shear modulus

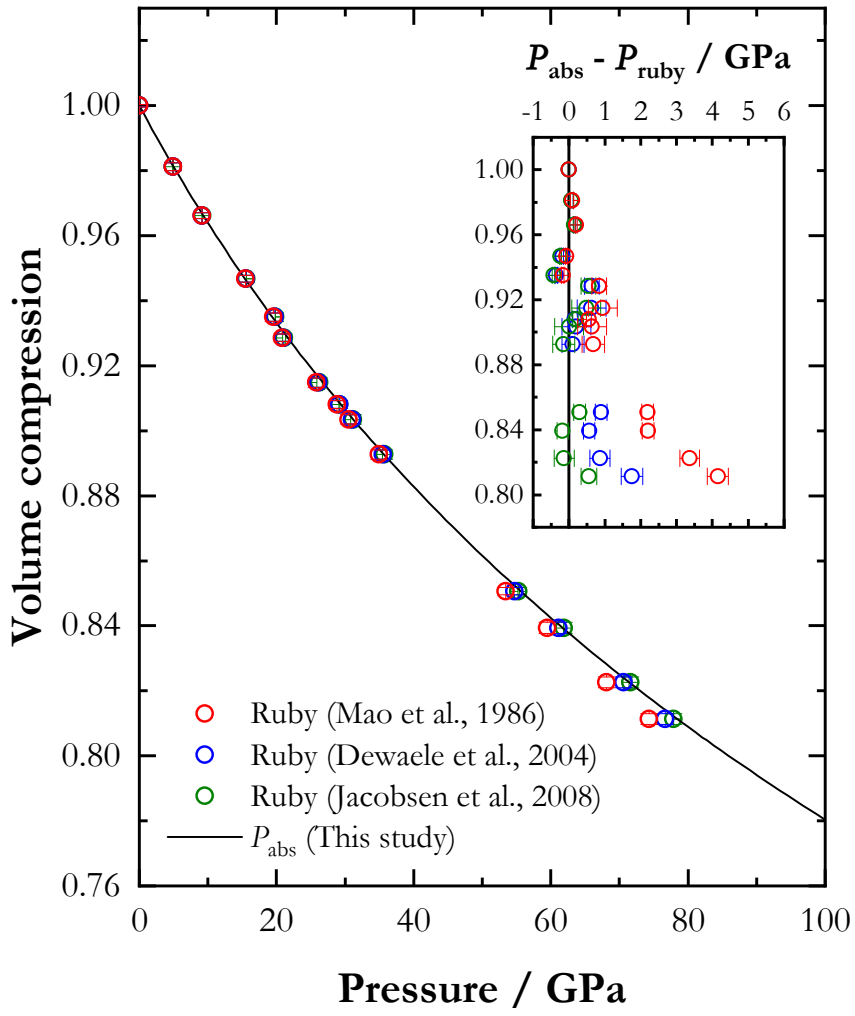

Figure A.4. Experimental *P-V* points of $MgSiO_3$ bridgmanite from run 1 and 2 plotted using different ruby pressure scales: Mao et al. (1986) (red); Dewaele et al. (2004) (green); Jacobsen et al. (2008) (blue). In the inset, it is shown the difference between P_{abs} and each ruby pressure scale.

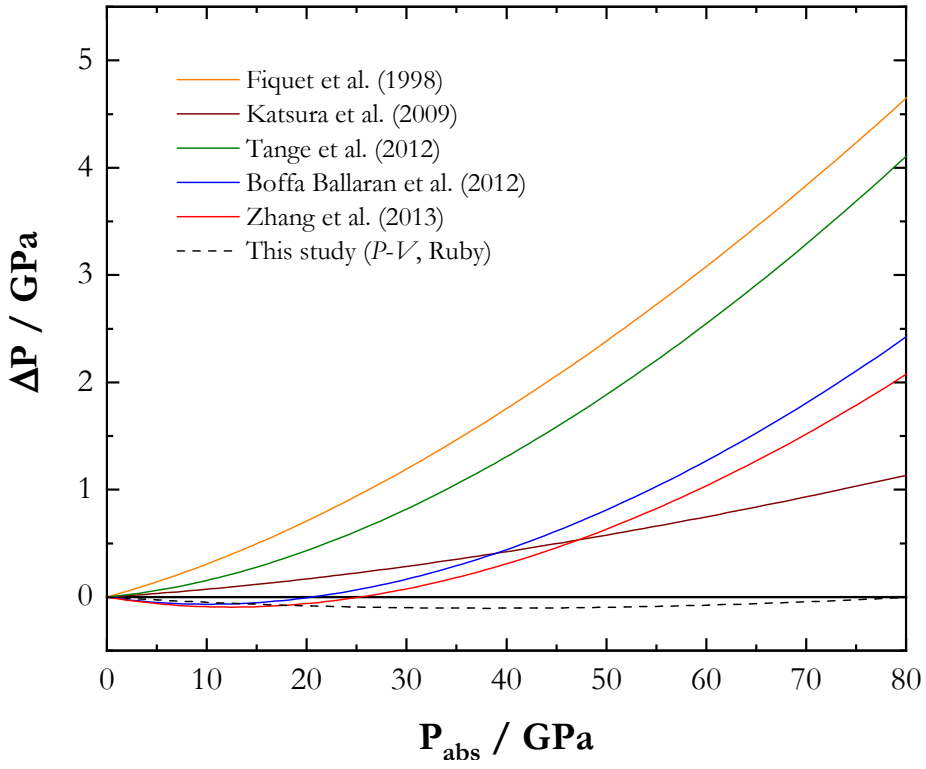

Figure A.5. Difference between P_{abs} and pressures calculated from $MgSiO_3$ bridgmanite *P-V* equations of state reported in previous studies.

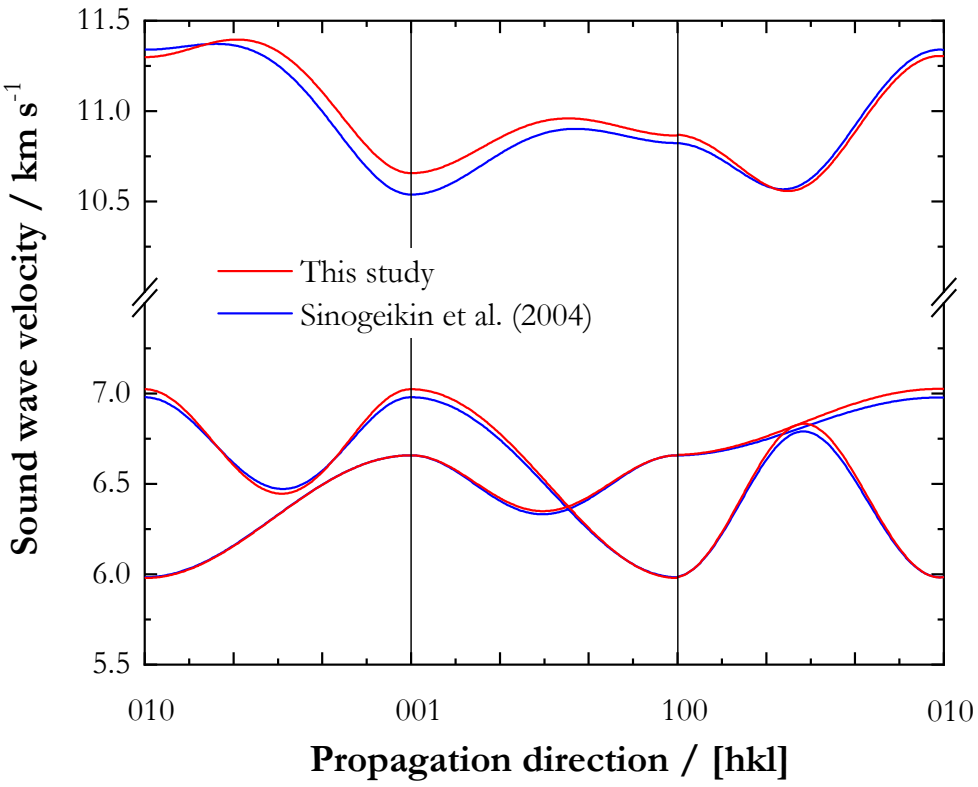

Figure A.6. Comparison between the dispersion curves at ambient conditions of $MgSiO_3$ bridgmanite from this study (global fit, red line) and from Sinogeikin et al. (2004) (blue line). The two curves are in excellent agreement.

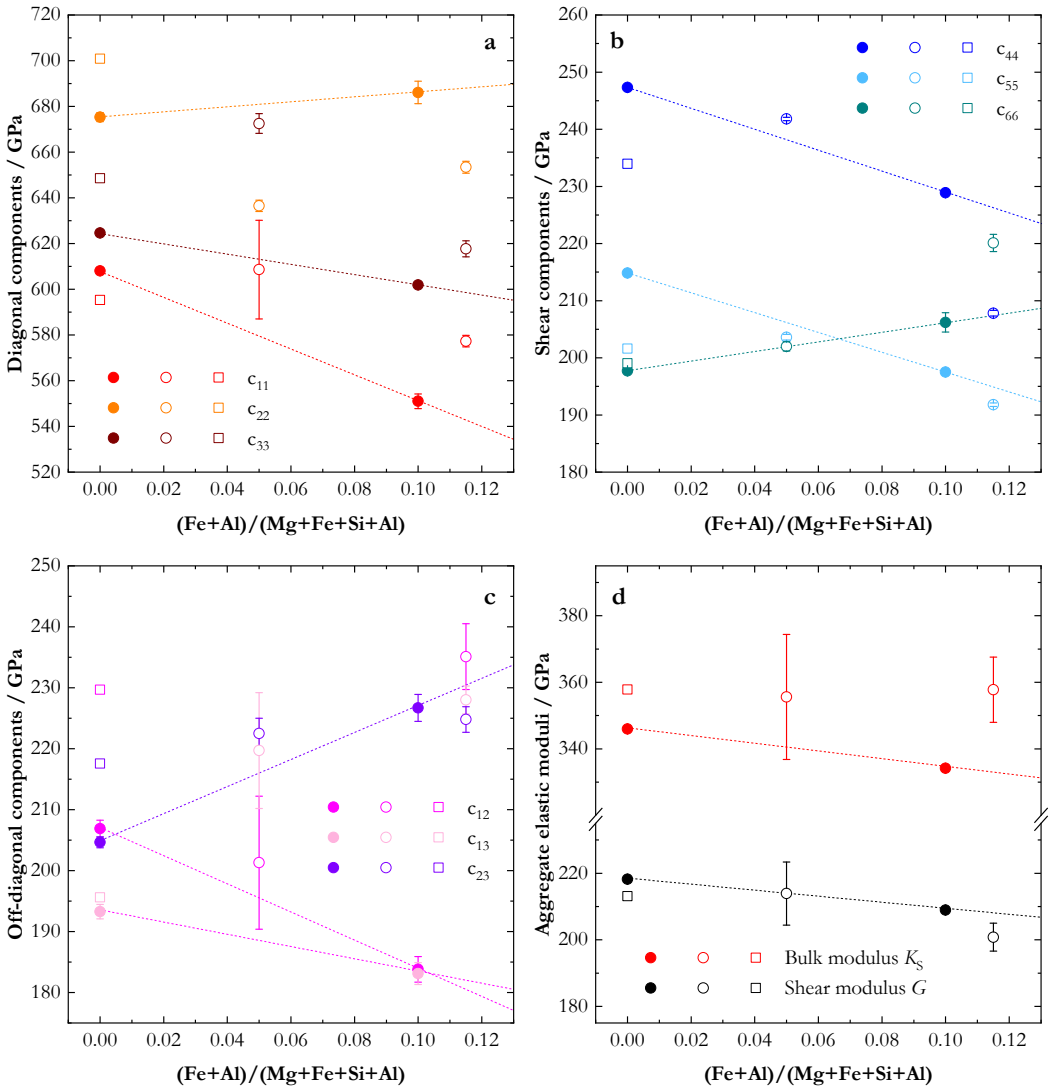

Figure A.7. Compositional dependence of elastic stiffness components (c_{ij}) and aggregate elastic moduli of bridgmanite at 25 GPa. Full circles: $MgSiO_3$ (this study) and $Mg_{0.9}Fe_{0.1}Al_{0.1}Si_{0.9}O_3$ (Kurnosov et al., 2017). Empty circles: $Mg_{0.94}Fe_{0.06}Al_{0.04}Si_{0.96}O_3$ (Fe6Al4) and $Mg_{0.88}Fe_{0.12}Al_{0.11}Si_{0.89}O_3$ (Fe12Al11) reported by Fu et al. (2019). Empty squares: $MgSiO_3$ (Wentzcovitch et al., 2004). When not shown, error bars are smaller than the symbols. Dashed lines: qualitative compositional trends of elastic parameters from this study and Kurnosov et al. (2017). Major differences between our qualitative trendlines and experimental data points of Fu et al. (2019) are c_{22} and c_{33} of Fe6Al4 (a), c_{44} and c_{66} of Fe12Al11(b), and c_{12} and c_{23} of both samples (c). Furthermore, in (d), our trendline shows that the bulk modulus decreases with increasing $FeAlO_3$ content, while data from Fu et al. (2019) suggest that the trend is opposite.

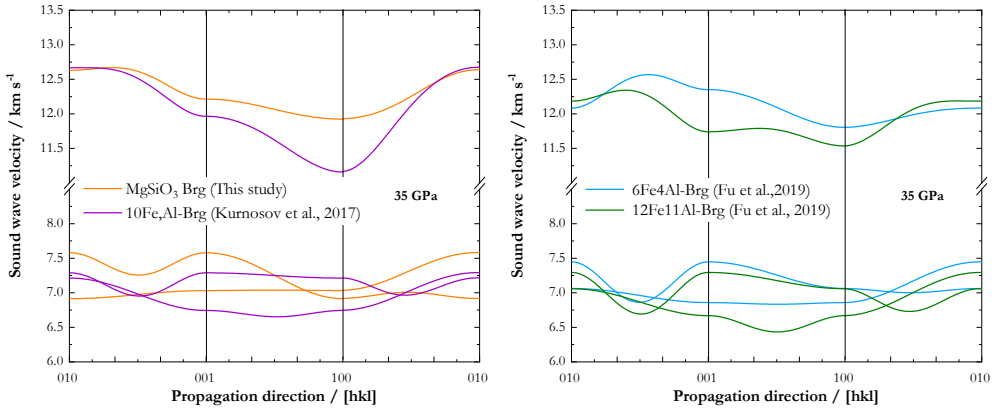

Figure A.8. Dispersion curves of bridgmanite at 35 GPa. The overall anisotropy of v_S is consistent among the three studies; however, discrepancies are still present in the anisotropy of v_P. This study: $MgSiO_3$, c_{ij} calculated from 3rd order EOS; Kurnosov et al. (2017): 10 mol% $FeAlO_3$, c_{ij} calculated from 3rd order EOS; Fu et al. (2019): 5 mol% $FeAlO_3$ and 11 mol% $FeAlO_3$, c_{ij} reported at 35 GPa.

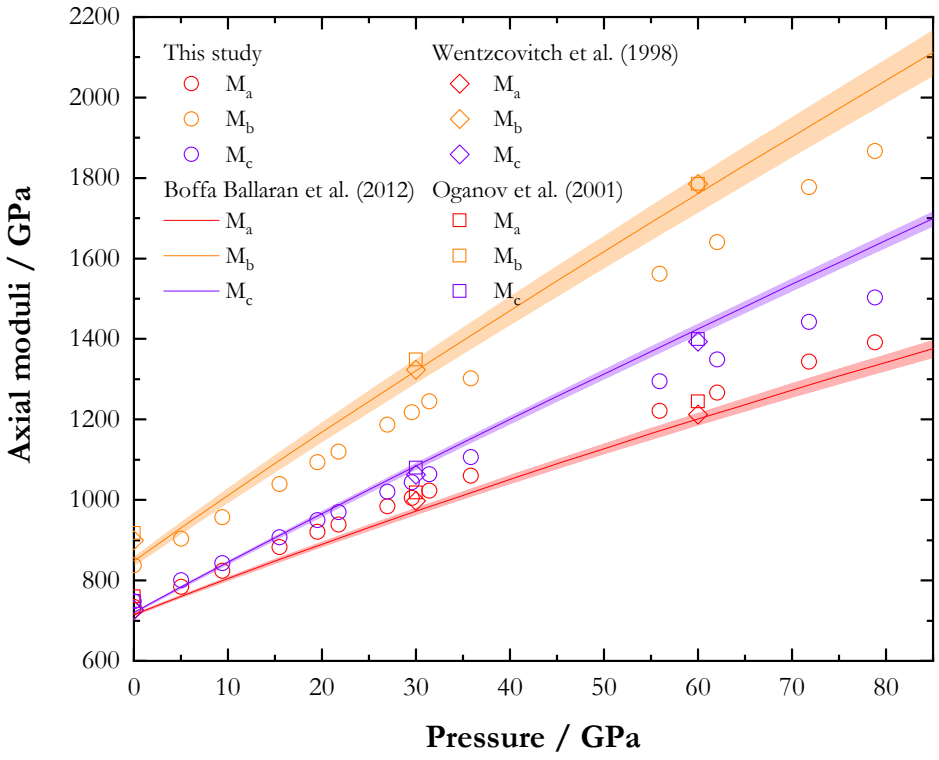

Figure A.9. Calculated axial moduli as a function of pressure. This study: Brillouin scattering (empty circles); Wentzcovitch et al. (1998): ab initio lattice dynamics (empty diamonds); Oganov et al. (2001): ab initio molecular dynamics (empty squares); Boffa Ballaran et al. (2012): single-crystal X-ray diffraction (solid lines and shaded area representing uncertainties).

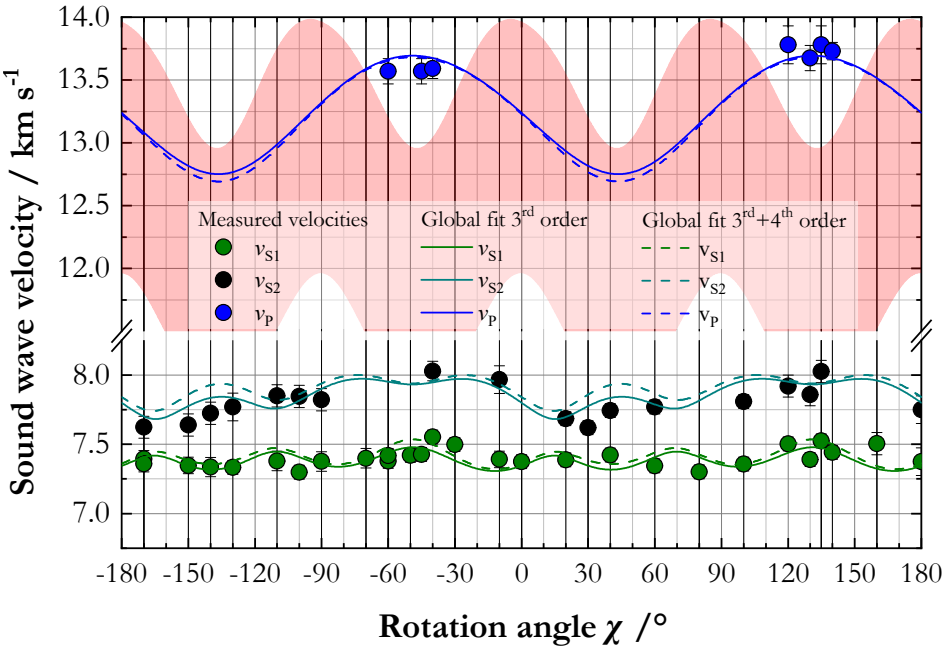

Figure A.10. Experimentally measured sound velocities (solid circles) and calculated dispersion curves for platelet 100 at 78.8(5) GPa. Solid lines are calculated using 3rd-order EOSs for all c_{ij}s. Dashed lines are calculated using 4th-order EOSs for shear components and 3rd-order EOSs for longitudinal and off diagonal components. The pink shaded area shows the velocity range where the v_P signal of the sample cannot be observed due to overlap with the diamond v_S. The hybrid 3rd and 4th-order fit (dashed lines) fails to accurately represent v_S2, showing deviations that are much larger than the experimental uncertainties.

Table A.1. Adiabatic bulk moduli and shear moduli of bridgmanite with different compositions from experimental and theoretical studies.

Composition	K_{S0} (GPa)	K'_{S0}	G_0 (GPa)	G'_0	P range (GPa)	Study
$MgSiO_3$	257.1(6)	3.71(4)	175.6(2)	1.86(1)	0-78.5	This study
$MgSiO_3$	253(3)		175(2)		0	Sinogeikin et al. (2004)
$MgSiO_3$	264(5)		177(4)		0	Yeganeh-Haeri (1994)
$MgSiO_3$	236(4)		166(2)		0	Fukui et al. (2016)
$MgSiO_3$	253(2)	4.4(1)	173(1)	2.0(1)	0-9	Li and Zhang (2005)
$MgSiO_3$	247(4)	4.5(2)	176(2)	1.6(1)	0-23	Chantel et al. (2012)
$MgSiO_3$	252(1)	4.1(1)	175(1)	1.7(1)	0-23	Chantel et al. (2012) + Li and Zhang (2005)
$MgSiO_3$			172.9(15)	1.56(4)	0-100	Murakami et al. (2007)
$MgSiO_3$			172.1(13)	1.70(3)	0-100	Recalculated from Murakami et al. (2007)
$MgSiO_3$	267		173		0	Wentzcovitch et al. (2004)
$MgSiO_3$	267		180		0	Oganov et al. (2001)
$MgSiO_3$	250.5	4.01	172.9	1.74	0-160	Zhang et al. (2013)
$MgSiO_3$	245.5	3.96	168.2	1.79	0-150	Schukla et al. (2015)
$Mg_{0.95}Fe_{0.05}SiO_3$	236(2)	4.7(1)	174(1)	1.56(5)	0-25	Chantel et al. (2012)
$Mg_{0.96}Fe_{0.05}Si_{0.99}O_3$ (HS)	254(8)	3.3(3)	166.2(5)	1.91(2)	25-43	Fu et al. (2018)
$Mg_{0.96}Fe_{0.05}Si_{0.99}O_3$ (LS)	234(11)	3.5(4)	190.0(7)	1.54(11)	58-70	Fu et al. (2018)
$Mg_{0.95}Fe_{0.05}SiO_3$	245.8	4.03	167.2	1.79	0-150	Schukla et al. (2015)
$Mg_{0.875}Fe_{0.250}Si_{0.875}O_3$	233.6	4.05	143.1	1.88	0-150	Schukla et al. (2016)
$Mg_{0.95}Al_{0.10}Si_{0.95}O_3$	252(5)	3.7(3)	165(2)	1.85	0-35	Jackson et al. (2005)
$Mg_{0.875}Al_{0.250}Si_{0.875}O_3$	242.5	4.06	162.7	1.85	0-150	Schukla et al. (2016)
$Mg_{0.9}Fe_{0.1}Al_{0.1}Si_{0.9}O_3$	250.8(4)	3.44(3)	159.7(2)	2.05(2)	0-40	Kurnosov et al. (2017)
$Mg_{0.943}Fe_{0.045}Al_{0.023}Si_{0.988}O_3$	244(3)		165(1)			Fukui et al. (2016)
$Mg_{0.875}Fe_{0.125}Al_{0.125}Si_{0.875}O_3$	239.4	4.05	156.3	1.83	0-150	Schukla et al. (2016)

Table A.2. Thermodynamic parameters used in the mineralogical model. Bold entries represent updated values with respect to Stixrude and Lithgow-Bertelloni (2011).

	V_0 (cm^3/mol)	K_{T0} (GPa)	K'_{T0}	Θ_0 (K)	γ_0	q_0	G_0 (GPa)	G'_0	η_0	F_0[f] (kJ/mol)
Bridgmanite										
$MgSiO_3$[a]	24.45	**254.5**	**3.73**	905	**1.44**	**1.4**	**175.6**	**1.86**	**3**	-1368
$Fe^{2+}SiO_3$[b]	**25.34**	272	4.1	**765**	**1.44**	**1.4**	**162**	**1.5**	**1.9**	**-1023**
Ferropericlase										
MgO[c]	**11.24**	**160.9**	**4.35**	**773**	1.53	**1.5**	**127.9**	**2.49**	**2.02**	**-570**
$Fe^{2+}O$[d]	12.26	**149.4**	**3.6**	**417**	**1.41**	**0.5**	59	1.4	-0.1	**-244**
Ca-perovskite (cubic)										
$CaSiO_3$[e]	**27.45**	**240.9**	**4.08**	**800**	**0.82**	**3**	**125.9**	**1.58**	**1.25**	

[a]: this study (room T) and Chantel et al. (2012) (high T)
[b]: Tange et al. (2009b), Nakajima et al. (2012), Xu et al. (2008), and Chantel et al. (2012)
[c]: Kono et al. (2010)
[d]: Fischer et al. (2011) and Stixrude and Lithgow-Bertelloni (2011)
[e]: refitted form Gréaux et al. (2019)
[f]: Nakajima et al. (2012)

Table A.3. Correlation matrices obtained from inversion of synthetic dataset at ambient conditions. Test 1: 38 phonon directions, 3 velocities per phonon direction, 114 total velocities, n_S/n_P = 2. Test 2: 38 phonon directions, 2 velocities per direction, 76 total velocities, n_S/n_P = 2. Test 3: 38 phonon directions, 2 velocities per direction, 76 total velocities, $n_S/n_P \sim 3.5$. Test 4: 38 phonon directions, 2 velocities per direction (2 shear velocities in one platelet, 1 shear and 1 compressional velocity in the other platelet), 76 total velocities, $n_S/n_P \sim 3.5$. Bold numbers indicate high correlation between c_{ij}.

	c_{22}	c_{33}	c_{44}	c_{55}	c_{66}	c_{12}	c_{13}	c_{23}
test 1								
c_{11}	-0.013	-0.089	-0.020	-0.144	-0.048	0.180	0.081	-0.048
c_{22}		-0.251	-0.218	-0.018	-0.022	0.229	-0.077	0.243
c_{33}			-0.343	-0.078	-0.027	-0.268	0.260	0.322
c_{44}				-0.002	-0.006	0.167	-0.096	-0.196
c_{55}					-0.205	0.036	-0.004	0.030
c_{66}						-0.022	0.094	0.020
c_{12}							0.045	0.038
c_{13}								-0.117
test 2								
c_{11}	-0.011	-0.072	-0.015	-0.118	-0.039	0.227	0.014	-0.044
c_{22}		-0.255	-0.157	-0.016	-0.033	0.230	-0.075	0.252
c_{33}			-0.376	-0.092	-0.034	-0.261	0.156	0.313
c_{44}				-0.002	-0.011	0.182	-0.095	-0.195
c_{55}					-0.251	0.039	0.034	0.022
c_{66}						-0.037	0.085	0.036
c_{12}							-0.064	0.033
c_{13}								-0.139
test 3								
c_{11}	-0.017	-0.057	-0.008	-0.067	-0.032	0.228	0.143	-0.046
c_{22}		-0.268	-0.081	-0.006	-0.024	0.407	-0.101	0.459
c_{33}			-0.236	-0.046	-0.008	-0.206	0.373	0.419
c_{44}				0.020	-0.001	0.191	-0.064	-0.056
c_{55}					-0.147	0.102	-0.105	0.061
c_{66}						0.033	0.142	0.011
c_{12}							0.027	0.234
c_{13}								0.049
test 4								
c_{11}	0.094	-0.119	-0.008	-0.110	-0.020	0.159	-0.161	0.017
c_{22}		**-0.972**	-0.051	0.099	0.005	**0.973**	**-0.867**	**0.902**
c_{33}			-0.049	-0.131	-0.011	**-0.953**	0.842	-0.805
c_{44}				0.024	-0.003	-0.002	0.012	-0.135
c_{55}					-0.237	0.110	-0.086	0.062
c_{66}						0.010	-0.026	-0.013

c_{12}	**-0.887**	**0.862**
c_{13}		-0.764

Table A.4. Elastic stiffness coefficients at ambient conditions and their pressure derivatives obtained from inversion of different velocity data sets using the global fit procedure. For comparison, the individual fit of room pressure data obtained from 4 platelets is also shown.

Test number	i	ii	iii	iv	v	Individual fits
Platelets used	100, 011	All	All	All	All	All
P_{max} (GPa)	29.4	35.6	61.7	78.8	78.8	0.0001
$c_{11,0}$ (GPa)	484(3)	483.6(18)	485(2)	487(2)	487(2)	482(3)
$c_{22,0}$ (GPa)	529(4)	528(3)	526(3)	524(3)	524(3)	523(4)
$c_{33,0}$ (GPa)	464(3)	464.6(17)	465.9(17)	467.7(16)	466.9(14)	468(3)
$c_{44,0}$ (GPa)	203.0(3)	203.0(2)	202.4(2)	202.3(2)	202.9(2)	202.3(3)
$c_{55,0}$ (GPa)	183.8(7)	183.4(5)	181.2(4)	180.2(4)	184.1(6)	182.8(10)
$c_{66,0}$ (GPa)	146.8(10)	150.5(6)	142.2(5)	141.9(5)	148.0(8)	148.6(14)
$c_{12,0}$ (GPa)	125(3)	121.7(16)	123.5(18)	124.3(18)	124.4(17)	122(3)
$c_{13,0}$ (GPa)	144.8(18)	146.8(13)	141.8(14)	140.9(13)	142.1(13)	146(2)
$c_{23,0}$ (GPa)	152.9(13)	152.5(9)	152.1(10)	152.6(10)	152.5(9)	154.3(14)
$c'_{11,0}$	5.32(12)	5.31(9)	5.29(10)	5.21(9)	5.14(9)	
$c'_{22,0}$	4.6(5)	5.5(3)	6.30(8)	6.35(6)	6.33(5)	
$c'_{33,0}$	6.85(17)	6.74(12)	6.70(8)	6.56(6)	6.54(5)	
$c'_{44,0}$	1.88(2)	1.88(1)	1.95(1)	1.95(1)	1.87(2)	
$c'_{55,0}$	1.33(3)	1.38(2)	1.51(1)	1.55(1)	1.23(4)	
$c'_{66,0}$	2.36(4)	1.98(2)	2.30(1)	2.30(1)	1.87(4)	
$c'_{12,0}$	2.3(3)	3.05(15)	3.33(7)	3.27(7)	3.22(6)	
$c'_{13,0}$	2.07(11)	1.83(7)	2.13(7)	2.17(6)	2.07(6)	
$c'_{23,0}$	1.6(2)	1.97(15)	2.26(4)	2.22(3)	2.19(3)	
$c''_{44,0}$ (GPa^{-1})					-0.119(9)	
$c''_{55,0}$ (GPa^{-1})					-0.0067(11)	
$c''_{66,0}$ (GPa^{-1})					0.0062(13)	

Table A.5. Root mean square (RMS) deviation between calculated and observed velocities for tests iv and v at selected pressures. Using 4^{th}-order EOS for the shear components the calculated RMS errors decrease at room pressure, but increase at very high pressure. Thus, the 3^{rd}-order fit is preferable due to the lower number and correlation of fitting parameters.

Method	RMS (m/s)			
	0 GPa	29.37 GPa	55.59 GPa	78.8 GPa
3^{rd}-order	43	66	73	66
Mixed 3^{rd} and 4^{th} order	29	65	62	80

References

Boffa Ballaran, T., A. Kurnosov, K. Glazyrin, D. J. Frost, M. Merlini, M. Hanfland, and R. Caracas (2012). "Effect of chemistry on the compressibility of silicate perovskite in the lower mantle". In: *Earth and Planetary Science Letters* 333-334, pp. 181–190. DOI: 10.1016/j.epsl.2012.03.029.

Buchen, J. (2018). "The Elastic Properties of Wadsleyite and Stishovite at High Pressures". URL: https://epub.uni-bayreuth.de/4410/.

Chantel, J., D. J. Frost, C. A. McCammon, Z. Jing, and Y. Wang (2012). "Acoustic velocities of pure and iron-bearing magnesium silicate perovskite measured to 25 GPa and 1200 K". In: *Geophysical Research Letters* 39 (19). DOI: 10.1029/2012GL053075.

Dewaele, A., P. Loubeyre, and M. Mezouar (2004). "Equations of state of six metals above 94 GPa". In: *Physical Review B - Condensed Matter and Materials Physics* 70 (9), p. 094112. DOI: 10.1103/PhysRevB.70.094112.

Fischer, R. A., A. J. Campbell, G. A. Shofner, O. T. Lord, P. Dera, and V. B. Prakapenka (2011). "Equation of state and phase diagram of FeO". In: *Earth and Planetary Science Letters* 304 (3-4), pp. 496–502. DOI: 10.1016/j.epsl.2011.02.025.

Fu, S., J. Yang, N. Tsujino, T. Okuchi, N. Purevjav, and J.-F. F. Lin (2019). "Single-crystal elasticity of (Al,Fe)-bearing bridgmanite and seismic shear wave radial anisotropy at the topmost lower mantle". In: *Earth and Planetary Science Letters* 518, pp. 116–126. DOI: 10.1016/j.epsl.2019.04.023.

Gréaux, S., T. Irifune, Y. Higo, Y. Tange, T. Arimoto, Z. Liu, and A. Yamada (2019). "Sound velocity of $CaSiO_3$ perovskite suggests the presence of basaltic crust in the Earth's lower mantle". In: *Nature* 565 (7738), pp. 218–221. DOI: 10.1038/s41586-018-0816-5.

Hill, R. (1963). "Elastic properties of reinforced solids: Some theoretical principles". In: *Journal of the Mechanics and Physics of Solids* 11 (5), pp. 357–372. DOI: 10.1016/0022-5096(63)90036-X.

Jacobsen, S. D., C. M. Holl, K. A. Adams, R. A. Fischer, E. S. Martin, C. R. Bina, J. F. Lin, V. B. Prakapenka, A. Kubo, and P. Dera (2008). "Compression of single-crystal magnesium oxide to 118 GPa and a ruby pressure gauge for helium pressure media". In: *American Mineralogist* 93 (11-12), pp. 1823–1828. DOI: 10.2138/am.2008.2988.

Kono, Y., T. Irifune, Y. Higo, T. Inoue, A. Barnhoorn, D. Suetsugu, C. Bina, T. Inoue, D. Wiens, and M. Jellinek (2010). "*P-V-T* relation of MgO derived by simultaneous elastic wave velocity and in situ X-ray measurements: A new pressure scale for the mantle transition region". In: *Physics of the Earth and Planetary Interiors* 183 (1-2), pp. 196–211. DOI: 10.1016/j.pepi.2010.03.010.

Kurnosov, A., H. Marquardt, D. J. Frost, T. B. Ballaran, and L. Ziberna (2018). "Kurnosov et al. reply". In: *Nature 2018 564:7736* 564 (7736), E27–E31. DOI: 10.1038/s41586-018-0742-6.

Kurnosov, A., H. Marquardt, D. J. Frost, T. B. Ballaran, and L. Ziberna (2017). "Evidence for a Fe^{3+}-rich pyrolitic lower mantle from (Al,Fe)-bearing bridgmanite elasticity data". In: *Nature* 543, pp. 543–546. DOI: 10.1038/nature21390.

Lin, J. F., Z. Mao, J. Yang, and S. Fu (2018). "Elasticity of lower-mantle bridgmanite". In: *Nature* 564 (7736), E18–E26. DOI: 10.1038/s41586-018-0741-7.

Mao, H. K., J. Xu, and P. M. Bell (1986). "Calibration of the ruby pressure gauge to 800 kbar under quasi-hydrostatic conditions". In: *Journal of Geophysical Research* 91 (B5), p. 4673. DOI: 10.1029/jb091ib05p04673.

Melinger-Cohen, A. and R. Jeanloz (2019). "Finite Strain Analysis of Shear and Compressional Wave Velocities". In: *Journal of Geophysical Research: Solid Earth* 124 (11), pp. 11651–11677. DOI: 10.1029/2019JB017868.

Nakajima, Y., D. J. Frost, and D. C. Rubie (2012). "Ferrous iron partitioning between magnesium silicate perovskite and ferropericlase and the composition of perovskite in the Earth's lower mantle". In: *Journal of Geophysical Research: Solid Earth* 117 (8), pp. 1–12. DOI: 10.1029/2012JB009151.

Nye, J. F. (1985). *Physical properties of crystals: their representation by tensors and matrices*. Oxford University Press. ISBN: 9780198511656.

Oganov, A. R., J. P. Brodholt, and G. D. Price (2001). "Ab initio elasticity and thermal equation of state of $MgSiO_3$ perovskite". In: *Earth and Planetary Science Letters* 184 (3-4), pp. 555–560. DOI: 10.1016/S0012-821X(00)00363-0.

Sinogeikin, S. V. and J. D. Bass (2000). "Single-crystal elasticity of pyrope and MgO to 20 GPa by Brillouin scattering in the diamond cell". In: *Physics of the Earth and Planetary Interiors* 120 (1), pp. 43–62. DOI: 10.1016/S0031-9201(00)00143-6.

Sinogeikin, S. V., J. Zhang, and J. D. Bass (2004). "Elasticity of single crystal and polycrystalline $MgSiO_3$ perovskite by Brillouin spectroscopy". In: *Geophysical Research Letters* 31 (6). DOI: 10.1029/2004gl019559.

Speziale, S., H. Marquardt, and T. S. Duffy (2014). "Brillouin scattering and its application in geosciences". In: *Reviews in Mineralogy and Geochemistry* 78 (1), pp. 543–603. DOI: 10.2138/rmg.2014.78.14.

Stixrude, L. and C. Lithgow-Bertelloni (2005). "Thermodynamics of mantle minerals - I. Physical properties". In: *Geophysical Journal International* 162 (2), pp. 610–632. DOI: 10.1111/j.1365-246X.2005.02642.x.

— (2011). "Thermodynamics of mantle minerals - II. Phase equilibria". In: *Geophysical Journal International* 184 (3), pp. 1180–1213. DOI: 10.1111/j.1365-246X.2010.04890.x.

Tange, Y., E. Takahashi, Y. Nishihara, K. I. Funakoshi, and N. Sata (2009b). "Phase relations in the system MgO-FeO-SiO_2 to 50 GPa and 2000°C: An application of experimental techniques using multianvil apparatus with sintered diamond anvils". In: *Journal of Geophysical Research: Solid Earth* 114 (2), pp. 1–12. DOI: 10.1029/2008JB005891.

Trots, D. M., A. Kurnosov, T. B. Ballaran, S. Tkachev, K. Zhuravlev, V. Prakapenka, M. Berkowski, and D. J. Frost (2013). "The Sm:YAG primary fluorescence pressure scale". In: *Journal of Geophysical Research: Solid Earth* 118 (11), pp. 5805–5813. DOI: 10.1002/2013JB010519.

Trots, D. M., A. Kurnosov, L. Vasylechko, M. Berkowski, T. B. Ballaran, and D. J. Frost (2011). "Elasticity and equation of state of $Li_2B_4O_7$". In: *Physics and Chemistry of Minerals* 38 (7), pp. 561–567. DOI: 10.1007/s00269-011-0428-1.

Wentzcovitch, R. M., B. B. Karki, M. Cococcioni, and S. de Gironcoli (2004). "Thermoelastic Properties of $MgSiO_3$-Perovskite: Insights on the Nature of the Earth's Lower Mantle". In: *Physical Review Letters* 92 (1). DOI: 10.1103/PhysRevLett.92.018501.

Wentzcovitch, R. M., B. B. Karki, S. Karato, and C. R. S. D. Silva (1998). "High pressure elastic anisotropy of $MgSiO_3$ perovskite and geophysical implications". In: *Earth and Planetary Science Letters* 164 (1-2), pp. 371–378. DOI: 10.1016/S0012-821X(98)00230-1.

Whitfield, C. H., E. M. Brody, and W. A. Bassett (1976). "Elastic moduli of NaCl by Brillouin scattering at high pressure in a diamond anvil cell". In: *Review of Scientific Instruments* 47 (8), pp. 942–947. DOI: 10.1063/1.1134778.

Xu, W., C. Lithgow-Bertelloni, L. Stixrude, and J. Ritsema (2008). "The effect of bulk composition and temperature on mantle seismic structure". In: *Earth and Planetary Science Letters* 275 (1-2), pp. 70–79. DOI: 10.1016/j.epsl.2008.08.012.

Zha, C. S., T. S. Duffy, R. T. Downs, H. K. Mao, and R. J. Hemley (1996). "Sound velocity and elasticity of single-crystal forsterite to 16 GPa". In: *Journal of Geophysical Research B: Solid Earth* 101 (8), pp. 17535–17545. DOI: 10.1029/96jb01266.

Appendix B

Supporting information to: Thermal Equation of State and Structural Evolution of Al-Bearing Bridgmanite

Contents of this file
Text B.1 to B.2
Figures B.1 to B.12
Tables B1, B.2, B.6, and B.7

Additional Supporting information: Files uploaded at https://figshare.com/s/ce5a9194e4e3a235e7bb

Table B.3. Unit-cell parameters and molar volume of CC2OV5 Al-bearing bridgmanite at high pressure and temperature. Bold pressure and temperature values were calculated using a cross correlation function between the ruby signal and the unit cell volume of W and/or Au.

Table B.4. Unit-cell parameters and molar volume of CC4OV2 Al-bearing bridgmanite at high pressure and temperature. Bold pressure and temperature values were calculated using a cross correlation function between the ruby signal and the unit cell volume of W and/or Au.

Table B.5. Unit-cell parameters and molar volume of CC7OV3 Al-bearing bridgmanite at high pressure and room temperature.

Supplementary Text B.1

In our analysis of pressure-volume-temperature (PVT) data, we employed the thermal pressure formulation of Stixrude and Lithgow-Bertelloni (2005). The formalism is based on a Debye model (e.g., Poirier, 2000) where the observed pressure is expressed as a function of

the experimentally measured volume (V) and temperature (T):

$$P(V,T) = P_c(V,T_0) + P_{th}(V,T) = P_c(V,T_0) + \frac{\gamma}{V_{\text{mol}}}\left(E(V,T) - E(V,T_0)\right) \tag{B.1}$$

where the term indicating cold pressure P_c is calculated at room temperature (T_0) using a 3$^{\text{rd}}$-order Birch-Murnaghan equation of state (see main text) and the thermal pressure (P_{th}) is expressed as a function of the molar volume (V_{mol}), the thermal Grüneisen parameter (γ) and the internal energy (E). E is then expressed a function of the Debye temperature (θ_D):

$$E = 9nRT\int_0^{\theta_D}\frac{t^3 dt}{e^t - 1} \tag{B.2}$$

where n is the number of atoms per formula unit and R is the gas constant. γ, its logarithmic derivave (q), and θ_D are then expressed as:

$$\theta_D^2 = \theta_{D0}^2\left[1 + 6\gamma f + \frac{1}{2}\left(36\gamma_0^2 - 12\gamma_0 - 18\gamma_0 q_0\right)f^2\right] \tag{B.3}$$

$$\gamma = \frac{1}{2}\frac{\theta_{D0}}{\theta_D}(2f+1)\left[6\gamma_0 + \left(36\gamma_0^2 - 12\gamma_0 - 18\gamma_0 q_0\right)f\right] \tag{B.4}$$

$$q = \frac{1}{9\gamma}\left[18\gamma^2 - 6\gamma - \frac{1}{2}\frac{\theta_{D0}}{\theta_D}(2f+1)^2\left(36\gamma_0^2 - 12\gamma_0 - 18\gamma_0 q_0\right)\right] \tag{B.5}$$

with γ_0, q_0, and θ_{D0} being the room pressure-temperature values of γ, q, and θ_D, and f being the finite Eulerian strain:

$$f = \frac{1}{2}\left[\left(\frac{V_0}{V}\right)^{2/3} - 1\right] \tag{B.6}$$

For comparison, we also employed the more conventional Mie-Grüneisen-Debye (MGD) formulation where q is fixed, while γ and θ_D are expressed as (Poirier, 2000):

$$\gamma = \gamma_0\left(\frac{V}{V_0}\right)^q \tag{B.7}$$

$$\theta_D = \theta_{D0}exp\left(\frac{\gamma_0 - \gamma}{q}\right) \tag{B.8}$$

Thermal EOSs based on the finite-strain-based and MGD formalisms were used to fit the above mentioned three *PVT* datasets using a script implemented in OriginPro2021 (OriginLab corporation, Northampton, MA, USA). Uncertainties on pressure, volume and temperature were propagated to the fit parameters through an orthogonal regression scheme. The script for the MGD EOS was benchmarked using the EosFit7-GUI software (Angel et al., 2014; Gonzalez-Platas et al., 2016) with both programs yielding very consistent refined fit parameters and estimated uncertainties. As shown in Supplementary Figure S8 and S9, the fitted curves obtained with the two formalisms are indistinguishable within the pressure range of interest to this study.

SupplementaryText B.2

To determine the best-fit equation of state of $MgSiO_3$ bridgmanite, we used the pressure-volume (PV) dataset of Boffa Ballaran et al. (2012) and the PVT datasets of Katsura et al. (2009) and Tange et al. (2012). Boffa Ballaran et al. (2012) determined the PV relations of $MgSiO_3$ bridgmanite up to 80 GPa using single-crystal XRD in a DAC loaded with He as the pressure transmitting medium and using the ruby scale of Jacobsen et al. (2008). Katsura et al. (2009) and Tange et al. (2012), on the other hand, determined PVT relations of $MgSiO_3$ bridgmanite between 20 and 60 GPa and up to 2600 K by means of powder XRD in a multi-anvil apparatus, using MgO as the pressure marker. Tange et al. (2012) also performed additional measurements in a laser-heated DAC at pressures of 50-105 GPa and temperatures up to 2400 K, with pressure estimates also based on the MgO scale. Tange et al. (2012) proposed a best-fit EOS based on experimental data from their and previous studies (Funamori et al., 1996; Katsura et al., 2009) based on the MgO pressure scale (Tange et al., 2009a). This pressure scale, however, increasingly deviates from the ruby scale of Jacobsen et al. (2008) that is also based on MgO, with differences of +1 to +2 GPa at 70-100 GPa. Here, instead, we employed the MgO pressure scale of Dorogokupets and Dewaele (2007), whose agreement with Jacobsen et al. (2008) is always within ±1 GPa up to 100 GPa. Additionally, it has the advantage of being intercalibrated with an EOS for Au (Dorogokupets and Dewaele, 2007), which was used as a pressure standard in our measurements of Al-bearing bridgmanite. In Figure B.8, we show the experimentally measured volumes reported by Katsura et al. (2009) and Tange et al. (2012) against the MgO pressure scale of Dorogokupets and Dewaele (2007). The room temperature data are in very good agreement with single-crystal measurements by Boffa Ballaran et al. (2012), which in turn are plotted against the ruby scale of Jacobsen et al. (2008). Pressure estimates at high temperature from Katsura et al. (2009) and Tange et al. (2012) were also corrected for the pressure effect on the electromotive force in type D (W/3%Re–W/25%Re) thermocouples, as recently proposed by Nishihara et al. (2020). In a preliminary stage, V_0, K_{T0}, K'_{T0}, γ_0, q_0 and θ_{D0} were refined, with T_0 fixed to 298 K. θ_{D0} was found to be 910(100) K, which is in excellent agreement with the value of 912(3) K determined by Akaogi et al. (2008) by means of low temperature heat capacity measurements. Therefore, θ_{D0} was fixed to 912 K in the final cycle of the fit to reduce the correlation with the other thermal parameters γ_0 and q_0 or q. The two PVT EOSs obtained by our best-fit approach are in excellent agreement with each other, except for the very low-pressure high-temperature region which is, however, out of the stability field of bridgmanite. Fit parameters obtained by the two fits are consistent with each other (Table 5.4 and B.4), with the exception of q_0, which was found to be about 50% higher using the finite strain-based formalism of Stixrude and Lithgow-Bertelloni (2005). This is likely related to the fact that q is fixed in the MGD formalism, while it scales with the finite Eulerian strain in the finite strain formalism (see Text B for details). By converting the refined K_{T0} = 251(2) GPa to the adiabatic bulk modulus $K_{S0} = K_{T0} + \gamma_0^2 C_V T_0/V_0$, we obtain 254(2) GPa, which is in good agreement with previous elasticity measurements by Sinogeikin et al. (2004) and Criniti et al. (2021), who found K_{S0} values of 253(3) and 256.7(4) GPa, respectively.

Supplementary Figures

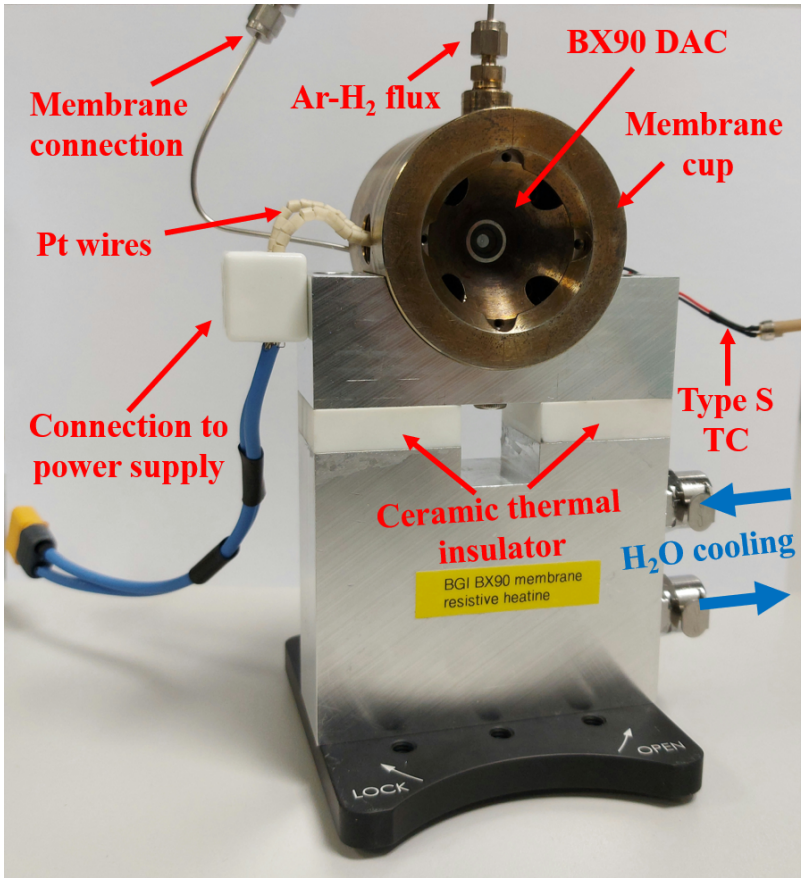

Figure B.1. The diamond anvil cell holder used for high-pressure and high-temperature diffraction measurements at beamline P02.2 of PETRA-III (Hamburg, Germany). The ceramic thermal insulator dividing the hot top part and water-cooled bottom part of the holder reduces the dissipation of heat and enhances the efficiency of the Pt-wire heater, enabling us to reach temperatures as high as 1000 K at about 25 GPa.

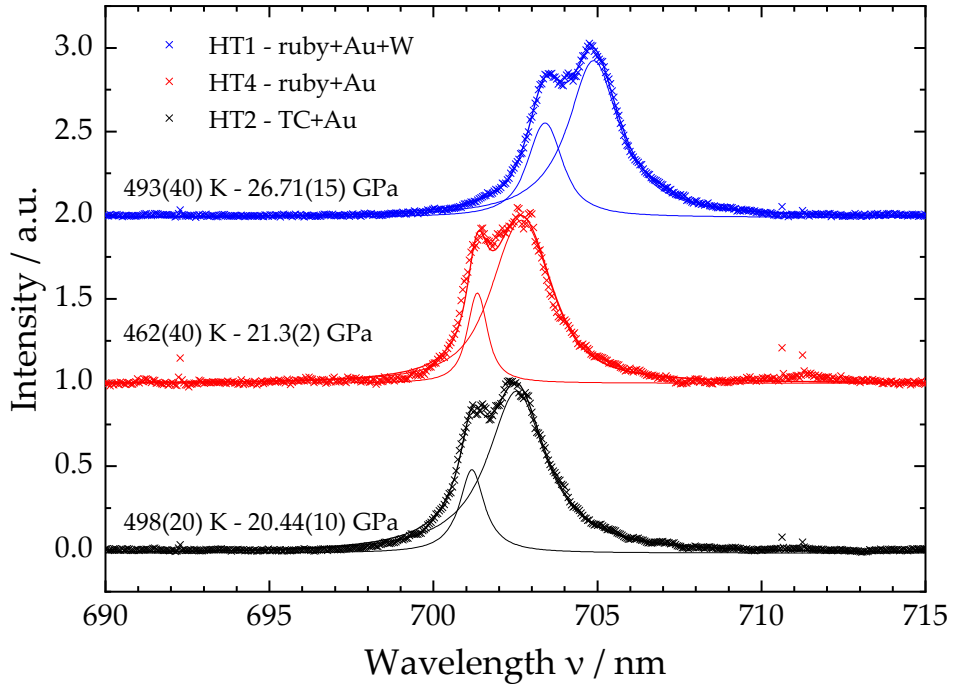

Figure B.2. Line shapes of ruby fluorescence spectra collected in different runs at temperature close to 500 K. Temperature determined either using a thermocouple (black symbols and lines) or using a cross correlation function between the R1 ruby line position (peak at higher wavelength) and the volume of W and/or Au measured by X-ray diffraction.

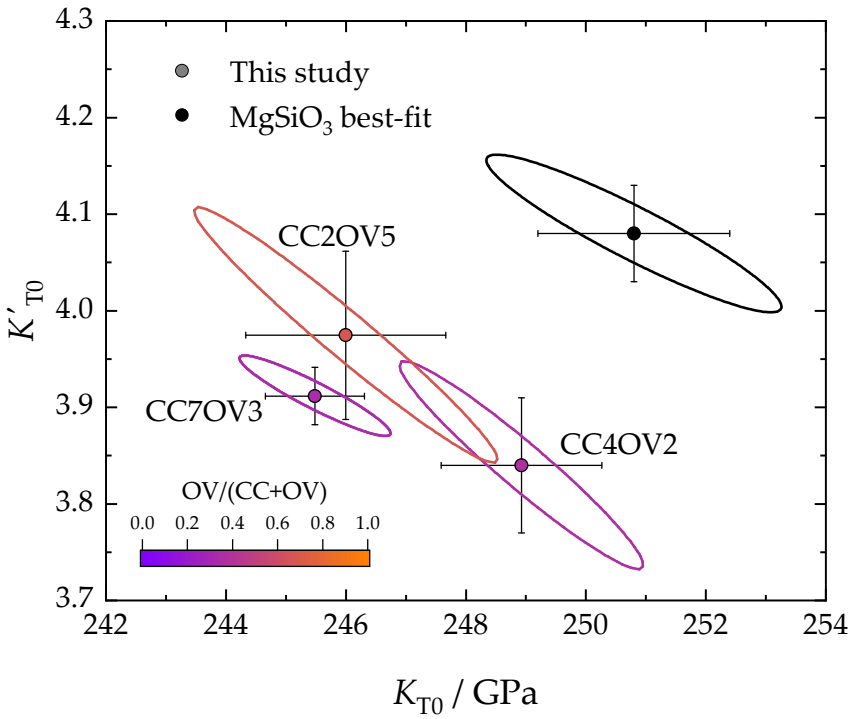

Figure B.3. Fit parameters K_{T0} and K'_{T0} for the best-fit equation of state of $MgSiO_3$ bridgmanite and isothermal equations of state of Al-bearing bridgmanite samples. The 68% (1 standard deviation) confidence ellipses are also plotted to show the correlation between the two fit parameters.

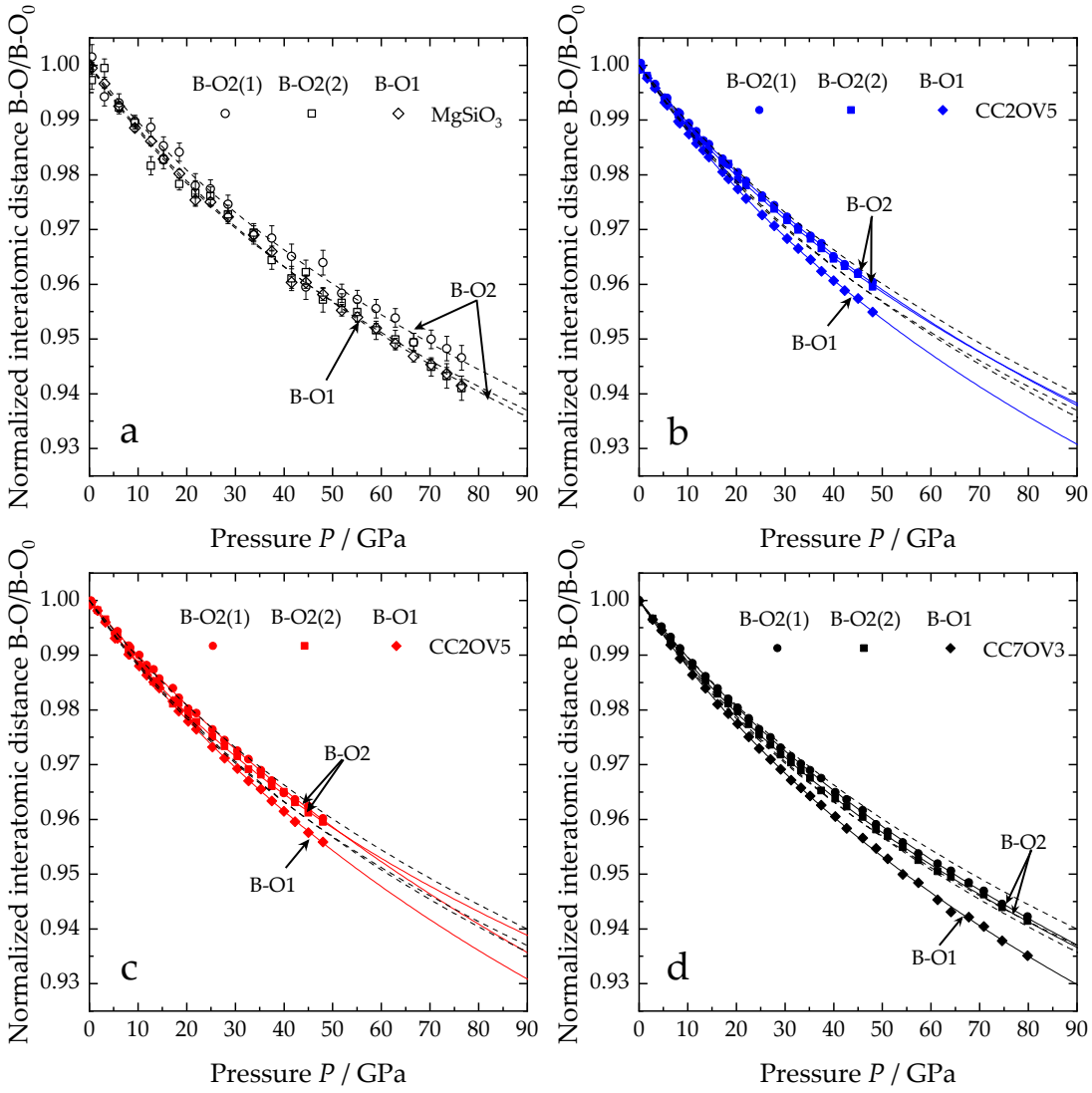

Figure B.4. Linear compressibility of B-O interatomic distances normalized by their room-pressure value. Lines represent linearized 3rd-order Brich-Murnaghan equations of state. Error bars are smaller than the symbols, where not shown. Equations of state for MgSiO
textsubscript3 (dashed black lines) are shown also in (b), (c) and (d) for reference.

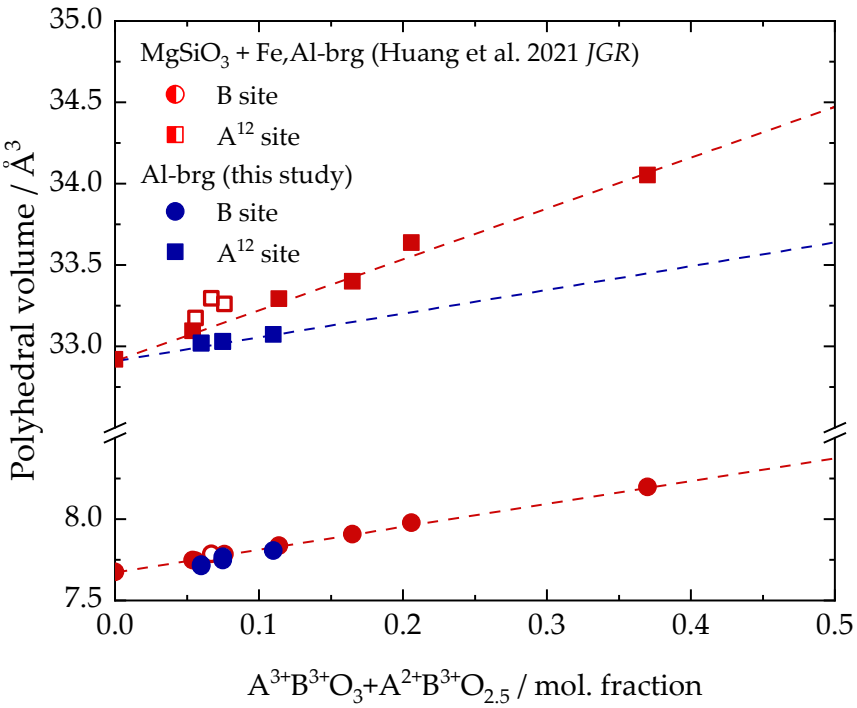

Figure B.5. Ambient pressure and temperature polyhedral volumes of 12-fold coordinated A (squares) and octahedral B (circles) sites of bridgmanite samples as a function of the trivalent cations content in their B site. Data from this study are plotted in blue. Solid and empty red symbols are Fe^{3+}-rich and Fe^{2+}-rich samples, respectively, from the previous study of Huang et al. (2021a)

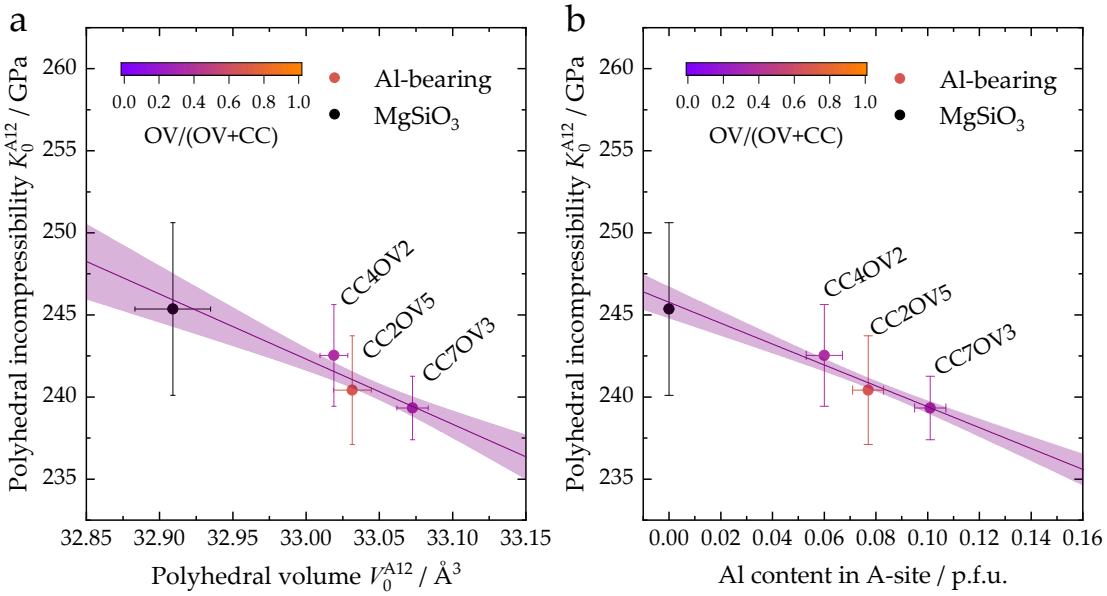

Figure B.6. Variation of the A-site polyhedral incompressibility ($K_0{}^{A12}$) as a function of (a) polyhedral volume and (b) Al content in the A site expressed in atoms per formula unit (p.f.u.). The concentration of CC and OV component in Al-bearing samples is expressed by the color scale.

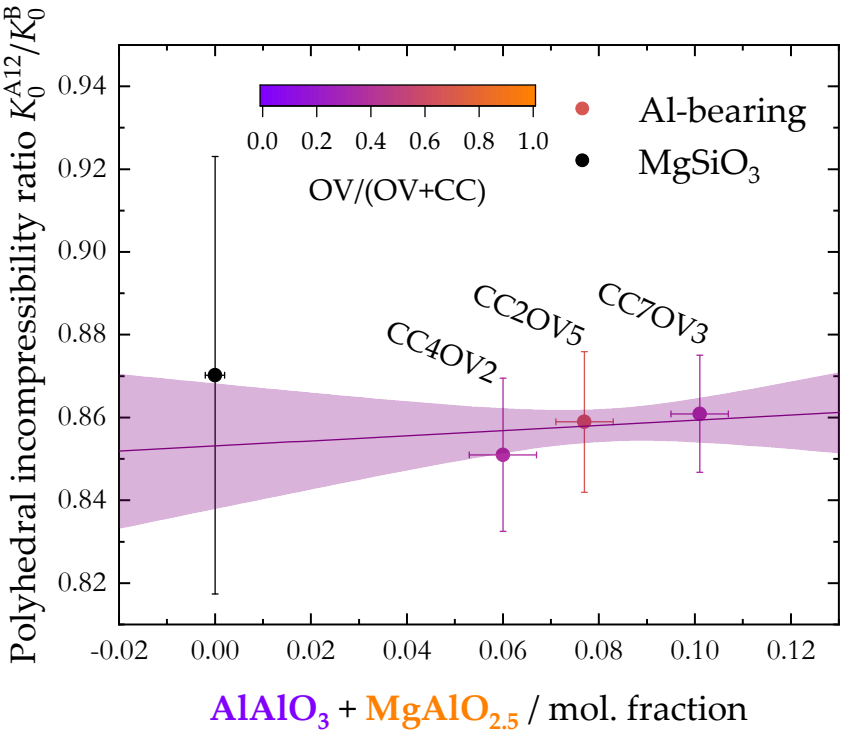

Figure B.7. Variation of the polyhedral incompressibility ratio $K_0{}^{A12}/K_0{}^{B}$ as a function of the Al content in the B site, represented by the sum of CC and OV substitutions. The purple line and shaded area represent a linear fit to the data and its 68% (i.e., one standard deviation) confidence band.

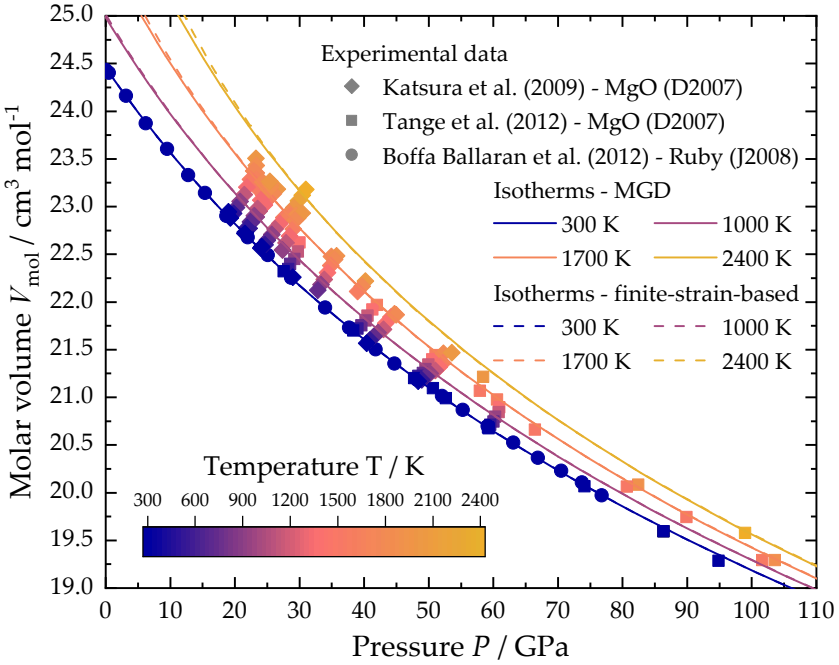

Figure B.8. Best-fit thermal EOSs of $MgSiO_3$ based on the MGD formalism (dashed lines) and on the formalism of Stixrude and Lithgow-Bertelloni (2005) (solid lines). Pressures from Katsura et al. (2009) and Tange et al. (2012) were recalculated using the MgO pressure scale of Dorogokupets and Dewaele (2007) (D2007), while data points from Boffa Ballaran et al. (2012) use the ruby scale of Jacobsen et al. (2008)(J2008).

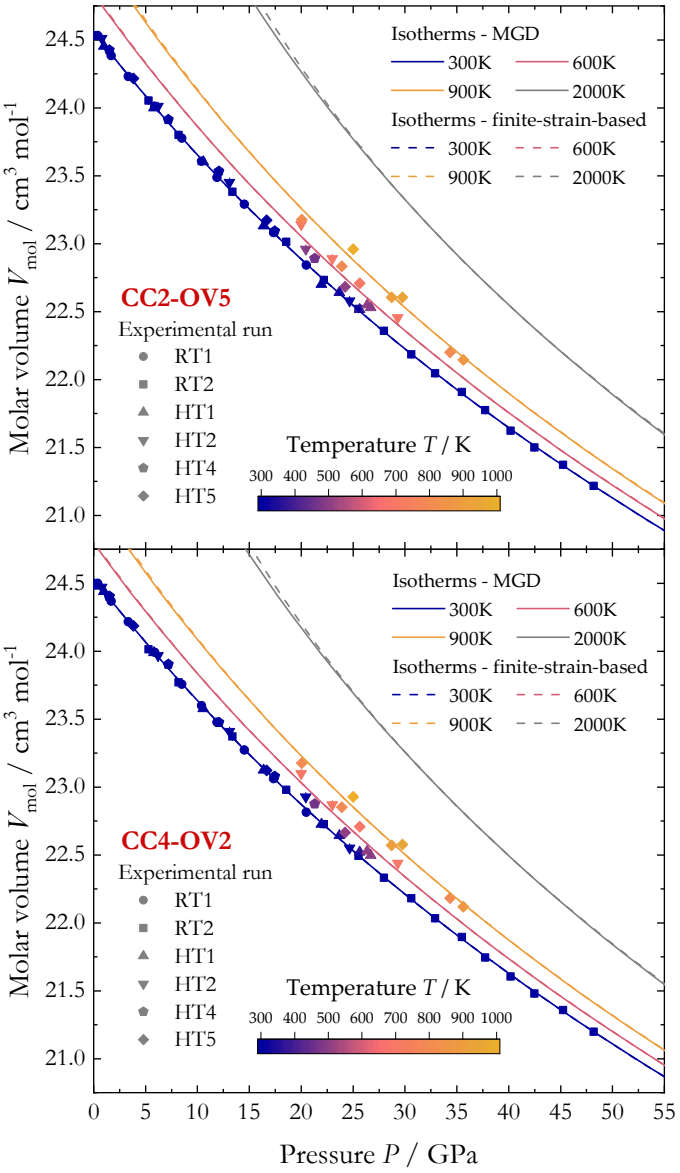

Figure B.9. *PVT* relations of CC2OV5 and CC4OV2 Al-bearing bridgmanite single-crystals collected over several experimental runs. Thermal EOSs based on the MGD (dashed lines) and finite-strain-based formalism (solid lines) are used to fit the experimental data. Experimental temperatures and calculated isotherms (300-900 K) are expressed as a color scale. The two models are in excellent agreement with one another, and the modelled isotherms perfectly overlap at the pressure conditions relevant to the topmost-lower mantle. Additional isotherms at 2000 K (purple lines) are also plotted to show that high-temperature extrapolation of the two EOS formalisms leads to consistent results in the stability field of bridgmanite (i.e., $P > 25$ GPa).

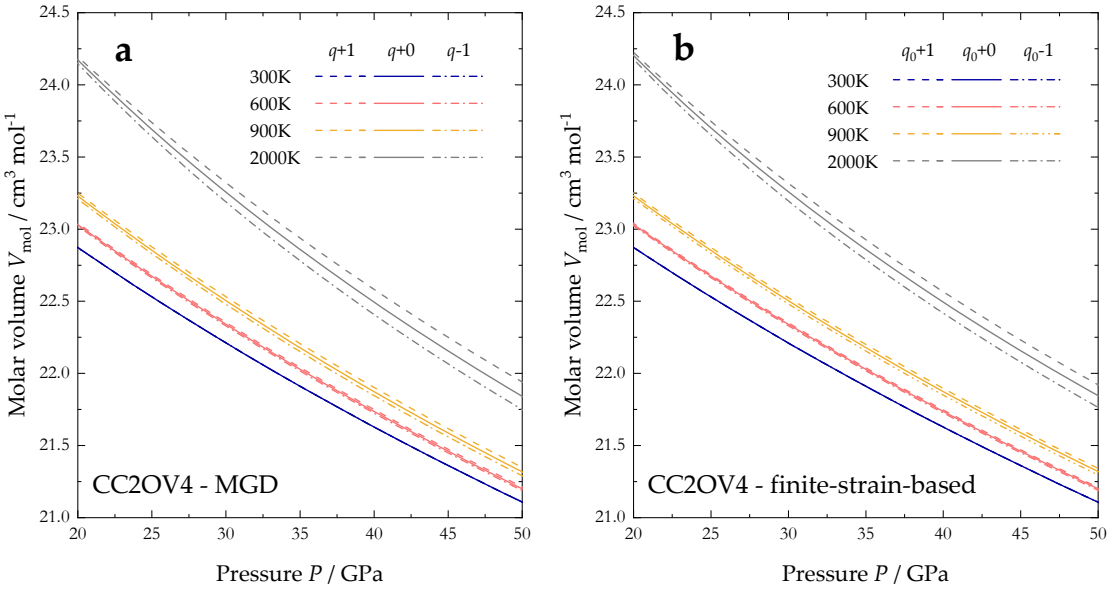

Figure B.10. Effect of the fit parameter (a) q and (b) q_0 on the thermal EOS of sample CC2OV4 employing the Mie-Grüneisen-Debye (MGD) and finite-strain-based (Stixrude and Lithgow-Bertelloni, 2005) formalisms, respectively. Solid lines represent the modelled isotherms using q or q_0 values determined for $MgSiO_3$ bridgmanite. Dashed and dot-dashed lines show the effect of varying q or q_0 values by one unit. Differences in the calculated pressure are about 0.5 GPa at 1000 K and 1-1.5 GPa at 2000 K.

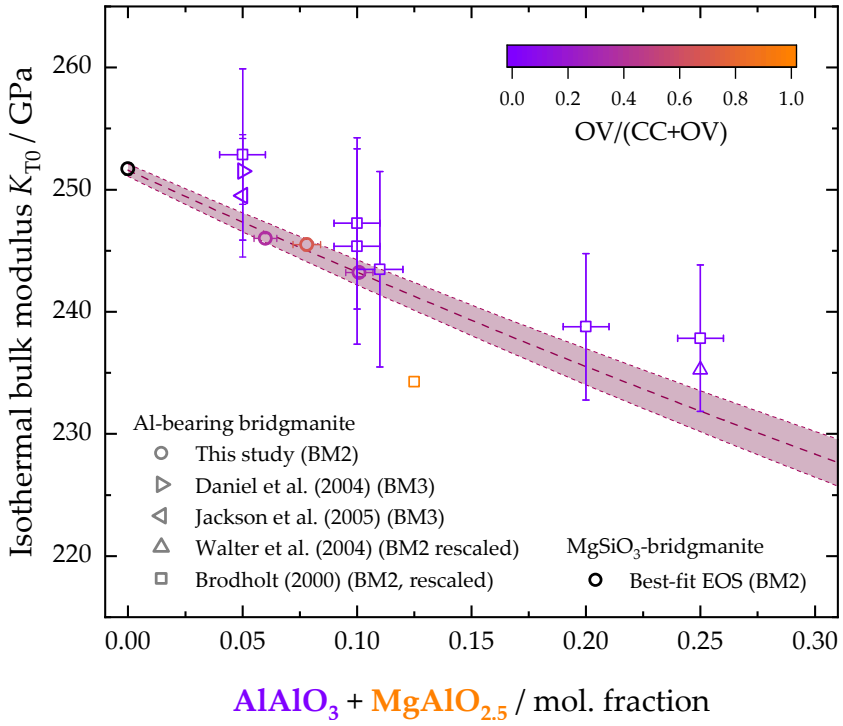

Figure B.11. Solid solution behavior of isothermal bulk modulus at ambient conditions (K_{T0}) for Al-bearing bridgmanite. The color scale indicates the degree of CC and OV substitution for each sample. The dashed line and shaded area represent the fit and estimated uncertainties for the $MgSiO_3$-$AlAlO_3$ and $MgSiO_3$-$MgAlO_3$ joins, under the assumption that $K_{AlAlO_3} = K_{MgAlO_{2.5}}$.

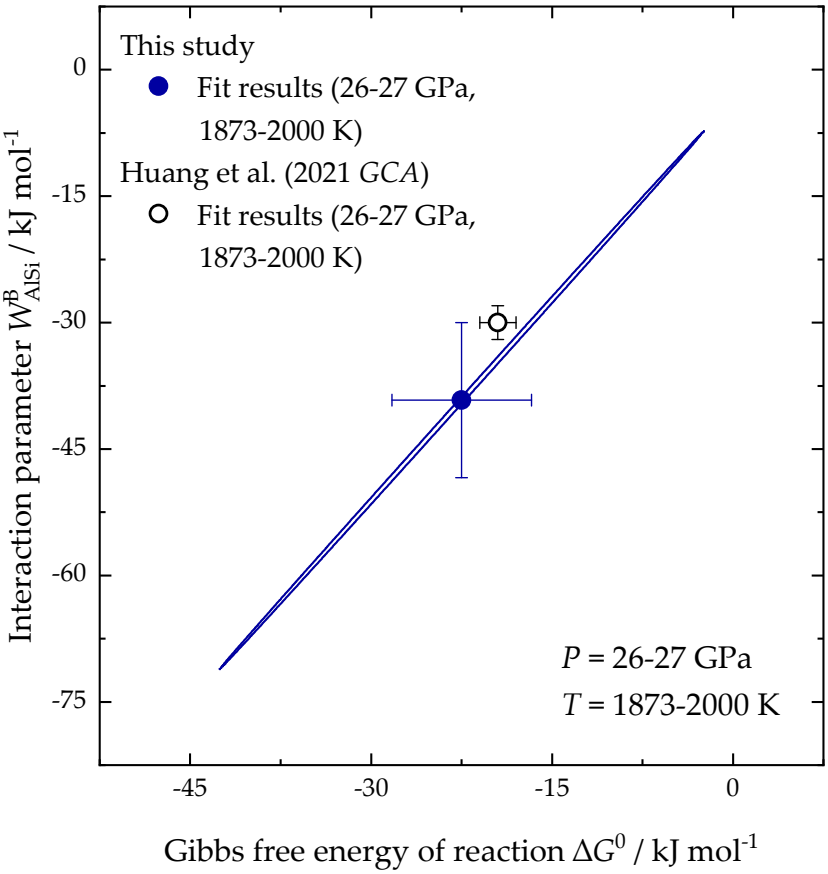

Figure B.12. Covariance ellipses for ΔG^0 and W^{B}_{AlSi} obtained by fitting phase relation data in the MgO-$AlO_{1.5}$-SiO_2 system at 26-27 GPa and 1873-2000 K using equation 5.14 (see main text). The values proposed by Huang et al. (2021a).

Supplementary Tables

Table B.1. Unit cell lattice parameters of Al-bearing bridgmanite samples determined by single-crystal X-ray diffraction at ambient conditions.

Sample	n^a	a (Å)	b (Å)	c (Å)	V (Å^3)
I701	32	4.77851(16)	4.93426(14)	6.91166(16)	162.966(8)
S7412	26	4.7751(5)	4.9399(3)	6.9331(4)	163.54(2)
S7464	21	4.77685(13)	4.93619(14)	6.92062(14)	163.184(7)
S7585	16	4.7760(5)	4.9397(2)	6.9282(8)	163.45(2)

[a] number of measured reflections

Table B.2. Results of electron microprobe analyses.

Run	Oxide composition				Atoms per 2 cations			
	MgO	SiO_2	$AlO_{1.5}$	Total	Mg	Al	Si	O
I701	38.50(26)	58.06(68)	4.96(42)	99.53(62)	0.962(6)	0.098(8)	0.940(7)	2.989(6)
S7412	37.60(64)	53.26(73)	9.28(59)	100.1(11)	0.932(9)	0.182(11)	0.886(9)	2.977(7)
S7464	39.35(50)	55.48(52)	5.21(47)	100.08(62)	0.975(10)	0.102(9)	0.922(6)	2.974(7)
S7585	37.45(34)	53.78(50)	8.54(32)	99.83(49)	0.932(6)	0.168(7)	0.899(6)	2.983(6)

Table B.3. 3rd-order Birch-Murnaghan equation of state parameters for polyhedral compression data of $MgSiO_3$ bridgmanite and Al-bearing bridgmanite.

	$MgSiO_3$	$MgSiO_3$*	CC2OV5	CC4OV2	CC7OV3
V_0^B (Å^3)	7.679(12)	7.674(4)	7.748(3)	7.713(3)	7.807(4)
K_0^B (GPa)	282(16)	294(2)	279(4)	285(5)	278(4)
K'^B_0	5.2(7)	4.65	4.8(2)	4.5(3)	4.66(16)
V_0^{12A} (Å^3)	32.91(3)	32.891(7)	33.032(13)	33.019(9)	33.073(11)
K_0^{12A} (GPa)	245(5)	250.4(6)	240(3)	243(3)	239(2)
K'^{12A}_0	3.93(19)	3.75	3.79(15)	3.71(17)	3.76(7)
K_0^{12A}/K_0^B	0.87(5)	0.852(2)	0.86(2)	0.85(2)	0.861(14)

* Pressure derivatives were fixed to be in the same range as Al-bearing samples.

Table B.4. Thermal EOS fit parameters for $MgSiO_3$ (best-fit) and Al-bearing bridgmanite (this study) using the Mie-Grüneisen-Debye (MGD) equation of state. Numbers in italics were fixed during the fitting procedure.

	$MgSiO_3$ best-fit	CC4OV2	CC2OV5
P scale	MgO[a], ruby[b]	Au[a], ruby[b]	Au[a], ruby[b]
V_{mol0} (cm^3/mol)	24.454(8)	24.536(3)	24.562(4)
T_0 (K)	*298*	*298*	*298*
K_{T0} (GPa)	251(2)	248.9(1.3)	246(2)
K'_{T0}	4.08(5)	3.84(7)	3.98(9)
γ_0	1.58(3)	2.06(12)	2.15(14)
q	2.3(2)	*2.3*	*2.3*
θ_{D0} (K)	*912*	*912*	*912*
n	*5*	*5*	*5*
reduced χ^2	1.52	2.86	3.48

[a] Dorogokupets and Dewaele (2007)

[b] Jacobsen et al. (2008)

References

Akaogi, M., H. Kojitani, T. Morita, H. Kawaji, and T. Atake (2008). "Low-temperature heat capacities, entropies and high-pressure phase relations of $MgSiO_3$ ilmenite and perovskite". In: *Physics and Chemistry of Minerals* 35 (5), pp. 287–297. DOI: 10.1007/s00269-008-0222-x.

Angel, R. J., J. Gonzalez-Platas, and M. Alvaro (2014). "EosFit7c and a Fortran module (library) for equation of state calculations". In: *Zeitschrift fur Kristallographie* 229 (5), pp. 405–419. DOI: 10.1515/zkri-2013-1711.

Boffa Ballaran, T., A. Kurnosov, K. Glazyrin, D. J. Frost, M. Merlini, M. Hanfland, and R. Caracas (2012). "Effect of chemistry on the compressibility of silicate perovskite in the lower mantle". In: *Earth and Planetary Science Letters* 333-334, pp. 181–190. DOI: 10.1016/j.epsl.2012.03.029.

Criniti, G., A. Kurnosov, T. B. Ballaran, and D. J. Frost (2021). "Single-Crystal Elasticity of $MgSiO_3$ Bridgmanite to Mid-Lower Mantle Pressure". In: *Journal of Geophysical Research: Solid Earth* 126 (5). DOI: 10.1029/2020JB020967.

Dorogokupets, P. I. and A. Dewaele (2007). "Equations of state of MgO, Au, Pt, NaCl-B1, and NaCl-B2: Internally consistent high-temperature pressure scales". In: *High Pressure Research* 27 (4), pp. 431–446. DOI: 10.1080/08957950701659700.

Funamori, N., T. Yagi, W. Utsumi, T. Kondo, and T. Uchida (1996). "Thermoelastic properties of $MgSiO_3$ perovskite determined by in situ X ray observations up to 30 GPa and 2000 K". In: *Journal of Geophysical Research: Solid Earth* 101, pp. 8257–8269.

Gonzalez-Platas, J., M. Alvaro, F. Nestola, and R. J. Angel (2016). "EosFit7-GUI: A new graphical user interface for equation of state calculations, analyses and teaching". In: *Journal of Applied Crystallography* 49 (4), pp. 1377–1382. DOI: 10.1107/S1600576716008050.

Huang, R., T. B. Ballaran, C. A. McCammon, N. Miyajima, D. Dolejš, and D. J. Frost (2021a). "The composition and redox state of bridgmanite in the lower mantle as a function of oxygen fugacity". In: *Geochimica et Cosmochimica Acta* 303, pp. 110–136. DOI: 10.1016/J.GCA.2021.02.036.

Jacobsen, S. D., C. M. Holl, K. A. Adams, R. A. Fischer, E. S. Martin, C. R. Bina, J. F. Lin, V. B. Prakapenka, A. Kubo, and P. Dera (2008). "Compression of single-crystal magnesium oxide to 118 GPa and a ruby pressure gauge for helium pressure media". In: *American Mineralogist* 93 (11-12), pp. 1823–1828. DOI: 10.2138/am.2008.2988.

Katsura, T., S. Yokoshi, K. Kawabe, A. Shatskiy, M. A. Manthilake, S. Zhai, H. Fukui, H. A. Hegoda, T. Yoshino, D. Yamazaki, T. Matsuzaki, A. Yoneda, E. Ito, M. Sugita, N. Tomioka, K. Hagiya, A. Nozawa, and K. I. Funakoshi (2009). "*P-V-T* relations of $MgSiO_3$ perovskite determined by in situ X-ray diffraction using a large-volume high-pressure apparatus". In: *Geophysical Research Letters* 36 (1), pp. 2–7. DOI: 10.1029/2008GL035658.

Nishihara, Y., S. Doi, S. Kakizawa, Y. Higo, and Y. Tange (2020). "Effect of pressure on temperature measurements using WRe thermocouple and its geophysical impact". In: *Physics of the Earth and Planetary Interiors* 298. DOI: 10.1016/j.pepi.2019.106348.

Poirier, J.-P. (2000). *Introduction to the Physics of the Earth's Interior*. Cambridge University Press. DOI: 10.1017/CBO9781139164467.

Sinogeikin, S. V., J. Zhang, and J. D. Bass (2004). "Elasticity of single crystal and polycrystalline $MgSiO_3$ perovskite by Brillouin spectroscopy". In: *Geophysical Research Letters* 31 (6). DOI: 10.1029/2004gl019559.

Stixrude, L. and C. Lithgow-Bertelloni (2005). "Thermodynamics of mantle minerals - I. Physical properties". In: *Geophysical Journal International* 162 (2), pp. 610–632. DOI: 10.1111/j.1365-246X.2005.02642.x.

Tange, Y., Y. Kuwayama, T. Irifune, K. I. Funakoshi, and Y. Ohishi (2012). "*P-V-T* equation of state of $MgSiO_3$ perovskite based on the MgO pressure scale: A comprehensive reference for mineralogy of the lower mantle". In: *Journal of Geophysical Research: Solid Earth* 117 (6), pp. 1–12. DOI: 10.1029/2011JB008988.

Tange, Y., Y. Nishihara, and T. Tsuchiya (2009a). "Unified analyses for *P-V-T* equation of state of MgO: A solution for pressure-scale problems in high *P-T* experiments". In: *Journal of Geophysical Research* 114 (B3), B03208. DOI: 10.1029/2008JB005813.

Appendix C

Supporting information to: High-pressure phase transition and equation of state of hydrous Al-bearing silica

Supplementary Figures and Tables

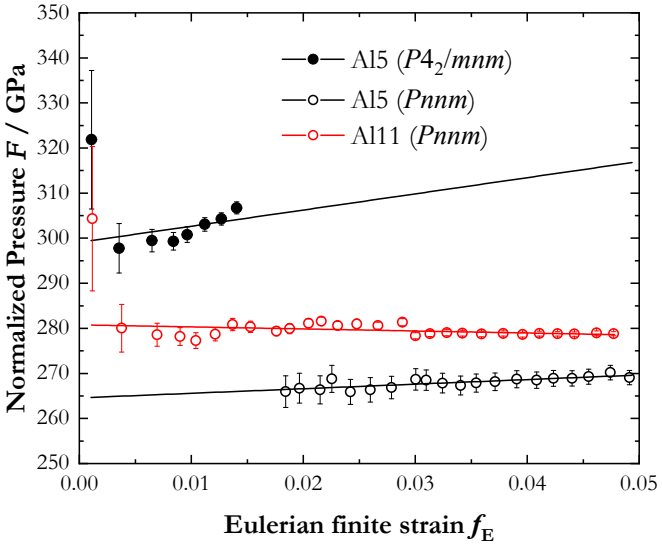

Figure C.1. f_E-F plot of the EOSs of Al5 ($P4_2/mnm$ and $Pnnm$ and Al11 ($Pnnm$). The normalized pressure F was calculated as $F = P/[3f_E(2f_E + 1)^{5/2}]$, where $f_E = [(V_0/V)^{2/3} - 1]/2$ is the Eulerian finite strain.

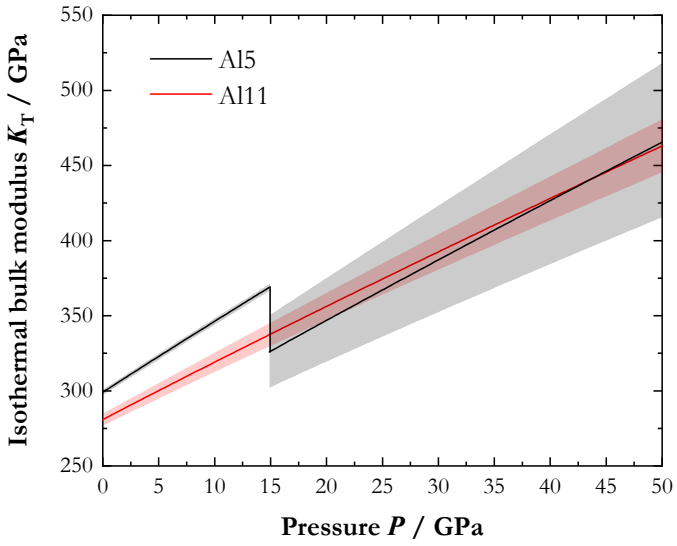

Figure C.2. Pressure evolution of the isothermal bulk modulus K_T of Al5 (black) and Al11 (red) samples investigated in this study. At about 16 GPa, a phase transition from tetragonal to orthorhombic occurs in Al5 and causes a drop in K_T. Shaded area represent propagated uncertainties.

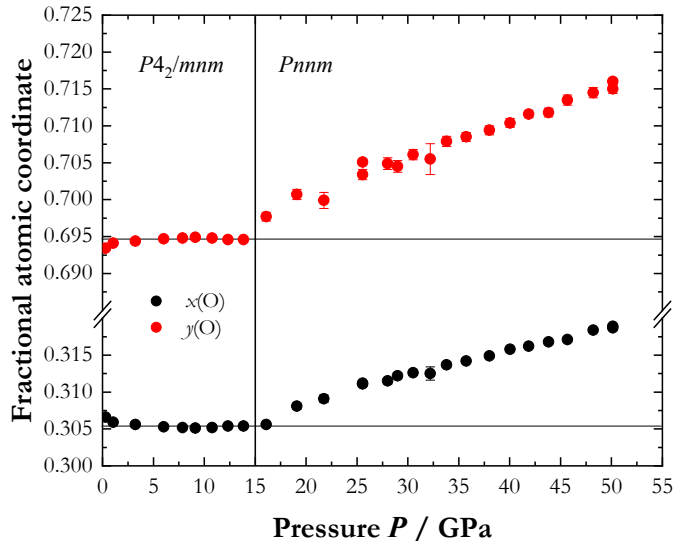

Figure C.3. Fractional x and y coordinates of O in the tetragonal ($P4_2/mnm$) and orthorhombic (*Pnnm*) phases of Al5 as a function of pressure. Horizontal lines represent values of x(O) and y(O) = 1- x(O)assumed for the tetragonal phase in the stability field of the orthorhombic phase, which are required in the symmetry-mode decomposition analysis.

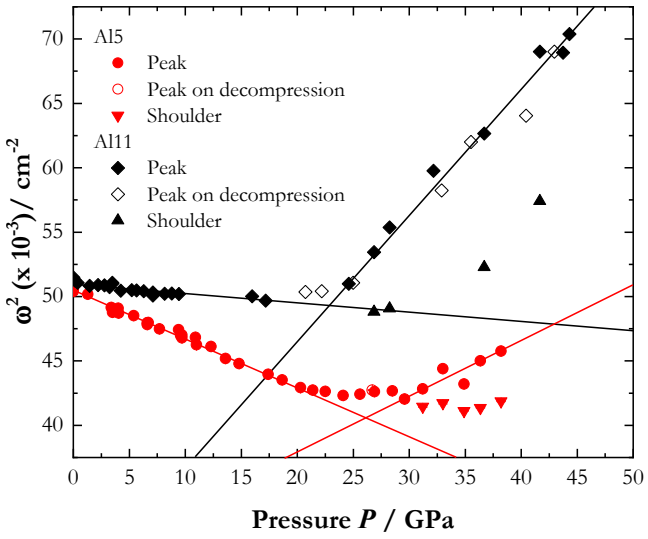

Figure C.4. Pressure evolution of Raman bands and their shoulders in Al5 and Al11. Empty symbols represent points collected upon decompression. The shoulder at lower wavenumber represented by black (Al11) and red (Al5) triangles is less intense and tend to disappear as pressure increases.

Table C.1. Details for the high-pressure experiments performed in this study.

Label	Sample(s)	Culet (μm)	Pressure medium	P range (GPa)	Technique
DACX	Al5, Al11	350	He	0-50.13(4)	XRD
DAC1	Al5	400	Ne	0-10.9(1)	Raman
DAC2	Al5	400	He	0-9.4(1)	Raman
DAC3	Al5	400	He	0-38.2(1)	Raman
DAC4	Al11	250	He	0-44.30(3)	Raman

Table C.2. Unit-cell lattice parameters of Al5 as a function of pressure. P is calculated as the average value between pressure measured before and after XRD measurements using the ruby fluorescence shift (Shen et al., 2020), and σP is the semi-difference between the two values. Errors on the cell parameters represent one standard deviation.

P (GPa)	σP (GPa)	a (Å)	σa (Å)	b (Å)	σb (Å)	c (Å)	σc (Å)	V (Å^3)	σV (Å^3)
1.06	0.02	4.1940	0.0001			2.6714	0.0001	46.988	0.003
3.23	0.04	4.1813	0.0001			2.6679	0.0001	46.644	0.003
6.02	0.02	4.1667	0.0001			2.6634	0.0001	46.239	0.003
7.86	0.02	4.1573	0.0001			2.6603	0.0001	45.979	0.003
9.13	0.02	4.1515	0.0001			2.6580	0.0001	45.810	0.003
10.78	0.02	4.1440	0.0002			2.6554	0.0001	45.599	0.003
12.33	0.02	4.1374	0.0001			2.6524	0.0001	45.403	0.003
13.86	0.03	4.1311	0.0002			2.6498	0.0001	45.222	0.003
16.09	0.02	4.1309	0.0003	4.1125	0.0003	2.6459	0.0001	44.949	0.005
17.32	0.03	4.1275	0.0002	4.1045	0.0003	2.6438	0.0001	44.789	0.005
19.10	0.04	4.1237	0.0002	4.0902	0.0003	2.6413	0.0001	44.550	0.005
20.30	0.03	4.1187	0.0002	4.0863	0.0003	2.6392	0.0001	44.418	0.005
21.75	0.03	4.1173	0.0002	4.0718	0.0004	2.6368	0.0001	44.205	0.005
23.57	0.07	4.1135	0.0002	4.0597	0.0004	2.6338	0.0001	43.983	0.005
25.56	0.03	4.1094	0.0002	4.0470	0.0004	2.6305	0.0001	43.747	0.005
28.02	0.05	4.1040	0.0002	4.0345	0.0004	2.6259	0.0001	43.479	0.005
29.00	0.02	4.1019	0.0002	4.0280	0.0003	2.6245	0.0001	43.364	0.004
30.51	0.03	4.0985	0.0002	4.0200	0.0003	2.6212	0.0001	43.185	0.004
32.21	0.04	4.0946	0.0002	4.0106	0.0003	2.6178	0.0001	42.989	0.004
33.79	0.03	4.0910	0.0002	4.0031	0.0003	2.6149	0.0001	42.824	0.004
35.72	0.04	4.0865	0.0002	3.9940	0.0003	2.6114	0.0001	42.622	0.004
38.02	0.04	4.0821	0.0002	3.9833	0.0003	2.6071	0.0001	42.391	0.004
40.04	0.03	4.0780	0.0002	3.9729	0.0003	2.6036	0.0001	42.183	0.004
41.87	0.03	4.0751	0.0002	3.9646	0.0003	2.6001	0.0001	42.007	0.004
43.83	0.02	4.0714	0.0002	3.9552	0.0003	2.5968	0.0001	41.816	0.004
45.69	0.03	4.0680	0.0002	3.9469	0.0003	2.5938	0.0001	41.645	0.004
48.21	0.04	4.0650	0.0002	3.9363	0.0003	2.5889	0.0001	41.425	0.004
50.13	0.04	4.0610	0.0002	3.9268	0.0003	2.5856	0.0001	41.232	0.004

Table C.3. Unit-cell lattice parameters of Al11 as a function of pressure. P is calculated as the average value between pressure measured before and after XRD measurements using the ruby fluorescence shift (Shen et al., 2020), and σP is the semi-difference between the two values. Errors on the cell parameters represent one standard deviation.

P (GPa)	σP (GPa)	a (Å)	σa (Å)	b (Å)	σb (Å)	c (Å)	σc (Å)	V (Å^3)	σV (Å^3)
1.06	0.02	4.2500	0.0002	4.1762	0.0003	2.6799	0.0001	47.566	0.004
3.23	0.04	4.2380	0.0002	4.1606	0.0002	2.6766	0.0001	47.196	0.004
6.02	0.02	4.2241	0.0002	4.1424	0.0002	2.6718	0.0001	46.752	0.004
7.86	0.02	4.2154	0.0002	4.1313	0.0002	2.6684	0.0001	46.470	0.004
9.13	0.02	4.2106	0.0002	4.1220	0.0002	2.6663	0.0001	46.277	0.004
10.78	0.02	4.2039	0.0002	4.1126	0.0002	2.6632	0.0001	46.043	0.003
12.33	0.02	4.1979	0.0002	4.1036	0.0002	2.6608	0.0001	45.837	0.004
13.86	0.03	4.1923	0.0002	4.0949	0.0002	2.6576	0.0001	45.623	0.003
16.09	0.02	4.1838	0.0002	4.0820	0.0002	2.6535	0.0001	45.317	0.003
17.32	0.03	4.1801	0.0002	4.0751	0.0002	2.6511	0.0001	45.160	0.004
19.10	0.04	4.1750	0.0002	4.0647	0.0002	2.6482	0.0001	44.941	0.003
20.30	0.03	4.1708	0.0002	4.0588	0.0002	2.6461	0.0001	44.795	0.003
21.75	0.03	4.1667	0.0002	4.0501	0.0002	2.6433	0.0001	44.607	0.004
23.57	0.07	4.1610	0.0002	4.0415	0.0002	2.6398	0.0001	44.391	0.003
25.56	0.03	4.1548	0.0002	4.0314	0.0002	2.6360	0.0001	44.152	0.003
28.02	0.05	4.1483	0.0002	4.0190	0.0002	2.6319	0.0001	43.879	0.003
29.00	0.02	4.1440	0.0002	4.0138	0.0002	2.6294	0.0001	43.734	0.004
30.51	0.03	4.1399	0.0002	4.0067	0.0002	2.6268	0.0001	43.572	0.003
32.21	0.04	4.1358	0.0002	3.9987	0.0002	2.6236	0.0001	43.389	0.003
33.79	0.03	4.1316	0.0002	3.9915	0.0002	2.6207	0.0001	43.219	0.003
35.72	0.04	4.1265	0.0002	3.9828	0.0002	2.6172	0.0001	43.014	0.003
38.02	0.04	4.1209	0.0002	3.9726	0.0002	2.6132	0.0001	42.780	0.003
40.04	0.03	4.1162	0.0002	3.9638	0.0001	2.6095	0.0001	42.575	0.003
41.87	0.03	4.1118	0.0002	3.9564	0.0001	2.6063	0.0001	42.399	0.003
43.83	0.02	4.1073	0.0002	3.9485	0.0002	2.6028	0.0001	42.210	0.003
45.69	0.03	4.1034	0.0002	3.9409	0.0002	2.5994	0.0001	42.034	0.003
48.21	0.04	4.098	0.0002	3.9315	0.0002	2.5949	0.0001	41.806	0.003
50.13	0.04	4.0938	0.0002	3.9239	0.0002	2.5916	0.0001	41.631	0.003

Table C.4. Observed Raman shifts of B_{1g} (stishovite) and A_g ($CaCl_2$-type phase) optic modes of Al5 (DAC1, DAC2, DAC3) as a function of pressure. Error on the peak position represent one standard deviation. P is calculated as the average value between pressure measured before and after Raman spectroscopy measurements using the ruby fluorescence shift (Shen et al., 2020), and σP is the semi-difference between the two values. Asterisks next to P values indicate measurements performed during decompression.

P (GPa)	σP (GPa)	ω (cm^{-1})	$\sigma\omega$ (cm^{-1})	P (GPa)	σP (GPa)	ω (cm^{-1})	$\sigma\omega$ (cm^{-1})
DAC1				DAC3			
0		224.99	0.09	11.0	0.1	215.05	0.05
1.3	0.1	224.01	0.07	13.6	0.1	212.59	0.05
3.5	0.1	220.86	0.04	14.8	0.1	211.63	0.1
5.4	0.1	220.24	0.11	17.4	0.1	209.66	0.05
6.6	0.1	218.67	0.06	18.65	0.1	208.64	0.12
7.7	0.1	217.91	0.07	20.3	0.2	207.17	0.05
9.7	0.2	216.3	0.04	21.4	0.1	206.73	0.06
10.9	0.1	216.42	0.09	22.5	0.1	206.47	0.08
9.6*	0.1	216.71	0.15	24.1	0.1	205.71	0.06
4.1*	0.1	220.71	0.05	24.7	0.1	204.34	0.08
DAC2				25.6	0.1	205.95	0.19
0		224.49	0.06	26.9	0.1	206.41	0.11
4.0	0.2	221.57	0.08	28.5	0.1	206.57	0.11
6.6	0.1	219.01	0.05	29.6	0.1	205.05	0.11
9.4	0.1	217.75	0.06	31.2	0.1	206.96	0.15
DAC3				33.0	0.2	210.7	0.3
0		225.18	0.03	34.9	0.1	207.86	0.06
3.4	0.1	221.69	0.06	36.3	0.2	212.15	0.06
6.7	0.1	219.05	0.04	38.2	0.2	213.92	0.07
9.7	0.1	216.81	0.04	26.7*	0.2	206.73	0.08

Table C.5. Observed Raman shifts of A_g ($CaCl_2$-type phase) optic modes of Al11 (DAC4) as a function of pressure. Error on the peak position represent one standard deviation. P is calculated as the average value between pressure measured before and after Raman spectroscopy measurements using the ruby fluorescence shift (Shen et al., 2020), and σP is the semi-difference between the two values. Asterisks next to P values indicate measurements performed during decompression.

P (GPa)	σP (GPa)	ω (cm^{-1})	$\sigma\omega$ (cm^{-1})	P (GPa)	σP (GPa)	ω (cm^{-1})	$\sigma\omega$ (cm^{-1})
DAC1				DAC3			
0		226.91	0.03	15.97	0.03	223.66	0.03
0.14	0.02	226.39	0.06	17.17	0.06	222.91	0.02
0.38	0.02	225.99	0.05	24.60	0.10	225.80	0.05
1.45	0.10	225.44	0.04	26.87	0.11	231.18	0.34
2.22	0.03	225.57	0.04	28.24	0.07	235.32	0.31
2.79	0.03	225.53	0.04	32.17	0.02	244.46	0.14
3.24	0.02	225.25	0.03	36.69	0.07	250.32	0.21
3.48	0.02	225.84	0.07	41.65	0.09	262.70	0.10
3.48	0.02	226.00	0.05	44.30	0.03	265.31	0.14
4.23	0.02	224.64	0.05	43.74*	0.02	262.56	0.13
5.22	0.02	224.73	0.03	42.95*	0.02	262.69	0.09
5.65	0.02	224.66	0.04	40.44*	0.02	253.05	0.16
6.28	0.02	224.52	0.04	35.50*	0.03	249.00	0.09
7.10	0.02	224.29	0.03	32.9*	0.2	241.32	0.19
7.10	0.02	223.76	0.03	25.0*	0.5	225.98	0.08
8.16	0.03	224.10	0.03	22.2*	0.8	224.55	0.06
8.79	0.02	224.16	0.03	20.7*	0.5	224.41	0.05
9.43	0.05	224.05	0.03				

Table C.6. Fractional atomic coordinates of oxygen and symmetry breaking mode Γ_{2+} as a function of pressure. P is calculated as the average value between pressure measured before and after XRD measurements, and σP is the semi-difference between the two values. Errors on the fractional atomic coordinates represent one standard deviation.

P	σP	x(O)	σx(O)	y(O)	σy(O)	Γ_{2+}
1.06	0.02	0.3059	0.0003			0
3.23	0.04	0.3056	0.0003			0
6.02	0.02	0.3053	0.0003			0
7.86	0.02	0.3052	0.0002			0
9.13	0.02	0.3051	0.0003			0
10.78	0.02	0.3052	0.0002			0
12.33	0.02	0.3054	0.0002			0
13.86	0.03	0.3054	0.0002			0
16.09	0.02	0.3056	0.0003	0.6977	0.0006	0.0192
19.10	0.04	0.3081	0.0004	0.7007	0.0004	0.0215
21.75	0.03	0.3091	0.0005	0.6999	0.0011	0.0522
25.56	0.03	0.3111	0.0003	0.7034	0.0007	0.0839
28.02	0.05	0.3115	0.0004	0.7049	0.0008	0.0947
29.00	0.02	0.3122	0.0004	0.7045	0.0008	0.0963
30.51	0.03	0.3126	0.0003	0.7161	0.0007	0.1078
32.21	0.04	0.3125	0.0009	0.7055	0.0021	0.1019
33.79	0.03	0.3137	0.0004	0.7079	0.0007	0.1242
35.72	0.04	0.3142	0.0003	0.7085	0.0006	0.1303
38.02	0.04	0.3149	0.0003	0.7094	0.0006	0.1393
40.04	0.03	0.3158	0.0003	0.7104	0.0006	0.1506
41.87	0.03	0.3162	0.0002	0.7116	0.0005	0.1590
43.83	0.02	0.3168	0.0003	0.7118	0.0006	0.1634
45.69	0.03	0.3171	0.0003	0.7135	0.0007	0.1740
48.21	0.04	0.3184	0.0003	0.7145	0.0007	0.1875
50.13	0.04	0.3187	0.0003	0.7150	0.0006	0.1918

References

Shen, G., Y. Wang, A. Dewaele, C. Wu, D. E. Fratanduono, J. Eggert, S. Klotz, K. F. Dziubek, P. Loubeyre, O. V. Fat'yanov, P. D. Asimow, T. Mashimo, and R. M. Wentzcovitch (2020). "Toward an international practical pressure scale: A proposal for an IPPS ruby gauge (IPPS-Ruby2020)". In: *High Pressure Research*, pp. 1–16. DOI: 10.1080/08957959.2020.1791107.

Appendix D

Supporting information to: Structure and Compressibility of Fe-Bearing Al-Phase D

Supplementary Figures and Tables

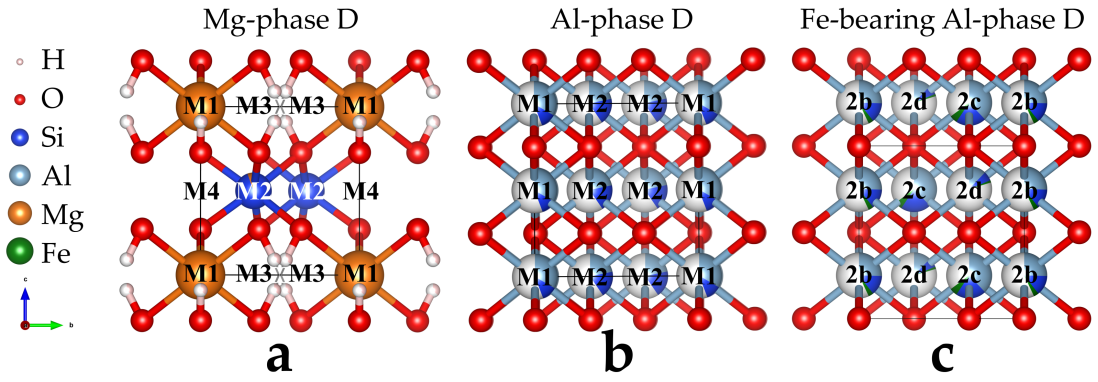

Figure D.1. Crystal structures of phase D samples having different Mg and Al content viewed along the *a* crystallographic axis. The arrows on the bottom left corner show the orientation of the three crystallographic axes. a) Mg-phase D, nominally $MgSi_2O_6H_2$, space group $P\bar{3}1m$ (Yang et al., 1997b). b) Al-phase D, nominally $Al_2SiO_6H_2$, space group $P6_3/mcm$ (Pamato et al., 2015). c) Fe-bearing Al-Phase D, space group $P6_322$ (this study)

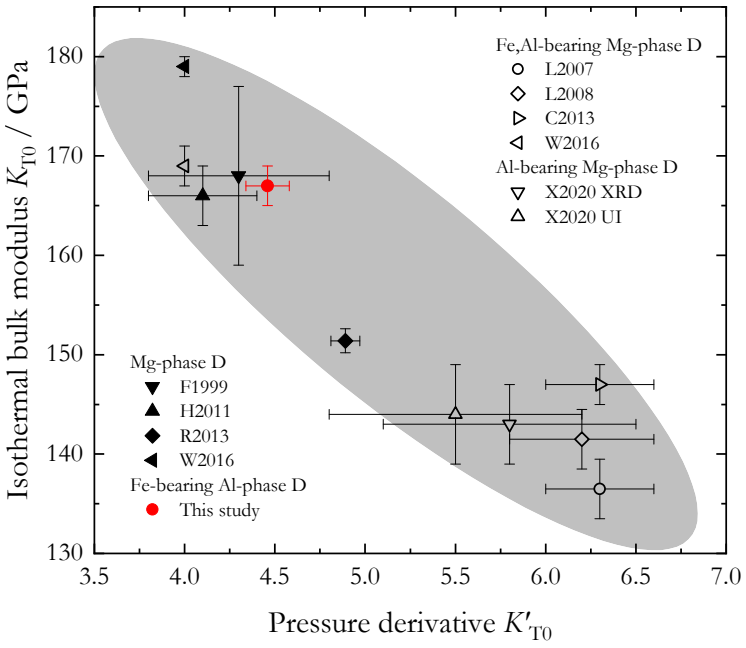

Figure D.2. Isothermal bulk moduli (K_{T0}) of high-pressure diffraction and elasticity studies of Phase D plotted against their pressure derivatives (K'_{T0}). The grey area is a guide to the eye showing the narrow range of K_{T0}-K'_{T0} values determined for Phase D samples in this and previous studies. F1999: Frost and Fei (1999), H2011: Hushur et al. (2011), R2013: Rosa et al. (2013), W2016: Wu et al. (2016), L2007: Litasov et al. (2007b), L2008: Litasov et al. (2008), C2013: Chang et al. (2013), X2020: Xu et al. (2020).

References

Chang, Y. Y., S. D. Jacobsen, J. F. Lin, C. R. Bina, S. M. Thomas, J. Wu, G. Shen, Y. Xiao, P. Chow, D. J. Frost, C. A. McCammon, and P. Dera (2013). "Spin transition of Fe^{3+} in Al-bearing phase D: An alternative explanation for small-scale seismic scatterers in the mid-lower mantle". In: *Earth and Planetary Science Letters* 382, pp. 1–9. DOI: 10.1016/j.epsl.2013.08.038.

Frost, D. J. and Y. Fei (1999). "Static compression of the hydrous magnesium silicate phase D to 30 GPa at room temperature". In: *Physics and Chemistry of Minerals* 26 (5), pp. 415–418. DOI: 10.1007/s002690050202.

Hushur, A., M. H. Manghnani, J. R. Smyth, Q. Williams, E. Hellebrand, D. Lonappan, Y. Ye, P. Dera, and D. J. Frost (2011). "Hydrogen bond symmetrization and equation of state of phase D". In: *Journal of Geophysical Research: Solid Earth* 116 (6), pp. 1–8. DOI: 10.1029/2010JB008087.

Litasov, K. D., E. Ohtani, Y. Nishihara, A. Suzuki, and K. Funakoshi (2008). "Thermal equation of state of Al- and Fe-bearing phase D". In: *Journal of Geophysical Research: Solid Earth* 113 (8), pp. 1–13. DOI: 10.1029/2007JB004937.

Litasov, K. D., E. Ohtani, A. Suzuki, and K. Funakoshi (2007b). "The compressibility of Fe- and Al-bearing phase D to 30 GPa". In: *Physics and Chemistry of Minerals* 34 (3), pp. 159–167. DOI: 10.1007/s00269-006-0136-4.

Pamato, M. G., R. Myhill, T. B. Ballaran, D. J. Frost, F. Heidelbach, and N. Miyajima (2015). "Lower-mantle water reservoir implied by the extreme stability of a hydrous aluminosilicate". In: *Nature Geoscience* 8 (1), pp. 75–79. DOI: 10.1038/ngeo2306.

Rosa, A. D., M. Mezouar, G. Garbarino, P. Bouvier, S. Ghosh, A. Rohrbach, and C. Sanchez-Valle (2013). "Single-crystal equation of state of phase D to lower mantle pressures and the effect of hydration on the buoyancy of deep subducted slabs". In: *Journal of Geophysical Research: Solid Earth* 118 (12), pp. 6124–6133. DOI: 10.1002/2013JB010060.

Wu, X., Y. Wu, J.-F. Lin, J. Liu, Z. Mao, X. Guo, Y. Takashi, C. McCammon, V. B. Prakapenka, and Y. Xiao (2016). "Two-stage spin transition of iron in FeAl-bearing phase D at lower mantle". In: *Journal of Geophysical Research: Solid Earth* 121, 6411–6420. DOI: 10.1002/2016JB013209.

Xu, C., S. Gréaux, T. Inoue, M. Noda, W. Sun, H. Kuwahara, and Y. Higo (2020). "Sound Velocities of Al-Bearing Phase D up to 22 GPa and 1300 K". In: *Geophysical Research Letters* 47 (18), pp. 1–10. DOI: 10.1029/2020GL088877.

Yang, H., C. T. Prewitt, and D. J. Frost (1997b). "Crystal structure of the dense hydrous magnesium silicate, phase D". In: *American Mineralogist* 82 (5-6), pp. 651–654. DOI: 10.2138/am-1997-5-627.

(Eidesstattliche) Versicherungen und Erklärungen

(§ 9 Satz 2 Nr. 3 PromO BayNAT)
Hiermit versichere ich eidesstattlich, dass ich die Arbeit selbstständig verfasst und keine anderen als die von mir angegebenen Quellen und Hilfsmittel benutzt habe (vgl. Art. 64 Abs. 1 Satz 6 BayHSchG).

(§ 9 Satz 2 Nr. 3 PromO BayNAT)
Hiermit erkläre ich, dass ich die Dissertation nicht bereits zur Erlangung eines akademischen Grades eingereicht habe und dass ich nicht bereits diese oder eine gleichartige Doktorprüfung endgültig nicht bestanden habe.

(§ 9 Satz 2 Nr. 4 PromO BayNAT)
Hiermit erkläre ich, dass ich Hilfe von gewerblichen Promotionsberatern bzw. -vermittlern oder ähnlichen Dienstleistern weder bisher in Anspruch genommen habe noch künftig in Anspruch nehmen werde.

(§ 9 Satz 2 Nr. 7 PromO BayNAT)
Hiermit erkläre ich mein Einverständnis, dass die elektronische Fassung meiner Dissertation unter Wahrung meiner Urheberrechte und des Datenschutzes einer gesonderten Überprüfung unterzogen werden kann.

(§ 9 Satz 2 Nr. 8 PromO BayNAT)
Hiermit erkläre ich mein Einverständnis, dass bei Verdacht wissenschaftlichen Fehlverhaltens Ermittlungen durch universitätsinterne Organe der wissenschaftlichen Selbstkontrolle stattfinden können.

Bayreuth, 04.10.2023 .....